# The Supercontinuum Laser Source

*Fundamentals with Updated References*

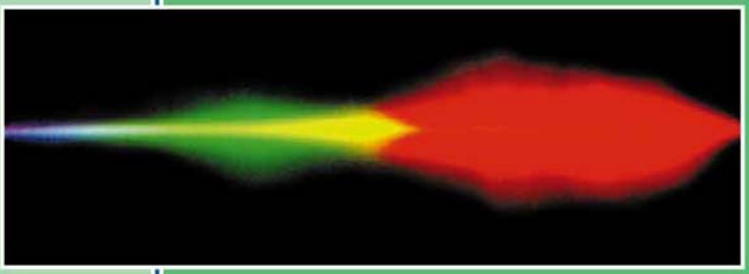

Second Edition

Robert R. Alfano
EDITOR

Springer

# The Supercontinuum Laser Source
Second Edition

Robert R. Alfano
Editor

# The Supercontinuum Laser Source

## Fundamentals with Updated References

Second Edition

With 259 Illustrations

Springer

Robert R. Alfano
Distinguished Professor of Science and Engineering
Department of Physics
City College of the City University of New York
New York, NY 10031
USA
ralfano@ccny.cuny.edu

*Cover illustration*: Shows the supercontinuum generation of intensity versus wavelength for 1 mm of carbon tetrachloride liquid excited by a 120-fs, 625-nm laser pulse. Photo by Robert R. Alfano, A. Katz, and P.P. Ho.

Library of Congress Cataloging-in-Publication Data
The supercontinuum laser source: fundamentals with updated references/[edited by]
Robert R. Alfano.
p. cm.
Includes bibliographical references and index.
ISBN 0-387-24504-9 (acid-free paper)
1. Laser pulses, Ultrashort. 2. Nonlinear optics. I. Alfano, Robert R., 1941–
QC689.5.L37S87 2005
621.36′6—dc22 2005042765

ISBN-10: 0-387-24504-9 e-ISBN 0-387-25097-2
ISBN-13: 978-0387-24504-1

Printed on acid-free paper.

© 2006, 1989 Springer Science+Business Media, Inc.
All rights reserved. This work may not be translated or copied in whole or in part without the written permission of the publisher (Springer Science+Business Media, Inc., 233 Spring Street, New York, NY 10013, USA), except for brief excerpts in connection with reviews or scholarly analysis. Use in connection with any form of information storage and retrieval, electronic adaptation, computer software, or by similar or dissimilar methodology now known or hereafter developed is forbidden.
The use in this publication of trade names, trademarks, service marks, and similar terms, even if they are not identified as such, is not to be taken as an expression of opinion as to whether or not they are subject to proprietary rights.

Printed in the United States of America. (BS/MVY)

9 8 7 6 5 4 3 2 1

springeronline.com

*To my father, Alfonso L. Alfano*
*and my father-in-law, Samuel J. Resnick*
*whose advice I deeply miss.*

# Preface to the Second Edition

The "supercontinuum" (SC) has become one of the hottest topics to study in optical and photonic sciences since the first book on the supercontinuum was published, entitled *The Supercontinuum Laser Source*, by Springer in 1989. That book, now becoming Part I in this second edition, reviewed the progress achieved on the experimental and theoretical understanding of the ultrafast nonlinear and linear processes responsible for the supercontinuum generation and related applications occurring over 20 years since its discovery by Robert R. Alfano and Stanley Shapiro in 1969.

There is a great need for a sequel part covering the recent worldwide surge of research activity on the supercontinuum phenomena and the numerous technological applications that have occurred over the past 15 years. This void will partly be covered in this new rejuvenated second edition, called Part II, by an overview of the recent advances with an updated compendium of references on the various breakthroughs to understand the supercontinuum and its new diverse applications.

The supercontinuum is the generation of intense ultrafast broadband "white-light" pulses spanning the ultraviolet to the near infrared that arises from the nonlinear interaction and propagation of ultrafast pulses focused into a transparent material. The supercontinuum can be generated in different states of matter—condensed media (liquids and solids) and gases. The supercontinuum is one of the most dramatic and elegant effects in optical physics. The conversion of one color to white-light is a startling result. This is multicolored light with many of the same desirable properties as conventional laser light: intense, collimated, and coherent. The supercontinuum has a beam divergence as good as that of the input pump laser pulse. Moreover, the coherence length of the supercontinuum is comparable with that of an incoherent white-light source from a light bulb. The interference pattern measured for the supercontinuum from a pair of filaments in water shows a constant phase relationship between the supercontinuum produced by each filament. There is a constant phase relationship between the pump laser pulse and its supercontinuum. The white-light supercontinuum is an ideal tunable ultrafast white-light laser source. Supercontinuum has overtaken the study of

other nonlinear optical effects such as second harmonic generation (SHG) and two-photon absorption for usefulness in a number of diverse applications. The supercontinuum field is still active after 36 years, and is today finding new and novel uses.

Various processes are involved in the supercontinuum generation. Whenever an intense ultrashort laser pulse propagates through a medium, it changes the refractive index from the distortion of the atomic and molecular configuration, which in turn changes the phase, amplitude, and frequency of the incident pulse. The phase change and amplitude change can cause a frequency sweep of the carrier wave within the pulse envelope and can alter the envelope and spatial distribution (self-focusing). There are various mechanisms responsible for the index of refraction change in material with intensity. The frequency broadening mechanisms are electronic cloud distortion, reorientational, librations, vibrational, and molecular redistribution, to name the major ones. The operation of these mechanisms depends on its relaxation time relevant to the laser pulse duration. The relaxation times associated with electronic distribution is of the order of Bohr orbit time ~150 as; reorientation time is ~1 ps; rocking and libration response about the field is ~1 ps; vibrational dephasing is ~0.1 ps; and molecular motion is ~1 ps. Most of these mechanisms are involved in the supercontinuum generation with 100 fs to ps laser pulses.

Soon after the supercontinuum discovery in 1969, it initially found applications in time-resolved pump-supercontinuum probe absorption and excitation spectroscopy to study the fundamental picosecond ($10^{-12}$ s) and femtosecond ($10^{-15}$ s) processes that occur in biology, chemistry, and solid-state physics. Briefly, in biology, the primary events in photosynthesis and vision were explored; in chemistry, a better understanding of the basic chemical dynamical steps in reactions and nonradiative processes in photoexcited chemicals was achieved; and in solid-state physics, the underlying kinetics of how elementary excitations behave and relax, such as optical phonons, polaritons, excitons, and carriers (electrons and holes) dynamics among the intervalleys and intravalley of semiconductors, were unraveled.

With the advent of microstructure fibers, there has been a rebirth of the supercontinuum field in the type of applications in which the supercontinuum can play a decisive role. These applications include frequency clocks, phase stabilization and control, timing, optical coherence tomography (OCT), ultrashort pulse compression, optical communication, broad spectrum LIDAR, atmospheric science, lighting control, attosecond ($10^{-18}$ s) pulse generation, and coherence control.

Over the past several years, supercontinuum generation in microstructure photonic crystal fibers by ultrashort pulse propagation has become a subject of great interest worldwide. The main reasons are the low pulse energies required to generate the supercontinuum; its coherences and high brightness makes the continuum an ideal white-light source for diverse applications; and the effects of zero dispersion and anomalous dispersion regions has resulted

in higher-order solutions generation, pulse compression, and an ultrabroadband continuum exceeding 1000 nm, extending from the ultraviolet to the infrared spectral regions.

In microstructural fibers, when pump wavelength lies in an anomalous dispersion region, it is the solitons that initiate the formation of the continuum. In a normal dispersion region, self-phase modulation is the process that initiates the continuum generation. The combination of four-wave mixing and Raman processes extends the spectral width of the continuum. In that regard, the pulse duration of an ultrafast laser determines the operational mechanisms—for 10 fs to 1000 fs laser pulses, self-phase modulation and soliton generation dominates; and for pulses >30 ps, stimulated Raman and four-wave mixing play a major role in extending the spectra. Of course, the pump wavelength location, relative to the zero dispersion wavelength and the anomalous dispersion region, plays a role in the active mechanism and coherence region of the supercontinuum. The supercontinuum spectra can span more than a two-optical octave bandwidth spread from 380 nm to 1600 nm using 200 fs pulses with energy in the tens of nanojoules. The span over an octave (i.e., 450 nm to 900 nm) is important in controlling the phase of the carrier wave inside the pulse envelope of a mode-locked pulse train. Using the $f$ and $2f$ waves in the supercontinuum, the carrier-envelope offset (CEO) phase can be detected using heterodyne beating between the high-frequency end of the supercontinuum with the doubled low end frequency of the supercontinuum in an interferometer. These phase-controlling effects are important for maintaining the accuracy of frequency combs for clocking and timing in metrology, high-intensity atomic studies, and attosecond pulse generation.

The increasing worldwide demand for large-capacity optical communication systems needs to incorporate both the wavelength and time. The ultrabroad bandwidth and ultrashort pulses of the supercontinuum may be the enabling technology to produce a cost-effective superdense wavelength division multiplexing (>1000 λ) and time multiplexing for the future Terabits/s to Pentabits/s communication systems and networks. The supercontinuum is an effective way to obtain numerous wavelength channels because it easily generates more than 1000 optical longitudinal modes while maintaining their coherency.

The propagation of ultrahigh power femtosecond pulses ~100 GW (10 mJ at 100 fs) in "air" creates the supercontinuum from the collapse of the beam by self-focusing into self-guided small-size filaments. These filament tracks in air are more or less stable over long distances of a few kilometers due to the balance between self-focusing by the nonlinear index of refraction ($n_2$) and the defocusing by the ionized plasma formation via multiphoton ionization. The supercontinuum in air can be used to monitor the amount of trace gases and biological agents in aerosols in the backscattering detection geometry for LIDAR applications. Furthermore, remote air ionization in the atmosphere by the intense femtosecond pulses in the filaments plasma (uses the supercontinuum as the onset marker) has the potential to trigger, control, and

guide lightning from one point to another and possibly even induce condensation by seeding clouds to make rain. This approach may be able to secure and protect airports and power stations from lightning and may be used to collect and store energy from lightning. Moreover, creating an ionized filament track in a desirable region may be used to confuse and redirect the pathway of incoming missiles for defense.

This new second edition will consist of two parts. The major portion (Part I) of the new book will be the reprinting of Chapters 1 to 10 from the first edition. These chapters lay down the understanding and foundation of the birth of the supercontinuum field. They go over the salient experimental and theoretical concepts in the research works produced up to 1989. The second part of this new second edition includes a new chapter (Chapter 11) highlighting the supercontinuum coherence and 10 additional chapters (Chapters 12 to 21) listing updated references of papers on the recent advances made in our understanding and applications of supercontinuum. These papers will be referenced and arranged within a topical group where a brief overview of the key features of these papers within a topic will be presented.

The following are the selected topics to be highlighted in the new Chapters 12 to 21 of updated references:

- Supercontinuum generation in materials (solids, liquids, gases, air).
- Supercontinuum generation in microstructure fibers.
- Supercontinuum in wavelength division multiplex telecommunication.
- Femtosecond pump—supercontinuum probe for applications in semiconductors, biology, and chemistry.
- Supercontinuum in optical coherence tomography.
- Supercontinuum in femtosecond carrier-envelope phase stabilization.
- Supercontinuum in ultrafast pulse compression.
- Supercontinuum in time and frequency metrology.
- Supercontinuum in atmospheric science.
- Coherence of the supercontinuum.

Special thanks to Ms. Lauren Gohara and Dr. Kestutis Sutkus for their assistance in the production of the second edition.

New York, New York — Robert R. Alfano

# Preface to the First Edition

This book deals with both ultrafast laser and nonlinear optics technologies. Over the past two decades, we have seen dramatic advances in the generation of ultrafast laser pulses and their applications to the study of phenomena in a variety of fields. It is now commonplace to produce picosecond ($10^{-12}$ s) pulses. New developments have extended this technology into the femtosecond ($10^{-15}$ s) time region. Soon pulses consisting of just a single cycle will be produced (i.e., 2 fs at 600 nm). These ultrafast pulses permit novel investigations to study phenomena in many disciplines. Sophisticated techniques based on these laser pulses have given rise to instruments with extremely high temporal resolution. Ultrafast laser technology offers the possibility of studying and discovering key processes unresolved in the past. A new era of time-resolved spectroscopy has emerged, with pulses so fast that one can now study the nonequilibrium states of matter, test quantum and light models, and explore new frontiers in science and technology. Ultrashort light pulses are a potential signal source in future high-bit-rate optical fiber communication systems. The shorter the pulses, the more can be packed into a given time interval and the higher is the data transmission rate for the tremendous bandwidth capacity of optical fiber transmission.

Nonlinear optics is an important field of science and engineering because it can generate, transmit, and control the spectrum of laser pulses in solids, liquids, gases, and fibers. One of the most important ultrafast nonlinear optical processes is the supercontinuum generation—the production of intense ultrafast broadband "white-light" pulses—that is the subject of this book.

The first study on the mechanism and generation of ultrafast supercontinuum dates back over 19 years to 1969, when Alfano and Shapiro observed the first "white" picosecond pulse continuum in liquids and solids. Spectra extended over ~6000 $cm^{-1}$ in the visible and infrared wavelength region. They attributed the large spectral broadening of ultrafast pulses to self-phase modulation (SPM) arising from an electronic mechanism and laid down the formulation of the supercontinuum generation model. Over the years, the improvement of mode-locked lasers led to the production of wider super-

continua in the visible, ultraviolet, and infrared wavelength regions using various materials.

The supercontinuum arises from the propagation of intense picosecond or shorter laser pulses through condensed or gaseous media. Various processes are responsible for continuum generation. These are called self-, induced-, and cross-phase modulations and four-photon parametric generation. Whenever an intense laser pulse propagates through a medium, it changes the refractive index, which in turn changes the phase, amplitude, and frequency of the pulse. However, when two laser pulses of different wavelengths propagate simultaneously in a condensed medium, coupled interactions (cross-phase modulation and gain) occur through the nonlinear susceptibility coefficients. These coupled interactions of two different wavelengths can introduce phase modulation, amplitude modulation, and spectral broadening in each pulse due to the other pulse using *cross-effects*.

An alternative coherent light source to the free electron laser, the supercontinuum laser source, can be wavelength selected and coded simultaneously over wide spectral ranges (up to $10{,}000\,cm^{-1}$) in the ultraviolet, visible, and infrared regions at high repetition rates, gigawatt output peak powers, and femtosecond pulse durations.

Ultrafast supercontinuum pulses have been used for time-resolved absorption spectroscopy and material characterization. Supercontinuum generation is a key step for the pulse compression technique, which is used to produce the shortest optical pulses. Future applications include signal processing, three-dimensional imaging, ranging, atmospheric remote sensing, and medical diagnosis.

Thus far, a great deal of information on supercontinuum technology has been obtained and has enhanced our understanding of how intense optical pulses propagate in materials. These developments are most often found in original research contributions and in review articles scattered in journals. Textbooks do not cover these subjects in great detail. There is a need for a book that covers the various aspects of ultrafast supercontinuum phenomena and technology.

This book reviews present and past progress on the experimental and theoretical understanding of ultrafast nonlinear processes responsible for supercontinuum generation and related effects such as pulse compression and ultrashort pulse generation on a picosecond and femtosecond time scale. The content of the chapters in the book is a mixture of both theoretical and experimental material. Overviews of the important breakthroughs and developments in the understanding of supercontinuum during the past 20 years are presented. The book is organized into 10 chapters.

Summarizing the highlights of the 10 chapters of the book:

In Chapter 1, Shen and Yang focus on the theoretical models and mechanisms behind supercontinuum generation arising mainly from self-phase modulation.

In Chapter 2, Wang, Ho, and Alfano review the experiments leading to the supercontinuum generation in condensed matter over the past 20 years.
In Chapter 3, Agrawal discusses the effects of dispersion on ultrafast light pulse propagation and supercontinuum generation in fibers.
In Chapter 4, Baldeck, Ho, and Alfano cover the latest experimental observations and applications of the cross-interactions in the frequency, time, and space domains of strong pulses on weak pulses.
In Chapter 5, Manassah reviews the theoretical models giving rise to many phenomena from self-phase and induced modulations.
In Chapter 6, Suydam highlights the effect of self-steepening of pulse profile on continuum generation.
In Chapter 7, Corkum and Rolland review the work on supercontinuum and self-focusing in gaseous media.
In Chapter 8, Glownia, Misewich, and Sorokin utilize the supercontinuum produced in gases for ultrafast spectroscopy in chemistry.
In Chapter 9, Dorsinville, Ho, Manassah, and Alfano cover the present and speculate on the possible future applications of the supercontinuum in various fields.
In Chapter 10, Johnson and Shank discuss pulse compression from the picosecond to femtosecond time domain using the continuum and optical dispersive effects of gratings, prisms, and materials.

The reader will find that these chapters review the basic principles, contain surveys of research results, and present the current thinking of experts in the supercontinuum field. The volume should be a useful source book and give young and seasoned scientists, engineers, and graduate students an opportunity to find the most necessary and relevant material on supercontinuum technology in one location.

I hope these efforts will stimulate future research on understanding the physics behind supercontinuum technology and exploring new applications.

I wish to thank all the expert contributors for their cooperation in this endeavor. Most thought it would not be completed. Special thanks goes to Mrs. Megan Gibbs for her administrative and secretarial assistance. I gratefully acknowledge T. Hiruma for his continued support. I pay particular tribute to my friend Stan Shapiro, who missed seeing the outgrowth of our first work in this field 20 years ago.

New York, New York ROBERT R. ALFANO

# Contents


Preface to the Second Edition . . . . . vii
Preface to the First Edition . . . . . xi
Contributors . . . . . xix

Part I Fundamentals

Chapter 1 Theory of Self-Phase Modulation and Spectral Broadening
Y.R. Shen and Guo-Zhen Yang . . . . . 1

Chapter 2 Supercontinuum Generation in Condensed Matter
Q.Z. Wang, P.P. Ho, and R.R. Alfano . . . . . 33

Chapter 3 Ultrashort Pulse Propagation in Nonlinear Dispersive Fibers
Govind P. Agrawal . . . . . 91

Chapter 4 Cross-Phase Modulation: A New Technique for Controlling the Spectral, Temporal, and Spatial Properties of Ultrashort Pulses
P.L. Baldeck, P.P. Ho, and R.R. Alfano . . . . . 117

Chapter 5 Simple Models of Self-Phase and Induced-Phase Modulation
Jamal T. Manassah . . . . . 184

Chapter 6 Self-Steepening of Optical Pulses
B.R. Suydam . . . . . 295

Chapter 7 Self-Focusing and Continuum Generation in Gases
Paul B. Corkum and Claude Rolland . . . . . 318

Chapter 8 Utilization of UV and IR Supercontinua in Gas-Phase Subpicosecond Kinetic Spectroscopy
J.H. Glownia, J. Misewich, and P.P. Sorokin ..... 337

Chapter 9 Applications of Supercontinuum: Present and Future
R. Dorsinville, P.P. Ho, Jamal T. Manassah, and R.R. Alfano ..... 377

Chapter 10 Pulse Compression in Single-Mode Fibers: Picoseconds to Femtoseconds
A.M. Johnson and C.V. Shank ..... 399

Part II New Developments

Chapter 11 Coherence Properties of the Supercontinuum Source
I. Zeylikovich and R.R. Alfano ..... 453

Chapter 12 Supercontinuum Generation in Materials (Solids, Liquids, Gases, Air) ..... 473
Summary ..... 473
Updated References ..... 473

Chapter 13 Supercontinuum Generation in Microstructure Fibers ..... 481
Summary ..... 481
Updated References ..... 482

Chapter 14 Supercontinuum in Wavelength Division Multiplex Telecommunication ..... 498
Summary ..... 498
Updated References ..... 498

Chapter 15 Femtosecond Pump: Supercontinuum Probe for Applications in Semiconductors, Biology, and Chemistry ..... 505
Summary ..... 505
Updated References ..... 506

Chapter 16 Supercontinuum in Optical Coherence Tomography ..... 510
Summary ..... 510
Updated References ..... 510

Chapter 17 Supercontinuum in Femtosecond Carrier-Envelope Phase Stabilization . . . . . 512
Summary . . . . . 512
Updated References . . . . . 514

Chapter 18 Supercontinuum in Ultrafast Pulse Compression . . . . 517
Summary . . . . . 517
Updated References . . . . . 517

Chapter 19 Supercontinuum in Time and Frequency Metrology . . 519
Summary . . . . . 519
Updated References . . . . . 519

Chapter 20 Supercontinuum in Atmospheric Science . . . . . 522
Summary . . . . . 522
Updated References . . . . . 522

Chapter 21 Coherence of the Supercontinuum . . . . . 524
Summary . . . . . 524
Updated References . . . . . 525

Index . . . . . 529

# Contributors

Govind P. Agrawal, Institute of Optics, University of Rochester, Rochester, New York 14627, USA

R.R. Alfano, Department of Physics, City College of the City University of New York, New York 10031, USA

P.L. Baldeck, Department of Electrical Engineering, City College of the City University of New York, New York 10031, USA

Paul B. Corkum, Division of Physics, National Research Council of Canada, Ottawa, Ontario K1A OR6, Canada

R. Dorsinville, Department of Electrical Engineering, City College of the City University of New York, New York 10031, USA

J.H. Glownia, IBM Research Division, Thomas J. Watson Research Center, Yorktown Heights, New York 10598, USA

P.P. Ho, Department of Electrical Engineering, City College of the City University of New York, New York 10031, USA

A.M. Johnson, AT&T Bell Laboratories, Holmdel, New Jersey 07733, USA

Jamal T. Manassah, Department of Electrical Engineering, City College of the City University of New York, New York 10031, USA

J. Misewich, IBM Research Division, Thomas J. Watson Research Center, Yorktown Heights, New York 10598, USA

Claude Rolland, Division of Physics, National Research Council of Canada, Ottawa, Ontario K1A OR6, Canada

C.V. Shank, AT&T Bell Laboratories, Holmdel, New Jersey 07733, USA

Y.R. Shen, Department of Physics, University of California, Berkeley, California 94720, USA

P.P. Sorokin, IBM Research Division, Thomas J. Watson Research Center, Yorktown Heights, New York 10598, USA

B.R. Suydam, Los Alamos National Laboratory, Los Alamos, New Mexico 87545, USA

Q.Z. Wang, Department of Physics, City College of the City University of New York, New York 10031, USA

Guo-Zhen Yang, Institute of Physics, Academy of Sciences, Beijing, China

I. Zeylikovich, Department of Physics, City College of the City University of New York, New York 10031, USA

# Part I
# Fundamentals

# 1
# Theory of Self-Phase Modulation and Spectral Broadening

Y.R. Shen and Guo-Zhen Yang

## 1. Introduction

Self-phase modulation refers to the phenomenon in which a laser beam propagating in a medium interacts with the medium and imposes a phase modulation on itself. It is one of those very fascinating effects discovered in the early days of nonlinear optics (Bloembergen and Lallemand, 1966; Brewer, 1967; Cheung et al., 1968; Lallemand, 1966; Jones and Stoicheff, 1964; Shimizu, 1967; Stoicheff, 1963). The physical origin of the phenomenon lies in the fact that the strong field of a laser beam is capable of inducing an appreciable intensity-dependent refractive index change in the medium. The medium then reacts back and inflicts a phase change on the incoming wave, resulting in self-phase modulation (SPM). Since a laser beam has a finite cross section, and hence a transverse intensity profile, SPM on the beam should have a transverse spatial dependence, equivalent to a distortion of the wave front. Consequently, the beam will appear to have self-diffracted. Such a self-diffraction action, resulting from SPM in space, is responsible for the well-known nonlinear optical phenomena of self-focusing and self-defocusing (Marburger, 1975; Shen, 1975). It can give rise to a multiple ring structure in the diffracted beam if the SPM is sufficiently strong (Durbin et al., 1981; Santamato and Shen, 1984). In the case of a pulsed laser input, the temporal variation of the laser intensity leads to an SPM in time. Since the time derivative of the phase of a wave is simply the angular frequency of the wave, SPM also appears as a frequency modulation. Thus, the output beam appears with a self-induced spectral broadening (Cheung et al., 1968; Gustafson et al., 1969; Shimizu, 1967).

In this chapter we are concerned mainly with SPM that leads to spectral broadening (Bloembergen and Lallemand, 1966; Brewer, 1967; Cheung et al., 1968; Lallemand, 1966; Jones and Stoicheff, 1964; Shimizu, 1967; Stoicheff, 1963). For large spectral broadening, we need a strong SPM in time (i.e., a large time derivative in the phase change). This obviously favors the use of short laser pulses. Consider, for example, a phase change of $6\pi$ occurring in $10^{-12}$ s. Such a phase modulation would yield a spectral broadening of

~100 $cm^{-1}$. In practice, with sufficiently intense femtosecond laser pulses, a spectral broadening of 20,000 $cm^{-1}$ is readily achievable by SPM in a condensed medium, which is essentially a white continuum (Alfano and Shapiro, 1970). The pulse duration of any frequency component (uncertainty limited) in the continuum is not very different from that of the input pulse (Topp and Rentzepis, 1971). This spectrally superbroadened output from SPM therefore provides a much needed light source in ultrafast spectroscopic studies—tunable femtosecond light pulses (Busch et al., 1973; Alfano and Shapiro, 1971). If the SPM and hence the frequency sweep in time on a laser pulse are known, then it is possible to send the pulse through a properly designed dispersive delay system to compensate the phase modulation and generate a compressed pulse with little phase modulation (Treacy, 1968, 1969). Such a scheme has been employed to produce the shortest light pulses ever known (Fork et al., 1987; Ippen and Shank, 1975; Nakatsuka and Grischkowsky, 1981; Nakatsuka et al., 1981; Nikolaus and Grischkowsky, 1983a, 1983b).

Self-phase modulation was first proposed by Shimizu (1967) to explain the observed spectrally broadened output from self-focusing of a *Q*-switched laser pulse in liquids with large optical Kerr constants (Bloembergen and Lallemand, 1966; Brewer, 1967; Cheung et al., 1968; Jones and Stoicheff, 1964; Lallemand, 1966; Shimizu, 1967; Stoicheff, 1963). In this case, the spectral broadening is generally of the order of a hundred reciprocal centimeters. Alfano and Shapiro (1970) showed that with picosecond laser pulses, it is possible to generate by SPM a spectrally broadened output extending over 10,000 $cm^{-1}$ in almost any transparent condensed medium. Self-focusing is believed to have played an important role in the SPM process in the latter case. In order to study the pure SPM process, one would like to keep the beam cross section constant over the entire propagation distance in the medium. This can be achieved in an optical fiber since the beam cross section of a guided wave should be constant and the self-focusing effect is often negligible. Stolin and Lin (1978) found that indeed the observed spectral broadening of a laser pulse propagating through a long fiber can be well explained by the simple SPM theory. Utilizing a well-defined SPM from an optical fiber, Grischkowsky and co-workers were then able to design a pulse compression system that could compress a laser pulse to a few hundredths of its original width (Nakatsuka and Grischkowsky, 1981; Nakatsuka et al., 1981; Nikolaus and Grischkowsky, 1983a, 1983b). With femtosecond laser pulses, a strong SPM on the pulses could be generated by simply passing the pulses through a thin film. In this case, the beam cross section is practically unchanged throughout the film, and one could again expect a pure SPM process. Fork et al. (1983) observed the generation of a white continuum by focusing an 80-fs pulse to an intensity of ~$10^{14}$ $W/cm^2$ on a 500-$\mu$m ethylene glycol film. Their results can be understood by SPM along with the self-steepening effect (Manassah et al., 1985, 1986; Yang and Shen, 1984).

Among other experiments, Corkum et al. (1985) demonstrated that SPM and spectral broadening can also occur in a medium with infrared laser pulses. More recently, Corkum et al. (1986) and Glownia et al. (1986) have independently shown that with femtosecond pulses it is even possible to generate a white continuum in gas media.

The phase modulation induced by one laser pulse can also be transferred to another pulse at a different wavelength via the induced refractive index change in a medium. A number of such experiments have been carried out by Alfano and co-workers (1986, 1987). Quantitative experiments on spectral superbroadening are generally difficult. Self-focusing often complicates the observation. Even without self-focusing, quantitative measurements of a spectrum that is generated via a nonlinear effect by a high-power laser pulse and extends from infrared to ultraviolet are not easy. Laser fluctuations could lead to large variations in the output.

The simple theory of SPM considering only the lower-order effect is quite straightforward (Gustafson et al., 1969; Shimizu, 1967). Even the more rigorous theory including the higher-order contribution is not difficult to grasp as long as the dispersive effect can be neglected (Manassah et al., 1985, 1986; Yang and Shen, 1984). Dispersion in the material response, however, could be important in SPM, and resonances in the medium would introduce pronounced resonant structure in the broadened spectrum. The SPM theory with dispersion is generally very complex; one often needs to resort to a numerical solution (Fischen and Bischel, 1975; Fisher et al., 1983). It is possible to describe the spectral broadening phenomenon as resulting from a parametric wave mixing process (in the pump depletion limit) (Bloembergen and Lallemand, 1966; Lallemand, 1966; Penzkofer, 1974; Penzkofer et al., 1973, 1975). In fact, in the studies of spectral broadening with femtosecond pulses, four-wave parametric generation of new frequency components in the phase-matched directions away from the main beam can be observed together with the spectrally broadened main beam. Unfortunately, a quantitative estimate of spectral broadening due to the parametric process is not easy. In the presence of self-focusing, more complication arises. Intermixing of SPM in space and SPM in time makes even numerical solution very difficult to manage, especially since a complete quantitative description of self-focusing is not yet available. No such attempt has ever been reported. Therefore, at present, we can only be satisfied with a qualitative, or at most a semiquantitative, description of the phenomenon (Marburger, 1975; Shen, 1975).

This chapter reviews the theory of SPM and associated spectral broadening. In the following section, we first discuss briefly the various physical mechanisms that can give rise to laser-induced refractive index changes responsible for SPM. Then in Section 3 we present the simple physical picture and theory of SPM and the associated spectral broadening. SPM in space is considered only briefly. Section 4 deals with a more rigorous theory of SPM that takes into account the higher-order effects of the induced refractive index change. Finally, in Section 5, a qualitative picture of how self-focusing can influence

and enhance SPM and spectral broadening is presented. Some semiquantitative estimates of the spectral broadening are given and compared with experiments, including the recent observations of supercontinuum generation in gases.

## 2. Optical-Field-Induced Refractive Indices

The material response to an applied laser field is often nonlinear. An explicit expression for the response is not readily available in general. Unless specified otherwise, we consider here only the case where the perturbative expansion in terms of the applied field is valid and the nonlocal response can be neglected. We can then express the induced polarization in a medium as (Shen, 1984)

$$\begin{aligned}
\mathbf{P}(t) &= \mathbf{P}^{(1)}(t) + \mathbf{P}^{(2)}(t) + \mathbf{P}^{(3)}(t) + \cdots, \\
\mathbf{P}^{(1)}(t) &= \int \chi^{(1)}(t-t') \cdot \mathbf{E}(t')dt' \\
&= \int \chi^{(1)}(\omega) \cdot \mathbf{E}(\omega)d\omega, \\
\mathbf{P}^{(n)}(t) &= \int \chi^{(n)}(t-t_1, \ldots, t-t_n) : \mathbf{E}(t_1) \ldots \mathbf{E}(t_n)dt_1 \ldots dt_n \\
&= \int \chi^{(n)}(\omega = \omega_1 + \omega_2 + \cdots + \omega_n) : \mathbf{E}(\omega_1) \ldots \mathbf{E}(\omega_n)d\omega_1 \ldots d\omega_n, \qquad (1)
\end{aligned}$$

where the applied field is

$$\mathbf{E}(t) = \int \mathbf{E}(\omega)d\omega \quad \text{with } \mathbf{E}(\omega) \propto \exp(-i\omega t) \qquad (2)$$

and the $n$th-order susceptibility is

$$\begin{aligned}
\chi^{(n)}(t-t_1, \ldots, t-t_n) = \int \chi^{(n)}(\omega = \omega_1 + \cdots + \omega_n) \exp[i\omega_1(t-t_1) \\
+ \cdots + i\omega_n(t-t_n)]d\omega_1 \ldots d\omega_n. \qquad (3)
\end{aligned}$$

We note that, strictly speaking, only for a set of monochromatic applied fields can we write

$$\mathbf{P}^{(n)} = \chi^{(n)}(\omega = \omega_1 + \cdots + \omega_n) : \mathbf{E}(\omega_1) \ldots E(\omega_n). \qquad (4)$$

In the case of instantaneous response (corresponding to a dispersionless medium), we have

$$\mathbf{P}^{(n)} = \chi^{(n)} : [E(t)]^n. \qquad (5)$$

Here, we are interested in the third-order nonlinearity that gives rise to the induced refractive index change. We consider only the self-induced refractive index change; extension to the cross-field-induced change should be straightforward. Thus we assume a pulsed quasi-monochromatic field $\mathbf{E}_w(t)$ =

$\mathscr{E}(t)\exp(-i\omega t)$. The third-order nonlinear polarization in a medium, in general, takes the form

$$\mathbf{P}_{\omega}^{(3)}(t) = \int \Delta\chi(t-t') \cdot \mathbf{E}_{\omega}(t')dt' \tag{6}$$

with $\Delta\chi(t-t') = \int\chi^{(3)}(t-t', t-t'', t-t''') : \mathbf{E}_{\omega}(t'')\mathbf{E}_{\omega}^{*}(t''')dt''\,dt'''$. If the optical field is sufficiently far from resonances that the transverse excitations are all virtual and can be considered as instantaneous, we can write

$$\begin{aligned}\mathbf{P}_{\omega}^{(3)}(t) &= \Delta\chi(t) \cdot \mathbf{E}_{\omega}(t),\\ \Delta\chi(t) &= \int \chi^{(3)}(t-t') : |\mathbf{E}_{\omega}(t')|^2 dt'.\end{aligned} \tag{7}$$

In the dispersionless limit, the latter becomes

$$\Delta\chi(t) = \chi^{(3)} : |E_{\omega}(t)|^2. \tag{8}$$

Equation (8) is a good approximation when the dispersion of $\Delta\chi$ is negligible within the bandwidth of the field. The optical-field-induced refractive index can be defined as

$$\Delta\mathbf{n} = (2\pi/n_0)\Delta\chi, \tag{9}$$

where $n_0$ is the average linear refractive index of the medium. With $\Delta n \equiv n_2|E_{\omega}|^2$, we have $n_2 = (2\pi/n_0)\chi^{(3)}$.

A number of physical mechanisms can give rise to $\Delta\chi$ or $\Delta\mathbf{n}$ (Shen, 1966). They have very different response times and different degrees of importance in different media. We discuss them separately in the following.

## 2.1 Electronic Mechanism

Classically, one can imagine that an applied optical field can distort the electronic distribution in a medium and hence induce a refractive index change. Quantum mechanically, the field can mix the electronic wave functions, shift the energy levels, and redistribute the population; all of these can contribute to the induced refractive index change. For a typical transparent liquid or solid, $n_2$ falls in the range between $10^{-13}$ and $10^{-15}$ esu. For gases at 1 atm pressure, $n_2 \sim 10^{-16}$ to $10^{-18}$ esu far away from resonances. The response time is of the order of the inverse bandwidth of the major absorption band (~$10^{-14}$ to $10^{-15}$ s in condensed media) except for the population redistribution part. As the optical frequency approaches an absorption band, $n_2$ is resonantly enhanced. In particular, when the population redistribution due to resonant excitation is significant, the enhancement of $n_2$ can be very large, but the time response will then be dominated by the relaxation of the population redistribution. In a strong laser field, saturation in population redistribution and multiphoton resonant excitations can become important. The perturbative expansion in Eq. (1) may then cease to be valid. For our discussion of SPM

in this chapter, we shall assume that the laser beam is deep in the transparent region and therefore all these electronic resonance effects on the induced refractive index are negligible.

## 2.2 Vibrational Contribution

The optical field can also mix the vibrational wave functions, shift the vibrational levels, and redistribute the populations in the vibrational levels. The corresponding induced refractive index change $\Delta n$ is, however, many orders (~5) of magnitude smaller than that from the electronic contribution because of the much weaker vibrational transitions. Therefore, the vibrational contribution to $\Delta n$ is important only for infrared laser beams close to vibrational resonances. For our discussion of SPM, we shall not consider such cases.

If the laser pulse is very short (10 fs corresponding to a bandwidth of 500 $cm^{-1}$), the vibrational contribution to $\Delta n$ can also come in via Raman excitations of modes in the few hundred $cm^{-1}$ range. The Raman transitions are also much weaker than the two-photon electronic transitions, so their contributions to the self-induced $\Delta n$ are usually not important for the discussion of SPM unless femtosecond pulses are used.

## 2.3 Rotation, Libration, and Reorientation of Molecules

Raman excitations of molecular rotations can, however, contribute effectively to $\Delta n$. This is because the rotational frequencies of molecules are usually in the few $cm^{-1}$ region except for the smaller molecules. Thus, even with a monochromatic field, one can visualize a Raman process (in which absorption and emission are at the same frequency $\omega$) that is nearly resonant. (The difference frequency of absorption and emission is zero, but it is only a few $cm^{-1}$ away from the rotational frequencies.) In condensed media, the rotational motion of molecules is, however, strongly impeded by the presence of neighboring molecules. Instead of simple rotations, the molecules may now librate in a potential well set up by the neighboring molecules. The librational frequencies determined by the potential well are often in the range of a few tens of $cm^{-1}$. The modes are usually heavily damped. Like the rotational modes, they can also contribute effectively to $\Delta n$ via the Raman process.

Molecules can also be reoriented by an optical field against rotational diffusion. This can be treated as an overdamped librational motion driven by the optical field. More explicitly, molecular reorientation arises because the field induces a dipole on each molecule and the molecules must then reorient themselves to minimize the energy of the system in the new environment.

All the above mechanisms involving rotations of molecules can contribute appreciably to $\Delta n$ if the molecules are highly anisotropic. Typically, in liquids, $n_2$ from such mechanisms falls in the range between $10^{-13}$ and $10^{-11}$ esu, with

a response time around $10^{-11}$ s for molecular reorientation and ~$10^{-13}$ s for libration. In liquid crystals, because of the correlated molecular motion, $n_2$ can be much larger, approaching 0.1 to 1, but the response time is much longer, of the order of 1 s. The rotational motion is usually frozen in solids, and therefore its contribution to $\Delta n$ in solids can be neglected.

## 2.4 Electrostriction, Molecular Redistribution, and Molecular Collisions

It is well known that the application of a dc or optical field to a local region in a medium will increase the density of the medium in that region. This is because the molecules in the medium must squeeze closer together to minimize the free energy of the system in the new environment. The effect is known as electrostriction. The induced density variation $\Delta\rho$ obeys the driven acoustic wave equation, and from $\Delta n = (\partial n/\partial\rho)\Delta\rho$ the induced refractive index change can be deduced. For liquids, we normally have $n_2 \sim 10^{-11}$ esu with a response time of the order of 100 ns across a transverse beam dimension of ~1 mm.

Molecules will also locally rearrange themselves in a field to minimize the energy of induced dipole–induced dipole interaction between molecules in the system. Whereas electrostriction yields an isotropic $\Delta n$, this molecular redistribution mechanism will lead to an anisotropic $\Delta n$. Molecular correlation and collisions could also affect molecular redistribution. A rigorous theory of molecular redistribution is therefore extremely difficult (Hellwarth, 1970). Experimentally, molecular redistribution is responsible for the anisotropic $\Delta n$ observed in liquids composed of nearly spherical molecules or atoms in cases where the electronic, electrostrictive, and rotational contributions should all be negligible. It yields an $n_2$ of the order of $10^{-13}$ esu with a response time in the subpicosecond range. In solids, the molecular motion is more or less frozen, so the contribution of molecular redistribution to $\Delta n$ is not significant.

## 2.5 Other Mechanisms

A number of other possible mechanisms can contribute to $\Delta n$. We have, for instance, laser heating, which increases the temperature of a medium and hence its refractive index; photorefraction, which comes from excitation and redistribution of charged carriers in a medium; and induced concentration variation in a mixture.

We conclude this section by noting that there is an intimate connection between third-order nonlinearities and light scattering (Hellwarth, 1977): each physical mechanism that contributes to $\Delta n$ (except the electronic mechanism) is also responsible for a certain type of light scattering. The third-order susceptibility from a given mechanism is directly proportional to the

Table 1.1.

| Physical mechanism | Magnitude of third-order nonlinearity $n_2$ (esu) | Response time $\tau$ (s) |
|---|---|---|
| Electronic contribution | $10^{-15}$–$10^{-13}$ | $10^{-14}$–$10^{-15}$ |
| Molecular reorientation | $10^{-13}$–$10^{-11}$ | ~$10^{-11}$ |
| Molecular libration and redistribution | ~$10^{-13}$ | ~$10^{-13}$ |
| Electrostriction | ~$10^{-11}$ | ~$10^{-16}$* |

* For a beam radius of ~1 mm.

scattering cross section related to the same mechanism, and the response time is inversely proportional to the linewidth of the scattering mode. Thus from the low-frequency light scattering spectrum, one can predict the value of $n_2$ for the induced refractive index. For example, in most liquids, light scattering shows a Rayleigh wing spectrum with a broad background extending to a few tens of $cm^{-1}$. This broad background is believed to arise from molecular libration, redistribution, and collisions (Febellinski, 1967), but the details have not yet been resolved. For our semiquantitative prediction of $n_2$ and the response time, however, we do not really need to know the details if the Rayleigh wing spectrum of the medium is available. A broad and strong Rayleigh wing spectrum is expected to yield a large $n_2$ with a fast response.

In Table 1.1 we summarize the results of our discussion of the various physical mechanisms contributing to $\Delta n$. It is seen that in nonabsorbing liquid, where all the mechanisms could operate, electrostriction and molecular reorientation may dominate if the laser pulses are longer than 100 ns; molecular reorientation, redistribution, and libration may dominate for pulses shorter than 100 ns and longer than 1 ps; molecular redistribution and libration and electronic contribution may dominate for femtosecond pulses. In transparent solids, usually only electrostriction and electronic contribution are important. Then for short pulses the latter is the only mechanism contributing to $\Delta n$.

## 3. Simple Theory of Self-Phase Modulation and Spectral Broadening

For our discussion of SPM of light, let us first consider the case where the propagation of a laser pulse in an isotropic medium can be described by the wave equation of a plane wave:

$$\left(\frac{\partial^2}{\partial z^2} - \frac{n_0^2}{c^2}\frac{\partial^2}{\partial t^2}\right)E = \frac{4\pi}{c^2}\frac{\partial^2}{\partial t^2}P^{(3)}, \tag{10}$$

where

$$E = \mathscr{E}(z,t)\exp(ik_0 z - i\omega_0 t),$$
$$P^{(3)} = \chi^{(3)}|E|^2 E,$$

and $n_0$ is the linear refractive index of the medium. In the simple theory of SPM (Cheung et al., 1968; Gustafson et al., 1969; Shimizu, 1967), we use the usual slowly varying amplitude approximation by neglecting the $\partial^2\mathscr{E}/\partial t^2$ term on the left and keeping only the $(4\pi/c^2)\chi^{(3)}|\mathscr{E}|^2\mathscr{E}$ term on the right of Eq. (10), which then becomes

$$\left(\frac{\partial}{\partial z} + \frac{n_0}{c}\frac{\partial}{\partial t}\right)\mathscr{E} = -\frac{4\pi\omega_0^2}{i2k_0c^2}\chi^{(3)}|\mathscr{E}|^2\mathscr{E}. \tag{11}$$

The approximation here also assumes an instantaneous response of $\chi^{(3)}$. Letting $z' \equiv z + ct/n_0$ and $\mathscr{E} = |\mathscr{E}|\exp(i\phi)$, we obtain from the above equation

$$\frac{\partial|\mathscr{E}|}{\partial z'} = 0,$$
$$\frac{\partial\phi}{\partial z'} = \frac{2\pi\omega_0^2}{c^2k_0}\chi^{(3)}|\mathscr{E}|^2. \tag{12}$$

They yield immediately the solution

$$|\mathscr{E}| = |\mathscr{E}(t)|, \tag{13a}$$

$$\phi(z,t) = \phi_0 + \frac{2\pi\omega_0^2}{c^2k_0}\chi^{(3)}|\mathscr{E}(t)|^2 z. \tag{13b}$$

Equation (13a) implies that the laser pulse propagates in the medium without any distortion of the pulse shape, while Eq. (13b) shows that the induced phase change $\Delta\phi(t) = \phi(z, t) - \phi_0$ is simply the additional phase shift experienced by the wave in its propagation from 0 to $z$ due to the presence of the induced refractive index $\Delta n = (2\pi/n_0)\chi^{(3)}|\mathscr{E}|^2$, namely $\Delta\phi = (\omega/c)\int_0^z \Delta n\, dz$. Since the frequency of the wave is $\omega = \omega_0(\partial\Delta\phi/\partial t)$, the phase modulation $\Delta\phi(t)$ leads to a frequency modulation

$$\Delta\omega(t) = -\partial(\Delta\phi)/\partial t$$
$$= -\frac{2\pi\omega_0^2}{c^2k_0}\chi^{(3)}\frac{\partial|\mathscr{E}|^2}{\partial t}z. \tag{14}$$

The spectrum of the self-phase-modulated field is, therefore, expected to be broadened. It can be calculated from the Fourier transformation

$$|E(\omega)|^2 = \left|\frac{1}{2\pi}\int_{-\infty}^{\infty}\mathscr{E}(t)e^{-i\omega_0 t + i\omega t}dt\right|^2. \tag{15}$$

An example is shown in Figure 1.1. We assume here a 4.5-ps full width at half-maximum (FWHM) Gaussian laser pulse propagating in a nonlinear medium that yields an SPM output with a maximum phase modulation of

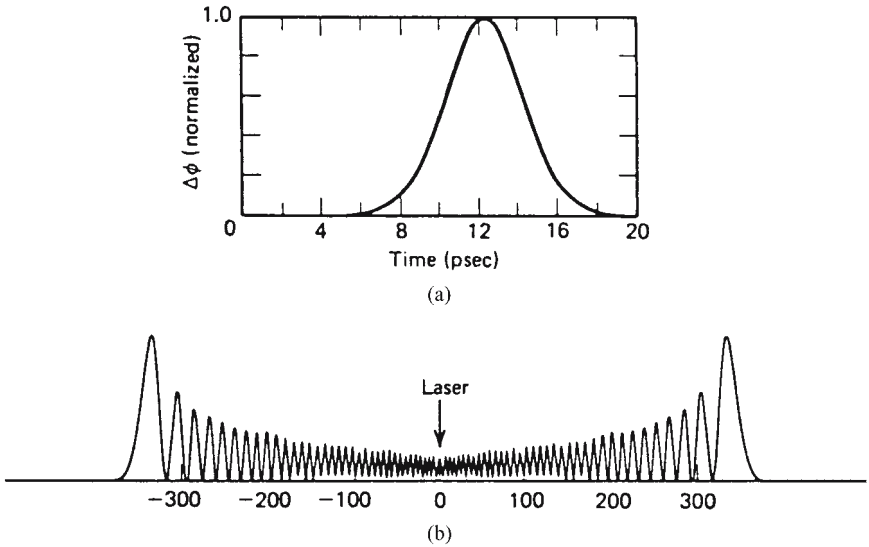


FIGURE 1.1. Theoretical power spectrum obtained by assuming an instantaneous response of $\Delta n$ to the intensity variation $|E(t)|^2$, so that the phase modulation $\Delta\phi(t)$ is proportional to $|E(t)|^2$. (a) $\Delta\phi$ versus $t$ and (b) power spectrum of the phase-modulated pulse.

$\Delta\phi_{max} \simeq 72\pi$ rad. The spectrum of the output shows a broadening of several hundred $cm^{-1}$ with a quasi-periodic oscillation. It is symmetric with respect to the incoming laser frequency because the SPM pulse is symmetric. The leading half of the $\Delta\phi$ pulse is responsible for the Stokes broadening and the lagging half for the anti-Stokes broadening. The structure of the spectrum can be understood roughly as follows. As shown in Figure 1.1, the $\Delta\phi$ curve following the laser pulse takes on a bell shape. For each point on such a curve, one can always find another point with the same slope, except, of course, the inflection points. Since $\partial\phi/\partial t = -\omega$, these two points describe radiated waves of the same frequency but different phases. These two waves will interfere with each other. They interfere constructively if the phase difference $\Delta\phi_{12}$ is an integer of $2\pi$ and destructively if $\Delta\phi_{12}$ is an odd integer of $\pi$. Such interference then gives rise to the peaks and valleys in the spectrum. The inflection points that have the largest slope on the curve naturally lead to the two outermost peaks with $|\omega_{max}| \sim |\partial\phi/\partial t|_{max}$. To find how many peaks we should expect in the spectrum, we need only to know $\phi_{max}$, as the number of pairs of constructive and destructive interferences is simply $N \sim \phi_{max}/2\pi$ on each side of the spectrum. The broadened spectrum has Stokes–anti-Stokes symmetry because $\Delta\phi(t)$ is directly proportional to $|E(t)|^2$ and is a symmetric pulse.

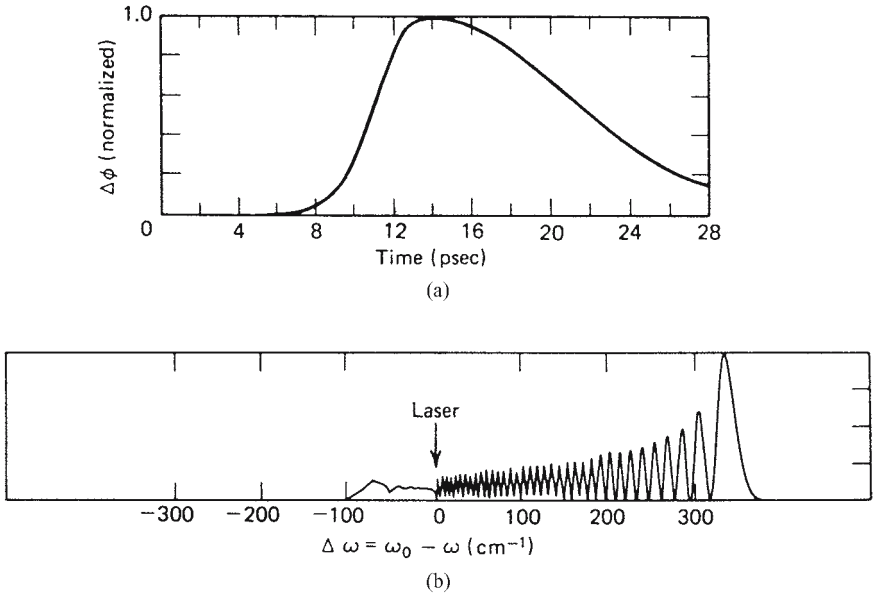


FIGURE 1.2. Theoretical power spectrum obtained by assuming a transient response of $\Delta n$ to the intensity variation $|E(t)|^2$ so that $\Delta\phi(t)$ is no longer proportional to $|E(t)|^2$. (a) $\Delta\phi$ versus $t$ and (b) power spectrum of the phase-modulated pulse.

With the above qualitative picture in mind, we can now generalize our discussion of SPM somewhat. The response of the medium to the laser pulse is generally not instantaneous. One therefore expects

$$\Delta\phi(z,t) = (\omega/c)\int_0^z \Delta n(z,t)dz,$$
$$\Delta n(z,t) = \int_{-\infty}^{z} n_2(z,t-t')|E(z,t')|^2 dt'. \tag{16}$$

Then, even if $|E(t)|^2$ is symmetric, $\Delta\phi(t)$ is asymmetric and is no longer proportional to $|E(t)|^2$. The consequence is a Stokes–anti-Stokes asymmetry. An example is given in Figure 1.2. Because of the finite response time of the medium, the leading part of the $\Delta\phi(t)$ curve always sees a larger portion of the intensity pulse $|E(t)|^2$, and therefore the Stokes side of the spectrum is always stronger. This Stokes–anti-Stokes asymmetry can be drastic if the response time becomes comparable to or smaller than the laser pulse width.

In the more rigorous theory, one should also expect a distortion of the pulse shape as the pulse propagates on in the nonlinear medium. Self-steepening of the pulse, for example, is possible and may also affect the spectral broadening (DeMartini et al., 1967; Gustafson et al., 1969; see Chapter 6). However, the above qualitative discussion still applies since the $\Delta\phi(t)$ curve should still take on an asymmetric bell shape in general.

The experimental situation is usually not as ideal as the simple theory describes. The laser beam has a finite cross section and will diffract. The transverse intensity variation also leads to a $\Delta n(\mathbf{r})$ that varies in the transverse directions. This causes self-focusing of the beam and complicates the simultaneously occurring SPM of the beam (Shen, 1975; Marburger, 1975). Moreover, stimulated light scattering could also occur simultaneously in the medium, in most cases initiated by self-focusing (Shen, 1975; Marburger, 1975). All these make the analysis of SPM extremely difficult.

One experimental case is, however, close to ideal, namely SPM of a laser pulse in an optical fiber. The transverse beam profile of a guided wave remains unchanged along the fiber. As long as the laser intensity is not too strong, self-focusing and stimulated scattering of light in the fiber can be neglected. For a sufficiently short pulse, the nonlinearity of the fiber is dominated by the electronic contribution and therefore has a nearly instantaneous response. Then if the pulse is not too short and the spectral broadening is not excessive, the slowly varying amplitude approximation is valid and $\partial^2 P^{(3)}/\partial t^2$ in the wave equation can be well approximated by $-\omega_0^2 P^{(3)}$. The only modification of the simple theory of SPM we have discussed is to take into account the fact that we now have a wave in a waveguide with a confined transverse dimension instead of an infinite plane wave in an open space. Thus the quantitative analysis can easily be worked out. Indeed, Stolen and Lin (1978) found excellent agreement between theory and experiment.

The above discussion of SPM in time can also be used to describe SPM in space. As we already mentioned, the transverse intensity variation of a laser beam can induce a spatial variation of $\Delta n$ in the transverse directions. Let us consider here, for simplicity, a continuous-wave (cw) laser beam with a Gaussian transverse profile. The phase increment $\Delta\phi(r, z)$ varying with the transverse coordinate $r$ is given by

$$\Delta\phi(r,z) = (\omega/c)\Delta n(r) z. \tag{17}$$

This leads to a distortion of the wave front. Since the beam energy should propagate along the ray path perpendicular to the wave front, this distortion of the wave front would cause the beam to self-focus. If the propagation length is sufficiently long, the beam will actually self-focus and drastically modify the beam cross section. However, if the length of the medium is much shorter than the self-focusing distance, then the self-focusing effect in the medium can be neglected and we are left with only the SPM effect on the beam. The results of Figure 1.1 can describe the spatial SPM equally well if we simply replace $t$ by $r$ and $\omega$ by $k_\perp$, where $k_\perp$ is the transverse component of the wave vector of the beam. We realize that $k_\perp$ defines the deflection angle $\theta$ of a beam by the relation $k_\perp = (\omega n_0/c)\sin\theta$. Therefore, the quasi-periodic spectrum in the $k_\perp$ space actually corresponds to a diffraction pattern with multiple bright and dark rings. This has indeed been observed experimentally (Durbin et al., 1981; Santamato and Shen, 1984). An example is shown in Figure 1.3. Self-focusing or diffraction in the medium can modify the spatial

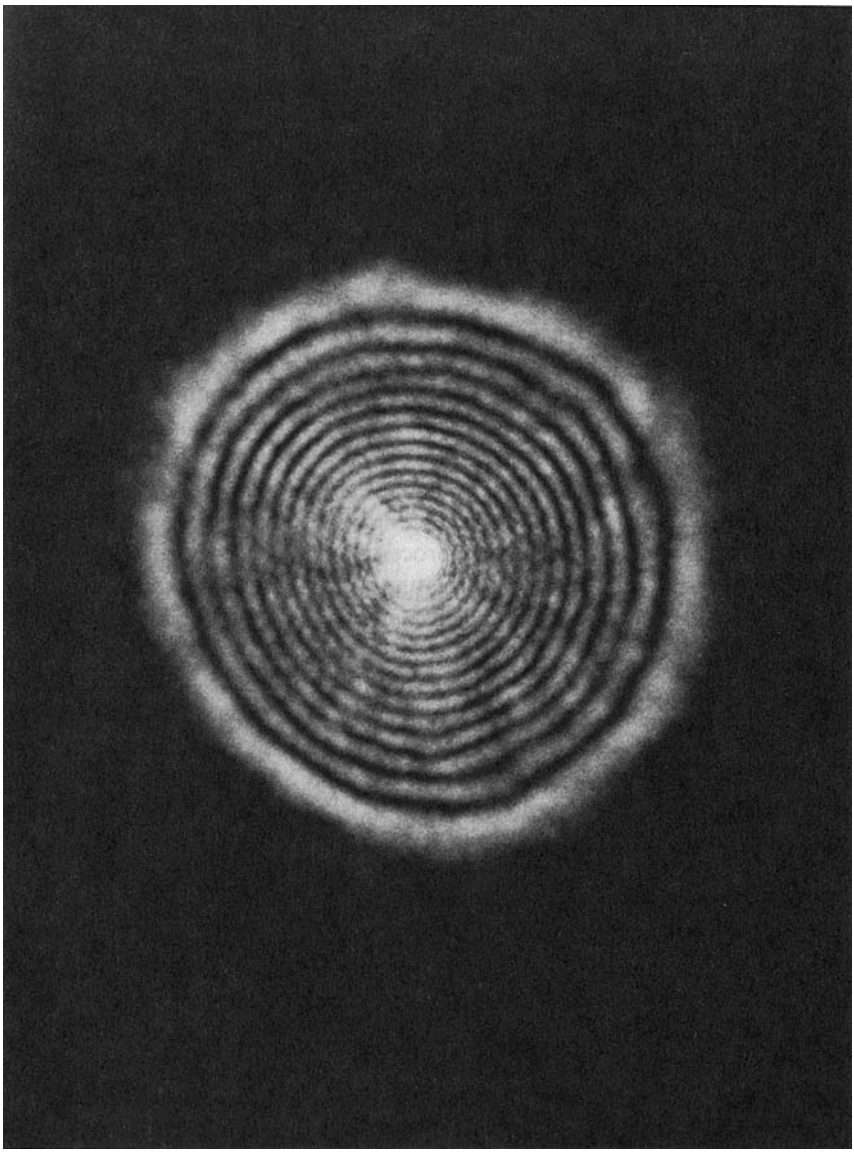

FIGURE 1.3. Diffraction ring pattern arising from spatial self-phase modulation of a CW $Ar^+$ laser beam passing through a 300-$\mu$m nematic liquid crystal film. (After Durbin et al., 1981; Santamato and Shen, 1984.)

SPM through its modification of the beam profile. This is analogous to the self-steepening effect on the temporal SPM through its modification of the pulse shape.

We now return to the discussion of temporal SPM and spectral broadening. In the next section we consider the case where the incoming laser pulse is very short and spectral broadening is very extensive so that the approximations used in the simple theory of SPM need improvement.

## 4. More Rigorous Theory of Self-Phase Modulation and Spectral Superbroadening

Another experimental case of SPM that could avoid complications arising from self-focusing, stimulated scattering, or other nonlinear optical effects involves the propagation of an ultrashort laser pulse through a thin nonlinear medium. In this case, the medium is thin enough so that the self-focusing effect on SPM in the medium can be ignored. The pulse is short enough so that the transient stimulated light-scattering processes are effectively suppressed. Yet the pulse intensity can still be so high as to induce a very strong SPM, but not high enough to result in appreciable multiphoton absorption or optical breakdown. This is the case first studied by Fork et al. (1987). Using an 80-fs pulse at 627 nm focused to an intensity of $10^{13}$ to $10^{14}$ W/cm on a 500-$\mu$m film of ethylene glycol, they observed in the output a huge spectral broadening that appears as a white continuum. Unlike the spectral broadening discussed in the previous section, the present case shows a Stokes–anti-Stokes asymmetry that emphasizes the anti-Stokes side instead. Such a spectral super-broadening was observed earlier by Alfano and Shapiro (1970) in much longer media with picosecond pulses, but SPM in those cases was definitely affected by self-focusing. Obviously, the results of Fork et al. cannot be explained by the simple theory of SPM. We must resort to a more rigorous analysis.

We first notice that the self-steepening effect on the pulse is not included in the simple theory. This means that the approximations neglecting the $\partial^2\mathscr{E}/\partial t^2$ term and the terms involving the time derivatives of $|P^{(3)}|$ in the wave equation are not quite appropriate. They become worse for shorter pulses. In the more rigorous analysis of SPM, we must improve on these approximations. Let us now go back to Eq. (10). Without any approximation, we can transform it into an equation for the field amplitude (Yang and Shen, 1984):

$$\left(\frac{\partial}{\partial z}+\frac{n_0}{c}\frac{\partial}{\partial t}\right)\mathscr{E}+\frac{1}{i2k_0}\left(\frac{\partial^2}{\partial z^2}-\frac{n_0^2}{c^2}\frac{\partial^2}{\partial t^2}\right)\mathscr{E}$$
$$=-\frac{4\pi\omega_0^2}{i2k_0c^2}\chi^{(3)}|\mathscr{E}|^2\mathscr{E}+\frac{2\pi}{ik_0c^2}\left(-i2\omega_0\frac{\partial}{\partial t}+\frac{\partial^2}{\partial t^2}\right)\chi^{(3)}|\mathscr{E}|^2\mathscr{E}. \qquad (18)$$

The last term on both sides of the equation has been neglected in the simple theory of SPM. By defining the differential operators $D_{\pm} \equiv (\partial/\partial z) \pm (n_0/c)(\partial/\partial t)$, Eq. (18) can be written as

$$D_+\mathscr{E} + \frac{1}{i2k_0} D_- D_+ \mathscr{E} = \frac{1}{i2k_0}\Pi,$$

$$\Pi = -\frac{4\pi\omega_0^2}{c^2}\left[1 + \frac{2i}{\omega_0}\frac{\partial}{\partial t} - \frac{1}{\omega_0^2}\frac{\partial^2}{\partial t^2}\right]\chi^{(3)}|\mathscr{E}|^2\mathscr{E}. \tag{19}$$

Since $D_- = -(2n_0/c)(\partial/\partial t) + D_+$, we have from Eq. (19)

$$D_+\mathscr{E} = \frac{1}{i2k_0}\left[\left(-\frac{2n_0}{c}\frac{\partial}{\partial t} + D_+\right)D_+\mathscr{E} + \Pi\right]$$

$$= \frac{1}{i2k_0}\sum_{m=0}^{\infty}\left[\left(-\frac{2n_0}{c}\frac{\partial}{\partial t} + D_+\right)\Big/ i2k_0\right]^m \Pi. \tag{20}$$

It is then simply a question of how many terms in the power series expansion we need to include to better describe the SPM.

The zeroth-order approximation corresponds to neglecting all derivatives of $\chi^{(3)}|\mathscr{E}|^2\mathscr{E}$ any yields

$$D_+\mathscr{E} = -(2\pi\omega_0^2/ic^2k_0)\chi^{(3)}|\mathscr{E}|^2\mathscr{E}, \tag{21}$$

which is identical to Eq. (11) used as the basis for the simple theory of SPM. We recognize that under this lowest-order approximation,

$$D_+\left(\chi^{(3)}|\mathscr{E}|^2\mathscr{E}\right) \propto \left(\chi^{(3)}|\mathscr{E}|^2\right)^2\mathscr{E}$$

$$\ll \chi^{(3)}|\mathscr{E}|^2\mathscr{E} \quad \text{if } \chi^{(3)}|\mathscr{E}|^2 \ll 1. \tag{22}$$

Therefore, we can use $D_+$ as an expansion parameter in the higher-order calculations. For the first-order approximation, we neglect terms involving $D_+^m(\chi^{(3)}|\mathscr{E}|^2\mathscr{E})$ with $m \geq 1$ in Eq. (20) and obtain

$$D_+\mathscr{E} = \frac{1}{i2k_0}\sum_{m=0}^{\infty}\left[\left(\frac{1}{i\omega_0}\frac{\partial}{\partial t}\right)^m \Pi\right]$$

$$= \left(1 + \frac{i}{\omega_0}\frac{\partial}{\partial t}\right)\left[-\frac{2\pi\omega_0^2}{ik_0c}\chi^{(3)}|\mathscr{E}|^2\mathscr{E}\right]. \tag{23}$$

The calculation here has in a sense used $\chi^{(3)}|\mathscr{E}|^2$ as the expansion parameter. In the above first-order approximation, we have kept the $(\chi^{(3)}|\mathscr{E}|^2)^n\mathscr{E}$ terms with $n \leq 1$ including all their time derivatives. In ordinary cases, this is a very good approximation because usually $\chi^{(3)}|\mathscr{E}|^2 \ll 1$ and therefore the higher-order terms involving $(\chi^{(3)}|\mathscr{E}|^2)^n\mathscr{E}$ with $n \geq 2$ are not very significant. For example, in the ultrashort pulse case, we have $\chi^{(3)} \sim 10^{-14}$ esu (or $n_2 \sim 10^{-13}$ esu) for a condensed medium; even if the laser pulse intensity is $I \sim 10^{14}\,\mathrm{W/cm^2}$, we find $\chi^{(3)}|\mathscr{E}|^2 \sim 4 \times 10^3 \ll 1$. For larger $\chi^{(3)}|\mathscr{E}|^2$, one may need to include

higher-order terms in the calculations. The next-order correction includes the $D_+(\chi^{(3)}|\mathscr{E}|^2\mathscr{E})$ term and all its time derivatives. They yield additional terms proportional to $(\chi^{(3)}|\mathscr{E}|^2)^2\mathscr{E}$ in the wave equation. If $\chi^{(3)}|\mathscr{E}|^2 \gtrsim 1$, then the approach with series expansion will not be useful and we have to go back to the original nonlinear wave equation (19).

In the following discussion, we consider only cases with $\chi^{(3)}|\mathscr{E}|^2 \ll 1$. We are therefore interested in the solution of Eq. (23), which, with $n_2 = (2\pi\omega_0/k_0c)\chi^{(3)}$, takes the form

$$\frac{\partial \mathscr{E}}{\partial z} + \frac{1}{c}\frac{\partial}{\partial t}\left(n_0\mathscr{E} + n_2|\mathscr{E}|^2\right) = i\frac{n_2\omega_0}{c}|\mathscr{E}|^2\mathscr{E}. \tag{24}$$

For simplicity, we now neglect the dispersion of the response of the medium. This, as we mentioned earlier, is equivalent to assuming an instantaneous response. Insertion of $\mathscr{E} = |\mathscr{E}|\exp(i\phi)$ into Eq. (24) yields two separate equations for the amplitude and phase:

$$\left[\frac{\partial}{\partial z} + \frac{n_0}{c}\left(1 + \frac{3n_2}{n_0}|\mathscr{E}|^2\right)\frac{\partial}{\partial t}\right]|\mathscr{E}| = 0, \tag{25a}$$

$$\left[\frac{\partial}{\partial z} + \frac{n_0}{c}\left(1 + \frac{n_2}{n_0}|\mathscr{E}|^2\right)\frac{\partial}{\partial t}\right]\phi = \frac{n_2\omega_0}{c}|\mathscr{E}|^2. \tag{25b}$$

In comparison with Eq. (12) for the simple theory of SPM, the only difference is the addition of the $n_2|\mathscr{E}|^2$ (= $\Delta n$) terms on the left-hand sides of Eqs. (25). Its effect is obvious in causing a pulse shape deformation during the pulse propagation. With $\Delta n > 0$, we expect a pulse steepening in the lagging edge. This is because the peak of the pulse then propagates at a lower velocity than either the leading or the lagging part of the pulse (DeMartini et al., 1967).

Let us first neglect the self-steepening effect on the amplitude pulse. Clearly, self-steepening in the lagging part of the $\phi$ pulse should lead to a spectral broadening with Stokes–anti-Stokes asymmetry emphasizing the anti-Stokes side, because it is the lagging part of the phase modulation that gives rise to the broadening on the anti-Stokes side. To be more quantitative, we assume an input laser pulse with $|\mathscr{E}(0, t)|^2 = A^2/\cosh(t/\tau)$, whose shape remains unchanged in propagating through the medium so that $|\mathscr{E}(z, t)|^2 = A^2/\cosh[(t - n_0/c)/\tau]$. The solution of Eq. (25b) can then be found analytically as

$$\phi = \omega_0\tau\left\{x - \sinh^{-1}\left[\sinh x - (n_2/c\tau)A^2 z\right]\right\} \tag{26}$$

with $x = [t - (n_0/c)z]/\tau$. The corresponding frequency modulation is given by

$$\Delta\omega/\omega_0 = \left[1 + \left(Q^2 - 2Q\sinh x\right)/\cosh x\right]^{-1/2} - 1. \tag{27}$$

Here we have defined

$$Q = n_2A^2\, z/c\tau \tag{28}$$

as a characteristic parameter for spectral broadening. For $Q \ll 1$, we have

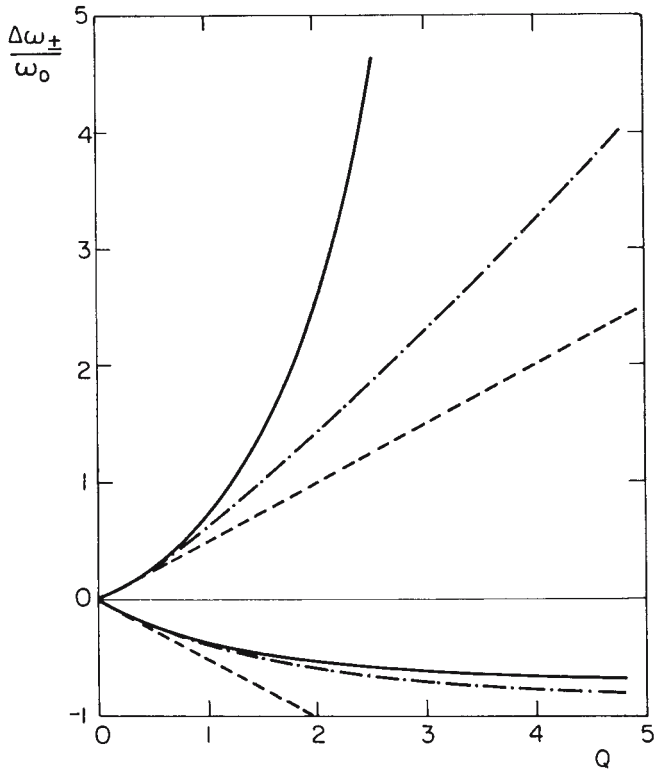


FIGURE 1.4. Maximum Stokes ($\Delta\omega_- < 0$) and anti-Stokes ($\Delta\omega_+ > 0$) shifts calculated with different models: simple theory of self-phase modulation (---); more rigorous theory without the self-steepening effect on the intensity pulse (–·–); more rigorous theory with the self-steepening effect (—). (After Yang and Shen, 1984.)

$$\Delta\omega/\omega_0 \simeq -Q\sinh x/\cosh^2 x, \tag{29}$$

which is identical to the result one would find from the simple theory of SPM. For $Q \gtrsim 1$, we expect spectral superbroadening with appreciable Stokes–anti-Stokes asymmetry and a maximum anti-Stokes shift $\Delta\omega_+ \gtrsim \omega_0$. The maximum Stokes and anti-Stokes shifts, $\Delta\omega_-$ and $\Delta\omega_+$, respectively, can be directly obtained from Eq. (27):

$$\Delta\omega_\pm/\omega_0 = \tfrac{1}{2}\left[(Q^2+4)^{1/2} \pm |Q|\right] - 1. \tag{30}$$

This is plotted in Figure 1.4 in comparison with the result calculated from the simple theory of SPM. For $|Q| \ll 1$ we have $\Delta\omega_\pm \simeq \pm(1/2)\omega_0|Q|$, and for $|Q| \gg 1$ we have $\Delta\omega_+ \simeq \omega_0|Q|$ and $\Delta\omega_- \simeq \omega_0(1/|Q| - 1)$. It is seen that Stokes broadening is always limited by $|\Delta\omega_-| < \omega_0$, as it should be.

We now include the effect of self-steepening on the amplitude pulse. It can be shown that with $|\mathscr{E}(0, t)|^2 = A^2/\cosh(t/\tau)$, the solution of Eq. (25a) must satisfy the implicit algebraic equation

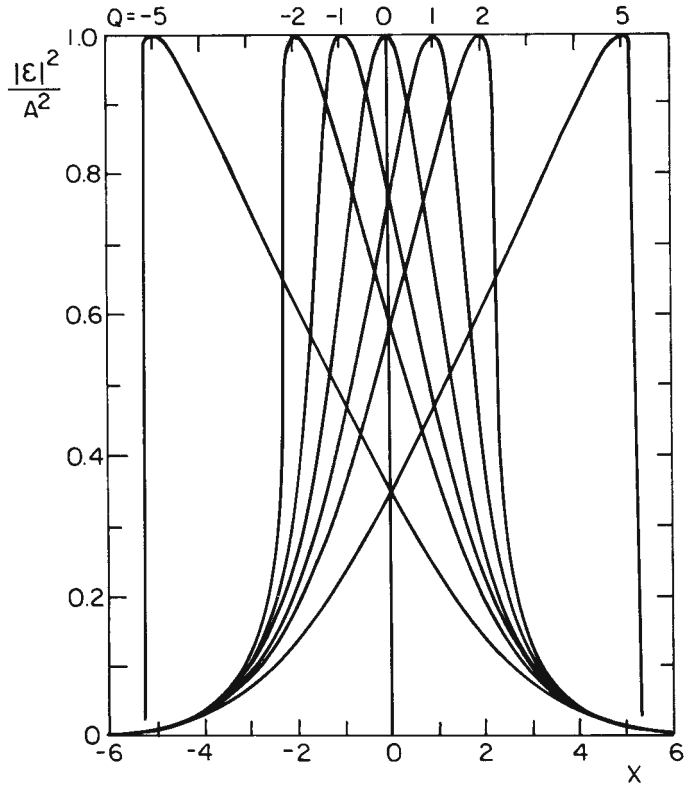


FIGURE 1.5. Self-steepening effect on the intensity pulse during its propagation in a nonlinear medium at various values of $Q = n_2 A^2 zc/\tau$, with $x = (t - n_0 z/c)/\tau$. (After Yang and Shen, 1984.)

$$|\mathscr{E}(z,t)|^2 = A^2 \Big/ \cosh\left[x - Q|\mathscr{E}(z,t)|^2 \Big/ A^2\right]. \tag{31}$$

A simple numerical calculation then allows us to find $|\mathscr{E}|^2$ as a function of $x$ for a given $Q$. The results are shown in Figure 1.5. For $|Q| \gtrsim 1$, the self-steepening effect is apparent. Knowing $|\mathscr{E}(z, t)|^2$, we can again solve for $\phi(z, t)$ from Eq. (25b) and find $\Delta\omega(z, t)$ and $\Delta\omega_{\pm}$. This can be done numerically; the results are also presented in Figure 1.4. It is seen that for $Q > 1$, self-steepening of the pulse amplitude has increased the spectral broadening on the anti-Stokes side quite significantly. The additional spectral broadening comes in because the steepening of the amplitude pulse enhances the steepening of the $\phi$ pulse.

The spectral broadening actually results from frequency chirping since $\partial\phi(t)/\partial t = -\omega(t)$. This is shown in Figure 1.6 for the numerical example discussed above. As expected, the Stokes and anti-Stokes shifts appear, respectively, in the leading and lagging parts of the self-steepened pulse. The $\Delta\omega = 0$ point appears at larger $x$ for larger values of $Q$ because self-steepening shifts the peak of the pulse to larger $x$ (see Figure 1.5).

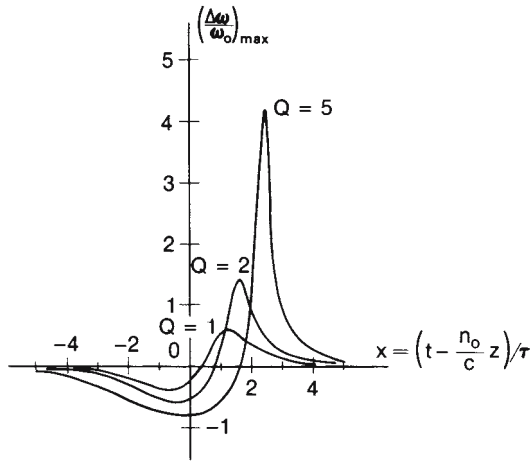


FIGURE 1.6. Frequency shift due to phase modulation as a function of $x = (t - n_0 z/c)/\tau$ at various value of $Q = n_2 A^2 zc/\tau$.

We can compare the calculation with the experiment of Fork et al. In their experiment, the relevant parameters are $n_2 \simeq 10^{-13}$ esu, $z = 0.05$ cm, $I \sim 10^{14}$ W/cm$^2$, and $\tau$ (pulse width) $\simeq 8 \times 10^{-14}$ s. The corresponding value of $Q$ is about 2.3. They observed a Stokes broadening $\Delta\omega_-/\omega_0 \simeq -0.6$ and an anti-Stokes broadening $\Delta\omega_+/\omega_0 \simeq 2.3$. Our calculation gives $\Delta\omega_-/\omega_0 \simeq -0.54$ and $\Delta\omega_+/\omega_0 \simeq 3.5$. Considering the uncertainty in the experimental parameters, we can regard the agreement between theory and experiment as reasonable.

Manassah et al. (1985, 1986) used the method of multiple scales to solve Eq. (18) (neglecting dispersion). They also took $n_2|\mathscr{E}|^2/n_0$ as the expansion parameter in their series expansion and therefore necessarily obtained the same results as we discussed above.*

We have neglected in the above calculation the dispersion of the medium response. Normal dispersion may also reshape the pulse (Fisher and Bischel, 1975; Fisher et al., 1983), but in the present case the length of the medium is so short that this effect is not likely to be important. Anomalous dispersion with resonances in $\chi^{(3)}$ or $n_2$ could, however, give rise to resonant structure in the broadened spectrum. The calculation including the dispersion of $\chi^{(3)}$ is much more complicated and, in general, must resort to numerical solution (Fisher and Bischel, 1975; Fisher et al., 1983). In obtaining the time-dependent solution of the wave equation with the third-order nonlinearity, we have already taken all the four-wave mixing contributions into account. By adding a noise term with a blackbody spectrum in the nonlinear wave equation, the four-wave parametric generation process proposed by Penzkofer et al. (1973, 1975) could also be inclued in the calculation.

* A factor of 3 in front of $n_2$ is mistakenly left out in Eq. (3a) of Yang and Shen (1984).

# 5. Self-Focusing and Self-Phase Modulation

For pulsed laser beam propagation in a nonlinear medium, SPM in time and SPM in space necessarily appear together. SPM in time causes self-steepening of the pulse, which in turn enhances SPM in time. Similarly, SPM in the transverse beam profile causes self-focusing of the beam, which in turn enhances the transverse SPM. If the propagation distance in the medium is sufficiently long, these effects can build up to a catastrophic stage, namely self-steepening to a shock front and self-focusing to a spot limited in dimensions only by higher-order nonlinear processes and diffraction. SPM in time and SPM in space are then tightly coupled and strongly influenced by each other. In many experiments, the observed strong temporal SPM and extensive spectral broadening are actually initiated by self-focusing. In such cases, the input laser pulse is so weak that without self-focusing in the nonlinear medium, SPM would not be very significant. Self-focusing to a limiting diameter greatly enhances the beam intensity, and hence SPM can appear several orders of magnitude stronger. A quantitative description of such cases is unfortunately very difficult, mainly because the quantitative theory for self-focusing is not yet available. We must therefore restrict ourselves to a more qualitative discussion of the problem.

## 5.1 Self-Phase Modulation with Quasi-Steady-State Self-Focusing

In the early experiments on self-focusing of single-mode nanosecond laser pulses, it was found that the output of the self-focused light had a spectral broadening of several hundred $cm^{-1}$ (Shen, 1975; Marburger, 1975). This was rather surprising because from the simple theory of SPM, picosecond pulses would be needed to create such a spectral broadening (Cheung et al., 1968; Gustafson et al., 1969; Shimizu, 1967). Later, the observation was explained by SPM of light trailing behind a moving focus (Shen and Loy, 1971; Wong and Shen, 1972). We briefly review the picture here and then use it to interpret the recently observed SPM and spectral superbroadening of ultrashort pulses in gases (Corkum et al., 1986; Glownia et al., 1986).

Figure 1.7 depicts the quasi-steady-state self-focusing of a laser pulse leading to a moving focus along the axis ($\hat{z}$) with a U-shaped trajectory described by the equation (Shen, 1975; Marburger, 1975)

$$z_f(t) = \frac{K}{\sqrt{P(t_R)} - \sqrt{P_0}}, \tag{32}$$

where $P_0$ is the critical power for self-focusing, $\sqrt{P(t_R)}$ is the laser power at the retarded time $t_R = t - z_f n_0/c$, and $K$ is a constant that can be determined from experiment. This equation assumes instantaneous response of $\Delta n$ to the applied field, which is a good approximation as long as the response time $\tau$ is much shorter than the laser pulse width. Here, we are interested only in the

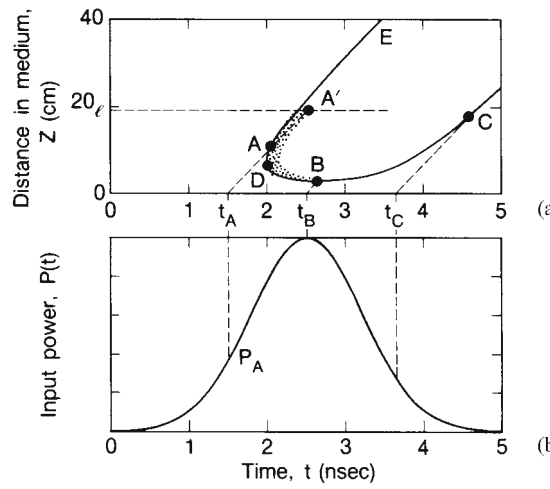


FIGURE 1.7. Self-focusing for an input laser pulse in (a) leading to the trajectory of a moving focus in the form of U curve in (b). The dashed lines in (b), with slope equal to the light velocity, depict how light propagates in the medium along the $z$ axis at various times. The shaded region around the U curve has appreciably larger $\Delta n$. Light traversing the medium along the dashed lines through the shaded region should acquire a phase increment $\Delta\phi$ that varies with time.

upper branch of the U curve, along which the focus has a forward velocity faster than light. Because of the high laser intensity in the focal spot, the locally induced $\Delta n$ should be appreciable and should last for a duration not shorter than the relaxation time $\tau$. Thus one can imagine that the moving focus creates in the medium a channel of $\Delta n$ at least $\tau\, dz_f/dt$ long trailing after the focus. Consider now the defocused light from a local focal spot. Since it lags behind the moving focus (which travels faster than light), it experiences the $\Delta n$ dielectric channel created by the focus over a certain distance and will diffract only weakly. In other words, the defocused light from the focus is partially trapped in the $\Delta n$ channel. This partial trapping of light in turn helps to maintain the $\Delta n$ channel and make it last longer. The emission from the focal spot at the end of the medium then takes the form of an asymmetric pulse (with a pulse width of the order of a few $\tau$) with a longer trailing edge.

The above picture is also illustrated in Figure 1.7. We use the shaded area around the U curve to denote the region with appreciable $\Delta n$. The laser input at $t_A$ focuses at $A$, but defocuses more gradually because of the existing $\Delta n$ channel in front of it. The partially trapped light then propagates along the axis from $A$ to the end of the medium at $A'$, crossing the shaded region with appreciable $\Delta n$. It therefore acquires a significant phase increment $\Delta\phi$. From the figure, one may visualize that $\Delta\phi$ can be strongly phase modulated in time, varying from nearly zero to a maximum and back to zero in a few relaxation times. This could yield appreciable spectral broadening in the output of the self-focused light.

To be more quantitative, we realize that the light pulse emitted from a focus in the medium must be asymmetric and must have a pulse width of several $\tau$. The shaded area in Figure 1.7 has a somewhat larger width since $\Delta n$ is induced by the focused light. Knowing the trajectory of the moving focus,

the beam intensity in the focal region, and how $\Delta n$ responds to the intensity, we can calculate $\Delta\phi(t)$ and hence $\Delta\omega(t)$ and the broadened spectrum (Shen and Loy, 1971; Wong and Shen, 1972). As an example, consider the case of a 1.2-ns laser pulse propagating into a 22.5-cm $CS_2$ cell. The trajectory of the moving focus (focal diameter $\simeq 5\,\mu$m) is described by Eq. (32) with $K = 5.7\,(\mathrm{kW})^{1/2}$-cm and $P_0 = 8\,\mathrm{kW}$. In this case, $\Delta n$ is dominated by molecular reorientation; it obeys the dynamic equation

$$\left(\frac{\partial}{\partial t}+\frac{1}{\tau}\right)\Delta n = \frac{n_2}{\tau}|E(z,t)|^2. \tag{33}$$

For $CS_2$, $\tau = 2\,\mathrm{ps}$ and $n_2 = 10^{-11}$ esu. The phase increment experienced by light waves traversing the cell along the axis is given by

$$\Delta\phi = \int_0^l (\omega/c)\Delta n[z, t' = t-(l-z)n_0/c]dz, \tag{34}$$

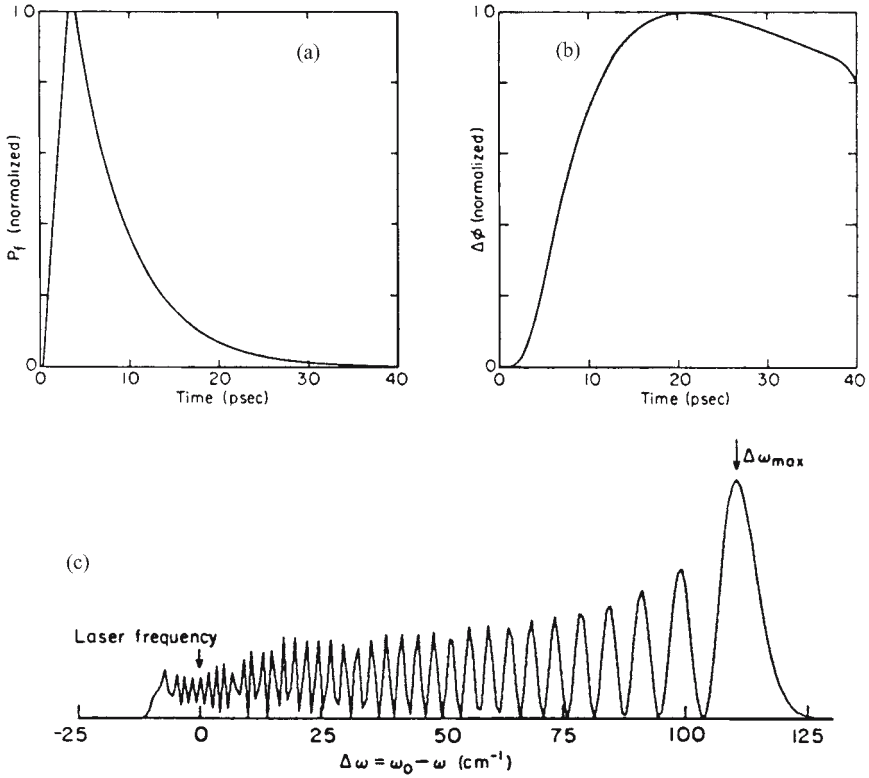


FIGURE 1.8. Theoretical power spectrum of a light pulse emitted from the focal region of a moving focus at the end of a $CS_2$ cell. (a) The intensity pulse; (b) $\Delta\phi$ versus $t$; (c) the power spectrum (see text for details). (After Shen and Loy, 1971; Wong and Shen, 1972.)

where $l$ is the cell length. (For this illustrative example, we have neglected the diffraction effect on $\Delta\phi$.) We now simply assume that $|E(z, t)|^2$ in the focal region resulting from self-focusing has a pulse width of $\sim 3\tau$ and a pulse shape as shown in Figure 1.8a. Equations (33) and (34) then allow us to find $\Delta n(z, t)$ and $\Delta\phi(t)$. Knowing $\Delta\phi(t)$ and $E(l, t)$, we can then calculate the spectrum of the output from the focal spot at the end of the cell, as shown in Figure 1.8c. The experimentally observed spectrum has in fact the predicted spectral broadening (Shen and Loy, 1971; Wong and Shen, 1972), but it often has a strong central peak (Figure 1.9). This is presumably because in the

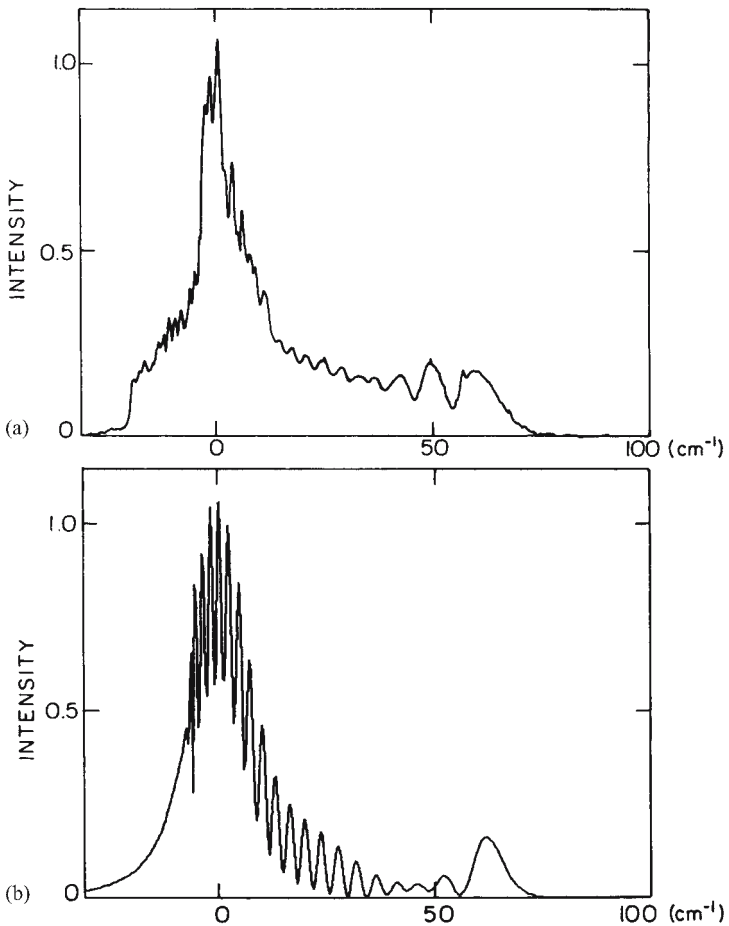


FIGURE 1.9. (a) Experimentally observed power spectrum of light emitted from the focal region at the end of a 10-cm $CS_2$ cell; the input pulse has a pulse width of 1.2 ns and a peak power of 27 kW. (b) Theoretical power spectrum using the moving focus model. (After Shen and Loy, 1971; Wong and Shen, 1972.)

calculation we have neglected a significant portion of the beam that self-focuses from the periphery and experiences little phase modulation. For shorter input pulses of longer cells, self-focusing of the beam toward the end of the cell is more gradual; accordingly, the weakly phase-modulated part is less and the central peak in the spectrum is reduced. We also note that in Figures 1.8 and 1.9 the anti-Stokes broadening is much weaker. This is because the negatively phase-modulated part of the pulse has little intensity, as seen in Figure 1.8.

Using the picture sketched in Figure 1.7, we can actually predict the Stokes broadening with the correct order of magnitude by the following rough estimate. We approximate the upper branch of the U curve toward the end of the medium by a straight line with a slope equal to the end velocity of the moving focus. If $\Delta n$ is the induced refractive index in the shaded area, then the phase modulation of the emitted light is given by

$$\Delta\phi(t) \simeq \left(\frac{\omega_0}{c}\right)\left(\frac{n_0}{c} - \frac{1}{v}\right)^{-1} \int_{t_0}^{t} \Delta n(l, t')dt', \tag{35}$$

where $l$ is the length of the medium and $t_0$ is the time when $\Delta n(l, t)$ starts to become appreciable. The extent of Stokes broadening is readily obtained from

$$\Delta\omega_{-} = (\partial\Delta\phi/\partial t)_{\max} \simeq \omega_0 Q \tag{36}$$

with $Q = \Delta n_{\max} l_{\text{eff}}/cT$ where $T \sim 2\tau$ and $l_{\text{eff}} = T/[(n_0/c) - (1/v)]$. For the above example with $CS_2$, we have $\Delta n_{\max} \sim 10^{-3}$, $T \sim 4\,\text{ps}$, $l_{\text{eff}} \sim 1\,\text{cm}$, and $Q \sim 0.01$. The resultant Stokes broadening should be $\Delta\omega_{-} \sim 150\,\text{cm}^{-1}$. The experimentally observed broadening is about $120\,\text{cm}^{-1}$.

## 5.2 Spectral Superbroadening of Ultrashort Pulses in Gases

The above discussion can be used to explain qualitatively the recently observed spectral superbroadening of ultrashort pulses in gas media (Corkum et al., 1986; Glownia et al., 1986). In those experiments, picosecond or femtosecond laser pulses with energies of several hundred microjoules were weakly focused into a high-pressure gas cell. Spectral superbroadening with $\Delta\omega \sim 10^4\,\text{cm}^{-1}$ was observed. A few examples are shown in Figure 1.10. Self-focusing was apparently present in the experiment. We therefore use the above simple model for SPM with quasi-steady-state self-focusing to estimate the spectral broadening (Loy and Shen, 1973), assuming that $\Delta n$ from the electronic contribution in the medium has a response time $\tau \sim 10\,\text{fs}$. In this case, the position of the moving focus is given by (Shen, 1975; Marburger, 1975)

$$\left(z_f^{-1}(t) - f^{-1}\right)^{-1} = \frac{K}{\sqrt{P(t_R)} - \sqrt{P_0}} \tag{37}$$

instead of Eq. (32), where $f$ is the focal length of the external focusing lens. Let us consider, for example, external focusing of a 250-$\mu J$, 100-fs pulse to a

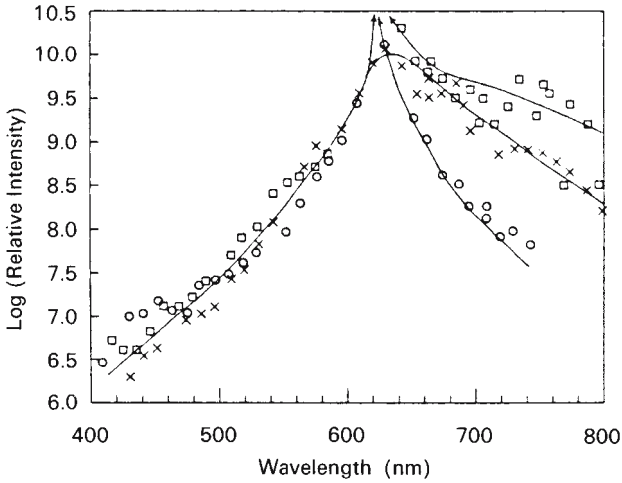


FIGURE 1.10. Continuum spectra of self-phase-modulated light from 70-fs pulses in 30-atm xenon (crosses), 2-ps pulses in 15-atm xenon (circles), and 2-ps pulses in 40-atm nitrogen (squares). The cell length is 90 cm. (After Corkum et al., 1986.)

nominally 100-$\mu$m focal spot in a 3-atm, 100-cm Xe cell. Self-focusing yields a smaller focus, assumed to be 50 $\mu$m. We then use the values $n_2 \sim 10^{-16}$ esu, $I \sim 10^{14}\,\mathrm{W/cm^2}$, $\Delta n_{\max} \sim 4 \times 10^{-5}$, $l_{\mathrm{eff}} \sim 10\,\mathrm{cm}$, and $T \sim 2\tau \sim 20\,\mathrm{fs}$; we find $Q \sim 1$ and hence $\Delta\omega_- \sim 10^4\,\mathrm{cm^{-1}}$. The above estimate is admittedly very crude because of uncertainties in the experimental parameters, but it does give a spectral superbroadening in order-of-magnitude agreement with the experiments.

Appreciable anti-Stokes broadening was also observed in the super-broadened spectrum of the SPM light from a gas medium. This seems to be characteristically different from what we have concluded from the discussion in the previous subsection. However, we realize that in the present case the moving focus terminates at $z = f$ instead of the end of the cell, and the total transmitted light is detected and spectrally analyzed. Thus the detected output pulse has essentially the same intensity envelope as the input pulse if we neglect the self-steepening effect, and the negatively phase-modulated part (the trailing edge) of the $\Delta\phi(t)$ pulse will overlap with the major part of the intensity pulse. Consequently, the spectral intensity of the anti-Stokes side should be nearly as strong as that of the Stokes side. The extent of the anti-Stokes broadening is expected to be somewhat less than that of the Stokes broadening because of the longer trailing edge of the $\Delta\phi$ pulse, unless the self-steepening effect becomes important.

Self-focusing in a gas medium should be more gradual than in a liquid cell. With weak external focusing, the focal dimensions resulting from combined external and self-focusing may not be very different from those resulting from external focusing alone. Thus, even with self-focusing, the SPM output from

the gas medium may not have a much larger diffraction angle than the linearly transmitted output, as was observed in the experiments.

## 5.3 Self-Phase Modulation with Transient Self-Focusing

We have used the picture of a moving focus with a trailing dielectric channel to describe SPM initiated by quasi-steady-state self-focusing. For shorter input pulses, the velocity of the forward moving focal spot is closer to the light velocity, and consequently more light is expected to be trapped in the dielectric channel for a longer distance. In fact, when the pulse width is comparable to or shorter than the relaxation time $\tau$, the entire self-focusing process becomes transient, and the input pulse will evolve into a dynamic trapping state (Loy and Shen, 1973).

The dynamic trapping model for transient self-focusing is an extension of the moving focus model for quasi-steady-state self-focusing. Consider the case where $\Delta n$ is governed by Eq. (33) or, more explicitly,

$$\Delta n(z,\xi) = \frac{1}{\tau}\int_{-\infty}^{\xi} n_2 |E(z,\xi')|^2 \exp[-(\xi-\xi')/\tau]\, d\xi', \tag{38}$$

where $\xi = t - zn_0/c$. Because of this transient response of $\Delta n$, the later part of the pulse propagating in the medium may see a larger $\Delta n$ than the earlier part. As a result, different parts of the pulse will propagate in the medium differently, as sketched in Figure 1.11 (Loy and Shen, 1973). The transient $\Delta n$ makes the very leading edge of the pulse diffract, the middle part self-focus weakly, and the lagging part self-focus to a limiting diameter. The result is that in

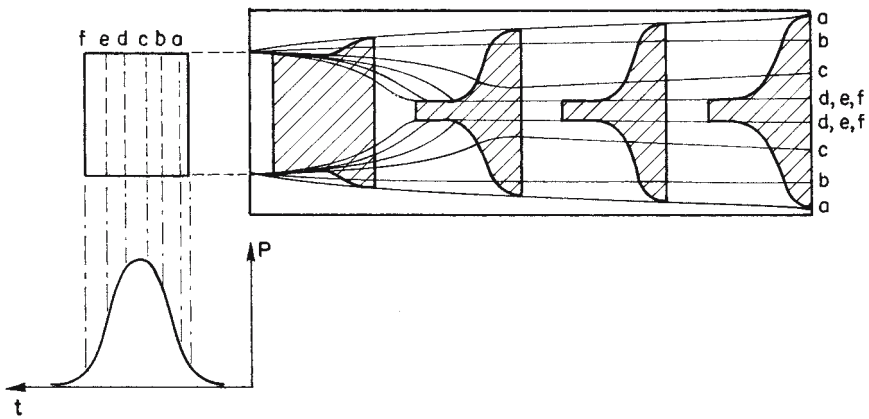


FIGURE 1.11. Sketch showing self-focusing of an ultrashort pulse in a medium with a transient response of $\Delta n$. Different parts (a, b, c, etc.) of the pulse focus and defocus along different ray paths. The pulse is first deformed into a horn shape and then propagates on without much further change. (After Loy and Shen, 1973.)

propagating through the medium, the pulse is first deformed into a horn-shaped pulse and then the horn-shaped pulse propagates on with only a slight change of the pulse shape due to diffraction of the front edge. In a long medium, the front-edge diffraction finally could blow up the deformed pulse. Note that this picture comes in because in transient self-focusing, both focusing and diffraction are much more gradual, leading to a long longitudinal focal dimension and hence the rather stable horn-shaped propagating pulse. Such a stable form of self-focused pulse propagation is known as dynamic trapping.

Since the various parts of the light pulse see different $\Delta n$'s along their paths, the phase increments $\Delta\phi$ they acquire are also different. This means phase modulation and hence spectral broadening. As an approximation, we can assume that the overall phase modulation is dominated by that of a stable horn-shaped pulse propagating in the nonlinear medium over a finite length $l_{\text{eff}}$. For illustration, let us take an example in which the horn-shaped pulse can be described by

$$|E(r,\xi)|^2 = A_0^2 \exp\left[-\xi^2 t_p^2 - 2r^2/r_0^2(\xi)\right] \tag{39}$$

with

$$\begin{aligned} r_0(\xi)/a &= 1 && \text{if } \xi \le \xi_1 \\ &= (1-\Delta)e^{-(\xi-\xi_1)/\tau_1} + \Delta && \text{if } \xi_1 \le \xi \le \xi_2 \\ &= (1-\Delta)e^{-(\xi_2-\xi_1)/\tau_1} + \Delta && \text{if } \xi \ge \xi_2, \end{aligned}$$

where $\xi = t - zn_0/c$. We have picosecond pulse propagation in Kerr liquids in mind and therefore choose $t_p = 1.25\tau$, $\xi_1 = 2.5\tau$, $\xi_2 = 2\tau$, $\tau_1 = \tau$, $\Delta = 0.05$, and $\tau = 2\,\text{ps}$ (for $CS_2$). We also choose the pulse intensity as $A_0^2 = 80(n_2/n_0)k^2a^2$, where $k$ is the wave vector and the effective pulse propagation distance $l_{\text{eff}} = 0.15\,ka^2$. From the three-dimensional wave equation, it can be shown that the phase modulation obeys the equation

$$\partial(\Delta\phi)/\partial z = k(\Delta n/n_0) - 2/kr_0^2(\xi). \tag{40}$$

The second term on the right of the equation is the diffractive contribution to $\Delta\phi$, which can be appreciable when $r_0$ is small. Knowing $|E(r, \xi)|^2$, we can find $\Delta n(z, \xi)$ from Eq. (38), and hence $\Delta\phi(z, \xi)$ from Eq. (40), and finally the broadened spectrum from $|E(r, \xi)|^2$, and $\Delta\phi(z, \xi)$ for $z = l_{\text{eff}}$, as shown in Figure 1.12.

The main qualitative result of the above calculation is that the spectrum has the quasi-periodic structure with nearly equal Stokes and anti-Stokes broadening, although the Stokes side is more intense. This agrees with the experimental observation (Cubbedu and Zagara, 1971; Cubbedu et al., 1971) and the more detailed numerical calculation of Shimizu and Courtens (1973). The reason is as follows. The Stokes–anti-Stokes symmetry results from a symmetric $\Delta\phi(t)$ pulse that overlaps well with the intensity pulse. The neck portion of the horn-shaped pulse with $\partial(\Delta\phi)/\partial t < 0$ contributes to the anti-Stokes broadening. As seen in Eq. (40), the time dependence of $\Delta\phi$ comes

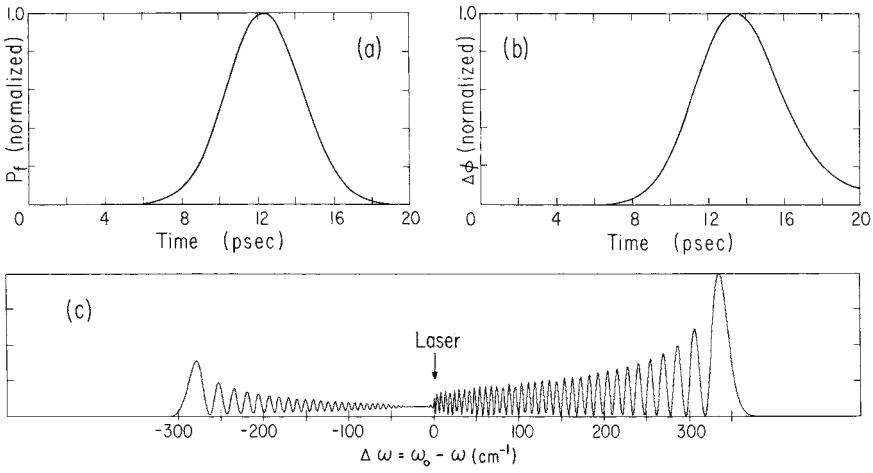


FIGURE 1.12. Theoretical power spectrum obtained by assuming a horn-shaped pulse propagating for a certain distance in a nonlinear medium without any change in its shape. (a) Normalized intensity output pulse; (b) $\Delta\phi$ versus $t$; (c) power spectrum of the output. (After Loy and Shen, 1973.)

solely from the time dependence in $(\Delta n/n_0 - 2/k^2 r_0^2)$. Without the diffraction term $(-1/k^2 r_0^2)$, the $\Delta\phi$ pulse would have a longer trailing edge because of the relaxation of $\Delta n$. With the diffraction term, the rapid reduction of $r_0$ toward the neck makes the $\Delta\phi$ pulse more symmetric. Thus it appears that the dynamic trapping model explains fairly well the qualitative features of SPM and spectral broadening initiated by transient self-focusing. The broadening is more extensive with more intense input pulses and longer propagation lengths. In a long medium, dynamic trapping may exist only over a limit section of the medium. In that case, the spectrally broadened light may seem to have originated from a source inside the medium. This has also been observed experimentally (Ho et al., 1987).

## 6. Conclusion

We have seen that the temporal SPM and the concomitant spectral broadening of light arise because an intense optical field can induce an appreciable refractive index change $\Delta n$ in a medium. The theory of pure SPM is, in principle, quite straightforward. If the input pulse intensity is not very strong, the zeroth-order approximation taking into account only the direct contribution of $\Delta n$ to the induced phase change $\Delta\phi$ should already give a fairly good description. The next-order approximation including the self-steepening effect on both $\Delta\phi$ and the amplitude pulse should satisfactorily cover the cases of strong SPM with spectral superbroadening.

Unfortunately, the temporal SPM is often complicated by the spatial SPM. The latter can lead to self-focusing, which dramatically alters the intensity distributions of the laser pulse in space and time and therefore drastically modifies the temporal SPM. In fact, in most practical cases, self-focusing occurs long before the temporal SPM becomes appreciable; it is actually self-focusing that increases the beam intensity in the medium and thus initiates a strong SPM in time. Only by using an optical waveguide or a very thin nonlinear medium can self-focusing be avoided. These are then the only experimental cases where a pure temporal SPM has been realized.

In the pure SPM case, the theoretical difficulty is in the description of $\Delta n$: it is not easy, in general, to predict quantitatively the nonlinear response of a medium from first principles; one must rely on experimental measurements. Quantitative measurements of $\Delta n(t)$ in the picosecond and femtosecond domains are still rare. In particular, measurements of $\Delta n$ with femtosecond time resolution are still rather difficult. The various low-frequency resonances could make the time dependence of $\Delta n$ very complex. Inclusion of the transient response of $\Delta n$ (or the dispersion of $\Delta n$) in the theory complicates the calculation; one may have to resort to numerical solution of the problem. Experimentally, SPM of laser pulses in optical fibers has been well studied; SPM of ultrashort pulses in thin nonlinear media is, however, still not well documented. More careful quantitative measurements are needed in order to have a more detailed comparison with theory.

With self-focusing, the theory of SPM becomes extremely complex. The main difficulty lies in the fact that a quantitative theory capable of describing the details of self-focusing is not yet available. We must then rely on the more qualitative physical pictures for self-focusing. Therefore, the discussion of the subsequently induced SPM can be at most semiquantitative. Thus, we find it quite satisfying that the predicted spectral broadening from such theoretical discussions can give order-of-magnitude agreement with the experimental observations in a number of very different cases: nanosecond pulse propagation in liquids to pico- or femtosecond pulse propagation in gases.

Spectral superbroadening is often observed with the propagation of ultrashort pulses in condensed media and is apparently initiated by self-focusing. In most cases, the details of the self-focusing process have not been measured; in some cases, even the quantitative information on $\Delta n$ is not available. The measurements on spectral broadening also tend to show strong fluctuations. All these made even an order-of-magnitude comparison between theory and experiment rather difficult.

A complete theory of SPM with self-focusing requires the solution of a time-dependent three-dimensional wave equation. With self-focusing modifying the laser pulse rapidly in both space and time, such a solution, even on the largest computer, is a formidable task. In our opinion, the best way to tackle the problem is to try to simplify the calculation by reasonable approximations derived from the physical picture that has already been established for self-focusing.

*Acknowledgment*. This work was supported by the Director, Office of Energy Research, Office of Basic Energy Sciences, Materials Sciences Division of the U.S. Department of Energy under Contract No. DE-AC03-76SF00098.

## References

Alfano, R.R. and S.L. Shapiro (1970) Emission in the region 4000–7000 A via four-photon coupling in glass; Observation of self-phase modulation and small scale filaments in crystals and glasses; Direct distortion of electronic clouds of rare-gas atoms in intense electric fields. Phys. Rev. Lett. **24**, 584, 592, 1219.

Alfano, R.R. and S.L. Shapiro (1971) Picosecond spectroscopy using the inverse Raman effect. Chem. Phys. Lett. **8**, 631.

Alfano, R.R., Q. Li, T. Jimbo, J.T. Manassah, and P.P. Ho (1986) Induced spectral broadening of a weak picosecond pulse in glass produced by an intense picosecond pulse. Opt. Lett. **11**, 626.

Alfano, R.R., Q. Wang, T. Jimbo, and P.P. Ho (1987) Induced spectral broadening about a second harmonic generated by an intense primary ultrashort laser pulse in ZuSe. Phys. Rev. A **35**, 459.

Bloembergen N. and P. Lallemand (1966) Complex intensity-dependent index of refraction, frequency broadening of stimulated Raman lines, and stimulated Rayleigh scattering. Phys. Rev. Lett. **16**, 81.

Brewer, R.G. (1967) Frequency shifts in self-focusing light. Phys. Rev. Lett. **19**, 8.

Busch, G.E., R.P. Jones, and P.M. Rentzepis (1973) Picosecond spectroscopy using a picosecond continuum. Chem. Phys. Lett. **18**, 178.

Cheung, A.C., D.M. Rank, R.Y. Chiao, and C.H. Townes (1968) Phase modulation of Q-switched laser beams in small-scale filaments. Phys. Rev. Lett. **20**, 786.

Corkum, P.B., P.P. Ho, R.R. Alfano, and J.T. Manassah (1985) Generation of infrared supercontinuum covering 3–14 $\mu$m in dielectrics and semiconductors. Opt. Lett. **10**, 624.

Corkum, P.B., C. Rolland, and T. Rao (1986) Supercontinuum generation in gases. Phys. Rev. Lett. **57**, 2268.

Cubbedu, R. and F. Zagara (1971) Nonlinear refractive index of $CS_2$ in small-scale filaments. Opt. Commun. **3**, 310.

Cubbedu, R., R. Polloni, C.A. Sacchi, O. Svelto, and F. Zagara (1971) Study of small-scale filaments of light in $CS_2$ under picosecond excitation. Phys. Rev. Lett. **26**, 1009.

DeMartini, F., C.H. Townes, T.K. Gustafson, and P.L. Kelley (1967) Self-steepening of light pulses. Phys. Rev. **164**, 312.

Durbin, S.D., S.M. Arakelian, and Y.R. Shen (1981) Laser-induced diffraction rings from a nematic liquid crystal film. Opt. Lett. **6**, 411.

Fabellinski, I.L. (1967) *Molecular Scattering of Light*. Plenum, New York, Chapter VIII.

Fisher, R.A. and W. Bischel (1975) Numerical studies of the interplay between self-phase modulation and dispersion for intense plane-wave light pulses. J. App. Phys. **46**, 4921.

Fisher, R.A., B. Suydam, and D. Yevich (1983) Optical phase conjugation for time domain undoing of dispersive self-phase modulation effects. Opt. Lett. **8**, 611.

Fork, R.L., C.V. Shank, C. Hirliman, and R. Yen (1983) Femtosecond white-light continuum pulses. Opt. Lett. **8**, 1.

Fork, R.L., C.H. Brito Cruz, P.C. Becker, and C.V. Shank (1987). Compression of optical pulses to six femtoseconds by using cubic phase compensation. Opt. Lett. **12**, 483.

Glownia, J., G. Arjavalingam, P. Sorokin, and J. Rothenberg (1986) Amplification of 350-fs pulses in XeCl excimer gain modules. Opt. Lett. **11**, 79.

Gustafson, T.K., J.P. Taran, H.A. Haus, J.R. Lifsitz, and P.L. Kelley (1969) Self-phase modulation, self steepening, and spectral development of light in small-scale trapped filaments. Phys. Rev. **177**, 306.

Hellwarth, R.W. (1970) Theory of molecular light scattering spectra using the linear-dipole approximation. J. Chem. Phys. **52**, 2128.

Hellwarth, R.W. (1977) Third-order optical susceptibilities of liquids and solids. Prog. Quantum Electron. **5**, 1.

Ho, P.P., Q.X. Li, T. Jimbo, Y.L. Ku, and R.R. Alfano (1987) Supercontinuum pulse generation and propagation in a liquid $CCl_4$. Appl. Opt. **26**, 2700.

Ippen, E.P. and C.V. Shank (1975) Dynamic spectroscopy and subpicosecond pulse compression. Appl. Phys. Lett. **27**, 488.

Jones, W.J. and B.P. Stoicheff (1964) Induced absorption at optical frequencies. Phys. Rev. Lett. **13**, 657.

Lallemand, P. (1996) Temperature variation of the width of stimulated Raman lines in liquids. Appl. Phys. Lett. **8**, 276.

Loy, M.M.T. and Y.R. Shen (1973) Study of self-focusing and small-scale filaments of light in nonlinear media. IEEE J. Quantum Electron. **QE-9**, 409.

Manassah, J.T., R.R. Shapiro, and M. Mustafa (1985) Spectral distribution of an ultrashort supercontinuum laser source. Phys. Lett. **A107**, 305.

Manassah, J.T., M.A. Mustafa, R.R. Alfano, and P.P. Ho (1986) Spectral extent and pulse shape of the supercontinuum for ultrashort laser pulse. IEEE J. Quantum Electron. **QE-22**, 197.

Marburger, J.H. (1975) Self-focusing: theory. Prog. Quantum Electron. **4**, 35.

Nakatsuka, H. and D. Grischkowsky (1981) Recompression of optical pulses broadened by passage through optical fibers. Opt. Lett. **6**, 13.

Nakatsuka, H., D. Grischkowsky, and A.C. Balant (1981) Nonlinear picosecond pulse propagation through optical fibers with positive group velocity dispersion. Phys. Rev. Lett. **47**, 910.

Nikolaus, B. and D. Grischkowsky (1983a) 12× pulse compression using optical fibers. Appl. Phys. Lett. **42**, 1.

Nikolaus, B. and D. Grischkowsky (1983b) 90-fs tunable optical pulses obtained by two-state pulse compression. Appl. Phys. Lett. **43**, 228.

Penzkofer, A. (1974) Parametrically generated spectra and optical breakdown in $H_2O$ and NaCl. Opt. Commun. **11**, 265.

Penzkofer, A., A. Laubereau, and W. Kaiser (1973) Stimulated short-wave radiation due to single-frequency resonances of $\chi^{(3)}$. Phys. Rev. Lett. **31**, 863.

Penzkofer, A., A. Seilmeier, and W. Kaiser (1975) Parametric four-photon generation of picosecond light at high conversion efficiency. Opt. Commun. **14**, 363.

Santamato, E. and Y.R. Shen (1984) Field curvature effect on the diffraction ring pattern of a laser beam dressed by spatial self-phase modulation in a nematic film. Opt. Lett. **9**, 564.

Shen, Y.R. (1966) Electrostriction, optical Kerr effect, and self-focusing of laser beams. Phys. Lett., **20**, 378.

Shen Y.R. (1975) Self-focusing: experimental. Prog. Quantum Electron. **4**, 1.

Shen, Y.R. (1984) *The Principles of Nonlinear Optics*. Wiley, New York, Chapters 1 and 16.

Shen, Y.R. and M.M.T. Loy (1971) Theoretical investigation of small-scale filaments of light originating from moving focal spots. Phys. Rev. A **3**, 2099.

Shimizu, F. (1967) Frequency broadening in liquids by a short light pulse. Phys. Rev. Lett. **19**, 1097.

Shimizu, F. and E. Courtens (1973) Recent results on self-focusing and trapping. In *Fundamental and Applied Laser Physics*, M.S. Feld, A. Javan, and N.A. Kurnit, eds. Wiley, New York, p. 67.

Stoicheff, B.P. (1963) Characteristics of stimulated Raman radiation generated by coherent light. Phys. Lett. **7**, 186.

Stolen, R. and C. Lin (1978) Self-phase modulation in silica optical fibers. Phys. Rev. A **17**, 1448.

Topp, M.R. and P.M. Rentzepis (1971) Time-resolved absorption spectroscopy in the $10^{-12}$-sec range. J. Appl. Phys. **42**, 3415.

Treacy, E.P. (1968) Compression of picosecond light pulses. Phys. Lett. **28A**, 34.

Treacy, E.P. (1969a) Measurements of picosecond pulse substructure using compression techniques. Appl. Phys. Lett. **14**, 112.

Treacy, E.P. (1969b) Optical pulse compression with diffraction gratings. IEEE J. Quantum Electron. **5**, 454.

Wong, G.K.L. and Y.R. Shen (1972) Study of spectral broadening in a filament of light. Appl. Phys. Lett. **21**, 163.

Yang, G. and Y.R. Shen (1984) Spectral broadening of ultrashort pulses in a nonlinear medium. Opt. Lett. **9**, 510.

# 2
# Supercontinuum Generation in Condensed Matter

Q.Z. Wang, P.P. Ho, and R.R. Alfano

## 1. Introduction

Supercontinuum generation, the production of intense ultrafast broadband "white light" pulses, arises from the propagation of intense picosecond or shorter laser pulses through condensed or gaseous media. Various processes are responsible for continuum generation. These are called self-, induced-, and cross-phase modulations and four-photon parametric generation. Whenever an intense laser pulse propagates through a medium, it changes the refractive index, which in turn changes the phase, amplitude, and frequency of the incident laser pulse. A phase change can cause a frequency sweep within the pulse envelope. This process has been called *self-phase modulation* (*SPM*) (Alfano and Shapiro, 1970a). Nondegenerate *four-photon parametric generation* (*FPPG*) usually occurs simultaneously with the SPM process (Alfano and Shapiro, 1970a). Photons at the laser frequency parametrically generate photons to be emitted at Stokes and anti-Stokes frequencies in an angular pattern due to the required phase-matching condition. When a coherent vibrational mode is excited by a laser, stimulated Raman scattering (SRS) occurs. SRS is an important process that competes and couples with SPM. The interference between SRS and SPM causes a change in the emission spectrum resulting in *stimulated Raman scattering cross-phase modulation* (*SRS-XPM*) (Gersten et al., 1980). A process similar to SRS-XPM occurs when an intense laser pulse propagates through a medium possessing a large second-order $\chi^2$ and third-order $\chi^3$ susceptibility. Both second harmonic generation (SHG) and SPM occur and can be coupled together. The interference between SHG and SPM alters the emission spectrum and is called *second harmonic generation cross-phase modulation* (*SHG-XPM*) (Alfano et al., 1987). A process closely related to XPM, called *induced phase modulation* (*IPM*) (Alfano, 1986), occurs when a weak pulse at a different frequency propagates through a disrupted medium whose index of refraction is changed by an intense laser pulse. The phase of the weak optical field can be modulated by the time variation of the index of refraction originating from the primary intense pulse.

Table 2.1. Brief history of experimental continuum generation.

| Investigator | Year | Material | Laser wavelength/ pulsewidth | Spectrum | Frequency ($cm^{-1}$) | Process |
|---|---|---|---|---|---|---|
| Alfano, Shapiro | 1968–1973 | Liquids and solids | 530 nm/ 8 ps or 1060 nm/ 8 ps | Visible and near IR | 6,000 | SPM |
| Stolen et al. | 1974–1976 | Fibers | 530 nm/ns | Visible | 500 | SPM |
| Shank, Fork et al. | 1983 | Glycerol | 620 nm/100 fs | UV, visible, near IR | 10,000 | SPM |
| Corkum, Ho, Alfano | 1985 | Semiconductors dielectrics | 10 $\mu$m/6 ps | IR | 1,000 | SPM |
| Corkum, Sorokin | 1986 | Gases | 600 nm/2 ps 300 nm/0.5 ps | Visible and UV | 5,000 | SPM |
| Alfano, Ho, Manassah, Jimbo | 1986 | Glass | 1,060 nm/ 530 nm/8 ps | Visible | 1,000 | IPM (XPM) |
| Alfano, Ho, Wang, Jimbo | 1986 | ZnSe | 1,060 nm/8 ps | Visible | 1,000 | SHG-XPM (ISB) |
| Alfano, Ho, Baldeck | 1987 | Fibers | 530 nm/30 ps | Visible | 1,000 | SRS-XPM |

The first study of the generation and mechanisms of the ultrafast supercontinuum dates back to the years 1968 to 1972, when Alfano and Shapiro first observed the "white" picosecond continuum in liquids and solids (Alfano and Shapiro, 1970a). Spectra extending over ~6000 $cm^{-1}$ in the visible and infrared wavelength region were observed. Over the years, improvements in the generation of ultrashort pulses from mode-locked lasers led to the production of wider supercontinua in the visible, ultraviolet, and infrared wavelength regions using various materials. Table 2.1 highlights the major accomplishments in this field over the past 20 years.

In this chapter we focus on the picosecond supercontinuum generation in liquids, solids, and crystals. Supercontinuum generation in gases, XPM, and IPM are discussed by Corkum and Rolland (Chapter 7), Glownia et al. (Chapter 8), Baldeck et al. (Chapter 4), Agrawal (Chapter 3), and Manassah (Chapter 5), respectively.

## 2. Simplified Model

Before we go further, let us first examine the nonlinear wave equation to describe the self-phase modulation mechanism. A thorough theoretical study of supercontinuum generation has been dealt with in Chapters 1, 3, and 5.

The optical electromagnetic field of a supercontinuum pulse satisfies Maxwell's equations:

$$\begin{aligned} \nabla \times \mathbf{E} &= -\frac{1}{c}\frac{\partial \mathbf{B}}{\partial t}, \\ \nabla \times \mathbf{H} &= \frac{1}{c}\frac{\partial \mathbf{D}}{\partial t} + \frac{4\pi}{c}\mathbf{J}, \\ \nabla \cdot \mathbf{D} &= 4\pi\rho, \\ \nabla \cdot \mathbf{B} &= 0. \end{aligned} \tag{1}$$

Equations (1) can be reduced to (see Appendix)

$$\frac{\partial A}{\partial z} + \frac{1}{v_g}\frac{\partial A}{\partial t} = i\frac{\omega_0 n_2}{2c}|A|^2 A, \tag{2}$$

where $A(z, t)$ is the complex envelope of the electric field and $v_g = 1/(\partial k/\partial\omega)_{\omega_0}$ is the group velocity. The total refractive index $n$ is defined by $n^2 = n_0^2 + 2n_0 n_2 |A(t)|^2$, where $n_2$ is the key parameter called the nonlinear refractive index. This coefficient is responsible for a host of nonlinear effects: self- and cross-phase modulation, self-focusing, and the optical Kerr effect, to name the important effects. Equation (2) was derived using the following approximations: (1) linearly polarized electric field, (2) homogeneous radial fields, (3) slowly varying envelope, (4) isotropic and nonmagnetic medium, (5) negligible Raman effect, (6) frequency-independent nonlinear susceptibility $\chi^{(3)}$, and (7) neglect of group velocity dispersion, absorption, self-steepening, and self-frequency shift.

Denoting by $a$ and $\alpha$ the amplitude and phase of the electric field envelope $A = ae^{i\alpha}$, Eq. (2) reduces to

$$\frac{\partial a}{\partial z} + \frac{1}{v_g}\frac{\partial a}{\partial t} = 0 \tag{3a}$$

and

$$\frac{\partial \alpha}{\partial z} + \frac{1}{v_g}\frac{\partial \alpha}{\partial t} = \frac{\omega_0 n_2}{2c}a^2. \tag{3b}$$

The analytical solutions for the amplitude and phase are

$$a(\tau) = a_0 F(\tau) \tag{4a}$$

and

$$\alpha(z,\tau) = \frac{\omega_0 n_2}{2c}\int_0^z a^2 dz' = \frac{\omega_0 n_2}{2c}a_0^2 F^2(\tau) z, \tag{4b}$$

where $a_0$ is the amplitude, $F(\tau)$ the pulse envelope, and $\tau$ the local time $\tau = t - z/v_g$. For materials whose response time is slower than pure electronic but faster than molecular orientation (i.e., coupled electronic, molecular

redistribution, libratory motion) the envelope is just the optical pulse shape. For a "pure" electronic response, the envelope should also include the optical cycles in the pulse shape.

The electric field envelope solution of Eq. (2) is given by

$$A(z,\tau) = a(\tau)\exp\left[i\frac{\omega_0 n_2}{2c}a_0^2 F^2(\tau)z\right]. \tag{5}$$

The main physics behind the supercontinuum generation by self-phase modulation is contained in Eq. (5) and is displayed in Figure 2.1. As shown in Figure 2.1a, the index change becomes time dependent and, therefore, the phase of a pulse propagating in a distorted medium becomes time dependent, resulting in self-phase modulation. The electric field frequency is continuously shifted (Figure 2.1c) in time. This process is most important in the generation of femtosecond pulses (see Chapter 10 by Johnson and Shank).

Since the pulse duration is much larger than the optical period $2\pi/\omega_0$ (slowly varying approximation), the electric field at each position $\tau$ within the

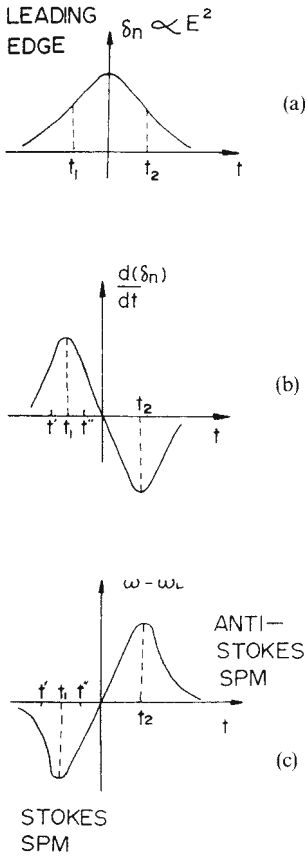


FIGURE 2.1. A simple mechanism for SPM for a non-linear index following the envelope of a symmetrical laser pulse: (a) time-dependent nonlinear index change; (b) time rate of change of index change; (c) time distribution of SPM-shifted frequencies $\omega(t) - \omega_0$.

pulse has a specific *local* and *instantaneous frequency* at given time that is given by

$$\omega(\tau) = \omega_0 + \delta\omega(\tau), \tag{6a}$$

where

$$\delta\omega(\tau) = -\frac{\partial\alpha}{\partial\tau} = -\frac{\omega_0}{2c} n_2 a_0^2 z \frac{\partial F^2(\tau)}{\partial\tau}. \tag{6b}$$

The $\delta\omega(\tau)$ is the frequency shift generated at a particular time location $\tau$ within the pulse shape. This frequency shift is proportional to the derivative of the pulse envelope, which corresponds to the generation of new frequencies resulting in wider spectra.

Pulses shorter than the excitation pulse can be produced at given frequencies. It was suggested by Y.R. Shen many years ago that Alfano and Shapiro in 1970 most likely produced femtosecond pulses via supercontinuum generation. Figure 2.1c shows the frequency distribution within the pulse shape. The leading edge, the pulse peak, and the trailing edge are red shifted, nonshifted, and blue shifted, respectively.

The spectrum of SPM pulses is obtained by taking the Fourier transform of the complex temporal envelope $A(z, \tau)$:

$$A(\Omega) = \frac{1}{2\pi}\int_{-\infty}^{\infty} A(z,\tau)\exp[i\Omega\tau]d\tau, \tag{7}$$

where $\Omega = \omega - \omega_0$. The intensity spectrum is given by

$$S(\Omega z) = \frac{c}{4\pi}|A(\Omega, z)|^2. \tag{8}$$

In practical cases, the phase of $A(z, \tau)$ is large compare with $\pi$, and the stationary phase method leads to

$$\Delta\omega(z)_{\max} = \frac{\omega_0}{2c} n_2 a_0^2 \left[ \left.\frac{\partial F^2}{\partial\tau}\right|_{\tau_1} - \left.\frac{\partial F^2}{\partial\tau}\right|_{\tau_2} \right] z. \tag{9}$$

The intensity

$$\begin{aligned} S(\Omega, z) = \left(\frac{c}{4\pi}\right)\left(\frac{4\pi c}{\omega_0 n_2 z}\right)\Bigg\{ & F^2(\tau') \Big/ \left.\frac{\partial F^2}{\partial\tau^2}\right|_{\tau'} + F^2(\tau'') \Big/ \left.\frac{\partial^2 F^2}{\partial\tau^2}\right|_{\tau''} \\ & + 2\frac{F(\tau')F(\tau'')}{\left[\partial^2 F^2/\partial\tau^2|_{\tau'}\,\partial^2 F^2/\partial\tau^2|_{\tau''}\right]^{1/2}} \\ & \times\cos\left[\Omega(\tau'-\tau'') + \frac{\omega_0}{2c} n_2 a_0^2 z\left(F^2(\tau') - F^2(\tau'')\right)\right]\Bigg\}, \end{aligned} \tag{10}$$

where $\Delta\omega_{\max}$ is the maximum frequency spread, $\tau_1$ and $\tau_2$ are the pulse envelope inflection points, and $\tau'$ and $\tau''$ are the points of the pulse shape that have the same frequency.

An estimate of the modulation frequency $\delta\omega_M$ can be made by calculating the maximum number of interference minima and dividing this number into the maximum frequency broadening. A straightforward calculation leads to

$$\delta\omega_M \approx 2\pi \left.\frac{\partial F^2}{\partial \tau}\right|_{\tau_1} / F^2(\tau_1) \approx 2\pi \left.\frac{\partial F^2}{\partial \tau}\right|_{\tau_2} / F^2(\tau_2). \tag{11}$$

For a Gaussian laser pulse given by

$$F(\tau) = \exp[-\tau^2/2\tau_0^2], \tag{12}$$

the modulation frequency of the SPM spectrum is (Alfano, 1972)

$$\delta\omega_M = \frac{4\pi}{\tau_0} \quad \text{or} \quad \delta\bar{\nu}_M = \frac{2}{\tau_0 c}. \tag{13}$$

Using this relation, the average modulation period of $13\,\text{cm}^{-1}$ corresponds to an initial pulse duration of 5 ps emitted from mode-locked Nd : glass laser. The maximum frequency extent in this case is (Alfano, 1972)

$$\Delta\omega_{\max} \approx \frac{\omega_0 n_2 a_0^2 z}{c\tau_0}. \tag{14}$$

The maximum frequency shift (Eq. (14)) indicates the following salient points:

- The frequency extent is inversely proportional to the pumping pulse duration. The shorter the incoming pulse, the greater the frequency extent. The first white light band supercontinuum pulses were generated using picosecond laser pulses (Alfano and Shapiro, 1970a,b).
- The spectral broadening is proportional to $n_2$. The supercontinuum generation can be enhanced by increasing the nonlinear refractive index. This is discussed in detail in Section 6.
- The spectral broadening is linearly proportional to amplitude $a_0^2$. Therefore, multiple-excitation laser beams of different wavelengths mat be used to increase the supercontinuum generation. This leads to the basic principle behind IPM and XPM. These processes are described by Baldeck et al. (Chapter 4) and Manassah (Chapter 5).
- The spectral broadening is proportional to $\omega_0$ and $z$.

The chirp—the temporal distribution of frequency in the pulse shape—is an important characteristic of SPM broadened pulse. In the linear chirp approximation, the chirp coefficient $C$ is usually defined by the phase relation

$$\alpha = C\tau^2. \tag{15}$$

For a Gaussian electric field envelope and linear approximation, the envelope reduces to

$$F^2(\tau) = \exp[-\tau^2/\tau_0^2] \approx 1 - \tau^2/\tau_0^2. \tag{16}$$

The linear chirp coefficient derived from Eqs. (5) and (16) becomes

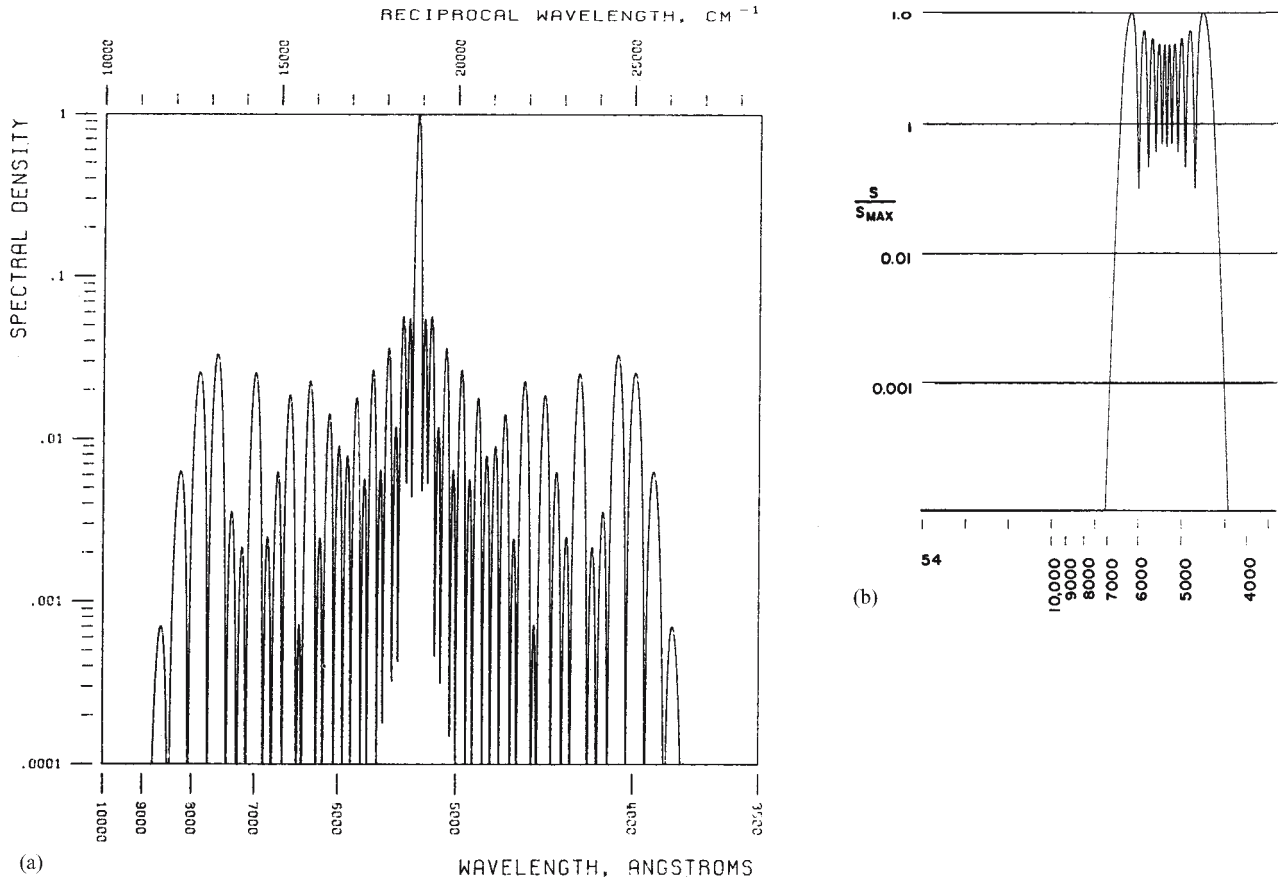


FIGURE 2.2. Calculated SPM spectrum: (a) for response time slower than pure electronic but faster than molecular orientation: $\beta = 30$ and $\tau = 0.1$ ps; (b) for pure electronic response: $\beta = 30$ and $\tau = 0.1$ ps. (From Alfano, 1972.)

$$C = \left(\frac{\omega_0}{2c}\right)\left(\frac{n_2 a_0^2 z}{\tau_0^2}\right). \tag{17}$$

Typical calculated SPM spectra are displayed in Figure 2.2. The spectral densities of the SPM light are normalized and $\beta$ is defined as $\beta = (n_2 a_0^2 \omega_0 z)/2c$, which measures the strength of the broadening process. Figure 2.2a shows the spectrum for a material response time slower than pure electronic but faster than molecular orientation for $\beta = 30$ and $\tau = 0.1$ ps. The extent of the spectrum is about 7000 $cm^{-1}$. Figure 2.2b shows the SPM spectrum for a quasi-pure electronic response for $\beta = 30$ and $\tau = 0.1$ ps. Typical SPM spectral characteristics are apparent in these spectra.

## 3. Experimental Arrangement for SPM Generation

To produce the supercontinuum, an ultrafast laser pulse is essential with a pulse duration in the picosecond and femtosecond time region. A modelocked laser is used to generate picosecond and femtosecond light pulses. Table 2.2 lists the available mode-locked lasers that can produce picosecond and femtosecond laser pulses. Measurements performed in the 1970s used a modelocked Nd : glass laser with output at 1.06 $\mu$m with power of ~$5 \times 10^9$ W and the second harmonic (SHG) at 530 nm with power of $2 \times 10^8$ W. Typically, one needs at least a few microjoulis of 100-fs pulse passing through a 1-mm sample to produce continuum.

A typical experimental setup for ultrafast supercontinuum generation is shown in Figure 2.3. Both spectral and spatial distributions are measured. The 8-ps SHG pulse of 5 mJ is reduced in size to a collimated 1.2-mm-diameter beam across the sample by an inverted telescope. For weaker excitation pulses, the beam is focused into the sample using a 10- to 25-cm focal lens. The typical sample length used is 10 to 15 cm for picosecond pulses and 0.1 to 1 cm for 100-f pulses. The intensity distribution of the light at the exit face of the sample was magnified 10 times and imaged on the slit of a spec-

Table 2.2. Available ultrafast mode-locked lasers.

| Oscillator | Wavelength (nm) | Pulse duration |
|---|---|---|
| Ruby | 694.3 | 30 ps |
| YAG | 1064 | 30 ps |
| Silicate glass | 1060 | 8 ps |
| Phosphate glass | 1054 | 6 ps |
| Dye | Tunable (SYNC or flash lamp) | 5–10 ps |
| Dye + $CO_2$ + semiconductor switches | 9300 | 1–10 ps |
| Dye (CPM) | 610–630 | 100 fs |
| Dye + pulse compression (SYNC) | Tunable | 300 fs |
| Dye + CPM (prisms in cavity) | 620 | 27–60 fs |
| Dye + SPM + pulse compression (prisms and grating pairs) | 620 | 6–10 fs |

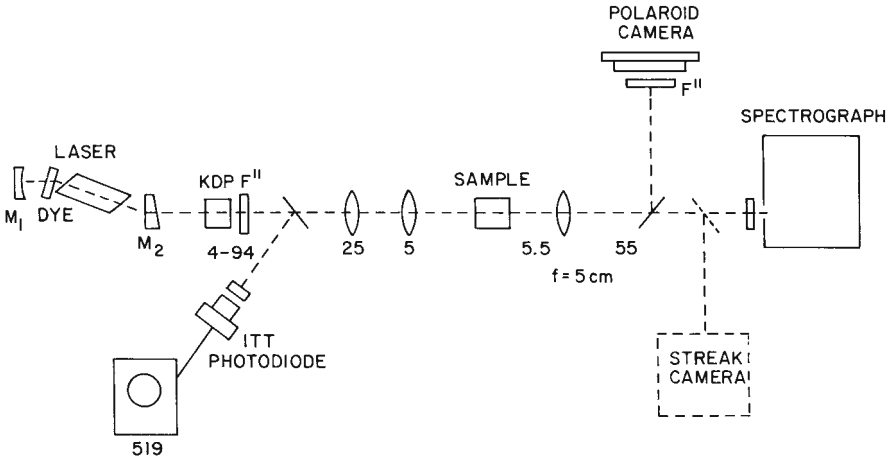


FIGURE 2.3. Experimental arrangement for generating and observing supercontinuum and self-focusing. (From Alfano, 1972.)

trograph. The spectrum of each individual filament within the slit was displayed. Usually there were 5 to 20 filaments. A thin quartz-wedge beam splitter was used to photograph filament formation of the Stokes (anti-Stokes) side of the spectra; three type 3-68 and three type 3-67 (two type 5-60) Corning filters were used to prevent the 530-nm direct laser light from entering the spectrograph. To reduce nonfilament light, a wire 2 mm in diameter was sometimes placed at the focal point of the imaging lens. Previously, spectra were taken on Polaroid type 57 film. At present, video systems such as an Silicon-intensified target (SIT) camera together with a PC computer are commonly used to display the spectra. Today, to obtain temporal information about the supercontinuum, a streak camera is added to the experimental system.

## 4. Generation of Supercontinuum in Solids

In the following sections, we review the experimental measurements of supercontinuum generated in condense matter. Topics discussed include supercontinuum generation in various kinds of solids and liquids, optical glass fibers, liquid argon, liquid and solid krypton, magnetic crystals, and dielectric crystals.

The mechanisms behind SPM are discussed in Chapter 1 by Shen and Yang. In general, various mechanisms are responsible for SPM in condensed matter and give rise to the coefficient of the intensity-dependent refractive index $n_2$. These are the orientational Kerr effect, electrostriction, molecular redistribution, librations, and electronic distribution. In suitably chosen media (central-symmetric molecules) these frequency-broadening mechanisms may be distinguished from the electronic mechanism through their dif-

ferent time responses (Lallemand, 1966). The relation times for these mechanisms are given approximately by (Brewer and Lee, 1968)

$$\tau(\text{orientation}) = \frac{4\pi}{3}\eta a^3/kT > 10^{-12}\,\text{s}, \tag{18}$$

$$\tau(\text{molecular types}) = \frac{\langle x^2\rangle}{D} = \frac{6\pi\eta a\langle x^2\rangle}{kT} > 10^{-12}\,\text{s}, \tag{19}$$

$$\tau(\text{libration about field}) = \sqrt{\frac{2I}{\alpha E_0^2}} > 10^{-12}\,\text{s}, \tag{20}$$

$$\tau(\text{electronic}) = \frac{2\pi a_0\hbar}{e^2} > 1.5\times 10^{-16}\,\text{s}, \tag{21}$$

where $\eta$ is the viscosity ($\eta = 0.4$ cp for liquids and $\eta = 10^6$ cp for glasses); $a$ is the molecular radius; $D$ is the diffusion coefficient ($\geq 10^{-5}$ cm/s for liquids) and $x$ is the diffusion distance of the clustering, ~$10^{-8}$ cm; $I$ is the moment of inertia, $I_{\text{argon}} = 9.3 \times 10^{-38}$ esu and $I_{CCl_4} = 1.75 \times 10^{-38}$ esu; $\alpha$ is the polarizability, $\alpha_{\text{argon}} = 1.6 \times 10^{-24}$ esu and $\alpha_{CCl_4} = 1.026 \times 10^{-24}$ esu; and $E_0$ is the amplitude of the electric field, taken as $10^5$ esu, which is close to the atomic field. The response time for an electron distortion is about the period of a Bohr orbit, ~$1.5 \times 10^{-16}$ s. Thus, typical calculated relaxation time responses for diffusional motions are $>10^{-12}$ s, while the electronic distortion response time is ~150 as.

With picosecond light pulses Brewer and Lee (1968) showed that the dominant mechanism for filament formation should be electronic in very viscous liquids. Molecular rocking has been suggested as the cause of broadening and self-focusing in $CS_2$. The molecules are driven by the laser field to rock about the equilibrium position of a potential well that has been set up by the neighboring molecules. This mechanism is characteristized by a relaxation time:

$$\tau_1 = \frac{\eta}{G} = 2.3\times 10^{-13}\,\text{s}, \tag{22}$$

where $G$ is the shear modulus ~$1.5 \times 10^{10}$ dynes/cm and viscosity $\eta = 3.7 \times 10^{-3}$ p for $CS_2$.

In solids, mechanisms giving rise to the coefficient of the intensity-dependent refractive index $n_2$ for picosecond pulse excitation are either direct distortion of electronic clouds around nuclei or one of several coupled electronic mechanisms: librational distortion, where electronic structure is distorted as the molecule rocks; electron-lattice distortion, where the electron cloud distorts as the lattice vibrates; and molecular distortion, where electronic shells are altered as the nuclei redistribute spatially. The electrostriction mechanism is rejected because it exhibits a negligible effect for picosecond and femtosecond pulses.

Typical supercontinuum spectra generated in solids and liquids using 8-ps pulses at 530 nm are displayed in Figure 2.4. All continuum spectra are similar despite the different materials.

## 4.1 Supercontinuum in Glasses

Spectra from the glass samples show modulation (see Figure 2.4a). The spectral modulation ranged from as small as a few wave numbers to hundreds of wave numbers. The filament size was approximately 5 to 50 $\mu$m. Typically, 5 to 20 small-scale filaments were observed. Occasionally, some laser output pulses from the samples did not show modulation or had no regular modulation pattern. Typical Stokes sweeps from these filaments were 1100 $cm^{-1}$ in extradense flint glass of length 7.55 cm and 4200 $cm^{-1}$ in both borosilicate crown (BK-7) and light barium (LBC-1) glass of length 8.9 cm. Sweeps on the anti-Stokes side were typically 7400 $cm^{-1}$ in BK and LBC glasses. The sweep is polarized in the direction of the incident laser polarization for unstrained glasses.

## 4.2 Supercontinuum in Quartz

SPM spectra from quartz using an 8-ps pulse at 530 nm are similar to the spectra from glasses displayed in Figure 2.4a. Typical Stokes sweeps from the filaments were 3900 $cm^{-1}$ in a quartz crystal of length 4.5 cm, and the anti-Stokes sweeps were 5500 $cm^{-1}$.

## 4.3 Supercontinuum in NaCl

Sweeps of 3900 $cm^{-1}$ in NaCl of length 4.7 cm to the red side of 530 nm were observed. Sweeps on the anti-Stokes side were about 7300 $cm^{-1}$. Some of the spectra show modulation with ranges from a few wave numbers to hundreds of wave numbers. Some laser shots showed no modulation or no regular modulation pattern. For unstrained NaCl, the supercontinuum light is polarized in the direction of the incident laser polarization.

## 4.4 Supercontinuum in Calcite

Sweeps of 4400 $cm^{-1}$ and 6100 $cm^{-1}$ to the Stokes and anti-Stokes sides of 530 nm were observed in a calcite crystal of length 4.5 cm (see Figure 2.4b). Some spectra showed modulation structure within the broadened spectra; some showed no modulation or no regular modulation pattern. The exit supercontinuum light has same polarization as the incident laser. The SRS threshold is lower for laser light traveling as an O-wave than an E-wave. SPM dominates the E-wave spectra.

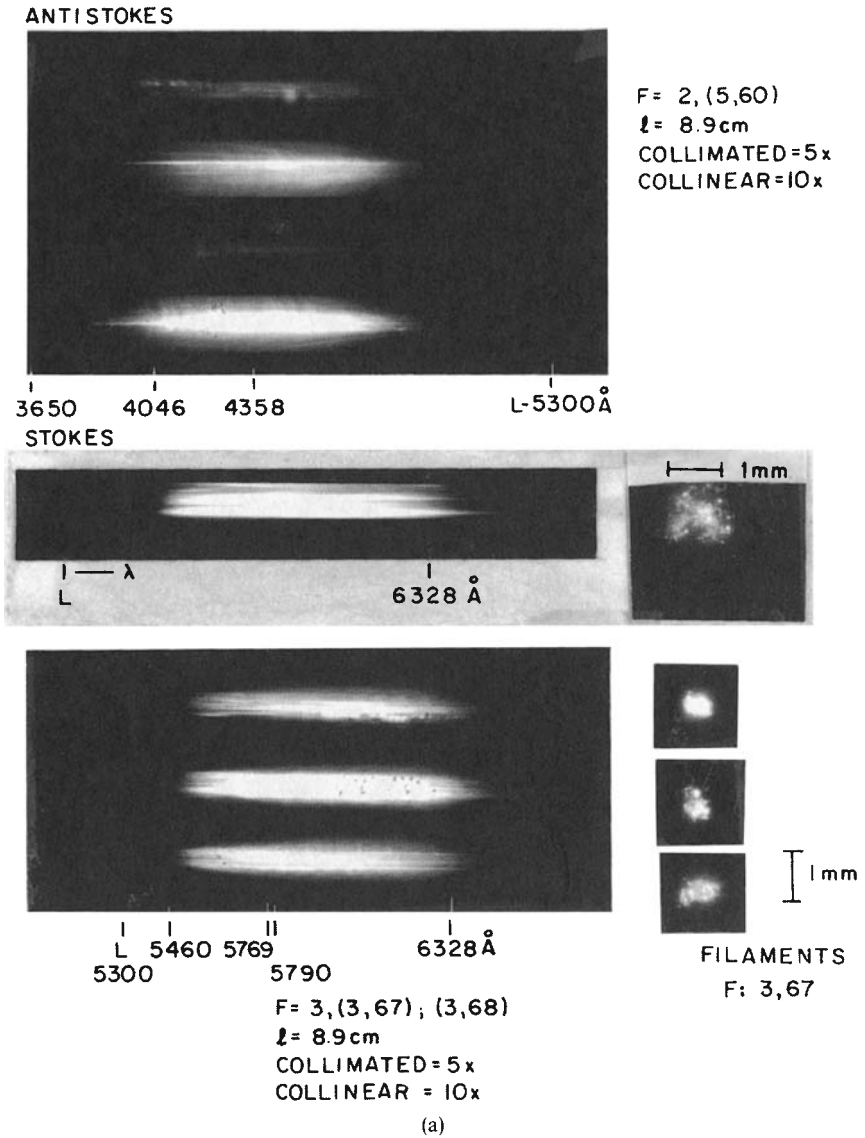


FIGURE 2.4. Supercontinuum spectra from various kind of solids and liquids. (a) Stokes and anti-Stokes SPM from BK-7 glass and filament formation for different laser shots. The filaments are viewed through Corning 3-67 filters. (b) Stokes and anti-Stokes SPM from calcite for different laser shots. The laser beam propagates as an O-wave through the sample. (c) Stokes and anti-Stokes SPM spectra from calcite for different laser shots. The laser beam propagates as an E-wave. (From Alfano, 1972.)

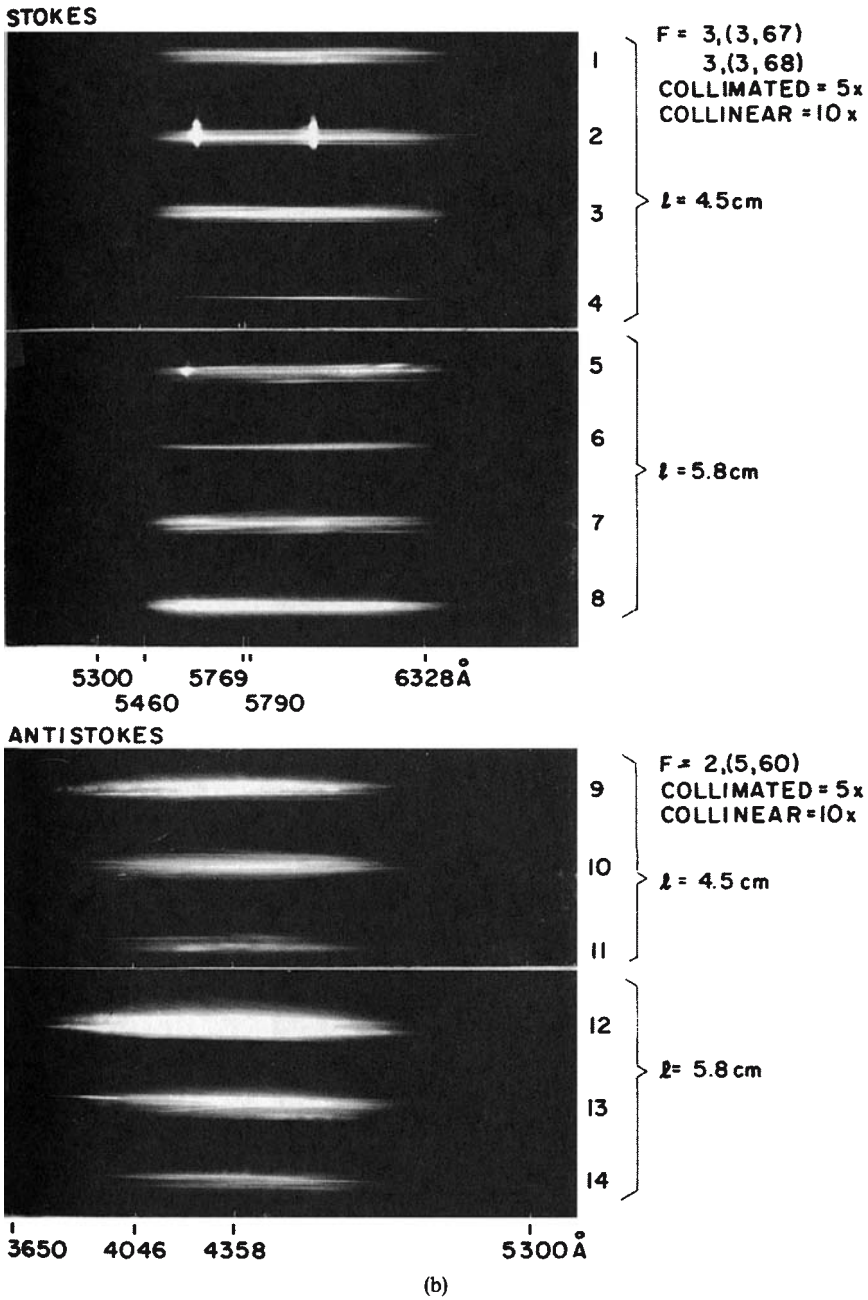


FIGURE 2.4. (*continued*)

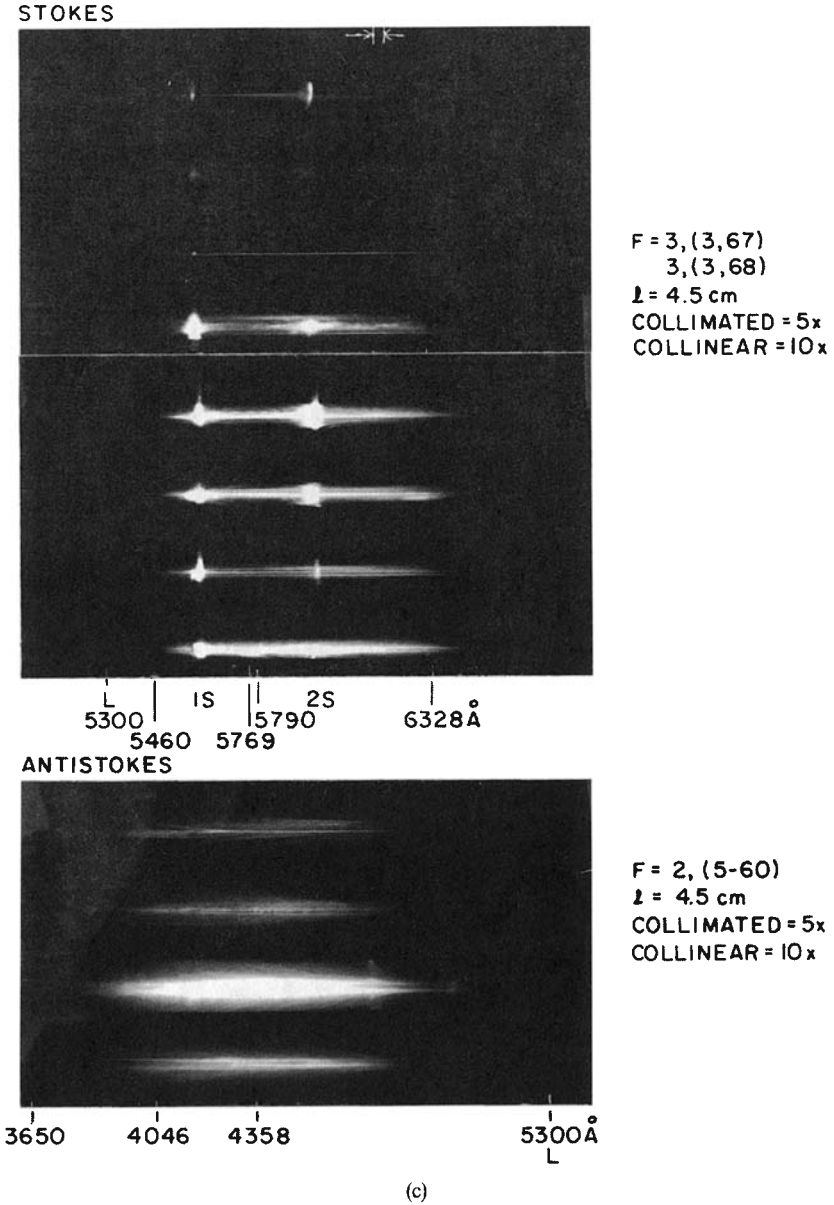


(c)

FIGURE 2.4. (*continued*)

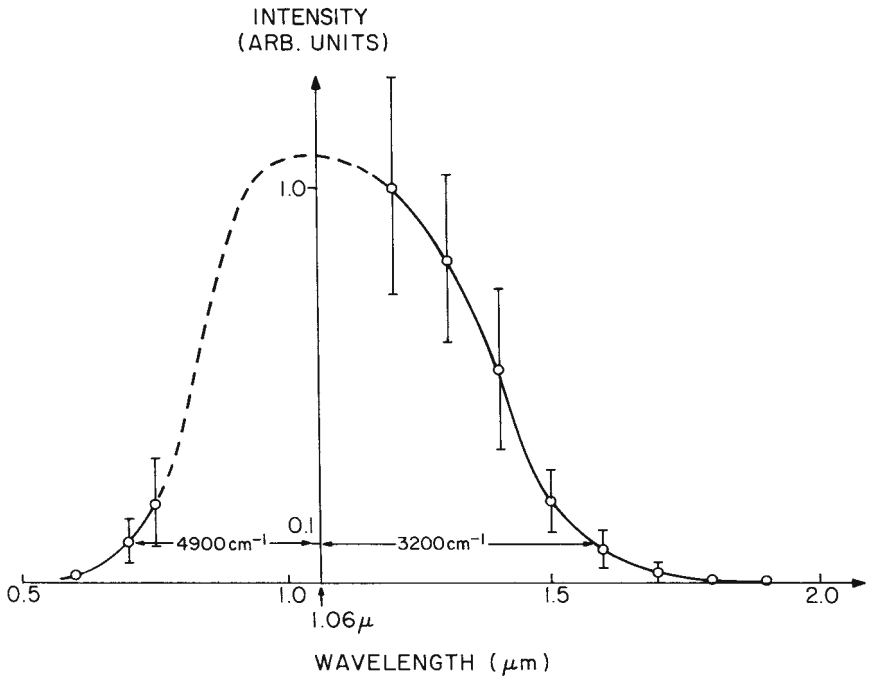


FIGURE 2.5. Relative emission intensity versus emission wavelength for KBr. Exciting wavelength = 1.06 $\mu$m. (From Yu et al., 1975.)

## 4.5 Supercontinuum in KBr

A high-power broadband coherent source in the near- and medium-infrared region can be realized by passing an intense 1.06-$\mu$m picosecond pulse through a KBr crystal. Figure 2.5 shows the spectra from 10-cm-long KBr crystal with excitation of a 9-ps, $10^{11}$ W/cm$^2$ pulse at 1.06 $\mu$m. On the Stokes side the maximum intensity occurs at 1.2 $\mu$m. When the signal drops to $10^{-1}$ the span of the spectral broadening is $\Delta\nu_s = 3200\,\text{cm}^{-1}$ on the Stokes side and $\Delta\nu_a = 4900\,\text{cm}^{-1}$ on the anti-Stokes side. Beyond 1.6 $\mu$m the signal level falls off rapidly. At 1.8 $\mu$m the signal is $10^{-2}$ and at 2 $\mu$m no detectable signal can be observed (Yu et al., 1975).

## 4.6 Supercontinuum in Semiconductors

Infrared supercontinuum spanning the range 3 to 14 $\mu$m can be obtained when an intense picoseond pulse generated from a $CO_2$ laser is passed into GaAs, AgBr, ZnSe, and CdS crystals (Corkum et al., 1985).

The supercontinuum spectra measured from a 6-cm-long Cr-doped GaAs crystal and a 3.8-cm AgBr crystal for different laser pulse durations and

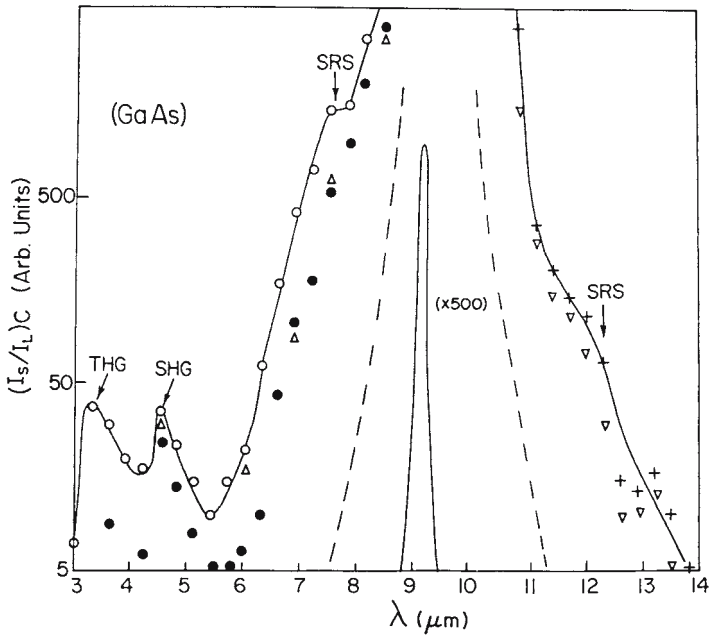


FIGURE 2.6. Supercontinuum spectra from a 6-cm-long Cr-doped GaAs crystal. (From Corkum et al., 1985.)

intensities and plotted in Figures 2.6 and 2.7, respectively. The signals were normalized for the input laser energy and the spectral sensitivity of filters, grating, and detectors. Each point represents the average of three shots. The salient feature of the curves displayed in Figures 2.6 and 2.7 is that the spectral broadening spans the wavelength region from 3 to 14 $\mu$m. The wave number spread on the anti-Stokes side is much greater than that on the Stokes side. From data displayed in Figure 2.6, the maximum anti-Stokes spectral broadening is $\Delta\omega_a = 793\,\text{cm}^{-1}$. Including second and third harmonic generation (SHG and THG), it spans $2000\,\text{cm}^{-1}$. On the Stokes side, $\Delta\omega_s = 360\,\text{cm}^{-1}$, yielding a value of $\delta\omega_a/\delta\omega_s \sim 2.2$. For AgBr, Figure 2.7 shows that $\Delta\omega_a = 743$ $\text{cm}^{-1}$ and $\Delta\omega_s = 242\,\text{cm}^{-1}$, yielding $\Delta\omega_a/\Delta\omega_s \sim 3$.

The spectral broadening mechanism for the supercontinuum can originate from several nonlinear optical processes. These include self-phase modulation, the four-wave parametric effect, higher-order harmonic generation, and stimulated Raman scattering. In Figure 2.6 the supercontinuum from the GaAs has two small peaks at 4.5 and 3.3 $\mu$m. These arise from the SHG and THG, respectively. Small plateaus are located at 7.5 and 12 $\mu$m. These arise from the first-order anti-Stokes and Stokes stimulated Raman scattering combined with SPM about these wavelengths. The SPM is attributed to an electronic mechanism.

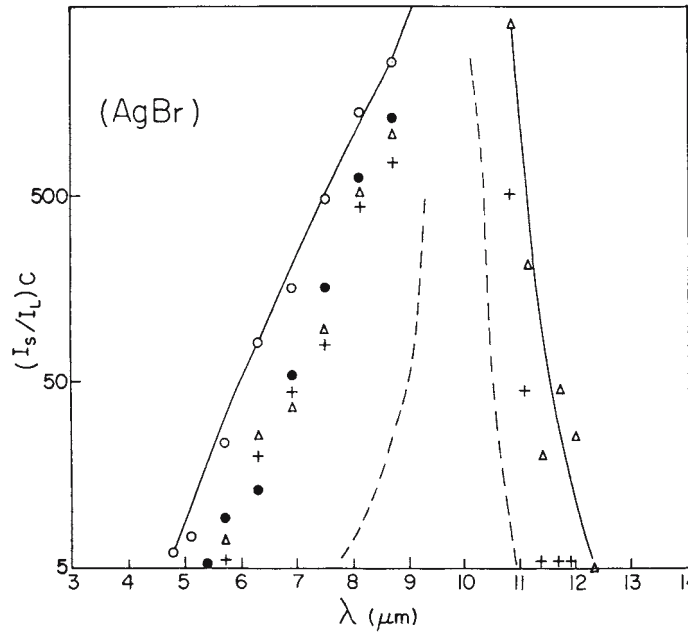


FIGURE 2.7. Supercontinuum spectra from a 3.8-cm-long AgBr crystal. (From Corkum et al., 1985.)

Summarizing the important experimental aspects of the spectra in condensed matter: The spectra are characterized by very large spectral widths and a nonperiodic or random substructure. Occasionally, a periodic structure interference minimum and maximum are observed. The modulation frequencies range from a few $cm^{-1}$ to hundreds of $cm^{-1}$, and some modulation progressively increases away from the central frequency. The Stokes and anti-Stokes spectra are approximately equal in intensity and roughly uniform. The extents on the Stokes and anti-Stokes sides are not symmetric. The peak intensity at the central frequency is $10^2$–$10^3$ the intensity of the SPM spectra at a given frequency.

## 5. Generation of Supercontinuum in Liquids

Nonlinear optical effects in solids are very effective; however, damage generated in solid media often limits their usefulness for ultrashort high-power effects. Various kinds of inorganic and organic liquids are useful media for generating picosecond or femtosecond supercontinuum light pulses since they are selfhealing media. The supercontinuum spectra produced in liquids (Alfano, 1972) are similar to the spectra displayed in Figure 2.4 (Alfano,

1972). The following highlights the supercontinuum phenomena in the various favorite liquid media of the authors. These liquids give the most intense and uniform supercontinuum spectral distributions.

## 5.1 Supercontinuum in $H_2O$ and $D_2O$

The supercontinuum generated in $H_2O$ and $D_2O$ by the second harmonic of a mode-locked neodymium glass laser spanned several thousand wave numbers. The time duration was equal to or less than the picosecond pulse that generated it (Busch et al., 1973). The continuum extended to below 310 nm on the anti-Stokes side and to the near-IR region on the Stokes side. There were sharp absorptions at 450 nm in the $H_2O$ continuum and at 470 nm in the $D_2O$ continuum resulting from the inverse Raman effect (Alfano and Shapiro, 1970b; Jones and Stoicheff, 1964). Focusing a 12-mJ, 1060-nm single pulse 14 ps in duration into 25 cm of liquid $D_2O$ resulted in a continuum that showed practically no structure, extending from 380 to at least 800 nm and highly directional and polarized (Sharma et al., 1976). Enhancing the supercontinuum intensity using water with ions is discussed in Section 10.

## 5.2 Supercontinuum in $CCl_4$

Another favorite liquid for producing a supercontinuum is $CCl_4$, in which the spectra produced are similar to the spectra displayed in Figure 2.4. A typical flat white supercontinuum extending from 430 nm through the visible and near infrared could be produced by focusing an 8-ps pulse at 1060 nm with about 15 mJ pulse energy into a cell containing $CCl_4$ (Magde and Windsor, 1974).

## 5.3 Supercontinuum in Phosphoric Acid

Orthophosphoric acid was found to be a useful medium for generating picosecond continuum light pulses ranging from the near UV to the near IR. By focusing a pulse train from a mode-locked ruby laser into a 10-cm-long cell containing phosphoric acid (60% by weight) solution in water by an 8-cm focal lens, a supercontinuum from near 450 nm to the near IR was obtained. The supercontinuum spectra contain structure arising from Raman lines (Kobayashi, 1979).

## 5.4 Supercontinuum in Polyphosphoric Acid

The supercontinuum from polyphosphoric acid was generated by focusing an optical pulse at 694.3 nm with 100 mJ pulse energy and a pulse width of 28 ps into a cell of any length from 2 to 20 cm containing polyphosphoric acid. It reaches 350 nm on the anti-Stokes side, being limited by the absorp-

tion of polyphosphoric acid, and 925 nm on the Stokes side, being cut off by limitations of IR film sensitivity (Nakashima and Mataga, 1975).

## 6. Supercontinuum Generated in Optical Fibers

The peak power and the interaction length can be controlled better in optical fibers than in bulk materials. Optical fibers are particularly interesting material for nonlinear optical experiments. In this section, we discuss supercontinuum generation in glass optical fibers. Details of the use of SPM for pulse compression are discussed in other chapters.

The generation of continua in glass optical fibers was performed by Stolen et al. in 1974. Continua covering ~500 $cm^{-1}$ were obtained. Shank et al. (1982) compressed 90-fs optical pulses to 30-fs pulses using SPM in an optical fiber followed by a grating compressor. Using the SPM in an optical fiber with a combination of prisms and diffraction gratings, they were able to compress 30 fs to 6 fs (Fork et al., 1987; also see Chapter 10 by Johnson and Shank).

A typical sequence of spectral broadening versus input peak power using 500-fs pulses (Baldeck et al., 1987b) is shown in Figure 2.8. The spectra show

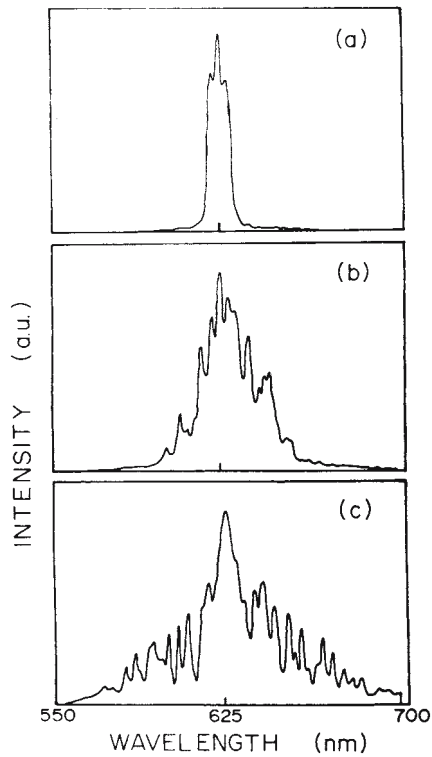


FIGURE 2.8. Sequence of spectral broadening versus increasing input energy in a single-mode optical fiber (length = 30 cm). The intensity of the 500-fs pulse was increased from (a) to (c). (From Baldeck et al., 1987b.)

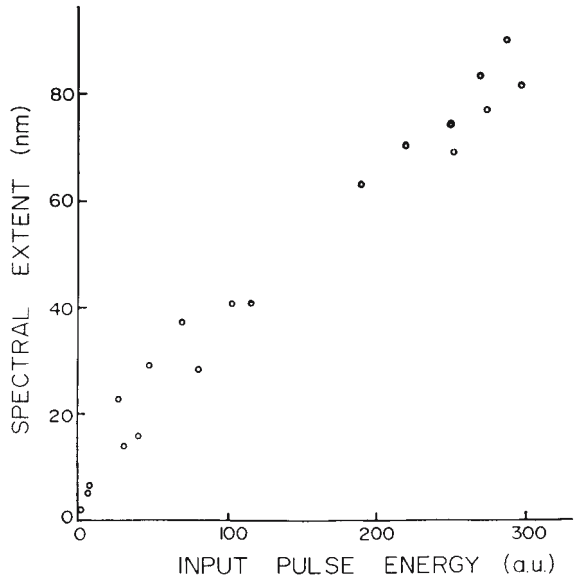


FIGURE 2.9. Supercontinuum spectra versus input pulse energy in a single-mode optical fiber (length = 30 cm) for a 500-fs pulse. (From Baldeck et al., 1987b.)

SPM characteristic of heavy modulation. The spectral extent is plotted against the energy in Figure 2.9 for 500-fs pulses (Baldeck et al., 1987b). The relative energy of each pulse was calculated by integrating its total broadened spectral distribution. The supercontinuum extent increased linearly with the pulse intensity. The fiber length dependence of the spectral broadening is plotted in Figure 2.10. The broadening was found to be independent of the length of the optical fiber for $l > 20$ cm. This is due to group velocity dispersion. The SPM spectral broadening occurs in the first few centimeters of the fiber for such short pulses (Baldeck et al., 1987b).

In multimode optical fibers, the mode dispersion is dominant and causes pulse distortion. Neglecting the detailed transverse distribution of each mode, the light field can be expressed by

$$E(t) = \sum_i a_i A_i(t) \exp[i\omega_0 t - ik_i z], \tag{23}$$

where $\omega_0$ is the incident laser frequency; $a_i$, $A_i(t)$, and $k_i = n_i\omega_0/c$ are the effective amplitude, electric field envelope function at the local time $\tau = t - z/v_{gi}$, and wave number of mode $i$, respectively; and $v_{gi}$ is the group velocity of mode $i$. The effective refractive index of mode $i$ is denoted by $n_i$ and

$$n_i = n_{0i} + n_{2i}|E(t)|^2, \tag{24}$$

where $n_{0i}$ and $n_{2i}$ are the linear refractive index and the nonlinear coefficient of the $i$th mode, respectively. The nonlinearities of different modes are

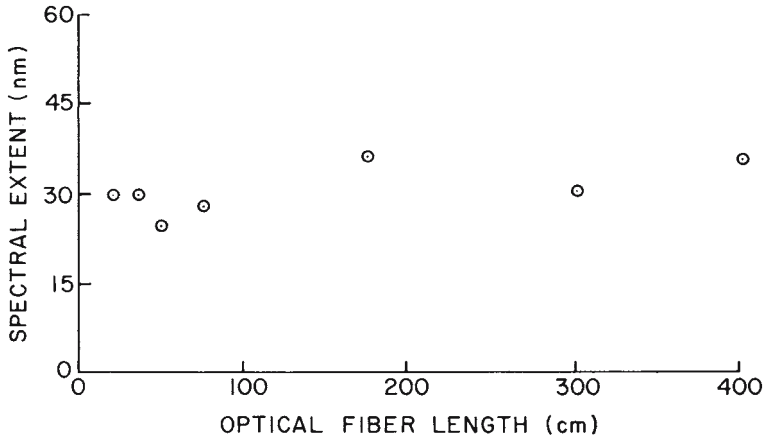


FIGURE 2.10. Supercontinuum spectra versus optical fiber length for a 500-fs pulse. (From Baldeck et al., 1987b.)

assumed to be the same, that is, $n_{2i} = n_2$. Substituting Eq. (21) into Eq. (20), we obtain

$$E(t) = \sum_i a_i A_i(t) \exp[i\omega_0 t - i n_{0i} \omega_0 z/c - i\Delta\phi(t)], \tag{25}$$

where

$$\Delta\phi(t) = (n_2 \omega_0 z/c)|E(t)|^2. \tag{26}$$

After inserting Eq. (23) into Eq. (26), the time-dependent phase factor $\Delta\phi(t)$ can be expanded in terms of $E_i(t)$:

$$\Delta\phi(t) = \sum_i \sum_j (n_2 \omega_0 z/c) a_i a_j A_i(t) A_j(t) \exp[i(n_{0i} - n_{0j})\omega_0 z/c]. \tag{27}$$

In the picosecond time envelope, the terms of $i \neq j$ oscillate rapidly. Their contributions to the time-dependent phase factor are washed out. The approximate $\Delta\phi(t)$ has the form

$$\Delta\phi = \sum_i (n_2 \omega_0 z/c) a_i^2 A_i^2(t). \tag{28}$$

The pulse shape changes due to the different group velocities of various modes. When most of the incident energy is coupled into the lower modes, the pulse will have a fast rising edge and a slow decay tail since the group velocity is faster for lower-order mode. This feature was observed using a streak camera. Therefore, the $\Delta\phi(t, z)$ of Eq. (28) will also have a fast rising edge and a slow decay tail. The time derivative of the phase $\Delta\phi(t, z)$ yields an asymmetric frequency broadening.

Figure 2.11 shows the spectral continuum generated from multimode glass optical fibers using 8-ps pulses at 530 nm. The spectral broadening is asym-

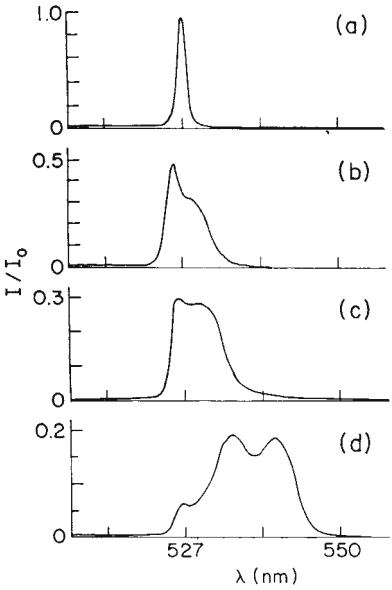


FIGURE 2.11. Output spectra for 8-ps laser pulses at 527 nm propagating through different lengths of multimode optical fibers: (a) no fiber; (b) 22 cm; (c) 42 cm; (d) 84 cm. (From Wang et al., 1988.)

metric about the incident laser frequency. It is shifted much more to the Stokes side than to the anti-Stokes side. The observed spectra did not show a modulation. This can be explained by the spectral resolution of the measurement system. The calculated modulation period is about 0.13 nm, which is much smaller than the resolution of the measurement system (about 1 nm) (Wang et al., 1988).

## 7. Supercontinuum Generation in Rare-Gas Liquids and Solids

Continuum generation is a general phenomenon that occurs in all states of matter. A system for testing the role of the electronic mechanism is rare-gas liquids and solids (Alfano and Shapiro, 1970a). Rare-gas liquids are composed of atoms possessing spherical symmetry. Thus, there are no orientational, librational, or electron-lattice contributions to the nonlinear refractive index $n_2$. However, interrupted rocking of argon can occur in which a distorted atom can rock about an equilibrium value before it collides with other atoms. Contributions to the nonlinear refractive index might be expected from electrostriction, molecular redistribution, interrupted rocking, and a distortion of the electron clouds:

$$n_2 = n_{2\text{ELECTRONIC}} + n_{2\text{MR}} + n_{2\text{LIBRATION}} + n_{2\text{ELECTROSTR}}. \tag{29}$$

Electrostriction is ruled out because picosecond exciting pulses are too short. Molecular redistribution arises from fluctuations in the local positional

arrangement of molecules and can contribute significantly to $n_2$. However, $n_2$ due to all mechanisms except electronic was estimated to be $\sim 2 \times 10^{-14}$ esu for liquid argon from depolarized inelastic-scattering data. Electronic distortion ($n_2 = 6 \times 10^{-14}$ esu) slightly dominates all nonlinear index contributions (Alfano and Shapiro, 1970a; Alfano, 1972). Furthermore, the depolarized inelastic light-scattering wing vanishes in solid xenon, implying that the molecular redistribution contribution to $n_2$ vanishes in rare-gas solids. Observations of self-focusing and SPM in rare-gas solids appear to provide a direct

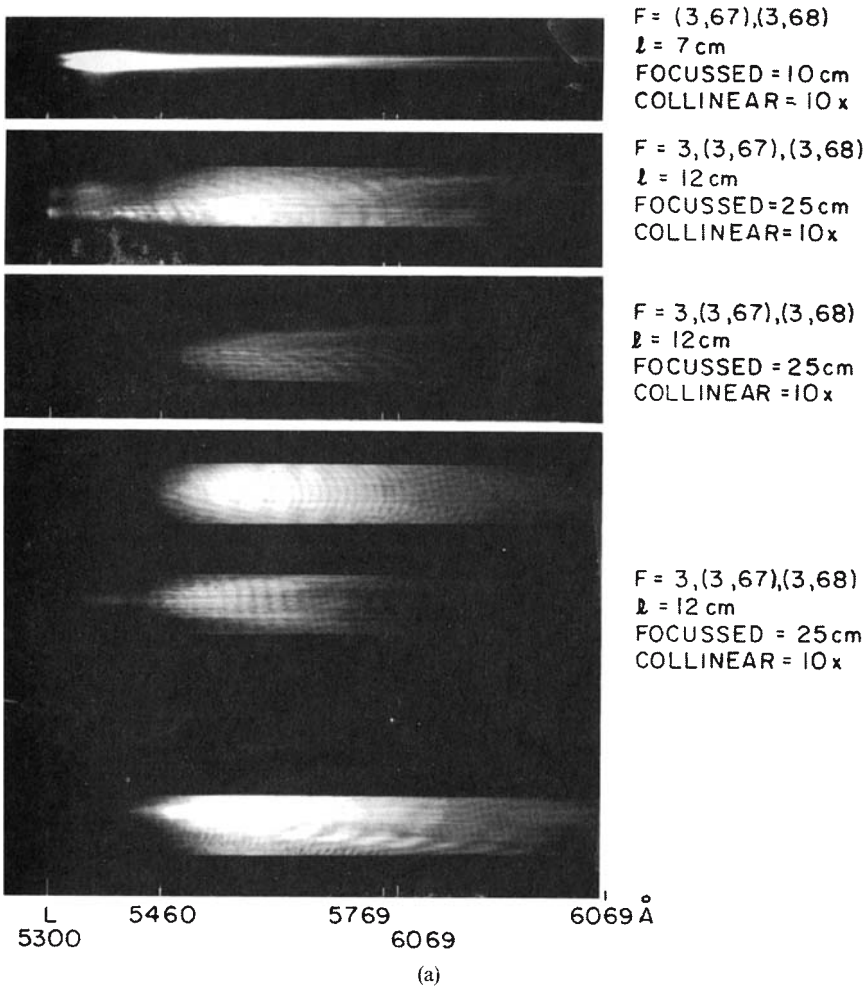


FIGURE 2.12. Supercontinuum spectra for picosecond laser pulses at 530 nm passing through rare-gas liquids and solids; (a) Stokes SPM from liquid argon for different laser shots; (b) anti-Stokes SPM for liquid argon for different laser shots; (c) Stokes SPM for liquid and solid krypton for different laser shots. (From Alfano, 1972.)

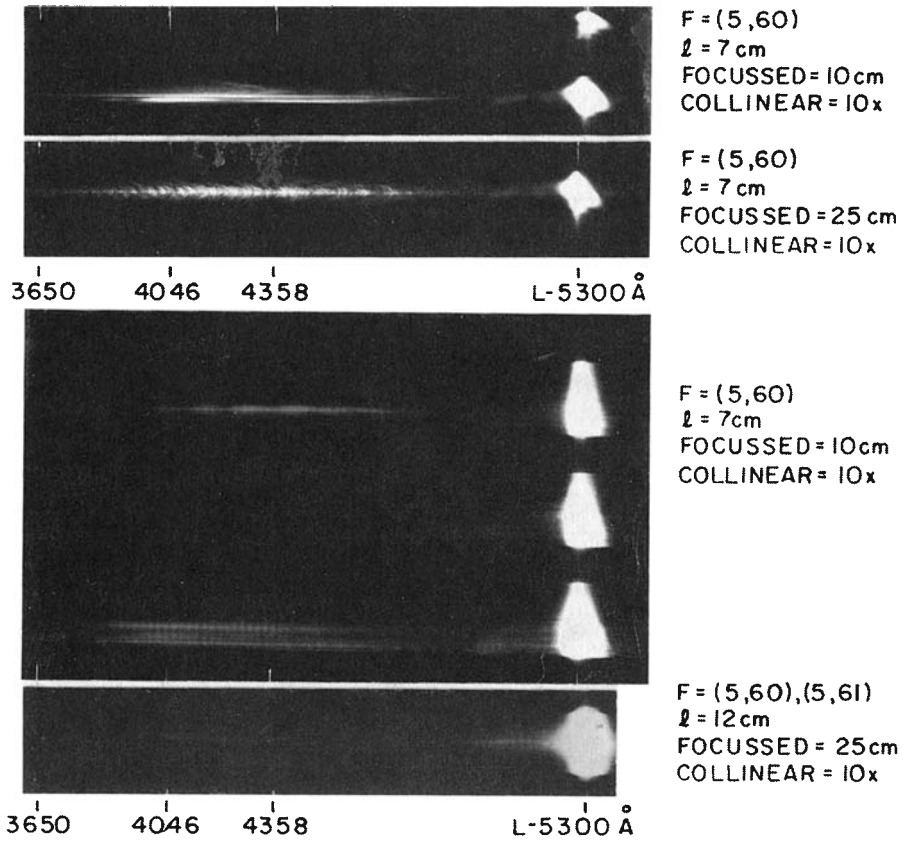


(b)

FIGURE 2.12. (*continued*)

proof that atomic electronic shells are distorted from their spherical symmetry under the action of the applied field. However, both pure electronic and molecular redistribution mechanisms contribute to $n_2$ in rare-gas liquids. The response time of the system for a combination of both of these mechanisms lies between $10^{-15}$ and $10^{-12}$ s. For femtosecond and subpicosecond pulses, the dominant mechanism for $n_2$ and SPM is electronic in origin.

The experimental setup used to generate and detect a supercontinuum in rare-gas liquids and solids is the same as that shown in Figure 2.3 with the exception that the samples are placed in an optical dewar.

Typical supercontinuum spectra from rare-gas liquids and solids are displayed in Figure 2.12. Sweeps of 1000 to 6000 $cm^{-1}$ were observed to both the Stokes and anti-Stokes sides of 530 nm in liquid argon. Modulation ranges from a few $cm^{-1}$ to hundreds of $cm^{-1}$. Similar spectral sweeps were observed in liquid and solid krypton.

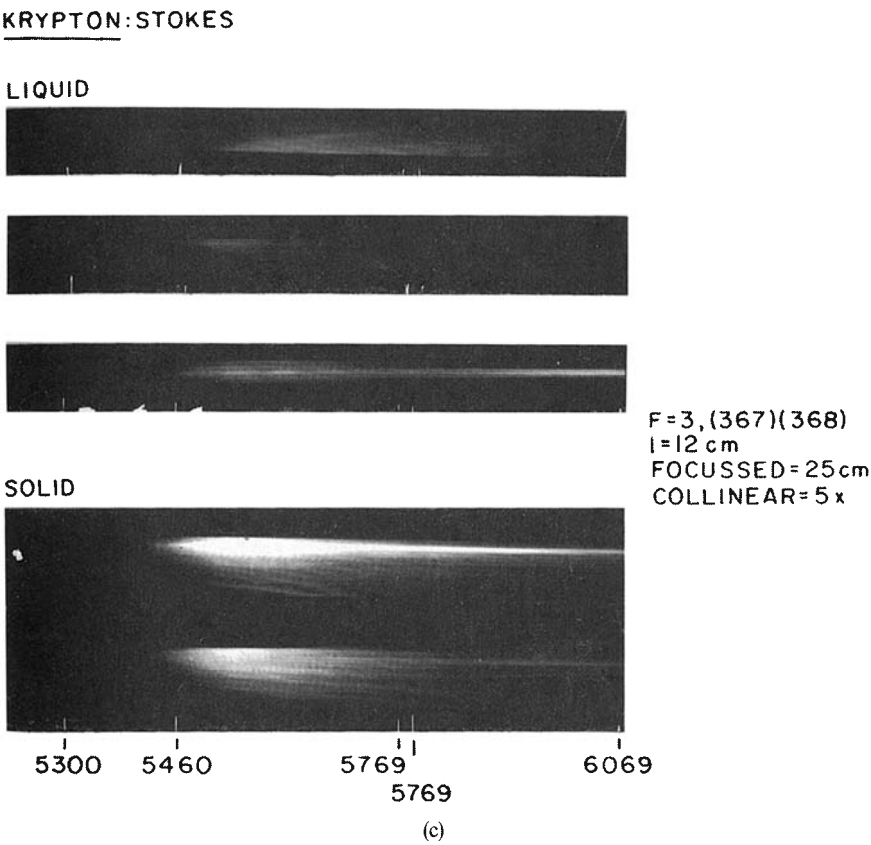


FIGURE 2.12. (*continued*)

A most important point is that the threshold for observing SPM in liquid krypton is $0.64 \pm 0.12$ that in liquid argon. The SPM threshold ratio of solid and liquid krypton is $0.86 \pm 0.15$. In liquid argon, SPM spectra appear at a threshold power of ~0.5 GW focused in a 12-cm sample. The swept light is also collimated, polarized, and modulated. These observations rule out dielectric breakdown.

The refractive index in rare-gas liquids is given by $n_{\|} = n_0 + n_2\langle E^2\rangle$, where $n_{\|}$ is the refractive index parallel to the field. $\langle E^2\rangle^{1/2}$ is the rms value of the electric field. The electronic nonlinear refractive index in rare gas liquids is given by

$$n_2 = \left[(n_0^2 + 2)^4 / 81 n_0\right] \pi N \rho, \tag{30}$$

where $n_0$ is the linear refractive index, $\rho$ is the second-order hyperpolarizability, and $N$ is the number of atoms per unit volume. The term $n_2 = 0.6 \times 10^{-13}$ esu in liquid argon and $\simeq 1.36 \times 10^{-13}$ in liquid krypton. For liquid argon

and liquid and solid krypton, the refractive indices are taken as 1.23, 1.30, and 1.35, respectively (McTague et al., 1969). Intense electric fields distort atoms and produce a birefringence. The anisotropy in refractive index between light traveling with the wave vector parallel and perpendicular to the applied electric field is given by (Alfano, 1972)

$$\delta n_{\parallel} - \delta n_{\perp} = \tfrac{1}{3} n_2 E_0^2, \tag{31}$$

where $\delta n_{\parallel}$ and $\delta n_{\perp}$ are the changes in refractive indices parallel and perpendicular to the field. The value of $n_2 E_0^2$ is $\sim 5 \times 10^{-5}$ V/m in liquid argon when $E_0 \sim 1.5 \times 10^7$ V/m ($\sim 4 \times 10^{11}$ W/cm$^2$). This change in index explains the self-focusing and SPM described above which was observed by Alfano and Shapiro in 1970. Similar SPM effects occur in organic and inorganic liquids, often accompanied by SRS and inverse Raman effects.

## 8. Supercontinuum Generation in Antiferromagnetic $KNiF_3$ Crystals

The influence of magnetic processes on nonlinear optical effects is an interesting topic. In this section, we discuss the supercontinuum generation associated with the onset of magnetic order in a $KNiF_3$ crystal (Alfano et al., 1976). Light at 530 nm is well suited for the excitation pulse because $KNiF_3$ exhibits a broad minimum in its absorption (Knox et al., 1963) between 480 and 610 nm.

Typical spectra from an unoriented 5-cm-long $KNiF_3$ single crystal are displayed in Figure 2.13 for 530-nm picosecond excitation (Alfano et al., 1976). The spectra are characterized by extensive spectral broadening ranging up to $\sim 3000\,\text{cm}^{-1}$ to either side of the laser frequency. The intensity, although not the spectral broadening, of the output exhibited the large temperature dependence illustrated in Figure 2.14. There is no sharp feature at 552 nm, the position expected for stimulated Raman scattering by the 746-cm$^{-1}$ magnon pair excitation. Usually, the spectra were smooth; however, occasionally structure was observed. A periodic structure with a modulation frequency of tens to hundreds of wave numbers was evident. The frequency broadening light is also polarized in the same direction as the incident 530-nm pulse. This property is the same observed in glass, crystals, and liquids (see Sections 3–6). Self-focusing was also observed, usually in the form of 10 to 40 small self-focused spots 5 to 20 $\mu$m in diameter at the exit face of the crystal. Using a focused beam, optical damage could also be produced. It should be emphasized that spectral broadening was always observed even in the absence of self-focusing, damage, or periodic spectral intensity modulation.

Figure 2.15 shows the output intensity at 570 nm as a function of input intensity for two temperatures: above and below the Néel temperature. The output intensity is approximately exponential in the input intensity at both

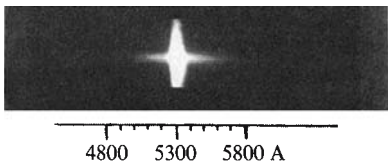


FIGURE 2.13. Spectra for picosecond laser pulse at 530 nm passing through 5-cm-long $KNiF_3$. (From Alfano et al., 1976.)

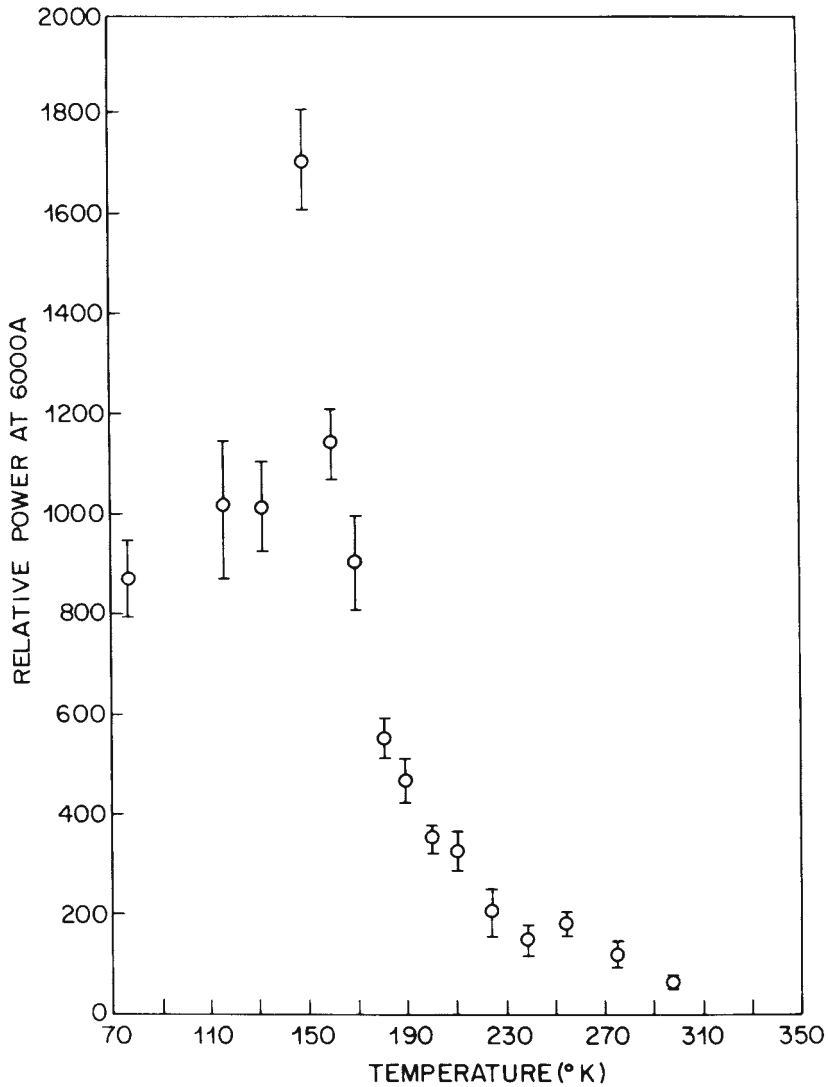


FIGURE 2.14. Intensity of the frequency-broadening emission from $KNiF_3$ as a function of temperature at fixed pump intensity at 552 nm. (From Alfano et al., 1976.)

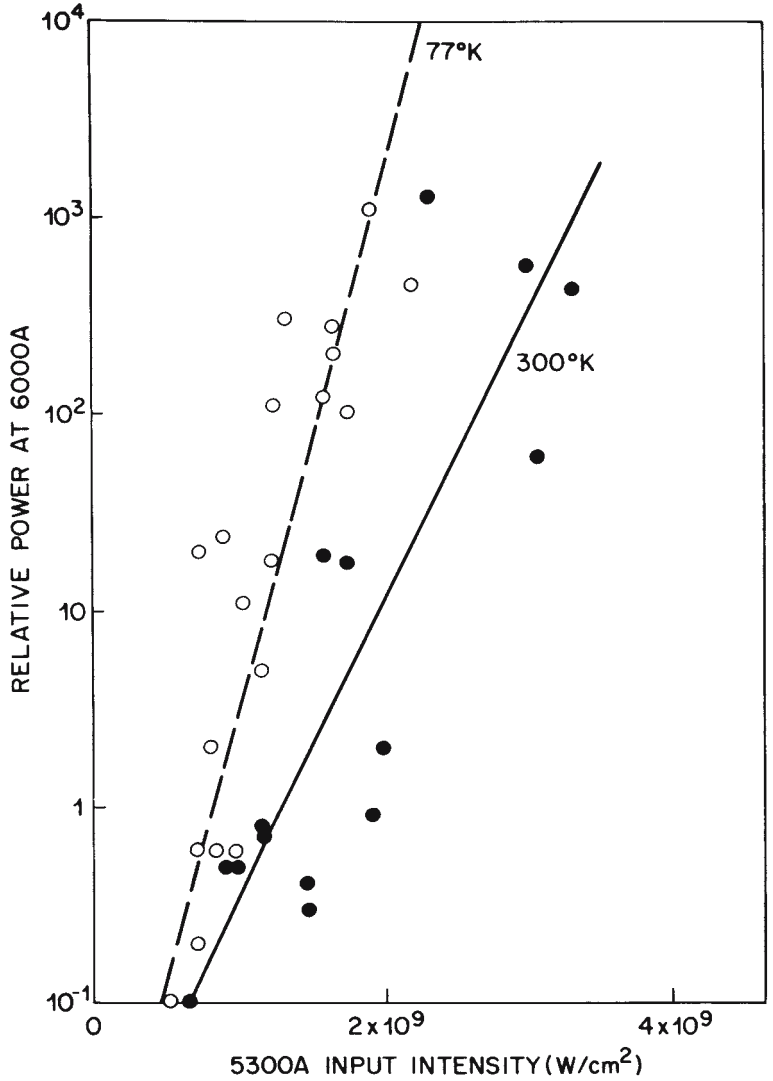


FIGURE 2.15. Intensity dependence of continuum spectra at 570 nm from $KNiF_3$ as a function of pumping laser intensity at fixed lattice temperature. (From Alfano et al., 1976.)

temperatures. However, the slope is more than a factor of two larger at 77 K than at 300 K. The rapid rise in conversion efficiency of four orders of magnitude within a small interval of input intensity is indicative of an amplification process with very large gain. Identical curves were obtained at 552 and 600 nm output wavelengths. The similarity in results for several output frequencies shows that simple stimulated magnon pair scattering is not the

dominant process. If it were, one would expect the behavior at 552 nm to differ considerably from that at other wavelengths.

The most novel experimental results in $KNiF_3$ are the large (~20×) intensity increases below $T_N$. Spectra at 552, 570, and 600 nm behave identically—within experimental error—consistent with the observations in Figure 2.15. The temperature dependence of the relative **peak** intensity for the spontaneous magnon pair scattering in the $KNiF_3$ sample (using 514.5 nm laser light) was measured and is potted in Figure 2.14. For $KNiF_3$ the magnon pair scattering accounts for the entire inelastic light scattering and therefore for the non-σ electronic contribution to $\chi^3$ (Hellwarth et al., 1975). The temperature dependence is compelling evidence for the magnetic origin of the low-temperature-enhanced nonlinear optical spectral broadened intensity.

The observation can be semiquantitatively accounted for in terms of a temperature-dependent spin contribution to the overall nonlinear susceptibility $\chi^{(3)}_{ijkl}$ that governs four-photon parametric mixing as the primary process. In general $\chi^{(3)}$ may be written as a sum of electronic and Raman contributions (Levenson and Bloembergen, 1974). For $KNiF_3$ we may consider the latter to consist solely of the magnon pair Raman scattering contribution (Chinn et al., 1971; Fleury et al., 1975), which we can approximate as a Lorentzian:

$$\chi^{(3)}_{ijkl}(-\omega_3,\omega_1,\omega_1,-\omega_2)=\chi^{(3)}_E+K\frac{\alpha^m_{ij}\alpha^m_{kl}+\alpha^m_{il}\alpha^m_{jk}}{\omega_m-(\omega_1-\omega_2)+i\Gamma_m}. \tag{32}$$

Here $\omega_m$ and $\Gamma_m$ denote the temperature-dependent frequency and linewidth, respectively, of the magnon pair excitations, $\alpha^m_{ij}$ is the magnon pair polarizability, and $\chi^{(3)}_E$ is the usual nonresonant, temperature-independent "electronic" contribution from nonlinear distortion of the electronic orbits. The second term in Eq. (32) is called magnetic $\chi^{(3)}_M$. Since the **integrated intensity** of the spontaneous magnon pair Raman spectrum, which is ~$|\alpha^m|^2$, has been measured and found to be essentially temperature independent (Chinn et al., 1971; Fleury et al., 1975), the only quantities in Eq. (32) that vary significantly with temperature are $\omega_m$ and $\Gamma_m$. The observed temperature independence of the extent of spectral broadening, $\delta\omega$, may be explained by noting that $\delta\omega \sim 2\Delta\omega n_2 k E_1^2 l$ due to self-phase modulation. Here $\Delta\omega$ is the spectral width of the input pulse, $k$ is its propagation constant, $E_1$ is the field amplitude, and $l$ is the path length. $n_2$ is the nonlinear refractive index, which contains a purely electronic contribution, $\sigma$, and a contribution proportional to the integrated Raman scattering cross section (Hellwarth et al., 1975). Since neither $\sigma$ nor $|\alpha^m|^2$ is temperature dependent in $KNiF_3$, $n_2$ and therefore $\Delta\omega$ should not vary either, in agreement with observations.

The observed strong temperature dependence of the intensity of the frequency-broadened spectrum (see Figure 2.14) arises from the resonant term in Eq. (32) through the primary process $2\omega_1 \rightarrow \omega_2 + \omega_3$, which is strongest when $\omega_2 = \omega_1 + \omega_m$ and increases as $\Gamma_m$ decreases (on cooling below the Néel

temperature). That is, the resonant contribution to $\chi^{(3)}$ in Eq. (32) varies with temperature in the same way as the peak spontaneous magnon pair cross section: $\Gamma_m^{-1}(T)$. However, the individual contribution to $\chi^{(3)}$ cannot be directly inferred from the dependence of the broadened spectrum. This is because the latter receives significant contributions from secondary processes of the form $\omega_1 + \omega_2' \rightarrow \omega_3' + \omega_4$ etc., in which products of the primary process interact with the pump to smooth the spectral distribution and wash out the sharp features that the resonant spin nonlinearity produces in the primary process. The large values of pump intensity and source spectral width make possible strong amplification in spite of imprecise phase matching in the forward direction. Such behavior (washing out of stimulated Raman features by the spectral broadening process) has frequently been observed in both liquids and crystals. Thus a full quantitative description of the nonlinear optical processes in $KNiF_3$ is not yet possible.

## 9. Generation of Supercontinuum near Electronic Resonances in Crystals

Since the active medium of a laser possesses well-defined electronic energy levels, knowledge of SPM near electronic levels is of paramount importance. SPM near electronic levels of a $PrF_3$ crystal has been investigated experimentally and theoretically to gain additional information on the SPM process—in particular, on the role played by the electronic levels and on how the continuum spectrum evolves through and beyond the electronic absorption levels (Alfano et al., 1974).

Experimentally, the Stokes and anti-Stokes spectrum and filament formation from the $PrF_3$ crystal are investigated under intense picosecond pulse excitation at the wavelength of 530 nm. The $c$ axis of the crystal is oriented along the optical axis. The intensity distribution at the exit face of the crystal is magnified by 10× and imaged on the slit of a Jarrell-Ash $\frac{1}{2}$-m-grating spectrograph so that the spectrum of each filament can be displayed. The spectra are recorded on Polaroid type 57 film. No visible damage occurred in the $PrF_3$ crystal.

The $PrF_3$ crystal was chosen for the experiment because its electronic levels are suitably located on the Stokes and anti-Stokes sides of the 530-nm excitation wavelength. The absorption spectra of a $\frac{1}{2}$-mm-thick $PrF_3$ crystal and the energy level scheme of $Pr^{3+}$ ions are shown in Figure 2.16. The fluorides of Pr have the structure of the naturally occurring mineral tysonite with $D_{34}^4$ symmetry.

Typical spectra of frequency broadening from $PrF_3$ about 530 nm are shown in Figure 2.17 for different laser shots. Because of the absorption associated with the electronic level, it is necessary to display the spectrum over different wavelength ranges at different intensity levels. In this manner, the

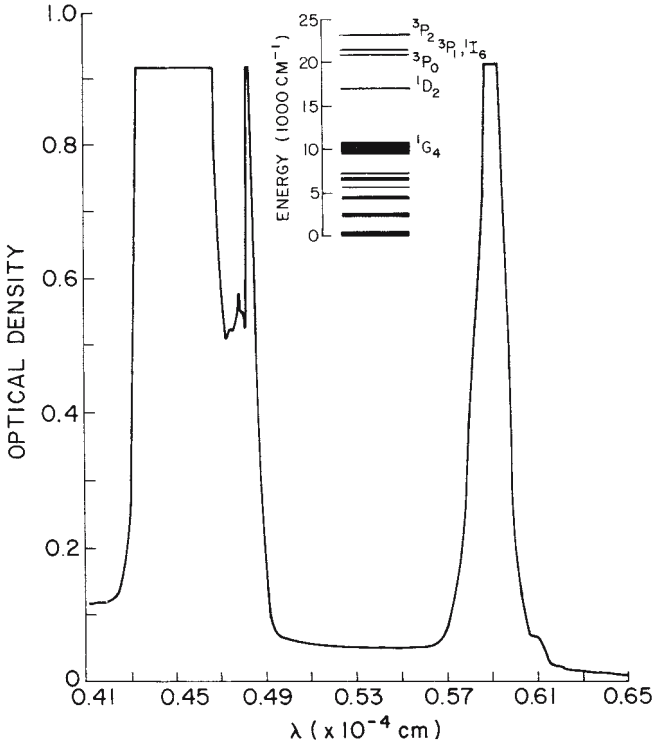


FIGURE 2.16. Absorption spectra of 0.5-mm-thick $PrF_3$ crystal; insert is the level scheme of $Pr^{3+}$ ions. (From Alfano et al., 1974.)

development of the SPM spectrum through the electronic absorption levels can be investigated. Using appropriate filters, different spectral ranges are studied and displayed in the following figures: in Figure 2.18a the Stokes side for frequency broadening $\bar{\nu}_B > 100\,\text{cm}^{-1}$ at an intensity level ($I_{\text{SPM}}$) of $\sim 10^{-2}$ of the laser intensity ($I_L$), in Figure 2.18b the Stokes side for $\bar{\nu}_B > 1500\,\text{cm}^{-1}$ at $I_{\text{SPM}} \sim 10^{-4} I_L$, in Figure 2.18c the anti-Stokes side for $\bar{\nu}_B > 100\,\text{cm}^{-1}$ at $I_{\text{SPM}} \sim 10^{-2} I_L$, and in Figure 2.18d the anti-Stokes side for $\bar{\nu}_B > 1500\,\text{cm}^{-1}$ at $I_{\text{SPM}} \sim 10^{-4} I_L$. Usually 50 to 100 small-scale filaments 5 to 50 $\mu$m in diameter are observed.

Several salient features are evident in the spectra displayed in Figures 2.17 and 2.18. In Figure 2.17 the Stokes and anti-Stokes spectra are approximately equal in intensity and frequency extent. The peak intensity at the central frequency is ~100 times the intensity of the SPM at a given frequency. The extent of the frequency broadening is $\sim 1500\,\text{cm}^{-1}$, ending approximately at the absorption lines. Occasionally a periodic structure of minima and maxima is observed that ranges from a few $\text{cm}^{-1}$ to $100\,\text{cm}^{-1}$, and for some observations no modulation is observed. Occasionally an absorption band appears on the

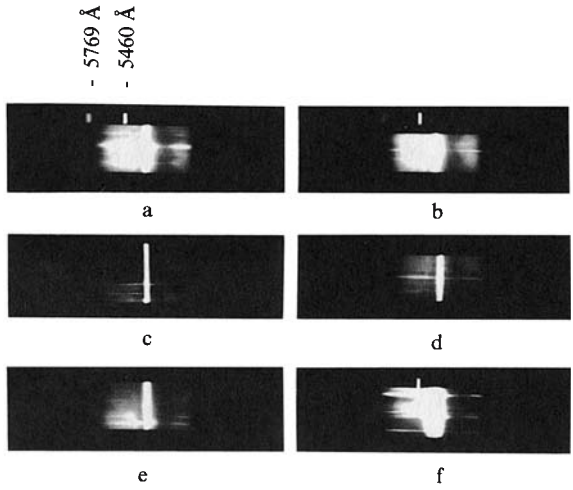


FIGURE 2.17. Spectra from $PrF_3$ excited by 4-ps laser pulses at 530 nm; neutral density (ND) filters: (a) ND = 1.5; (b) ND = 1.5; (c) ND = 2.0; (d) ND = 2.0; (e) ND = 1.7; (f) ND = 1.4. A wire is positioned after the collection lens at the focal length. (From Alfano et al., 1974.)

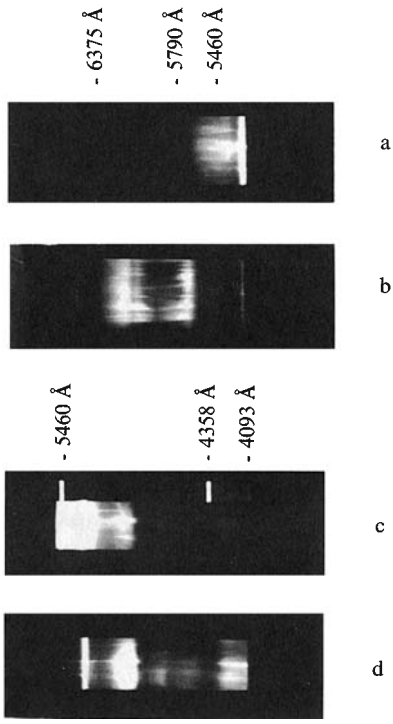


FIGURE 2.18. Spectra on the Stokes and anti-Stokes sides of the 530-nm excitation: (a) Stokes side, Corning 3-68 filter, wire inserted, ND = 2.0; (b) Stokes side, Corning 3-66 filter, wire inserted; (c) anti-Stokes side, wire inserted, ND = 1.0; (d) anti-Stokes side, Corning 5-61, wire inserted. (From Alfano et al., 1974.)

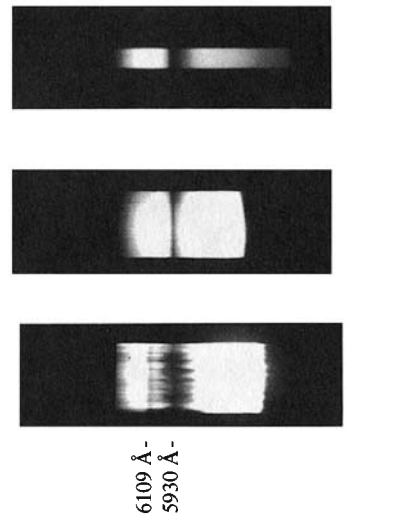


FIGURE 2.19. Comparison of the Stokes absorption spectra of $PrF_3$ photographed with different light sources: (a) light emitted from a tungsten lamp is passed through 0.5-cm-thick crystal; (b) SPM light emitted from BK-7 glass is passed through 0.5-mm-thick crystal; (c) SPM light is generated within the 5-cm $PrF_3$. (From Alfano et al., 1974.)

anti-Stokes side of the 530-nm line whose displacement is $430\,cm^{-1}$. In Figure 2.18 the main feature is the presence of a much weaker super-broadband continuum whose frequency extends through and past the well-defined absorption lines of the $Pr^{3+}$ ion to a maximum frequency of $>3000\,cm^{-1}$ on the Stokes side (end of film sensitivity) and $>6000\,cm^{-1}$ on the anti-Stokes side. The intensity of the continuum at a given frequency outside absorption lines is $\sim 10^{-4}$ the laser intensity.

The observed absorption lines on the anti-Stokes side of 530 nm are located at 441.5, 465.3, and 484.5 nm and on the Stokes side at 593 and 610.9 nm. These lines correspond within ±0.7 nm to the absorption lines measured with a Cary 14. The absorption lines measured from the Cary spectra are $\sim 3\,cm^{-1}$ at 611.2 nm, $62\,cm^{-1}$ at 5938.8 nm, $46\,cm^{-1}$ at 485.2 nm, and $>100\,cm^{-1}$ at 441.2 nm. Figure 2.19 compares the Stokes absorption spectra of a $PrF_3$ crystal photographed with a $\frac{1}{2}$-m Jarrell-Ash spectrograph with different broadband light sources. Figure 2.19a was obtained with light emitted from a tungsten lamp passing through a $\frac{1}{2}$-mm $PrF_3$ crystal, Figure 2.19b was obtained with the Stokes side of the broadband picosecond continuum generated in BK-7 glass passing through a $\frac{1}{2}$-mm $PrF_3$, and Figure 2.19c was obtained with the broadband light generated in a 5-cm $PrF_3$ crystal. Notice that the absorption line at 611.2 nm is very pronounced in the spectra obtained with the continuum generated in $PrF_3$, whereas with conventional absorption techniques it is barely visible. The anti-Stokes spectrum obtained with light emitted from a tungsten filament lamp passing through a $\frac{1}{2}$-mm $PrF_3$ crystal is shown in Figure 2.20a. This is compared with the spectrum obtained with broadband light generated in a 5-cm $PrF_3$ crystal shown in Figure 2.20b.

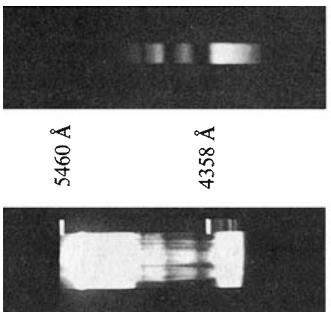


FIGURE 2.20. Comparison of the anti-Stokes absorption spectrum of $PrF_3$ photographed with (a) light emitted from a tungsten lamp passing through 0.5-mm-thick crystal and (b) SPM light generated within the 5-cm $PrF_3$. (From Alfano et al., 1974.)

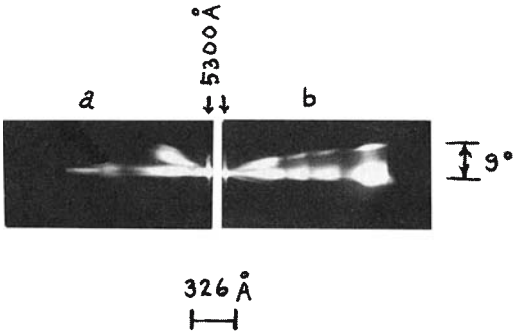


FIGURE 2.21. Angular variation of the (a) Stokes and (b) anti-Stokes spectral patterns emitted from $PrF_3$ crystal: (a) Corning 4(3-67) filters, ND = 1.0; (b) Corning 2(5-60) filters. (From Alfano et al., 1974.)

The angular variation of the anti-Stokes and Stokes spectral emission from $PrF_3$ is displayed in Figure 2.21. The light emitted from the sample is focused on the slit of a $\frac{1}{2}$-m Jarrell-Ash spectrograph with a 5-cm focal length lens with the laser beam positioned near the bottom of the slit so that only the upper half of the angular spectrum curve is displayed. In this fashion, a larger angular variation of the spectrum is displayed. Emission angles >9° go off slit and are not displayed. This spectrum is similar to four-photon emission patterns observed from glass and liquids under picosecond excitation.

The experimental results show that a discontinuity in intensity occurs when the self-phase modulation frequency extends beyond the absorption line frequency. This is due to almost total suppression of the signal beyond the absorption resonance (Alfano et al., 1974). A similar argument and conclusion hold for the blue side of the laser line. The residual weak intensity that exists beyond the absorption line is not due to SPM. It can arise, however, from three-wave mixing. Since there was a continuum of frequencies created by SPM, it might be possible for three such frequencies, $\omega_1$, $\omega_2$, and $\omega_3$, to mix to create a signal at frequency $\omega_1 + \omega_2 - \omega_3$ that lies beyond the absorption line. Since the frequencies are chosen from a continuum, it is also possible for phase matching to be achieved. For the spectrum in the domain between the laser frequency and the absorption line, the extent of self-broadening is proportional to the intensity. Since the energy in the pulse is proportional to the product of the frequency extent and the intensity spectrum, the intensity spectrum remains approximately constant. The observed

absorption band in the continuum on the anti-Stokes side about 400 $cm^{-1}$ away from the excitation frequency (see Figure 2.17) is probably due to the inverse Raman effect (Jones and Stoicheff, 1964). The observed absorption band is located in the vicinity of strong Raman bands: 401, 370, and 321 $cm^{-1}$.

A curious feature of the associated weak broadband spectrum is the existence of a pronounced absorption line at a position (611.2 nm) where the linear absorption would be expected to be rather weak. A possible explanation for this is as follows: Imagine tracing the spatial development of the phase modulation spectrum. At a short distance, where the bounds of the spectrum have not yet intersected a strong absorption line, the spectrum is reasonably flat. On intersecting the absorption line, the spectrum abruptly drops (Alfano et al., 1974). The mechanism of FFPG is presumably responsible for the appearance of the signal beyond the absorption line limit. This explanation is also supported by the appearance of the angular emission pattern (see Figure 2.21). As the spectrum continues to develop, one reaches a point where the limit of the regenerated spectrum crosses a weak absorption line. One can again expect a drastic drop in the spectrum at the position of this line. At still greater distances renewed four-photon parametric regeneration accounts for the feeble signal. A continuum is generated behind absorption bands due to contributions from SPM, three-wave mixing (TWM), and FFPG.

## 10. Enhancement of Supercontinuum in Water by Addition of Ions

The most common liquids used to generate a continuum for various applications are $CCl_4$, $H_2O$, and $D_2O$. In most applications of the ultrafast supercontinuum, it is necessary to increase the conversion efficiency of laser excitation energy to the supercontinuum. One method for accomplishing this is based on the induced- or cross-phase modulation. Another way is to increase $n_2$ in materials. In this section, chemical means are used to obtain a tenfold enhancement of the ultrafast supercontinuum in water by adding $Zn^{2+}$ or $K^+$ ions (Jimbo et al., 1987) for 8-ps pulse generation.

The optical Kerr gate (OKG) (Ho and Alfano, 1979) was used to measure the nonlinear refractive index of the salt solutions. The primary and second harmonic light beams were separated by a dichroic mirror and then focused into a 1-cm-long sample cell filled with the same salt solutions that produced the ultrafast supercontinuum pulse enhancements. The size of the nonlinear index of refraction, $n_2$, was determined from the transmission of the probe beam through the OKG.

Three different two-component salt solutions of various concentrations were tasted. The solutes were KCl, $ZnCl_2$, and $K_2ZnCl_4$. All measurements were performed at 20 ± 1°C. Typical spectra of ultrafast supercontinuum

pulses exhibited both SPM and FPPG features. The collinear profile arising from SPM has nearly the same spatial distribution as the incident 8-ps, 530-nm laser pulse. The two wings correspond to FPPG pulse propagation. The angle arises from the phase-matching condition of the generated wavelength emitted at different angles from the incident laser beam direction. FPPG spectra sometimes appear as multiple cones and sometimes show modulated features. SPM spectra also show modulated patterns. These features can be explained by multiple filaments.

Typical ultrafast supercontinuum pulse spectra on the Stokes side for different aqueous solutions and neat water, measured with the optical multichannel analyzer, are shown in Figure 2.22. The salient features in Figure 2.22 are a wideband SPM spectrum together with the stimulated Raman scattering of the OH stretching vibration around 645 nm. The addition of salts causes the SRS signal to shift toward the longer-wavelength region and sometimes causes the SRS to be weak (Figure 2.22a). The SRS signal of pure water and dilute solution appears in the hydrogen-bonded OH stretching region (~3400 $cm^{-1}$). In a high-concentration solution, it appears in the non-hydrogen-bonded OH stretching region (~3600 $cm^{-1}$). The latter features of SRS were observed in an aqueous solution of $NaClO_4$ by Walrafen (1972).

To evaluate quantitatively the effect of cations on ultrafast supercontinuum generation, the ultrafast supercontinuum signal intensity for various samples at a fixed wavelength were measured and compared. Figure 2.23 shows the dependence of the supercontinuum (mainly from the SPM contribution) signal intensity on salt concentration for aqueous solutions of $K_2ZnCl_4$, $ZnCl_2$, and KCl at 570 nm (Figure 2.23a) and 500 nm (Figure 2.23b). The data were normalized with respect to the average ultrafast supercontinuum signal intensity obtained from neat water. These data indicated that the supercontinuum pulse intensity was highly dependent on salt concentration and that both the Stokes and the anti-Stokes sides of the supercontinuum signals from a saturated $K_2ZnCl_4$ solution were about 10 times larger than from neat water. The insets in Figure 2.23 are the same data plotted as a function of $K^+$ ion concentration for KCl and $K_2ZnCl_4$ aqueous solutions. Solutions of KCl and $K_2ZnCl_4$ generate almost the same amount of supercontinuum if the $K^+$ cation concentration is same, even though they contain different amounts of $Cl^-$ anions. This indicates that the $Cl^-$ anion has little effect on generation of the supercontinuum. The $Zn^{2+}$ cations also enhanced the supercontinuum, though to a lesser extent than the $K^+$ cations.

The measurements of the optical Kerr effect and the ultrafast supercontinuum in salt-saturated aqueous solutions are summarized in Table 2.3. The measured $n_2$ (pure $H_2O$) is about 220 times smaller than $n_2$ ($CS_2$). The value $G_{SPM}(\lambda)$ represents the ratio of the SPM signal intensity from a particular salt solution to that from neat water at wavelength $\lambda$. $G_{Kerr}$ is defined as the ratio of the transmitted intensity caused by a polarization change of the probe beam in a particular salt solution to that in neat water; $G_{Kerr}$ is equal to [$n_2$ (particular solution/$n_2$ (water)]$^2$. Table 2.3 shows that, at saturation, $K_2ZnCl_4$

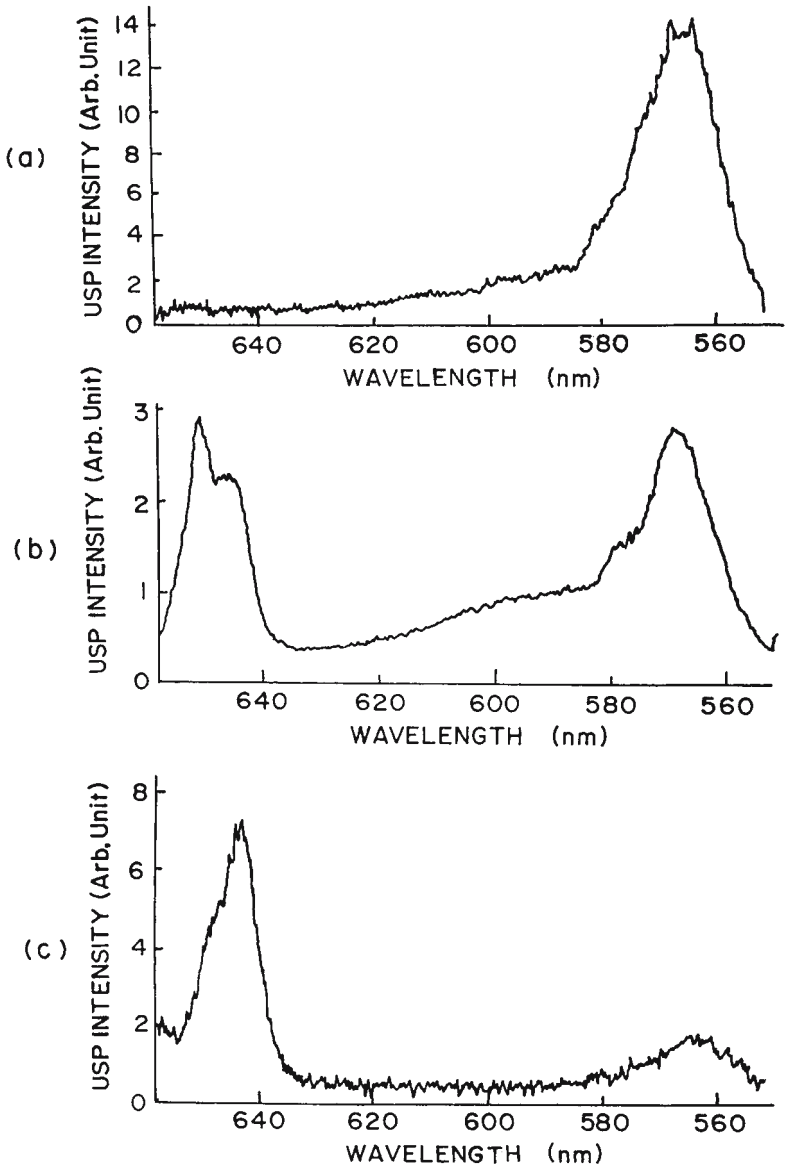


FIGURE 2.22. SPM spectrum of (a) saturated $K_2ZnCl_4$ solution, (b) 0.6-m $K_2ZnCl_4$, and (c) pure water. The SRS signal (645 nm) is stronger in pure water, and it disappears in high-concentration solution. (From Jimbo et al., 1987.)

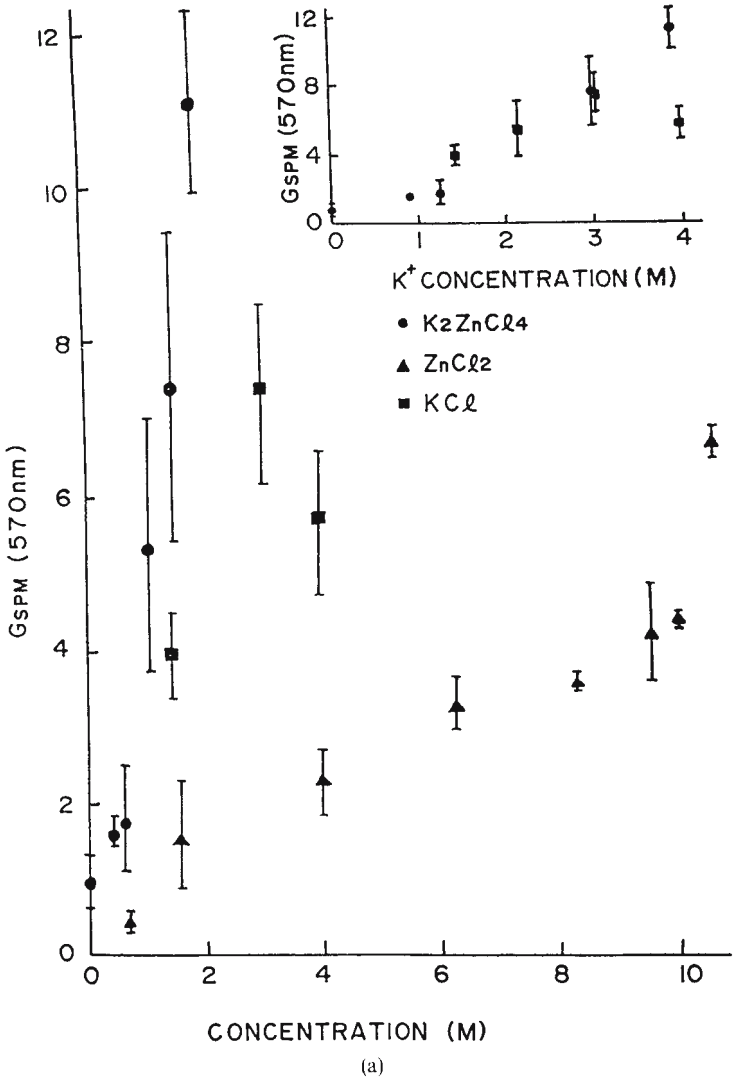


FIGURE 2.23. Salt concentration dependence of the SPM signal (a) on the Stokes side and (b) on the anti-Stokes side 20°C. Each data point is the average of about 10 laser shots. The inserts are the same data plotted as a function of $K^+$ ion concentration for KCl and $K_2ZnCl_4$ aqueous solutions. (From Jimbo et al., 1987.)

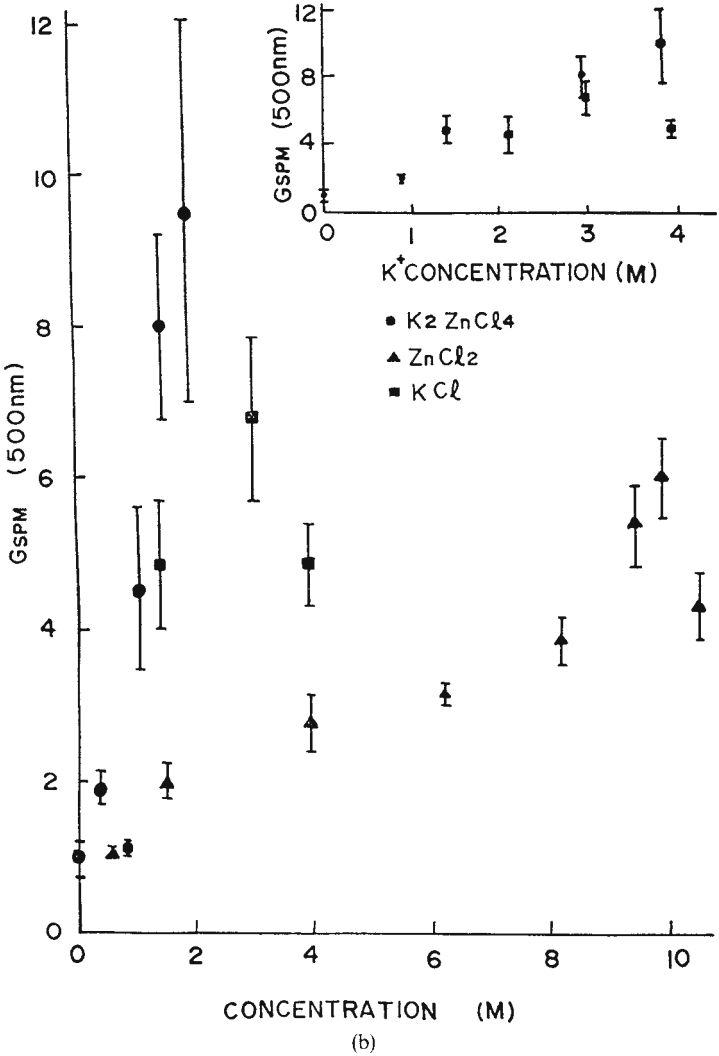


FIGURE 2.23. (*continued*)

TABLE 2.3. Enhancement of the supercontinuum and optical Kerr effects signals in saturated aqueous solutions at 20°C.[a]

| Signal | $K_2ZnCl_4$ (1.9 M) | KCl (4.0 M) | $ZnCl_2$ (10.6 M) |
|---|---|---|---|
| $G_{SPM}$ (570) | 11 ± 1 | 5.6 ± 0.9 | 6.6 ± 0.4 |
| $G_{SPM}$ (500) | 9.5 ± 2.5 | 4.9 ± 0.2 | 4.3 ± 0.5 |
| $G_{Kerr}$ | 16 ± 1 | 6.1 ± 1.4 | 35 ± 9 |

[a] $G_{SPM}(\lambda) = [I_{SPM}(\lambda)/I_{laser}(530\,nm)]_{solution}/[I_{SPM}(\lambda)/I_{laser}\,(530\,nm)]_{water}$ and $G_{Kerr} = [I_{Kerr}(solution)]/[I_{Kerr}\,(water)]$.

produced the greatest increase in the supercontinuum. Although $ZnCl_2$ generated the largest enhancement of the optical Kerr effect, it did not play an important role in the enhancement of the ultrafast supercontinuum (a possible reason for this is discussed below). The optical Kerr effect signal from saturated solutions of $ZnCl_2$ was about 2 to 3 times greater than that from saturated solutions of $K_2ZnCl_4$.

The enhancement of the optical nonlinearity of water by the addition of cations can be explained by the cations' disruption of the tetrahedral hydrogen-bonded water structures and their formation of hydrated units (Walrafen, 1972). Since the nonlinear index $n_2$ is proportional to the number density of molecules, hydration increases the number density of water molecules and thereby increases $n_2$. The ratio of the hydration numbers of $Zn^{2+}$ and $K^+$ has been estimated from measurements of $G_{Kerr}$ and compared with their values based on ionic mobility measurements. At the same concentration of KCl and $ZnCl_2$ acqueous solution, ($G_{Kerr}$ generated by $ZnCl_2$ solution)/($G_{Kerr}$ generated by KCl solution) = $[N(Zn^{2+})/N(K^+)]^2 \sim 2.6$, where $N(Zn^{2+}) \sim 11.2 \pm 1.3$ and $N(K^+) \sim 7 \pm 1$ represent the hydration numbers for the $Zn^{2+}$ and $K^+$ cations, respectively. The calculation of the hydration number of $N(Zn^{2+})/N(K^+) \sim 1.5$ is in good agreement with the Kerr non-linearity measurements displayed in Table 2.3.

In addition, from our previous measurements and discussions of nonlinear processes in mixed binary liquids (Ho and Alfano, 1978), the total optical nonlinearity of a mixture modeled from a generalized Langevin equation was determined by the coupled interactions of solute-solute, solute-solvent, and solvent-solvent molecules. The high salt solution concentration may contribute additional optical nonlinearity to the water owing to the distortion from the salt ions and the salt-water molecular interactions.

The finding that $Zn^{2+}$ cations increased $G_{Kerr}$ more than $G_{SPM}$ is consistent with the hydration picture. The transmitted signal of the OKG depends on $\Delta n$, while the ultrafast supercontinuum signal is determined by $\partial n/\partial t$. The ultrafast supercontinuum also depends on the response time of the hydrated units. Since the $Zn^{2+}$ hydrated units are larger than those of $K^+$, the response time will be longer. These effects will be reduced for longer pulses. Two addi-

tional factors may contribute to part of the small discrepancy between $G_{SPM}$ and $G_{Kerr}$ for $ZnCl_2$. The first one is related to the mechanism of $\delta n$ generation in which $\chi_{1111}$ is involved in the generation of SPM while the difference $\chi_{1111} - \chi_{1112}$ is responsible for the optical Kerr effect. The second is the possible dispersion of $n_2$ because of the difference in wavelength between the exciting beams of the ultrafast supercontinuum and the optical Kerr effects.

The optical Kerr effect is enhanced 35 times by using $ZnCl_2$ as a solute, and the ultrafast supercontinuum is enhanced about 10 times by using $K_2ZnCl_4$ as a solute. The enhancement of the optical nonlinearity has been attributed to an increase in the number density of water molecules owing to hydration and the coupled interactions of solute and solvent molecules. Addition of ions can be used to increase $n_2$ for SPM generation and gating.

## 11. Temporal Behavior of SPM

In addition to spectral features, the temporal properties of the supercontinuum light source are important for understanding the generation and compression processes. In this section, the local generation, propagation, and pulse duration reduction of SPM are discussed.

### 11.1 Temporal Distribution of SPM

In Section 2, using the stationary phase method, it was described theoretically that the Stokes and anti-Stokes frequencies should appear at well-defined locations in time within leading and trailing edges of the pump pulse profile (Alfano, 1972). Theoretical analyses by Stolen and Lin (1978) and Yang and Shen (1984) obtained similar conclusions.

Passing an 80-fs laser pulse through a 500-$\mu$m-thick ethylene glycol jet stream, the pulse duration of the spectrum in time was measured by the autocorrelation method (Fork et al., 1983). These results supported the SPM mechanism for supercontinuum generation. In the following, the measurements of the distribution of various wavelengths for the supercontinuum generated in $CCl_4$ by intense 8-ps laser pulses (Li et al., 1986) are presented. Reduction of the pulse duration using the SPM principle is discussed in Section 10.3.

The incident 530-nm laser pulse temporal profile is shown in Figure 2.24. The pulse shape can be fitted with a Gaussian distribution with duration $\tau$(FWHM) = 8 ps. The spectral and temporal distributions of the supercontinuum pulse were obtained by measuring the time difference using a streak camera. The measured results are shown as circles in Figure 2.25. Each data point corresponds to an average of about six laser shots. The observation is consistent with the SPM and group velocity dispersion. To determine the temporal distribution of the wavelengths generated within a supercontinuum, the group velocity dispersion effect (Topp and Orner, 1975) in $CCl_4$

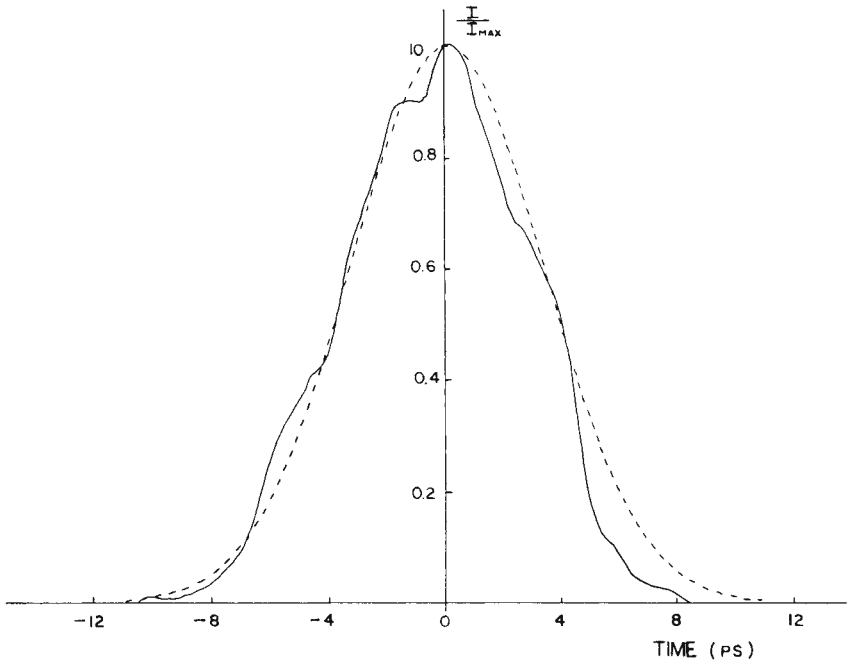


FIGURE 2.24. Temporal profile of a 530-nm incident laser pulse measured by a 2-ps-resolution streak camera. The dashed line is a theoretical fit to an 8-ps EWHM Gaussian pulse. (From Li et al., 1986.)

was corrected. Results corrected for both the optical delay in the added filters and the group velocity are displayed as triangles in Figure 2.25.The salient feature of Figure 2.25 indicates that the Stokes wavelengths of the continuum lead the anti-Stokes wavelengths.

Using the stationary phase SPM method [Eq. (6)], the generated instantaneous frequency $\omega$ of the supercontinuum can be expressed by

$$\omega(t) - \omega_L = -(\omega_L l/c)\partial(\Delta n)/\partial t, \tag{33}$$

where $\omega_L$ is the incident laser angular frequency, $l$ is the length of the sample, and $\Delta n$ is the induced nonlinear refractive index $n_2 E^2$. A theoretical calculated curve for the sweep is displayed in Figure 2.26 by choosing appropriate parameters to fit the experimental data of Figure 2.25. An excellent fit using a stationary phase model up to maximum sweep demonstrates that the generation mechanism of the temporal distribution of the supercontinuum arises from the SPM. During the SPM process, a wavelength occurs at a well-defined time within the pulse. The above analysis will be supported by the additional experimental evidence for SPM described in Section 10.3 (see Figure 2.29).

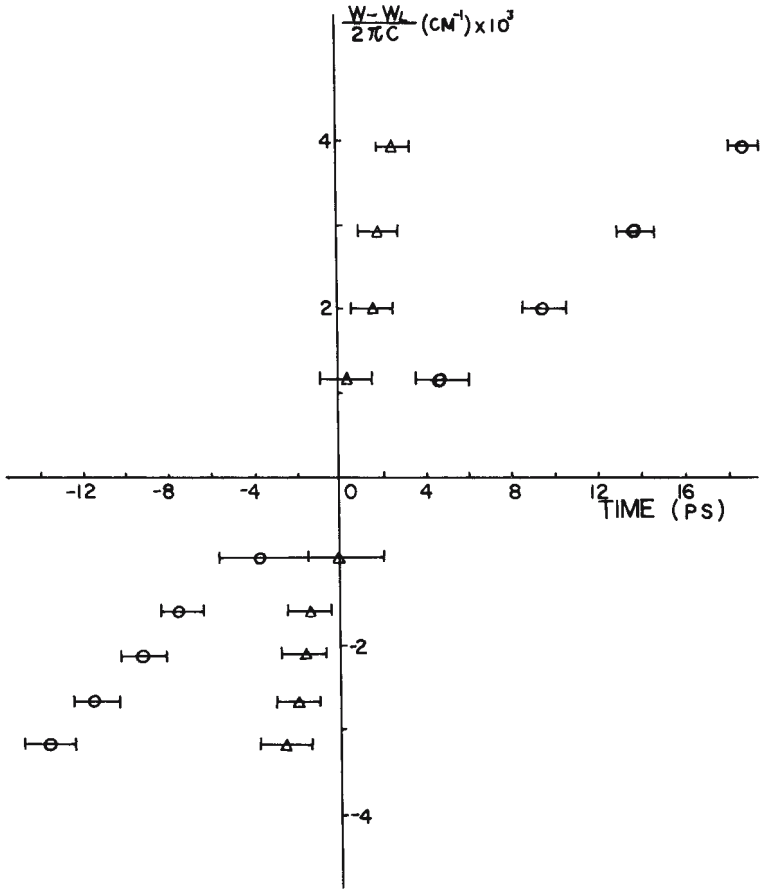


FIGURE 2.25. Measured supercontinuum temporal distribution at different wavelengths: (o) data points with correction of the optical path in filters; (Δ) data points with correction of both the optical path in filters and group velocity dispersion in liquid. (From Li et al., 1986.)

## 11.2 Local Generation and Propagation

The dominant mechanisms responsible for the generation of the ultrafast supercontinuum as mentioned in Sections 1 and 2 are SPM, FPPG, XPM, and SRS. In the SPM process, a newly generated wavelength could have bandwidth-limited duration at a well-defined time location (Alfano, 1972) in the pulse envelope. In the FPPG and SRS processes, the duration of the supercontinuum pulse could be shorter than the pump pulse duration due to the high gain about the peak of the pulse. In either case, the supercontinuum pulse will be shorter than the incident pulse at the local spatial point of generation. These pulses will be broadened in time due to the group velocity dispersion in condensed matter (Ho et al., 1987).

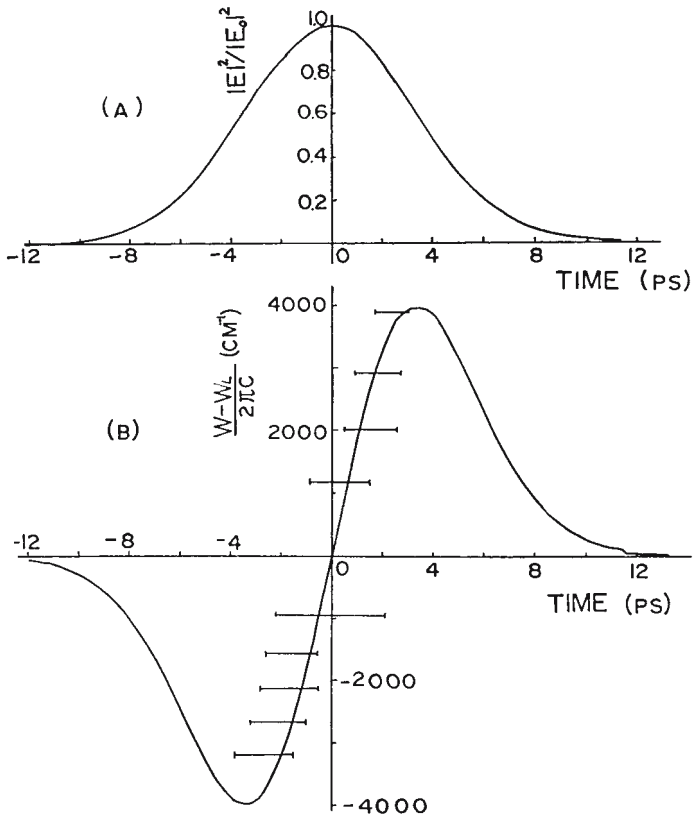


FIGURE 2.26. Comparison of the measured temporal distribution of supercontinuum with the SPM model. (From Li et al., 1986.)

Typical data on the time delay of 10-nm-bandwith pulses centered at 530, 650, and 450 nm wavelengths of the supercontinuum generated from a 20-cm-long cell filled with $CCl_4$ are displayed in Figure 2.27. The peak locations of 530, 650, and 450 nm are –49, –63, and –30 ps, respectively. The salient features in Figure 2.27 (Ho et al., 1987) indicate that the duration of all 10-nm-band supercontinuum pulses is only 6 ps, which is shorter than the incident pulse of 8 ps, the Stokes side (650 nm) of the supercontinuum pulse travels ahead of the pumping 530 nm by 14 ps, and the anti-Stokes side (450 nm) of the supercontinuum pulse lags the 530 nm by 10 ps.

If the supercontinuum could be generated throughout the entire length of the sample, the Stokes side supercontinuum pulse generated by the 530-nm incident laser pulse at $z = 0$ cm of the sample would be ahead of the 530-nm incident pulse after propagating through the length of the sample. Over this path, 530 nm could continuously generate the supercontinuum pulse. Thus, the Stokes side supercontinuum generated at the end of the sample coincides in time with the 530-nm incident pulse. In this manner, a supercontinuum

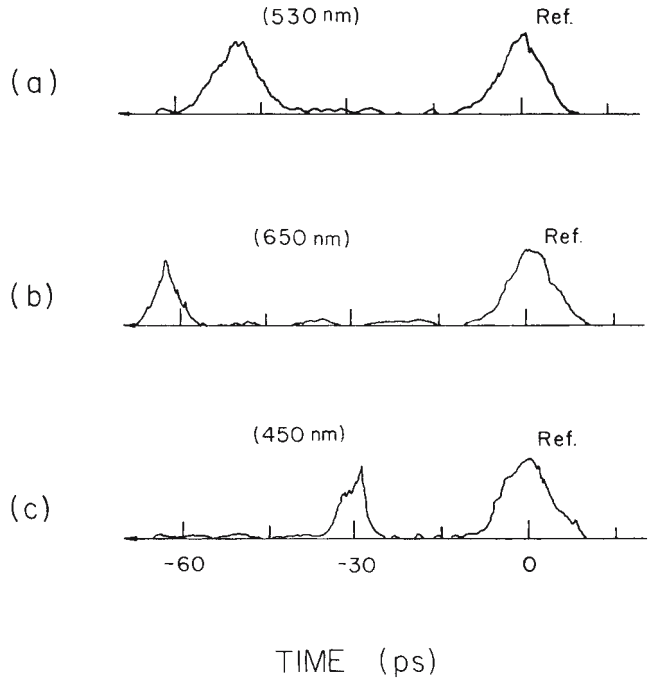


FIGURE 2.27. Temporal profiles and pulse locations of a selected 10-nm band of a supercontinuum pulse at different wavelengths propagated through a 20-cm-long $CCl_4$ cell: (a) $\lambda = 530$ nm; (b) $\lambda = 650$ nm; (c) $\lambda = 450$ nm. Filter effects were compensated. (From Ho et al., 1987.)

pulse centered at a particular Stokes frequency could have a pulse greater than the incident pulse extending in time from the energing of the 530-nm pulse to the position where the Stokes frequency was originally produced at $z \sim 0$ cm. From a similar consideration, the anti-Stokes side supercontinuum pulse would also be broadened. However, no slow asymmetric tail for the Stokes pulse or rise for the anti-Stokes pulse is displayed in Figure 2.27. These observation suggest the local generation of supercontinuum pulses.

A model to describe the generation and propagation features of the supercontinuum pulse has been formulated based on local generation. The time delay of Stokes and anti-Stokes supercontinuum pulses relative to the 530-nm pump pulse is accounted for by the filaments formed ~5 cm from the sample cell entrance window. The 5-cm location is calculated from data in Figure 2.27 by using the equation.

$$T_{530} - T_{\text{supercon.}} = \Delta x \left( \frac{1}{v_{530}} - \frac{1}{v_{\text{supercon.}}} \right), \tag{34}$$

where $\Delta x$ is the total length of supercontinuum pulse travel in $CCl_4$ after the generation. $T_{350}$ and $T_{\text{supercon.}}$ are the 530-nm and supercontinuum pulse peak

time locations in Figure 2.27, and $v_{530}$ and $v_{\text{supercon.}}$ are the group velocities of the 530-nm and supercontinuum pulses, respectively.

The duration of the supercontinuum pulse right at the generation location is either limited by the bandwidth of the measurement from the SPM process or shortened by the parametric generation process. In either cases, a 10-nm-bandwidth supercontinuum pulse will have a shorter duration than the incident pulse. After being generated, each of these 10-nm-bandwidth supercontinuum pulses will travel through the rest of the sample and will continuously generated by the incident 530 nm over a certain interaction length before these two pulses walk off. The interaction length can be calculated as (Alfano, 1972).

$$l = \tau \frac{v_{530} v_{\text{supercon.}}}{v_{530} - v_{\text{supercon.}}}, \tag{35}$$

where $l$ is the interaction length over the pump and the supercontinuum pulses stay spatially coincident by less than the duration (FWHM) of the incident pump pulse, and $\tau$ is the duration of the supercontinuum pulse envelope. From Eq. (35), one can estimate the interaction length from the measured $\tau$ of the supercontinuum pulse. Using parameters $\tau$ = 6 ps, $v_{530} = c/1.4868$, and $v_{\text{supercon.}} = c/1.4656$, the interaction length $l$ = 8.45 cm is calculated. This length agrees well with the measured beam waist length of 8 cm for the pump pulse in $CCl_4$.

Since no long tails were observed from the supercontinuum pulses to the dispersion delay times of the Stokes and anti-Stokes supercontinuum pulses, the supercontinuum was not generated over the entire length of 20 cm but only over 1 to 9 cm. This length is equivalent to the beam waist length of the laser in $CCl_4$. The length of the local SPM generation over a distance of 8.45 cm yields a possible explanation for the 6-ps supercontinuum pulse duration. In addition, a pulse broadening of 0.3 ps calculated from the group velocity dispersion of a 10-nm band at 650-nm supercontinuum traveling over 20 cm of liquid $CCl_4$ is negligible in this case.

Therefore, the SPM pulses have shorter durations than the pump pulse and were generated over local spatial domains in the liquid cell.

## 11.3 SPM Pulse Duration Reduction

The principle behind the pulse narrowing based on the spectral temporal distribution of the SPM spectrally broadened in time within the pulse is described in Sections 2 and 10.1. At each time $t$ within the pulse there is a frequency $\omega(t)$. When a pulse undergoes SPM, the changes in the optical carrier frequency within the temporal profile are greatest on the rising and falling edges, where the frequency is decreased and increased, respectively. Near the peak of the profile, and in the far leading and trailing wings, the carrier frequency structure is essentially unchanged. The maximum frequency shift is proportional to the intensity gradient on the sides of the pulse, and

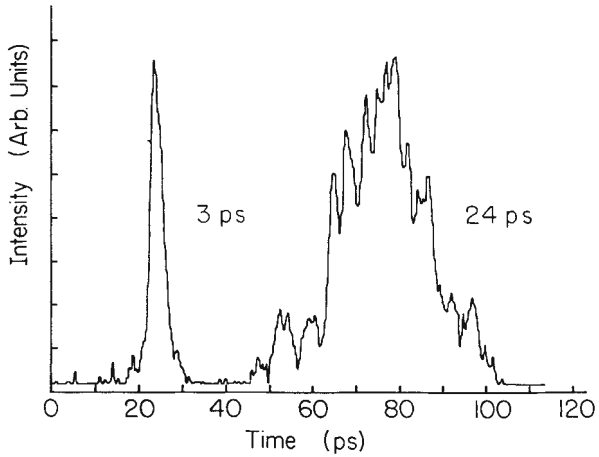


FIGURE 2.28. Streak camera temporal profile of the 25-ps, 530-nm incident laser pulse and 10-nm-bandwidth pulse at 580 nm. The 3-ps pulse was obtained by spectral filtering a SPM frequency continuum generated in $D_2O$. (From Dorsinville et al., 1987.)

this determines the position of the outer lobes of the power spectrum. If these are then attenuated by a spectral window of suitably chosen width, the wings of the profile where the high- and low-frequency components are chiefly concentrated will be depressed, while the central peak will be largely unaffected. The overall effect is to create a pulse that is significantly narrower in time than the original pulse duration. A file can be used to select a narrow portion of the pulse, giving rise to a narrower pulse in time.

A threefold shortening of 80-ps pulses to 30 ps from an Nd:YAG laser broadened from 0.3 to 4 Å after propagation through 125 m of optical fiber with a monochromator as a spectral window was demonstrated using this technique (Gomes et al., 1986). The measurements of pulses at different wave-lengths of the frequency sweep of supercontinuum pulses generated by 8-ps laser pulses propagating in $CCl_4$ show that the continuum pulses have a shorter duration (~6 ps) than the pumping pulses (Li et al., 1986).

A major advance occurred when a 25-ps laser pulse was focused into a 5-cm-long cell filled with $D_2O$. A continuum was produced. Using 10-nm-bandwidth narrowband filters, tunable pulses of less than 3 ps in the spectral range from 480 to 590 nm (Figure 2.28) were produced (Dorsinville et al., 1987).

To identify the SPM generation mechanism, the temporal distribution of the continuum spectrum was determined by measuring the time delay between the continuum and a reference beam at different wavelengths using a streak camera. The results are displayed in Figure 2.29, which is similar to data displayed in Figure 2.25. The time delay was ~22 ps for a 140-nm change in wavelength; as predicted by the SPM mechanism, the Stokes wavelength led the anti-Stokes wavelength (Alfano, 1972). The delay due to group velocity over a 5-cm $D_2O$ cell for the 140-nm wavelength change is less than 3 ps.

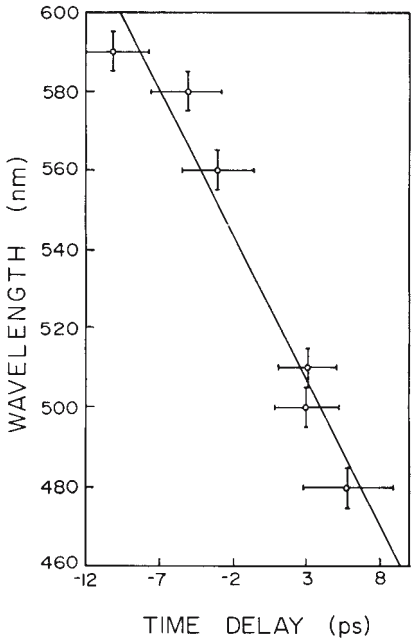


FIGURE 2.29. Continuum temporal distribution at different wavelengths. Horizontal error bars correspond to 10-nm band-widths of the filter. (From Dorsinville et al., 1987.)

The remaining 18 ps is well accounted for by the SPM mechanism using a 25-ps (FWHM) pulse and the stationary phase method (Alfano, 1972). Furthermore, a 10-nm selected region in the temporal distribution curve corresponds to an ~2.6-ps width matching the measured pulse duration (Figure 2.28). This observation suggests that by using narrower bandwidth filters the pulse duration can be shortened to the uncertainty limit.

## 12. Higher-Order Effects on Self-Phase Modulation

A complete description of SPM-generated spectral broadening should take into account higher-order effects such as self-focusing, group velocity dispersion, self-steepening, and initial pulse chirping. Some of these effects are described by Suydam (Chapter 6), Shen (Chapter 1), and Agrawal (Chapter 3). These effects will influence the observed spectral profiles.

### 12.1 Self-Focusing

In the earliest experiments using picosecond pulses, the supercontinuum pulses were often generated in small-scale filaments resulting from the self-focusing of intense laser beams (Alfano, 1972). Self-focusing arises from the radial dependence of the nonlinear refractive index $n(r) = n_0 + n_2E^2(r)$ (Shen, 1984; Auston, 1977). It has been observed in many liquids, bulk materials (Shen, 1984), and optical fibers (Baldeck et al., 1987a). It effects on the continuum pulse generation can be viewed as good and bad. On the one hand,

it facilitates the spectral broadening by concentrating the laser beam energy. On the other hand, self-focusing is a random and unstable phenomenon that is not controllable. Femtosecond supercontinua are generated with thinner samples than picosecond supercontinua, so it can reduce but not totally eliminate self-focusing effects.

## 12.2 Dispersion

Group velocity dispersion (GVD) arises from the frequency dependence of the refractive index. These effects are described by Agrawal (Chapter 3). The first-order GVD term leads to a symmetric temporal broadening (Marcuse, 1980). A typical value for the broadening rate arising from $\partial^2 k/\partial\omega^2$ is 500 fs/m · nm (in silica at 532 nm). In the case of supercontinuum generation, spectral widths are generally large (several hundred nanometers), but interaction lengths are usually small (<1 cm). Therefore, the temporal broadening arising from GVD is often negligible for picosecond pulses but is important for femtosecond pulses. Limitations on the spectral extent of supercontinuum generation are also related to GVD. Although the spectral broadening should increase linearly with the medium length (i.e., $\Delta\omega(z)_{\max} = \omega_0 n_2 a^2 z/c\,\Delta\tau$), it quickly reaches a maximum as shown in Figure 2.10. This is because GVD, which is large for pulses having SPM-broadened spectra, reduces the pulse peak power $a^2$ and broadens the pulse duration $\Delta\tau$. As shown in Figure 2.25, the linear chirp parameter is decreased by the GVD chirp in the normal dispersion regime. This effect is used to linearize chirp in the pulse compression technique.

The second-order term $\partial^3 k/\partial\omega^3$ has been found to be responsible for asymmetric distortion of temporal shapes and modulation of pulse propagation in the lower region of the optical fiber (Agrawal and Potasek, 1986). Since the spectra of supercontinuum pulses are exceptionally broad, this term should also lead to asymmetric distortions of temporal and spectral shapes of supercontinuum pulses generated in thick samples. These effects have been observed.

In multimode optical fibers, the mode dispersion dominates and causes distortion of the temporal shapes. This in turn yields asymmetric spectral broadening (Wang et al., 1988).

## 12.3 Self-Steepening

Pulse shapes and spectra of intense supercontinuum pulses have been found to be asymmetric (De Martini et al., 1967). There are two potential sources of asymmetric broadening in supercontinuum generation. The first one is the second-order GVD term. The second one is self-steepening, which is intrinsic to the SPM process and occurs even in nondispersion media. Details of the effects of self-steepening can be found in Suydam (Chapter 6), Shen and Yang (Chapter 1), and Manassah (Chapter 5).

Because of the intensity and time dependence of the refractive index, $n = n_0 + n_2 E(t)^2$, the supercontinuum pulse peak sees a higher refractive index than its edges. Because $v = c/n$, the pulse peak travels slower than the leading and

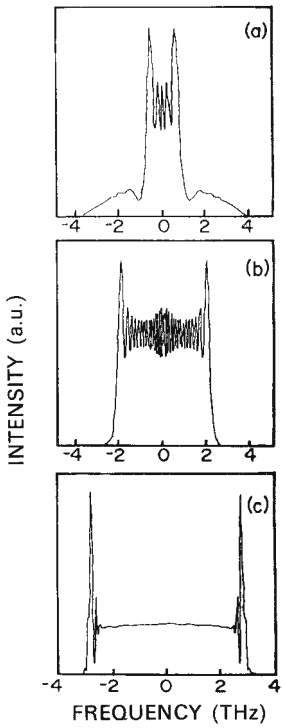


FIGURE 2.30. Influence of initial pulse chirping on SPM-broadened spectra in optical fibers. Peak power = 1000 W. (a) $C = 50$; (b) $C = 0$; (c) $C = -50$ [see Eq. (17)]. (From Baldeck et al., 1987b.)

trailing edges. This results in a sharpened trailing edge. Self-steepening occurs and more blue-shifted frequencies (sharp trailing edge) are generated than red frequencies. Several theoretical approaches have given approximate solutions for the electric field envelope distorted by self-steepening and asymmetric spectral extent. Actual self-steepening effects have not been observed in the time domain.

### 12.4 Initial Pulse Chirping

Most femtosecond and picosecond pulses are generated with initial chirps. Chirps arise mainly from GVD and SPM in the laser cavity. As shown in Figure 2.30, the spectral broadening is reduced for positive chirps and enhanced for negative chirps in the normal dispersion regime. The spectral distribution of SPM is also affected by the initial chirp.

## 13. Overview

Supercontinuum generation is the generation of bursts of "white" light, which can be obtained by passing intense picosecond or femtosecond pulses through various materials. Because of the nonlinear response of the medium,

the pulse envelope yields a phase modulation that initiates the wide frequency broadening (up to 10,000 $cm^{-1}$). The phase modulation can be generated by the pulse itself, a copropagating pump pulse, or the copropagating stronger pulse. These different configurations are called self-phase modulation (SPM), induced-phase modulation (IPM), and cross-phase modulation (XPM), respectively. The SPM process for supercontinuum generation in various materials was reviewed in this chapter. This latter two processes are closely related to each other and are described by Baldeck et al. (Chapter 4), Agrawal (Chapter 3), and Manassah (Chapter 5).

Using an 8-ps laser at 530 nm, typical Stokes sweeps were 4400 $cm^{-1}$ in a calcite crystal of length 4 cm, 3900 $cm^{-1}$ in a quartz crystal of length 4.5 cm, 1100 $cm^{-1}$ in extra-dense flint glass of length 7.55 cm, 3900 $cm^{-1}$ in NaCl of length 4.7 cm, and 4200 $cm^{-1}$ in both BK-7 and LBC-1 glasses of length 8.9 cm. Sweeps on the anti-Stokes side were typically 6100 $cm^{-1}$ in calcite, 5500 $cm^{-1}$ in quartz, 7300 $cm^{-1}$ in NaCl, and 7400 $cm^{-1}$ in BK-7 and LBC-1 glasses. An infrared supercontinuum spanning the range from 3 to 14 $\mu$m can be obtained by passing an intense laser pulse generated from a $CO_2$ laser through GaAs, AgBr, ZnSe, and CdS crystals. Near- and medium-infrared spectral sweeps of 3200 $cm^{-1}$ on the Stokes side and 4900 $cm^{-1}$ on the anti-Stokes side can be realized by passing a strong 1.06-$\mu$m pulse through a KBr crystal of length 10 cm. Sweeps on the order of 1000 $cm^{-1}$ are observed to both the red and blue sides of 530 nm in liquid argon. Similar spectral sweeps are observed in liquid and solid krypton arising from electronic mechanism for SPM. Using a picosecond laser train of wavelength 530 nm, the spectra were broadened up to 3000 $cm^{-1}$ to either side of the laser frequency in a 5-cm-long magnetic $KNiF_3$ single crystal. Production of SPM near electronic levels of $PrF_3$ crystal and enhancement of supercontinuum in water by addition of $Zn^{2+}$ and $K^+$ cations have been also discussed. The temporal properties of supercontinuum pulses have been described. Higher-order effects on SPM arising from dispersion, self-focusing, self-steepening, and initial pulse chirping were briefly described.

SPM will continue to be an important nonlinear process in science and technology and has been one of the most important ultrafast nonlinear optical processes for more than 20 years since the advent of ultrashort laser pulses!

## References

Agrawal, G.P. and M.J. Potasek (1986) Nonlinear pulse distortion in single-mode optical fibers at the zero-dispersion wavelength. Phys. Rev. A **33**, 1765–1776.

Alfano, R.R. (1972) Interaction of picosecond laser pulses with matter. GTE Technical Report TR 72–330. Published as Ph.D. thesis at New York University, 1972.

Alfano, R.R. (1986) The ultrafast supercontinuum laser source. *Proc. International Conference Laser* '85. STS Press, McLean, Virigina, pp. 110–122.

Alfano, R.R. and P.P. Ho (1988) Self-, cross-, and induced-phase modulations of ultrashort laser pulse propagation. IEEE J. Quantum Electron. **QE-24**, 351–363.

Alfano, R.R. and S.L. Shapiro (1970a) Emission in the region 4000–7000 A via four-photon coupling in glass. Phys. Rev. Lett. **24**, 584–587; Observation of self-phase modulation and small scale filaments in crystals and glasses. Phys. Rev. Lett. **24**, 592–594; Direct distortion of electronic clouds of rare-gas atoms in intense electric fields. Phys. Rev. Lett. **24**, 1219–1222.

Alfano, R.R. and S.L. Shapiro (1970b) Picosecond spectroscopy using the inverse Raman effect. Chem. Phys. Lett. **8**, 631–633.

Alfano, R.R., L. Hope, and S. Shapiro (1972) Electronic mechanism for production of self-phase modulation. Phys. Rev. A **6**, 433–438.

Alfano, R.R., J. Gersten, G. Zawadzkas, and N. Tzoar (1974) Self-phase-modulation near the electronic resonances of a crystal. Phys. Rev. A **10**, 698–708.

Alfano, R.R., P. Ho, P. Fleury, and H. Guggeneheim (1976) Nonlinear optical effects in antiferromagnetic $KNiF_3$. Opt. Commun. **19**, 261–264.

Alfano, R.R., Q. Li, T. Jimbo, J. Manassah, and P. Ho (1986) Induced spectral broadening of a weak picosecond pulse in glass produced by an intense ps pulse. Opt. Lett. **11**, 626–628.

Alfano, R.R., Q.Z. Wang, T. Jimbo, and P.P. Ho (1987) Induced spectral broadening about a second harmonic generated by an intense primary ultrashort laser pulse in ZnSe crystals. Phys. Rev. A **35**, 459–462.

Alfano, R.R., Q.Z. Wang, D. Ji, and P.P. Ho (1989) Harmonic cross-phase-modulation in ZnSe. App. Phys. Lett, **54**, 111–113.

Anderson, D. and M. Lisak (1983) Nonlinear asymmetric self-phase modulation and self-steepening of pulses in long optical waveguides. Phys. Rev. A **27**, 1393–1398.

Auston, D.H. (1977) In *Ultrafast Light Pulses*, S.L. Shapiro, ed., Springer, Verlag, New York.

Baldeck, P.L., F. Raccah, and R.R. Alfano (1987a) Observation of self-focusing in optical fibers with picosecond pulses. Opt. Lett. **12**, 588–589.

Baldeck, P.L., P.P. Ho, and R.R. Alfano (1987b) Effects of self-, induced-, and cross-phase modulations on the generation of ps and fs white light supercontinuum. Rev. Phys. Appl. **22**, 1877–1894.

Bloembergen, N. and P. Lallemand (1966) Complex intensity dependent index of refraction frequency broadening of stimulated Raman lines and stimulated Rayleigh scattering. Phys. Rev. Lett. **16**, 81–84.

Bourkoff, E., W. Zhao, and R.I. Joseph (1987) Evolution of femtosecond pulses in single-mode fibers having higher-order nonlinearity and dispersion. Opt. Lett, **12**, 272–274.

Brewer, R.G. (1967) Frequency shifts in self-focused light. Phys. Rev. Lett. **19**, 8–10.

Brewer, R.G. and C.H. Lee (1968) Self-trapping with picosecond light pulses. Phys. Rev. Lett. **21**, 267–270.

Busch, G.E., R.P. Jones, and P.M. Rentzepis (1973) Picosecond spectroscopy using a picosecond continuum. Chem. Phys. Lett. **18**, 178–185.

Chinn, S.R., H. Zeiger, and J. O'Connor (1971) Two-magnon Raman scattering and exchange interactions in antiferromagnetic $KNiF_3$ and $K_2NiF_4$ and ferrimagnetic $RbNiF_3$. Phys. Rev. **B3**, 1709–1735.

Corkum, P., P. Ho, R. Alfano, and J. Manassah (1985) Generation of infrared supercontinuum covering 3–14 $\mu$m in dielectrics and semiconductors. Opt. Lett. **10**, 624–626.

Corkum, P.B., C. Rolland, and T. Rao (1986) Supercontinuum generation in gases. Phys. Rev. Lett. **57**, 2268–2271.

Cornelius, P. and L. Harris (1981) Role of self-phase modulation in stimulated Raman scattering from more than one mode. Opt. Lett. **6**, 129–131.
DeMartini, F., C.H. Townes, T.K. Gustafson, and P.L. Kelly (1967) Self-steepening of light pulses. Phys. Rev. **164**, 312–322.
Dorsinville, R., P. Delfyett, and R.R. Alfano (1987) Generation of 3 ps pulses by spectral selection of the supercontinuum generated by a 30 ps second harmonic Nd: YAG laser pulse in a liquid. Appl. Opt. **27**, 16–18.
Fisher, R.A. and W. Bischel (1975) Numerical studies of the interplay wave laser pulse. J. Appl. Phys. **46**, 4921–4934.
Fisher, R.A., B. Suydam, and D. Yevich (1983) Optical phase conjugation for time domain undoing of dispersion self-phase modulation effects. Opt. Lett. **8**, 611–613.
Fleury, P.A., W. Hayes, and H.J. Guggenheim (1975) Magnetic scattering of light in $K(NiMg)F_3$. J. Phys. C: Solid State **8**, 2183–2189.
Fork, R.L., C.V. Shank, C. Hirliman, R. Yen, and J. Tomlinson (1983) Femtosecond white-light continuum pulse. Opt. Lett. **8**, 1–3.
Fork, R.L., C.H. Brito Cruz, P.C. Becker, and C.V. Shank (1987) Compression of optical pulses to six femtoseconds by using cubic phase compensation. Opt. Lett. **12**, 483–485.
Gersten, J., R. Alfano, and M. Belic (1980) Combined stimulated Raman scattering in fibers. Phys. Rev. A **21**, 1222–1224.
Girodmaine, J.A. (1962) Mixing of light beams in crystals. Phys. Rev. Lett. **8**, 19–20.
Glownia, J., G. Arjavalingam, P. Sorokin, and J. Rothenberg (1986) Amplification of 350-fs pulses in XeCl excimer gain modules. Opt. Lett. **11**, 79–81.
Goldberg, L. (1982) Broadband CARS probe using the picosecond continua. In *Ultrafast Phenomena III*. Springer-Verlag, New York, pp. 94–97.
Gomes, A.S.L., A.S. Gouveia-Neto, J.R. Taylor, H. Avramopoulos, and G.H.C. New (1986) Optical pulse narrowing by the spectral windowing of self-phase modulated picosecond pulses. Opt. Commun. **59**, 399.
Gustafson, T.K., I.P. Taran, H.A. Haus, J.R. Lifisitz, and P.L. Kelly (1969) Self-modulation, self-steepening, and spectral development of light in small-scale trapped filaments. Phys. Rev **177**, 306–313.
Gustafson, T.K., J. Taran, P. Kelley, and R. Chiao (1970) Self-modulation of picosecond pulse in electro-optical crystals. Opt. Commun. **2**, 17–21.
Hellwarth, R.W. (1970) Theory of molecular light scattering spectra using linear-dipole approximation. J. Chem. Phys. **52**, 2128–2138.
Hellwarth, R.W., J. Cherlow, and T.T. Yang (1975) Origin and frequency dependence of nonlinear optical susceptibilities of glasses. Phys. Rev. B **11**, 964–967.
Heritage, J., A. Weiner, and P. Thurston (1985) Picasecond pulse shaping by spectral phase and amplitude manipulation. Opt. Lett. **10**, 609–611.
Ho, P.P. and R.R. Alfano (1978) Coupled molecular reorientational relaxation kinetics in mixed binary liquids directly measured by picosecond laser techniques. J. Chem. Phys. **68**, 4551–4563.
Ho, P.P. and R.R. Alfano (1979) Optical Kerr effect in liquids. Phys. Rev. A **20**, 2170–4564.
Ho, P.P., Q.X. Li, T. Jimbo, Y.L. Ku, and R.R. Alfano (1987) Supercontinuum pulse generation and propagation in a liqud carbon tetrachloride. Appl. Opt. **26**, 2700–2702.
Ishida, Y., K. Naganuma, T. Yagima, and C. Lin (1984) Ultrafast self-phase modulation in a colliding pulse mode-locking ring dye laser. In *Ultrafast Phenomena IV*. Springer-Verlag, New York, pp. 69–71.

Jimbo, T., V.L. Caplan, Q.X. Li, Q.Z. Wang, P.P. Ho, and R.R. Alfano (1987) Enhancement of ultrafast supercontinuum generation in water by addition of $Zn^{2+}$ and $K^+$ cations. Opt. Lett. **12**, 477–479.

Johnson, A., R. Stolen, and W. Simpson (1986) The observation of chirped stimulated Raman scattering light in fibers. In *Ultrafast Phenomena* V.G.R. Fleming and A.E. Siegman ed. Springer-Verlag, New York, pp. 160–163.

Jones, W.J. and B.P. Stoicheff (1964) Inverse Raman spectra: induced absorption at optical frequencies. Phys. Rev. Lett. **13**, 657–659.

Knox, K., R.G. Shulman, and S. Sugano (1963) Covalency effects in $KNiF_3$. II. Optical studies. Phys. Rev. **130**, 512–516.

Knox, W., R. Fork, M. Dower, R. Stolen, and C. Shank (1985) Optical pulse compression to 8-fs at 5-kHz repetition rate. Appl. Phys. Lett. **46**, 1120–1121.

Kobayashi, T. (1979) Broadband picosecond light generation in phosphoric acid by a mode-locked laser. Opt. Commun. **28**, 147–149.

Lallemand, P. (1966) Temperature variation of the width of stimulated Raman lines in liquids. Appl. Phys. Lett. **8**, 276–277.

Levenson, M.D. and N. Bloembergen (1974) Dispersion of the nonlinear optical susceptibility tensor in centrosymmetric media. Phys. Rev. B **10**, 4447–4463.

L, Q.X., T. Jimbo, P.P. Ho, and R.R. Alfano (1986) Temporal distribution of picosecond super-continuum generated in a liquid measured by a streak camera. Appl. Opt. **25**, 1869–1871.

Lozobkin, V., A. Malytin, and A. Prohorov (1970) Phase self-modulation of Nd: glass radiation with mode-locking. JETP Lett. **12**, 150–152.

Magde, D. and M.W. Windsor (1974) Picosecond flash photolysis and spectroscopy: 3,3'-diethyloxadicarbocyanine iodide (DODCI). Chem. Phys. Lett. **27**, 31–36.

Manassah, J.T., P.P. Ho, A. Katz, and R.R. Alfano (1984) Ultrafast supercontinuum laser source. Photonics Spectra **18** November, 53–59.

Manassah, J.T, R.R., Alfano and M. Mustafa (1985a) Spectral distribution of an ultrashort supercontinuum laser source. Phys. Lett. A **107**, 305–309.

Manassah, J.T., M. Mustafa, R. Alfano, and P. Ho (1985b) Induced supercontinuum and steepening of an ultrafast laser pulse. Phys. Lett. **113A**, 242–247.

Manassah, J.T., M. Mustafa, R.R. Alfano, and P.P. Ho (1986) Spectral extent and pulse shape of the supercontinuum for ultrashort laser pulse. IEEE J. Quantum Electron. **QE-22**, 197–204.

Marcuse, D. (1980) Pulse distortion in single-mode optical fibers Appl. Opt. **19**, 1653–1660.

Masuhara, H., H. Miyasaka, A. Karen, N. Mataga, and Y. Tsuchiya (1983) Temporal characteristics of picosecond continuum as revealed by two-dimensional analysis of streak images. Opt. Commun. **4**, 426.

McTague, J., P., Fleury, and D. DuPre (1969) Intermolecular light scattering in liquids. Phys. Rev. **188**, 303–308.

Nakashima, N. and N. Mataga (1975) Picosecond flash photolysis and transient spectral measurements over the entire visible, near ultraviolet and near infrared regions. Chem. Phys. Lett. **35**, 487–492.

Patel, C.K.N. and E.D. Shaw (1971) Tunable stimulated Raman scattering from mobile carriers in semiconductors. Phys. Rev. **B 3**, 1279–1295.

Penzokfer, A., A. Laubereau, and W. Kasier (1973) Stimulated short-wave radiation due to single frequency resonances of $\chi^{(3)}$. Phys. Rev. Lett. **31** 863–866.

Potasek, M.J., G.P. Agrawal, and S.C. Pinault (1986) Analytical and numerical study of pulse broadening in nonlinear dispersive optical fibers. J. Opt. Soc. Am. **B 3**, 205–211.
Shank, C. (1983) Measurement of ultrafast phenomena in the femtosecond domain. Science **219**, 1027.
Shank, C.V., R.L. Fork, R. Yen, and R.H. Stolen (1982) Compression of femtosecond optical pulses. Appl. Phys. Lett. **40**, 761–763.
Sharma, D.K., R.W. Yid, D.F. Williams, S.E. Sugamori, and L.L.T. Bradley (1976) Generation of an intense picosecond continuum in $D_2O$ by a single picosecond 1.06 $\mu$ pulse. Chem. Phys. Lett. **41**, 460–465.
Shen, Y.R. (1966) Electrostriction, optical Kerr effect and self-focusing of laser beams. Phys. Lett. **20**, 378.
Shen Y.R. (1984) *The Principles of Nonlinear Optics.* Wiley, New York.
Shimizu, F. (1967) Frequency broadening in liquids by a short light pulse. Phys. Rev. Lett. **19**, 1097–1100.
Stolen, R.H. and A.M. Johnson (1986) The effect of pulse walkoff on stimulated Raman scattering in optical fibers. IEEE J. Quantum Electron. **QE-22**, 2154–2160.
Stolen, R.H. and C. Lin (1978) Self-phase modulation in silica optical fibers. Phys. Rev. A **17**, 1448–1453.
Topp, M.R. and G.C. Orner (1975) Group velocity dispersion effects in picosecond spectroscopy. Opt. Commun. **13**, 276.
Tzoar, N. and M. Jain (1981) Self-phase modulation in long-geometry waveguide. Phys. Rev. A **23**, 1266–1270.
Walrafen, G.E. (1972) Stimulated Raman scattering and the mixture model of water structure. Adv. Mol. Relaxation Processes **3**, 43–49.
Wang, Q.Z., D. Ji, Lina Yang, P.P. Ho, and R.R. Alfano (1989) Self-phase modulation in multimode optical fibers with modest high power. Produced by moderately high power picosecond pulses. *Opt. Lett.*, in press.
Yablonovitch, E. and N. Bloembergen (1972) Avalanche ionization of the limiting diameter of filaments induced by light pulses in transparent media. Phys. Rev. Lett. **29**, 907–910.
Yang, G. and Y.R. Shen (1984) Spectral broadening of ultrashort pulse in a nonlinear medium. Opt. Lett. **9**, 510–512.
Yu, W., R. Alfano, C.L. Sam, and R.J. Seymour (1975) Spectral broadening of picosecond 1.06 $\mu$m pulse in KBr. Opt. Commun. **14**, 344.

## Appendix: Nonlinear Wave Equation with Group Velocity Dispersion

We start with Maxwell equations for the electric and magnetic fields **E** and **H** in Gaussian units

$$\begin{aligned}
\nabla \times \mathbf{E} &= -\frac{1}{c}\frac{\partial \mathbf{B}}{\partial t}, \\
\nabla \times \mathbf{H} &= \frac{1}{c}\frac{\partial D}{\partial t} + \frac{4\pi}{c}\mathbf{J}, \\
\nabla \cdot \mathbf{D} &= 4\pi\rho, \\
\nabla \cdot \mathbf{B} &= 0.
\end{aligned} \tag{A.1}$$

The helping equations are $\mathbf{D} = \varepsilon\mathbf{E}$ and $\mathbf{B} = \mu\mathbf{H}$, and $\mathbf{J}$ and $\rho$ are the current and charge densities, respectively. For nonmagnetic material, $\mathbf{B} \approx \mathbf{H}$. The refractive index of an isotropic material possessing nonlinearity can be written as

$$n(\omega) = [\varepsilon(\omega)]^{1/2} = n_0(\omega) + n_2|\mathbf{E}|^2, \tag{A.2}$$

where $n_0(\omega)$ is the linear refractive index and $n_2$ the nonlinear refractive index. In the absence of sources, from Maxwell equations one can readily obtain the wave equation

$$\nabla^2\mathbf{E}(\mathbf{r},t) - \frac{1}{c^2}\frac{\partial^2}{\partial t^2}\mathbf{D}_L(\mathbf{r},t) = \frac{2n_0n_2}{c^2}\frac{\partial^2}{\partial t^2}\left(|\mathbf{E}|^2\,\mathbf{E}(\mathbf{r},t)\right), \tag{A.3}$$

where $\mathbf{D}_L(\mathbf{r}, t)$ is the linear electric displacement vector. In obtaining the equation, we have used $\nabla \times (\nabla \times \mathbf{E}) = \nabla(\nabla\cdot\mathbf{E}) - \nabla^2\mathbf{E}) \approx -\nabla^2\mathbf{E}$ and neglected the $(n_2)^2$ term.

The electric field can be written as

$$\mathbf{E}(\mathbf{r},t) = \Phi(x,y)\mathbf{E}(z,t), \tag{A.4}$$

where $\Phi(x, y)$ is the transverse distribition function. Substitute Eq. (A.4) into the wave equation and averaging over transverse coordinates, we have

$$\frac{\partial^2}{\partial z^2}\mathbf{E}(z,t) - \frac{1}{c}\frac{\partial^2}{\partial t^2}\mathbf{D}_L(z,t) = \frac{2n_0\bar{n}_2}{c^2}\frac{\partial^2}{\partial t^2}|\mathbf{E}(z,t)|^2\,\mathbf{E}(z,t). \tag{A.5}$$

We have neglected the $\partial^2/\partial x^2$ and $\partial^2/\partial y^2$ terms. The effective nonlinear refractive index $\bar{n}_2$ is

$$\bar{n}_2 = \frac{\int n_2\Phi^2(x,y)dxdy}{\int \Phi^2(x,y)dxdy} \approx \frac{1}{2}n_2. \tag{A.6}$$

Using a plane wave approximation with $(k_0z - \omega_0t)$ representation, a linearly polarized electric field propagating along $z$ direction can be written as

$$\mathbf{E}(z,t) = \hat{\mathbf{e}}A(z,t)\exp[i(k_0z - \omega_0t)], \tag{A.7}$$

where ê is the unit vector of polarization of electric field, $\omega_0$ the carrier frequency, $k_0$ the carrier wave number, and $A(z, t)$ the pulse envelope function. The form of $\mathbf{D}_L(z, t)$ becomes

$$\mathbf{D}_L(z,t) = \int_{-\infty}^{+\infty} n_0^2(\omega)\tilde{E}(z,\omega)\exp(-i\omega t)d\omega, \tag{A.8}$$

where

$$\tilde{E}(z,\omega) = \frac{1}{2\pi}\int_{-\infty}^{+\infty} E(z,t)\exp(i\omega t)dt. \tag{A.9}$$

If the $(\omega_0 t - k_0 z)$ representation is used, one obtains sign changes in the final reduced wave equation.

Using the foregoing equations, we can write the linear polarization term on the left-hand side of the one-dimensional wave equation as

$$\begin{aligned} &-\frac{1}{c^2}\frac{\partial^2}{\partial t^2}\mathbf{D}_L(z,t) \\ &= -\frac{1}{c^2}\int_{-\infty}^{+\infty}(-\omega^2)n_0^2(\omega)\tilde{E}(z,\omega)\exp(-i\omega t)d\omega \\ &= \frac{1}{2\pi}\int_{-\infty}^{\infty}\int_{-\infty}^{\infty}k^2(\omega)A(z,t')\exp[i\omega(t'-t)]\exp[i(k_0 z-\omega_0 t')]d\omega dt'. \end{aligned} \quad \text{(A.10)}$$

The derivation of the wave equation then proceeds by expanding $k^2(\omega)$ about the carrier frequency $\omega_0$ in the form:

$$k^2(\omega) \approx k_0^2 + 2k_0 k_0^{(1)}(\omega-\omega_0) + k_0 k_P^{(2)}(\omega-\omega_0)^2 + \cdots, \quad \text{(A.11)}$$

where $k_0 = k(\omega_0)$ is the propagation constant, $k_0^{(1)} = \left.\frac{\partial k}{\partial \omega}\right|_{\omega=\omega_0}$ is the inverse of group velocity, and $k_0^{(2)} = \left.\frac{\partial^2 k}{\partial \omega}\right|_{\omega=\omega_0}$ is the inverse of group velocity of dispersion. It is then possible to evaluate the integral of Eq. (A.10) by using the convenient delta function identities

$$\frac{1}{2\pi}\int_{-\infty}^{\infty}\exp[i(\omega-\omega_0)(t'-t)]d\omega = \delta(t'-t) \quad \text{(A.12)}$$

as well as

$$\frac{1}{2\pi}\int_{-\infty}^{\infty}(\omega-\omega_0)\exp[i(\omega-\omega_0)(t'-t)]d\omega = i\delta^{(1)}(t'-t), \quad \text{(A.13)}$$

and

$$\frac{1}{2\pi}\int_{-\infty}^{\infty}(\omega-\omega_0)^2\exp[i(\omega-\omega_0)(t'-t)]d\omega = -\delta^{(2)}(t'-t). \quad \text{(A.14)}$$

In these relations, $\delta^{(n)}(t)$ is an $n$th-order derivative of the Dirac delta function, with the property that

$$\int_{-\infty}^{\infty}\delta^{(n)}(t-t_0)f(t)dt = \left.\frac{d^n f(t)}{\partial t^n}\right|_{t=t_0} \quad \text{(A.15)}$$

when applied to a function $f(t)$. Substitute Eq. (A.11) into Eq. (A.10) and use Eq. (A.12) to (A.15), the second term on the left-hand side of Eq. (1.5) becomes

$$
\begin{aligned}
&-\frac{1}{c^2}\frac{\partial^2}{\partial t^2}\mathbf{D}_L(z,t)\\
&=\frac{1}{2\pi}\int_{-\infty}^{\infty}\int_{-\infty}^{\infty}\left[k_0^2+2k_0k_0^{(1)}(\omega-\omega_0)+k_0k_0^{(2)}(\omega-\omega_0)^2\right]A(z,t')\\
&\quad\times\exp[i\omega(t'-t)]\exp[i(k_0z-\omega_0t)]d\omega dt'\\
&=\int_{-\infty}^{\infty}\left[k_0^2\delta(t'-t)+i2k_0k_0^{(1)}\delta^{(1)}(t'-t)-k_0k_0^{(2)}\delta^{(2)}(t'-t)\right]A(z,t')\\
&\quad\times\exp[i(k_0z-\omega_0t)]dt'\\
&=\left[k_0^2A+i2k_0k_0^{(2)}\frac{\partial A}{\partial t}-k_0k_0^{(2)}\frac{\partial^2A}{\partial t^2}\right]\exp[i(k_0z-\omega_0t)].
\end{aligned}
\tag{A.16}
$$

Neglecting the second derivative of $A(z, t)$ with respect to $z$ and $\frac{\partial^2}{\partial t^2}|A(z,t)|^2$. $A(z, t)$, the first term on the left-hand side and the term on the right-hand side of Eq. (1.5) are simply

$$
\frac{\partial^2E(z,t)}{\partial z^2}\approx\left[-k_0^2A(z,t)+i2k_0\frac{\partial A(z,t)}{\partial z}\right]\exp[i(k_0z-\omega_0t)],
\tag{A.17}
$$

and

$$
\frac{2n_0\bar{n}_2}{c^2}\frac{\partial^2}{\partial t^2}|E|^2E\approx-\frac{n_0n_2\omega_0^2}{c^2}|A|^2A\exp[i(k_0z-\omega_0t)],
\tag{A.18}
$$

respectively.

Inserting Eqs. (A.16) to (A.18) into Eq. (1.5), the wave equation for electric field reduces to the wave equation for the pulse envelope

$$
i\left(\frac{\partial A}{\partial z}+\frac{1}{v_g}\frac{\partial A}{\partial t}\right)-\frac{1}{2}k_0^{(2)}\frac{\partial^2A}{\partial t^2}+\frac{\omega_0}{2c}n_2|A|^2A=0,
\tag{A.19}
$$

where $v_g \equiv 1/k_0^{(1)}$ is the group velocity. In Eq. (A.19), the first two terms describe the envelope propagation at the group velocity $v_g$; the third term determines the temporal pulse broadening due to group velocity dispersion; the fourth characterizes the second order of the nonlinear polarization, which is responsible for the self-phase modulation effect and spectral broadening. Neglecting the group velocity dispersion term in Eq. (A.19), we obtain

$$
\frac{\partial A}{\partial z}+\frac{1}{v_g}\frac{\partial A}{\partial t}=i\frac{\omega_0}{2c}n_2|A|^2A.
\tag{A.20}
$$

This is Eq. (2.2).

# 3
# Ultrashort Pulse Propagation in Nonlinear Dispersive Fibers

Govind P. Agrawal

## 1. Introduction

The use of silica fibers for transmission of optical pulses has become widespread, as is evident from the recent advances in optical fiber communications (Basch, 1986; Miller and Kaminow, 1988). For pulses not too short (pulse width >1 ns) and not too intense (peak power <10 mW), the fiber plays a passive role (except for energy loss) and acts as a transporter of optical pulses from one place to another without significantly affecting their shape or spectrum. However, as pulses become shorter and more intense, two physical mechanisms, chromatic dispersion and index nonlinearity, both intrinsic to the silica material, start to affect the pulse shape and spectrum during propagation.

The fiber has found many novel and interesting applications in this active role. It has been used for pulse compression (Shank et al., 1982; Nikolaus and Grischkowsky, 1983), and pulses with durations as short as 6 fs have been produced (Fork et al., 1987). Such short pulses provide the capability for ultrafast continuum spectroscopy with a time resolution approximating that allowed by the transform-limited bandwidth (Shank et al., 1986). In the anomalous dispersion regime the fiber supports optical solitons resulting from a balance between the dispersive and nonlinear effects (Hasegawa and Tappert, 1973; Mollenauer et al., 1980). The solitons may be useful for high-speed optical communications over long distances (Hasegawa, 1983; Mollenauer et al., 1986). The soliton formation capacity of optical fibers has also been exploited to develop the soliton laser (Mollenauer and Stolen, 1984). An important application of optical fibers is in the field of ultrafast super-continuum generation (Alfano, 1985; Shank et al., 1986). Several nonlinear effects such as self-phase modulation (SPM), cross-phase modulation (XPM), and stimulated Raman scattering (SRS) can lead to an extensive spectral broadening of the incident pulse, resulting in an almost "white" spectrum (Alfano and Shapiro, 1970). Although SPM in optical fibers was studied nearly a decade ago (Stolen and Lin, 1978), it is only recently that the effect of XPM on propagation of ultrashort pulses in optical fibers has attracted

attention (Alfano et al., 1987; Islam et al., 1987; Agrawal, 1987; Schadt and Jaskorzynska, 1987; Baldeck et al., 1987).

This chapter reviews how the nonlinear and dispersive effects in optical fibers influence the propagation characteristics of ultrashort pulses with widths in the picosecond range. In Section 2 we outline the derivation of the basic propagation equation satisfied by the amplitude of the pulse envelope. In the presence of SRS it becomes necessary to consider the coupled amplitude equations satisfied by the pump and Raman pulses. These equations include the effect of group velocity mismatch, group velocity dispersion, SPM, XPM, SRS gain, and pump depletion. Section 3 considers the propagation of a single pulse below the SRS threshold and identifies various propagation regimes. Sections 4 and 5 then consider the cases of normal dispersion and anomalous dispersion regimes separately. The effect of SRS on pulse propagation is studied in Section 6, where the results of numerical simulations are presented and compared with the experiments. Particular attention is paid to the XPM effects in Section 7, where the case of two incident pulses is investigated. Finally, Section 8 gives a brief summary of the main conclusions of the chapter.

## 2. Propagation Equation

As is the case for all electromagnetic phenomena, pulse propagation in optical fibers is governed by Maxwell's equations. For a nonmagnetic medium, this amounts to solving the wave equation

$$\nabla \times \nabla \times \mathbf{E} = -\mu_0 \frac{\partial^2 \mathbf{D}}{\partial t^2}, \tag{1}$$

where $\mathbf{E}$ is the electric field, $\mu_0$ is the vacuum permeability, and $\mathbf{D}$ is the electric flux density. The constitutive relation between $\mathbf{D}$ and $\mathbf{E}$ takes a simple form in the frequency domain and can be written as

$$\tilde{\mathbf{D}}(\mathbf{r}, \omega) = \varepsilon_0 \tilde{n}^2 \tilde{\mathbf{E}}(\mathbf{r}, \omega), \tag{2}$$

where $\varepsilon_0$ is the vacuum permittivity, $\tilde{n}$ is the refractive index, and $\tilde{\mathbf{E}}$ and $\tilde{\mathbf{D}}$ are the Fourier transforms of $\mathbf{E}$ and $\mathbf{D}$ respectively, i.e.,

$$\tilde{\mathbf{E}}(\mathbf{r}, \omega) = \frac{1}{2\pi} \int_{-\infty}^{\infty} \mathbf{E}(\mathbf{r}, t) \exp(i\omega t) dt \tag{3}$$

with a similar relation for $\tilde{\mathbf{D}}(\mathbf{r}, \omega)$. Using Eqs. (1)–(3), we obtain

$$\nabla^2 \tilde{\mathbf{E}} + (\tilde{n}\omega/c)^2 \tilde{\mathbf{E}} = 0, \tag{4}$$

where we have assumed that $\nabla \cdot \mathbf{E} \cong 0$. A suitable form for the refractive index in optical fibers is

$$\tilde{n} = n(\mathbf{r}, \omega) + i\alpha c/2\omega + n_2 |\mathbf{E}|^2, \tag{5}$$

where the linear index $n(\mathbf{r}, \omega)$ is inhomogeneous (in the transverse dimensions $x$ and $y$) to account for dielectric waveguiding and is frequency dependent to account for chromatic dispersion in silica fibers. The fiber loss is taken into account by the absorption coefficient $\alpha$. Finally, the last term in Eq. (5) accounts for the fiber nonlinearity. The nonlinear coefficient $n_2 = 3.2 \times 10^{-16}\,\text{cm}^2/\text{W}$ for silica fibers and is nearly frequency independent in the frequency range of interest. It is implicitly assumed that the nonlinear response is instantaneous, an assumption that becomes questionable for ultrashort optical pulses with widths <0.1 ps.

Since the refractive index does not vary appreciably along the fiber length ($z$ direction), Eq. (4) can be solved by assuming that

$$\tilde{\mathbf{E}}(x, y, z, \omega) = \hat{e}\tilde{a}(z, \omega)\psi(x, y) = \hat{e}E_0\psi(x, y)\exp(i\tilde{\beta}z), \tag{6}$$

where $\hat{e}$ is the polarization unit vector, $\tilde{\beta}$ is the wave number, and $\psi(x, y)$ is obtained by solving

$$\frac{\partial^2\psi}{\partial x^2} + \frac{\partial^2\psi}{\partial y^2} + \left(\frac{\tilde{n}^2\omega^2}{c^2} - \tilde{\beta}^2\right)\psi = 0. \tag{7}$$

Since the last two terms in Eq. (5) are much smaller than the linear index $n(x, y, \omega)$, they can be treated by first-order perturbation theory. The complex wave number $\tilde{\beta}$ is thus well approximated by

$$\tilde{\beta} \cong \beta(\omega) + i\alpha/2 + \Delta\beta_{\text{NL}}, \tag{8}$$

where

$$\Delta\beta_{\text{NL}} = \frac{n_2\omega}{c}\iint_{\sigma}|\psi(x, y)|^2|\mathbf{E}|^2\,dxdy \tag{9}$$

and $\beta(\omega)$ is obtained by solving the eigenvalue equation

$$\frac{\partial^2\psi}{\partial x^2} + \frac{\partial^2\psi}{\partial y^2} + \left(n(x, y, \omega)\frac{\omega^2}{c^2} - \beta^2(\omega)\right)\psi = 0 \tag{10}$$

for a given index distribution of the fiber. For a single-mode fiber, $\psi(x, y)$ is the field distribution of the fundamental fiber mode and has been taken to satisfy the normalization condition

$$\iint_{\sigma}|\psi(x, y)|^2\,dxdy = 1, \tag{11}$$

where the integration is carried over the fiber cross section $\sigma$.

The dispersion relation (8) can be used to obtain the envelope propagation equation by noting from Eq. (6) that

$$\frac{\partial\tilde{a}}{\partial z} = i[\beta(\omega) + i\alpha/2 + \Delta\beta_{\text{NL}}]\tilde{a}. \tag{12}$$

Since the pulse spectrum is centered at the carrier frequency $\omega_0$, it is useful to expand $\beta(\omega)$ in a Taylor series

$$\beta(\omega) = \beta_0 + (\omega - \omega_0)\beta_1 + \tfrac{1}{2}(\omega - \omega_0)^2 \beta_2 + \tfrac{1}{6}(\omega - \omega_0)^3 \beta_3 + \cdots, \tag{13}$$

where $\beta_n = d^n\beta/d\omega^n$ is evaluated at $\omega_0$. The cubic and higher-order terms are generally neglected by assuming that the spectral width $\Delta\omega \ll \omega_0$. If $\beta_2 \simeq 0$ for some specific values of $\omega_0$ or if the pulses are ultrashort (<0.1 ps), it may be necessary to include the cubic term. It is useful to define the slowly varying pulse amplitude $A(z, t)$ by using

$$a(z, t) = A(z, t)\exp[i(\beta_0 z - \omega_0 t)], \tag{14}$$

where $a(z, t)$ is the inverse Fourier transform of $\tilde{a}(z, \omega)$. During the Fourier transform operation $\omega - \omega_0$ is replaced by the differential operator $i(\partial/\partial t)$. The use of Eqs. (12)–(14) then leads to the following propagation equation:

$$\frac{\partial A}{\partial z} + \beta_1 \frac{\partial A}{\partial t} + \frac{\alpha}{2} A + \frac{i}{2}\beta_2 \frac{\partial^2 A}{\partial t^2} = i\gamma |A|^2 A, \tag{15}$$

where the nonlinearity coefficient

$$\gamma = n_2 \omega_0 / c A_{\text{eff}}. \tag{16}$$

The parameter $A_{\text{eff}}$ is known as the effective fiber core area and from Eq. (9) is given by (noting that $E = A\psi$)

$$A_{\text{eff}}^{-1} = \iint_{\sigma} |\psi(x, y)|^4 \, dx dy. \tag{17}$$

Equation (15) describes the propagation of an optical pulse in single-mode fibers. The pulse envelope moves at the group velocity $v_g = 1/\beta_1$. The group velocity dispersion (GVD) is included through the parameter $\beta_2$ while the parameter $\gamma$ takes into account the fiber nonlinearity responsible for SPM. Both material dispersion and waveguide dispersion contribute to $\beta_2$. However, the contribution of material dispersion generally dominates. In that case $\beta_2$ can be approximated by

$$\beta_2 \simeq (\lambda/2\pi c^2) D(\lambda), \tag{18}$$

where $\lambda = 2\pi c/\omega_0$ is the carrier wavelength and $D(\lambda) = \lambda^2(d^2n/d\lambda^2)$. For silica fibers $D(\lambda) = 0.066$ at $\lambda = 0.53\,\mu$m, and therefore $\beta_2 \simeq 0.06\,\text{ps}^2/\text{m}$. The nonlinearity parameter $\gamma$ depends on the fiber parameters through $A_{\text{eff}}$. Its estimated values are in the range 0.01 to $0.02\,\text{W}^{-1}\,\text{m}^{-1}$. The GVD parameter $\beta_2$ becomes negative for $\lambda > \lambda_{ZD}$, where $\lambda_{ZD}$ is sometimes referred to as the zero-dispersion wavelength. In the anomalous dispersion regime ($\beta_2 < 0$), the fiber can support optical solitons. The wavelength $\lambda_{ZD} \cong 1.3\,\mu$m but can be changed in the range 1.2 to 1.6 $\mu$m by modifying the fiber design that changes the waveguide dispersion contribution to $\beta_2$.

Depending on the experimental conditions, Eq. (15) may need modification. For example, this equation does not include the effect of SRS that

becomes important at high power levels. SRS transfers the pulse energy to the Stokes pulse (shifted downward in frequency by about 13 THz) as the pump pulse propagates inside the fiber. Equation (15) can be generalized to include SRS if we include the Raman gain and consider a coupled set of equations describing the interaction between the pump and Stokes pulses with amplitudes $A_1$ and $A_2$, respectively;

$$\frac{\partial A_1}{\partial z}+\frac{1}{v_{g1}}\frac{\partial A_1}{\partial t}+\frac{1}{2}\left(\alpha_1+g_1|A_2|^2\right)A_1 + \frac{i}{2}\beta_{21}\frac{\partial^2 A_1}{\partial t^2}-i\gamma_1\left(|A_1|^2+2|A_2|^2\right)A_1=0, \tag{19}$$

$$\frac{\partial A_2}{\partial z}+\frac{1}{v_{g2}}\frac{\partial A_2}{\partial t}+\frac{1}{2}\left(\alpha_2-g_2|A_1|^2\right)A_2 + \frac{i}{2}\beta_{22}\frac{\partial^2 A_2}{\partial t^2}-i\gamma_2\left(|A_2|^2+2|A_1|^2\right)A_2=0. \tag{20}$$

Here $v_{gj}=\beta_j^{-1}$ is the group velocity, $g_j$ is the Raman gain coefficient, $\beta_{2j}$ is the GVD coefficient, and $\gamma_j$ is the nonlinear coefficient ($j=1$ and 2 for pump and Stokes pulses, respectively). It is important to include both SPM and XPM in the nonlinear term (Gersten et al., 1980; Schadt and Jaskorzynska, 1987; Agrawal, 1987).

Equation (15) should also be modified for ultrashort optical pulses with widths $\lesssim 0.1$ ps. The spectral width $\Delta\omega$ of such pulses becomes comparable to the carrier frequency $\omega_0$, and several approximations made in the derivation of Eq. (15) become questionable. Furthermore, the pulse spectrum is wide enough that the low-frequency components get amplified from the Raman gain at the expense of the high-frequency components. As a result, the spectrum shifts toward shorter frequencies as the pulse propagates inside the fiber, a phenomenon referred to as self-frequency shift (Mitschke and Mollenauer, 1986; Gordon, 1986). One can no longer consider the pump and Stokes pulses separately. Rather than using Eqs. (19) and (20) to describe SRS and related nonlinear effects, a generalization of Eq. (15) is needed. Kodama and Hasegawa (1987) have carried out such a generalization. The resulting propagation equation is

$$\frac{\partial A}{\partial z}+\beta_1\frac{\partial A}{\partial t}+\frac{\alpha}{2}A=-\frac{i}{2}\beta_2\frac{\partial^2 A}{\partial t^2}+i\gamma|A|^2A+\frac{1}{6}\beta_3\frac{\partial^3 A}{\partial t^3} -a_1\frac{\partial}{\partial t}\left(|A|^2A\right)-a_2A\frac{\partial|A|^2}{\partial t}. \tag{21}$$

This equation has three additional terms compared with Eq. (15). The term proportional to $\beta_3$ results from including the cubic term in the expansion (13). The term proportional to $a_1$ is responsible for self-steepening; $a_1$ is generally approximated by $a_1 \simeq 2\gamma/\omega_0$. The term proportional to $a_2$ includes the effect

of SRS among other things. In particular, the imaginary part of $a_2$ is responsible for the self-frequency shift. The physical origin of this effect is related to the retarded nonlinear response of the fiber. In this chapter we do not consider these effects and only refer to the recent work (Zysset et al., 1987; Bourkoff et al., 1987; Golovchenko et al., 1987; Vysloukh and Matveeva, 1987; Serkin, 1987).

## 3. Propagation Regimes

We first consider the case of pulse propagation below the SRS threshold such that Eq. (15) is applicable. It is useful to define the normalized variables

$$\tau = (t - \beta_1 z)/T_0, \qquad A = \sqrt{P_0}\exp(-\alpha z/2)U, \tag{22}$$

where $T_0$ and $P_0$ are related to the width and the peak power of the incident pulse. Equation (15) then takes the form

$$i\frac{\partial U}{\partial z} = \pm\frac{1}{2L_D}\frac{\partial^2 U}{\partial \tau^2} - \frac{1}{L_{NL}}e^{-\alpha z}|U|^2 U, \tag{23}$$

where

$$L_D = T_0^2/|\beta_2| \quad \text{and} \quad L_{NL} = (\gamma P_0)^{-1}. \tag{24}$$

The choice of the sign in the dispersion term depends on the sign of $\beta_2$; a plus sign is chosen for normal GVD ($\beta_2 > 0$) and a minus sign is chosen for anomalous GVD ($\beta_2 < 0$). The dispersion length $L_D$ and the nonlinear length $L_{NL}$ provide the length scales over which dispersive and nonlinear effects become important. Depending on their relative magnitudes, pulse propagation in optical fibers can be classified in three different categories.

### 3.1 Dispersion-Dominant Regime

If the fiber length $L$ is such that $L \ll L_{NL}$ while $L \sim L_D$, the nonlinear term in Eq. (23) plays a relatively minor role and can be neglected. The resulting linear equation is readily solved to yield

$$U(z,\tau) = \int_{-\infty}^{\infty}\tilde{U}(0,\omega)\exp[-i\omega\tau \pm i\omega^2(z/2L_D)]d\omega, \tag{25}$$

where $\tilde{U}(0, \omega)$ is the Fourier transform of the incident pulse amplitude $U(0, \tau)$. Equation (25) has been widely used to study pulse broadening in the dispersion-dominant regime. In particular, a simple analytic expression for the pulse width can be obtained for Gaussian pulses (Marcuse, 1981). For an unchirped Gaussian pulse, $U(0, \tau) = \exp(-\tau^2/2)$, and the pulse broadens by a factor of $(1 + z^2/L_D^2)^{1/2}$ as it propagates along the fiber. The dispersion length $L_D$ corresponds to the fiber length over which the pulse width increases by

about 40% (in the absence of nonlinear effects). The dispersion-dominant regime or Eq. (25) is applicable when the fiber and pulse parameters are such that

$$\frac{L_D}{L_{NL}} = \frac{\gamma P_0 T_0^2}{|\beta_2|} \ll 1. \tag{26}$$

As a rough estimate, $P_0$ should be less than 10 mW for 10-ps pulses.

## 3.2 Nonlinearity-Dominant Regime

If the fiber length $L$ is such that $L \ll L_D$ while $L \gtrsim L_{NL}$, the dispersion term in Eq. (23) plays a relatively minor role and can be neglected as long as the pulse shape is relatively smooth so that $|\partial^2 U/\partial\tau^2|$ is not too large. The resulting equation can be solved analytically with the result

$$U(z,\tau) = U(0,\tau)\exp[i\phi_{\text{SPM}}(z,\tau)], \tag{27}$$

where

$$\phi_{\text{SPM}}(z,\tau) = \left(\frac{1-e^{-\alpha z}}{\alpha L_{NL}}\right)|U(0,\tau)|^2. \tag{28}$$

Equation (27) shows that the nonlinearity gives rise to SPM while it does not affect the pulse shape. The effect of SPM is to broaden the pulse spectrum with considerable internal structure. Figure 3.1 shows the calculated SPM spectra for a Gaussian pulse obtained by taking the Fourier transform of Eq. (27) with $\alpha = 0$ and $z = 40L_{NL}$. Quite generally, the number of internal peaks increases linearly with the fiber length (for $\alpha = 0$), and the dominant peaks occur near the spectral boundaries. The spectral range is determined by $\Delta\omega_{\max} = |\partial\phi_{\text{SPM}}/\partial t|_{\max}$, which is the maximum chirp induced by the nonlinearity. The SPM-induced spectral features have been observed in optical fibers and were used to estimate $n_2$ (Stolen and Lin, 1978).

## 3.3 Dispersive Nonlinear Regime

When the fiber length $L$ is longer than or comparable to both $L_D$ and $L_{NL}$, dispersion and nonlinearity act together as the pulse propagates along the fiber. Their mutual interaction plays an important role and has been used to generate solitons and to compress optical pulses. To understand this interaction theoretically, Eq. (23) is solved numerically and has been found to be extremely helpful in interpreting the experimental results (Mollenauer et al., 1980; Grischowsky and Balant, 1982; Tomlinson et al., 1984). It is useful to normalize the fiber length by introducing $\xi = z/L_D$ and to write Eq. (23) in the following normalized form:

$$i\frac{\partial U}{\partial \xi} = \pm\frac{1}{2}\frac{\partial^2 U}{\partial \tau^2} - N^2 e^{-\alpha z}|U|^2 U, \tag{29}$$

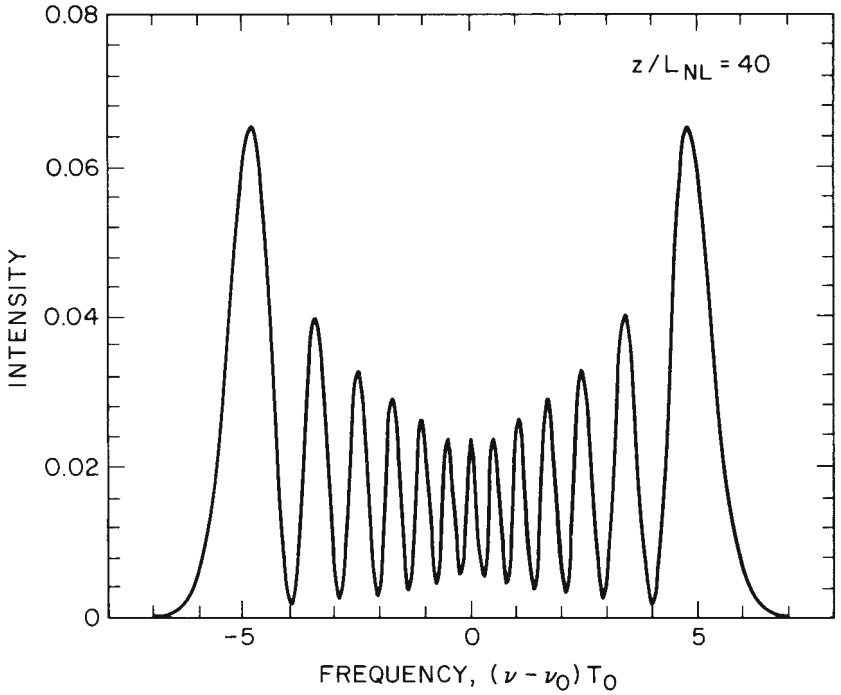


FIGURE 3.1. Calculated SPM spectrum of a Gaussian pulse (in the absence of dispersion) at a distance $z = 40L_{NL}$, where $L_{NL}$ is the nonlinear length defined by Eq. (24).

where

$$N^2 = \frac{L_D}{L_{NL}} = \frac{\gamma P_0 T_0^2}{|\beta_2|}. \tag{30}$$

In the lossless case ($\alpha = 0$), Eq. (29) is often referred to as the nonlinear Schrödinger equation (NSE). In the anomalous dispersion regime (corresponding to the choice of minus sign), the NSE is known to have exact solutions, known as solitons (Zakharov and Shabat, 1972; Hasegawa and Tappert, 1973). For an initial pulse shape $U(0, \tau) = \text{sech}(\tau)$ and integer values of the parameter $N$, the solitons follow a periodic evolution pattern with the period $\xi_0 = \pi/2$. In the unnormalized units, the soliton period $z_0$ becomes

$$z_0 = \frac{\pi}{2} L_D = \frac{\pi T_0^2}{2|\beta_2|}. \tag{31}$$

The fundamental soliton corresponds to $N = 1$ and propagates without change in its shape. From Eq. (30), the peak power necessary to excite the fundamental soliton is $P_1 = |\beta_2|/\gamma T_0^2$. For a hyperbolic secant pulse, the pulse width $T_p$ (FWHM) is related to $T_0$ by $T_p \simeq 1.76T_0$. This relation should be

used for comparison with experiments. As a rough estimate, for 1.55-$\mu$m solitons in silica fibers, $z_0 \sim 25\,\text{m}$ and $P_1 \sim 1\,\text{W}$ when $T_p = 1\,\text{ps}$.

In the next two sections we consider the pulse propagation characteristics in the normal and anomalous GVD regimes based on the numerical solution of Eq. (29). A fast Fourier transform (FFT)-based beam propagation method (Fleck et al., 1976; Lax et al., 1981; Agrawal and Potasek, 1986) was used for the numerical solution. Although a finite-difference scheme can be used, the FFT method is considerably faster for a given accuracy (typically by more than a factor of 10). In the FFT method, Eq. (29) is formally written as

$$\frac{\partial U}{\partial \xi} = (D+Q)U, \tag{32}$$

where

$$D = \pm\frac{i}{2}\frac{\partial^2}{\partial \tau^2} \quad \text{and} \quad Q = iN^2 e^{-\alpha z}|U|^2. \tag{33}$$

The field is propagated inside the fiber by a small distance $\delta$ using the following prescription:

$$U(\xi+\delta,\tau) = \left[\exp\left(\frac{\delta D}{2}\right)\exp\left(\int_{\xi}^{\xi+\delta} Q(\xi')d\xi'\right)\exp\left(\frac{\delta D}{2}\right)\right]U(\xi,\tau). \tag{34}$$

The numerical procedure consists of propagating the field by a distance $\delta/2$ with dispersion only, multiplying the result by a nonlinear term that represents the effect of nonlinearity over the whole step length $\delta$, and then propagating the field for the remaining distance $\delta/2$ with dispersion only. In effect, the nonlinearity is assumed to be lumped at the midplane of each segment. This technique is a generalization of the split-step method (Hasegawa and Tappert, 1973; Fisher and Bischel, 1975).

The propagation in a linear dispersive medium indicated by the exponential operator $\exp(\delta D/2)$ in Eq. (34) can be accomplished using the Fourier transform method. The use of the FFT algorithm makes this step relatively fast. The integral in Eq. (34) is well approximated using the trapezoidal rule:

$$\int_{\xi}^{\xi+\delta} Q(\xi')d\xi' \simeq \frac{1}{2}\delta[Q(\xi)+Q(\xi+\delta)]. \tag{35}$$

However, $Q(\xi+\delta)$ cannot be evaluated since $U(\xi+\delta,\tau)$ is not known while evaluating Eq. (35) at the midsegment located at $\xi+\delta/2$. One can approximate $Q(\xi+\delta)$ by $Q(\xi)$ if $|U|^2$ has not significantly changed in going from $\xi$ to $\xi+\delta$. This approximation can, however, restrict the step size $\delta$ to relatively small values. Another approach is to follow an iterative procedure in which Eq. (35) is evaluated several times with increasingly accurate values of $Q(\xi+\delta)$. In practice, two iterations are often sufficient to obtain the desired accuracy.

## 4. Normal Dispersion

In the normal dispersion regime, the GVD parameter $\beta_2 > 0$. For silica fibers, this regime corresponds to $\lambda < 1.3\,\mu$m and has been extensively studied because of the availability of solid-state and dye lasers in the visible region. At $\lambda = 0.53\,\mu$m, $\beta_2 \simeq 0.06\,\text{ps}^2\text{m}$ and $\gamma \simeq 0.01\,\text{W}^{-1}\text{m}^{-1}$ for typical fiber parameters. From Eq. (24), $L_D \sim 100\,$m for $T_0 \simeq 3$–$5\,$ps and $L_{NL} \sim 1\,$m for $P_0 \sim 100\,$W. Thus the parameter $N \sim 10$ under typical experimental conditions, although $N \sim 100$ is feasible for wider and more intense pulses. Figure 3.2 shows the evolution of pulse shape along the fiber for $N = 30$ after assuming $\alpha = 0$ and a Gaussian pulse with $U(0, \tau) = \exp(-\tau^2/2)$. As the pulse propagates, it broadens and develops a nearly rectangular profile with sharp leading and trailing edges. The combination of rapidly varying intensity and SPM in these steep-slope regions broadens the pulse spectrum. Because the new frequency components are mainly generated near the edges, the pulse develops a nearly linear frequency chirp across its entire width (Grischkowsky and Balant, 1982; Tomlinson et al., 1984). This linear chirp helps to compress the pulse by passing it subsequently through a dispersive delay line (often a grating pair).

An interesting feature of Figure 3.2 is the presence of rapid oscillations in the wings of the pulse. Tomlinson et al. (1985) have interpreted these oscillations in terms of optical wave breaking resulting from a mixing of the SPM-induced frequency-shifted components with the unshifted light in the wings. This phenomenon can also be understood as a four-wave mixing process and should be manifest through the presence of sidelobes in the pulse spectrum. Figure 3.3 shows the pulse shape and spectrum at $\xi = 0.08$. As seen there, oscillations near the pulse edges are accompanied by the sidelobes in the pulse spectrum. The central structure in the spectrum is due to SPM (see Figure 3.1).

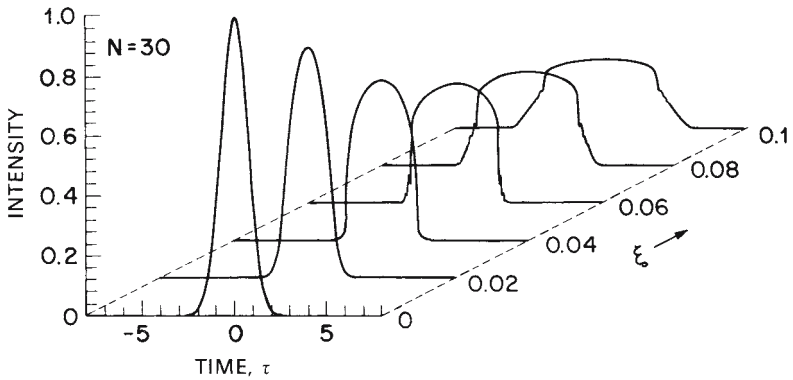


FIGURE 3.2. Evolution of the pulse shape of an unchirped Gaussian pulse along the fiber length ($\xi = z/L_D$) for $N = 30$ in the normal dispersion regime. The peak power is related to $N$ through Eq. (30).

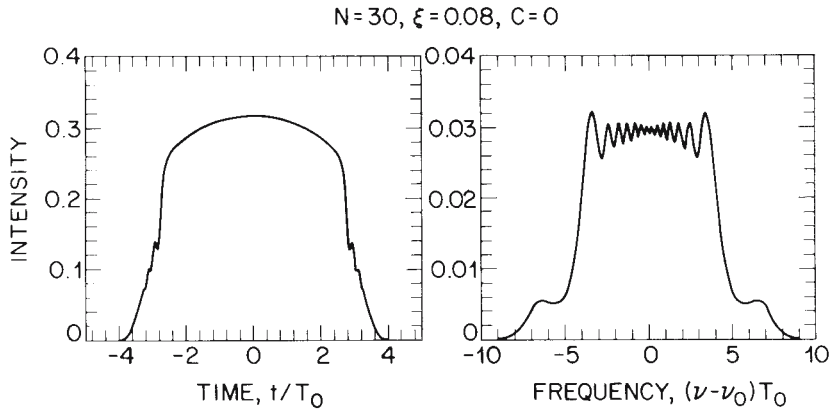


FIGURE 3.3. Pulse shape and spectrum of an unchirped Gaussian pulse at $\xi = 0.08$ for $N = 30$. Sidelobes in the spectrum and oscillations near the pulse edges are due to optical wave breaking.

The results shown in Figures 3.2 and 3.3 are for an initially unchirped pulse. The pulses emitted by practical laser sources are often chirped and may follow quite a different evolution pattern than that shown in Figure 3.2 (Lassen et al., 1985). To include the effect of initial chirp, the incident amplitude is taken to be

$$U(0,\tau) = \exp[-\tfrac{1}{2}(1+iC)\tau^2], \tag{36}$$

where $C$ is a measure of chirp. $C$ can be estimated by noting that the spectral width of the chirped pulse is larger by a factor of $(1 + C^2)^{1/2}$ than the transform-limited value for $C = 0$. Figure 3.4 shows the pulse shape and spectrum under conditions identical to those of Figure 3.3 except for the chirp parameter that has a value of $C = 20$. A comparison of Figures 3.3 and 3.4 shows how much an initial chirp can modify the propagation behavior. For example, the shape for the initially chirped pulse is nearly triangular rather than rectangular. The pulse evolution is also sensitive to the fiber loss (Lassen et al., 1985). Thus, for an actual comparison between theory and experiment it is necessary to include both the chirp and the loss in numerical simulations.

## 5. Anomalous Dispersion

In the anomalous dispersion regime, the GVD parameter $\beta_2 < 0$. For silica fibers, this regime corresponds to $\lambda > 1.3\,\mu$m and has been extensively studied, using color-center lasers, for example (Mollenauer et al., 1980). At $\lambda = 1.55\,\mu$m, $\beta_2 \simeq -0.02\,\text{ps}^2/\text{m}$ and $\gamma \simeq 0.01\,\text{W}^{-1}\,\text{m}^{-1}$ for typical fiber parameters. For $T_0 \simeq 1\,$ps, the dispersion length $L_D \simeq 50\,$m; the peak power correspond-

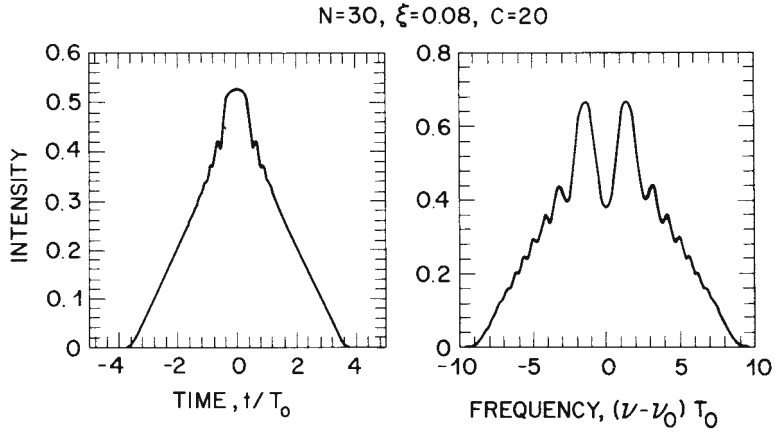


FIGURE 3.4. Pulse shape and spectrum for parameters identical to those of Figure 3.3 except for the chirp parameter, which has a value $C = 20$ instead of 0.

ing to the fundamental soliton ($N = 1$) can be estimated from Eq. (30) and is $P_0 \sim 1$ W. In the absence of fiber loss, the fundamental soliton can propagate undistorted for arbitrarily long distances. This is the reason behind the current interest in soliton-based communication systems (Hasegawa and Tappert, 1973). In practice, however, the fiber loss leads to a gradual broadening of the soliton. Periodic compensation of the loss by Raman gain has been proposed to restore the original soliton (Mollenauer et al., 1986).

The higher-order solitons ($N > 1$) follow a periodic evolution pattern along the fiber with a period $z_0 = (\pi/2)L_D$. Figure 3.5 shows, as an example, the evolution pattern of an $N = 3$ soliton over one period obtained by solving Eq. (29) with $N = 3$, $\alpha = 0$, and $U(0, \tau) = \text{sech}(\tau)$. The pulse initially narrows, develops a two-peak structure, and then reverses its propagation behavior beyond $z/z_0 = 0.5$ such that the original pulse is restored at $z = z_0$. Both pulse narrowing and pulse restoration at the soliton period have been observed experimentally (Stolen et al., 1983). In particular, initial narrowing of the higher-order soliton has been used to compress the optical pulses by suitably selecting the peak power and the fiber length. A combination of a normal dispersion fiber with a grating pair followed by an anomalous dispersion fiber has been used to compress optical pulses by more than three orders of magnitude (Tai and Tomita, 1986) and to generate pulses as short as 33 fs (Gouveia-Neto et al., 1987).

The soliton formation capacity of optical fibers has led to the development of the soliton laser (Mollenauer and Stolen, 1984). A piece of single-mode fiber inside the cavity is used to shape the pulses. The pulse width can be controlled by adjusting the fiber length. Pulses as short as 50 fs have been generated directly from a soliton laser and compressed to about 19 fs using

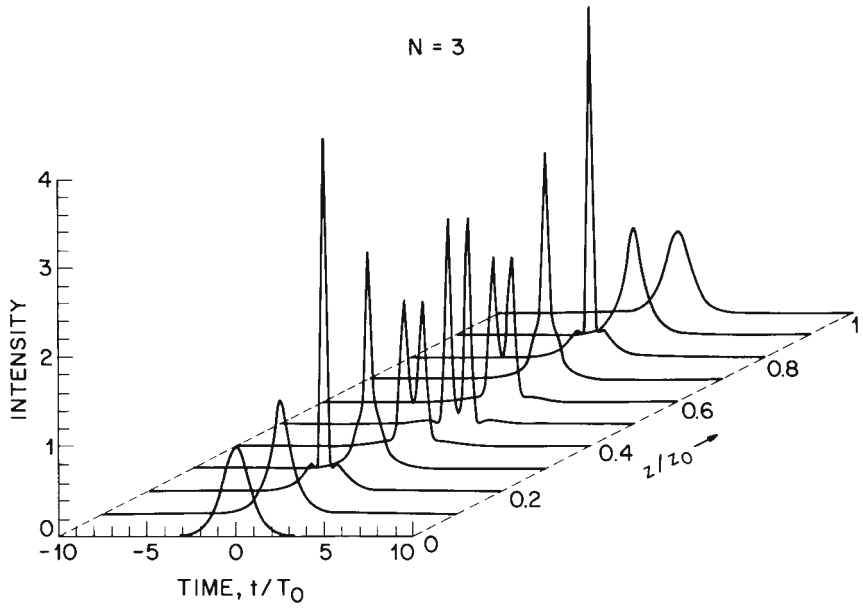


FIGURE 3.5. Evolution of $N = 3$ soliton over one period. Note the initial pulse narrowing in the anomalous dispersion regime.

the high-order soliton effect in an external fiber (Mitschke and Mollenauer, 1987).

Equation (29) has proved to be very useful in understanding the propagation behavior in the anomalous dispersion regime of optical fibers. However, as discussed in Section 2, for ultrashort pulses ($T_0 \lesssim 0.1$ ps) Eq. (29) is no longer adequate, and Eq. (21) should be used in its place. The necessity of including the higher-order nonlinear terms in Eq. (21) was established in a recent experiment where a new effect known as the self-frequency shift was observed (Mitschke and Mollenauer, 1986). In this phenomenon the center frequency of the soliton shifts toward red as the pulse propagates inside the fiber. Physically, the low-frequency components are amplified from the Raman gain at the expense of the high-frequency components. Equation (21) includes the Raman gain through the last term and can be used to study such self-frequency shifts (Gordon, 1986; Kodama and Hasegawa, 1987).

The effect of higher-order dispersion on the soliton behavior [governed by the term proportional to $\beta_3$ in Eq. (21)] has also attracted attention. In general, such effects become significant only when the pulse wavelength nearly coincides with the zero-dispersion wavelength of the fiber and can lead to considerable pulse distortion (Agrawal and Potasek, 1986). It has been shown that the fiber can support a soliton even at the zero-dispersion wavelength (Wai et al., 1987) by shifting the center wavelength toward the anomalous dispersion regime.

## 6. Stimulated Raman Scattering

In preceding sections the peak power of the incident pulse has been assumed to be considerably below the SRS threshold (Smith, 1972). When this condition is not satisfied, the Raman gain provided by the fiber leads to a rapid buildup of the Stokes pulse. Figure 3.6 shows the Raman gain spectrum for silica fibers (Stolen, 1980). The large spectral width results from the amorphous nature of fused silica. Since the largest gain occurs at a frequency shifted downward by about 13 THz from the pump frequency, the Stokes pulse appears red-shifted by that amount. If the incident pulse is so short ($\lesssim$0.1 ps) that its spectral width exceeds the Raman shift, the distinction between the pump and Stokes pulses is not sharp since their spectra overlap. In that case pulse evolution is governed by Eq. (21). However, for pulse widths $\gtrsim$1 ps, the pump and Stokes pulses can be treated separately, and their propagation in optical fibers is described by the coupled set of Eqs. (19) and (20). In this section we consider numerical solution of these equations and compare the results with the experimental work on SRS. The numerical method is a generalization of that used to solve the NSE, described in Section 3.3.

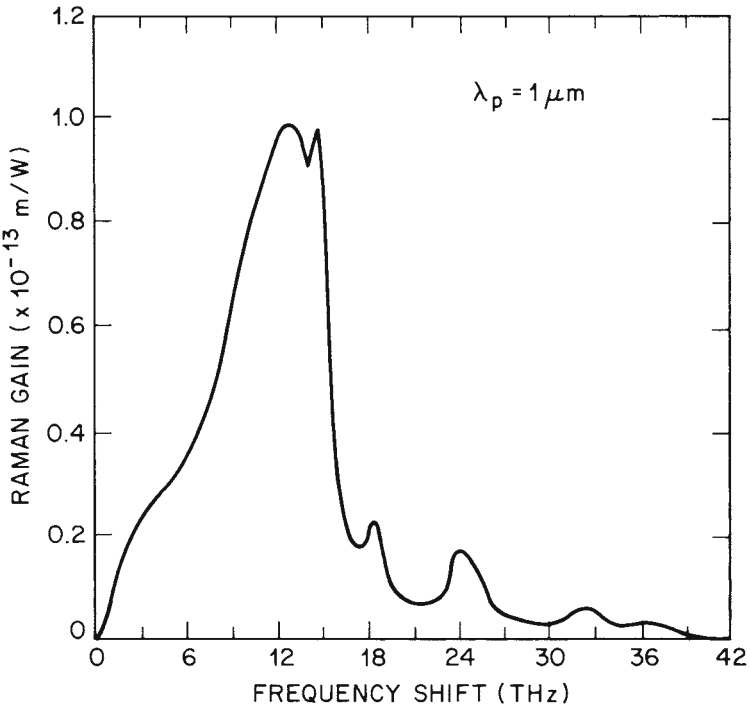


FIGURE 3.6. Raman gain spectrum for silica fibers (after Stolen, 1980) The peak gain is about $1 \times 10^{-13}$ m/W for a 1-$\mu$m pump and scales as $\lambda_p^{-1}$ with change in the wavelength.

For the purpose of computations, it is convenient to define the reduced time

$$T = t - z/v_{g1} \tag{37}$$

and write Eqs. (19) and (20) in the form

$$\frac{\partial A_p}{\partial z} + \frac{1}{2}\left(\alpha_p + g_p|A_s|^2\right)A_p + \frac{i}{2}\beta_p \frac{\partial^2 A_p}{\partial T^2} - i\gamma_p\left(|A_p|^2 + 2|A_s|^2\right)A_s = 0, \tag{38}$$

$$\frac{\partial A_s}{\partial z} + d\frac{\partial A_s}{\partial T} + \frac{1}{2}\left(\alpha_s - g_s|A_p|^2\right)A_s + \frac{i}{2}\beta_s \frac{\partial^2 A_s}{\partial T^2} - i\gamma_s\left(|A_s|^2 + 2|A_p|^2\right)A_p = 0, \tag{39}$$

where we have used the subscripts $p$ and $s$ to identify the pump and Stokes variables. The parameter

$$d = \frac{v_{gp} - v_{gs}}{v_{gp}v_{gs}} \tag{40}$$

accounts for the group velocity mismatch between the pump and Raman pulses. Because of the Stokes shift of about 13 THz, the parameters $\beta_j$, $\gamma_j$, and $g_j$ are slightly different for $j = p$ and $s$. In particular, form Eqs. (16) and (18)

$$\beta_s = (\lambda_s/\lambda_p)\beta_p, \qquad \gamma_s = (\lambda_p/\lambda_s)\gamma_p, \tag{41}$$

where $\lambda_p$ and $\lambda_s$ are the center wavelengths for the pump and Raman pulses, respectively. Similarly, the gains are related by

$$g_s = (\lambda_p/\lambda_s)g_p. \tag{42}$$

For definiteness, the numerical results for SRS are presented here for $\lambda_p \simeq 0.53$ $\mu$m; qualitatively similar behavior is expected to occur for other wavelengths. Using typical values for the fiber parameters, we estimate that $\alpha_p = 0.0012\,\mathrm{m}^{-1}$, $\beta_p = 0.06\,\mathrm{ps}^2\mathrm{m}^{-1}$, $\gamma_p = 0.015\,\mathrm{W}^{-1}\,\mathrm{m}^{-1}$, and $g_p = 0.015\,\mathrm{W}^{-1}\,\mathrm{m}^{-1}$. Assuming a Gaussian unchirped pump pulse, the incident field $A_p(0, \tau)$ is taken to be

$$A_p(0, \tau) = \sqrt{P_0}\,\exp(-T^2/2T_0^2). \tag{43}$$

We choose $T_0 = 10$ ps, which corresponds to a full width at half-maximum (FWHM) of about 16 ps. The peak pump power is taken to be $P_0 = 500$ W. Numerical simulations require the use of a seed Raman pulse. It was taken to be a Gaussian pulse with a width identical to that of the pump pulse but with a power of $10^{-6}$ of the pump pulse. The two pulses overlap initially but the Raman pulse travels faster than the pump pulse inside the fiber because of the group velocity mismatch. The walk-off effect is included through the parameter $d$ in Eq. (39); its value is estimated to be about 5 ps/m. Because of the use of a specific seed pulse, the results presented here are applicable more directly to the case of Raman amplification rather than noise-induced SRS. Most of the qualitative features are, however, expected to apply to SRS as well.

Figure 3.7 shows the evolution of the pump and Raman pulses as they copropagate inside a 5-m-long fiber. As the Raman pulse moves ahead of the

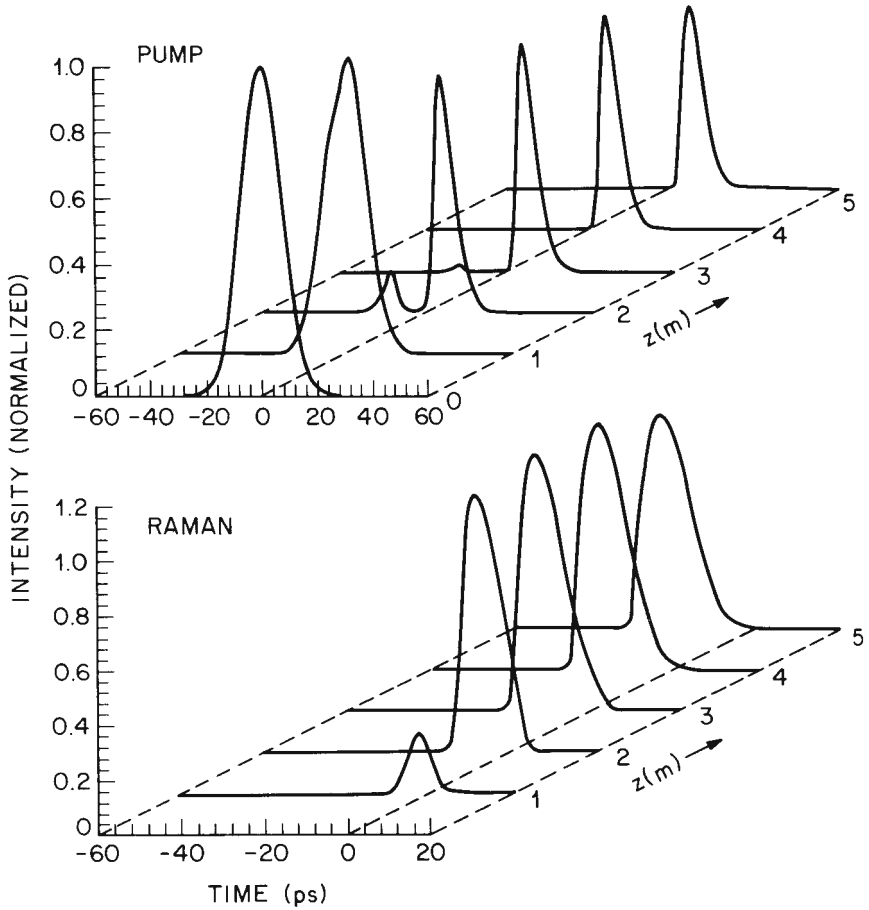


FIGURE 3.7. Evolution of pump pulse and Raman pulse along the fiber length. Pump pulse parameters are $\lambda_p = 0.53\,\mu$m, $T_0 = 10$ ps, and $P_0 = 500$ W. Pulse walk-off is included by taking $d = -5$ ps/m.

pump pulse, the energy for the generation of the Raman pulse comes from the leading edge of the pump pulse. This is seen clearly in Figure 3.8, where the pulse shapes are shown overlapped at $z = 2$ m and 5 m. At $z = 2$ m, the creation of the Raman pulse has led to a two-peak structure for the pump pulse as a result of pump depletion. The peak near the leading edge disappears with further propagation as the Raman pulse walks through it. At $z = 5$ m, the two pulses are completely separated. Because of the walk-off effect, both pulses are asymmetric and narrower than the incident pulse. In particular, the pump pulse consists of the trailing portion of the incident pulse that remained undepleted because of the walk-off of the Raman pulse.

The spectral evolution of the two pulses along the fiber length is shown in Figure 3.9. Both pulses exhibit asymmetric spectral broadening with

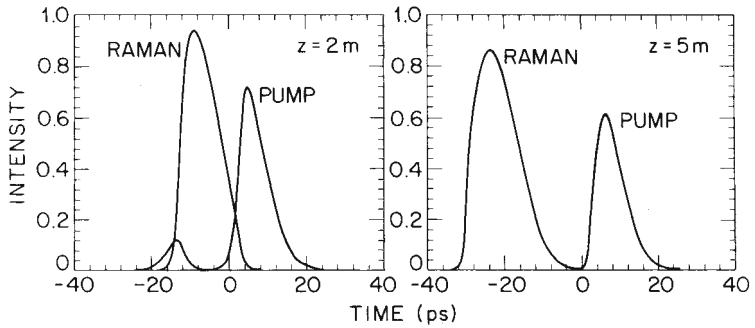


FIGURE 3.8. Comparison of pump and Raman pulse shapes at $z = 2\,\text{m}$ and $z = 5\,\text{m}$ with parameters of Figure 3.7. At $z = 2\,\text{m}$, the pump pulse develops a two-peak structure because of pump depletion occurring at the location of the Raman pulse. Two pulses are completely separated after propagating a distance of 5 m.

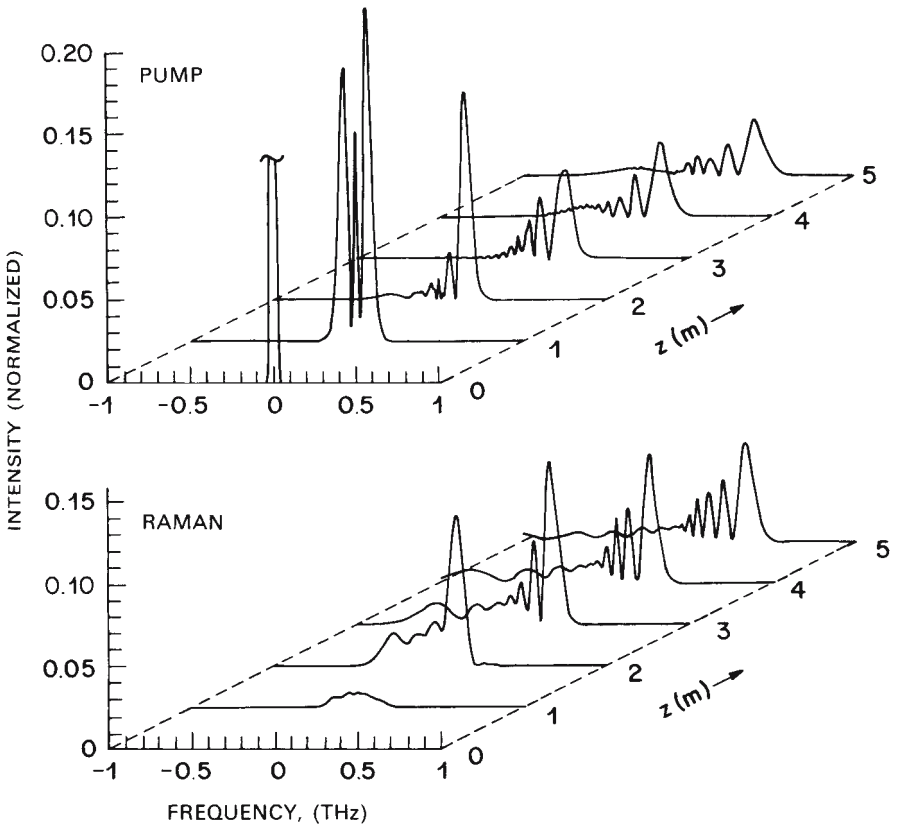


FIGURE 3.9. Evolution of pump and Raman pulse spectra along the fiber length. The parameter values are identical to those of Figure 3.7.

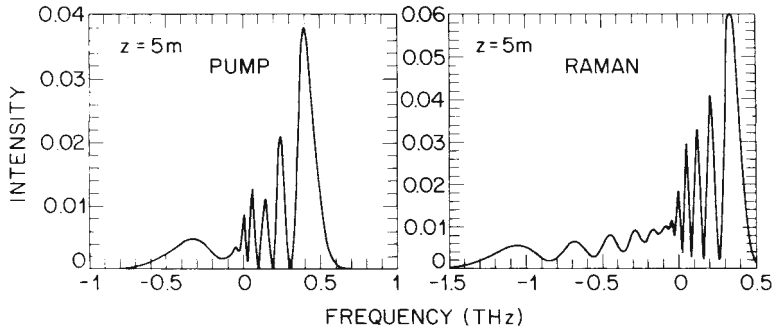


FIGURE 3.10. Comparison of pump and Raman pulse spectra at $z = 5$ m. Note the spectral broadening of the Raman pulse by more than a factor of 2 compared with that of the pump pulse.

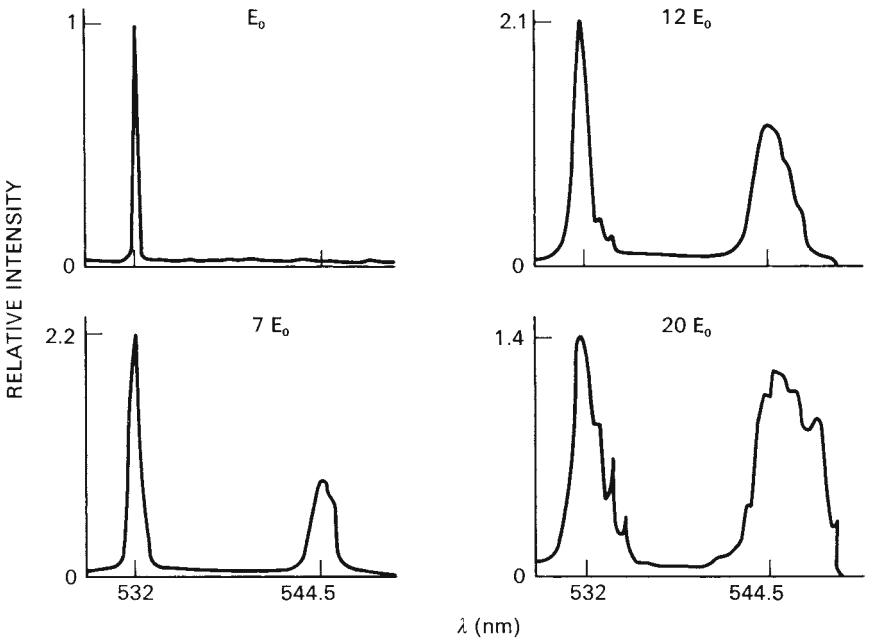


FIGURE 3.11. Experimental spectra of pump and Raman pulses after a 25-ps pump pulse at 532 nm has propagated 10 m inside a fiber. Four spectra correspond to different pump pulse energies normalized to $E_0$, an energy below the Raman threshold. (After Alfano et al., 1987.)

considerable internal structure. In general, the spectral width of the Raman pulse exceeds that of the pump pulse by a factor of 2 or more. These features are more clearly seen in Figure 3.10, where the spectra at $z = 5$ m are shown on an expanded scale. Note that the spectral range of the Raman pulse is about 2.5 times that of the pump pulse. This feature was predicted by Gersten et al. (1980) and has been verified by Alfano et al. (1987). Figure 3.11 shows their experimentally observed spectra at the output end of a 10-m-long fiber for a 25-ps pump pulse with increasing pump pulse energies. The Raman line is broader by about a factor of 2.8. The spectral asymmetry of the pump line is also evident. Similar qualitative features have been observed at other pump wavelengths. Figure 3.12 shows, as an example, the observed pump spectra at various peak power levels when 140-ps-wide pump pulses at 1.06 $\mu$m are propagated along a 150-m-long fiber (Kean et al., 1987). For peak powers below 100 W, the observed spectra are due to SPM (see Figure 3.1). The Raman threshold is reached near 100 W. The spectrum at 148 W shows the asymmetric spectral broadening resulting from the Raman interaction and should be compared with that shown in Figure 3.10. The physical origin of

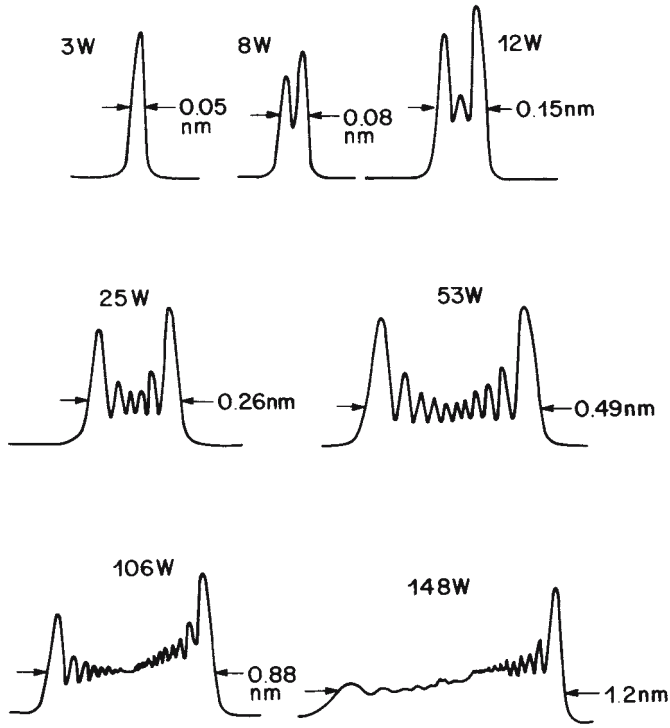


FIGURE 3.12. Experimental spectra of the pump pulse at different peak powers after a 140-ps pulse at 1.06 $\mu$m has propagated inside a 150-m-long fiber. The Raman threshold is reached at about 100 W. (After Dean et al., 1987.)

spectral broadening is related to XPM, while the physical origin of spectral asymmetry is related to the pulse walk-off. These features are discussed further in the following section.

## 7. Cross-Phase Modulation

Although the major qualitative features seen in the pulse spectra of Figures 3.9 and 3.10 are due to XPM, it is difficult to isolate the XPM-induced features. For this reason, we consider in this section the interaction of two incident pulses copropagating along the fiber without SRS; that is, $g_p = 0$ and $g_s = 0$ in Eqs. (38) and (39). The other parameters are identical to those used in Section 6 except for the incident peak powers, which we take to be $P_1 = P_2 = 200$ W. For these power levels both pulses are below the Raman threshold for $L = 5$ m; that is, $g_s PL < 16$ (Smith, 1972; Stolen, 1980). Both incident pulses are assumed to be Gaussian with $T_0 = 10$ ps; they overlap completely at the input end of the fiber. The pulse walk-off effects are included by taking $d = -2$ ps/m, a value appropriate when the center wavelengths of two pulses are spaced by about 5 nm. Similar to the SRS case shown in Figures 3.7 and 3.9, the evolution of the pulse shapes and spectra along a 5-m-long fiber was studied. It was found that the shapes of both pulses remain largely unaffected during XPM interaction except for the walk-off effect; that is, the peaks of the Gaussian pulses drifted apart at a rate of about 2 ps/m, as one would have expected.

The spectral evolution is, however, governed by the combined effect of SPM and XPM. Figure 3.13 shows the pulse spectra at $z = 5$ m for the two pulses. Similar to the case of SPM (see Figure 3.1), the spectra exhibit inter-

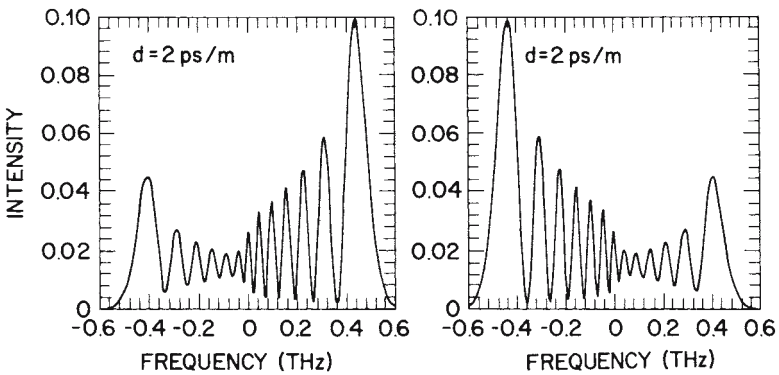


FIGURE 3.13. Calculated spectra of two pulses at $z = 5$ m. Both pulses are identical (except for their center wavelengths) and launched simultaneously inside the fiber with parameters $T_1 = T_2 = 10$ ps and $P_1 = P_2 = 200$ W. Group velocity mismatch is included by taking $d = -2$ ps/m.

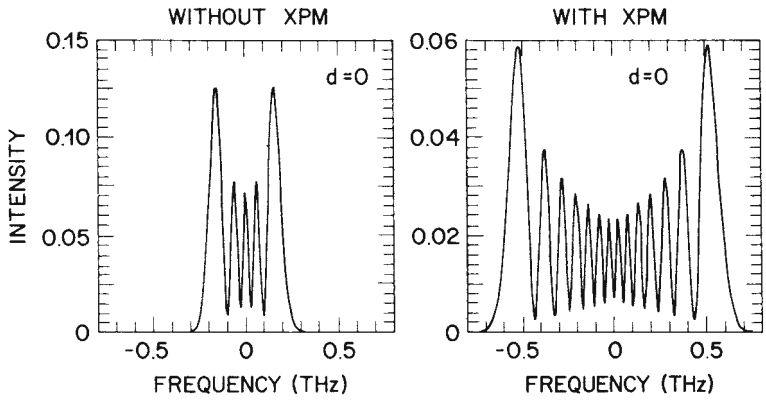


FIGURE 3.14. Same as in Figure 3.13 except that the group velocity mismatch is ignored by setting $d = 0$. Since the spectra are identical, only the spectrum of one pulse is shown. The right and left plots show the spectrum without and with XPM, respectively. Note the XPM-induced broadening by a factor of about 3.

nal structure with multiple peaks. The noticeable new features are (1) that the spectrum of each pulse is asymmetric and (2) that the spectrum of one pulse is the mirror image of the other (shifted by the initial wavelength separation of the two pulses). In general, blue-shifted components are more intense for the slower pulse while the opposite occurs for the fast-moving pulse.

In order to isolate the features related to XPM and group velocity msmatch, Figure 3.14 shows the spectrum for the case $d = 0$. Also included for comparison is the spectrum expected in the absence of XPM. Since the spectra of both pulses are found to be identical for $d = 0$, the spectra of only one pulse are shown in Figure 3.15. A comparison of the two spectra in Figure 3.14 shows that in the absence of group velocity mismatch ($d = 0$), the effect of XPM is to broaden the spectrum by nearly a factor of 3 over that expected by SPM alone. By comparing Figures 3.13 and 3.14 we conclude that it is the pulse walk-off that is responsible for the spectral asymmetry seen in Figure 3.13. It should, however, be stressed that XPM is also necessary for spectral asymmetry since it is XPM that provides the physical mechanism for two pulses to interact with each other.

A simple analytic model for the XPM interaction between two copropagating pulses can be developed to understand the origin of spectral features seen in Figures 3.13 and 3.14. The model makes the following three assumptions to simplify the coupled-amplitude Eqs. (19) and (20). (1) The effects of GVD are negligible so that $\beta_{21} = \beta_{22} = 0$. This approximation is justified if the fiber length is much shorter than the dispersion length $L_D$ associated with each pulse [see Eq. (23)]. (2) The peak powers of the incident pulses are below the Raman threshold so that $g_1 = g_2 = 0$. (3) The fiber loss is negligible so that $\alpha_1 = \alpha_2 = 0$. The last assumption is not necessary but is made to simplify the

treatment. The inclusion of fiber loss does not affect the conclusions drawn here.

It can readily be verified by using Eqs. (19) and (20) with these simplifications that the pulse shapes remain unchanged during propagation. The effect of SPM and XPM is to generate a nonlinear phase shift accumulated over the fiber length $L$ (Islam et al., 1987). The phase shift for pulse 1 is given by

$$\Phi_1(T) = \gamma_1 \int_0^L \left[ |A_1(0,T)|^2 + 2|A_2(0,T-zd)|^2 \right] dz, \tag{44}$$

where $T$ is the reduced time given by Eq. (37) and $d$ is the group velocity mismatch defined in a way similar to Eq. (40). If the two pulses are Gaussian in shape and are launched simultaneously with complete overlap, the incident fields are given by

$$A_m(0,T) = \sqrt{P_m}\, \exp(-T^2/2T_m^2), \tag{45}$$

where $m = 1$ or 2, $P_m$ is the peak power, and $T_m$ is the $1/e$ half-width. We assume equal pulse widths, $T_1 = T_2 = T_0$, but allow for unequal peak powers. By using Eq. (45) in Eq. (44) and performing the integration, we obtain

$$\Phi_1(\tau) = \gamma_1 L \left\{ P_1 \exp(-\tau^2) + P_2 \frac{\sqrt{\pi}}{\delta} [\mathrm{erf}(\tau) - \mathrm{erf}(\tau - \delta)] \right\}, \tag{46}$$

where erf stands for the error function, $\tau = T/T_0$ is the normalized time coordinate, and

$$\delta = Ld/T_0 \tag{47}$$

is the normalized walk-off parameter.

The nonlinearity-induced chirp is obtained by using $\Delta\nu_1 = -(1/2\pi)\partial\Phi_1/\partial T$. By differentiating Eq. (46), it is given by

$$\Delta\nu_1(\tau) = \frac{\gamma_1 L}{\pi T_0} e^{-\tau^2} \left\{ P_1 \tau + \frac{P_2}{\delta} [\exp(2\tau\delta - \delta^2) - 1] \right\}. \tag{48}$$

To the lowest order in $\delta$, the chirp is given by the simple relation

$$\Delta\nu_1(\tau) \simeq \frac{\gamma_1 L}{\pi T_0} e^{-\tau^2} [P_1 \tau + P_2(2\tau - \delta)]. \tag{49}$$

The chirp $\Delta\nu_2$ can be obtained by interchanging the subscripts 1 and 2 and replacing $\delta$ by $-\delta$ in Eq. (49) and is given by

$$\Delta\nu_2(\tau) = \frac{\gamma_2 L}{\pi T_0} e^{-\tau^2} [P_2 \tau + P_1(2\tau + \delta)]. \tag{50}$$

Equations (49) and (50) can be used to understand all the spectral features seen in Figures 3.13 and 3.14. Consider first the case $\delta = 0$ (no walk-off), for which the numerical pulse spectra are shown in Figure 3.14. Since $P_1 = P_2$ was assumed in numerical simulations, Eq. (49) indicates that the effect of

XPM is to broaden the pulse spectrum by a factor of 3 over that expected from the SPM alone. This is in agreement with the results of Figure 3.14. The fact that the broadening factor is slightly smaller than 3 in Figure 3.14 is related to the GVD, which reduces the peak powers slightly by broadening the pulse during its propagation inside the fiber.

In the presence of group velocity mismatch ($\delta \neq 0$), Eq. (49) shows that the chirp can be larger or smaller depending on the relative signs of $\tau$ and $\delta$. For the results shown in Figure 3.13, $\delta < 0$. As a consequence, the chirp is larger near the trailing edge ($\tau > 0$) and smaller near the leading edge ($\tau < 0$) for pulse 1 while the opposite occurs for pulse 2. Since blue components are generated near the trailing edge, they are expected to be more intense for pulse 1. For the same reason, the spectral spread should be larger toward the blue side than the red side for pulse 1. This feature is clearly seen in Figure 3.13. Using a similar argument, Eq. (50) predicts that the spectrum of pulse 2 will have a larger spread on the red side, and the red components will be more intense. For the specific case of $\gamma_1 \simeq \gamma_2$ and $P_1 = P_2$, the two spectra should be mirror images of each other since $\Delta\nu_2(\tau) = -\Delta\nu_1(-\tau)$. This feature would, of course, be absent for unequal peak powers.

Equations (49) and (50) can be used to predict the relative spectral widths of two spectra for the case of $P_1 \neq P_2$. Since the spectral range is relatively unaffected by pulse walk-off (compare Figures 3.13 and 3.14), we set $\delta = 0$. The ratio of the spectral widths is then given by

$$\frac{\Delta\nu_2}{\Delta\nu_1} = \frac{\lambda_1}{\lambda_2}\left(\frac{P_2 + 2P_1}{P_1 + 2P_2}\right), \tag{51}$$

where we used Eq. (16) to show the dependence on wavelengths. For $\lambda_1 \simeq \lambda_2$, the width ratio can vary from 0.5 to 2 depending on the power ratio $P_2/P_1$. In particular, when a weak probe pulse copropagates with an intense pulse ($P_2 \ll P_1$), its spectrum is broadened by a factor of more than 2 over that of the pump pulse because of XPM (Gersten et al., 1980; Alfano et al., 1987). Note, however, that the width ratio can be quite different if $\lambda_1$ and $\lambda_2$ differ significantly. For example, the spectral broadening would be by a factor of 4 if the probe pulse is at the second harmonic of the pump pulse.

## 8. Conclusion

This chapter has reviewed the propagation characteristics of ultrashort optical pulses in single-mode fibers influenced by the dispersive and nonlinear effects. When the pulse peak power is below the Raman threshold, the propagation behavior is modeled well by the nonlinear Schrödinger equation (29). New qualitative features arise depending on whether the propagation occurs in the normal or the anomalous dispersion regime. In the latter case, the fiber supports optical solitons and has found applications in the design of the soliton laser. When the pulse peak power exceeds the Raman thresh-

old, the evolution of the pump and Raman pulses is governed by the coupled set of Eqs. (38) and (39). In this case it is important to take into account both the group velocity mismatch and XPM. In particular, XPM is responsible for new spectral features such as an additional broadening of the Raman pulse spectrum by a factor of 2 or more over that of the pump pulse. Of course, SRS is not a prerequisite for the observation of these novel qualitative features; similar propagation characteristics can be observed by launching simultaneously two optical pulses inside the fiber. Clearly, optical fibers are extremely versatile for studying nonlinear phenomena and should find new applications, including one in the design of ultrafast supercontinuum laser sources.

## References

Agrawal, G.P. (1987) Modulation instability induced by cross-phase modulation. Phys. Rev. Lett. **59**, 880–883.

Agrawal, G.P. and M.J. Potasek (1986) Nonlinear pulse distortion in single-mode optical fibers at the zero-dispersion wavelength. Phys. Rev. A **33**, 1765–1776.

Alfano, R.R. (1985) Ultrafast supercontinuum laser source. *Proc. Lasers '85*, pp. 110–122.

Alfano, R.R., P.L. Baldeck, F. Raccah, and P.P. Ho (1987) Cross-phase modulation measured in optical fibers. Appl. Opt. **26**, 3491–3492.

Alfano R.R. and S.L. Shapiro (1970) Observation of self-phase modulation in crystals and glasses. Phys. Rev. Lett. **24**, 592–594.

Baldeck, P.L., P.P. Ho, and R.R. Alfano (1987) Effects of self, induced and cross phase modulations on the generation of picosecond and femtosecond white light supercontinua. Rev. Phys. Appl. **22**, 1677–1694.

Basch, E.E., ed. (1986) *Optical-Fiber Transmission*. Sams, Indianapolis, Indiana.

Bourkoff, E., W. Zhao, R.L. Joseph, and D.N. Christodoulides (1987) Evolution of femtosecond pulses in single-mode fibers having higher-order nonlinearity and dispersion. Opt. Lett. **12**, 272–274.

Fisher, R.A. and W.K. Bischel (1975) Numerical studies of the interplay between self-phase modulation and dispersion for intense plane-wave laser pulses. J. Appl. Phys. **46**, 4921–4934.

Fleck, J.A., J.R. Morris, and M.D. Feit (1976) Time-dependent propagation of high-energy laser beams through the atmosphere. Appl. Phys. **10**, 129–160.

Fork, R.L., C.H. Brito Cruz, P.C. Becker, and C.V. Shank (1987) Compression of optical pulses to six femtoseconds by using cubic phase compensation. Opt. Lett. **12**, 483–485.

Gersten, J.I., R.R. Alfano, and M. Belic (1980) Combined stimulated Raman scattering and continuum self-phase modulations. Phys. Rev. A **21**, 1222–1224.

Golovchenko, E.A., E.M. Dianov, A.N. Pilipetskii A.M. Prokhorov, and V.N. Serkin (1987) Self-effect and maximum contraction of optical femtosecond wave packets in a nonlinear dispersive medium. JETP Lett. **45**, 91–95.

Gordon, J.P. (1986) Theory of the soliton self-frequency shift. Opt. Lett. **11**, 662–664.

Gouveia-Neto, A.S., A.S.L. Gomes, and J.R. Taylor (1987) Generation of 33-fsec pulses at 1.32 $\mu$m through a high-order soliton effect in a single-mode optical fiber. Opt. Lett. **12**, 395–397.

Grischkowsky, D. and A.C. Balant (1982) Optical pulse compression based on enhanced frequency chirping. Appl. Phys. Lett. **41**, 1–3.

Hasegawa, A. (1983) Amplification and reshaping of optical solitons in glass fiber—IV. Opt. Lett. **8**, 650–652.

Hasegawa, A. and F. Tappert (1973) transmission of stationary nonlinear optical pulses in dispersive dielectric fibers. I. Anomalous dispersion. App. Phys. Lett. **23**, 142–144.

Islam, M.N., L.F. Mollenauer, R.H. Stolen, J.R. Simpson, and H.T. Shang (1987) Cross-phase modulation in optical fibers. Opt. Lett. **12**, 625–627.

Kean, P.N., K. Smith, and W. Sibbett (1987) Spectral and temporal investigation of self-phase modulation and stimulated Raman scattering in a single-mode optical fiber. IEE Proc. **134**, 163–170.

Kodama, Y. and A. Hasegawa (1987). Nonlinear pulse propagation in a monomode dielectric guide. IEEE J. Quantum Electron. **QE-23**, 510–524.

Lassen, H.E., F. Mengel, B. Tromborg, N.C. Albertsen, and P.L. Christiansen (1985). Evolution of chirped pulses in nonlinear single-mode fibers. Opt. Lett. **10**, 34–36.

Lax, M., J.H. Batteh, and G.P. Agrawal (1981) Chenneling of intense electromagnetic beams. J. Appl. Phys. **52**, 109–125.

Marcuse, D. (1981) Pulse distortion in single-mode fibers. Appl. Opt. **19**, 1653–1660.

Miller, S.E. and I.P. Kaminow, eds. (1988) *Optical Fiber Telecommunications II*. Academic Press, Boston, Massachusetts.

Mitschke, F.M. and L.F. Mollenauer (1986) Discovery of the soliton self-frequency shift. Opt. Lett. **11**, 659–661.

Mitschke, F.M. and L.F. Mollenauer (1987) Ultrashort pulses from the soliton laser. Opt. Lett. **12**, 407–409.

Mollenauer, L.F. and R.H. Stolen (1984) The soliton laser. Opt. Lett. **9**, 13–15.

Mollenauer, L.F., R.H. Stolen, and J.P. Gordon (1980) Experimental observation of picosecond pulse narrowing and solitons in optical fibers. Phys. Rev. Lett. **45**, 1095–1097.

Mollenauer, L.F., J.P. Gordon, and M.N. Islam (1986) Soliton propagation in long fibers with periodically compensated loss. IEEE J. Quantum Electron. **QE-22**, 157–173.

Nikolaus, B. and D. Grischkowsky (1983) 12 × pulse compression using optical fibers. Appl. Phys. Lett. **42**, 1–2.

Schadt, D. and B. Jaskorzynska (1987) Frequency chirp and stimulated Raman scattering influenced by pulse walk-off in optical fibers. J. Opt. Soc. Am. **4**, 856–862.

Serkin, V.N. (1987) Colored envelope solitons in optical fibers. Sov. Tech. Phys. Lett. **13**, 320–321.

Shank, C.V., R.L. Fork, R. Yen, R.H. Stolen, and W.J. Tomlinson (1982) Compression of femtosecond optical pulses. Appl. Phys. Lett. **40**, 761–763.

Shank, C.V., R.L. Fork, C.H. Brito Cruz, and W. Knox (1986). In *Ultrafast Phenomena V*, G.R. Fleming and A.E. Siegman, eds. Springer-Verlag, Heidelberg.

Smith, R.G. (1972) Optical power handling capacity of low loss optical fibers as determined by stimulated Raman and Brillouin scattering. Appl. Opt. **11**, 2489–2494.

Stolen, R.H.(1980) Nonlinearity in fiber transmission. Proc. IEEE **68**, 1232–1236.

Stolen, R.H. and C. Lin (1978) Self-phase modulation in silica optical fibers. Phys. Rev. A **17**, 1448–1453.

Stolen, R.H., L.F. Mollenauer, and W.J. Tomlinson (1983) Observation of pulse restoration at the soliton period in optical fibers. Opt. Lett. **8**, 186–188.

Tai, K. and A. Tomita (1986) 1100 × optical fiber pulse compression using grating pair and soliton effect at 1.319 $\mu$m. Appl. Phys. Lett. **48**, 1033–1035.

Tomlinson, W.J., R.H. Stolen, and C.V. Shank (1984) Compression of optical pulses chirped by self-phase modulation in fibers. J. opt. Soc. Am. B **1**, 139–149.

Tomlinson, W.J., R.H., Stolen, and A.M. Johnson (1985) Optical wave breaking in nonlinear optical fibers. Opt. Lett. **10**, 457–459.

Vysloukh, V.A. and T.A. Matveeva (1987) Influence of inertia of nonlinear response on compression of femtosecond pulses. Sov. J. Quantum Electron. **17**, 498–500.

Wai, P.K., C.R. Menyuk, H.H. Chen, and Y.C. Lee (1987) Soliton at the zero-group-dispersion wavelength of a single-mode fiber. Opt. Lett. **12**, 628–630.

Zakharov, V.E. and A.B. Shabat (1972) Exact theory of two-dimensional self-focusing and one-dimensional self-modulation of waves in nonlinear media. Sov. Phys. JETP **34**, 62–69.

Zysset, B., P. Beaud, and W. Hodel (1987) Generation of optical solitons in the wavelength region 1.37–1.49 $\mu$m. Appl. Phys. Lett. **50**, 1027–1029.

# 4
# Cross-Phase Modulation: A New Technique for Controlling the Spectral, Temporal, and Spatial Properties of Ultrashort Pulses

P.L. Baldeck, P.P. Ho, and R.R. Alfano

## 1. Introduction

Self-phase modulation (SPM) is the principal mechanism responsible for the generation of picosecond and femtosecond white-light supercontinua. When an intense ultrashort pulse progagates through a medium, it distorts the atomic configuration of the material, which changes the refractive index. The pulse phase is time modulated, which causes the generation of new frequencies. This phase modulation originates from the pulse itself (*self*-phase modulation). It can also be generated by a copropagating pulse (*cross*-phase modulation).

Several schemes of nonlinear interaction between optical pulses can lead to cross-phase modulation (XPM). For example, XPM is intrinsic to the generation processes of stimulated Raman scattering (SRS) pulses, second harmonic generation (SHG) pulses, and stimulated four-photon mixing (SFPM) pulses. More important, the XPM generated by pump pulses can be used to control, with femtosecond time response, the spectral, temporal, and spatial properties of ultrashort probe pulses.

Early studies on XPM characterized induced polarization effects (optical Kerr effect) and induced phase changes, but did not investigate spectral, temporal and spatial effects on the properties of ultrashort pulses. In 1980, Gersten, Alfano, and Belic predicted that Raman spectra of ultrashort pulses would be broadened by XPM (Gersten et al., 1980). The first experimental observation of XPM spectral effects dates to early 1986, when it was reported that intense picosecond pulses could be used to enhance the spectral broadening of weaker pulses copropagating in bulk glasses (Alfano et al., 1986). Since then, several groups have been studying XPM effects generated by ultrashort pump pulses on copropagating Raman pulses (Schadt et al., 1986; Schadt and Jaskorzynska, 1987a; Islam et al., 1987a; Alfano et al., 1987b; Baldeck et al., 1987b–d; Manassah, 1987a, b; Hook et al., 1988), second harmonic pulses (Alfano et al., 1987a; Manassah, 1987c; Manassah and Cockings, 1987; Ho et al., 1988), stimulated four-photon mixing pulses (Baldeck and Alfano, 1987), and probe pulses (Manassah et al., 1985;

Agrawal et al., 1989a; Baldeck et al., 1988a, c). Recently, it has been shown that XPM leads to the generation of modulation instability (Agrawal, 1987; Agrawal et al., 1989b; Schadt and Jaskorzynska, 1987b; Baldeck et al., 1988b, 1988d; Gouveia-Neto et al., 1988a, b), solitary waves (Islam et al., 1987b; Trillo et al., 1988), and pulse compression (Jaskorzynska and Schadt, 1988; Manassah, 1988; Agrawal et al., 1988). Finally, XPM effects on ultrashort pulses have been proposed to tune the frequency of probe pulses (Baldeck et al., 1988a), to eliminate the soliton self-frequency shift effect (Schadt and Jaskorzynska, 1988), and to control the spatial distribution of light in large core optical fibers (Baldeck et al., 1987a).

This chapter reviews some of the key theoretical and experimental works that have predicted and described spectral, temporal, and spatial effects attributed to XPM. In Section 2, the basis of the XPM theory is outlined. The nonlinear polarizations, XPM phases, and spectral distributions of coprapagating pulses are computed. The effects of pulse walk-off, input time delay, and group velocity dispersion broadening are particularly discussed. (Additional work on XPM and on SPM theories can be found in Manassah (Chapter 5) and Agrawal (Chapter 3).) Experimental evidence for spectral broadening enhancement, induced-frequency shift, and XPM-induced optical amplification is presented in Section 3. Sections 4, 5, and 6 consider the effects of XPM on Raman pulses, second harmonic pulses, and stimulated four-photon mixing pulses, respectively. Section 7 shows how induced focusing can be initiated by XPM in optical fibers. Section 8 presents measurements of modulation instability induced by cross-phase modulation in the normal dispersion region of optical fibers. Section 9 describes XPM-based devices that could be developed for the optical processing of ultrashort pulses with terahertz repetition rates. Finally, Section 10 summarizes the chapter and highlights future trends.

## 2. Cross-Phase Modulation Theory

### 2.1 Coupled Nonlinear Equations of Copropagating Pulses

The methods of multiple scales and slowly varying amplitude (SVA) are the two independent approximations used to derive the coupled nonlinear equations of copropagating pulses. The multiple scale method, which has been used for the first theoretical study on induced-phase modulation, is described in Manassah (Chapter 5). The following derivation is based on the SVA approximation.

The optical electromagnetic field of two copropagating pulses must ultimately satisfy Maxwell's vector equation:

$$\nabla \times \nabla \times \mathbf{E} = -\mu_0 \frac{\partial \mathbf{D}}{\partial t} \tag{1a}$$

and

$$\mathbf{D} = \varepsilon \mathbf{E} + \mathbf{P}^{NL}, \tag{1b}$$

where $\varepsilon$ is the medium permitivity at low intensity and $\mathbf{P}^{NL}$ is the nonlinear polarization vector.

Assuming a pulse duration much longer than the response time of the medium, an isotropic medium, the same linear polarization for the copropagating fields, and no frequency dependence for the nonlinear susceptibility $\chi^{(3)}$, the nonlinear polarization reduces to

$$P^{NL}(r, z, t) = \chi^{(3)} E^3(r, z, t), \tag{2}$$

where the transverse component of the total electric field can be approximated by

$$E(r, z, t) = \tfrac{1}{2}\{A_1(r, z, t)e^{i(\omega_1 t - \beta_1 z)} + A_2(r, z, t)e^{i(\omega_2 t - \beta_2 z)} + c.c.\}. \tag{3}$$

$A_1$ and $A_2$ refer to the envelopes of copropagating pulses of carrier frequencies $\omega_1$ and $\omega_2$, and $\beta_1$ and $\beta_2$ are the corresponding propagation constants, respectively.

Substituting Eq. (3) into Eq. (2) and keeping only the terms synchronized with $\omega_1$ and $\omega_2$, one obtains

$$P^{NL}(r, z, t) = P_1^{NL}(r, z, t) + P_2^{NL}(r, z, t), \tag{4a}$$

$$P_1^{NL}(r, z, t) = \tfrac{3}{8}\chi^{(3)}\left(|A_1|^2 + 2|A_2|^2\right)A_1 e^{i(w_1 t - \beta_1 z)}, \tag{4b}$$

$$P_2^{NL}(r, z, t) = \tfrac{3}{8}\chi^{(3)}\left(|A_2|^2 + 2|A_1|^2\right)A_2 e^{i(w_2 t - \beta_2 z)}, \tag{4c}$$

where $P_1^{NL}$ and $P_2^{NL}$ are the nonlinear polarizations at frequencies $\omega_1$ and $\omega_2$, respectively. The second terms in the right sides of Eqs. (4b) and (4c) are cross-phase modulations terms. Note the factor of 2.

Combining Eqs. (1)–(4) and using the slowly varying envelope approximation (at the first order for the nonlinearity), one obtains the coupled nonlinear wave equations:

$$\frac{\partial A_1}{\partial z} + \frac{1}{v_{g1}}\frac{\partial A_1}{\partial t} + \frac{i}{2}\beta_1^{(2)}\frac{\partial^2 A_1}{\partial t^2} = i\frac{\omega_1}{c}n_2\left[|A_1|^2 + 2|A_2|^2\right]A_1, \tag{5a}$$

$$\frac{\partial A_2}{\partial z} + \frac{1}{v_{g2}}\frac{\partial A_2}{\partial t} + \frac{i}{2}\beta_2^{(2)}\frac{\partial^2 A_2}{\partial t^2} = i\frac{\omega_2}{c}n_2\left[|A_2|^2 + 2|A_1|^2\right]A_2, \tag{5b}$$

where $v_{gi}$ is the group velocity for the wave $i$, $\beta_i^{(2)}$ is the group velocity dispersion for the wave $i$, and $n_2 = 3\chi^{(3)}/8n$ is the nonlinear refractive index.

In the most general case, numerical methods are used to solve Eqs. (5). However, they have analytical solutions when the group velocity dispersion temporal broadening can be neglected.

Denoting the amplitude and phase of the pulse envelope by $a$ and $\alpha$, that is,

$$A_1(\tau, z) = a_1(\tau, z)e^{i\alpha_1(\tau,z)} \quad \text{and} \quad A_2(\tau, z) = a_2(\tau, z)e^{i\alpha_2(\tau,z)}, \tag{6}$$

and assuming $\beta_1^{(2)} \approx \beta_2^{(2)} \approx 0$, Eqs. (5a) and (5b) reduce to

$$\frac{\partial a_1}{\partial z} = 0, \tag{7a}$$

$$\frac{\partial a_1}{\partial z} = i\frac{\omega_1}{c}n_2\left[a_1^2 + 2a_2^2\right], \tag{7b}$$

$$\frac{\partial a_2}{\partial z} + \left(\frac{1}{v_{g2}} - \frac{1}{v_{g1}}\right)\frac{\partial a_2}{\partial \tau} = 0, \tag{7c}$$

$$\frac{\partial \alpha_2}{\partial z} = i\frac{\omega_2}{c}n_2\left[a_2^2 + 2a_1^2\right], \tag{7d}$$

where $\tau = (t - z/v_{g1})/T_0$ and $T_0$ is the $1/e$ pulse duration.

In addition, Gaussian pulses are chosen at $z = 0$:

$$A_1(\tau, z = 0) = \sqrt{\frac{P_1}{A_{\text{eff}}}}e^{-\tau^2/2}, \tag{8a}$$

$$A_2(\tau, z = 0) = \sqrt{\frac{P_2}{A_{\text{eff}}}}e^{-(\tau-\tau_d)^2/2}, \tag{8b}$$

where $P$ is the pulse peak power, $A_{\text{eff}}$ is the effective cross-sectional area, and $\tau_d = T_d/T_0$ is the normalized time delay between pulses at $z = 0$. With the initial conditions defined by Eqs. (8), Eqs. (5) have analytical solutions when temporal broadenings are neglected:

$$A_1(\tau, z) = \sqrt{\frac{P_1}{A_{\text{eff}}}}e^{-\tau^2/2}e^{i\alpha_1(t,z)}, \tag{9a}$$

$$A_2(\tau, z) = \sqrt{\frac{P_2}{A_{\text{eff}}}}e^{-(\tau-\tau_d-z/L_w)^2/2}e^{i\alpha_2(\tau,z)}, \tag{9b}$$

$$\alpha_1(\tau, z) = \frac{\omega_1}{c}n_2\frac{P_1}{A_{\text{eff}}}ze^{-\tau^2} + \sqrt{\pi}\frac{\omega_1}{c}n_2\frac{P_2}{A_{\text{eff}}}L_w\left[\text{erf}(\tau - \tau_d) - \text{erf}\left(\tau - \tau_d - \frac{z}{L_w}\right)\right], \tag{9c}$$

$$\alpha_2(\tau, z) = \frac{\omega_2}{c}n_2\frac{P_2}{A_{\text{eff}}}ze^{-(\tau-\tau_d-z/L_w)^2} + \sqrt{\pi}\frac{\omega_2}{c}n_2\frac{P_1}{A_{\text{eff}}}L_w\left[\text{erf}(\tau) - \text{erf}\left(\tau - \frac{z}{L_w}\right)\right], \tag{9d}$$

where $L_w = T_0/(1/v_{g1} - 1/v_{g2})$ is defined as the walk-off length.

Equations (9c) and (9d) show that the phases $\alpha_1(\tau, z)$ of copropagating pulses that overlap in a nonlinear Kerr medium are modified by a cross-phase modulation via the peak power $P_{j\neq i}$. In the case of ultrashort pulses this cross-

phase modulation gives rise to the generation of new frequencies, as does self-phase modulation.

The instantaneous XPM-induced frequency chirps are obtained by differentiating Eqs. (9c) and (9d) according to the instantaneous frequency formula $\Delta\omega = -\partial\alpha/\partial\tau$. These are

$$\Delta\omega_1(\tau, z) = 2\frac{\omega_1}{c}n_2\frac{P_1}{A_{\text{eff}}}\frac{z}{T_0}\tau e^{-\tau^2} 2\frac{\omega_1}{c}n_2\frac{P_2}{A_{\text{eff}}}\frac{L_w}{T_0}\left[e^{-(\tau-\tau_d-2/L_w)^2} - e^{-(\tau-\tau_d-z/L_w)^2}\right], \tag{10a}$$

$$\Delta\omega_2(\tau, z) = 2\frac{\omega_2}{c}n_2\frac{P_2}{A_{\text{eff}}}\frac{z}{T_0}(\tau - \tau_d - 2/L_w)e^{-(\tau-\tau_d-z/L_w)^2} + 2\frac{\omega_2}{c}n_2\frac{P_1}{A_{\text{eff}}}\frac{L_w}{T_0}\left[e^{-\tau^2} - e^{-(\tau-2/L_w)^2}\right], \tag{10b}$$

where $\Delta\omega_1 = \omega - \omega_1$ and $\Delta\omega_2 = \omega - \omega_2$. The first and second terms on the right sides of Eqs. (10a) and (10b) are contributions arising from SPM and XPM, respectively. It is interesting to notice in Eq. (10) than the maximum frequency chirp arising from XPM is inversely proportional to the group velocity mismatch $L_w/T_0 = 1/(1/v_{g1} - 1/v_{g2})$ rather than the pump pulse time duration or distance traveled $z$ as for ZPM. Therefore, the time duration of pump pulses does not have to be as short as the time duration of probe pulses for XPM applications.

More generally, spectral profiles affected by XPM can be studied by computing the Fourier transform:

$$S(\omega - \omega_0, z) = \frac{1}{2\pi}\int_{-\infty}^{+\infty} a(\tau, z)e^{i\alpha(\tau, z)}e^{i(\omega-\omega_0)\tau}d\tau, \tag{11}$$

where $|S(\omega - \omega_0, z)|^2$ represents the spectral intensity distribution of the pulse. Equation (10) is readily evaluated numerically using fast Fourier transform algorithms.

Analytical results of Eqs. (9) take in account XPM, SPM, and group velocity mismatch. These results are used in the Section 2.2 to isolate the specific spectral features arising from the nonlinear interaction of copropagating pulses. Higher-order effects due to group velocity dispersion broadening are discussed in Section 2.3.

## 2.2 Spectral Broadening Enhancement

The spectral evolution of ultrashort pulses interacting in a nonlinear Kerr medium is affected by the combined effects of XPM, SPM, and pulse walk-off.

For a negligible group velocity mismatch, XPM causes the pulse spectrum to broaden more than expected from SPM alone. The pulse phase of Eqs. (9c) and (9d) reduces to

$$\alpha_i(\tau, z)\frac{\omega_i}{c}n_2\frac{(P_i + 2P_j)}{A_{\text{eff}}}ze^{-\tau^2}. \tag{12}$$

The maximum spectral broadening of Gaussian pulses, computed using Eq. (12), is given by

$$\Delta\omega_i(z) \approx \frac{\omega_i}{c} n_2 \frac{(P_i + 2P_j)}{A_{\text{eff}}} \frac{z}{T_0}. \tag{13}$$

Thus, the spectral broadening enhancement arising from XPM is given by

$$\frac{\Delta\omega_{i\text{SPM+XPM}}}{\Delta\omega_{\text{iSPM}}} = 1 + \frac{2P_j}{P_i}. \tag{14}$$

Therefore, XPM can be used to control the spectral broadening of probe pulses using strong command pulses. This spectral control is important, for it is based on the electronic response of the interacting medium. It could be turned on and off in a few femtoseconds, which could lead to applications such as the pulse compression of weak probe pulses, frequency-based optical computation schemes, and the frequency multiplexing of ultrashort optical pulses with terahertz repetition rates.

The effect of pulse walk-off on XPM-induced spectral broadening can be neglected when wavelengths of pulses are in the low dispersion region of the nonlinear material, the wavelength difference or/and the sample length are small, and the time duration of pulses is not too short. For other physical situations, the group velocity mismatch and initial time delay between pulses affect strongly the spectral shape of interacting pulses (Islam et al., 1987a; Manassah 1987a; Agrawal et al., 1988, 1989a; Baldeck et al., 1988a).

Figure 4.1 shows how the spectrum of a weak probe pulse can be affected by the XPM generated by a strong copropagating pulse. The wavelength of the pump pulse was chosen where the pump pulse travels faster than the probe pulse. Initial time delays between pulses at the entrance of the nonlinear medium were selected to display the most characteristic interaction schemes. Figures 4.1a and 4.1b are displayed for reference. They show the probe pulse spectrum without XPM interaction (Figure 4.1a) and after the XPM interaction but for negligible group velocity mismatch (Figure 4.1b). Figure 4.1c is for the case of no initial time delay and total walk-off. The probe spectrum is shifted and broadened by XPM. The anti-Stokes shift is characteristic of the probe and pump pulse walk-off. The probe pulse is blue shifted because it is modulated only by the back of the faster pump pulse. When the time delay is chosen such that the pump pulse enters the nonlinear medium after the probe and has just time to catch up with the probe pulse, one obtains a broadening similar to that in Figure 4.1c but with a reverse Stokes shift (Figure 4.1d). The XPM broadening becomes symmetrical when the input time delay allows the pump pulse not only to catch up with but also to pass partially through the probe pulse (Figure 4.1e). However, if the interaction length is long enough to allow the pump pulse to completely overcome the probe pulse, there is no XPM-induced broadening (Figure 4.1f).

The diversity of spectral features displayed in Figure 4.1 can easily be understood by computing the phase and frequency chirp given by Eqs. (9)

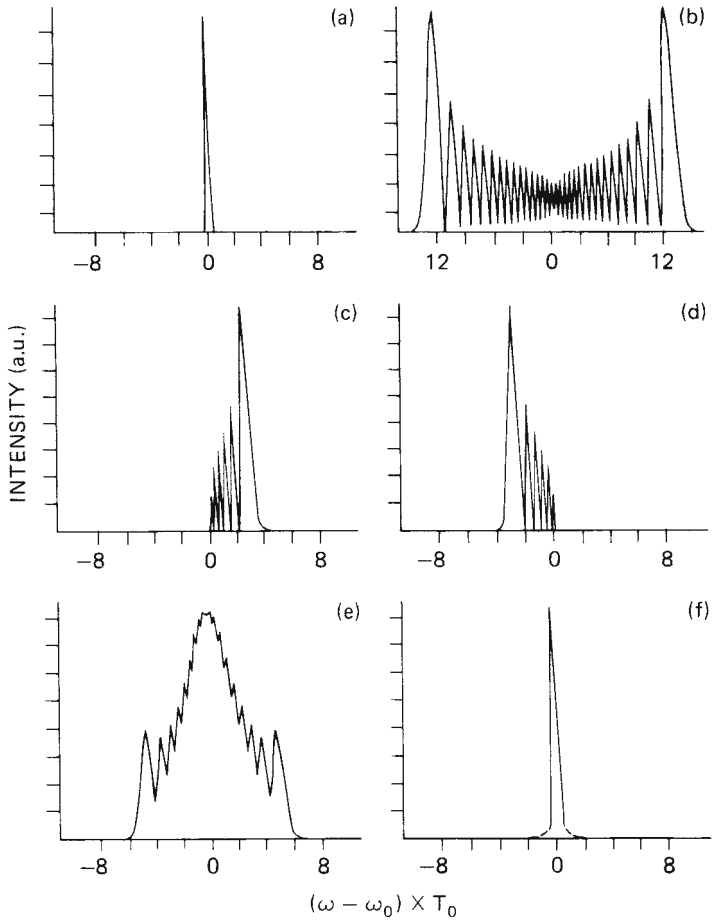


FIGURE 4.1. Influence of cross-phase modulation, walk-off, and input time delay on the spectrum of a probe pulse from Eqs. (9) and (11) with $P_1 \ll P_2$. $\phi = 2(\omega_1/c)n_2P_2L_w$, $\delta = z/L_w$, and $\tau_d$ are the XPM, walk-off, and input time delay parameters, respectively. (a) Reference spectrum with no XPM; i.e., $\phi = 0$. (b) XPM in the absence of walk-off; i.e., $\phi = 50$ and $\delta = 0$. (c) XPM, total walk-off, and no initial time delay; i.e., $\phi = 50$, $\delta = -5$, and $\tau_d = 0$. (d) XPM and initial time delay to compensate the walk-off; i.e., $\phi = 50$, $\delta = -5$, and $\tau_d = 5$. (e) XPM and symmetrical *partial* walk-off; i.e., $\phi = 50$, $\delta = -3$, and $\tau_d = 1.5$. (f) XPM and symmetrical *total* walk-off; i.e., $\phi = 50$, $\delta = -5$, and $\tau_d = 2.5$.

and (10) (Figure 4.2). For reference, Figure 4.2a shows the locations of the pump pulse (solid line) and the probe pulse (dotted line) at the output of the nonlinear sample (case of no initial delay and total walk-off). In this case the XPM phase, which is integrated over the fiber length, has the characteristic shape of an error function whose maximum corresponds to neither the probe pulse maximum nor the pump pulse maximum (Figure 4.2b). The probe pulse (dotted line in Figure 4.2c) sees only the blue part of the frequency chirp (solid line in Figure 4.2c) generated by the pump pulse. As a result, the probe

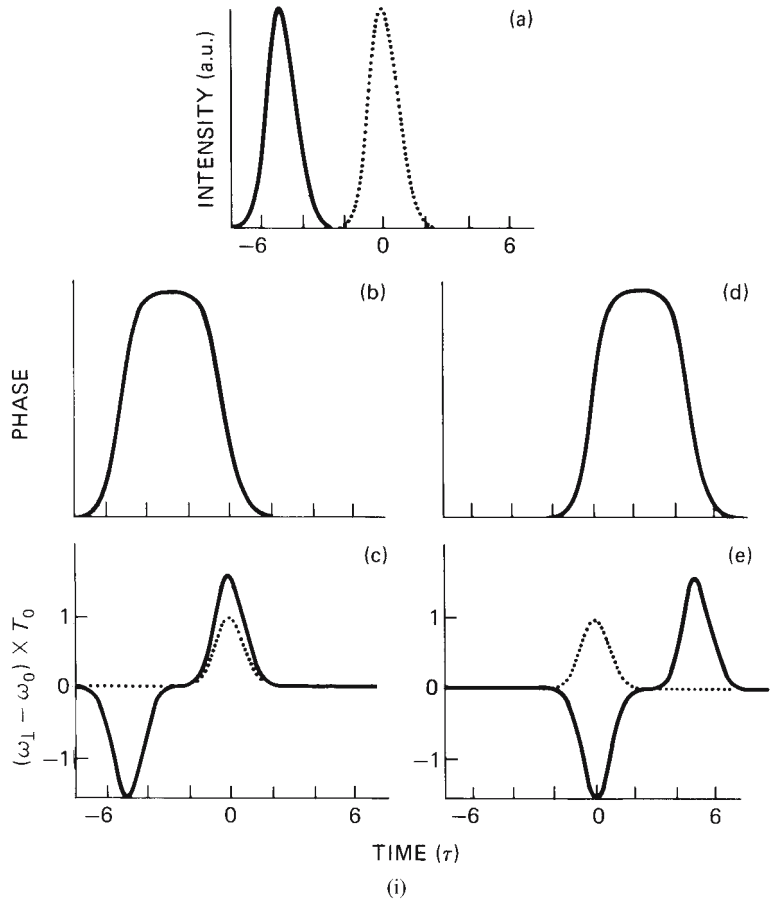


FIGURE 4.2. Influence of cross-phase modulation, walk-off, and input time delay on the phase and frequency chirp of a probe pulse. (a) Locations of pump (solid line) and probe (dotted line) at the output of the nonlinear medium for total walk-off and no initial time-delay; i.e., $\delta = -5$ and $\tau_d = 0$. (b) XPM phase with a total walk-off and no initial time delay; i.e., $\phi = 50$, $\delta = -5$, and $\tau_d = 0$. (c) XPM-induced chirp (solid line) with total walk-off and no initial time delay. (Dotted line) Probe pulse intensity. (d) XPM phase with an initial time delay to compensate the walk-off; i.e., $\phi = 50$, $\delta = -5$, and $\tau_d = 5$. (e) XPM-induced chirp (solid line) with an initial time delay to compensate the walk-off. (Dotted line) Probe pulse intensity. (f) XPM phase and symmetrical *partial* walk-off; i.e., $\phi = 50$, $\delta = -3$, and $\tau_d = 1.5$. (g) XPM-induced chirp (solid line) and symmetrical *partial* walk-off. (Dotted line) Probe pulse intensity. (h) XPM phase and symmetrical *total* walk-off; i.e., $\phi = 50$, $\delta = -5$, and $\tau_d = 2.5$. (i) XPM-induced chirp (solid line) and symmetrical *total* walk-off. (Dotted line) Probe pulse intensity.

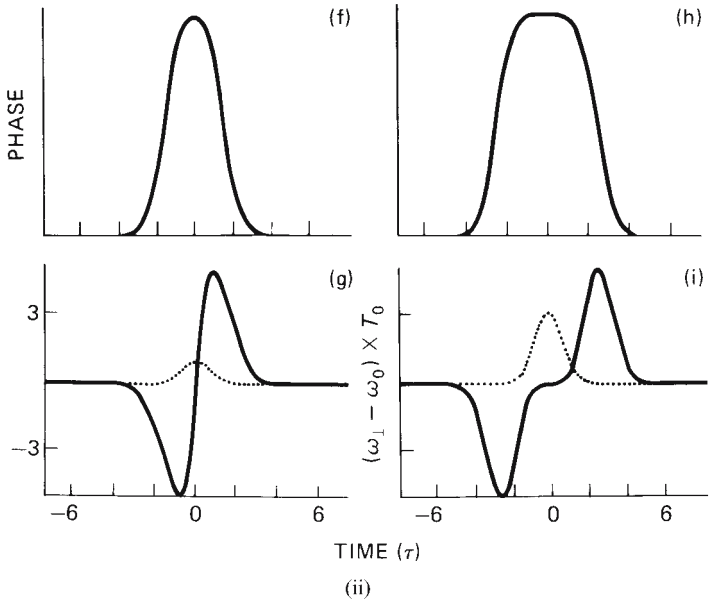


FIGURE 4.2. (*continued*)

spectrum is simultaneously broadened and shifted toward the highest frequencies (Figure 4.1c). One should notice that opposite to the SPM frequency chirp, the XPM chirp in Figure 4.2c is not monotonic. The pulse leading edge and trailing edge have a positive chirp and negative chirp, respectively. As a result, dispersive effects (GVD, grating pair, . . .) are different for the pulse front and the pulse back. In the regime of normal dispersion ($\beta^{(2)} > 0$), the pulse front would be broadened by GVD while the pulse back would be sharpened. Figures 4.2d and 4.2e show XPM-induced phase and frequency chirp for the mirror image case of Figures 4.2b and 4.2c. The probe spectrum is now shifted toward the smallest frequencies. Its leading edge has a negative frequency chirp, while the trailing edge has a positive one. A positive GVD would compress the pulse front and broaden the pulse back. The case of a partial symmetrical walk-off is displayed in Figures 4.2f and 4.2g. In first approximation, the time dependence of the XPM phase associated with the probe pulse energy is parabolic (Figure 4.2f), and the frequency chirp is quasi-linear (4.2 g). This is the prime quality needed for the compression of a weak pulse by following the XPM interaction by a grating pair compressor (Manassah, 1988). Figures 4.2h and 4.2i show why there is almost no spectral broadening enhancement when the pump pulse passes completely through the probe pulse (Figure 4.1f): the part of XPM associated with the probe pulse energy is constant (Figure 4.2h). The probe pulse is phase modulated, but *the phase shift is time independent*. Therefore, there is neither frequency chirp (Figure 4.2i) nor spectral broadening enhancement by XPM.

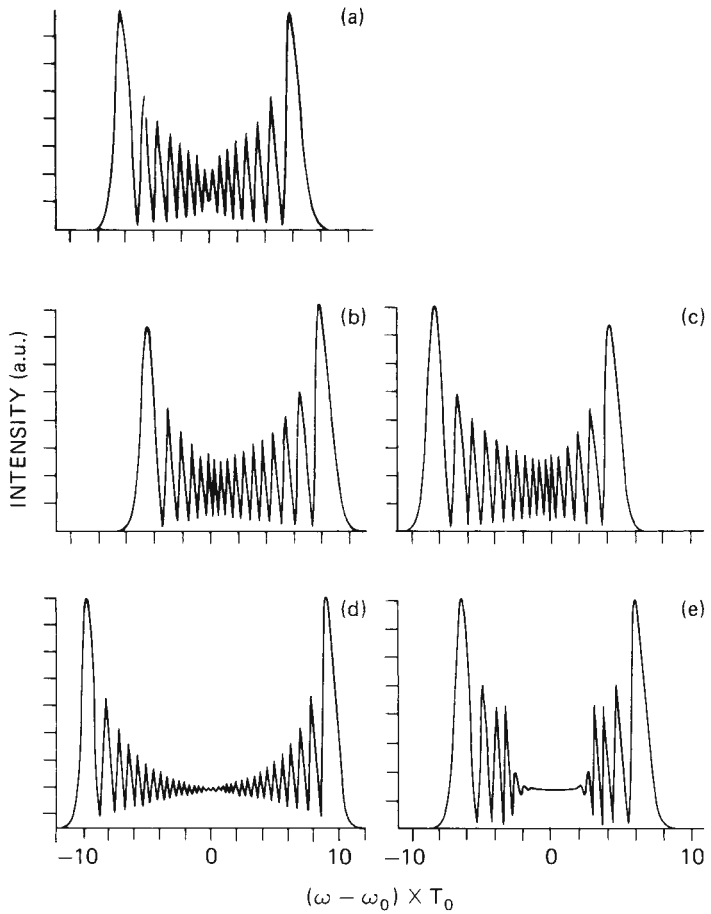


FIGURE 4.3. Influence of self-phase modulation, cross-phase modulation, walk-off, and input time delay on the spectrum of a probe pulse from Eqs. (9) and (11) with $P_1 = P_2$. The parameter values in Figure 4.1 are used.

The combined effects of XPM and walk-off on the spectra of weak probe pulses (negligible SPM) have been shown in Figure 4.1 and 4.2. When the group velocity mismatch is large, the spectral broadening is not significant and the above spectral features reduce to a tunable induced-frequency shift of the probe pulse frequency (see Section 3.2). When strong probe pulses are used, the SPM contribution has to be included in the analysis. Figure 4.3 show how the results of Figure 4.1 are modified when the probe power is the same as the pump power, that is, the SPM has to be taken in account. Figure 4.3a shows the spectral broadening arising from the SPM alone. Combined effects of SPM and XPM are displayed in Figures 4.3b to 4.3e with the same initial delays as in Figure 4.1. The SPM contribution to the spectral broad-

ening is larger than the XPM contribution because the XPM interaction length is limited by the walk-off between pump and probe pulses.

The XPM spectral features described in this section have been obtained using first-order approximation of the nonlinear polarization, propagation constant, and nonlinearity in the nonlinear wave equation (Eq. 1). Moreover, plane wave solutions and peak powers below the stimulated Raman scattering threshold have been assumed. For practical purposes it is often necessary to include the effects of (1) first- and second-order group velocity dispersion broadening, $\beta^{(2)}$ and $\beta^{(3)}$, (2) induced- and self-steepening, (3) four-wave mixing occurring when pump and probe pulses are coupled through $\chi^{(3)}$, (4) stimulated Raman scattering generation, (5) the finite time response of the nonlinearity, and (6) the spatial distribution of interacting fields (i.e., induced- and self-focusing, diffraction, Gaussian profile of beams, . . .). In Section 2.3 the combined effect of XPM and group velocity dispersion broadening $\beta^{(2)}$ is shown to lead to new kinds of optical wave breaking and pulse compression. Some other effects that lead to additional spectral, temporal, and spatial features of XPM are discussed by Agrawal (Chapter 3) and Manassah (Chapter 5).

## 2.3 Optical Wave Breaking and Pulse Compression due to Cross-Phase Modulation in Optical Fibers

When an ultrashort light pulse propagates through an optical fiber, its shape and spectrum change considerably as a result of the combined effect of group velocity dispersion $\beta^{(2)}$ and self-phase modulation. In the normal dispersion regime of the fiber ($\lambda \leq 1.3\,\mu$m), the pulse can develop rapid oscillations in the wings together with spectral sidelobes as a result of a phenomenon known as optical wave breaking (Tomlinson et al., 1985). In this section it is shown that a similar phenomenon can lead to rapid oscillations near one edge of a weak pulse that copropagates with a strong pulse (Agrawal et al., 1988).

To isolate the effects of XPM from those of SPM, a pump-probe configuration is chosen ($P_2 \ll P_1$) so that pulse 1 plays the role of the pump pulse and propagates without being affected by the copropagating probe pulse. The probe pulse, however, interacts with the pump pulse through XPM. To study how XPM affects the probe evolution along the fiber, Eqs. (5a) and (5b) have been solved numerically using a generalization of the beam propagation or the split-step method (Agrawal and Potasek, 1986). The numerical results depend strongly on the relative magnitudes of the length scales $L_d$ and $L_w$, where $L_d = T_0^2/|\beta_2|$ is the dispersion length and $L_w = v_{g1}v_{g2}T_0/|v_{g1} - v_{g2}|$ is the walk-off length. If $L_w \ll L_d$, the pulses walk off from each other before GVD has an opportunity to influence the pulse evolution. However, if $L_w$ and $L_d$ become comparable, XPM and GVD can act together and modify the pulse shape and spectra with new features.

To show these features as simply as possible, a specific case is considered in which $L_w/L_d = 0.1$ and $\lambda_1/\lambda_2 = 1.2$. Both pulses are assumed to propagate

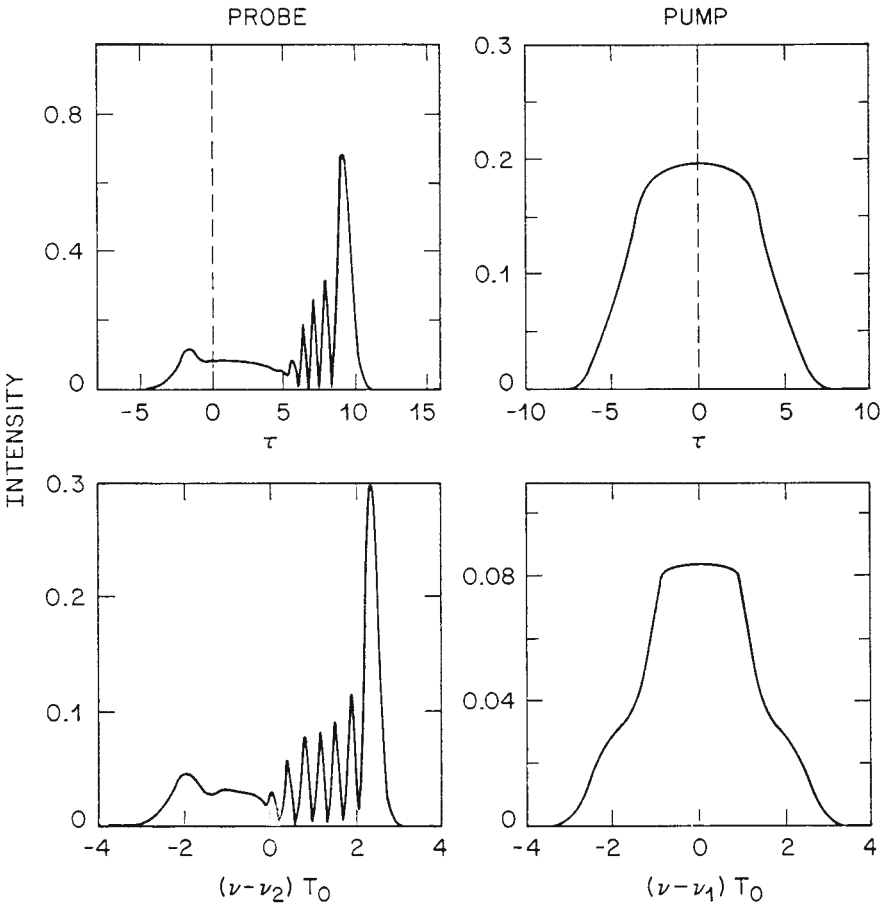


FIGURE 4.4. Shape and spectrum of probe pulse (left) and pump pulse (right) at $z/L_d = 0.4$ when the two pulses copropagate in the normal dispersion regime of a single-mode fiber. The parameters are $N = 10$, $L_w/L_d = 0.1$, $\lambda_1/\lambda_2 = 1.2$, and $\tau_d = 0$. Oscillations near the trailing edge (positive time) of the probe pulse are due to XPM-induced optical wave breaking. (From Agrawal et al., 1988.)

in the normal GVD regime with $\beta_1 = \beta_2 > 0$. It is assumed that the pump pulse goes faster than the probe pulse ($v_{g1} > v_{g2}$). At the fiber input both pulses are taken to be a Gaussian of the same width with an initial delay $\tau_d$ between them. First, the case $\tau_d = 0$ is considered, so the two pulses overlap completely at $z = 0$. Figure 4.4 shows the shapes and spectra of the pump and probe pulses at $z/L_d = 0.4$ obtained by solving Eqs. (5a) and (5b) numerically with $N = (\gamma_1 P_1 L_d)^{0.5} = 10$. For comparison, Figure 4.5 shows the probe and pump spectra under identical conditions but without GVD effects ($\beta_1 = \beta_2 = 0$). The pulse shapes are not shown since they remain unchanged when the GVD effects are excluded.

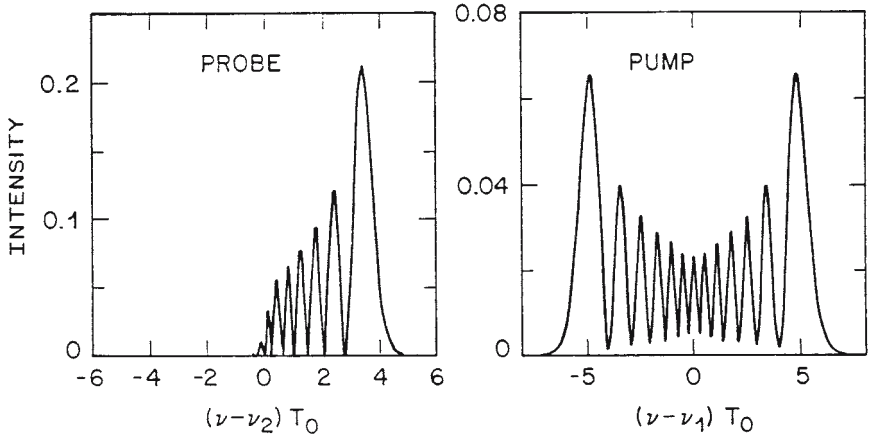


FIGURE 4.5. Spectra of probe and pump pulses under conditions identical to those of Figure 4.4 but without the GVD effects ($\beta_1 = \beta_2 = 0$). Pulse shapes are not shown as they remain unchanged. (From Agrawal et al., 1988.)

From a comparison of Figures 4.4 and 4.5, it is evident that GVD can substantially affect the evolution of features expected from SPM or XPM alone. Consider first the pump pulse for which XPM effects are absent. The expected from dispersive SPM for $N = 10$. With further propagation, the pump pulse eventually develops rapid oscillations in the wings as a result of conventional SPM-induced optical wave breaking. Consider now the probe pulse for which SPM effects are absent and probe pulse evolution is governed by dispersive XPM. In absence of GVD, the pulse shape would be a narrow Gaussian centered at $\tau = 4$ (the relative delay at the fiber output because of group velocity mismatch). The GVD effects not only broaden the pulse considerably but also induce rapid oscillations near the trailing edge of the probe pulse. These oscillations are due to XPM-induced optical wave breaking.

To understand the origin of XPM-induced optical wave breaking, it is useful to consider the frequency chirp imposed on the probe pulse by the copropagating pulse. As there is total walk-off and no initial delay, maximum chirp occurs at the center of the probe pulse. Since the chirp is positive, blue-shifted components are generated by XPM near the pulse center. As a result of the normal GVD, the peak of the probe pulse moves slower than its tails. Since the peak lags behind as the probe pulse propagates, it interferes with the trailing edge. Oscillations seen near the trailing edge of the probe pulse in Figure 4.4 result from such an interference. Since the basic mechanism is analogous to the optical wave-breaking phenomenon occurring in the case of dispersive XPM, we call it XPM-induced optical wave breaking.

In spite of the identical nature of the underlying physical mechanism, optical wave breaking exhibits different qualitative features in the XPM case

compared with the SPM case. The most striking difference is that the pulse shape is asymmetric with only one edge developing oscillations. For the case shown in Figure 4.4 oscillations occur near the trailing edge. If the probe and pump wavelengths were reversed so that the pump pulse moved slower than the probe pulse, oscillations would occur near the leading edge since the pump pulse would interact mainly with that edge. In fact, in that case the shape and the spectrum of the probe pulse are just the mirror images of those shown in Figures 4.4 and 4.5.

The effect of initial delay between probe and pump pulses is now investigated. The effect of initial delay on XPM-induced spectral broadening has been discussed in the dispersionless limit ($\beta_1 = \beta_2 = 0$) in Section 2.2. For example, if the pump pulse is delayed by the right amount so that it catches

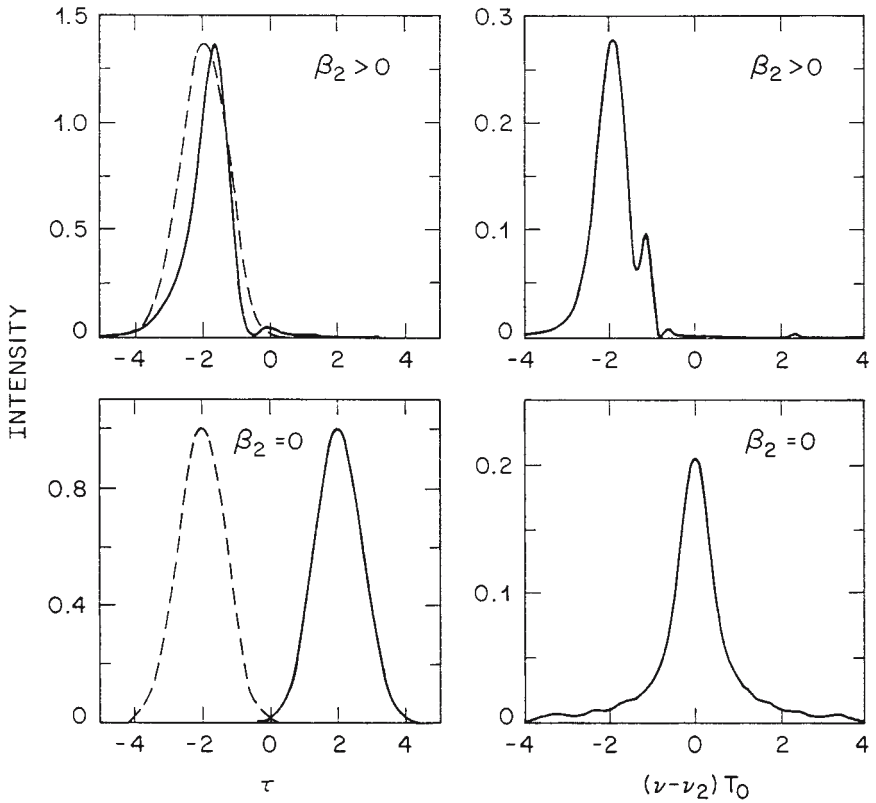


FIGURE 4.6. Probe shape and spectrum with (top) and without (bottom) the GVD effects under conditions identical to those of Figure 4.5 except that $\tau_d = -2$. Note the important effect on pulse evolution of the initial time delay between the pump and probe pulses. (From Agrawal et al., 1988.)

up with the probe pulse at the fiber output, the probe spectrum is just the mirror image of that shown in Figure 4.4, exhibiting a red shift rather than a blue shift. Futhermore, if $\tau_d$ is adjusted such that the pump pulse catches up with the probe pulse halfway through the fiber, the probe spectrum is symmetrically broadened since the pump walks through the probe in a symmetric manner. Our numerical results show that the inclusion of GVD completely alters this behavior. Figure 4.6 shows the probe shape and spectrum under conditions identical to those of Figure 4.4 except that the probe pulse is advanced ($\tau_d = -2$) such that the pump pulse would catch it halfway through the fiber in the absence of GVD effects. The lower row shows the expected behavior in the dispersionless limit, showing the symmetrical spectral broadening in this case of symmetrical walk-off. A direct comparison reveals how much the presence of GVD can affect the SPM effects on the pulse evolution. In particular, both the pulse shape and spectra are asymmetric. More interestingly, the probe pulse is compressed, in sharp contrast to the case of Figure 4.4, where GVD led to a huge broadening. This can be understood qualitatively from Eq. (10). For the case shown in Figure 4.6, the XPM-induced chirp is negative and nearly linear across the trailing part of the probe pulse. Because of this chirp, the traveling part is compressed as the probe pulse propagates inside the fiber.

Experimental observation of XPM-induced optical wave breaking would require the use of femtosecond pulses. This can be seen by noting that for picosecond pulses with $T_0 = 5$–$10$ ps, typically $L_d \approx 1$ km while $L_w \approx 1$ m even if the pump-probe wavelengths differ by as little as 10 nm. By contrast, if $T_0 = 100$ fs, both $L_d$ and $L_w$ become comparable ($\approx$10 cm), and the temporal changes in the probe shape discussed here can occur in a fiber less than a meter long. Pulses much shorter than 100 fs should also not be used since higher-order nonlinear effects such as self-steepening and a delayed nonlinear response then become increasingly important. Although these effects are not expected to eliminate the phenomenon of XPM-induced optical wave breaking, they may interfere with the interpretation of experimental data.

## 3. Pump-Probe Cross-Phase Modulation Experiments

Cross-phase modulation is intrinsic to numerous schemes of ultrashort pulse interaction. The first observation of spectral effects arising from XPM was reported using a pump-probe scheme (Alfano et al., 1986). The phase modulation generated by the infrared pulse at the probe wavelength was referred to as an induced-phase modulation (PM). More recently, the induced-frequency shift and spectral broadening enhancement of picosecond probe pulses have been observed using optical fibers as nonlinear media (Baldeck et al., 1988a; Islam et al., 1987a, b). Pump-probe experiments on XPM are of prime importance for they could lead to applications for pulse compres-

sion, optical communication, and optical computation purposes. Results of the pump-probe experiments on XPM are discussed in this section.

## 3.1 Spectral Broadening Enhancement by Cross-Phase Modulation in BK-7 Glass

The possibility of enhancing the spectral broadening of a probe pulse using a copropagating pump pulse was first observed experimentally in early 1986 (Alfano et al., 1986). The spectral broadening of a weak 80-$\mu$J picosecond 530-nm laser in BK-7 glass was enhanced over the entire spectral band by the presence of an intense millijoule picosecond 1060-nm laser pulse. The spectral distributions of the self-phase modulation and the cross-phase modulation signals were found to be similar. The dominant enhancement mechanism for the induced supercontinuum was determined to be a cross-phase modulation process, not stimulated four-photon scattering.

The experimental setup is shown in Figure 4.7. A single 8-ps laser pulse at 1060 nm generated from a mode-locked glass laser system was used as the pump beam. Its second harmonic was used as the probe beam. These pulses at the primary 1060-nm and the second harmonic 530-nm wavelengths were weakly focused into a 9-cm-long BK-7 glass. A weak supercontinuum signal was observed when both 530- and 1060-nm laser pulses were sent through the sample at the same time. This signal could arise from the IPM process and/or stimulated four-photon parametric generation (FPPG).

In this induced supercontinuum experiment, the 530-nm laser pulse intensity was kept nearly constant with a pulse energy of about 80 $\mu$J. The primary 1060-nm laser pulse energy was a controlled variable changing from 0 to 2 mJ. Filters were used to adjust the 1060-nm pump-laser pump intensity. The output beam was separated into three paths for diagnosis.

The output beam along path 1 was imaged onto the slit of a 0.5-m Jarrel-Ash spectrograph to separate the contributions from the possible different mechanisms for the supercontinuum by analyzing the spatial distribution of the spectrum from phase modulation and stimulated four-photon scattering processes. In this spectrograph measurement, films were used to measure the spatial distribution of the supercontinuum spectrum and a photomultiplier tube was used to obtain quantitative reading. To distinguish different contributions from either phase modulation or stimulated four-photon scattering, geometric blocks were arranged in the path for the selection of a particular process. An aperture of 6 mm diameter was placed in front of the entrance slit of the spectrograph to measure the signal contributed phase modulation, while an aluminum plate of 7 mm width was placed in front of the spectrograph entrance slit to measure the $\lambda = 570$ nm contribution.

The beam along path 2 was directed into a spectrometer with an optical multichannel analyzer to measure the supercontinuum spectral intensity distribution. The spectrum was digitized, displayed, and stored in 500 channels

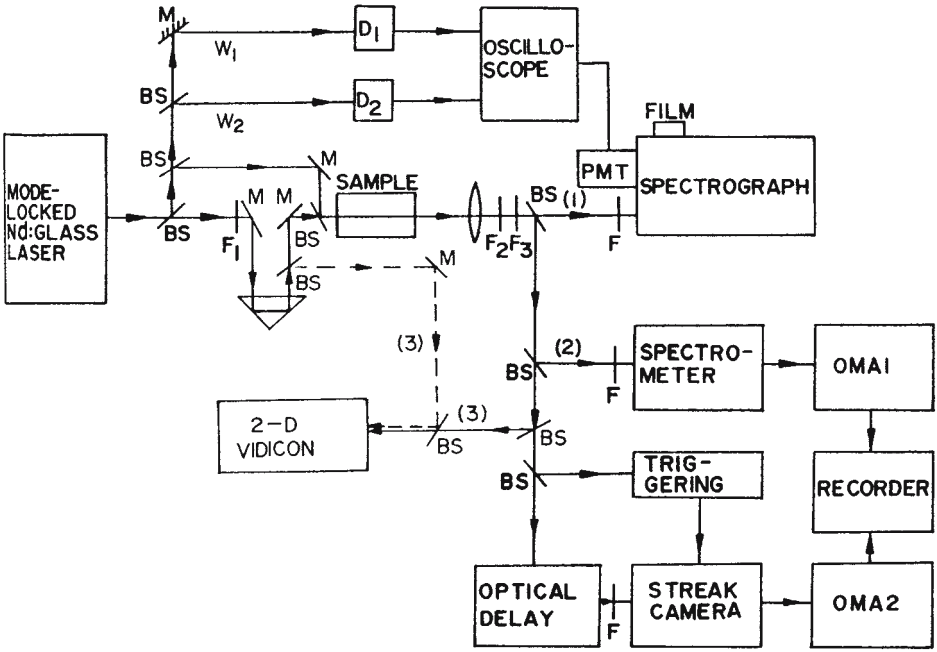


FIGURE 4.7. Schematic diagram of the experimental arrangment for measuring the spectral broadening enhancement of probe pulses by induced-phase modulation. $F_1$: Hoya HA30 (0.03%), R72 (82%), Corning 1-75 (1%), 1-59 (15%), 0-51 (69%), 3-75 (80%). The numbers in parentheses correspond to the transmittivity at 1054 nm. All these color filters have about 82% transmittivity at 527 nm. $F_2$: 1-75 + 3-67 for Stokes side measurements; $F_2$: 1-75 + 2 (5-57) for anti-Stokes side measurements; $F_3$: neutral density filters; $F$: ND3 + 1-75; D1, D2; detectors; M: dielectric-coated mirror; BS: beam splitter. (From Alfano et al., 1986.)

as a function of wavelength. The beam along path 3 was delayed and directed into a Hamamatsu Model C1587 streak camera to measure the temporal distribution of the laser pulse and induced supercontinuum. The duration of the induced supercontinuum with a selected 10-nm bandwidth was measured to be about the same as the incident laser pulse duration.

Experimental results for the spectral distribution of induced supercontinuum and supercontinuum are displayed in Figure 4.8. More than 20 laser shots for each data point in each instance have been normalized and smoothed. The average gain of the induced supercontinuum in a BK-7 glass from 410- to 660-nm wavelength was about 11 times that of the supercontinuum. In this instance, both the 530- and 1060-nm laser pulse energies were maintained nearly constant: 80 $\mu$J for 530 nm and 2 mJ for 1060 nm. In this experiment, the 530-nm laser pulse generated a weak supercontinuum and the intense 1060-nm laser pulse served as a catalyst to enhance the super-

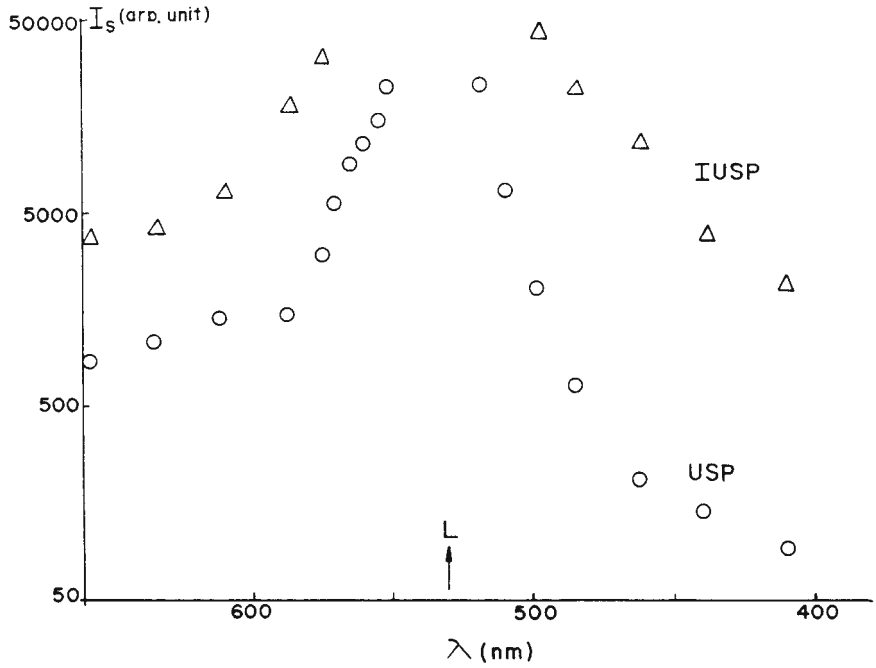


FIGURE 4.8. Intensities of the induced ultrafast supercontinuum pulse (IUSP) and the ultrafast supercontinuum pulse (USP). Each data point was an average of about 20 laser shots and was corrected for the detector, filter, and spectrometer spectral sensitivity. (Δ) IUSP ($F_1$: 3-75); (○) USP from 527 nm ($F_1$: HA30). USP from 1054 nm, which is not shown here was ≈1% of the IUSP signal. The measured 527-nm probe pulse was about $5 \times 10$ counts on this arbitrary unit scale. The error bar of each data point is about ±20%. (From Alfano et al., 1986.)

continuum in the 530-nm pulse. The supercontinuum generated by the 1060-nm pulse alone in this spectral region was less than 1% of the total induced supercontinuum. The spectral shapes of the induced supercontinuum pulse and the supercontinuum pulse in Figure 4.8 are similar. Use of several liquid samples such as water, nitrobenzene, $CS_2$, and $CCl_4$ has also been attempted to obtain the induced supercontinuum. There was no significant (twofold) enhancement from all other samples that we tested.

A plot of the intensity dependence of the induced supercontinuum is displayed in Figure 4.9 as a function of the 1060-nm pump pulse energy. The wavelengths plotted in Figure 4.9 were $\lambda = 570$ nm for the Stokes side and $\lambda = 498$ nm for the anti-Stokes side. The 530-nm pulse energy was set at $80 \pm 15\,\mu$J. The induced supercontinuum increased linearly as the added 1060-nm laser pulse energy was increased from 0 to $200\,\mu$J. When the 1060-nm pump pulse was over 1 mJ, the supercontinuum enhancement reached a plateau and saturated at a gain factor of about 11 times over the supercontinuum inten-

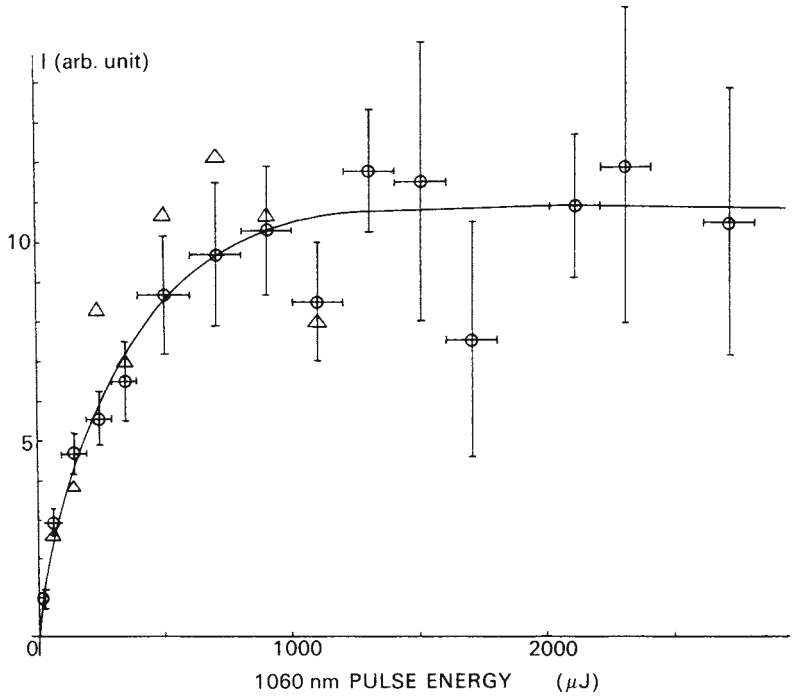


FIGURE 4.9. Dependence of the IUSP signal on the intensity of the 1.06-$\mu$m pump pulse. (○) Stokes side at $\lambda = 570$ nm; (Δ) anti-Stokes side at $\lambda = 498$ nm. The error bars of the anti-Stokes side were similar to those of the Stokes side. The solid line is a guide for the eye. The vertical axis is the normalized $I_{\text{IUSP}}/I_{527\,\text{nm}}$. (From Alfano et al., 1986.)

sity generated by only the 530-nm pulse. This gain saturation may be due to the trailing edge of the pulse shape function being maximally distorted when the primary pulse intensity reaches a certain critical value. This implies a saturation of the PM spectral distribution intensity when the pumped primary pulse energy is above 1 mJ, as shown in Figure 4.9.

Since the supercontinuum generation can be due to the phase modulation and/or the stimulated four-photon scattering processes, it is important to distinguish between these two different contributions to the induced supercontinuum signal. Spatial filtering of the signal was used to separate the two main contributions. The induced supercontinuum spectrum shows a spatial spectral distribution similar to that of the conventional supercontinuum. The collinear profile that is due to the phase modulation has nearly the same spatial distribution as the incident laser pulse. Two emission wings at noncollinear angles correspond to the stimulated four-photon scattering continuum arising from the phase-matching condition of the generated wavelengths emitted at different angles from the incident laser beam direction. Using a

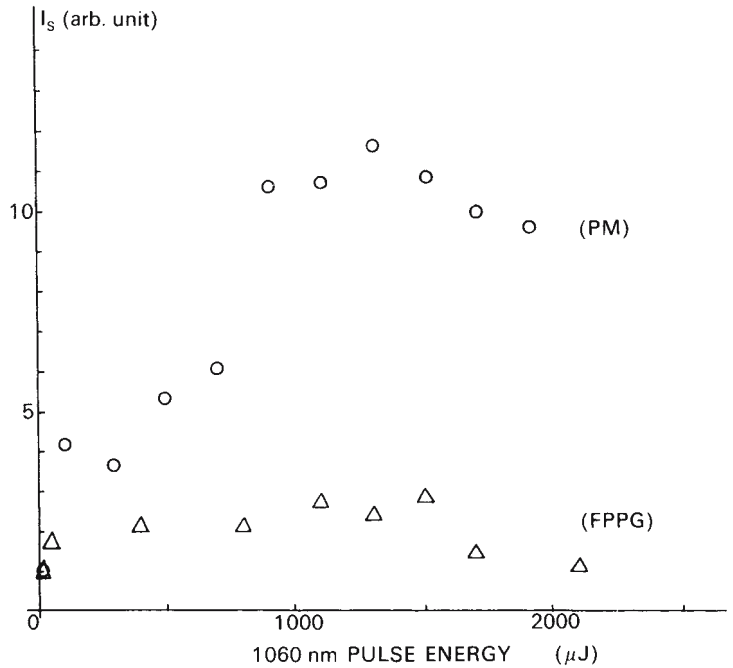


FIGURE 4.10. Dependence of $I_s$ (PM) and $I_s$ (FPPG) at $\lambda = 570$ nm or the intensity of the 1054-nm pump laser pulse. (○) PM; (Δ) FPPG. The measured signal has been normalized with the incident 527-nm pulse energy. The error bar of each data point is about ±20% of the average value. (From Alfano et al., 1986.)

photomultiplier system and spatial filtering, quantitative measurements of the induced supercontinuum contributions from the collinear PM and the noncollinear stimulated four-photon scattering parts were obtained (Figure 4.10). These signals, measured at $\lambda = 570$ nm from the collinear PM and the noncollinear parts of the induced supercontinuum, are plotted as a function of the pump pulse energy. There was little gain from the contribution of the stimulated four-photon scattering process over the entire pulse-energy-dependent measurement as shown in Figure 4.10. The main enhancement of the induced supercontinuum generation is consequently attributed to the PM mechanism, which corresponds to the collinear geometry. Another possible mechanism for the observed induced supercontinuum could be associated with the enhanced self-focusing of the second harmonic pulse induced by the primary pulse. There was no significant difference in the spatial intensity distribution of the 530-nm probe beam with and without the added intense 1060-nm pulse.

In this experiment the spectral broadening of 530-nm pulses was enhanced by nonlinear interaction with copropagating strong infrared pulses in a BK-

7 glass sample. The spectral change has been found to arise from a phase modulation process rather than a stimulated four-photon mixing process. It is in good agreement with predictions of the induced-phase modulation theory. This experiment showed the first clear evidence of a cross-phase modulation spectral effect.

## 3.2 Induced-Frequency Shift of Copropagating Pulses

Optical fibers are convenient for the study of nonlinear optical processes. The optical energy is concentrated into small cross section (typically $10^{-7}\,\mathrm{cm}^2$) for long interaction lengths. Thus, large nonlinear effects are possible with moderate peak powers (10–$10^4$ W). Optical fibers appear to be an ideal medium in which to investigate XPM effects. The first pump probe experiment using picosecond pulses propagating in optical fibers demonstrated the importance of the pulse walk-off in XPM spectral effects (Baldeck et al., 1988a). It was shown that ultrashort pulses that overlap in a nonlinear and highly dispersive medium undergo a substantial shift of their carrier frequencies. This new coherent effect, which was referred to as an induced-frequency shift, resulted from the combined effect of cross-phase modulation and pulse walk-off. In the experiment, the induced-frequency shift was observed by using strong infrared pulses that shifted the frequency of weak picosecond green pulses copropagating in a 1-m-long single-mode optical fiber. Tunable red and blue shifts were obtained at the fiber output by changing the time delay between infrared and green pulses at the fiber input.

A schematic of the experimental setup is shown in Figure 4.11. A mode-locked Nd: YAG laser with a second harmonic crystal was used to produce

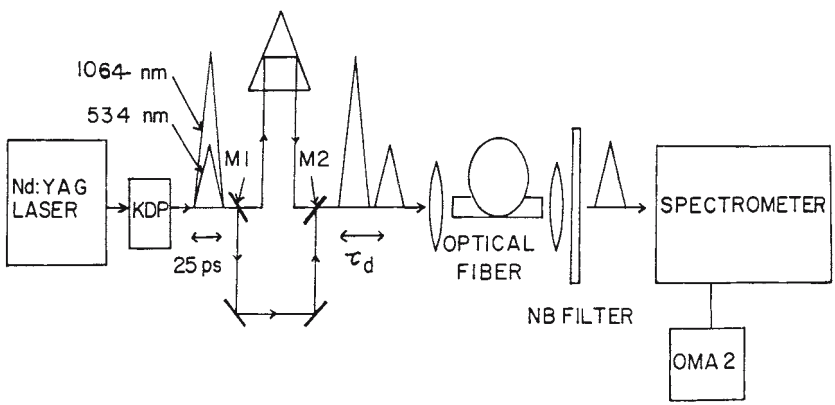


FIGURE 4.11. Experimental setup used to measure the induced-frequency shift of 532-nm pulses as a function of the time delay between pump and probe pulses at the optical fiber input. Mirrors $M_1$ and $M_2$ are wavelength selective; i.e., they reflect 532-nm pulses and transmit 1064-nm pulses. (From Baldeck et al., 1988a.)

33-ps infrared pulses and 25-ps green pulses. These pulses were separated using a Mach-Zehnder interferometer delay scheme with wavelength-selective mirrors. The infrared and green pulses propagated in different interferometer arms. The optical path of each pulse was controlled using variable optical delays. The energy of infrared pulses was adjusted with neutral density filters in the range 1 to 100 nJ while the energy of green pulses was set to about 1 nJ. The nonlinear dispersive medium was a 1-m-long single-mode optical fiber (Corguide of Corning Glass). This length was chosen to allow for total walk-off without losing control of the pulse delay at the fiber output. The group velocity mismatch between 532 and 1064-nm pulses was calculated to be about 76 ps/m in fused silica. The spectrum of green pulses was measured using a grating spectrometer (1 meter, 1200 lines/mm) and an optical multichannel analyzer (OMA2).

The spectra of green pulses propagating with and without infrared pulses are plotted in Figure 4.12. The dashed spectrum corresponds to the case of green pulses propagating alone. The blue-shifted and red-shifted spectra are those of green pulses copropagating with infrared pulses after the input delays were set at 0 and 80 ps, respectively. The main effect of the nonlinear interaction was to shift the carrier frequency of green pulses. The induced-wavelength shift versus the input delay between infrared and green pulses is

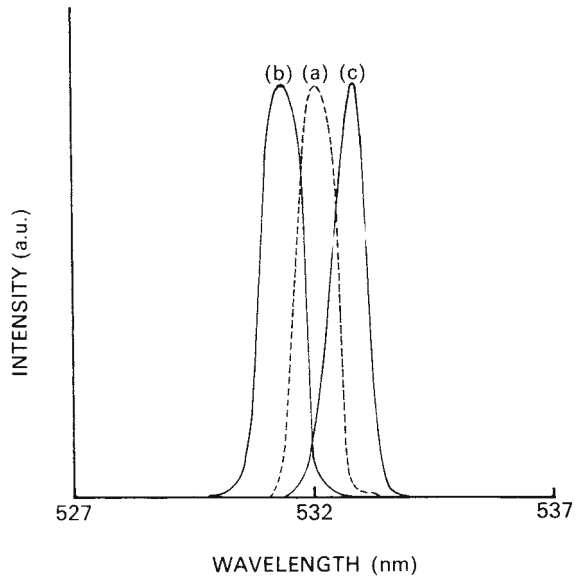


FIGURE 4.12. Cross-phase modulation effects on spectra of green 532-nm pulses. (a) Reference spectrum (no copropagating infrared pulse). (b) Infrared and green pulses overlapped at the fiber input. (c) Infrared pulse delayed by 80 ps at the fiber input. (From Baldeck et al., 1988a.)

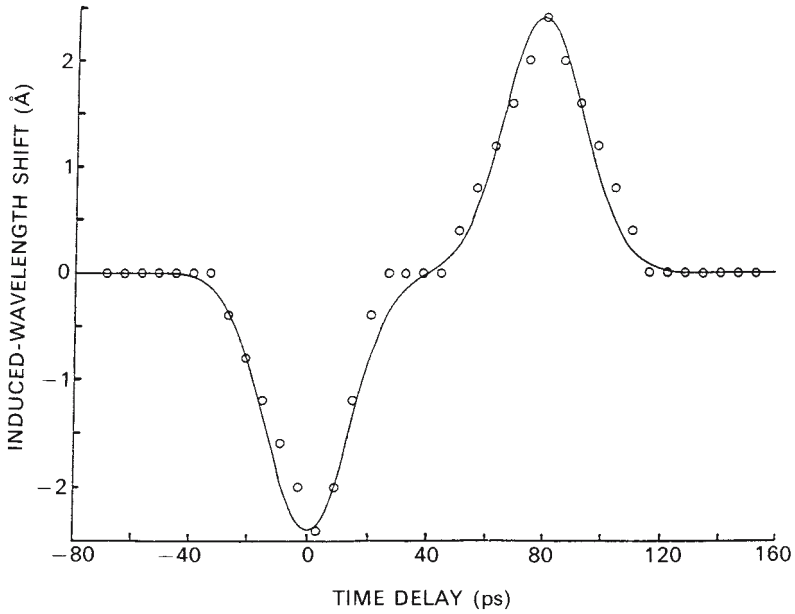


FIGURE 4.13. Induced wavelength shift of green 532-nm pulses as a function of the input time delay between 532-nm pulses and infrared 1064-nm pulses at the input of a 1-m-long optical fiber. (○) Experimental points. The solid line is the theoretical prediction from Eq. (3.3). (From Baldeck et al., 1988a.)

plotted in Figure 4.13. The maximum induced-wavelength shift increased linearly with the infrared pulse peak power (Figure 4.14). Hence, the carrier wavelength of green pulses could be tuned up to 4 Å toward both the red and blue sides by varying the time delay between infrared and green pulses at the fiber input. The solid curves in Figures 4.13 and 4.14 are from theory.

When weak probe pulses are used the SPM contribution can be neglected in Eqs. (9) and (10). Thus, nonlinear phase shifts and frequency chirps are given by

$$\alpha_1(\tau, z) \approx \sqrt{\pi}\,\frac{\omega_1}{c}\,n_2\,\frac{P_2}{A_{\text{eff}}}\,L_w\left[\operatorname{erf}(\tau-\tau_d)-\operatorname{erf}\left(\tau-\tau_d+\frac{z}{L_w}\right)\right], \tag{15}$$

$$\delta\omega_1(\tau, z) \approx -2\,\frac{\omega_1}{c}\,n_2\,\frac{P_2}{A_{\text{eff}}}\,\frac{L_w}{T_0}\left[e^{-(\tau-\tau_d)^2}-e^{-(\tau-\tau_d-z/L_w)^2}\right]. \tag{16}$$

When the pulses coincide at the fiber entrance ($t_d$ = 0) the point of maximum phase is generated ahead of the green pulse peak because of the group velocity mismatch (Eq. 15). The green pulse sees only the trailing part of the XPM profile because it travels slower than the pump pulse. This leads to a blue induced-frequency shift (Eq. 16). Similarly, when the initial delay is set at 80 ps, the infrared pulse has just sufficient time to catch up with the

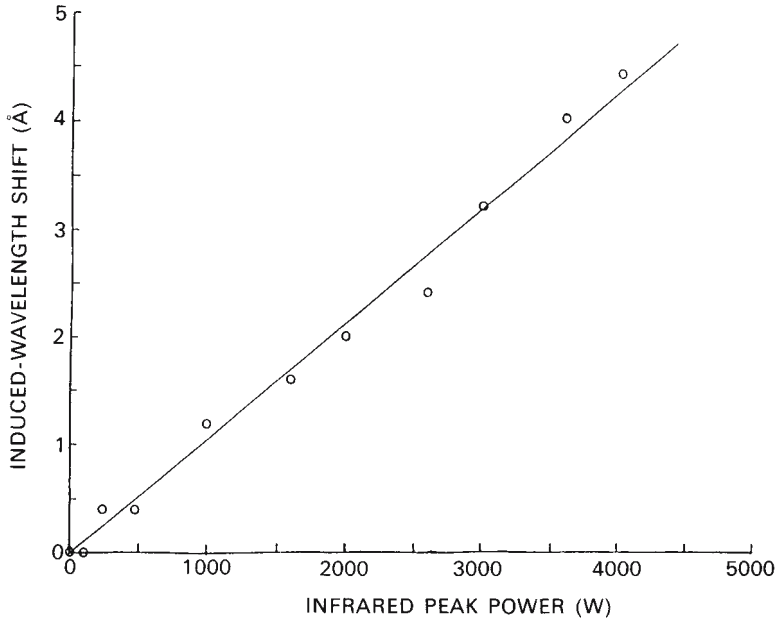


FIGURE 4.14. Maximum induced wavelength shift of 532-nm pulses versus the peak power of infrared pump pulses. (o) Experimental points. The solid line is the theoretical prediction from Eq. (3.4). (From Baldeck et al., 1988a.)

green pulse. The green pulse sees only the leading part of the XPM phase shift, which gives rise to a red induced-frequency shift. When the initial delay is about 40 ps, the infrared pulse has time to pass entirely through the green pulse. The pulse envelope sees a constant dephasing and there is no shift of the green spectrum (Figure 4.13).

Equations (15) and (16) can be used to fit our experimental data shown in Figures 4.13 and 4.14. Assuming that the central part of the pump pulses provides the dominant contribution to XPM, we set $t = 0$ in Eq. (16) and obtain

$$\delta\omega_1(\tau, z) \approx \frac{\omega_1}{c} n_2 \frac{P_2}{A_{\text{eff}}} \frac{L_w}{T_0} \left[ e^{-(\tau-\tau_d)^2} - e^{-(\tau-\tau_d+z/L_w)^2} \right]. \tag{17}$$

The maximum induced-frequency shift occurs at $t_d = d = z/L_w$ and is given by

$$|\Delta\omega_{\max}| = \frac{\omega_1}{c} n_2 \frac{P_2}{A_{\text{eff}}} \frac{L_w}{T_0}. \tag{18}$$

Equations (17) and (18) are plotted in Figures 4.13 and 4.14, respectively. There is very good agreement between this simple analytical model and experimental data. It should be noted that only a simple parameter (i.e., the

infrared peak power at the maximum induced-frequency shift) has been adjusted to fit the data. Experimental parameters were $\lambda = 532\,\text{nm}$, $T_0 = 19.8\,\text{ps}$ (33 ps FWHM), $L_w = 26\,\text{cm}$, and $\delta = 4$.

We have shown experimentally and theoretically that ultrashort optical pulses that overlap in a nonlinear and highly dispersive medium can undergo a substantial shift of their carrier frequency. This induced-frequency shift has been demonstrated using strong infrared pulses to shift the frequency of copropagating green pulses. The results are well explained by an analytical model that includes the effect of cross-phase modulation and pulse walk-off. This experiment led to a conclusive observation of XPM spectral effects.

## 3.3 XPM-Induced Spectral Broadening and Optical Amplification in Optical Fibers

This section presents additional features that can arise from the XPM interaction between a pump pulse at 630 nm and a probe pulse at 532 nm. With this choice of wavelengths, the group velocity dispersion between the pump pulse and the probe pulse is reduced and the XPM interaction enhanced. The spectral width and the energy of the probe pulse were found to increase in the presence of the copropagating pump pulse (Baldeck et al., 1988c).

A schematic of the experimental setup is shown in Figure 4.15. A mode-locked Nd: YAG laser with a second harmonic crystal was used to produce pulses of 25-ps duration at 532 nm. Pump pulses were obtained through stimulated Raman scattering by focusing 90% of the 532-nm pulse energy into a 1-cm cell filled with ethanol and using a narrowband filter centered at 630 nm. Resulting pump pulses at 630 nm were recombined with probe pulses and coupled into a 3-m-long single-mode optical fiber. Spectra of probe pulses were recorded for increasing pump intensities and varying input time delays between pump and probe pulses.

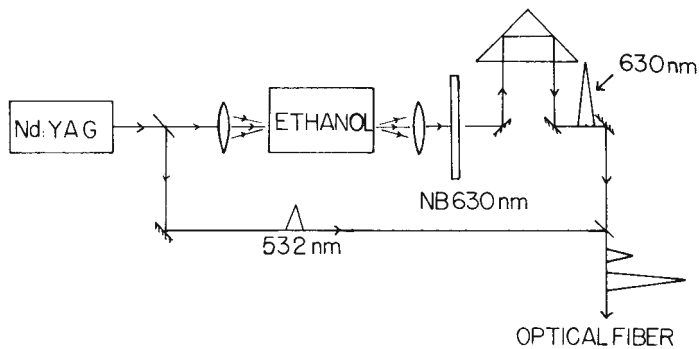


FIGURE 4.15. Experimental setup for generating copropagating picosecond pulses at 630 and 532 nm. (From Baldeck et al., 1988c.)

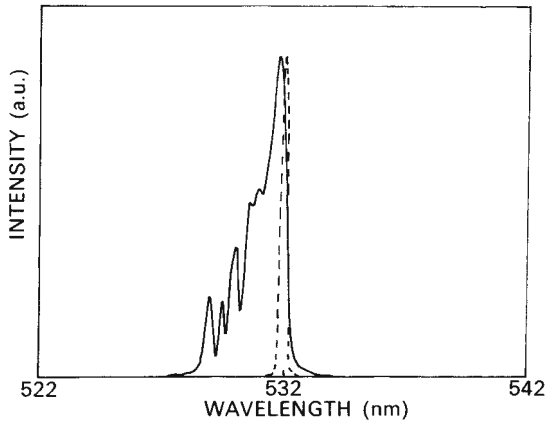


FIGURE 4.16. Cross-phase modulation effects on the spectrum of a probe picosecond pulse. (Dashed line) Reference spectrum without XPM. (Solid line) With XPM and no time delay between pump and probe pulses at the optical fiber input. (From Baldeck et al., 1988c.)

With negative delays (late pump at the optical fiber input), the spectrum of the probe pulse was red shifted as in the 1064 nm/532 nm experiment (Figure 4.12). A new XPM effect was obtained when both pulses entered the fiber simultaneously. The spectrum of the probe pulse not only shifted toward blue frequencies as expected but also broadened (Figure 4.16). An spectral broadening as wide as 10 nm could be induced, which was, surprisingly, at least one order of magnitude larger than predicted by the XPM theory. As shown in Figure 4.16, the probe spectrum extended toward the blue-shifted frequencies with periodic resonant lines. These lines could be related to modulation instability sidelobes that have been predicted theoretically to occur with cross-phase modulation (see Section 8).

The optical amplification of the probe pulse is another new and unexpected feature arising from the XPM interaction. Pump power-dependent gain factors of 3 or 7 were measured using probe pulses at 532 nm and pump pulses at 630 or 1064 nm, respectively. Figure 4.17 shows the dependence of the XPM-induced gain for the probe pulse at 532 nm with the input time delay between the probe pulse and the pump pulse at 630 nm. The shape of the gain curve corresponds to the overlap function of pump and probe pulses. Figure 4.18 shows the dependence or the gain factor on the intensity of pump pulses at 1064 nm. This curve is typical of a parametric amplification with pump depletion. The physical origin of this XPM-induced gain is still under investigation. It could originate from an XPM-phase-matched four-wave mixing process.

The spectral distribution of probe pulses can be significantly affected by the XPM generated by a copropagating pulse. In real time, the probe pulse frequency can be tuned, its spectrum broadened, and its energy increased.

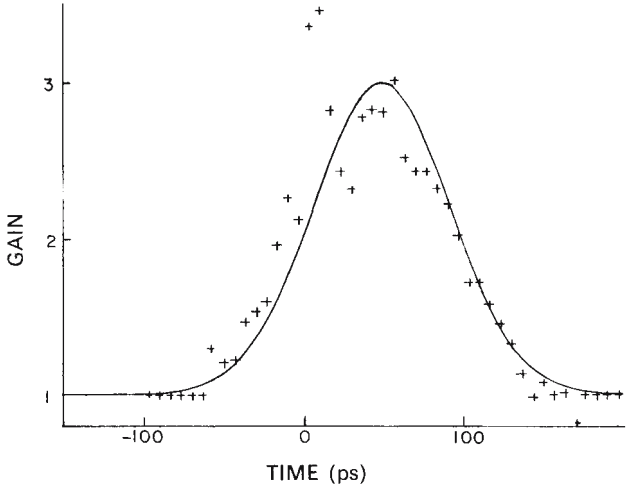


FIGURE 4.17. XPM-induced optical gain $I_{532}(\text{out})/I_{532}(\text{in})$ versus input time delay between pump pulses at 630 nm and probe pulses at 532 nm. (Crosses) Experimental data; (solid line) fit obtained by taking the convolution of pump and probe pulses. (From Baldeck and Alfano, 1988c.)

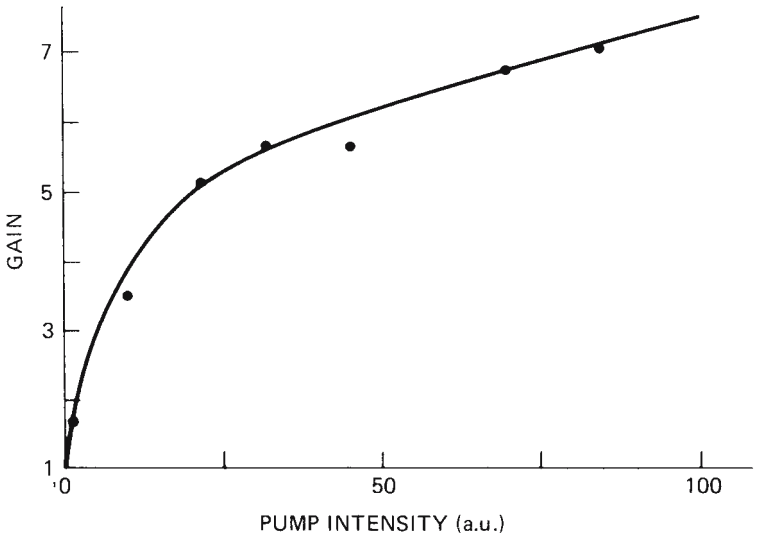


FIGURE 4.18. XPM-induced optical gain $I_{532}(\text{out})/I_{532}(\text{in})$ versus intensity of pump pulses at 1064 nm. (From Baldeck et al., 1987c–d.)

XPM appears as a new technique for controlling the spectral properties and regenerating ultrashort optical pulses with terahertz repetition rates.

## 4. Cross-Phase Modulation with Stimulated Raman Scattering

When long samples are studied optically, stimulated Raman scattering (SRS) contributes to the formation of ultrafast supercontinua. In 1980, Gersten, Alfano, and Belic predicted that ultrashort pulses should generate broad Raman lines due to the coupling among laser photons and vibrational phonons (Gersten et al., 1980). This phenomenon was called cross-pulse modulation (XPM). It characterized the phase modulation of the Raman pulse by the intense pump laser pulse. Cornelius and Harris (1981) stressed the role of SPM in SRS from more than one mode. Recently, a great deal of attention has been focused on the combined effects of SRS, SPM, and group velocity dispersion for the purposes of pulse compression and soliton generation (Dianov et al., 1984; Lu Hian-Hua et al., 1985; Stolen and Johnson, 1986; French et al., 1986; Nakashima et al., 1987; Johnson et al., 1986; Gomes et al., 1988; Weiner et al., 1986–1988, to name a few). Schadt et al. numerically simulated the coupled wave equations describing the changes of pump and Stokes envelopes (Schadt et al., 1986) and the effect of XPM on pump and Stokes spectra (Schadt and Jaskorzynska, 1987a) in nonlinear and dispersive optical fibers. Manassah (1987a, b) obtained analytical solutions for the phase and shape of a weak Raman pulse amplified during the pump and Raman pulse walk-off. The spectral effects of XPM on picosecond Raman pulses propagating in optical fibers were measured and characterized (Islam et al., 1987a, b; Alfano et al., 1987b; Baldeck et al., 1987b, d). In this section we review (1) Schadt and Jaskorzynska theoretical analysis of stimulated Raman scattering in optical fibers and (2) measurements of XPM and SPM effects on stimulated Raman scattering.

### 4.1 Theory of XPM with SRS

The following theoretical study of stimulated Raman scattering generation of picosecond pulses in optical fibers is from excerpts from Schadt et al. (1986) and Schadt and Jaskorzynska (1987a).

In the presence of copropagating Raman and pump pulses the nonlinear polarization can be approximated in the same way as in Section 2.1 by

$$P^{NL}(r, z, t) = \chi^{(3)} E^3(r, z, t), \tag{19}$$

where the total electric field $E^3(r, z, t)$ is given by

$$E(r, z, t) = \tfrac{1}{2}\{A_p(r, z, t)e^{i(\omega_p t - \beta_p z)} + A_s(r, z, t)e^{i(\omega_S t - \beta_S z)} + c.c.\}. \tag{20}$$

In this case, $A_1 = A_p$ and $A_2 = A_s$.

The subscripts $P$ and $S$ refer to the pump and Stokes Raman pulses, respectively. The anti-Stokes Raman is neglected. Substituting Eq. (20) into Eq. (19) and keeping only terms synchronized with either pump or Stokes carrier frequency, the nonlinear polarization becomes

$$P_P^{NL}(z,t) = \tfrac{3}{8}\left\{i2\chi_R^{(3)}|A_S|^2 + \chi_{PM}^{(3)}\left[|A_P|^2 + 2|A_S|^2\right]\right\}A_P e^{i(\omega_P t - \beta_P z)} + c.c., \tag{21a}$$

$$P_S^{NL}(z,t) = \tfrac{3}{8}\left\{-i2\chi_R^{(3)}|A_P|^2 + \chi_{PM}^{(3)}\left[|A_S|^2 + 2|A_P|^2\right]\right\}A_S e^{i(\omega_S t - \beta_S z)} + c.c., \tag{21b}$$

where $\chi^{(3)} = \chi_{PM}^{(3)} + i\chi_R^{(3)}$, $\chi_R^{(3)}$ gives rise to the Raman gain (or depletion) of the probe (or pump), and $\chi_{PM}^{(3)}$ leads to self- and cross-phase modulations. Note the factor 2 associated with XPM.

As in the pump-probe case, the phase shift contribution of the nonlinear polarization at the pump (or Raman) frequency depends not only on the pump (or Raman) peak power but also on the Raman (or pump) peak power. This gives rise to cross-phase modulation during the Raman scattering process.

Using the expressions for $P_P^{NL}$ and $P_S^{NL}$ in the nonlinear wave equation, leads to the coupled nonlinear dispersive equations for Raman and pump pulses:

$$\frac{\partial A_P}{\partial Z} + \frac{z_K}{z_W}\frac{\partial A_P}{\partial T} + \frac{i}{2}\frac{z_K}{z_D}\frac{\partial^2 A_P}{\partial T^2} = -\frac{1}{2}\frac{\Omega_P}{\Omega_S}\frac{z_K}{z_A}|A_S|^2 A_P + \frac{i}{2}\left[|A_P|^2 + 2|A_S|^2\right]A_P - \frac{z_K}{z_L}A_P, \tag{22a}$$

$$\frac{\partial A_S}{\partial Z} + \frac{i}{2}\frac{k_R''}{k_P''}\frac{z_K}{z_D}\frac{\partial^2 A_S}{\partial T^2} = \frac{1}{2}\frac{z_K}{z_A}|A_P|^2 A_S + \frac{i}{2}\frac{\Omega_S}{\Omega_P}\left[|A_S|^2 + 2|A_P|^2\right]A_S - \frac{\Gamma_S}{\Gamma_P}\frac{z_K}{z_L}A_S, \tag{22b}$$

where $A_1 = a_1/|a_{0P}|$ are the complex amplitudes $a_1$ normalized with respect to the initial peak amplitude $|a_{0P}|$ of the pump pulse. The index $1 = P$ refers to the pump, whereas $1 = S$ refers to the Stokes pulse. $Z = z/z_K$ and $T = (t - z/v_s)/\tau_0$ are the normalized propagation distance and the retarded time normalized with respect to the duration of the initial pump pulse. $\Omega = \omega/(1/\tau_0)$ is a normalized frequency. Moreover, the following quantities were introduced:

- $z_K = 1/\gamma_P|a_{0P}|^2 = 1/(|a_{0P}|^2 n_2 \omega_P/c)$ is the Kerr distance, with the PM coefficient $\gamma_P$, the Kerr coefficient $n_2$, and $\omega_P$ as the carrier frequency of the pump pulse; $c$ is the velocity of light.
- $z_W = \tau_0/(v_p^{-1} - v_s^{-1})$ is the walk-off distance; $v_p$ and $v_s$ are the group velocities at the pump and Stokes frequencies, respectively.
- $z_D = \tau_0^2/k_P''$ is the dispersion length; $k_P'' = \partial^2 k_P/\partial\omega^2$, where $k_P$ is the propagation constant of the pump.
- $z_D = 1/\alpha_s|a_{0P}|^2 = 1/\gamma|a_{0P}|^2$ is the amplification length, with $g$ the Raman gain coefficient.

$z_L = 1/\Gamma_P$ is the pump loss distance, where $\Gamma_P$ is the attenuation coefficient at the pump frequency.

The derivation of Eqs. (22) assumes that a quasi-steady-state approximation holds. Thus, it restricts the model to pulses much longer than the vibrational dephasing time (~100 fs) of fused silica. The Raman gain or loss is assumed to be constant over the spectral regions occupied by the Stokes and pump pulses, respectively. Furthermore, the quasi-monochromatic approximation is used, which is justified as long as the spectral widths of the pulses are much smaller than their carrier frequencies. As a consequence of these simplifications, the considered spectral broadening of the pulses is a result only of phase modulations and pulse reshaping. The direct transfer of the chirp from the pump to the Stokes pulse by SRS is not described by the model. The frequency dependence of the linear refractive index is included to a second-order term, so both the walk-off arising from a group velocity mismatch between the pump and Stokes pulses and the temporal broadening of the pulses are considered.

Using Eqs. (22a) and (22b), Schadt and Jaskorzynska numerically simulated the generation of picosecond Raman pulses in optical fibers. They particularly investigated the influence of walk-off on the symmetry properties of pulse spectra and temporal shapes and the contributions from SPM and XPM to the chirp of the pulses.

### 4.1.1 Influence of Walk-Off on the Symmetry Properties of the Pulse Spectra

Results obtained in absence of walk-off are shown in Figure 4.19 (Schadt and Jaskorzynska, 1987a). The pump spectrum, broadened and modulated by SPM, is slightly depleted at its center due the energy transfer toward the Raman pulse (Figure 4.19a). The Raman spectrum is almost as wide as the pump spectrum, but without modulations (Figure 4.19b). The spectral broadening of the Raman spectrum arises mainly from XPM. The modulationless feature appears because the Raman pulse, being much shorter than the pump pulse, picks up only the linear part of the XPM-induced chirp. Such a linearly chirped Raman pulse could be efficiently compressed using a grating-pair pulse compressor.

The influence of the walk-off on the Raman process is displayed in Figure 4.20. The pronounced asymmetry of the spectra in Figure 4.20a and 4.20b is connected with the presence of the pulse walk-off in two different ways. When the Stokes pulse has grown strong enough to deplete the pump pulse visibly, it has also moved toward the leading edge of the pump (it is referred only to regions of normal dipersion). The leading edge has in the meantime been downshifted in frequency as a result of SPM. Consequently, the pump pulse loses energy from the lower-frequency side. On the other hand, the asymmetric depletion of the pump gives rise to the asymmetric depletion buildup of the frequency shift itself, as can be seen from Figures 4.20c and 4.20d.

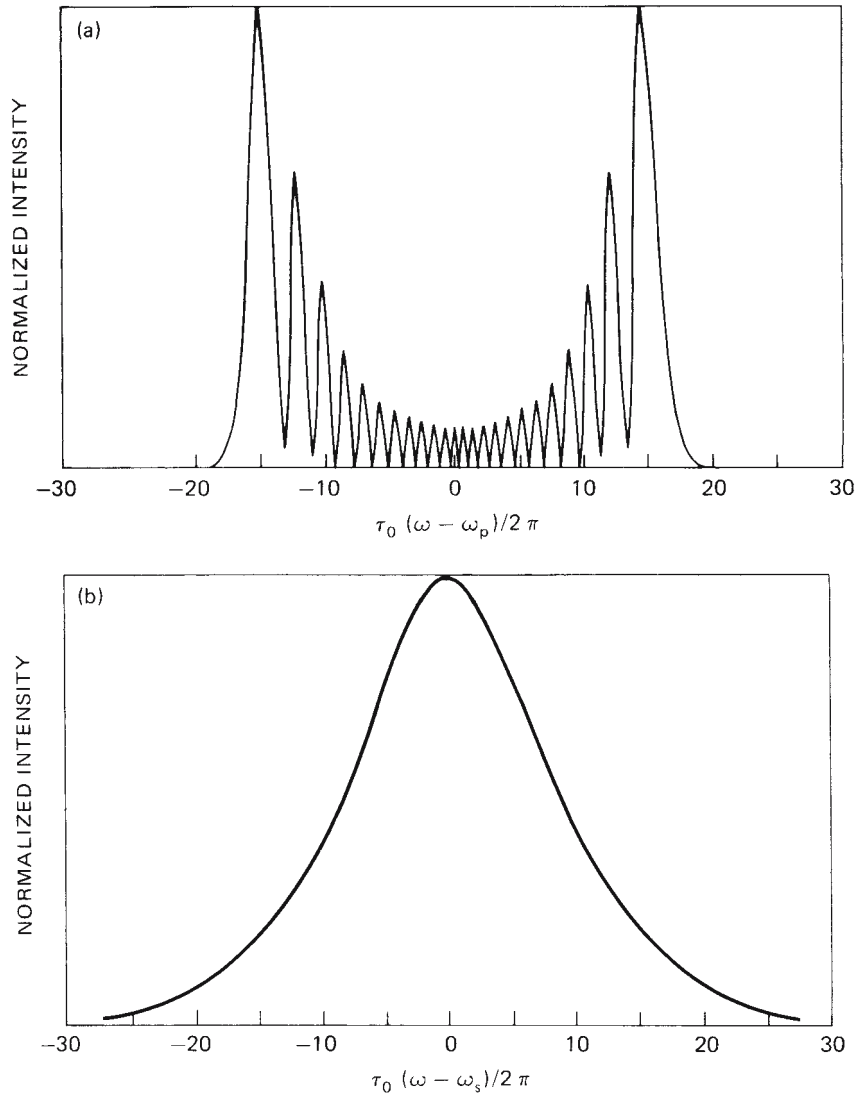


FIGURE 4.19. Spectra of pump and Stokes Raman pulses in the absence of walk-off. (a) Spectrum of the pump pulse. (b) Spectral broadening of the Stokes pulse because of phase modulations. (From Schadt and Jaskorzynska, 1987a.)

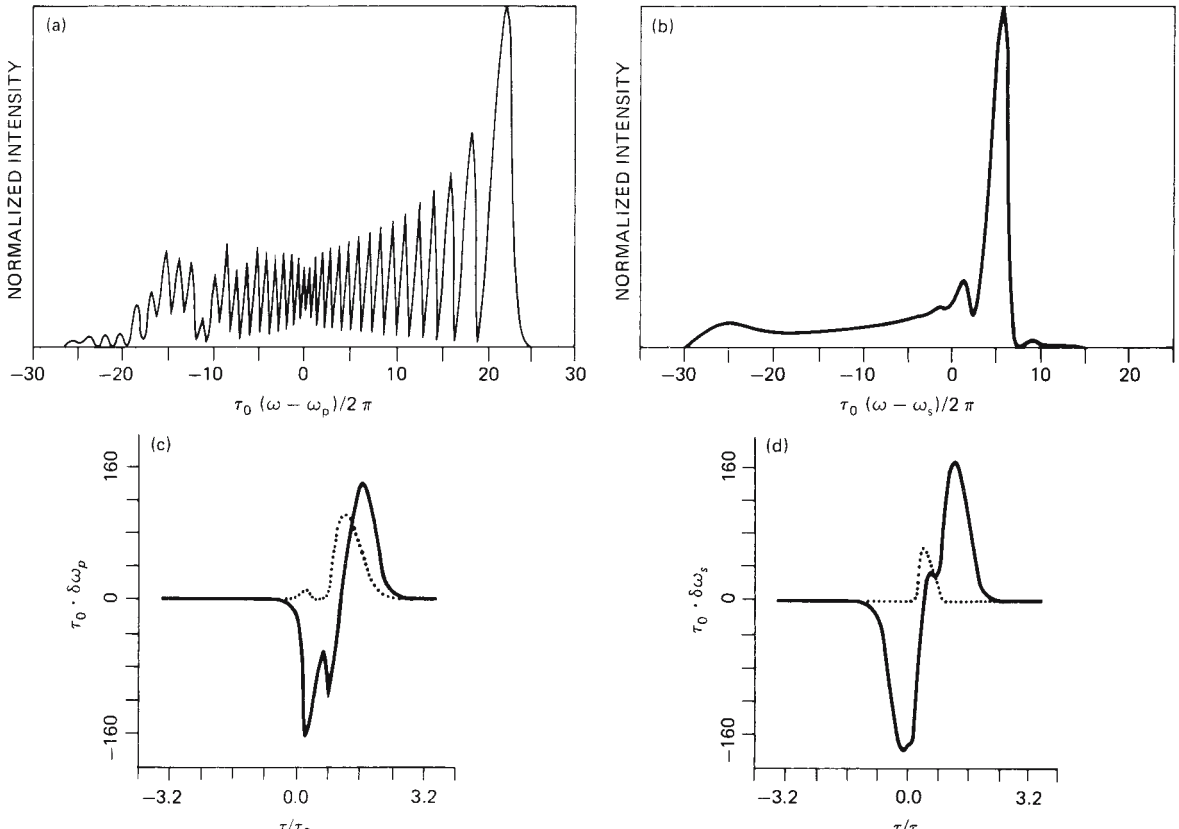


FIGURE 4.20. Influence of walk-off on spectra and chirps of pump and Stokes Raman pulses. (a) Spectrum of the pump pulse. (b) Spectral broadening of the Stokes pulse because of phase modulations. (c) Chirp (solid line) and shape (dashed line) of the pump pulse. (d) Chirp (solid line) and shape (dashed line) of the Stokes pulse. (From Schadt and Jaskorzynska, 1987a.)

Theoretical spectra in Figure 4.20 agree very well with measured spectra (Gomes et al., 1986; Weiner et al., 1986; Zysset and Weber, 1986).

### 4.1.2 Contributions from Self-Phase Modulation and Cross-Phase Modulation to the Chirp of Pulses

The chirps of Raman and pump pulses originate from SPM and XPM. The contributions from SPM and XPM are independent as long as the effect of second-order dispersion is negligible. In Figure 4.21 are plotted the contributions to the pump and Stokes chirps coming from either SPM only (Figures

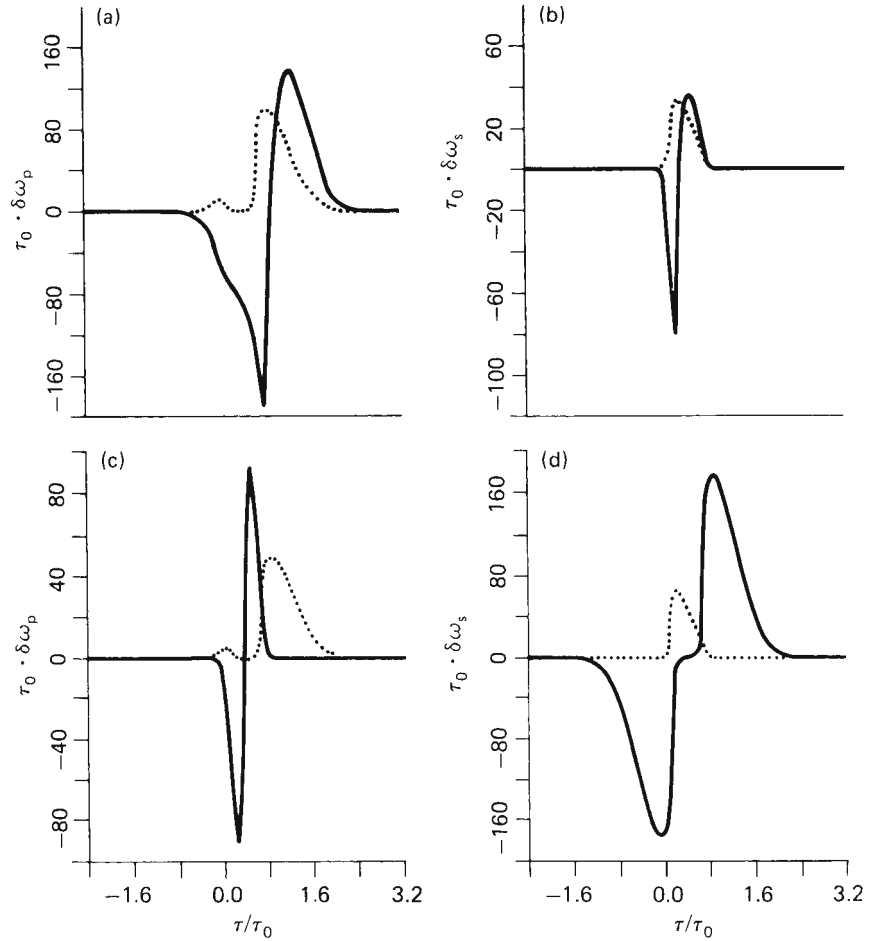


Figure 4.21. Chirp components that are due to SPM and XPM for the case of walk-off. (a) Pump chirp due to SPM only. (b) Stokes chirp due to SPM only. (c) Pump chirp due to XPM only. (d) Stokes chirp due to XPM only. (From Schadt and Jaskorzynska, 1987a.)

4.21a, 4.21b) or XPM only (Figures 4.21c, 4.21d). The shapes of SPM contributions shown in Figures 4.21a and 4.21b apparently reflect the history of their buildup according to the changes of pulse shapes during the propagation. Their strong asymmetry is a result of an asymmetric development of the pulse shapes that is due to walk-off. The XPM affecting the pump pulse in the initial stage of the Raman process plays a lesser role as the pump depletion becomes larger. This constituent of the chirp, associated with the Stokes pulse is built up just in the region where most of the pump energy is scattered to the Stokes frequency if the Raman process goes fast enough. However, if for a fixed walk-off SRS is slow, as in the case illustrated by Figure 4.21c, the leading part of the pump pulse will remain affected by the XPM.

The most characteristic feature of the XPM-induced part of the Stokes chirp, shown in Figure 4.21d, is a plateau on the central part of the Stokes pulse. In the case of the lower input power (Figure 4.21d) this plateau can be attributed mainly to the effect of walk-off. Since pump depletion becomes considerable only close to the end of the propagation distance, it has little influence on the buildup of the chirp. For higher input powers the range over which the chirp vanishes is wider. Consequently, after the walk-off distance the effect of XPM on the Stokes chirp is negligible for a severely depleted pump, whereas in the case of insignificant pump depletion the leading part of the Stokes pulse will remain influenced by XPM.

Schadt et al. have developed a numerical model to describe combined effects of SRS, SPM, XPM, and walk-off in single-mode optical fibers. They explained the influence of the above effects on pump and Stokes spectra and chirps. They separately studied the contributions of SPM and XPM to the chirps and found that both walk-off and pump depletion tend to cancel the effect of XPM on the chirp in the interesting pulse regions. However, for more conclusive results an investigation of the direct transfer of the pump chirp and consideration of the finite width of the Raman gain curve are needed.

## 4.2 Experiments

In the late 1970s and early 1980s, numerous experimental studies investigated the possibility of using SRS to generate and amplify Raman pulses in optical fibers (Stolen, 1979). However, most of these studies involved "long" nanosecond pulses and/or neglected to evaluate SPM and XPM contributions to the pump and Raman spectral broadenings. It was not until 1987, after the success of the first spectral broadening enhancement experiment (Alfano et al., 1986), that measurements of XPM effects on Raman pulses were reported (Islam et al., 1987a; Alfano et al., 1987b). In this section, research work at AT&T Bell Laboratories and at the City College of New York is reported.

### 4.2.1 XPM Measurements with the Fiber Raman Amplification Soliton Laser

Islam et al. showed the effects of pulse walk-off on XPM experimentally in the Fiber Raman Amplification Soliton Laser (FRASL) (Islam et al., 1986).

They proved that XPM prevents a fiber Raman laser from producing pedestal-free, transform limited pulses except under restrictive conditions (Islam et al., 1987b). The following simple picture of walk-off effects and experimental evidence is excerpted from reference (Islam et al., 1987a).

The spectral features and broadening resulting from XPM depend on the walk-off between the pump and signal pulses. These spectral features can be confusing and complicated, but Islam et al. show that they can be understood both qualitatively and quantitively and quantitatively by concentrating on the phase change as a function of walk-off. XPM is most pronounced when the pump and signal are of comparable pulse widths and when they track each other. The phase change $\Delta\phi$ induced on the signal is proportional to the pump intensity, and the signal spectrum (Figure 4.22a) looks like that obtained from self-phase-modulation (SPM).

The opposite extreme occurs when the phase shift is uniform over the width of the signal pulse. This may happen in the absence of pump depletion or spreading if the pump walks completely through the signal, or if the signal is much narrower than the pump and precisely tracks the pump. XPM is canceled in this limit, and the original spectral width of the signal (much narrower than any shown in Figure 4.22) results.

A third simple limit exists when the pump and signal coincide at first, but then the pump walks off. This is most characteristic of stimulated amplification processes (i.e., starting from noise), and may occur also in synchronously-pumped systems such as the FRASL. The net phase change turns out to be proportional to the integral of the initial pump pulse, and, as Figure 4.22b shows, the signal spectrum is asymmetric and has "wiggles." Figure 4.22c treats the intermediate case where the pump starts at the trailing edge of the signal, and in the fiber walks through to the leading edge. A symmetric spectrum results if the walk-off is symmetric.

A FRASL consists of a optical fiber ring cavity that is synchronously pumped by picosecond pulses and designed to lase at the stimulated Raman scattering Stokes wavelength (Figure 4.23). To obtain the generation of soliton Raman pulses the pump wavelength is chosen in the positive group velocity dispersion region of the optical fiber, whereas the Raman wavelength is in the negative group velocity dispersion region. Inserting a narrowband tunable etalon in the resonant ring, Islam et al. turned their laser in a pump-probe configuration in which they could control the seed feedback into the fiber and observe the spectral broadening in a single pass. The effect of walk-off on XPM could be studied by changing the fiber length in the cavity. Output Raman signals were passed through a bandpass filter to eliminate the pump and then sent to a scanning Fabry-Perot and an autocorrelator.

When a 50-m fiber is used in the FRASL ($l < l_w$), the signal remains with the pump throughout the fiber. With no etalon in the cavity, the signal spectrum is wider than the 300-$cm^{-1}$ free spectral range of the Fabry-Perot. Even with the narrow-passband etalon introduced into the cavity, the spectral width remains greater than 300 $cm^{-1}$ (Figure 4.24a). Therefore, more or less independent of the seed, the pump in a single pass severely

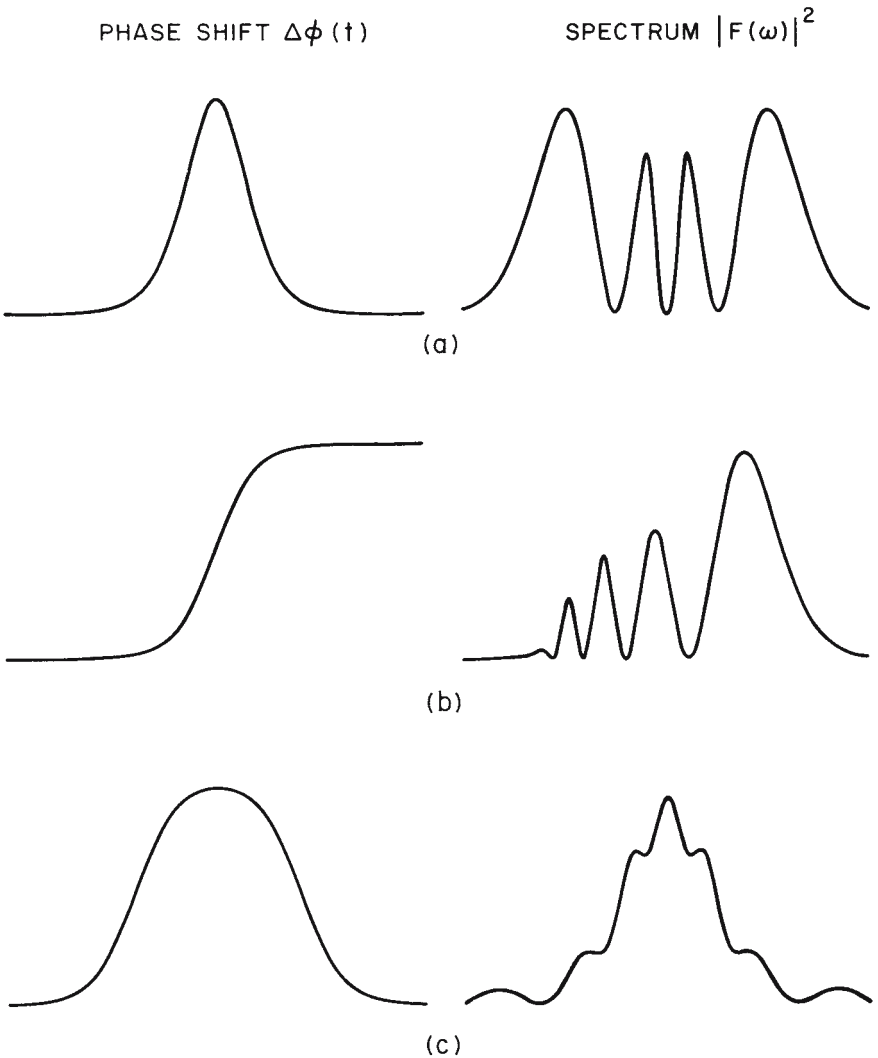


FIGURE 4.22. Phase shifts and spectra corresponding to various degrees of walk-off between pump and signal pulses. (a) Perfect tracking case ($t_0 = \beta = 0$, $2A^2l = 3.5\pi$, $\alpha = 1$); (b) pump and signal coincide initially, and then pump walks off ($t_0 = 0$, $\beta l = 4$, $2A^2/\beta = 3.5\pi$, $\alpha = 1$); and (c) pump walks from trailing edge of signal to the leading edge ($t_0 = -2$, $\beta l = 4$, $2A^2/\beta = 3.5\pi$, $\alpha = 1$). (From Islam et al., 1987a.)

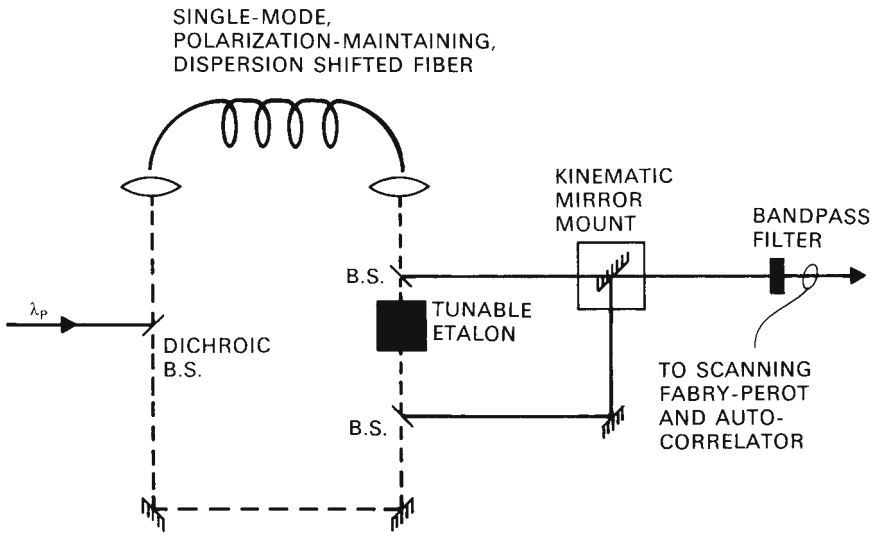


FIGURE 4.23. Modified fiber Raman amplification soliton laser (FRASL). B.S., beam splitter. (From Islam et al., 1987a.)

broadens the signal spectrum. As expected from theory, the Raman spectrum is featureless.

If the fiber length is increased to 100 m ($l \approx l_w$), there is partial walk-off between the pump and signal and XPM again dominates the spectral features. Without an etalon in the FEASL cavity, the emerging spectrum is wide and has wiggles (Figure 4.24b). By time dispersion tuning the FRASL, thus varying the amount of walk-off, the details of the spectrum can be changed as shown in Figure 4.24c. Even after the etalon is inserted and the cavity length appropriately adjusted, the spectrum remained qualitatively the same (Figure 4.24d).

When there is complete walk-off between pump and signal ($l = 400\,\text{m} \gg l_w$), without an etalon the spectrum is symmetric and secant-hyperboliclike, althoug still broad (Figure 4.24e). The effects of XPM are reduced considerably, but they are not canceleled completely because the walk-off is asymmetrized by pump depletion. As Figure 4.24f shows, the addition of the etalon narrows the spectrum (the narrow peak mimics the seed spectrum). However, XPM still produces a broad spectral feature (at the base of the peak), which is comparable in width to the spectrum without the filter (Figure 4.24e). In autocorrelation, it was found that the low-level wider feature corresponded to a $\tau \approx 250\,\text{fs}$ peak, while the narrow spectral peak results in a broader $\tau \approx 2.5\,\text{ps}$ pulse.

With these experimental results, Islam et al. have conclusively assessed the effects of walk-off on Raman XPM. It should be noted that, despite the long nonlinear interaction lengths, spectral broadenings were small and the SPM

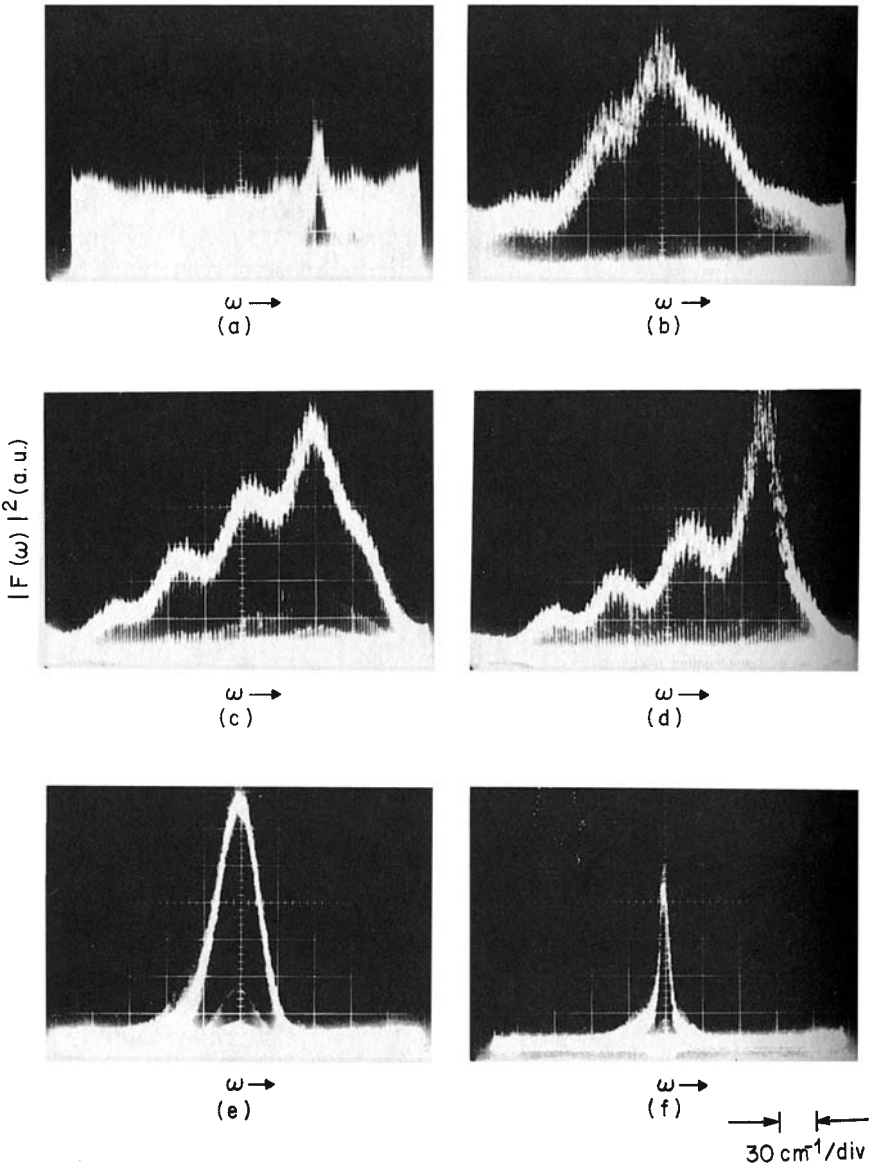


FIGURE 4.24. Experimental spectra for various fiber lengths ($l$) with and without the tunable etalon in the FRASL cavity. (a) $l = 50$ m with etalon in cavity. (b) $l = 100$ m, no etalon. (c) $l = 100$ m, no etalon, but different FRASL cavity length than in (b). (d) Same as (c), except with etalon inserted. (e) $l = 400$ m, no etalon. (f) Same as (e), except with etalon inserted. Here, except for the wings, the spectrum is nearly that of the etalon. The vertical scales are in arbitrary units, and the signal strength increases for increasing fiber lengths. (From Islam et al., 1987a.)

generated by the Raman pulse itself was negligible. Furthermore, measured spectral features were characteristic of XPM for the Raman amplification scheme, as expected for the injection of Raman seed pulses in the optical fiber loop.

### 4.2.2 Generation of Picosecond Raman Pulses in Optical Fibers

Stimulated Raman scattering of ultrashort pulses in optical fibers attracts a great deal of interest because of its potential applications for tunable fiber lasers and all-optical amplifiers. XPM effects on weak Raman pulses propagating in long low-dispersive optical fibers were characterized in the preceding section. Temporal and spectral modifications of pump and Raman pulses are more complex to analyze when Raman pulses are generated in short lengths (i.e., high Raman threshold) of very dispersive optical fibers. In addition to XPM and walk-off, one has to take into account pump depletion, SPM of the Raman pulse, Raman-induced XPM of the pump pulse, group velocity dispersion broadening, higher-order SRS, and XPM-induced modulation instability. This section presents measurements of the generation of Raman picosecond pulses from the noise using short lengths of a single-mode optical fiber (Alfano et al., 1987b; Baldeck et al., 1987b–d).

A mode-locked Nd:YAG laser was used to generate 25-ps time duration pulses at $\lambda = 532\,\text{nm}$ with a repetition rate of 10 Hz. The optical fiber was custom-made by Corning Glass. It has a 3-$\mu$m core diameter, a 0.24% refractive index difference, and a single-mode cutoff at $\lambda = 462\,\text{nm}$. Spectra of output pulses were measured using a grating spectrometer (1 m, 600 lines/mm) and recorded with an optical multichannel analyzer OMA2. Temporal profiles of pump and Raman pulses were measured using a 2-ps resolution Hamamatsu streak camera.

Spectra of pump and Raman pulses, which were measured for increasing pump energy at the output of short fiber lengths, are plotted in Figure 4.25. The dashed line in Figure 4.25a is the reference laser spectrum at low intensity. Figures 4.25a (solid line) and 4.25b show spectra measured at the Raman threshold at the output of 1- and 6-m-long optical fibers, respectively. The Raman line appears at $\lambda = 544.5\,\text{nm}$ (about $440\,\text{cm}^{-1}$). The laser line is broadened by SPM and shows XPM-induced sidebands, which are discussed in Section 8. For moderate pump intensities above the stimulated Raman scattering threshold, spectra of Raman pulses are broad, modulated, and symmetrical in both cases (Figures 4.25c and d). For these pump intensities, the pulse walk-off (6 m corresponds to two walk-off lengths) does not lead to asymmetric spectral broadening. For higher pump intensities, Raman spectra become much wider (Figures 4.25e and f). In addition, spectra of Raman pulses generated in the long fiber are highly asymmetric (Figure 4.25f). The intensity-dependent features observed in Figure 4.24 are characteristic of spectral broadenings arising from nonlinear phase modulations such as SPM and XPM as predicted by the theory (Section 4.1). At the lowest intensities XPM dominates, while at the highest intensities the SPM generated by the

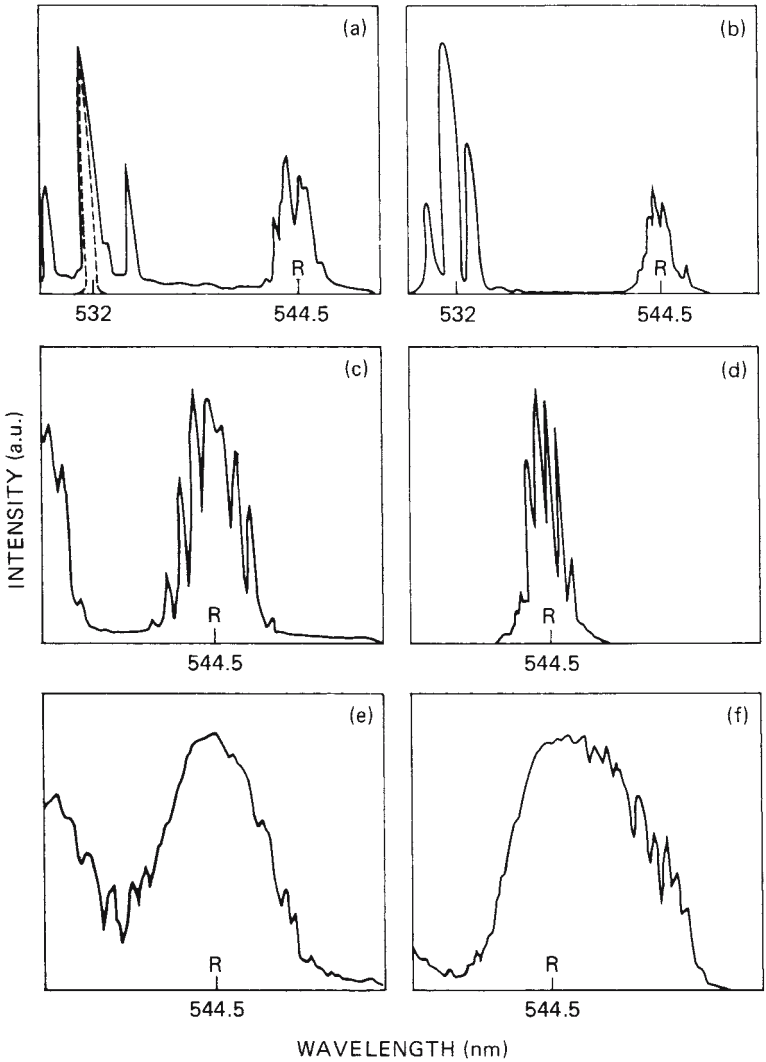


FIGURE 4.25. Spectra of picosecond Raman pulses generated in short lengths of a single-mode optical fiber. The laser and Raman lines are at 532 and 544.5 nm, respectively. Results in the left column and right column were obtained with 1- and 6-m-long single-mode optical fibers, respectively. (a and b) Dashed line: referenced of laser spectrum at low intensity; solid line: pump and Raman lines near the stimulated Raman scattering threshold. Frequency sidebands about the laser line are XPM-induced modulation instability sidebands (see Section 8). (c and d) Raman spectra for moderate pump peak powers above threshold. (e and f) Raman spectra for higher pump peak powers. (From Baldeck et al., 1987c–d.)

Raman pulse itself is the most important. However, it should be noted that the widths of Raman spectra shown in Figure 4.25 are one order of magnitude larger than expected from the theory. Modulation instability induced by pump pulses could explain such a discrepancy between measurements and theory (Section 8).

Temporal measurements of the generation process were performed to test whether the spectral asymmetry originated from the pump depletion reshaping as in the case of longer pulses (Schadt et al., 1986). Pump and Raman profiles were measured at the output of a 17-m-long fiber (Figure 4.26). The dotted line is for a pump intensity at the SRS threshold and the solid line for a higher pump intensity. The leading edge of the pump pulse is partially "eaten" but is not completely emptied because of the quick walk-off between pump and Raman pulses. Thus, the leading edge of the pump pulse does not become very sharp, and the contribution of pump depletion effects to the spectral asymmetry of pump and Raman pulses does not seem to be significant.

Figure 4.26 shows a typical sequence of temporal profiles measured for input pump intensities strong enough to generate higher-order stimulated Raman scattering lines. The temporal peaks are the maxima of high-order SRS scatterings that satisfy the group velocity dispersion delay of 6 ps/m for each frequency shift of 440 $cm^{-1}$. These measurements show that (1) the Raman process clamps the peak power of pulses propagating into an optical fiber to a maximum value and (2) high-order stimulated Raman scatterings occur in cascade during the laser pulse propagation.

### 4.2.3 Generation of Femtosecond Raman Pulses in Ethanol

Nonlinear phenomena such as supercontinuum generation and stimulated Raman scattering were first produced in unstable self-focusing filaments generated by intense ultrashort pulses in many liquids and solids. Optical fibers are convenient media for studying such nonlinear phenomena without the catastrophic features of collapsing beams. However, optical fibers are not suitable for certain applications such as high-power experiments, the generation of larger Raman shifts (>1000 $cm^{-1}$), and Raman pulses having high peak powers (>1 MW). In this section, spectral measurements of SRS generation in ethanol are presented. Spectral shapes are shown to result from the combined effects of XPM, SPM, and walk-off.

Spectral measurements of SRS in ethanol have been performed using the output from a CPM ring dye amplifier system (Baldeck et al., 1987b). Pulses of 500 fs duration at 625 nm were amplified to an energy of about 1 mJ at a repetition rate of 20 Hz. Pulses were weakly focused into a 20-cm-long cell filled with ethanol. Output pulses were imaged on the slit of a $\frac{1}{2}$-m Jarrell-Ash spectrometer and spectra were recorded using an optical multichannel analyzer OMA2.

Ethanol has a Raman line shifted by 2928 $cm^{-1}$. Figure 4.27 shows how the Stokes spectrum of the Raman line changes as a function of the pump intensity. Results are comparable to those obtained using optical fibers. At low

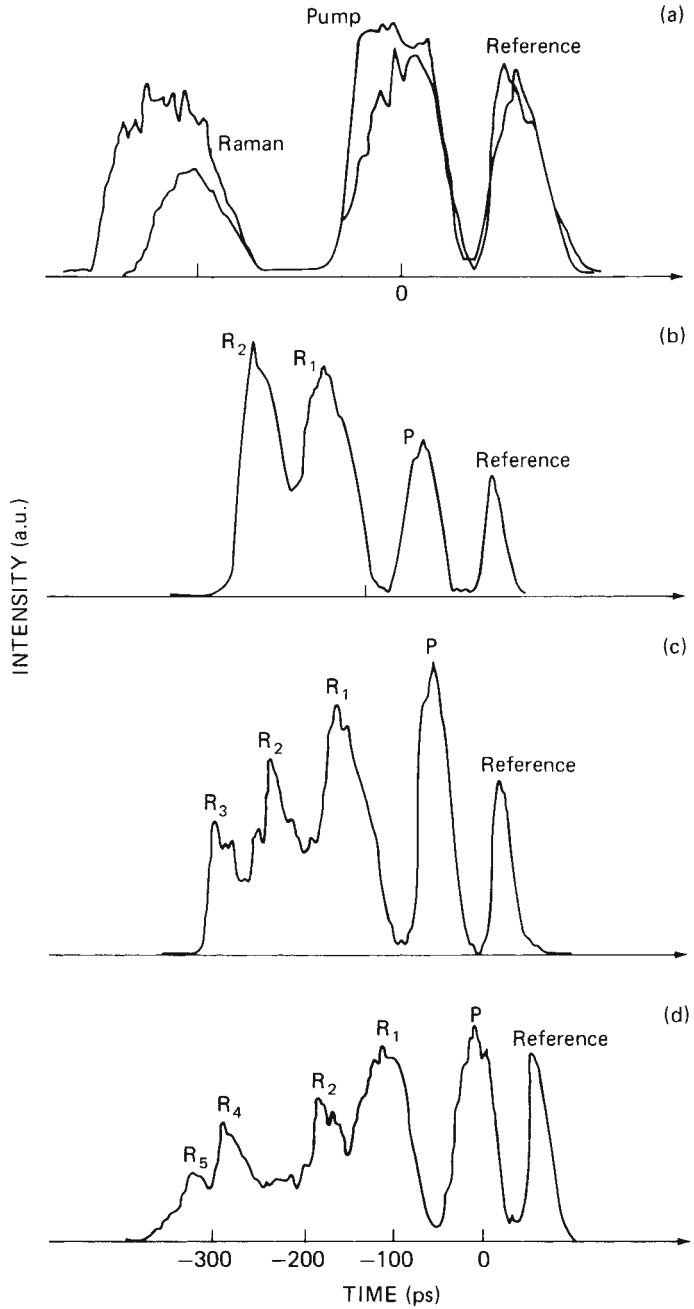


FIGURE 4.26. Temporal shapes of reference pulse, pump pulse, and SRS pulses at the output of a 17-m-long single-mode optical fiber for increasing pump intensity. (a) First-order SRS for slightly different pump intensity near threshold. (b) First- and second-order SRS. (c) First- to third-order SRS. (d) First- to fifth-order SRS. (From Baldeck et al., 1987d.)

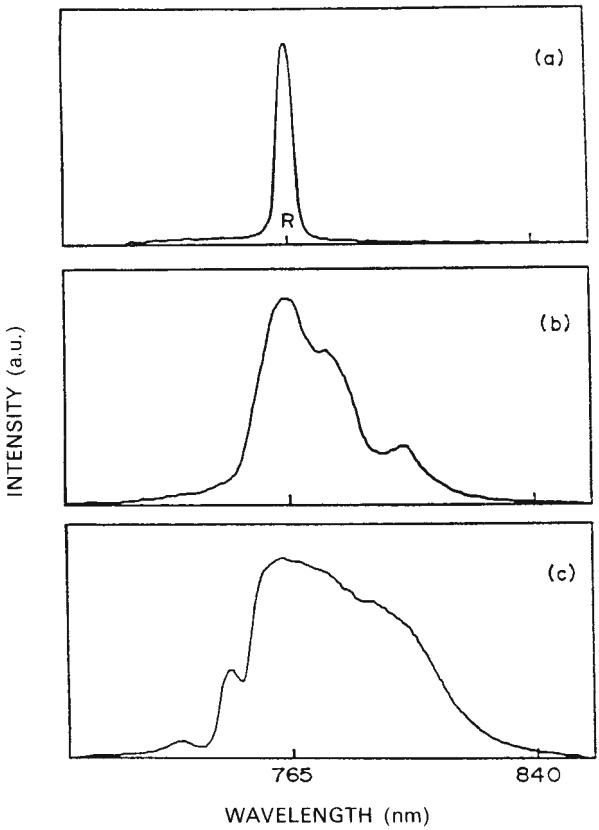


FIGURE 4.27. Effects of cross- and self-phase modulations on the Stokes-shifted Raman line generated by 500-fs pulses in ethanol. (a to c) Increasing laser intensity. (From Baldeck et al., 1987b.)

intensity the Stokes spectrum is narrow and symmetrical (Figure 4.27). As the pump intensity increases the Raman spectrum broadens asymmetrically with a long tail pointing toward the longer wavelengths. Spectra of the anti-Stokes Raman line were also measured (Baldeck et al., 1987b). They were as wide as Stokes spectra but with tails pointing toward the shortest wavelengths, as predicted by the sign of the walk-off parameter.

## 5. Harmonic Cross-Phase Modulation Generation in ZnSe

Like stimulated Raman scattering, the second harmonic generation (SHG) process involves the copropagation of a weak generated-from-the-noise pulse with an intense pump pulse. The SHG of ultrashort pulses occurs simulta-

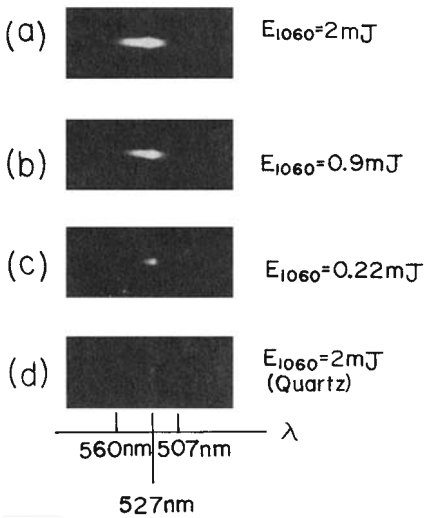


FIGURE 4.28. Induced-spectral-broadening spectra in ZnSe crystal excited by an intense 1060-nm laser pump. In (d) the ZnSe crystal was replaced by a 3.7-cm-long quartz crystal. (From Alfano et al., 1987a.)

neously with cross-phase modulation, which affects both the temporal and spectral properties of second harmonic pulses. In this section, measurements of XPM on the second harmonic generated by an intense primary picosecond pulse in ZnSe crystals are reported (Alfano et al., 1987a; Ho et al., 1988).

The laser system consisted of a mode-locked Nd:galss laser with single-pulse selector and amplifier. The output laser pulse had about 2 mJ energy and 8 ps duration at a wavelength of 1054 nm. The 1054-nm laser pulse was weakly focused into the sample. The spot size at the sample was about 1.5 mm in diameter. The second harmonic produced in this sample was about 10 nJ. The incident laser energy was controlled using neutral density filters. The output light was sent through a $\frac{1}{2}$-m Jarrell-Ash spectrometer to measure the spectral distribution of the signal light. The 1054-nm incident laser light was filtered out before detection. A 2-ps time resolution Hamamatsu streak camera system was used to measure the temporal characteristics of the signal pulse. Polycrystalline ZnSe samples 2, 5, 10, 22, and 50 mm thick were purchased from Janos, Inc. and a single crystal of ZnSe 16 mm thick was grown at Philips.

Typical spectra of non-phase-matched SHG pulses generated in a ZnSe crystal by 1054-nm laser pulses of various pulse energies are displayed in Figure 4.28. The spectrum from a quartz sample is included in Figure 4.28d for reference. The salient features of the ZnSe spectra indicate that the extent of the spectral broadening about the second harmonic line at 527 nm depends on the intensity of the 1054-nm laser pulse. When the incident laser pulse energy was 2 mJ, there was significant spectral broadening of about 1100 $cm^{-1}$ on the Stokes side and 770 $cm^{-1}$ on the anti-Stokes side (Figure 4.29). There was no significant difference in the spectral broadening distribution measured in the single and polycrystalline materials. The spectral width of the SHG

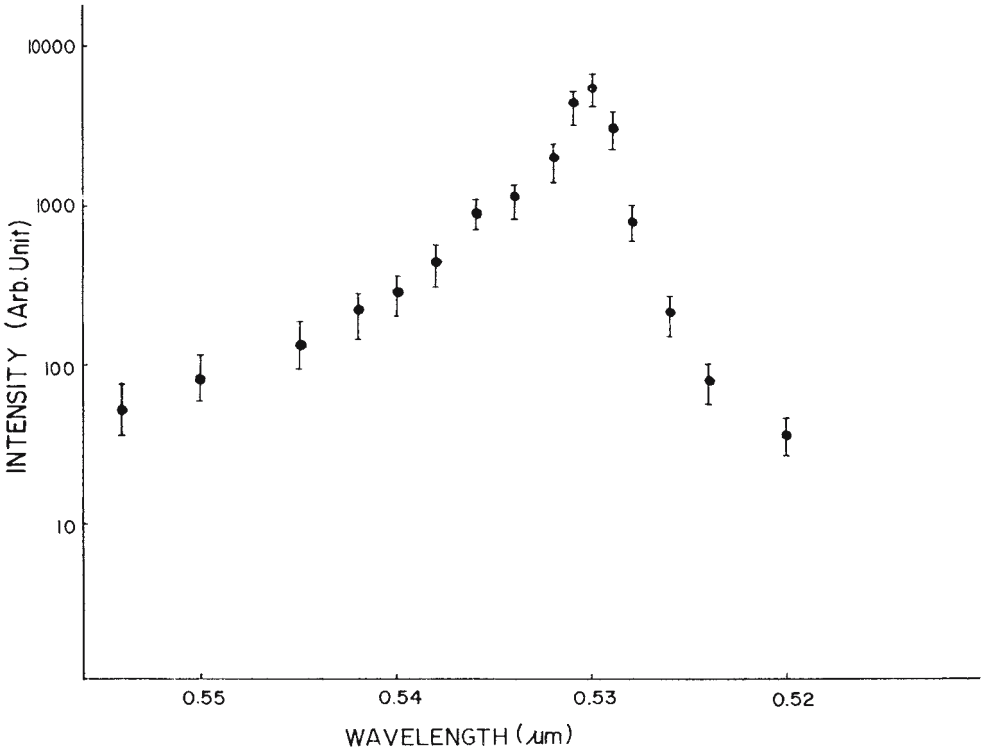


FIGURE 4.29. Spectral measurement of the induced spectrally broadened pulse about $\lambda = 527$ nm by sending a 1054-nm pulse through 22-mm ZnSe. (From Alfano et al., 1988.)

signal is plotted for the Stokes and anti-Stokes sides as a function of the incident pulse energy in Figure 4.30. The salient feature of Figure 4.30 is that the Stokes side of the spectrum is broader than the anti-Stokes side. When the incident pulse energy was less than 1 mJ, the spectral broadening was found to be monotonically increasing on the pulse energy of 1054 nm. The spectral broadening generated by sending an intense 80-$\mu$J, 527-nm, 8-ps laser pulse alone through these ZnSe crystals was also measured for comparison with the $\pm 1000\,\text{cm}^{-1}$ induced spectral broadening. The observed spectral broadening was only $200\,\text{cm}^{-1}$ when the energy of the 527-nm pulse was over 0.2 mJ. This measurement suggests that the self-phase modulation process from the 10-nJ SHG pulse in ZnSe is too insignificant to explain the observed $1000\,\text{cm}^{-1}$. Most likely, the broad spectral width of the SHG signal arises from the XPM generated by the pump during the generation process.

The temporal profile and propagation time of the intense 1054-nm pump pulse and the second harmonic pulse propagating through a 22-mm ZnSe polycrystalline sample is shown in Figure 4.31. A pulse delay of ~189 ps at

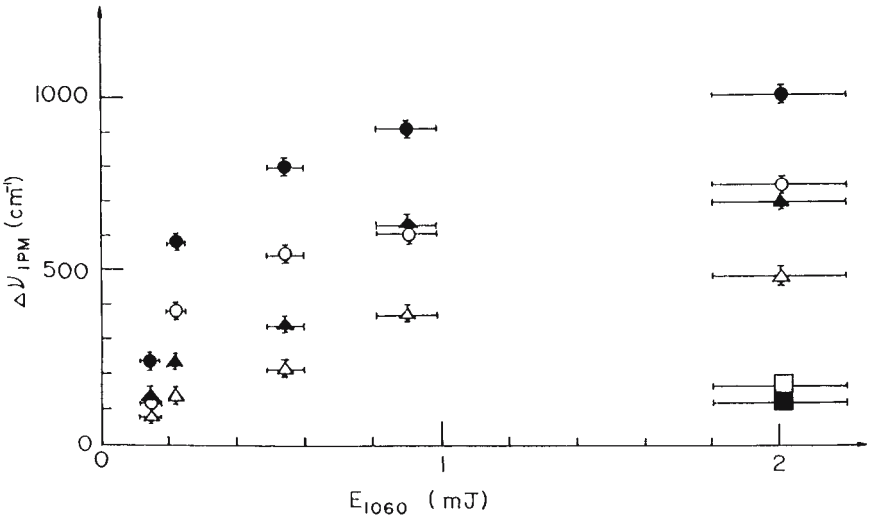


FIGURE 4.30. Intensity dependence of induced spectral width about 530 nm in ZnSe pumped by a 1060-nm laser pulse. The horizontal axis is the incident laser pulse energy. (○) 2.2-cm-long polycrystalline ZnSe anti-Stokes broadening. (●) 2.2-cm-long polycrystalline ZnSe Stokes broadening. (▲) 1.6-cm-long single-crystal ZnSe anti-Stokes broadening. (△) 1.6-cm-long single-crystal ZnSe Stokes broadening. (□) 3.7-cm-long quartz crystal anti-Stokes broadening. (■) 3.7-cm-long quartz crystal Stokes broadening. The measured $\Delta n$ is defined as the frequency spread from 527 nm to the farthest detectable wavelengths measured either photographically or by an optical multi-channel analyzer. (From Alfano and Ho, 1988.)

1054 nm was observed (Figure 4.31a) when an intense 1054-nm pulse passed through the crystal. The second harmonic signal, which spread from 500 to 570 nm, indicated a sharp spike at 189 ps and a long plateau from 189 to 249 ps (Figure 4.31b). Using 10-nm bandwidth narrowband filters, pulses of selected wavelengths from the second harmonic signal were also measured. For example, time delays corresponding to the propagation of two pulses with wavelengths centered at 530 and 550 nm are displayed in Figures 4.31c and d, respectively. All traces from Figure 4.31 indicated that the induced spectrally broadened pulses have one major component emitted at nearly the same time as the incident pulse (Figure 4.31a). The selected wavelength shifted 10 nm from the second harmonic wavelength has shown a dominant pulse distribution generated at the end of the crystal. Furthermore, when a weak 3-nJ, 527-nm calibration pulse propagated alone through the 22-mm ZnSe, a propagation time of about 249 ps was observed, as expected from the group velocity.

The difference in the propagation times of a weak 527-nm calibration pulse and a 1054-nm pump pulse through a ZnSe crystal can be predicted perfectly

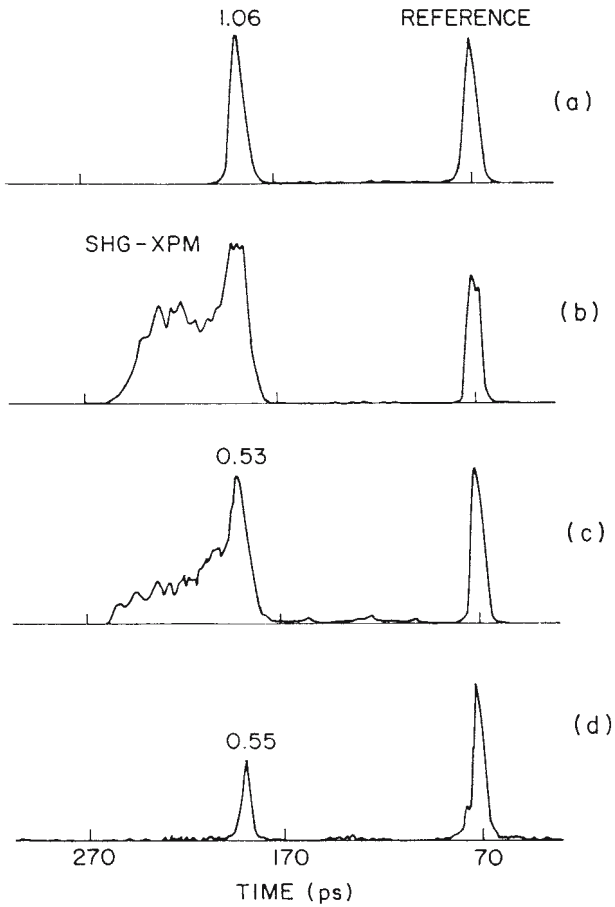


FIGURE 4.31. Temporal profile and propagation delay time of (a) incident 1054 nm, (b) SHG-XPM signal of all visible spectra, and (c) selected 530 nm from SHG-XPM of a 22-nm-long ZnSe crystal measured by a 2-ps resolution streak camera system. (d) same as (c) for a signal selected at 550 nm. The reference time corresponds to a laser pulse traveling through air without the crystal. The right side of the time scale is the leading time. The vertical scale is an arbitrary intensity scale. (From Alfano and Ho, 1988.)

by the difference in group velocities. The measured group refractive indices of ZnSe can be fitted to $n_{g,1054} = 3.39$ and $n_{g,1054} = 2.57$, respectively. These values are in agreement with the calculated values.

The sharp spike and plateau of the second harmonic pulse can be explained using the XPM model of second harmonic generation (Ho et al., 1980). Because of lack of phase matching, i.e., destructive interferences, the energy of the second harmonic pulse cannot build up along the crystal length. As a result, most of the second harmonic power is generated at the exit face of the

crystal, which explains the observed spike. However, since very intense pump pulses are involved there is a partial phase matching due to the cross-phase modulation and two photon absorption effects at the second harmonic wavelength. Some second harmonic energy can build up between the entrance and exit faces of the sample, which explains the plateau feature.

## 6. Cross-Phase Modulation and Stimulated Four-Photon Mixing in Optical Fibers

Stimulated four-photon mixing (SFPM) is an ideal process for designing parametric optical amplifiers and frequency converters. SFPM is produced when two high-intensity pump photons are coupled by the third-order susceptibility $\chi^{(3)}$ to generate a Stokes photon and an anti-Stokes photon. The frequency shifts of the SFPM waves are determined by the phase-matching conditions, which depend on the optical geometry. SFPM was produced in glass by Alfano and Shapiro (1970) using picosecond pulses. Later, SFPM was successfully demonstrated by a number of investigators in few mode, birefringent, and single-mode optical fibers (Stolen, 1975; Stolen et al., 1981; Washio et al., 1980). Most of the earlier experiments using optical fibers were performed with nanosecond pulses. Lin and Bosch (1981) obtained large-frequency shifts; however, the spectral dependence on the input intensity was not investigated. In the following, measurements of the intensity dependence of SFPM spectra generated by 25-ps pulses in an optical fiber are reported (Baldeck and Alfano, 1987). For such short pulses, spectra are influenced by the combined effects of SPM and XPM. The broadening of SFPM lines and the formation of frequency continua are investigated.

The experimental method is as follows. A Quantel frequency-doubled mode-locked Nd: YAG laser produced 25-ps pulses. An X20 microscope lens was used to couple the laser beam into the optical fiber. The spectra of the output pulses were measured using a 1-m, 1200 lines/mm grating spectrometer. Spectra were recorded on photographic film and with an optical multichannel analyzer OMA2. Average powers coupled in the fiber were measured with a power meter at the optical fiber output. The 15-m-long optical fiber had a core diameter of 8 mm and a normalized frequency $V = 4.44$ at 532 nm. At this wavelength, the four first LP modes ($LP_{01}$, $LP_{11}$, $LP_{21}$, and $LP_{02}$) were allowed to propagate.

Typical intensity-Dependent spectra are displayed in Figures 4.32, 4.33, and 4.34. At low intensity, $I < 10^8\,W/cm^2$, the output spectrum contains only the pump wavelength $\lambda = 532\,nm$ (Figure 4.32a). At approximately $5 \times 10^8\,W/cm^2$ three sets of symmetrical SFPM lines (at $\Omega = 50$, 160, and $210\,cm^{-1}$) and the first SRS Stokes line (at $440\,cm^{-1}$) appear (Figures 4.32b and c). As the intensity increases the SFPM and SRS lines broaden, and a Stokes frequency continuum is generated (Figures 4.32d and e). Above an intensity threshold of $20 \times 10^8\,W/cm^2$, new sets of SFPM lines appear on the Stokes and

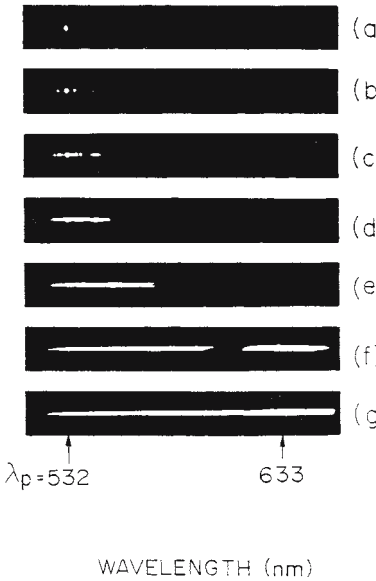


FIGURE 4.32. Evolution of a stimulated four-photon spectrum with increasing pulse intensity. (a) $I < 10^8$ W/cm$^2$; (b and c) $I = 5 \times 10^8$ W/cm$^2$; (d) $I = 10 \times 10^8$ W/cm$^2$; (e) $I = 15 \times 10^8$ W/cm$^2$; (f) $I = 30 \times 10^8$ W/cm$^2$; (g) $I = 35 \times 10^8$ W/cm$^2$. (From Baldeck and Alfano, 1987.)

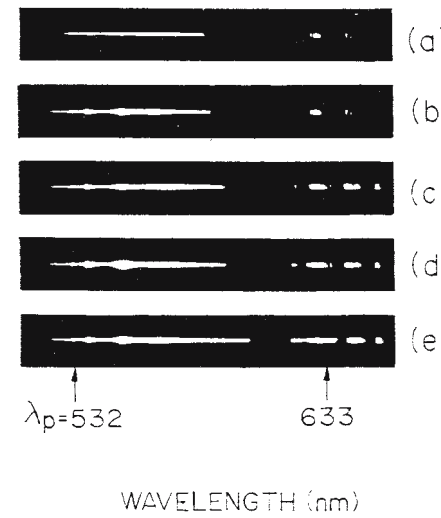


FIGURE 4.33. (a to e) Sequence of the large-shift SFPM line broadening. The pulse peak intensity increases from $I = 20 \times 10^8$ W/cm$^2$ in (a) to $I = 30 \times 10^8$ W/cm$^2$ in (e) in steps of $2.5 \times 10^8$ W/cm$^2$. (From Baldeck and Alfano, 1987.)

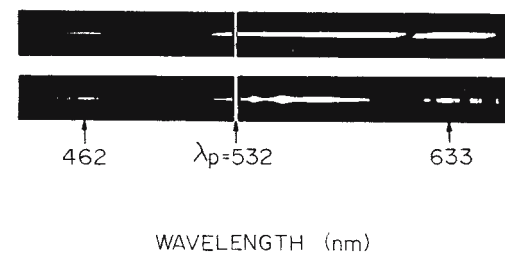


FIGURE 4.34. Examples of large-shift Stokes lines with their corresponding anti-Stokes lines. Photographs of the Stokes and anti-Stokes regions were spliced together. (From Baldeck and Alfano, 1987.)

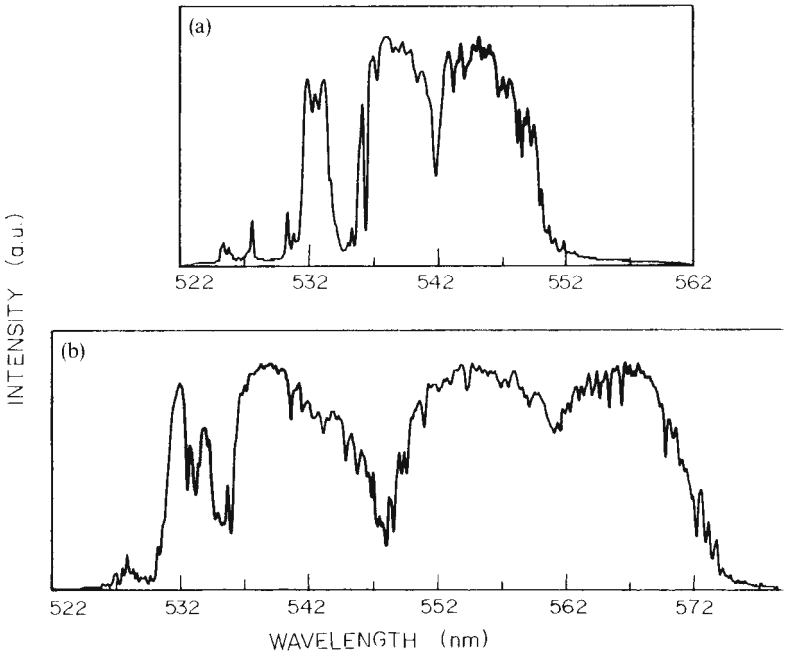


FIGURE 4.35. Supercontinuum generation. (a) The pump, SFPM, and first SRS Stokes lines are broadened at $I = 10 \times 10^8\,\mathrm{W/cm^2}$. (b) The broadened second and third SRS Stokes lines appear and extend the spectrum toward the Stokes wavelengths at $I = 15 \times 10^8\,\mathrm{W/cm^2}$. (From Baldeck and Alfano, 1987.)

anti-Stokes sides with frequency ranging from 2700 to 3865 $\mathrm{cm^{-1}}$. Finally, the large shifts merge (Figure 4.32f) and contribute to the formation of a 4000 $\mathrm{cm^{-1}}$ frequency continuum (Figure 4.32g). Figure 4.33 shows how the large Stokes shift SFPM lines are generated and broaden when the pump intensity increases from $20 \times 10^8$ to $30 \times 10^8\,\mathrm{W/cm^2}$. Figure 4.34 gives two examples of complete spectra including the large-shift anti-Stokes and Stokes lines. The measured SFPM shifts correspond well with the phase-matching condition of SFPM in optical fibers.

Figure 4.35 shows the development of a Stokes continuum from the combined effects of SFPM, SRS, SPM, and XPM. As the pump intensity is increased, the pump, SFPM, and first SRS lines broaden and merge (Figure 4.35a). For stronger pump intensities, the continuum is duplicated by stimulated Raman scattering, and the continuum expands toward the lowest optical frequencies (Figure 4.35b). As shown, the maximum intensities of new frequencies are self-limited.

The broadening of the SFPM and SRS lines arises from self- and cross-phase modulation effects. It is established that spectral broadenings generated by SPM are inversely proportional to the pulse duration and linearly

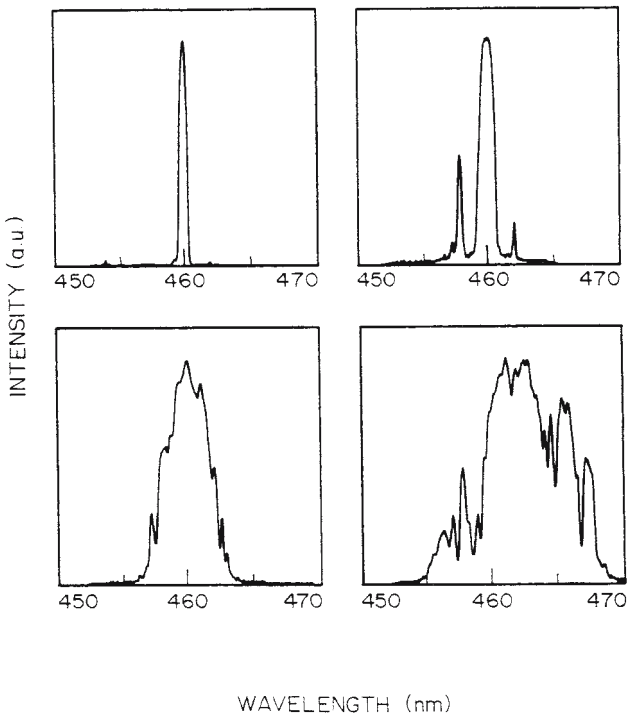


FIGURE 4.36. (a to d) Spectral broadening of the anti-Stokes SFPM line generated at 460 nm. The pulse peak intensity increases from $I = 20 \times 10^8$ W/cm$^2$ in (a) to $I = 30 \times 10^8$ W/cm$^2$ in (e) in steps of $2.5 \times 10^8$ W/cm$^2$. (From Baldeck and Alfano, 1987.)

proportional to the pump intensity. In this experiment, SPM effects are important because of the pump pulse shortness (25 ps) and intensity ($10^9$ W/cm$^2$). Furthermore, the modulation that is seen in the continuum spectrum fits well with the spectrum modulation predicted by phase modulation theories.

Figure 4.36 shows the spectral broadening of the anti-Stokes SFPM line of $\lambda = 460$ nm ($\Omega = 2990$ cm$^{-1}$). This line is a large-shift SFPM anti-Stokes line generated simultaneously with the $\lambda = 633$ nm SFPM Stokes line by the laser pump of $\lambda = 532$ nm (see Figure 4.34). The corresponding frequency shift and mode distribution are $W = 2990$ cm$^{-1}$ and $LP_{01}$ (pump)–$LP_{11}$ (Stokes and anti-Stokes), respectively. From Figures 4.36a to d, the peak intensity of the $\lambda = 460$ nm line increases from approximately $20 \times 10^8$ to $30 \times 10^8$ W/cm$^2$ in steps of $2.5 \times 10^8$ W/cm$^2$. In Figure 4.36a, the spectrum contains only the 460-nm SFPM line generated by the laser pump ($\lambda = 532$ nm). In Figure 4.36b, the line begins to broaden and two symmetrical lines appear with a frequency shift of 100 cm$^{-1}$. This set of lines could be a new set of small-shift SFPM lines generated by the 460-nm SFPM line acting as a new pump wavelength.

Figures 4.36c and d show significant broadening, by a combined action of SFPM, SPM, and XPM, of the 460 nm into a frequency continuum. Similar effects were observed on the Stokes side as displayed in Figure 4.33.

The intensity effects on SFPM spectra generated by 25-ps pulses propagating in optical fibers have been investigated experimentally. In contrast to SFPM lines generated by nanosecond pulses, spectra were broadened by self-phase modulation and cross-phase modulation. Intensity-saturated wide frequency continua covering the whole visible spectrum were generated for increasing intensities. Applications are for the design of wideband amplifiers, the generation of "white" picosecond pulses, and the generation by pulse compression of femtosecond pulses at new wavelengths.

## 7. Induced Focusing by Cross-Phase Modulation in Optical Fibers

Cross-phase modulation originates from the nonlinear refractive index $\Delta n(r, t) = 2n_2E_p^2(r, t)$ generated by the pump pulse at the wavelength of the probe pulse. Consequently, XPM has not only temporal and spectral effects but also spatial effects. Induced focusing is a spatial effect of XPM on the probe beam diameter. Induced focusing is the focusing of a probe beam because of the radial change of the refractive index induced by a copropagating pump beam. Induced focusing is similar to the self-focusing (Kelley, 1965) of intense lasers beams that has been observed in many liquids and solids. Overviews and references on self-focusing in condensed media are given by Auston (1977) and Shen (1984).

In 1987, Baldeck, Raccah, and Alfano reported on experimental evidence for focusing of picosecond pulses propagating in an optical fiber (Baldeck et al., 1987a). Focusing occurred at Raman frequencies for which the spatial effect of the nonlinear refractive index was enhanced by cross-phase modulation. Results of this experiment on induced focusing by cross-phase modulation in optical fibers are summarized in this section.

The experimental setup is shown in Figure 4.37. A Quantel frequency-doubled mode-locked Nd: YAG laser produced 25-ps pulses at 532 nm. The laser beam was coupled into the optical fiber with a 10× microscope lens. A stable modal distribution was obtained with a Newport FM-1 mode scrambler. Images of the intensity distribution at the output face were magnified by 350× and recorded on photographic film. Narrowband (NB) filters were used to select frequencies of the output pulses. The optical fiber was a commercial multimode step-index fiber (Newport F-MLD). Its core diameter was 100 $\mu$m, its numerical aperture 0.3, and its length 7.5 m.

Several magnified images of the intensity distributions that were observed at the output face of the fiber for different input pulse energies are shown in

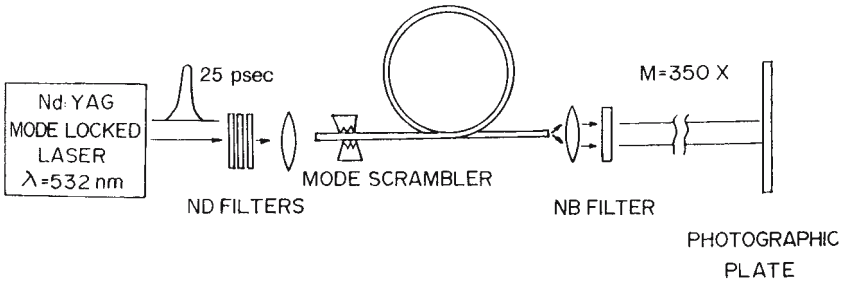


FIGURE 4.37. Experimental setup for the observation of Raman focusing in a large-core optical fiber. (From Baldeck et al., 1987.)

Figure 4.38. The intensity distribution obtained for low pulse energies ($E <$ 1 nJ) is shown in Figure 4.38a. It consists of a disk profile with a speckle pattern. The intensity distribution of the disk covers the entire fiber core area. The disk diameter, measured by comparison with images of calibrated slits, is 100 $\mu$m, which corresponds to the core diameter. The characteristics of this fiber allow for the excitation of about 200,000 modes. The mode scrambler distributed the input energy to most of the different modes. The speckle pattern is due to the interference of these modes on the output face. Figure 4.37b shows the intensity distribution in the core for intense pulses ($E >$ 10 nJ). At the center of the 100-mm-diameter disk image, there is an intense smaller (11-mm) ring of a Stokes-shifted frequency continuum of light. About 50% of the input energy propagated in this small-ring pattern. The corresponding intensities and nonlinear refractive indices are in the ranges of gigawatts per square centimeter and $10^{-6}$, respectively. For such intensities, there is a combined effect of stimulated Raman scattering, self-phase modulation, and cross-phase modulation that generates the observed frequency continuum. In Figure 4.37c, an NB filter selected the output light pattern at 550 nm. This clearly shows the ring distribution of the Stokes-shifted wavelengths. Such a ring distribution was observed for a continuum of Stokes-shifted wavelengths up to 620 nm for the highest input energy before damage.

The small-ring intensity profile is a signature of induced focusing at the Raman wavelengths. First, the small ring is speckleless, which is characteristic of single-mode propagation. This single-mode propagation means that the guiding properties of the fiber are dramatically changed by the incoming pulses. Second, SRS, SPM, and XPM occur only in the ring structure, i.e., where the maximum input energy has been concentrated. Our experimental results may be explained by an induced-gradient-index model for induced focusing. For high input energies, the Gaussian beam induces a radial change of the refractive index in the optical fiber core. The step-index fiber becomes a gradient-index fiber, which modifies its light-guiding properties. There is

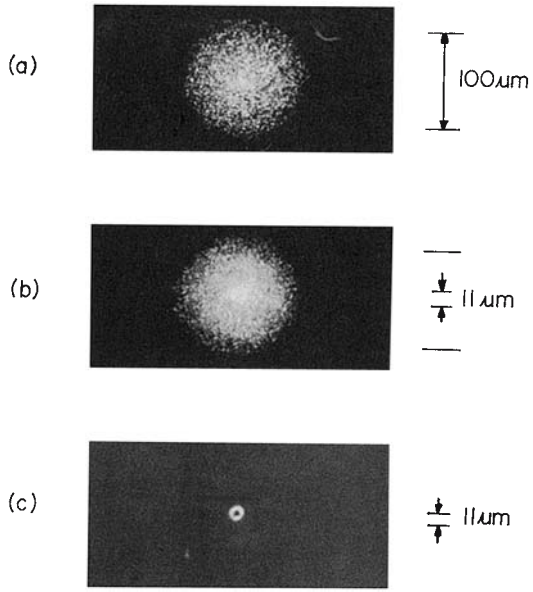


FIGURE 4.38. Images of the intensity distributions at the optical fiber output: (a) input pulses of low energies ($E < 1$ nJ); (b) input pulses of high energies ($E > 10$ nJ); (c) same as (b) with an additional narrowband filter centered at $\lambda = 550$ nm. ($M = 350\chi$). (From Baldeck et al., 1987a.)

further enhancement of the nonlinear refractive index at Raman frequencies because of XPM. Thus, Stokes-shifted light propagates in a well-marked induced-gradient-index fiber. The ray propagation characteristics of a gradient-index fiber are shown schematically in Figure 4.39 (Keiser, 1983). The cross-sectional view of a skew-ray trajectory in a graded-index fiber is shown. For a given mode $u$, there are two values for the radii, $r_1$ and $r_2$, between which the mode is guided. The path followed by the corresponding ray lies completely within the boundaries of two coaxial cylindrical surfaces that form a well-defined ring. These surfaces are known as the caustic surfaces. They have inner and outer radii $r_1$ and $r_2$, respectively. Hence, Figure 4.39 shows that skew rays propagate in a ring structure comparable to the one shown in Figure 4.38c. This seems to support the induced-gradient-index model for induced focusing in optical fibers.

Induced focusing of Raman picosecond pulses has been observed in optical fibers. Experimental results may be explained by an induced-gradient-index model of induced focusing. An immediate application of this observation could be the single-mode propagation of high-bit-rate optical signals in large-core optical fibers.

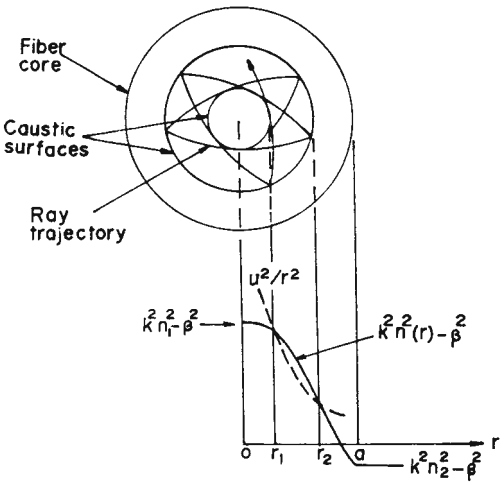


FIGURE 4.39. Cross-sectional projection of a skew ray in a gradient-index fiber and the graphical representation of its mode solution from the WBK method. The field is oscillatory between the turning points $r_1$ and $r_2$ and is evanescent outside this region.

## 8. Modulation Instability Induced by Cross-Phase Modulation in Optical Fibers

Modulation instability refers to the sudden breakup in time of waves propagating in nonlinear dispersive media. It is a common nonlinear phenomenon studied in several branches of physics (an overview on modulation instability can be found in Hasegawa, 1975). Modulation instabilities occur when the steady state becomes unstable as a result of an interplay between the dispersive and nonlinear effects. Tai, Hasegawa, and Tomita have observed the modulation instability in the anomalous dispersion regime of silica fibers, i.e., for wavelengths greater than 1.3 $\mu$m (Tai et al., 1986). Most recently, Agrawal (1987) has suggested that a new kind of modulation instability can occur even in the normal dispersion regime when two copropagating fields interact with each other through the nonlinearity-induced cross-phase modulation. This section summarizes the first observation by Baldeck, Alfano, and Agrawal of such a modulation instability initiated by cross-phase modulation in the normal dispersion regime of silica optical fibers (Baldeck et al., 1988b, 1989d).

Optical pulses at 532 nm were generated by either a mode-locked Nd: YAG laser or a $Q$-switched Nd: YAG laser with widths of 25 ps or 10 ns, respectively. In both cases the repetition rate of pulses was 10 Hz. Pulses were coupled into a single-mode optical fiber using a microscope lens with a magnification of 40. The peak power of pulses into the fiber could be adjusted in the range 1 to $10^4$ W by changing the coupling conditions and by using neutral density filters. The optical fiber was custom-made by Corning Glass. It has a 3-$\mu$m core diameter, a 0.24% refractive index difference, and a single-

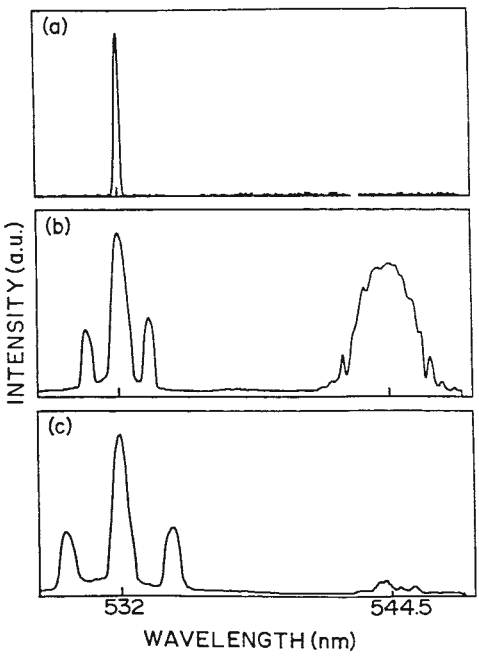


FIGURE 4.40. Characteristic frequency sidebands of modulation instability resulting from cross-phase modulation induced by the simultaneously generated Raman pulses in lengths $L$ of a single-mode optical fiber. The laser line is at $\lambda = 532$ nm and the Raman line at $\lambda = 544.5$ nm. The time duration of input pulses is 25 ps. (a) Reference spectrum at low intensity; (b) Spectrum at about the modulation instability threshold and $L = 3$ m; (c) same as (b) for $L = 0.8$ m. (From Baldeck et al., 1988d–1989.)

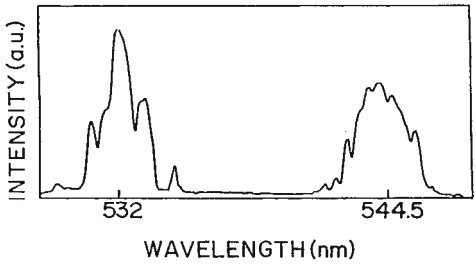


FIGURE 4.41. Secondary sidebands observed for pulse energies well above the modulation instability threshold. (From Baldeck et al., 1988d–1989.)

mode cutoff at $\lambda = 462$ nm. Spectra of output pulses were measured using a grating spectrometer (1 m, 600 lines/mm) and recorded with an optical multichannel analyzer OMA2.

Figures 4.40 and 4.41 show spectra of intense 25-ps pulses recorded for different peak powers and fiber lengths. Figure 4.40a is the reference spectrum of low-intensity pulses. Figures 4.40b and c show spectra measured at about the modulation instability threshold for fiber lengths of 3 and 0.8 m, respectively. They show modulation instability sidebands on both sides of the laser wavelength at 532 nm and the first-order stimulated Raman scattering line at 544.5 nm. Notice that the frequency shift of sidebands is larger for the shorter fiber. Secondary sidebands were also observed for pulse energy well

above the modulation instability threshold and longer optical fibers as shown in Figure 4.41.

Similar to spectra in the experiment of Tai et al., spectra shown in Figures 4.40 and 4.41 are undoubtedly signatures of modulation instability. A major salient difference in the spectra in Figures 4.40 and 4.41 is that they show modulation instability about 532 nm, a wavelength in the *normal dispersion regime* of the fiber. According to the theory, modulation instability at this wavelength is possible only if there is a cross-phase modulation interaction (Agrawal, 1987). As shown in Figure 4.40, modulation instability sidebands were observed only in the presence of stimulated Raman scattering light. It has recently been demonstrated that cross-phase modulation is intrinsic to the stimulated Raman scattering process (see Section 4). Therefore, sideband features observed in Figures 4.40 and 4.41 are conclusively a result of the cross-phase modulation induced by the simultaneously generated Raman pulses. To rule out the possibility of a multimode or single-mode stimulated four-photon mixing process as the origin of the sidebands, Baldeck et al. note that the fiber is truly single-mode (cutoff wavelength at 462 nm) and that the sideband separation changes with the fiber length.

The strengthen the conclusion that the sidebands are due to modulation instability induced by cross-phase modulation, Baldeck et al. measured and compared with theory the dependence of sideband shifts on the fiber lengths. For this measurement, they used 10-ns pulses from the *Q*-switched Nd:YAG laser to ensure quasi-CW operation. The spectra were similar to those obtained with 25-ps pulses (Figure 4.40). As shown in Figure 4.42, the sidelobe separation, defined as the half-distance between sideband maxima, varied from 1.5 to 8.5 nm for fiber lengths ranging from 4 to 0.1 m, respectively. The energy of input pulses was set at approximately the modulation instability threshold for each fiber length. The solid line in Figure 4.42 cor-

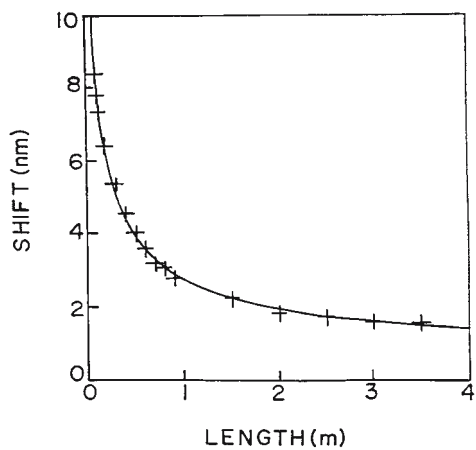


FIGURE 4.42. Sideband shifts versus fiber length near the modulation instability threshold. The time duration of input pulses is 10 ns. Crosses are experimental points. The solid line is the theoretical fit from Eq. (25). (From Baldeck et al., 1988d–1989.)

responds to the theoretical fit. As discussed in Agrawal (1987), the maximum gain of modulation instability sidebands is given by $g_{\max} = k''\Omega_m^2$, where $\Omega_m = 2\pi f_m$ is the sideband shift. Thus, the power of a sideband for an optical fiber length $L$ is given by

$$P(\Omega_m, L) = P_{\text{noise}} \exp(k''\Omega_m^2 L), \tag{23}$$

where $P_{\text{noise}}$ is the initial spontaneous noise and $k'' = \partial(v_g)^{-1}/\partial\omega$ is the group velocity dispersion at the laser frequency.

For such amplified spontaneous emission, it is common to define a threshold gain $g_{\text{th}}$ by

$$P_{\text{th}}(L) = P_{\text{noise}} \exp(g_{\text{th}}), \tag{24}$$

where $P_{\text{th}}$ is the sideband power near threshold such that each sideband contains about 10% of the input energy. A typical value for $g_{\text{th}}$ is 16 (Tai et al., 1986).

From Eqs. (23) and (24) the dependence of the sideband shift on the fiber length near threshold is given by

$$\Omega_m = (g_{\text{th}}/k''L)^{1/2}. \tag{25}$$

At $\lambda = 532\,\text{nm}$, the group velocity dispersion in $k'' \approx 0.06\,\text{ps}^2/\text{m}$. The theoretical fit shown in Figure 4.42 (solid line) is obtained using this value and $g_{\text{th}} = 18.1$ in Eq. (25). The good agreement between the experimental data and the theory of modulation instability supports the belief of Baldeck et al. that they have observed cross-phase modulation-induced modulation instability, as predicted in Agrawal (1987).

Tai et al. have shown that modulation instability leads to the breakup of long quasi-CW pulses in trains of picosecond subpulses. The data in Figure 4.42 show that the maximum sideband shift is $\Delta\lambda_{\max} \approx 8.5\,\text{nm}$ or $8.5\,\text{THz}$, which corresponds to the generation of femtosecond subpulses within the envelope of the 10-ns input pulses with a repetition time of 120 fs. Even though autocorrelation measurements were not possible because of the low repetition rate (10 Hz) needed to generate pulses with kilowatt peak powers, Baldeck et al. believe they have generated for the first time modulation instability subpulses shorter than 100 fs.

Baldeck et al. (1988b) observed modulation instability in the normal dispersion regime of optical fibers. Modulation instability sidebands appear about the pump frequency as a result of cross-phase modulation induced by the simultaneously generated Raman pulses. Sideband frequency shifts were measured for many fiber lengths and found to be in good agreement with theory. In this experiment, cross-phase modulation originated from an optical wave generated inside the nonlinear medium, but similar results are expected when both waves are incident externally. Modulation instability induced by cross-phase modulation represents a new kind of modulation instability that not only occurs in normally dispersive materials but also, most important, has the potential to be controlled in real time by switching on or off the

copropagating pulse responsible for the cross-phase modulation. Using optical fibers, such modulation instabilities could lead to the design of a novel source of femtosecond pulses at visible wavelengths.

## 9. Applications of Cross-Phase Modulation for Ultrashort Pulse Technology

Over the last 20 years, picosecond and femtosecond laser sources have been developed. Researchers are now investigating new applications of the unique properties of these ultrashort pulses. The main efforts are toward the design of communication networks and optical computers with data streams in, eventually, the tens of terahertz. For these high repetition rates, electronic components are too slow and all-optical schemes are needed. The discovery of cross-phase modulation effects on ultrashort pulses appears to be a major breakthrough toward the real-time all-optical coding/decoding of such short pulses. As examples, this section describes the original schemes for a frequency shifter, a pulse compression switch, and a spatial light deflector. These all-optical devices are based on spectral, temporal, and spatial effects of cross-phase modulation on ultrashort pulses.

The first XPM-based technique to control ultrashort pulses was developed in the early 1970s. It is the well-known optical Kerr gate, which is shown in Figure 4.43. A probe pulse can be transmitted through a pair of cross-polarizers only when a pump pulse induces the (cross-) phase (modulation) needed for the change of polarization of the probe pulse. The principle of the optical Kerr gate was demonstrated using nonlinear liquids (Shimizu and Stoicheff, 1969; Duguay and Hansen, 1969) and optical fibers (Stolen and Ashkin, 1972; Dziedzic et al., 1981; Ayral et al., 1984). In optical fibers, induced-phase effects can be generated with milliwatt peak powers because of their long interaction lengths and small cross sections (White et al., 1988). XPM effects in optical fibers have been shown to alter the transmission of frequency

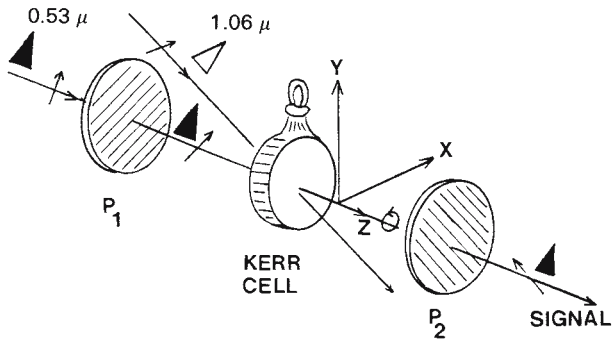


FIGURE 4.43. Schematic diagram of an optical Kerr gate.

multiplexed signals (Chraplyvy et al., 1984) and also to allow quantum nondemolition measurements (Levenson et al., 1986; Imoto et al., 1987). In addition, phase effects arising from XPM have been used to make all-fiber logic gates (Kitayama et al., 1985a), ultrafast optical multi/demultiplexers (Morioka et al., 1987), and nonlinear interferometers (Monerie and Durteste, 1987).

The novelty of our most recent work was to show that XPM leads not only to phase effects but also to spectral, temporal, and spatial effects on ultrashort pulses. New schemes for XPM-based optical signal processors are proposed in Figure 4.44. The design of an ultrafast frequency shifter is shown in Figure 4.44a. It is based on spectral changes that occur when pulses copropagate in a nonlinear dispersive medium. In the absence of a pump pulse, the weak signal pulse passes undistorted through the nonlinear medium. When the signal pulse copropagates in the nonlinear medium with a pump pulse, its carrier wavelength can be changed by an amount $\Delta\lambda$ that is linearly proportional to the peak power of the pump pulse (see Section 3.2). Thus, in Figure 4.44 the signal pulses S1 and S2 have their frequencies shifted by $\Delta\lambda_1$ and $\Delta\lambda_2$ by the pump pulses P1 and P2, while S3 is not affected by the stream of pump pulses.

The design of a pulse-compression switch is proposed in Figure 4.44b. It is a modified version of the usual optical fiber/grating-pair pulse compression scheme (see Chapter 9 by Dorsinville et al. and Chapter 10 by Johnson and Shank). First, the probe pulse is spectrally broadened by a copropagating pump pulse in the nonlinear medium (case of negligible group velocity mismatch; see Sections 2.2 and 3.1). Then, or simultaneously, it is compressed in time by a dispersive element. Thus, in the presence of the pump pulse, the signal pulse is compressed ("on" state), while in its absence, the signal pulse is widely broadened ("off" state) by the device.

An example of an all-optical spatial light deflector based on spatial effects of XPM is shown in Figure 4.44c. In this scheme, the pump pulse profile leads to an induced focusing of the signal pulse through the induced nonlinear refractive index (Section 7). The key point in Figure 4.43c is that half of the pump pulse profile is cut by a mask, which leads to an asymmetric induced-focusing effect and a spatial deflection of the signal pulse. This effect is very similar to the self-deflection of asymmetric optical beams (Swartlander and Kaplan, 1988). In the proposed device, pump pulses originate from either path P1 or path P2, which have, respectively, their left side or right side blocked. Thus, if a signal pulse copropagates with a pump pulse from P1 or P2, it is deflected on, respectively, the right or left side of the nondeflected signal pulse.

The prime property of future XPM-based optical devices will be their switching speed. They will be controlled by ultrashort pulses that will turn on or off the induced nonlinearity responsible for XPM effects. With short pulses, the nonlinearity originates from the fast electronic response of the interacting material. As an example, the time response of electronic nonlinearity in optical fibers is about 2 to 4 fs (Grudinin et al., 1987). With such

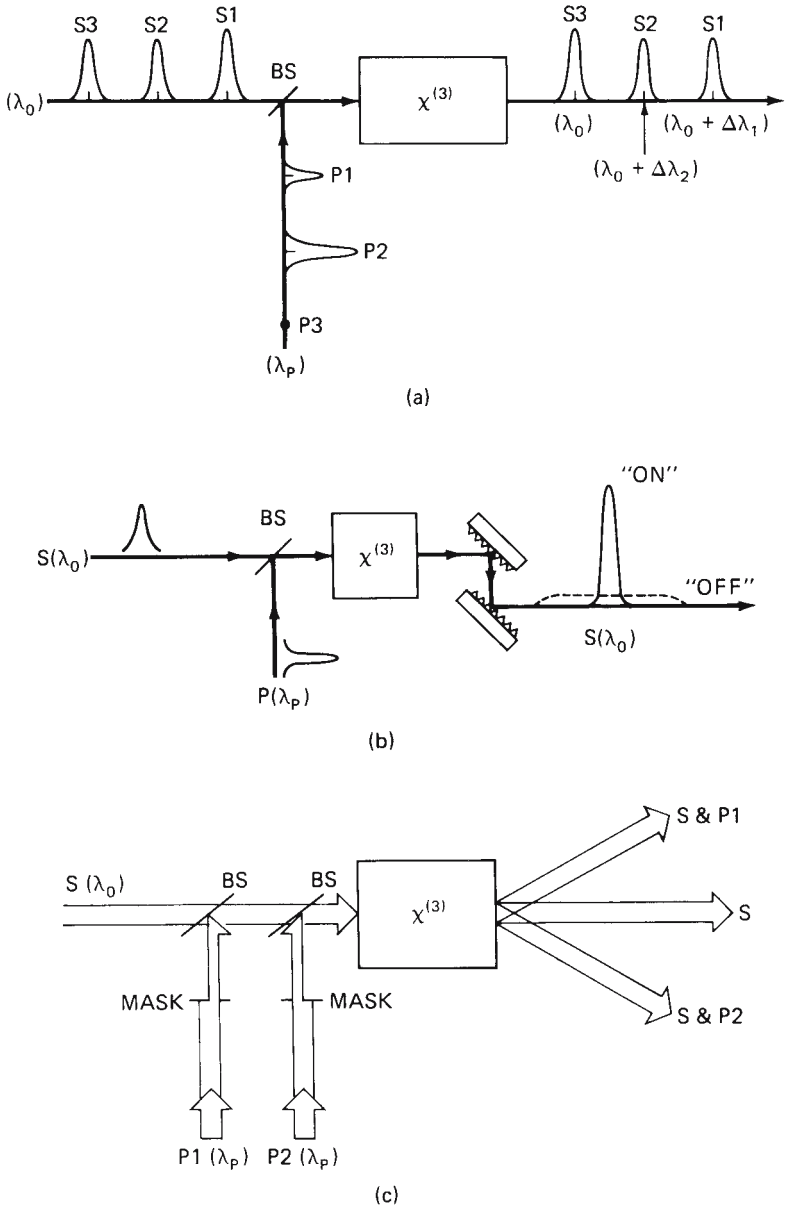


FIGURE 4.44. Schematic diagrams of ultrafast optical processors based on cross-phase modulation effects. (a) Ultrafast frequency shifter; (b) all-optical pulse compression switch; (c) all-optical spatial light deflector.

a response time, one can envision the optical processing of femtosecond pulses with repetition rates up to 100 THz.

## 10. Conclusion

This chapter reviewed cross-phase modulation effects on ultrashort optical pulses. It presented XPM measurements that were obtained during the years 1986 to 1988. XPM is a newly identified physical phenomenon with important potential applications based on the picosecond and femtosecond pulse technology. XPM is similar to SPM but corresponds to the phase modulation caused by the nonlinear refractive index *induced by a copropagating pulse.* As for SPM, the time and space dependences of XPM lead to spectral, temporal, and spatial changes of ultrashort pulses.

Experimental investigations of cross-phase modulation effects began in 1986, when the spectral broadening enhancement of a probe pulse was reported for the first time. Subsequently, spectra of Raman, second harmonic, and stimulated four-photon mixing picosecond pulses were found to broaden with increasing pump intensities. Moreover, it was demonstrated that the spectral shape of Raman pulses was affected by the pulse walk-off, that the frequency of copropagating pulses could be tuned by changing the input time delay between probe and pump pulses, and that modulation instability could be obtained in the normal dispersion regime of optical fibers. All these results are well understood in terms of the XPM theory. Furthermore, induced focusing of Raman pulses, which was recently observed in optical fibers, was explained as a spatial effect of XPM.

The research trends are now toward more quantitative comparisons between measurement and theory and the development of XPM-based applications. Future experiments should clarify the relative contributions of SPM, XPM, and modulation instability to the spectral broadening of Raman, second harmonic, and stimulated four-photon mixing pulses. As, XPM appears to be a new tool for controlling (with the fast femtosecond time response of electronic nonlinearities) the spectral, temporal, and spatial properties of ultrashort pulses. Applications could include the frequency tuning in real time of picosecond pulses, the compression of weak pulses, the generation of femtosecond pulse trains from CW beams by XPM-induced modulation instability, and the spatial scanning of ultrashort pulses. The unique controllability of XPM should open up a broad range of new applications for the supercontinuum laser source.

Experiments on induced- and cross-phase modulations have been performed by the authors in close collaboration with T. Jimbo, Z. Li, Q.Z. Wang, D. Ji, and F. Raccah. Theoretical studies were undertaken in collaboration with J. Gersten and Jamal Manassah of the City College of New York and, most recently, with Govind P. Agrawal of AT&T Bell Laboratories.

We gratefully acknowledge partial support from Hamamatsu Photonics K.K.

## 11. Addendum

This chapter was written during the spring of 1988. Since then many more of new theoretical and experimental results on XPM effects have been or are being published by various research groups. The reference list in the introduction section of this chapter has been updated. The interested readers should refer themselves to original reports in the most recent issues of optics and applied physics publications.

### References

Agrawal, G.P. (1987) Modulation instability induced by cross-phase modulation. Phys. Rev. Lett. **59**, 880–883.

Agrawal, G.P. and M.J. Potasek (1986) Nonlinear pulse distortion in single-mode optical fibers at the zero-dispersion wavelength. Phys. Rev. **3**, 1765–1776.

Agrawal, G.P., P.L. Baldeck, and R.R. Alfano (1988) Optical wave breaking and pulse compression due to cross-phase modulation in optical fibers. Conference abstract #MW3, in *Digest of the 1988 OSA annual meeting*. Optical Society of America, Washington, D.C. Opt. Lett. **14**, 137–139 (1989).

Agrawal, G.P., P.L. Baldeck, and R.R. Alfano (1989a) Temporal and spectral effects of cross-phase modulation on copropagating ultrashort pulses in optical fibers. Submitted for publication in Phys. Rev. A.

Agrawal, G.P., P.L. Baldeck, and R.R. Alfano (1989b) Modulation instability induced by cross-phase modulation in optical fibers. Phys. Rev. A (April 1989).

Alfano, R.R. and P.P. Ho (1988) Self-, cross-, and induced-phase modulations of ultrashort laser pulse propagation. IEEE J. Quantum Electron. **24**, 351–364.

Alfano, R.R. and S.L. Shapiro (1970) Emission in the region 4000–7000 Å via four-photon coupling in glass. Phys. Rev. Lett. **24**, 584–587. Observation of self-phase modulation and small scale filaments in crystals and glasses. Phys. Rev. Lett. **24**, 592–594.

Alfano, R.R., Q. Li, T. Jimbo, J.T. Manassah, and P.P. Ho (1986) Induced spectral broadening of a weak picosecond pulse in glass produced by an intense ps pulse. Opt. Lett. **11**, 626–628.

Alfano, R.R., Q.Z. Wang, T. Jimbo, and P.P. Ho (1987a) Induced spectral broadening about a second harmonic generated by an intense primary ultrafast laser pulse in ZnSe crystals. Phys. Rev. **A35**, 459–462.

Alfano, R.R., P.L. Baldeck, F. Raccah, and P.P. Ho (1987b) Cross-phase modulation measured in optical fibers. Appl. Opt. **26**, 3491–3492.

Alfano, R.R., P.L. Baldeck, and P.P. Ho (1988) Cross-phase modulation and induced-focusing of optical nonlinearities in optical fibers and bulk materials. Conference abstract #ThA3, In *Digest of the OSA topical meeting on nonlinear optical properties of materials.* Optical Society of America, Washington, D.C.

Auston, D.H. (1977) In *Ultrafast Light Pulses* S.L. Shapiro, ed. Springer-Verlag, Berlin, 1977.

Ayral, J.L., J.P. Pochelle, J. Raffy, and M. Papuchon (1984) Optical Kerr coefficient measurement at 1.15 $\mu$m in single-mode optical fivers. Opt. Commun. **49**, 405–408.

Baldeck, P.L. and R.R. Alfano (1987) Intensity effects on the stimulated four-photon spectra generated by picosecond pulses in optical fibers. Conference abstract #FQ7,

March meeting of the American Physical Society, New York, New York, 1987; J. Lightwave Technol. L. T-5, 1712–1715.

Baldeck, P.L., F. Raccah, and R.R. Alfano (1987a) Observation of self-focusing in optical fibers with picosecond pulses. Opt. Lett. **12**, 588–589.

Baldeck, P.L., P.P. Ho, and R.R. Alfano (1987b) Effects of self, induced-, and cross-phase modulations on the generation of picosecond and femtosecond white light supercontinua. Rev. Phys. Appl. **22**, 1677–1694.

Baldeck, P.L., P.P. Ho, and R.R. Alfano (1987c) Experimental evidences for cross-phase modulation, induced-phase modulation and self-focusing on picosecond pulses in optical fibers. Conference abstract #TuV4, in *Digest of the 1987 OSA annual meeting.* Optical Society of America, Washington, D.C.

Baldeck, P.L., F. Raccah, R. Garuthara, and R.R. Alfano (1987d) Spectral and temporal investigation of cross-phase modulation effects on picosecond pulses in singlemode optical fibers. Proceeding paper #TuC4, International Laser Science conference ILS-III, Atlantic City, New Jersey, 1987.

Baldeck, P.L., R.R. Alfano, and G.P. Agrawal (1988a) Induced-frequency shift of copropagating pulses. Appl. Phys. Lett. **52**, 1939–1941.

Baldeck, P.L., R.R. Alfano, and G.P. Agrawal (1988b) Observation of modulation instability in the normal dispersion regime of optical fibers. Conference abstract #MBB7, in *Digest of the 1988 OSA annual meeting.* Optical Society of America, Washington, D.C.

Baldeck, P.L., R.R. Alfano, and G.P. Agrawal (1988c) Induced-frequency shift, induced spectral broadening and optical amplification of picosecond pulses in a single-mode optical fiber. Proceeding paper #624, Electrochemical Society symposium on nonlinear optics and ultrafast phenomena, Chicago, Illinois, 1988.

Baldeck, P.L., R.R. Alfano, and G.P. Agrawal (1988d) Generation of sub-100-fsec pulses at 532 nm from modulation instability induced by cross-phase modulation in single-mode optical fibers. Proceeding paper #PD2, in *Utrafast Phenomena 6.* Springer-Verlag, Berlin.

Baldeck, P.L. and R.R. Alfano (1989) Cross-phase modulation: a new technique for controlling the spectral, temporal and spatial properties of ultrashort pulses. SPIE Proceedings of the 1989 Optical Science Engineering conference, Paris, France.

Chraplyvy, A.R. and J. Stone (1984) Measurement of cross-phase modulation in coherent wavelength-division multiplexing using injection lasers. Electron. Lett. **20**, 996–997.

Chraplyvy, A.R., D. Marcuse and P.S. Henry (1984) Carrier-induced phase noise in angel-modulated optical-fiber systems. J. Lightwave Technol. **LT-2**, 6–10.

Cornelius, P. and L. Harris (1981) Role of self-phase modulation in stimulated Raman scattering from more than one mode. Opt. Lett. **6**, 129–131.

Dianov, E.M., A.Y. Karasik, P.V. Mamyshev, G.I. Onishchukov, A.M. Prokhorov, M.F. Stel'Marh, and A.A. Formichev (1984) Picosecond structure of the pump pulse in stimulated Raman scattering in optical fibers. Opt. Quantum Electron. **17**, 187.

Duguay, M.A. and J.W. Hansen (1969) An ultrafast light gate. Appl. Phys. Lett. **15**, 192–194.

Dziedzic, J.M., R.H. Stolen, and A. Ashkin (1981) Optical Kerr effect in ling fibers, Appl. Opt. **20**, 1403–1406.

French, P.M.W., A.S.L. Gomes, A.S. Gouveia-Neto, and J.R. Taylor (1986) Picosecond stimulated Raman generation, pump pulse fragmentation, and fragment compression in single-mode optical fibers. IEEE J. Quantum Electron. **QE-22**, 2230.

Gersten, J., R.R. Alfano, and M. Belic (1980) Combined stimulated Raman scattering and continuum self-phase modulation. Phys. Rev. **A#21**, 1222–1224.

Gomes, A.S.L., W. Sibbet, and J.R. Taylor (1986) Spectral and temporal study of picosecond-pulse propagation in a single-mode optical fibers. Appl. Phys. **B#39**, 44–46.

Gomes, A.S.L., V.L. da Silva, and J.R. Taylor (1988) Direct measurement of nonlinear frequency chirp of Raman radiation in single-mode optical fibers using a spectral window method. J. Opt. Soc. Am. **B#5**, 373–380.

Gouveia-Neto, A.S., M.E. Faldon, A.S.B. Sombra, P.G.J. Wigley, and J.R. Taylor (1988a) Subpicosecond-pulse generation through cross-phase modulation-induced modulation instability in optical fibers. Opt. Lett. **12**, 901–906.

Gouveia-Neto, A.S., M.E. Faldon, and J.R. Taylor (1988b) Raman amplification of modulation instability and solitary-wave formation. Opt. Lett. **12**, 1029–1031.

Grudinin, A.B., E.M. Dianov, D.V. Korobkin, A.M. Prokhorov, V.N. Serkinand, and D.V. Khaidarov (1987) Decay of femtosecond pulses in single-mode optical fibers. Pis'ma Zh. Eksp. Teor. Fiz. **46**, 175–177. [Sov. Phys. JETP Lett. **46**, 221, 225.]

Hasegawa, A. (1975). *Plasma Instabilities and Nonlinear Effects.* Springer-Verlag, Heidelberg.

Ho, P.P., Q.Z. Wang, D. Ji, and R.R. Alfano (1988) Propagation of harmonic cross-phase-modulation pulses in ZnSe. Appl. Phys. Lett. 111–113.

Hook, A.D. Anderson, and M. Lisak (1988) Soliton-like pulses in stimulated Raman scattering. Opt. Lett. **12**, 114–116.

Imoto, N., S. Watkins, and Y. Sasaki (1987) A nonlinear optical-fiber interferometer for nondemolition measurement of photon number. Optics Commun. **61**, 159–163.

Islam, M.N., L.F. Mollenauer, and R.H. Stolen (1986) Fiber Raman amplification soliton laser, in *Ultrafast Phenomena 5.* Springer-Verlag, Berlin.

Islam, M.N., L.F. Mollenauer, R.H. Stolen, J.R. Simson, and H.T. Shang (1987a) Cross-phase modulation in optical fibers. Opt. Lett. **12**, 625–627.

Islam, M.N., L.F. Mollenauer, R.H. Stolen, J.R. Simson, and H.T. Shang (1987b) Amplifier/compressor fiber Raman lasers. Opt. Lett. **12**, 814–816.

Jaskorzynska, B. and D. Schadt (1988) All-fiber distributed compression of weak pulses in the regime of negative group-velocity dispersion. IEEE J. Quantum Electron. **QE-24**, 2117–2120.

Johnson, A.M., R.H. Stolen, and W.M. Simpson (1986) The observation of chirped stimulated Raman scattered light in fibers. In *Ultrafast Phenomena 5.* Springer-Verlag, Berlin.

Keiser, G. (1983) In *Optical Fiber Communications.* McGraw-Hill, New York.

Kelley, P.L. (1965) Self-focusing of optical beams. Phys. Rev. Lett. **15**, 1085.

Kimura, Y., K.I. Kitayama, N. Shibata, and S. Seikai (1986) All-fibre-optic logic "AND" gate. Electron. Lett. **22**, 277–278.

Kitayama, K.I., Y. Kimura, and S. Seikai (1985a) Fiber-optic logic gate. Appl. Phys. Lett. **46**, 317–319.

Kitayama, K.I., Y. Kimura, K. Okamoto, and S. Seikai (1985) Optical sampling using an all-fiber optical Kerr shutter. Appl. Phys. Lett. **46**, 623–625.

Levenson, M.D., R.M. Shelby, M. Reid, and D.F. Walls (1986) Quantum nondemolition detection of optical quadrature amplitudes. Phys. Rev. Lett. **57**, 2473–2476.

Lin, C. and M.A. Bosh (1981) Large Stokes-shift stimulated four-photon mixing in optical fibers. Appl. Phys. Lett. **38**, 479–481.

Lu, Hian-Hua, Yu-Lin Li, and Jia-Lin Jiang (1985) On combined self-phase modulation and stimulated Raman scattering in fibers. Opt. Quantum Electron. **17**, 187.
Manassah, J.T. (1987a) Induced phase modulation of the Raman pulse in optical fibers. Appl. Opt. **26**, 3747–3749.
Manassah, J.T. (1987b) Time-domain characteristics of a Raman pulse in the presence of a pump. Appl. Opt. **26**, 3750–3751.
Manassah, J.T. (1987c) Amplitude and phase of a pulsed second-harmonic signal. J. Opt. Soc. Am. **B#4**, 1235–1240.
Manassah, J.T. (1988) Pulse compression of an induced-phase modulated weak signal. Opt. Lett. **13**, 752–755.
Manassah, J.T. and O.R. Cockings (1987) Induced phase modulation of a generated second-harmonic signal. Opt. Lett. **12**, 1005–1007.
Manassah, J.T., M. Mustafa, R.R. Alfano, and P.P. Ho (1985) Induced supercontinuum and steepening of an ultrafast laser pulse. Phys. Lett. **113A**, 242–247.
Monerie, M. and Y. Durteste (1987) Direct interferometric measurement of nonlinear refractive index of optical fibers by cross-phase modulation. Electron. Lett. **23**, 961–962.
Morioka, T., M. Saruwatari, and A. Takada (1987) Ultrafast optical multi/demultiplexer utilising optical Kerr effect in polarisation-maintaining single-mode optical fibers. Electron. Lett. **23**, 453–454.
Nakashima, T., M. Nakazawa, K. Nishi, and H. Kubuta (1987) Effect of stimulated Raman scattering on pulse-compression characteristics. Opt. Lett. **12**, 404–406.
Schadt, D., B. Jaskorzynska, and U. Osterberg (1986) Numerical study on combined stimulated Raman scattering and self-phase modulation in optical fibers influenced by walk-off between pump and Stokes pulses. J. Opt. Soc. Am. **B#3**, 1257–1260.
Schadt, D. and B. Jaskorzynska (1987a) Frequency chirp and spectra due to self-phase modulation and stimulated Raman scattering influenced by walk-off in optical fibers. J. Opt. Soc. Am. **B#4**, 856–862.
Schadt, D. and B. Jaskorzynska (1987b) Generation of short pulses from CW light by influence of cross-phase modulation in optical fibers. Electron. Lett. **23**, 1091–1092.
Schadt, D. and B. Jaskorzynska (1988) Suppression of the Raman self-frequency shift by cross-phase modulation. J. Opt. Soc. Am. **B#5**, 2374–2378.
Shen, Y.R. (1984) In *The Principles of Nonlinear Optics.* Wiley, New York.
Shimizu, F. and B.P. Stoicheff (1969) Study of the duration and birefringence of self-trapped filaments in $CS_2$. IEEE J. Quantum Electron. **QE-5**, 544.
Stolen, R.H. (1975) Phase-matched stimulated four-photon mixing. IEEE J. Quantum Electron. **QE-11**, 213–215.
Stolen, R.H. (1979) In *Nonlinear properties of Optical fibers,* S.E. Miller and A.G. Chynoweth, eds. Academic Press, New York, Chapter 5.
Stolen, R.H. and A. Ashkin (1972) Optical Kerr effect in glass waveguide. Appl. Phys. Lett. **22**, 294–296.
Stolen, R.H., M.A. Bosh, and C. Lin (1981) Phase matching in birefringent fibers. Opt. Lett. **6**, 213–215.
Stolen, R.H. and A.M. Johnson (1986) The effect of pulse walk-off on stimulated Raman scattering in optical fibers. IEEE J. Quantum Electron. **QE-22**, 2230.
Swartzlander, G.A., Jr., and A.E. Kaplan (1988) Self-deflection of laser beams in a thin nonlinear film. J. Opt. Soc. Am. **B5**, 765–768.
Tai, K., A. Hasegawa, and A. Tomita (1986) Observation of modulation instability in optical fibers. Phys. Rev. Lett. **56**, 135–138.

Tomlinson, W.J., R.H. Stolen, and A.M. Johnson (1985) Optical wave breaking of pulses in nonlinear optical fibers. Opt. Lett. **10**, 457–459.

Trillo, S., S. Wabnitz, E.M. Wright, and G.I. Stegeman (1988) Optical solitary waves induced by cross-phase modulation. Opt. Lett. **13**, 871–873.

Wahio, K., K. Inoue, and T. Tanigawa (1980) Efficient generation near-IR stimulated light scattering in optical fibers pumped in low-dispersion region at 1.3 mm. Electron. Lett. **16**, 331–333.

Weiner, A.M., J.P. Heritage, and R.H. Stolen (1986) Effect of stimulated Raman scattering and pulse walk-off on self-phase modulation in optical fibers. In *Digest of the Conference on Lasers and Electro-Optics.* Optical Society of America, Washington, D.C., p. 246.

Weiner, A.M., J.P. Heritage, and R.H. Stolen (1988) Self-phase modulation and optical pulse compression influenced by stimulated Raman scattering in fibers. J. Opt. Soc. Am. **B5**, 364–372.

White, I.H., R.V. Penty, and R.E. Epworth (1988) Demonstration of the optical Kerr effect in an all-fibre Mach-Zehnder interferometer at laser diode powers. Electron. Lett. **24**, 172–173.

Zysset, B. and H.P. Weber (1986) Temporal and spectral investigation of Nd:YAG pulse compression in optical fibers and its application to pulse compression. In *Digest of the Conference on Lasers and Electro-Optics.* Optical Society of America, Washington, D.C., p. 182.

# 5
# Simple Models of Self-Phase and Induced-Phase Modulation

Jamal T. Manassah

## Introduction

Supercontinuum (Alfano and Shapiro, 1970) generation is the production of nearly continuous spectra by propagating intense picosecond and subpicosecond laser pulses through nonlinear media. Induced supercontinuum (Manassah et al., 1985; Alfano et al., 1986) is the superbroadening of the spectrum of a weak pulse due to the presence of a strong pulse propagating simultaneously with it in a nonlinear medium. These observable physical effects form the motivation for the study of self-phase and induced-phase modulation. This chapter examines, for some idealized simple models of the nonlinear material and incoming pulse, the amplitude, phase, geometric shape, and spectral distribution of an outgoing pulse on exiting from the nonlinear material for cases of both absent and present pump. The chapter is limited in scope and extent; it is confined to some analytical and semianalytical cases developed by the author and co-workers. Effects related to group velocity dispersion (GVD) are not generally included among our models.

To define the nomenclature for the different models, we next write the general form of Maxwell's equation in a nonlinear medium. The propagation of a monochromatic electromagnetic wave in a linear medium is described by the equation

$$\left(\Delta_T^2 + \frac{\partial^2}{\partial z^2}\right)\tilde{E}(\mathbf{r},\omega) + k^2(\omega)\tilde{E}(\mathbf{r},\omega) = 0.$$

Denoting, $k(\omega_0) \equiv k_0$, the above Maxwell's equation can be described for any $\omega$ near $\omega_0$ to second order in the difference $(\omega - \omega_0)$ by

$$\left(\Delta_T^2 \tilde{E} + \frac{\partial^2 E}{\partial z^2}\right) + \left[k_0^2 + 2k_0 k_0'(\omega - \omega_0) + (k_0'^2 + k_0 k_0')(\omega - \omega_b)^2\right]\tilde{E} = 0,$$

where

$$k_0' = \left.\frac{dk}{d\omega}\right|_{\omega=\omega_0} \quad \text{and} \quad k'' = \left.\frac{d^2k}{d\omega^2}\right|_{\omega=\omega_0},$$

where $k'$ is the group velocity and $k''$ is the group velocity dispersion. Consequently, for a pulse with center frequency $\omega_0$, the electric field then obeys the equation (Tzoar and Jain, 1979)

$$\nabla_T^2 E(\mathbf{r},t) + \frac{\partial^2 E(\mathbf{r},t)}{\partial z^2} + \exp(-i\omega_0 t)\left[k_0^2 + 2k_0 k_0' i\left(\frac{\partial}{\partial t}\right) - (k_0'^2 + k_0 k_0'')\frac{\partial^2}{\partial_t^2}\right] \times \exp(i\omega_0 t)E(\mathbf{r},t) = 0,$$

where $\omega$ in Fourier space has been replaced by $[i(\partial/\partial t)]$ in the time domain. In normalized coordinates defined by

$$E = E_0\Phi, \qquad T = t/\tau, \qquad \mathbf{R}' = \mathbf{r}/c\tau,$$
$$W_0 = \omega_0\tau, \qquad K_0 = (c\tau)/k_0,$$

where $E_0$ is the maximum pulse amplitude and $\tau$ is its width, Maxwell's equation for the function $\Phi$ can be written as

$$\frac{E_0}{c^2\tau^2}\left\{\nabla_T'^2\Phi + \frac{\partial^2}{\partial Z'^2}\Phi + \exp(-iW_0T)\left[K_0^2 + 2K_0K_0'\left(i\frac{\partial}{\partial T}\right) - (K_0'^2 + K_0K_0'')\frac{\partial^2}{\partial T^2}\right]\Phi\exp(iW_0T)\right\} = 0,$$

where

$$K_0' = \left.\frac{dK}{dW}\right|_{W_0} = ck_0' \quad \text{and} \quad K_0'' = \left.\frac{d^2K}{dW^2}\right|_{W_0} = \frac{c}{\tau}k_0''.$$

The source term for Maxwell's equation in a nonlinear medium is given by (Bloembergen, 1965)

$$\mu_0\frac{\partial^2}{\partial t}P_{NL},$$

where $P_{NL}$ is the nonlinear polarization ($\chi^{(2)}$ medium means that $P_{NL}$ is proportional to $E^2$; $\chi^{(3)}$ medium means that $P_{NL}$ is proportional to $|E|^2E$, etc.). In all phenomenological treatment (i.e., Sections 1 through 4), we assume the instantaneous form for the polarization, which implies physically that the pulse duration is much longer than the material relaxation time.

In the following, plane wave refers to the case where the $\nabla_T^2$ term of Maxwell's equation is neglected, finite beam size refers to the case where $\nabla_T^2$ effects are incorporated in the analysis, dispersionless refers to the case where the $k_0''$ term in Maxwell's equation is neglected, steepened pulse refers to the case where the time derivative of the envelope of the nonlinear polarization is kept (see also Chapter 6, by Suydam), and low-intensity pulse refers to the case where this steepening is negligible.

# 1. Low-Intensity Pulse in $\chi^{(3)}$ Dispersionless Medium

In this section we review the conventional self-phase modulation theory (Alfano and Shapiro, 1970) and generalize its results to the case of finite beam size. We show that the effects of diffraction can combine with those of self-phase modulation and self-focusing to exhibit many new features both in the shapes of the pulse and phase and in the spectral distribution.

## 1.1 Conventional Self-Phase Modulation Theory

The topic is covered in greater detail by Shen and Yang (Chapter 1 and Wang et al., Chapter 2), but for completeness we will quickly review it. The simplified nonlinear wave equation for the electric field envelope is given by

$$\frac{\partial A}{\partial z}+\frac{1}{v_g}\frac{\partial A}{\partial t}=i\frac{\omega}{2c}n_2|A|^2A, \tag{1}$$

where $v_g$ is the group velocity and $n_2$ is the Kerr index of refraction. In this equation we neglected group velocity dispersion, self-steepening (De Martini et al., 1967), and absorption and we assumed that $\chi^{(3)}$ is instantaneous (i.e., we neglect all effects associated with nonzero relaxation time). Denoting the amplitude and phase of the envelope $A$ by $a$ and $\alpha$, respectively, their differential equations are given by

$$\frac{\partial a}{\partial z}+\frac{1}{v_g}\frac{\partial a}{\partial t}=0, \tag{2}$$

$$\frac{\partial \alpha}{\partial z}+\frac{1}{v_g}\frac{\partial \alpha}{\partial t}=\frac{\omega}{2c}n_2a^2, \tag{3}$$

and the solutions are

$$a(\bar{u})=a_0F(\bar{u}), \tag{4}$$

$$\alpha(z,\bar{u})=\frac{\omega_0}{2c}n_2a_0^2F^2(\bar{u})z, \tag{5}$$

where $\bar{u}$ is the pulse comoving coordinate defined by

$$\bar{u}=t-z/v_g, \tag{6}$$

$a_0$ is the amplitude at $z=0$, and $F$ is the pulse shape form function. The above solution assumes that $\alpha(z=0)=0$; otherwise this initial phase should be added to the solution of Eq. (5). It should be noted that in this approximation the amplitude of the pulse is unmodified and only the phase of the pulse is affected, hence the name self-phase modulation. At this point, we refer the reader to other articles (Alfano, 1972 and Chapter 2) for the analysis of the experimental consequences of the above solutions.

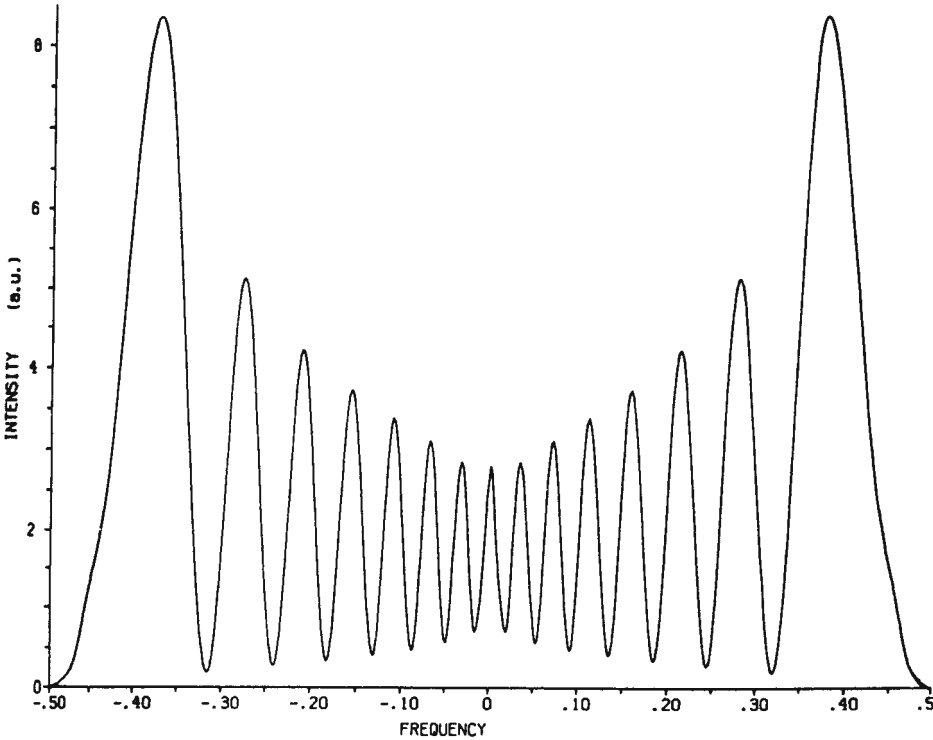


FIGURE 5.1. A typical spectral distribution predicted by the conventional self-phase modulation theory.

The spectral extent of a Gaussian pulse associated with the above supercontinuum is

$$\Delta\omega \approx \frac{\omega_0}{c}\frac{n_2 a_0^2 z}{\tau}, \tag{7}$$

where $\tau$ is the incoming pulse width. The spectral distribution is symmetric (see Fig. 5.1), and its modulation period is

$$\delta\omega \approx 4\pi/\tau. \tag{8}$$

The linear chirp coefficient for the self-phase modulated pulse in the above approximation is given for a Gaussian pulse by

$$|m| = \frac{\omega_0}{2c}\frac{n_2 a_0^2 z}{\tau^2}, \tag{9}$$

where the coefficient $m$ is related to the curvature of the phase at its extremum, that is,

$$\alpha|_{\text{extremum}} = m\bar{u}^2. \tag{10}$$

## 1.2 Grating Transform and Pulse Compression

The frequency sweep in the self-phase modulated pulse is used as the first step in the fiber-grating compressor (Tomlinson et al., 1984; Grischkowsky and Balant, 1986). In this section, we find the characteristics of the grating that optimizes the compressor for a self-phase modulated signal in the same approximations as in Section 1.1. Other details are given in Chapter 10 by Johnson and Shank. To find the grating transform of an incoming pulse we use the techniques of Fourier optics (Goodman, 1968). Essentially, in the Fourier domain, the outgoing signal is equal to the incoming signal multiplied by the optical element transfer function (Gaskill, 1978). The transfer function of a grating is described by (Treacy, 1969; Martinez et al., 1984)

$$H(\omega) = \exp[i\Phi(\omega)], \tag{11}$$

where

$$\Phi(\omega) = c(\omega - \omega_g)^2, \tag{12}$$

that is, the transfer function is a pure phase. Using the properties of the Fourier transform, the outgoing pulse can be written as the convolution of the incoming pulse with the time representation of the grating transfer function. Thus, the outgoing pulse electric field can be written as a function of the incoming pulse amplitude and phase as

$$E_{\text{out}}(\overline{U}) = \exp[iK\overline{U}]\frac{(1+i)}{(8\pi g)^{1/2}}\int_{-\infty}^{\infty} d\overline{U}'a(\overline{U}-\overline{U}')\exp[i\alpha(\overline{U}=\overline{U}')] \times \exp\left[-\frac{i\overline{U}'^2}{4g}\right]d\overline{U}', \tag{13}$$

where $K$ is the incoming pulse center frequency normalized to the pulse duration (i.e., $K = \omega\tau$) and $g = c/\tau^2$.

For an incoming Gaussian pulse that is weakly self-phase modulated, the amplitude and the phase are given by (4) and (5) but the integration in Eq. (13) with these expressions cannot be performed except numerically. However, an approximation to this integral can be obtained by approximating the phase to a Gaussian as given by Eq. (10). Under these conditions the outgoing pulse can be approximated by

$$E_{\text{out}}(\overline{U}) = \exp[iK\overline{U}]\exp\left[-\frac{i\overline{U}^2}{4g}\right]\frac{(1+i)}{(8g)^{1/2}} \times\left\{\frac{E_0}{\left[1/4+(m-1/4g)^2\right]^{1/4}}\exp\left[-\frac{\overline{U}^2}{2(4g)^2}\frac{1}{1/4+(m-1/4g)^2}\right]\right\}. \tag{14}$$

The optimum compression condition then can be directly deduced to give

$$g = m/(1+4p^2). \tag{15}$$

The amplitude scaling factor and the compression ratio under this optimization condition are respectively related to the parameter given by

$$S = (1 + 4m^2)^{1/4}. \tag{16}$$

The outgoing pulse (amplitude)$^2$ is then written as

$$|E_{\text{out}}|^2 = (SE_0)^2 \exp[-S^4 \overline{U}^2]. \tag{17}$$

The numerically derived $|E_{\text{out}}|^2$ actually deviates on the wings from Eq. (18) results, because of the deviation of the phase from the approximate parabolic shape assumed in the derivation of (17). Experimentally, these deviations were compensated for by the addition of prisms (Fork et al., 1987) that correct for cubic terms in the exact phase expression.

## 1.3 Self-Focusing and Self-Phase Modulation in a Parabolic Graded Index Medium

In this section we examine the combined effects of Kerr nonlinearity, diffraction, and graded index waveguiding on the spatial and spectral profiles of an intense pulse propagating in a parabolic graded index material with the same axis of symmetry as the pulse (Manassah et al., 1988a). The beam transverse geometric shape, radius of curvature, phase, and spectrum are computed as functions of the material parameters and pulse peak powers. Approximate analytical results are derived for the beam waist radius of curvature and phase. This calculation is motivated by two considerations:

1. Graded-index optical fibers (Thomas et al., 1982) are closely approximated by such materials.
2. The results for homogeneous bulk material in the presence of heating due to absorption of the laser beam can be closely approximated by this model for thermal positive lensing materials.

The approximations that we make in the following calculation are that

1. the graded index profile is approximated by

$$n = n_0(1 - Ar^2/2n_0);$$

2. the GRIN material boundary with other materials is at a distance larger than the beam radius (in the language of optical fibers this translates into neglecting the core-cladding boundary conditions) and the beam radius $a$ is much smaller than the core radius $r_c$;
3. effects of group velocity dispersion are neglected;
4. the self-steepening (De Martini et al., 1967) of the amplitude is neglected (i.e., the time derivative of the nonlinear polarization is neglected);
5. the quadratic index of refraction $n_2$ is not modified by the radial variation in the ordinary index of refraction;

6. one component of the electric field is kept (i.e., we are neglecting the vector nature of the electic field);
7. the graded index of refraction is of the order required to guide the beam within the material transverse dimension; and
8. the spatial changes in the physical quantities over the light wavelength are unimportant. Under these assumptions, $\varepsilon$, the envelope of the electric field, obeys the equation

$$\Delta_T^2\varepsilon - 2ik\varepsilon' - kk_2r^2\varepsilon + \frac{n_2k^2}{n_0}|\varepsilon|^2\varepsilon = 0, \tag{18}$$

where $\nabla_T^2$ is the transverse component of the Laplacian, $\varepsilon' = \partial\varepsilon/\partial z$, $k_2 = kA = 2kn_0\Delta/r_c^2$, and $\Delta$ is the relative index difference between the core center and the cladding.

If the initial condition for the incoming pulse is given by

$$\varepsilon(r,0,\bar{u}) = \varepsilon_0 \exp\left(-\frac{r^2}{a^2}\right)\exp\left(-\frac{\bar{u}^2}{2\tau^2}\right), \tag{19}$$

that is, the initial pulse is assumed to be Gaussian both in the transverse plane and in the comoving coordinate system, $\bar{u} = (z/v_g - t)$, where $v_g$ is the pulse group velocity, $a$ the initial beam radius, $\tau$ the pulse duration, and $\varepsilon_0$ the magnitude of the pulse amplitude.

In the following, the product $\varepsilon_0 \exp(-\bar{u}^2/2\tau^2)$ is denoted by $\tilde{\varepsilon}_0$. Then an approximate solution to Eq. (18) with the boundary condition given by Eq. (19), correct to order $r^2/a^2$, can be obtained through the trial solution (Marburger, 1975)

$$\varepsilon(r,z,\bar{u}) = \frac{\tilde{\varepsilon}_0}{\bar{\omega}(z,\bar{u})}\exp\left[-\frac{r^2}{a^2\bar{\omega}^2(z,\bar{u})} - \frac{ik}{2}\rho(z,\bar{u})r^2 + ik\alpha(z,\bar{u})\right], \tag{20}$$

where the different functions can be interpreted as follows: $\bar{\omega}$ is the normalized beam radius, $\rho$ is the inverse of the beam radius of curvature, and $k\alpha$ is the longitudinal phase on the material axis. This approximation of self-similarity of the beam is well justified for powers smaller than the critical power (i.e., the power at which self-focusing becomes possible), in particular for instances where $\bar{\omega}_{\max}$ and $\bar{\omega}_{\min}$ are not too far apart.

The equations satisfied by the subsidiary functions $\bar{\omega}$, $\rho$, and $\alpha$ are given by

$$\rho = \frac{1}{\bar{\omega}}\frac{\partial\bar{\omega}}{\partial z}, \tag{21}$$

$$\frac{\partial\alpha}{\partial z} = \frac{a^2}{2\bar{\omega}^2}[B - C], \tag{22}$$

$$\frac{\partial^2\bar{\omega}}{\partial z^2} + A\bar{\omega} + [2C - B]\frac{1}{\bar{\omega}^3} = 0, \tag{23}$$

where

$$A = \frac{k_2}{k} \equiv \frac{1}{L_w^2}, \tag{24}$$

$$B = \frac{4}{a^4 k^2} \equiv \frac{1}{L_d^2}, \tag{25}$$

$$C = \frac{n_2 \tilde{\varepsilon}_0^2}{n_0 a^2}, \tag{26}$$

and $L_w$ and $L_d$ are the characteristic lengths for waveguiding and diffraction, respectively.

The solutions to Eqs (21), (22), and (23) satisfying the boundary conditions $\bar{\omega} = 1$, $\rho = 0$, and $\alpha = 0$ at $z = 0$ are

1. the normalized beam radius:

$$\bar{\omega} = [\beta \cos(\gamma z) + \delta]^{1/2}; \tag{27}$$

2. the inverse of the radius of curvature:

$$\rho = -\frac{1}{2} \frac{\beta\gamma \sin(\gamma z)}{[\beta \cos(\gamma z) + \delta]}; \tag{28}$$

3. the longitudinal phase:

$$k\alpha = \frac{ka^2(B - C)}{2[B - 2C]^{1/2}} \operatorname{arctg}\left[\left(\frac{B - 2C}{A}\right)^{1/2} \operatorname{tg}(A^{1/2} z)\right] \tag{29}$$

for $B - 2C \geq 0$ and

$$k\alpha = \frac{ka^2}{4} \frac{B - C}{[2C - B]^{1/2}} \ln\left\{\frac{1 + \left(\frac{2C - B}{A}\right)^{1/2} \operatorname{tg}(A^{1/2} z)}{1 - \left(\frac{2C - B}{A}\right)^{1/2} \operatorname{tg}(A^{1/2} z)}\right\} \tag{30}$$

for $B - 2C \leq 0$, where

$$\gamma = 2A^{1/2}, \tag{31}$$

$$\beta = \frac{2C - B + A}{2A}, \tag{32}$$

$$\delta = \frac{A - 2C + B}{2A}. \tag{33}$$

For negative $n_2$ (i.e., defocusing medium), $\beta < \delta$ is satisfied for all values of $\varepsilon$ and Eq. (29) is the solution for the longitudinal phase everywhere. For positive $n_2$ (i.e., focusing medium), $\beta = \delta$ for the critical field $\varepsilon_c$, which is given by (Kelley, 1965)

$$\varepsilon_c^2 = 2n_0 / a^2 k^2 n_2 . \tag{34}$$

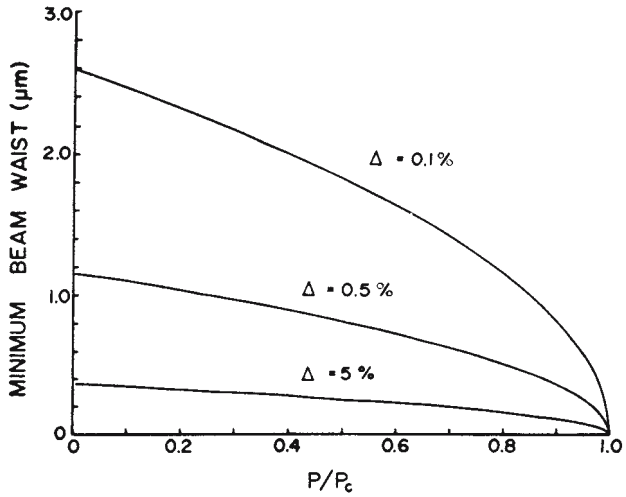


FIGURE 5.2. Minimum beam waist as a function of the normalized peak power $P/P_c$. $\Delta$ is the relative refraction index difference between the GRIN core center and the cladding. In silica fibers $P_c \approx 10^6$ W.

It should be noted that, in the low intensity limit, Eqs. (27), (28), and (29) lead to the usual results for Gaussian beams propagating in lenslike media (Kogelnik, 1965; Kogelnik and Li, 1966).

Equation (27) shows that the normalized beam radius $\bar{\omega}$ varies periodically along the optical axis length. The period of variation depends only on the waveguiding characteristic length $L_w$. The magnitude of $\bar{\omega}_{\min}$, the minimum normalized beam radius, depends on all three characteristic lengths associated with $A$, $B$, and $C$. In Figure 5.2, the minimum beam radius is plotted as a function of the pulse normalized peak power $P/P_c$ for different values of the graded index parameter $\Delta$, where $P_c$ is the critical power for self-focusing. The minimum beam radius decreases for increasing peak powers and collapses at $P = P_c$.

The inverse of the radius of curvature $\rho$ is plotted in Figure 5.3 as a function of the normalized length $2z/\pi L_w$. For increasing peak powers, the curvature is clearly enhanced periodically by self-focusing at the beam waist (i.e., minimum beam diameter) locations.

The total phase of the electric field can be computed using Eqs. (20), (28), and (29). This phase, and consequently the spectral broadening arising from self-phase modulation, is radially dependent. It is worth noting that the time-dependent part of the phase $\phi'$, denoted $\phi'_t$, which is equal to total phase – $\omega_0 t$, reduces to that of the conventional SPM theory in the case of a homogeneous medium ($k_2 = 0$) and for an incoming plane wave ($a \Rightarrow \infty$). Furthermore, for weak waveguiding ($k_2 \Rightarrow 0$), but finite initial beam diameter, the time-dependent phase $\phi'_t$ reduces to

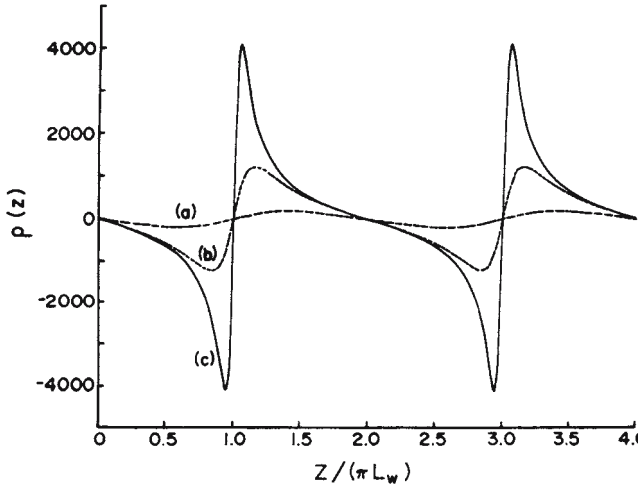


FIGURE 5.3. Inverse of radius of curvature as a function of normalized length $2z/\pi L_w$ for a graded-index fiber. ($a = 1.5\,\mu$m, $\Delta = 0.48\%$, and $L_w = 15.3\,\mu$m). (a) $P/P_c = 0.1$; (b) $P/P_c = 0.9$; (c) $P/P_c = 0.99$.

$$\lim_{k_2 \Rightarrow 0} \phi_t' = \phi_{\text{SPM}}\left(1 - \frac{2r^2}{a^2}\right), \tag{35}$$

Thus, in this limit the spectral extent as a function of the radius varies as $(1 - 2r^2/a^2)$. This approximation is valid for $r/a \ll 1$ and reflects the $|\varepsilon|^2$ change.

In Figure 5.4 the longitudinal phase contribution $k\alpha(z, \bar{u} = 0)$, denoted the $\alpha$-phase, is plotted as a function of the normalized material length for different power levels. As shown, the $\alpha$-phase mostly increases by steps at $z$ locations corresponding to the periodic positions of the minimum beam waist. As a result, the total amount of the longitudinal phase yielded by the pulse is often much larger than the usual SPM, and it depends strongly on the waveguiding, diffraction, and nonlinear parameters. It is worth noting that for $z \ll L_w$ the regularized $\alpha$-phase, defined as the value of the $\alpha$-phase at a certain power minus its value for zero intensity, has the same sign as $\phi_{\text{SPM}}$; however, this sign changes for $z > L_w$. Physically, this result leads to the reverse of the red leading the blue in the supercontinuum and may have important consequences for soliton propagation in graded-index fibers and for pulse compression. Finally, one notices that the $\alpha$-phase approaches a ladder function for values of $\varepsilon$ that equalize $B$ and $2C$ (i.e., $P \Rightarrow P_c$).

The temporal distribution of the longitudinal phase, the $\alpha$-phase, can be studied using Eq. (29). If we define the parameter $p$ by

$$C = \frac{p}{2} B \exp\left(\frac{-\bar{u}^2}{\tau^2}\right), \tag{36}$$

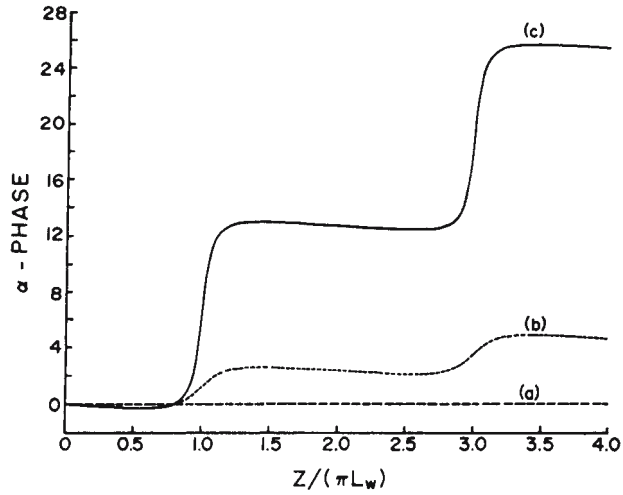


FIGURE 5.4. Longitudinal $\alpha$-phase as a function of the material normalized length $2z/\pi L_w$ for a grade-index fiber. (a) $P/P_c = 0.1$; (b) $P/P_c = 0.9$; (c) $P/P_c = 0.99$.

where $p = 1$ corresponds to $P = P_c$, then

$$\frac{(\alpha - phase)_{reg.}}{\phi_{\rm SPM}(\bar{u}=0)} \approx \left(\frac{A}{B}\right)^{1/2} \frac{2}{p} \frac{\left[\left(1 - p\exp(-\bar{u}^2/\tau^2)\right)^{1/2} + (p/2)\exp(-\bar{u}^2/\tau^2) - 1\right]}{\left(1 - p\exp(-\bar{u}^2/\tau^2)\right)^{1/2}}. \tag{37}$$

It is worth noting that for small $p$, Eq. (37) can be approximated by

$$\lim_{p\ll 1} \frac{(\alpha - \text{phase})_{\text{reg.}}}{\phi_{\rm SPM}(\bar{u}=0)} \approx -\frac{P}{4}\left(\frac{A}{B}\right)^{1/2} \exp\left(-\frac{2\bar{u}^2}{\tau^2}\right). \tag{38}$$

In Figure 5.5 the $\alpha$-phase, normalized to its maximum value, is plotted as a function of time for different power levels. For small peak powers the width of the phase envelope is $\sqrt{2}$ smaller than the conventional SPM phase, as shown by Eq. (38). As the pulse peak power increases and tends to the critical power, the phase width significantly decreases, and the value of the phase at its maximum increases dramatically.

The spectral distribution of a pulse propagating in this medium can be obtained by taking the Fourier transform of the electric field and then taking its magnitude squared. It should be noted that all time dependence as given by Eq. (20) should be incorporated in the numerical calculation. Special care should be exercised at the beam waist, where $\bar{\omega}$ as a function of time features the same narrowing characteristics observed above for the longitudinal phase. At locations other than the waists, most of the pulse energy is not modulated. For small peak powers ($P \ll P_c$) the SPM spectra generated in parabolic GRIN material are similar to the conventional SPM broadened spectra,

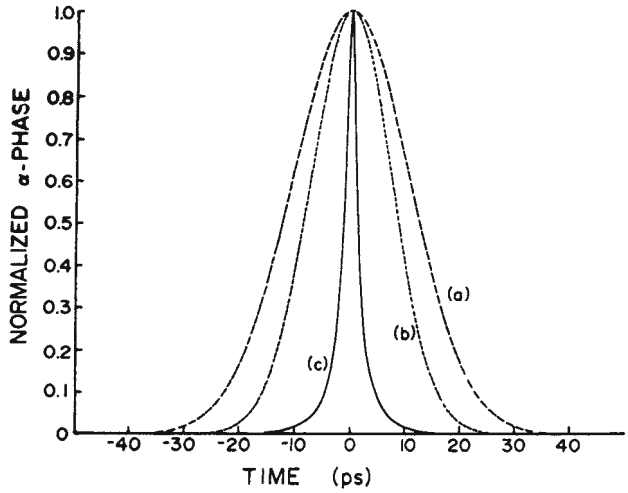


FIGURE 5.5. The $\alpha$-phase normalized to its maximum value plotted versus time for a graded-index fiber. (a) Conventional SPM phase for $P/P_c = 0.1$; (b) $P/P_c = 0.1$; (c) $P/P_c = 0.992$. Maximum values of the phase are, respectively, 0.92, 0.55, and 1880 radians. ($a = 25\,\mu$m, $\Delta = 0.48\%$, $z = 10$ cm, and $\tau = 15$ ps.)

as observed in Figure 5.6a. On the other hand, for peak powers near the critical power for self-focusing ($P \approx P_c$) new SPM features appear, see Figure 5.6b. There is an intense peak at the laser wavelength over a much weaker background of white light. This effect is due to the narrowing of the $\alpha$-phase and the limited modulation over the pulse duration.

In conclusion, the combined effects of self-focusing, diffraction, and waveguiding lead to novel features in both the time and frequency domains of the electric field of a pulse. Novel features in the SPM spectra, distinct from conventional SPM theory, appear.

## 1.4 Self-Focusing, Self-Phase Modulation, and Diffraction in Bulk Homogeneous Material

In this section we specialize the results of the previous section to $k_2 \Rightarrow 0$ (i.e., homogeneous bulk material) (Manassah et al., 1988b), We explore the simultaneous effects of self-focusing, self-phase modulation, and diffraction on the propagation of an ultrafast pulse in a homogeneous Kerr medium. The competing effects of self-focusing and diffraction are shown to modify the shape and magnitude of the pulse amplitude and phase. These modifications are shown to affect the spectral distribution of the supercontinuum compared to that predicted by conventional self-phase modulation theory.

In the case of a homogeneous medium ($A \Rightarrow 0$), the results of Section 1.3 can be written as

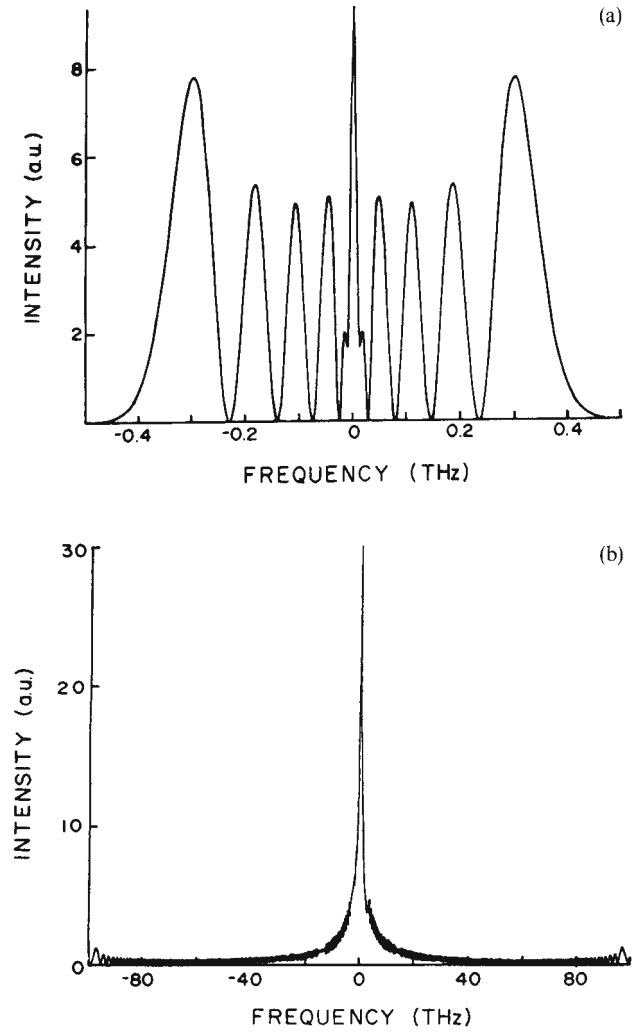


FIGURE 5.6. Spectral broadening of a Gaussian pulse ($\tau = 15\,\text{ps}$) outgoing from a graded-index fiber ($a = 25\,\mu\text{m}$, $\Delta = 0.48\%$). (a) $P/P_c = 0.1$ and $z = 0.5\,\text{m}$; (b) $P/P_c = 0.997$ and $z = 0.1\,\text{m}$.

$$\bar{\omega} = \left[1 + y^2(1 - p')\right]^{1/2}, \tag{39}$$

$$L_d\rho = \frac{y(1-p')}{\left[1 + y^2(1-p')\right]}, \tag{40}$$

$$k\alpha = \frac{\left[1 - \frac{1}{2}p'\right]}{\left[1 - p'\right]^{1/2}} \operatorname{arctg}\left[(1-p')^{1/2} y\right] \tag{41}$$

for $p' < 1$, and

$$k\alpha = \frac{\left[1 - \frac{1}{2}p'\right]}{\left[p' - 1\right]^{1/2}} \ln\left\{\frac{1 + y(p'-1)^{1/2}}{1 - y(p'-1)^{1/2}}\right\} \tag{42}$$

for $p' < 1$, where

$$p' = p \exp(-\bar{u}^2/\tau^2), \tag{43}$$

$p = \varepsilon_0^2/\varepsilon_c^2$, $\varepsilon_c$ is the critical field for self-focusing, and $y$ is the material length in units of the Rayleigh diffraction length $L_d$, that is,

$$y = z/L_d\,. \tag{44}$$

In the above notation, the normalized self-focusing distance (Kelley, 1965) is

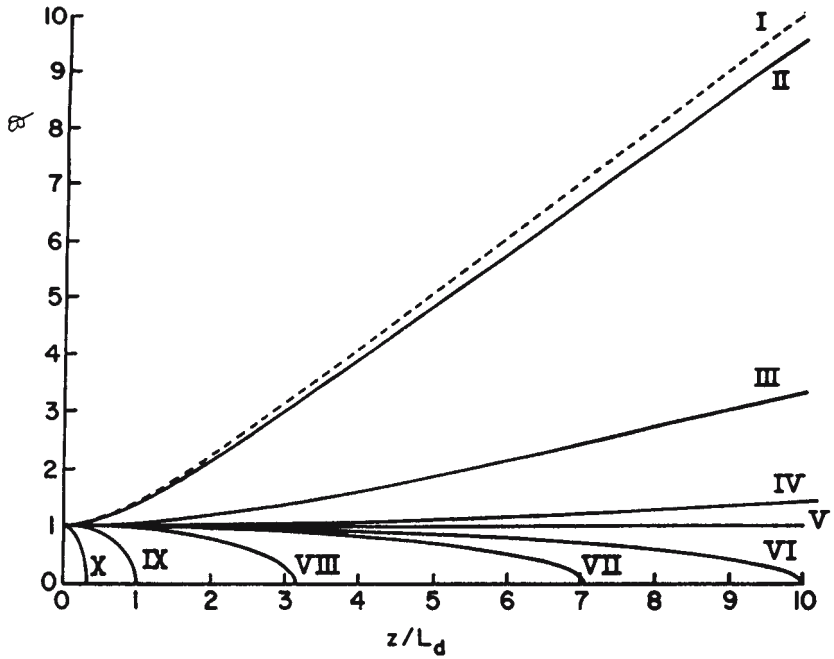


FIGURE 5.7. Normalized beam radius for a pulse propagating in a homogeneous medium at $u = 0$ as a function of the normalized length ($z/L_d$). (I) $p \ll 1$; (II) $p = 0.1$; (III) $p = 0.9$; (IV) $p = 0.99$; (V) $p = 1$; (VI) $p = 1.01$; (VII) $p = 1.02$; (VIII) $p = 1.1$; (IX) $p = 2$; (X) $p = 10$.

$$y_{\text{foc}} = 1/(p-1)^{1/2}. \tag{45}$$

In the following, the analysis is limited to $y < y_{\text{foc}}$, where the above solutions are valid.

It should be noted that the solutions of $\bar{\omega}$, $\rho$, and $\alpha$ in the linear regime ($\varepsilon_0 \Rightarrow 0$) reduce to the standard formulas of a Gaussian pulse propagating in a homogeneous medium (Tien et al., 1965), specifically:

$$\bar{\omega} = (1+y^2)^{1/2}, \tag{46}$$

$$\rho L_d = y/(1+y^2), \tag{47}$$

$$k\alpha = \text{arctg}(y) \equiv \eta(z). \tag{48}$$

In Figure 5.7 the normalized beam radius is plotted for $\bar{u} = 0$ as a function of the normalized length ($z/L_d$) and for different electric field intensities [$p = \varepsilon_0^2/\varepsilon_c^2$]. For weak fields ($p < 1$) diffraction is the dominant effect, while for the most intense fields ($p > 1$) the nonlinearity is dominant, there is self-focusing, and $\bar{\omega}$ approaches zero as the length approaches the self-focusing distance.

In Figure 5.8 the normalized inverse radius of curvature ($L_d/R = \rho L_d$) is plotted for $\bar{u} = 0$ as a function of the normalized length. For $p < 1$, this quan-

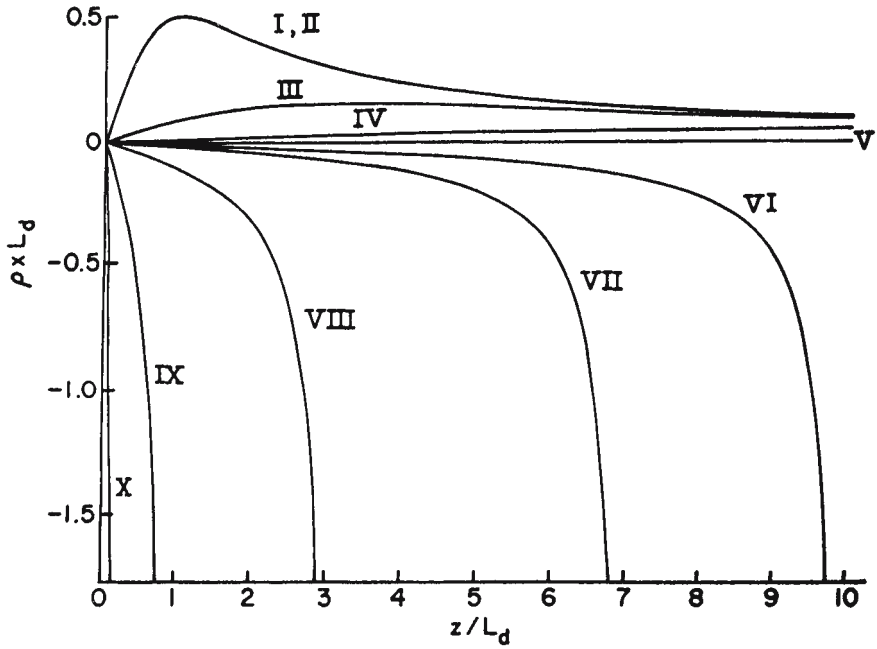


FIGURE 5.8. Normalized inverse radius of curvature ($\rho L_d$) for a pulse propagating in a homogeneous medium at $u = 0$ as a function of the normalized length ($z/L_d$). (I) $p \ll 1$; (II) $p = 0.1$; (III) $p = 0.9$; (IV) $p = 0.99$; (V) $p = 1$; (VI) $p = 1.01$; (VII) $p = 1.02$; (VIII) $p = 1.1$; (IX) $p = 2$; (X) $p = 10$.

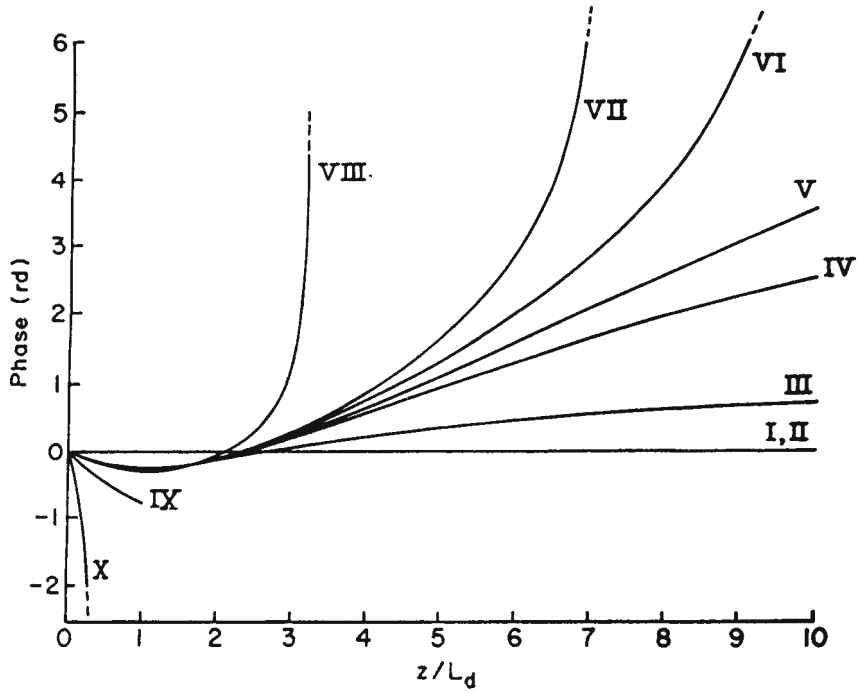


FIGURE 5.9. Regularized longitudinal phase for a pulse propagating in a homogeneous medium at $u = 0$ as a function of the normalized length ($z/L_d$). (I) $p \ll 1$; (II) $p = 0.1$; (III) $p = 0.9$; (IV) $p = 0.99$; (V) $p = 1$; (VI) $p = 1.01$; (VII) $p = 1.02$; (VIII) $p = 1.1$; (IX) $p = 2$; (X) $p = 10$.

tity is positive, has a maximum for $y = 1/(1-p)^{1/2}$, and goes to zero for very large distances; that is, diffraction is the dominant effect. For $p > 1$, this quantity is negative, monotonically decreasing, and approaches $-\infty$ at the self-focusing distance.

In Figure 5.9 the regularized longitudinal phase (i.e., its value for a specific $p$ minus its value for $p = 0$) is plotted for $\bar{u} = 0$ as a function of the normalized length. For $0 < p < 2$ the longitudinal phase changes sign in the total length interval; when positive it is the reverse sign of that predicted by the conventional self-phase modulation theory. For $1 < p < 2$ this phase has a positive asymptote for the sample length equal to the self-focusing distance. For $p > 2$ this phase is everywhere negative, admits the conventional self-phase modulation curve as a tangent at the origin, but decreases much faster than the SPM result as the length increases until it reaches a negative asymptote at the self-focusing distance.

In Figure 5.10a the electric field intensity ($\varepsilon_0^2/\bar{\omega}^2$) is plotted for $p \approx 1$ as a function of the normalized time ($\bar{u}/\tau$) for different normalized lengths of the sample; as can be observed, the pulse compresses with increasing length.

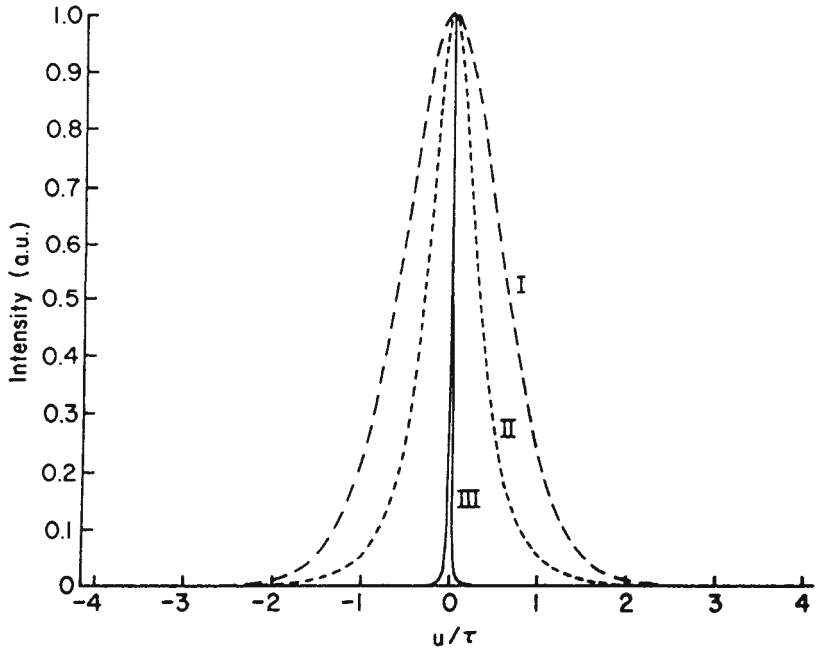


(a)

FIGURE 5.10. (a) Normalized intensity of the pulse as a function of time for $p = 0.9999$. Homogeneous material. (I) $z/L_d = 1$; (II) $z/L_d = 3$; (III) $z/L_d = 100$. (b) Regularized longitudinal phase as a function of time for $p = 0.9999$. Homogeneous material. (I) $z/L_d = 1$; (II) $z/L_d = 3$; (III) $z/L_d = 100$. [The values of the phase peaks are, respectively, 0.285, 0.25, and 46.87. The corresponding phases for SPM theory are, respectively, −0.5, −1.5, and −50.] (c) Spectral distribution intensity as a function of the normalized frequency difference. $p = 0.9999$ and $z/L_d = 100$.

Physically it should be noted that for very large distances the dispersion effects will impose a limit on the value of this compression. In Figure 5.10b the regularized longitudinal phase is plotted for $p < 1$ as function of the normalized time for different normalized lengths of the sample. As can be observed, for small length the phase has the same sign as in conventional SPM theory, for intermediate length the phase changes sign in its width interval, and for large length the phase is always positive, leading to the reverse of the red leading the blue in the supercontinuum. In Figure 5.10c the spectral distribution for $p \cong 1$ and large $z$ is plotted; it should be noted that a central peak appears in the spectrum.

In Figure 5.11 the electric field intensity, phase, and spectral distribution are plotted as a function of $\bar{u}$ for length close to the self-focusing distance. Both the field intensity and the phase narrow, albeit at different rates. The magnitudes of the maxima of both intensity and phase increase dramatically

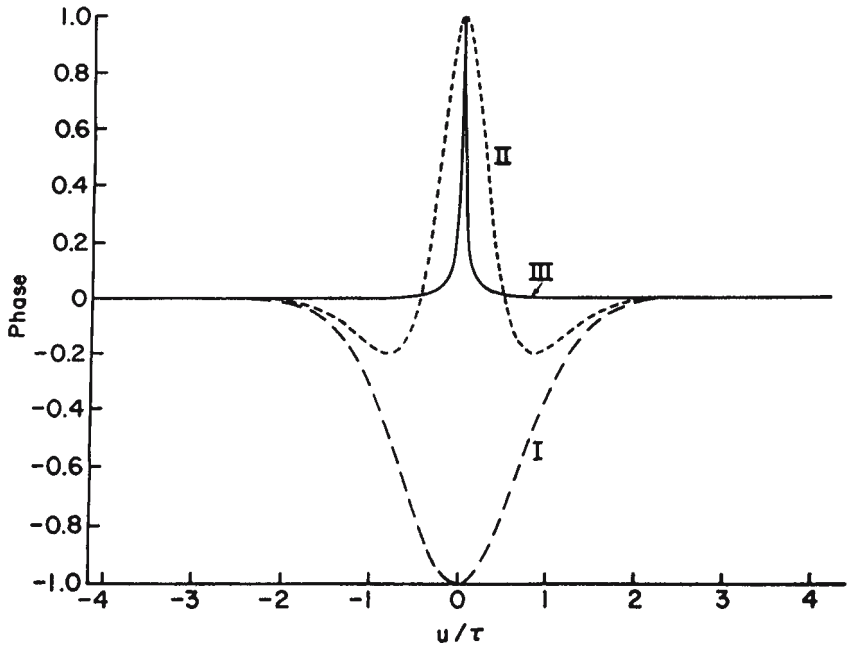


(b)

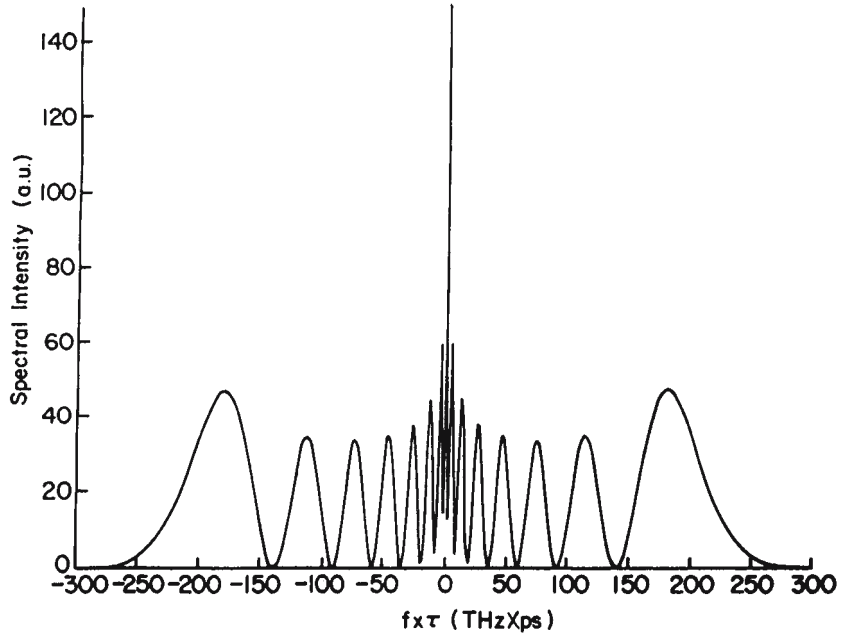


(c)

FIGURE 5.10. (*continued*)

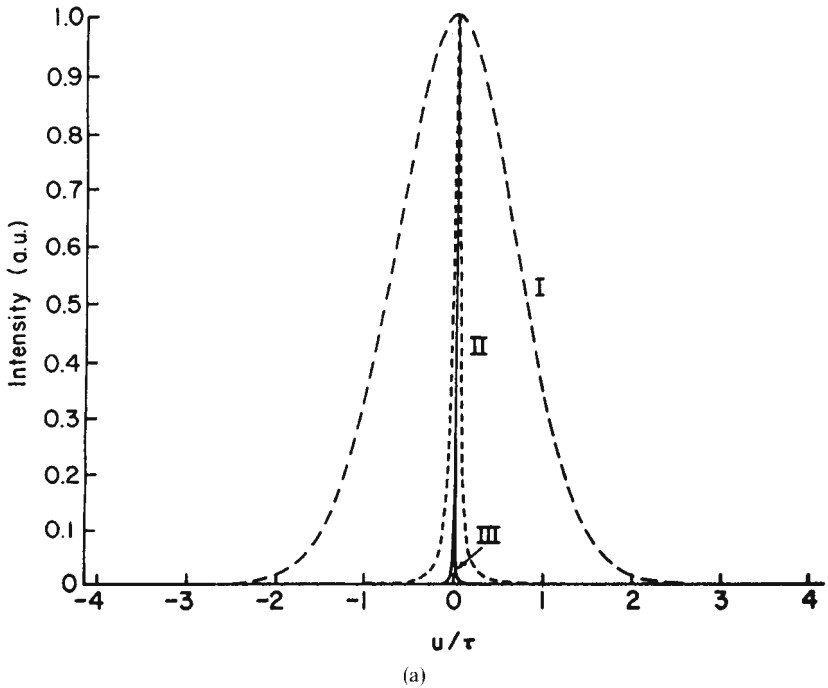


FIGURE 5.11. (a) Normalized intensity ($\varepsilon^2/\bar{\omega}^2$) of the pulse as a function of time. $p$ = 10. (I) $z/L_d = 0$; (II) $z/L_d = 0.333$; (III) $z/L_d = 0.3333$. [The focusing distance for this case corresponds to 1/3.] (b) Regularized longitudinal phase as a function of time. $p$ = 10. (I) $z/L_d = 0$; (II) $z/L_d = 0.333$; (III) $z/L_d = 0.3333$. [The values of the phase peaks are, respectively, 0.51, −5.4, and −8.4. The corresponding phases for SPM theory are, respectively, −0.5, −1.67, and −1.67.] (c) Spectral distribution intensity as a function of the normalized frequency difference. $p$ = 10. (I) $z/L_d = 0.333$; (II) $z/L_d = 0.3333$. [$z/L_d = 1/3$ is the self-focusing length for $p$ = 10.]

from those of conventional SPM theory because of the strong self-focusing effect. If the electric field can still be supported by the medium (i.e., no breakdown occurs), Figure 5.11c shows the dramatic change in the spectral extent over an infinitesimal change in the sample length.

## 1.5 Thermal Focusing Effects on the Supercontinuum

It has long been recognized (Gordon et al., 1965) that the propagation of a laser beam in a material produces local heating in its vicinity and that the temperature gradient in the material induces a transverse gradient of the refractive index, which leads to a lensing effect. In Section 1.3 we showed that the phase shape and spectral distribution of a pulse propagating in a parabolic graded-index material differ significantly from the conventional self-

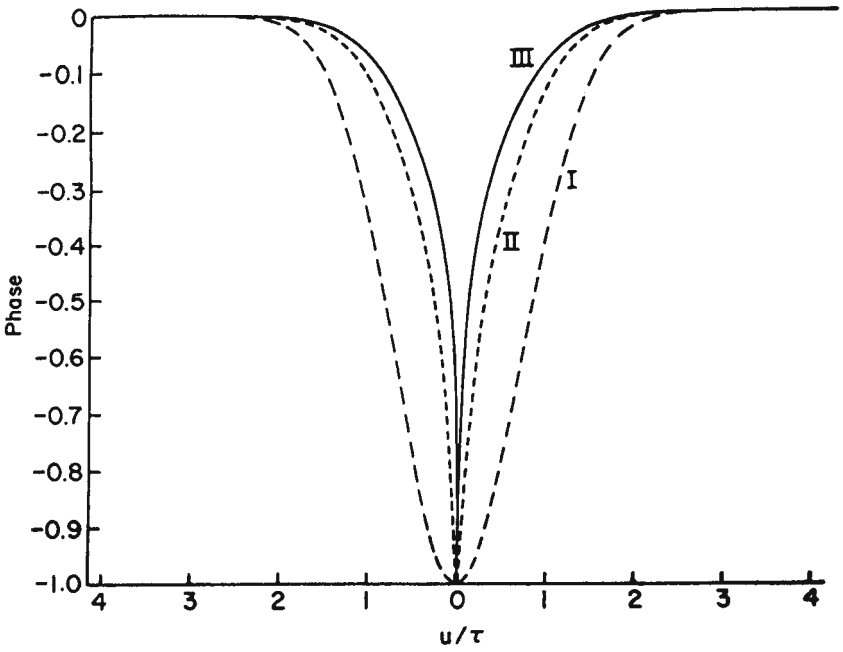


(b)

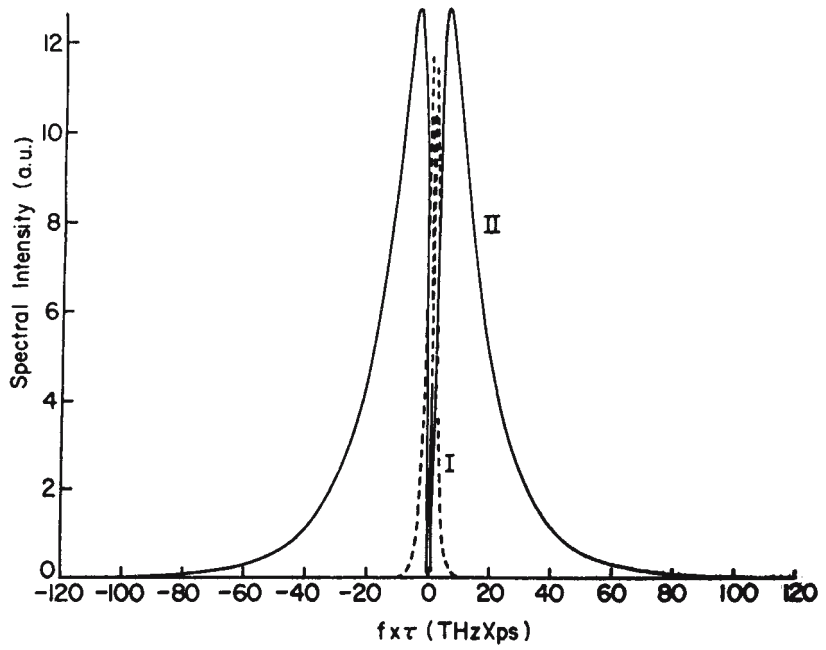


(c)

FIGURE 5.11. (*continued*)

phase modulation results of Section 1.1. The temperature gradient can, in the case of supercontinuum generation with high repetition rate, thus produce significant variations in the spectral extent and shape. Properly controlled (e.g., by using a CW heating beam), it is also possible to use this effect in optical fibers, lead glass, and certain semiconductors where $dn/dT > 0$ (Dabby and Whinnery, 1968) to control the sign of the pulse phase so as to reverse the red leading the blue in the supercontinuum and possibly to compress pulses within $\chi^{(3)}$ materials without the need for external gratings or prisms (Manassah et al., 1988c). In this section we review the effects of heating on the index of refraction profile and show how a homogeneous bulk material transforms in the vicinity of the heating beam into a graded-index material.

The following derivation is due to Gordon et al. (1965). If the field of the heating laser beam is given by

$$E(r) = E_0 \exp(-r^2/r_H^2), \tag{49}$$

the heat generated per unit length is proportional to the square of this field. The Green's function for the heat diffusion equation is given by

$$G(r,r',t) = \frac{1}{4\pi\kappa t} \exp\left[-\frac{(r^2 + r'^2)}{4Dt}\right] I_0\left[\frac{rr'}{2Dt}\right], \tag{50}$$

where

$$D = \kappa/\rho C_p\,, \tag{51}$$

$\kappa$ is the thermal conductivity (cal/cm·s·K), $\rho$ is the density (g/cm$^3$), and $C_p$ is the specific heat (cal/g·K). The temperature distribution for the distributed source is

$$\Delta T(r,t) = \int_0^\infty \int_0^t 2\pi r' Q(r') G(r,r',t') dr' dt', \tag{52}$$

where $Q(r)$ is the heat generated per unit length. The solution for $\Delta T$ is given as function of the exponential integrals:

$$\Delta T(r,t) = \frac{A r_H^2}{8\kappa} \left\{ Ei\left(\frac{-2r^2}{r_H^2}\right) - Ei\left(\frac{-2r^2}{8Dt + r_H^2}\right)\right\}, \tag{53}$$

where $A$ can be related to the heating beam total power and the material rate of dissipation through

$$A r_H^2 = 0.48 bP/\pi\,, \tag{54}$$

where $b$ is the fractional dissipation per centimeter.

For a temperature rise $\Delta T$, the corresponding index of refraction is

$$n(r,t) = n_0 + \left(\frac{dn}{dT}\right) \Delta T(r,t) \tag{55}$$

where $dn/dT$ measures the change in the material index of refraction for a change in its temperature. For small $r$, combining Eqs. (53) and (55), due to the temperature gradient, the index of refraction in the material is given by

$$n = n_0\left[1 + \frac{\delta'}{r_H^2} r^2\right], \tag{56}$$

where

$$\delta' = -\frac{0.12Pb}{n_0 \kappa \pi}\left(\frac{dn}{dT}\right)\frac{8Dt}{r_H^2 + 8Dt}; \tag{57}$$

that is, the problem reduces to a case similar to that treated in Section 1.3. The conclusions are as follows for $dn/dT$ positive:

1. The normalized beam diameter is a periodic function in $z$. The wavelength of this periodicity is proportional to $|\delta'|^{-1/2}$. In Figure 5.12, $\bar{\omega}$ is plotted for selected values of $|\delta'|$.
2. The longitudinal phase, for $u = 0$, as function of $z$ mostly increases by steps at $z$ locations corresponding to the periodic positions of the minimum

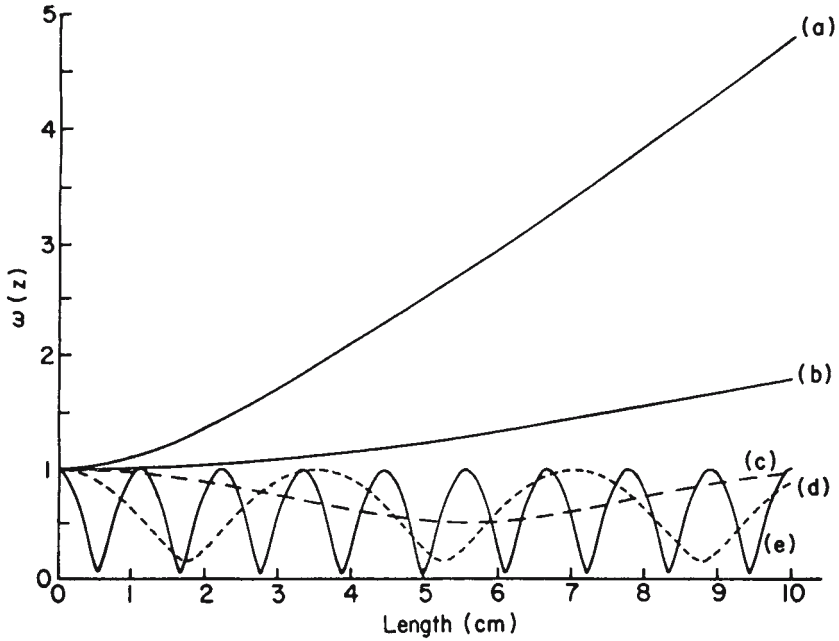


FIGURE 5.12. Normalized probe beam diameter as a function of the material thickness in the presence of thermal focusing. (a) $p = 0$, $|\delta'| = 0$; (b) $p = 0.9$, $|\delta'| = 0$; (c) $p = 0.9$, $|\delta'| = 2.5 \times 10^{-3}$; (d) $p = 0.9$, $|\delta'| = 7.8 \times 10^{-3}$; (e) $p = 0.9$, $|\delta'| = 2.5 \times 10^{-2}$.

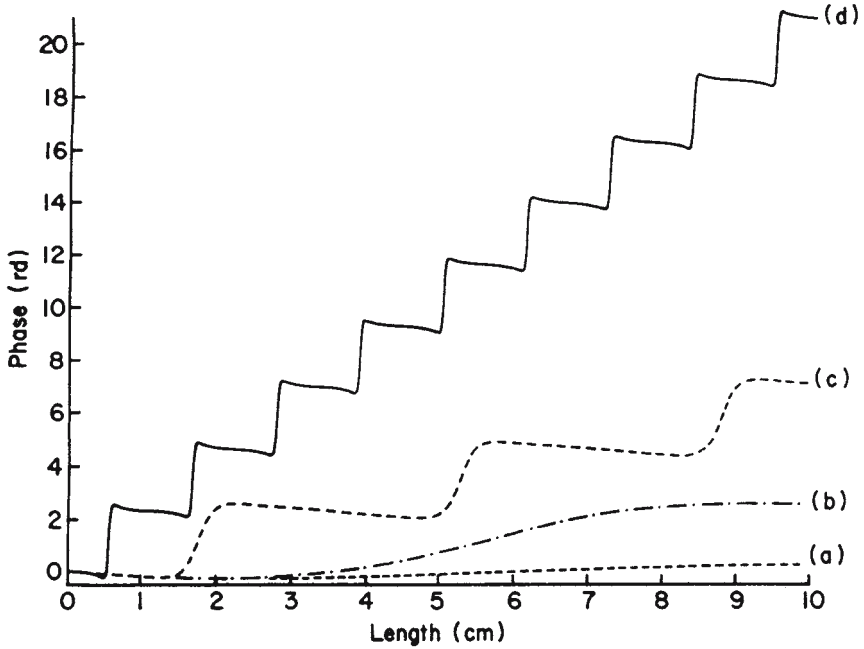


FIGURE 5.13. Longitudinal probe phase at $\bar{u} = 0$ as a function of the material thickness in the presence of thermal focusing. $p = 0.9$. (a) $|\delta'| = 0$; (b) $|\delta'| = 2.5 \times 10^{-3}$; (c) $|\delta'| = 7.8 \times 10^{-3}$; (d) $|\delta'| = 2.5 \times 10^{-2}$.

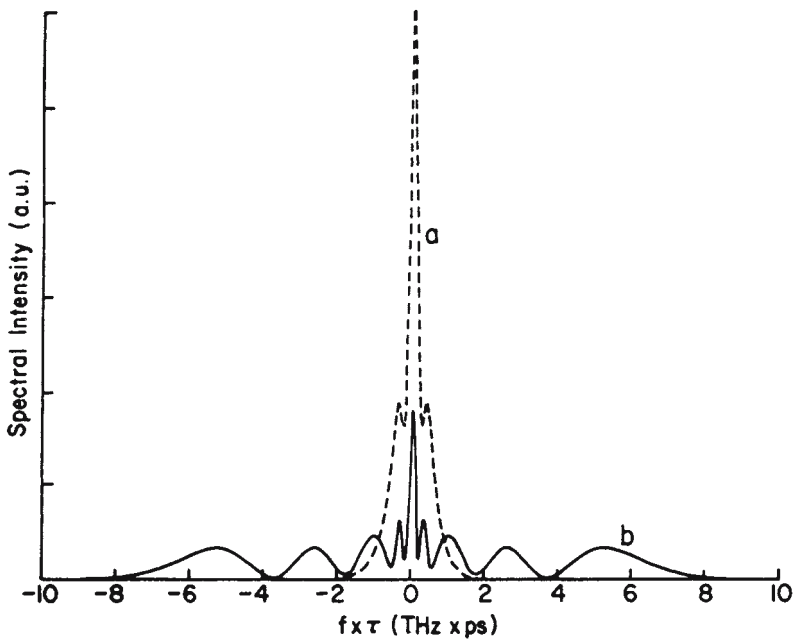


FIGURE 5.14. Probe spectral distribution in the presence of thermal focusing for $r = 0$, $z = 10\,\text{cm}$, and $p = 0.9$. (a) $|\delta'| = 2.5 \times 10^{-3}$; (b) $|\delta'| = 2.5 \times 10^{-2}$.

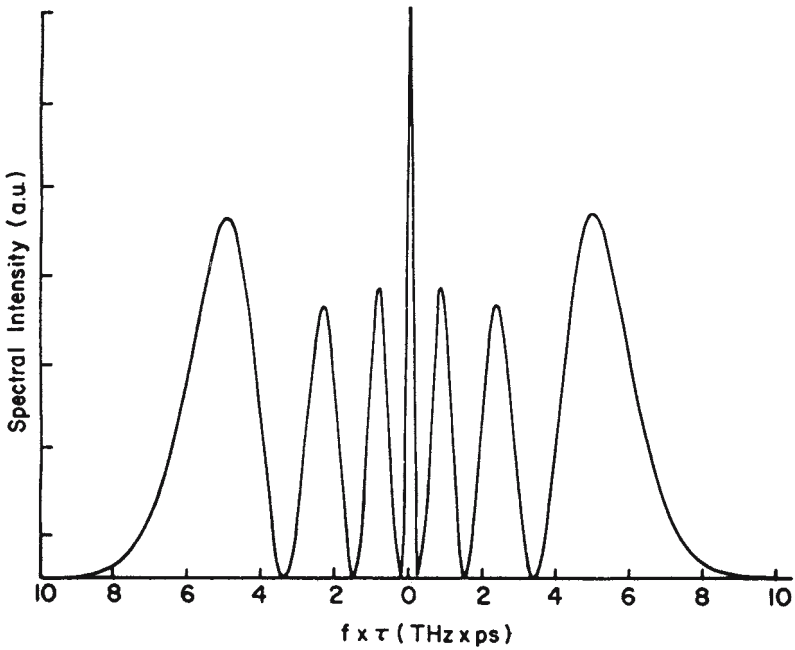


FIGURE 5.15. Probe spectral distribution in the presence of thermal focusing for $r = 0$, $z = 9.44\,\text{cm}$, $p = 0.9$, and $|\delta'| = 2.5 \times 10^{-2}$.

beam diameter. As a result, this phase is not linear in $z$ like the conventional self-phase modulation theory phase. Furthermore, its magnitude can be much larger. In Figure 5.13 this phase is plotted for different values of the $\delta'$ parameter.

3. The time-dependent portion of the longitudinal phase may have the reverse sign to that of conventional SPM. Physically, this result leads to the reverse of the red leading the blue in the supercontinuum. Furthermore, as the pulse peak magnitude increases and tends to the critical field of the nonlinear medium, the phase which decreases significantly. Therefore, for $\bar{\omega}$ close to its maximum, only a short period over the pulse duration is modulated; this portion increases as $\bar{\omega}$ approaches its minimum.

In Figure 5.14 the spectral intensity is plotted for the same length $z$ but for different $\delta'$ parameters. For larger $\delta'$ the spectral extent is larger.

In Figure 5.15 the spectral intensity is plotted for the $\delta'$ of the curve in Figure 5.14b, but for a slightly different sample length. As can be observed, the spectral extent does not change significantly with a small variation in $z$; however, the spectral shape can be altered dramatically. Actually, the two lengths chosen correspond to successive maximum and minimum positions of the normalized beam diameter.

## 2. Pulse Steepening in a $\chi^{(3)}$ Dispersionless Medium: Plane-Wave Approximation

### 2.1 Nonlinear Wave Equation

Maxwell's equation, in a $\chi^{(3)}$ nonlinear medium where the dispersion of the linear index of refraction and its imaginary part are neglected, is given by

$$\nabla^2\mathbf{E} - \frac{n^2}{c^2}\frac{\partial^2\mathbf{E}}{\partial t^2} = \frac{2nn_2}{c^2}\frac{\partial^2}{\partial t^2}\langle\mathbf{E}\cdot\mathbf{E}\rangle\mathbf{E}, \tag{58}$$

where $n$ is the linear index of refraction and $n_2$ is the nonlinear index of refraction. In the instance that the transverse variation of $\mathbf{E}$ is neglected (i.e., diffraction is neglected), one component of $\mathbf{E}$ is present and $<\mathbf{E}\cdot\mathbf{E}> = |E|^2/2$, the wave equation reduces to

$$\frac{\partial^2 E}{\partial z^2} - \frac{1}{v_g^2}\frac{\partial^2 E}{\partial t^2} = \frac{nn_2}{c^2}\frac{\partial^2}{\partial t^2}|E|^2 E, \tag{59}$$

where $v_g$ is the group velocity in the medium, assumed constant over the light bandwidth. To reduce the differential equation to a dimensionless form, we introduce the new dimensionless variables $\Phi$, $T$, and $Z$ defined as

$$T = t/\tau, \quad Z = z/v_g\tau, \quad E = E_0\Phi, \tag{60}$$

where $\tau$ is the pulse width and $E_0$ is the maximum amplitude of the electric field at the entrance plane of the $\chi^{(3)}$ medium. Introducing the nonlinear coupling constant $\varepsilon$, defined as

$$\varepsilon \equiv n_2|E_0|^2/n, \tag{61}$$

the wave equation in dimensionless form reduces to

$$\left(\frac{\partial^2}{\partial Z^2} - \frac{\partial^2}{\partial T^2}\right)\Phi = \varepsilon\frac{\partial^2}{\partial T^2}|\Phi|^2\Phi. \tag{62}$$

Typical values for the above parameters are

$$\tau \sim 10^{-14} \text{ to } 10^{-12}\text{s},$$
$$n_2 \sim 10^{-22} \text{ to } 10^{-18}\text{MKS},$$
$$v_g \sim 2\times10^8\ \text{m/s}.$$

### 2.2 Method of Multiple Scales

The functional dependence of $\Phi$ on $Z$, $T$, and $\varepsilon$ in the solution of (62) is not disjoint (Nayfeh, 1981). To first order in $\varepsilon$, $\Phi$ depends on the combinations $\varepsilon T$ and $\varepsilon Z$ as well as on the individual $T$, $Z$, and $\varepsilon$. Carrying the perturbation to higher orders, $\Phi$ additionally depends on $\varepsilon^2 T$, $\varepsilon^2 Z$, $\varepsilon^3 T$, $\varepsilon^3 Z$, .... Hence it is convenient to write $\Phi$ as

$$\Phi(Z,T;\varepsilon)=\Phi(Z_0,T_0,Z_1,T_1,Z_2,T_2,\ldots;\varepsilon), \tag{63}$$

where the new scaled variables $Z_1$, $T_1$, $Z_2$, $T_2$, etc., are defined as

$$T_0=T, \qquad T_1=\varepsilon T,\ldots,T_n=\varepsilon^n T, \tag{64}$$

$$Z_0=Z, \qquad Z_1=\varepsilon Z,\ldots,Z_n=\varepsilon^n Z. \tag{65}$$

The $T_n$'s and $Z_n$'s represent different time and distance scales. $\Phi$ is then determined as a function of the old and new variables. Next, we seek a uniform expansion solution to $\Phi$ in the form

$$\begin{aligned}\Phi=&\Phi_0(T_0,Z_0,T_1,Z_1,T_2,Z_2,\ldots)\\&+\varepsilon\Phi_1(T_0,Z_0,T_1,Z_1,T_2,Z_2,\ldots)\\&+\varepsilon^2\Phi_2(T_0,Z_0,T_1,Z_1,T_2,Z_2,\ldots)+\ldots.\end{aligned} \tag{66}$$

To express the derivatives in (62) as functions of the new variables, we use the chain rules for derivatives; then

$$\begin{aligned}\frac{\partial}{\partial T}&=\frac{\partial}{\partial T_0}+\varepsilon\frac{\partial}{\partial T_1}+\varepsilon^2\frac{\partial}{\partial T_2}+\ldots,\\ \frac{\partial}{\partial Z}&=\frac{\partial}{\partial Z_0}+\varepsilon\frac{\partial}{\partial Z_1}+\varepsilon^2\frac{\partial}{\partial Z_2}+\ldots,\\ \frac{\partial^2}{\partial T^2}&=\frac{\partial^2}{\partial T_0^2}+2\varepsilon\frac{\partial^2}{\partial T_0\partial T_1}+\varepsilon^2\left(2\frac{\partial^2}{\partial T_0\partial T_2}+\frac{\partial^2}{\partial T_1^2}\right)+\ldots,\\ \frac{\partial^2}{\partial Z^2}&=\frac{\partial^2}{\partial Z_0^2}+\varepsilon\frac{\partial^2}{\partial Z_0\partial Z_1}+\varepsilon^2\left(2\frac{\partial^2}{\partial Z_0\partial Z_2}+\frac{\partial^2}{\partial Z_1^2}\right)+\ldots.\end{aligned} \tag{67}$$

Using expressions (66) and (67) in the partial differential equation (62) and equating the respective coefficients of $\varepsilon^n$, one obtains, respectively, for the terms multiplying $\varepsilon^0$, $\varepsilon$, and $\varepsilon^2$ the following equations:

$$\left(\frac{\partial^2}{\partial Z_0^2}-\frac{\partial^2}{\partial T_0^2}\right)\Phi_0=0, \tag{68}$$

$$\left(\frac{\partial^2}{\partial Z_0^2}-\frac{\partial^2}{\partial T_0^2}\right)\Phi_0+2\left(\frac{\partial^2}{\partial Z_1\partial Z_0}-\frac{\partial^2}{\partial T_1\partial T_0}\right)\Phi_0=\frac{\partial^2}{\partial T_0^2}|\Phi_0|^2\Phi_0, \tag{69}$$

and

$$\begin{aligned}&\left(\frac{\partial^2}{\partial Z_0^2}-\frac{\partial^2}{\partial T_0^2}\right)\Phi_2+2\left(\frac{\partial^2}{\partial Z_1\partial Z_0}-\frac{\partial^2}{\partial T_1\partial T_0}\right)\Phi_1\\&\quad+\left(\frac{\partial^2}{\partial Z_1^2}-\frac{\partial^2}{\partial T_1^2}+2\frac{\partial^2}{\partial Z_0\partial Z_2}-2\frac{\partial^2}{\partial T_0\partial T_2}\right)\Phi_0\\&\quad=2\frac{\partial^2}{\partial T_0\partial T_1}|\Phi_0|^2\Phi_0+2\frac{\partial^2}{\partial T_0^2}|\Phi_0|^2\Phi_1+\frac{\partial^2}{\partial T_0^2}\Phi_0^2\Phi_1^*.\end{aligned} \tag{70}$$

Since the incoming pulse is described most easily by a comoving coordinate system (i.e., a new coordinate system that is moving with the pulse), we will define the $U_n$ and $V_n$ families of new coordinates as

$$\begin{aligned} U_0 &= Z_0 - T_0, \qquad V_0 = Z_0, \\ U_1 &= Z_1 - T_1, \qquad V_1 = Z_1, \\ U_2 &= Z_2 - T_2, \qquad V_2 = Z_2. \end{aligned} \tag{71}$$

The partial derivatives can be described in the new coordinates as

$$\begin{aligned} \frac{\partial}{\partial Z_n} &= \frac{\partial}{\partial U_n} + \frac{\partial}{\partial V_n}, \\ \frac{\partial}{\partial T_n} &= -\frac{\partial}{\partial U_n}, \\ \frac{\partial^2}{\partial Z_n^2} &= \frac{\partial^2}{\partial U_n^2} + \frac{\partial^2}{\partial V_n^2} + 2\frac{\partial^2}{\partial U_n \partial V_n}, \\ \frac{\partial^2}{\partial T_n^2} &= \frac{\partial^2}{\partial U_n^2}, \\ \frac{\partial^2}{\partial Z_n \partial Z_m} &= \frac{\partial^2}{\partial U_n \partial U_m} + \frac{\partial^2}{\partial V_n \partial V_m} + \frac{\partial^2}{\partial U_n \partial V_m} + \frac{\partial^2}{\partial U_m \partial V_n}. \end{aligned} \tag{72}$$

The partial differential equations (68), (69), and (70) are then given by

$$\left[\frac{\partial^2}{\partial V_0^2} + 2\frac{\partial}{\partial U_0}\frac{\partial}{\partial V_0}\right]\Phi_0 = 0, \tag{73}$$

$$\left[\frac{\partial^2}{\partial V_0^2} + 2\frac{\partial}{\partial U_0}\frac{\partial}{\partial V_0}\right]\Phi_1 + 2\left[\frac{\partial}{\partial U_1}\frac{\partial}{\partial V_0} + \frac{\partial}{\partial U_0}\frac{\partial}{\partial V_1} + \frac{\partial}{\partial V_1}\frac{\partial}{\partial V_0}\right]\Phi_0 = \frac{\partial^2}{\partial U_0^2}|\Phi_0|^2\Phi \tag{74}$$

and

$$\begin{aligned} &\left[\frac{\partial^2}{\partial V_0^2} + 2\frac{\partial}{\partial U_0}\frac{\partial}{\partial V_0}\right]\Phi_2 + 2\left[\frac{\partial}{\partial U_1}\frac{\partial}{\partial V_0} + \frac{\partial}{\partial U_0}\frac{\partial}{\partial V_1} + \frac{\partial}{\partial V_1}\frac{\partial}{\partial V_0}\right]\Phi_1 \\ &\quad + \left[\frac{\partial^2}{\partial V_1^2} + 2\frac{\partial}{\partial U_1}\cdot\frac{\partial}{\partial V_1} + 2\frac{\partial}{\partial U_0}\cdot\frac{\partial}{\partial V_2} + 2\frac{\partial}{\partial U_2}\cdot\frac{\partial}{\partial V_0} + 2\frac{\partial}{\partial V_2}\cdot\frac{\partial}{\partial V_0}\right]\Phi_0 \\ &= 2\frac{\partial}{\partial U_0}\cdot\frac{\partial}{\partial U_1}|\Phi_0|^2\Phi_0 + 2\frac{\partial^2}{\partial U_0^2}|\Phi_0|^2\Phi_1 + \frac{\partial^2}{\partial U_0^2}\Phi_0^2\Phi_1^*. \end{aligned} \tag{75}$$

An ansatz that solves the above partial differential equations correct to order $\varepsilon$ in the (66) expansion is

$$\begin{aligned} \Phi_0 &= A(U_1, V_1, U_2, V_2)e^{iKU_0}, \\ \Phi_1 &= 0, \\ \Phi_2 &= C(U_1, V_1, U_2, V_2,)e^{iKU_0}, \end{aligned} \tag{76}$$

where $K = \omega\tau = W$ and $\omega$ is the pulse center frequency. It is worth noting at this point that the solutions thus obtained are valid for $\varepsilon V \sim O(1)$ while those deduced from ordinary perturbation theory would have been valid only for $V \sim O(1)$. Furthermore, note that the specific form for $C$ cannot be obtained from the above equations. With the above ansatz, the above system of partial differential equations reduces to (Manassah et al., 1986)

$$2iK\frac{\partial A}{\partial V_1} = -K^2|A|^2 A, \tag{77}$$

$$\left[\frac{\partial^2}{\partial V_1^2} + 2\frac{\partial}{\partial U_1}\cdot\frac{\partial}{\partial V_1} + 2iK\frac{\partial}{\partial V_2}\right]A = 2iK\frac{\partial}{\partial U_1}|A|^2 A. \tag{78}$$

## 2.3 Quasi-Linear Partial Differential Equations

Starting with Eqs. (77) and (78) we obtain the system of quasi-linear partial differential equations for the amplitude and phase of the pulse. Denote $A$ by

$$A = ae^{i\alpha}. \tag{79}$$

Then the system of partial differential equations is given by

$$\frac{\partial a}{\partial V_1} = 0, \tag{80}$$

$$\frac{\partial \alpha}{\partial V_1} = \frac{K}{2}a^2, \tag{81}$$

$$3a^2\frac{\partial a}{\partial U_1} = 2\frac{\partial a}{\partial V_2}, \tag{82}$$

$$\frac{K}{4}a^4 + 2\frac{\partial \alpha}{\partial V_2} = a^2\frac{\partial \alpha}{\partial U_1}. \tag{83}$$

In variables $U$ and $V$, the above equations lead to

$$\frac{\partial a}{\partial V} - \frac{3}{2}\varepsilon a^2\frac{\partial a}{\partial U} = 0, \tag{84}$$

$$\frac{\partial \alpha}{\partial V} - \frac{\varepsilon}{2}a^2\frac{\partial \alpha}{\partial U} = \frac{\varepsilon K}{2}a^2 - \frac{\varepsilon^2 K}{8}a^4. \tag{85}$$

In the same notation, the quasi-linear partial differential equations in other work are:

1. Conventional theory (Alfano and Shapiro, 1970):

$$\frac{\partial a}{\partial V} = 0, \tag{86}$$

$$\frac{\partial \alpha}{\partial V} = \frac{\varepsilon K}{2}a^2. \tag{87}$$

TABLE 5.1. Range of experimental parameters in supercontinuum generation experiments.[a]

| $P_c$, critical power for self-focusing | $n_2 = 10^{-22}$ (MKS) $= 0.9 \times 10^{-13}$ (esu) | | | $n_2 = 10^{-20}$ (MKS) $= 0.9 \times 10^{-11}$ (esu) | | |
|---|---|---|---|---|---|---|
| | $2 \times 10^6$ W | | | $2 \times 10^4$ W | | |
| $P_{in}$, pulse input power, W | $10^7$ | $10^9$ | $10^{11}$ | $10^7$ | $10^9$ | $10^{11}$ |
| $E_0$, maximum amplitude of the incoming pulse, V/m | $9 \times 10^7$ | $9 \times 10^8$ | $9 \times 10^9$ | $9 \times 10^7$ | $9 \times 10^8$ | $9 \times 10^9$ |
| $S_f$, distance to focusing point; m | 0.4 | 0.04 | 0.004 | 0.04 | 0.004 | 0.0004 |
| $\varepsilon = n_2\|E_0\|^2/n$ ($n = 1.5$) | $\frac{2}{3} \times 10^{-6}$ | $\frac{2}{3} \times 10^{-4}$ | $\frac{2}{3} \times 10^{-2}$ | $\frac{2}{3} \times 10^{-4}$ | $\frac{2}{3} \times 10^{-2}$ | $\frac{2}{3}$ |
| $\varepsilon V = n_2\|E_0\|^2 z/c\tau$ ($z = 1\,\mu$m of sample thickness) | $\frac{1}{3} \times 10^{-7}$ | $\frac{1}{3} \times 10^{-5}$ | $\frac{1}{3} \times 10^{-3}$ | $\frac{1}{3} \times 10^{-5}$ | $\frac{1}{3} \times 10^{-3}$ | $\frac{1}{3} \times 10^{-1}$ |

[a] Source wavelength = 1 $\mu$m, pulse width = $10^{-13}$ s, and beam diameter at input plane = 1 mm.

2. Slowly varying approximation (Anderson and Lisak, 1983):

$$\frac{\partial a}{\partial V} - 3\varepsilon a^2 \frac{\partial a}{\partial U} = 0, \tag{88}$$

$$\frac{\partial \alpha}{\partial V} - \varepsilon a^2 \frac{\partial \alpha}{\partial U} = \frac{\varepsilon K}{2} a^2. \tag{89}$$

3. Yang and Shen approximation (Yang and Shen, 1984)

$$\frac{\partial a}{\partial V} - \frac{\varepsilon}{2} a^2 \frac{\partial a}{\partial U} = 0, \tag{90}$$

$$\frac{\partial \alpha}{\partial V} - \frac{\varepsilon a^2}{2} \frac{\partial \alpha}{\partial U} = \frac{\varepsilon K}{2} a^2. \tag{91}$$

Next we will find the solution for $a$ and $\alpha$ for a pulse whose initial shape is a sech pulse. In Manassah et al. (1986) the Gaussian pulse results are also given. In Table 5.1 some physical quantities in the present notation are given.

## 2.4 Pulse Amplitude

The solution of Eq. (84) with the boundary condition

$$a(U, 0) = \operatorname{sech}(U) \tag{92}$$

can be obtained by the usual technique of first-order partial differential equations; it is given by (Anderson and Lisak, 1983)

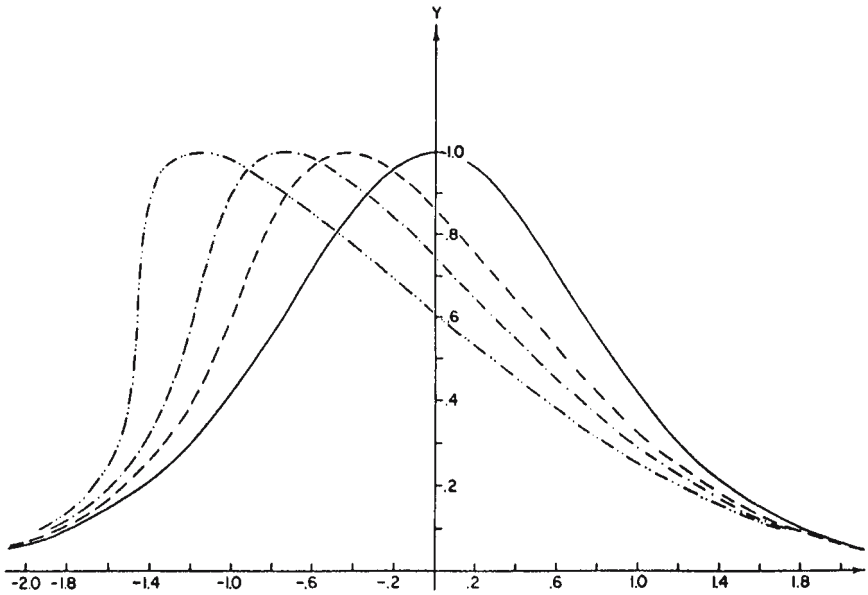


FIGURE 5.16. Steepened pulse amplitude as a function of $U$. —— $\varepsilon V = 0.0$; – – – $\varepsilon V = 0.3$; –·– $\varepsilon V = 0.5$; –··– $\varepsilon V = 0.8$.

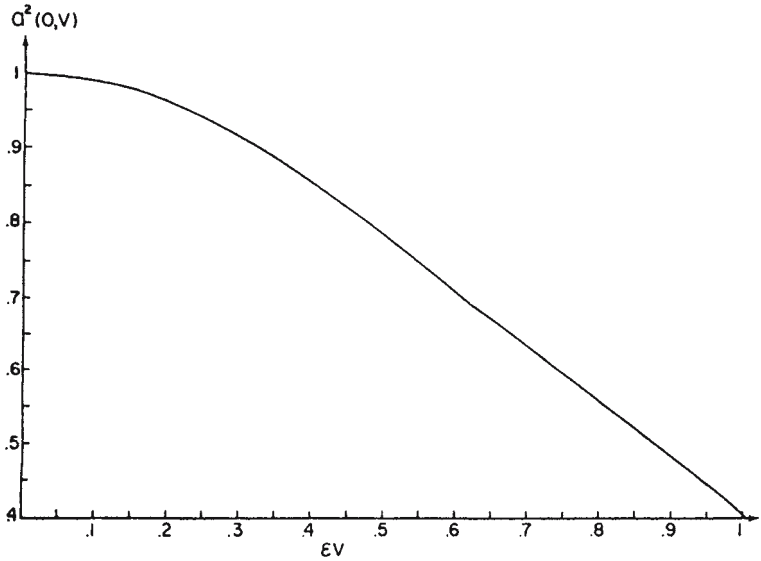


FIGURE 5.17. Magnitude of the steepened (amplitude)$^2$ at $U = 0$ as a function of $\varepsilon V$.

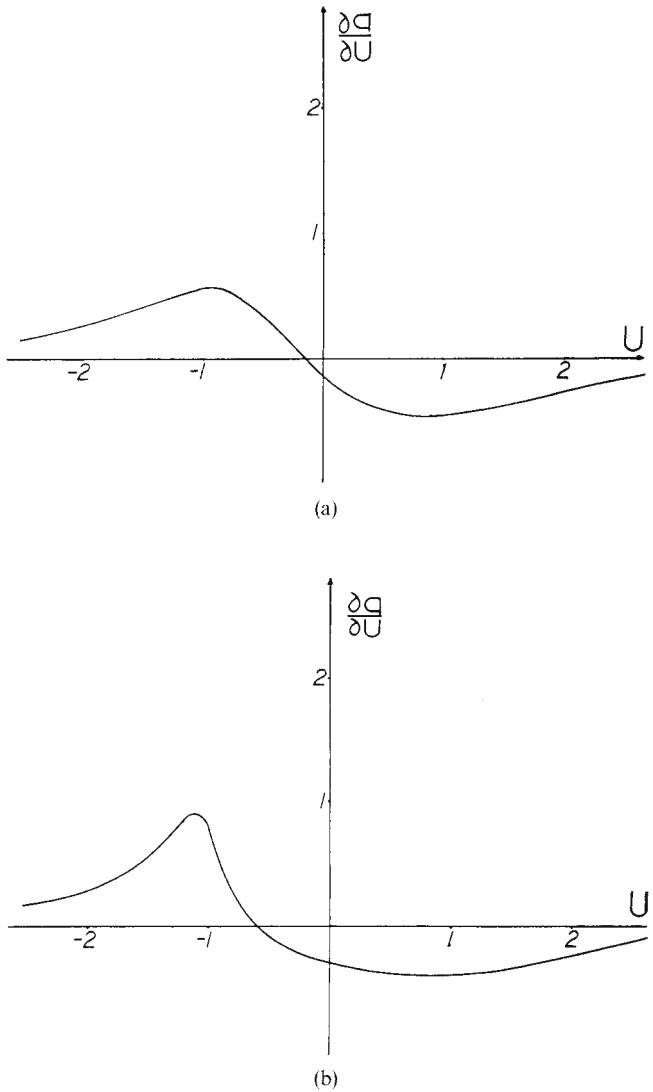


FIGURE 5.18. Slope of the steepened pulse as a function of $U$. (a) $\varepsilon V = 0.1$; (b) $\varepsilon V = 0.4$; (c) $\varepsilon V = 0.8$.

$$a^2 = \operatorname{sech}^2\left[U + \tfrac{3}{2}\varepsilon V a^2\right]. \tag{93}$$

The amplitude is maximum for

$$U_m = -\tfrac{3}{2}\varepsilon V. \tag{94}$$

The (amplitude)$^2$ of the pulse at $U = 0$ is given by the solution of

$$a_0^2 = \operatorname{sech}^2\left[\tfrac{3}{2}\varepsilon V a_0^2\right] \tag{95}$$

or

$$\varepsilon V = \frac{2}{3a_0^2}\ln\left[\frac{1}{a_0} + \left(\frac{1}{a_0^2} - 1\right)^{1/2}\right], \tag{96}$$

where $a_0 = a(0, V)$.

The partial derivative of the amplitude with respect to $U$ is given by

$$\frac{\partial a}{\partial U} = \frac{-a(1-a^2)^{1/2}}{3\varepsilon V a^2(1-a^2)^{1/2} \pm 1}, \tag{97}$$

where (–) refers to $U < -\frac{3}{2}\varepsilon V$ and (+) otherwise.

The present model produces an amplitude that is asymmetric; this distortion is called self-steepening. A shock in the amplitude can develop for $\varepsilon V > \sqrt{\frac{3}{2}}$.

In Figure 5.16 the amplitude $a$ is plotted as a function of $U$ for different values of $\varepsilon V$, in Figure 5.17 $a_0$ is plotted as a function of $\varepsilon V$, and in Figure 5.18 $\partial a_0/\partial U$ is plotted as a function of $U$.

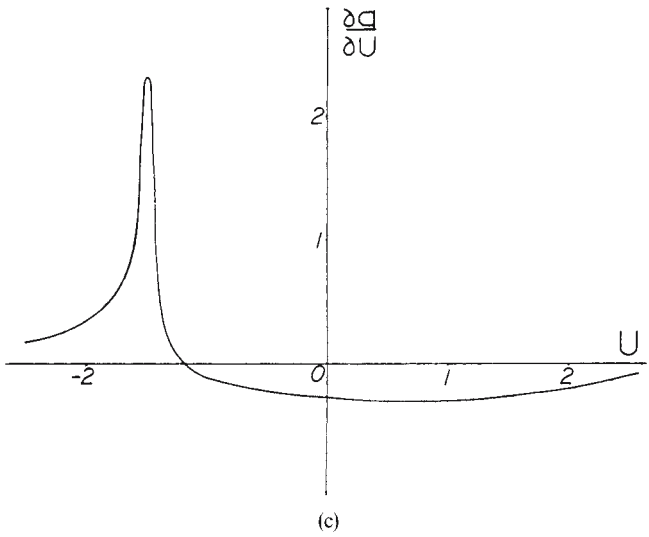


(c)

FIGURE 5.18. (*continued*)

## 2.5 Pulse Phase

The general solution of Eq. (85) is given by (Manassah et al., 1986)

$$\alpha = -KU - \frac{K\varepsilon}{2}\int_0^U a^2(p,V)dp - \frac{3K}{8}\varepsilon^2\int_0^V a^4(0,q)dq + F(U,V), \tag{98}$$

where the function $F(U, V)$ is a solution of the equation

$$\frac{\partial F}{\partial V} - \frac{\varepsilon}{2}a^2\frac{\partial F}{\partial U} = 0. \tag{99}$$

The boundary condition imposed by the physical condition of no initial chirp is that at the input plane (i.e., $V = 0$), $\alpha$ should be zero for all values of $U$. This implies that, for an incoming sech pulse, we have

$$F(U,0) = KU + \frac{K\varepsilon}{2}\tanh U. \tag{100}$$

The general solution of Eq. (99) is given by

$$F(f) = F\left(\frac{\varepsilon}{2}\int_0^V a^3(U,q)dq + \int_0^U a(p,0)dp\right). \tag{101}$$

The special form of $\alpha$ satisfying the boundary condition (100) is given by

$$\begin{aligned}\overline{\alpha} \equiv \frac{\alpha}{K} = -U - \frac{\varepsilon}{2}\int_0^U a^2(p,V)dp - \frac{3\varepsilon^2}{8}\int_0^V a^4(0,q)dq \\ + \tanh^{-1}\sin f(U,V) + \frac{\varepsilon}{2}\sin f(U,V),\end{aligned} \tag{102}$$

where

$$f(U,V) = \frac{\varepsilon}{2}\int_0^V a^3(U,q)dq + \sin^{-1}\tanh U. \tag{103}$$

The maximum of $\alpha$, denoted by $\alpha^M$, and its position, denoted by $U_\alpha$, are respectively given by (Manassah and Mustafa, 1988a)

$$\alpha^M \approx K\varepsilon V/2 \tag{104}$$

and

$$U_\alpha \approx -\varepsilon V. \tag{105}$$

We note that the positions of the maxima of $a$ and $\alpha$ are shifted from each other. Furthermore, this shift is linear in $\varepsilon V$. Also note that while the value of the maximum of the amplitude is equal to 1 for all $\varepsilon V$, $\alpha^M$, the value of the phase maximum, increases linearly with $\varepsilon V$. In Figure 5.19, $\alpha(U, V)$ is plotted for different values of the parameter $\varepsilon V$. As can be observed, for small values of $\varepsilon V$, $\alpha$ is symmetric and is centered on the $U = 0$ axis. However, as $\varepsilon V$ increases the $\alpha$ curve becomes skewed and its maximum is shifted to the

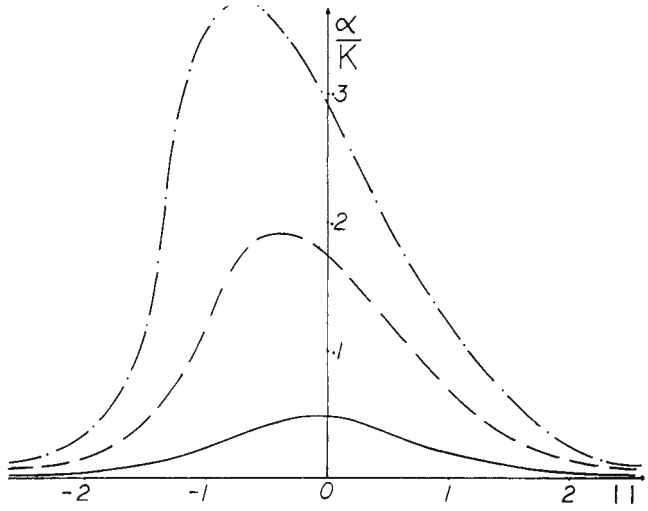


FIGURE 5.19. Phase of the steepened pulse as function of $\varepsilon V$. (a) —— $\varepsilon V = 0.1$; (b) –– $\varepsilon V = 0.4$; (c) –·– $\varepsilon V = 0.8$.

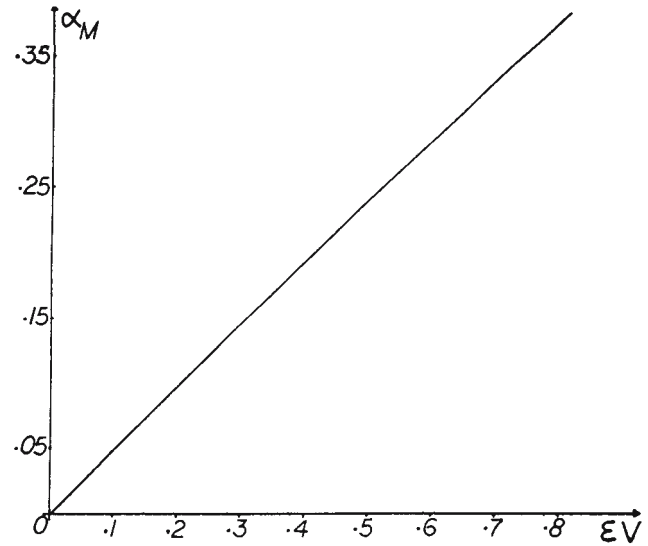


FIGURE 5.20. Computed magnitude of the maximum of the steepened pulse phase as function of $\varepsilon V$.

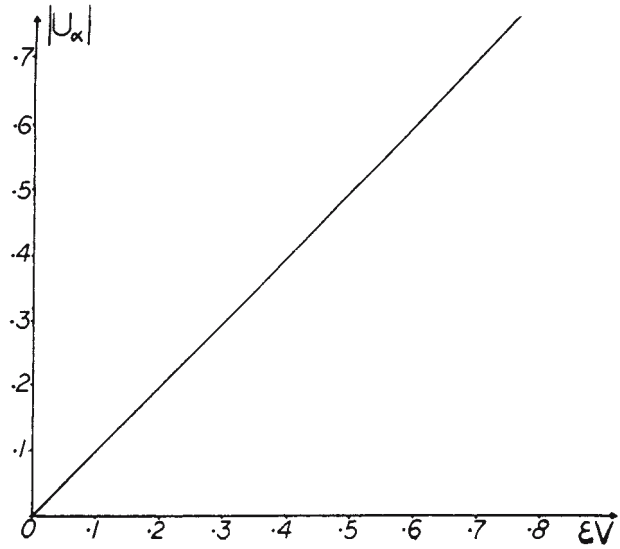


FIGURE 5.21. Computed position of the maximum of the steepened pulse phase as a function $\varepsilon V$.

left of the $U = 0$ axis. In Figures 5.20 and 5.21 the computed values of $\alpha^M$ and $U_\alpha$ are plotted as functions of $\varepsilon V$. As can be seen, the computed curves are well approximated by Eqs. (104) and (105).

The expression for the derivative of the phase with respect to $U$, also called the instantaneous frequency sweep, is given by

$$\frac{1}{K}\frac{\partial \alpha}{\partial U} = \bar{\alpha}' = -1 + a(U,V)(\cos f(U,V))^{-1} + \frac{\varepsilon}{2}\{a(U,V)\cos[f(U,V)] - a^2(U,V)\}. \tag{106}$$

The second partial derivative of the phase is given by

$$\frac{1}{K}\frac{\partial^2 \alpha}{\partial U^2} = \bar{\alpha}'' = \left[\frac{\partial a(U,V)}{\partial U} + a^2(U,V)\tan f(U,V)\right][\cos fU,V]^{-1} + \frac{\varepsilon}{2}\left[\frac{\partial a(U,V)}{\partial U}\cos f(U,V) - a^2(U,V)\sin f(U,V) - 2a(U,V)\frac{\partial a(U,V)}{\partial U}\right]. \tag{107}$$

In Figures 5.22 and 5.23 the phase partial derivatives are plotted for different values of the parameter $\varepsilon V$. It should be observed that $\bar{\alpha}'$ and $\bar{\alpha}''$ for a self-phase modulated pulse are qualitatively different from those of a chirped

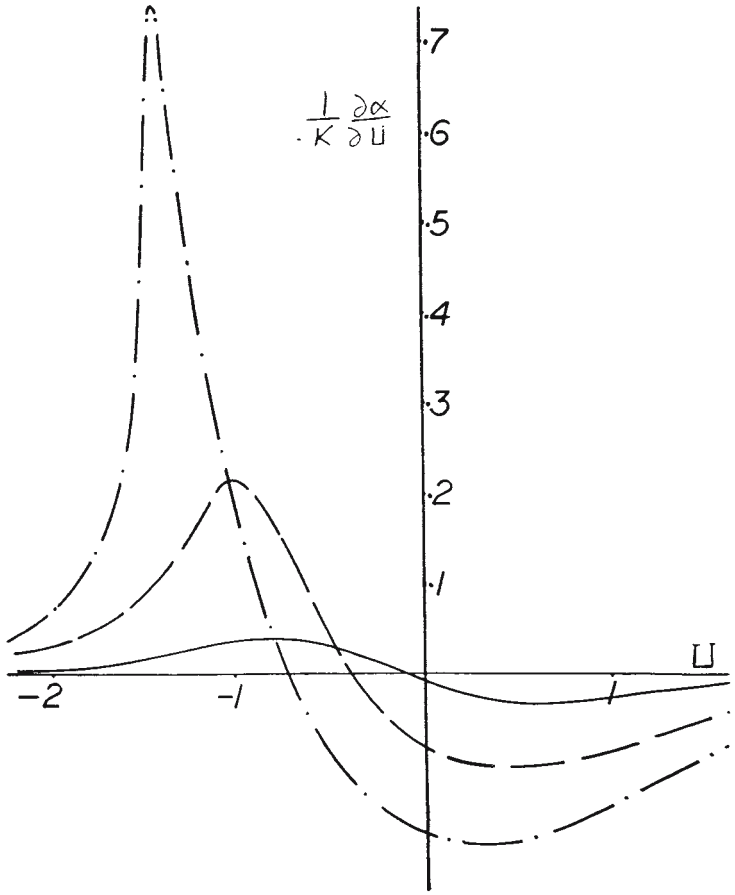


FIGURE 5.22. The $U$ partial derivative of the steepened pulse phase as a function of $\varepsilon V$. (a) —— $\varepsilon V = 0.1$; (b) – – $\varepsilon V = 0.4$; (c) –·– $\varepsilon V = 0.8$.

Gaussian pulse, where $\alpha'$ is linear in $U$ and $\alpha''$ is a constant. Consequently, whereas in the time domain for small $\varepsilon V$ the phase can be approximated by a chirped Gaussian, in the frequency domain, where the values of $\bar{\alpha}'$ and $\bar{\alpha}''$ are critical, such an approximation is not valid. We will return to this point when we discuss the spectral distribution and the filter transform of this pulse. The critical results of this section are the asymmetries of the phase and its derivatives. In the following section, we discuss a direct method for measuring the asymmetry in the phase.

## 2.6 Direct Time Measurement of the Phase

The phase of the pulse can be directly measured using the Rothenberg-Grischkowsky interferometric technique (Rothenberg and Grischkowsky,

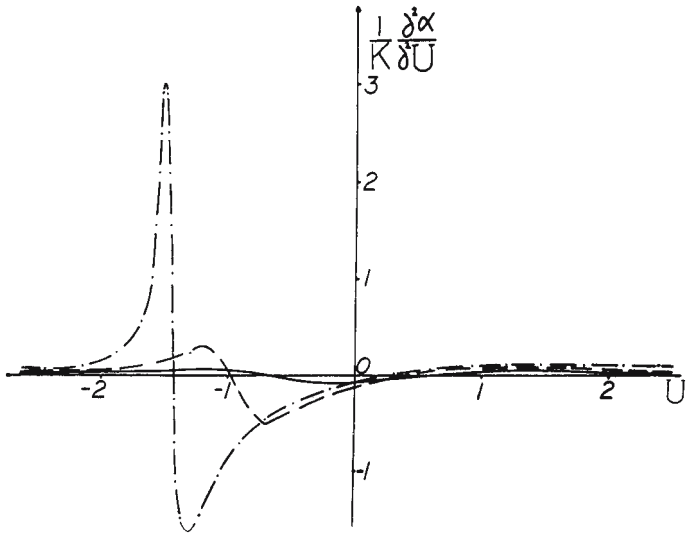


FIGURE 5.23. The $U$ second partial derivative of the steepened pulse phase as a function of $U$. (a) —— $\varepsilon V = 0.1$; (b) – – $\varepsilon V = 0.4$; (c) –·– $\varepsilon V = 0.8$.

1987). Essentially, the measurement technique consists of adding two pulses, a reference pulse of known width and zero chirp and a signal pulse described by the above amplitude and phase, and then subtracting the sum of the intensities of the reference pulse and the signal pulse. The resultant is given by

$$I(U) = 2R(U)a(U)\cos[\alpha(U)]. \tag{108}$$

If the reference pulse $R(U)$ is obtained as a portion of the incoming pulse (i.e., sech $U$), then $I(U)$ is given by

$$I(U) = 2\operatorname{sech} Ua(U)\cos[\alpha(U)]. \tag{109}$$

In Figure 5.24, $I(U)$ is plotted using the above theory and is compared to the results of conventional self-phase modulation theory. As can be observed (Manassah and Mustafa, 1988a), the asymmetry in the amplitude and phase are translated into an asymmetry in $I(U)$.

## 2.7 Interference Pattern of the Supercontinuum

In this section we compute the interference pattern generated by a self-phase-modulated pulse (Manassah and Mustafa, 1988b). We prove that the presence of the amplitude-phase time shift generates fringe position shifts. We also compute the Fourier transform of the interferometric intensity distribution and prove that the range of this transform is directly related to the range of $\bar{\alpha}'$.

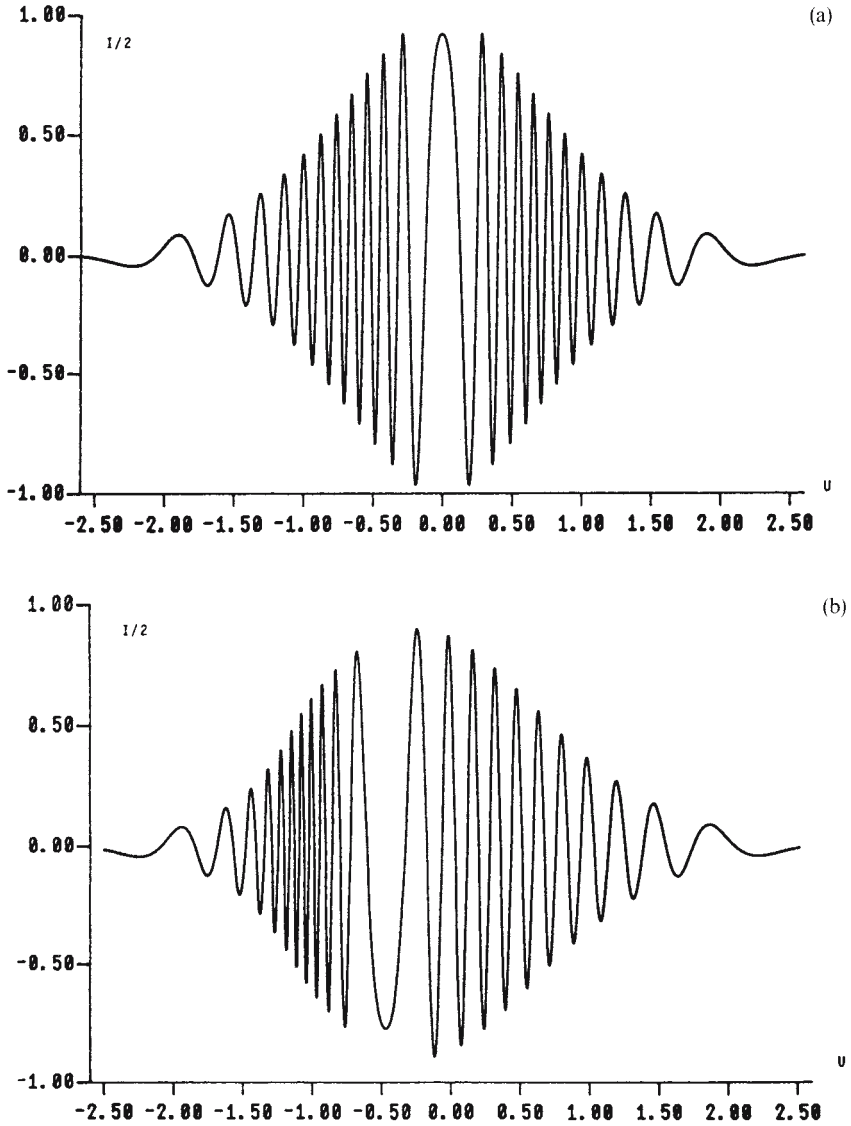


FIGURE 5.24. Difference signal between the output from a Mach-Zehnder interferometer and the sum of the input pulse to the interferometer (i.e., the SPM pulse) and the reference pulse (i.e., sech pulse). $K = 300$, $\varepsilon V = 0.5$. (a) Conventional SPM theory; (b) self-steepened theory.

For all interferometric problems (Born and Wolf, 1975), the method of analysis of nonmonochromatic light is first to find the intensity distribution for a specific frequency as a function of the path time delays of the specific physical setup and then to sum incoherently over the intensities of all frequency components. Therefore, if a light that is incident on a Young/Michelson interferometric system has an input spectral distribution given by $I_{\text{in}}(\omega)$, the output intensity $I_{\text{out}}$ from this system is then given by (Manassah, 1987a)

$$I_{\text{out}}(\Delta) = \int I_{\text{in}}(\omega) H(\omega, \Delta) d\omega, \tag{110}$$

where $\Delta$ is the time delay associated with the two paths and $H(\omega, \Delta)$ is the response of the system to the incoming field of unit amplitude and frequency $\omega$. Specifically, the monochromatic response function for the Young configuration is given by

$$H(\omega, \Delta) = 2\{1 + \cos(\omega\Delta)\}. \tag{111}$$

The relative output intensity for any $\Delta$, normalized to the intensity for $\Delta = 0$, is then given by

$$\frac{I(\Delta)}{I(0)} = \frac{1}{2} + \frac{1}{2} \frac{\int_{-\infty}^{-\infty} dt a(t) a(t-\Delta) \cos\{\omega\Delta + \alpha(t) - \alpha(t-\Delta)\}}{\int_{-\infty}^{\infty} a^2(t) dt}. \tag{112}$$

For CW radiation, the minima of the interferometric intensity are located at

$$\Delta(n) = \frac{(2n+1)\pi}{\omega}.$$

In normalized time $T$, and using normalized frequency $K$, the normalized time delay $\Delta/\tau$ is parametrized as $y/K$. In these units, the CW minima correspond to

$$y(n) = (2n+1)\pi \tag{113}$$

and the expression for the relative intensity of the interference pattern reduces to

$$I_R(y) = \frac{I(y)}{I(0)} = \frac{1}{2} + \frac{1}{2} \frac{\int_{-\infty}^{\infty} dT a(T) a(T - y/K) \cos\{y + \alpha(T) - \alpha(T - y/K)\}}{\int_{-\infty}^{\infty} dT a^2(T)}. \tag{114}$$

In Figure 5.25 we plot $I_R(y)$ for fixed $K$ (i.e., fixed pulse width) but variable $\varepsilon V$ (i.e., changing pulse energy). As can be observed, both the values and positions of the extrema change with $\varepsilon V$. Furthermore, for large $n$, the ratio of the magnitude of a maximum intensity to that of its neighboring minimum

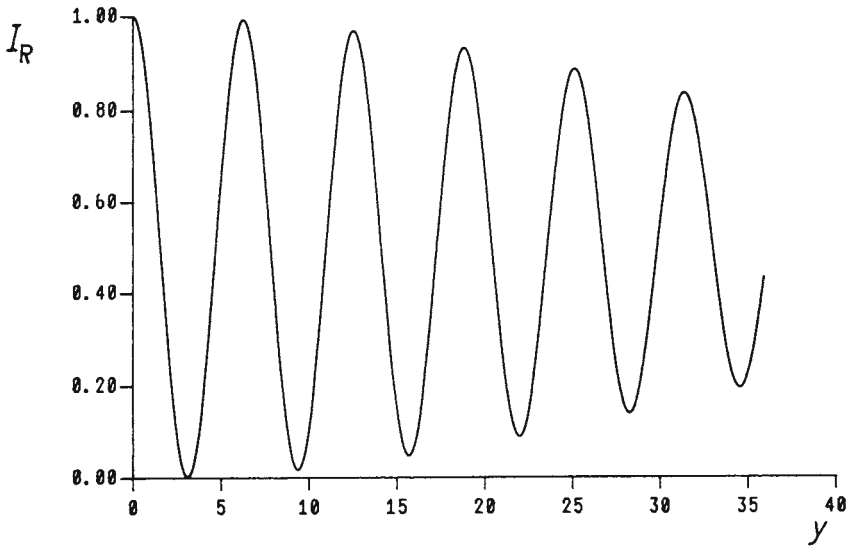


(a)

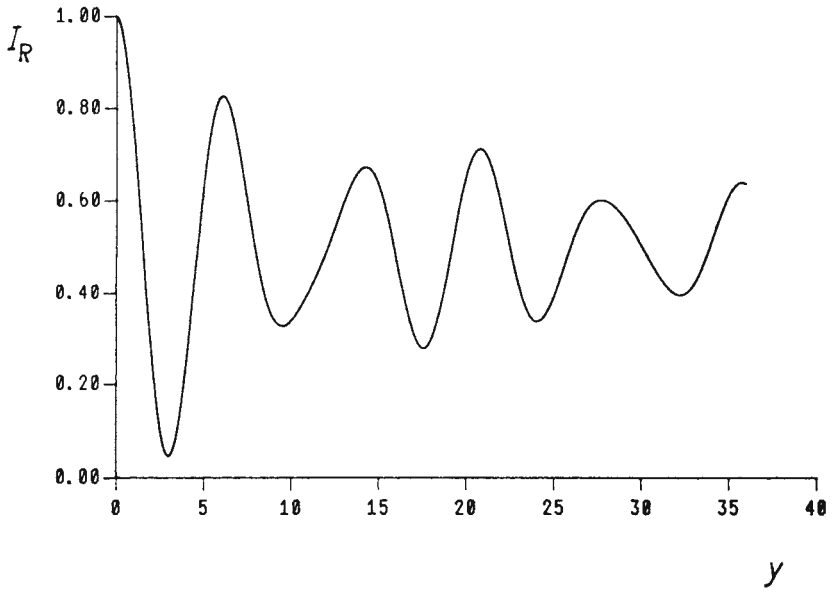


(b)

FIGURE 5.25. Young/Michelson normalized interferometric intensity distribution $I_R(y)$, for a steepened self-phase-modulated input, as a function of $y$ ($= \omega_0\Delta$). $K = 50$. (a) $\varepsilon V = 0.1$; (b) $\varepsilon V = 0.5$; (c) $\varepsilon V = 0.8$.

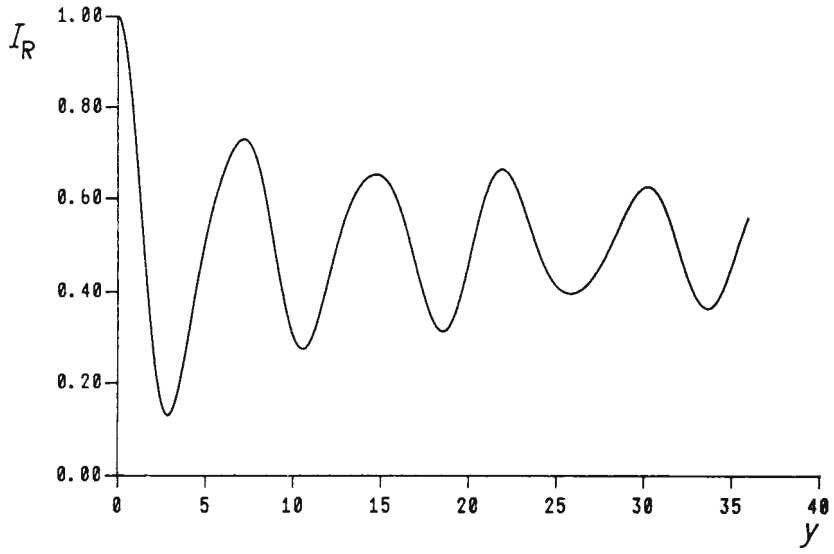


(c)

FIGURE 5.25. (*continued*)

intensity decreases with increasing $\varepsilon V$. This ratio goes asymptotically, for large $n$, to 1.

In Figure 5.26 we plot the shifts in the position of the third minimum (i.e., the minimum that corresponds to $y(2) = 5\pi$ for CW radiation) as a function of $K$, but fixed $\varepsilon V$. As can be observed, this shift depends only weakly on $K$. The approximate scaling—i.e., the strong dependence of the shift in fringe positions on the ratio $\varepsilon V$, essentially the pulse intensity over the pulse duration, and not independently on the pulse width—will be discussed next. The phase of an SPM signal was shown in Section 2.5 to depend only on the parameter $K$ through a multiplicative factor, $\alpha = K\bar{\alpha}$, where $\bar{\alpha}$ depends only on the parameter $\varepsilon V$. Consequently, if for $y/K < 1$ we approximate Eq. (114) by the leading term of its Taylor series, we obtain

$$I_R^A(y) \approx \frac{1}{2} + \frac{1}{2} \frac{\int_{-\infty}^{\infty} dU a^2(U) \cos\{y(1 + \partial\bar{\alpha}/\partial U)\}}{\int_{-\infty}^{\infty} dU a^2(U)}. \tag{115}$$

This approximate expression for $I_R$ does not have an explicit dependence on $K$. We notice from Figure 5.26 that this asymptotic value for $I_R$ is already within 2% of its exact value for $K \sim 90$ (i.e., a 30-fs pulse for $\lambda \sim 0.6\mu$m). Furthermore, by examining Eq. (114) it also becomes clear why the $\varepsilon V$-dependent amplitude-phase time shift is responsible for the interferometric

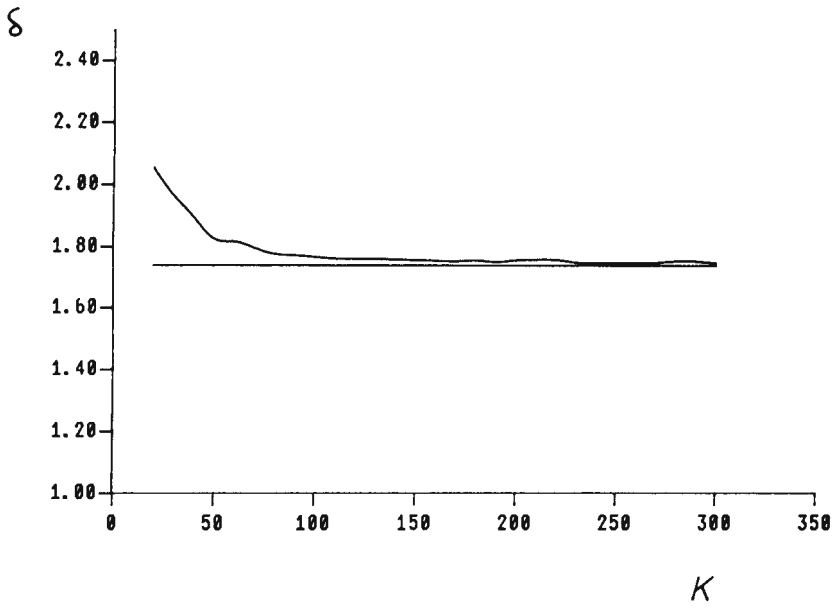


FIGURE 5.26. Shifts in the positions of the Young interferometric third-order minimum, for a steepened self-phase-modulated input, $\varepsilon V = 0.5$, as a function of $K$ $(= \omega_0 \tau)$.

TABLE 5.2. Shifts in the positions of the asymptotic interfero-metric intensity minima for various orders and $\varepsilon V$ values.

| $\varepsilon V$ \ $n$ | 0 | 1 | 2 | 3 | 4 |
|---|---|---|---|---|---|
| 0.1 | –0.006 | –0.016 | –0.021 | –0.029 | –0.034 |
| 0.2 | –0.018 | –0.051 | –0.073 | –0.045 | –0.343 |
| 0.3 | –0.040 | –0.101 | –0.010 | 1.14 | 2.29 |
| 0.4 | –0.072 | –0.127 | 1.84 | 2.02 | 2.20 |
| 0.5 | –0.113 | 0.115 | 1.74 | 2.20 | 3.63 |
| 0.6 | –0.161 | 1.29 | 1.59 | 3.15 | 4.59 |
| 0.7 | –0.213 | 1.19 | 2.62 | 3.84 | 4.87 |
| 0.8 | –0.254 | 1.04 | 2.51 | 4.01 | 5.67 |

minima shifts; in effect $\partial\bar{\alpha}/\partial U \neq 0$ for $U = U_a$ and the argument of the cosine function at that point is $\varepsilon V$ dependent.

In Table 5.2 the shifts in the positions of the $I_R^A$ minima are tabulated as functions of the order of the minima and of the parameter $\varepsilon V$. A shift is defined as the difference between the actual minimum of $I_R^A(y)$ and the corresponding CW minimum as defined in Eq. (113). As can be observed, each $\varepsilon V$ has a distinct signature for the shifts.

A nonspectroscopic method for deducing $\varepsilon V$ is through an analysis of the Fourier transform of $I_R^A$. The expression for the Fourier transform can be directly deduced from Eq. (116) and the integral representation of the Dirac delta function, specifically:

$$F(x) \equiv \int_{-\infty}^{\infty} e^{ixy}\left[I_R^A(y) - \frac{1}{2}\right]dy$$
$$= \frac{\pi}{2N}\left\{\sum_i \left|\frac{a^2(U)}{\partial^2 \overline{\alpha}/\partial U^2}\right|_{U=U_i} + \sum_j \left|\frac{a^2(U)}{\partial^2 \overline{\alpha}/\partial U^2}\right|_{U=U_j}\right\}, \tag{116}$$

where $U_i$ and $U_j$ are respectively the solutions of

$$x + 1 + \partial\overline{\alpha}/\partial U = 0, \tag{117}$$

$$X - 1 - \partial\overline{\alpha}/\partial U = 0, \tag{118}$$

and $N$ is the $a^2$ integral normalization factor. $F(x)$ is an even function of $x$. For $x > 0$, only Eq. (117) admits a solution since $|\partial\overline{\alpha}/\partial U| < 1$. The function $F(x)$ is not identically zero in the interval $[a, b]$, where

$$a = \min(\partial\overline{\alpha}/\partial U) + 1, \tag{119}$$

$$b = \max(\partial\overline{\alpha}/\partial U) + 1 \tag{120}$$

(i.e., a determination of the range of $F(x)$ specifies the value of the parameter $\varepsilon V$). In Figure 5.27 the maximum and minimum of $(\partial\overline{\alpha}/\partial U)$ are plotted as functions of the parameter $\varepsilon V$. It should also be observed here that, as we will see in Section 2.8, the spectral distribution extents on the Stokes and anti-Stokes sides are determined by the extrema of $(\partial\overline{\alpha}/\partial U)$. In Figure 5.28, the function $F(x)$ is plotted for selected values of $\varepsilon V$.

## 2.8 Spectral Distribution

The spectral distribution for a signal is proportional to the magnitude squared of the time Fourier transform of the electric field, which is given by

$$\tilde{E}(K') = \int_{-\infty}^{\infty} \exp(-iK'U)E(U)dU. \tag{121}$$

In Figure 5.29 the spectral intensity (Manassah and Mustafa, 1988a) of the supercontinuum is computed from the specific values of the amplitude $a$ and phase $\alpha$, earlier computed. However, to gain an intuitive feeling for this spectrum structure, we observe that the stationary phase method can be applied to the integral of Eq. (121). Specifically, this equation can be approximated by

$$\tilde{E}(K) \approx \left(\frac{2\pi}{K}\right)^{1/2}\left\{\frac{a(U_1)\exp[iK(\delta + \overline{\alpha}(U_1)) + i\pi/4]}{[\alpha''(U_1)]^{1/2}}\right.$$
$$\left. + \frac{a(U_2)\exp[iK(\delta + \overline{\alpha}(U_2)) - i\pi/4]}{|\overline{\alpha}''(U_2)|^{1/2}}\right\}, \tag{122}$$

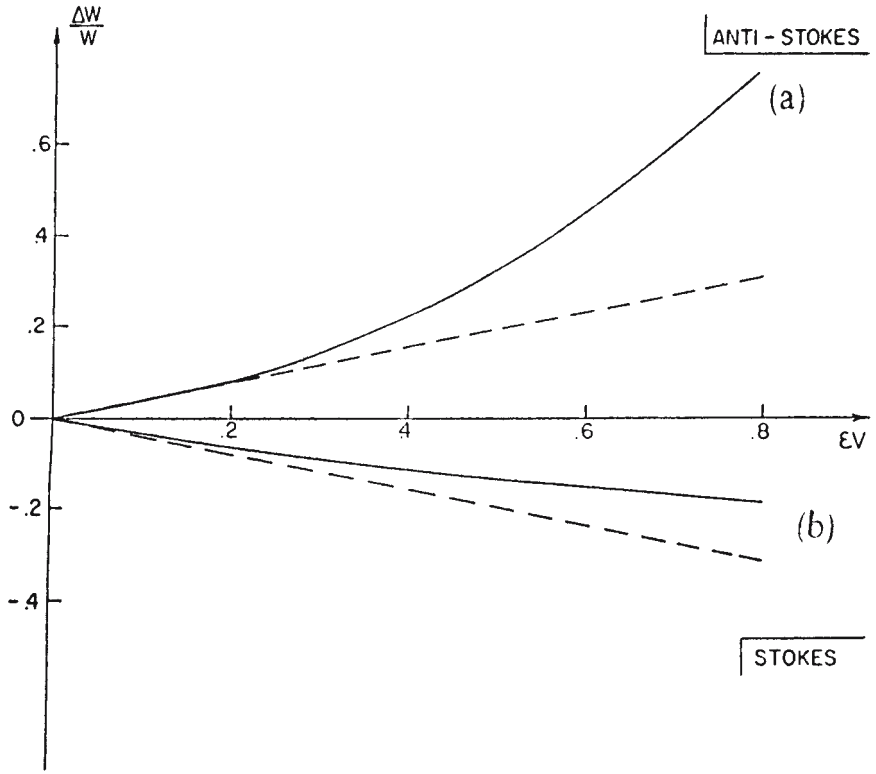


FIGURE 5.27. Values of the extrema of the $U$ partial derivative of the steepened pulse phase as a function of $\varepsilon V$. (a) Maxima; (b) minima. (Dashed line) Conventional SPM; (full line) steepened pulse.

where $K - K' = \delta K$ and $U_1$ and $U_2$ are the roots of the equation

$$\delta + \overline{\alpha}'(U) = 0 \tag{123}$$

(i.e., the stationary points), and $U_1$ and $U_2$ are chosen such that $\alpha''(U_1) > 0$ and $\alpha''(U_2) < 0$. Two stationary points exist for any $(-\delta)$ in the interval spanning the domain of $\alpha'$. We observe the following features for the spectral distribution of the self-phase modulated supercontinuum:

1. The spectral extents are given by

$$K' - K|_{\text{anti-Stokes}} \approx \text{Max}(\partial\alpha/\partial U), \tag{124}$$

$$K' - K|_{\text{Stokes}} \approx \text{Min}(\partial\alpha/\partial U). \tag{125}$$

Since $\text{Max}(\partial\alpha/\partial U) > |\text{min}(\partial\alpha/\partial U)|$ (see Figure 5.27), the spectral extent on the anti-Stokes side ($\delta < 0$) is appreciably larger than the corresponding quantity on the Stokes side, a result clearly exhibited in Figure 5.29.

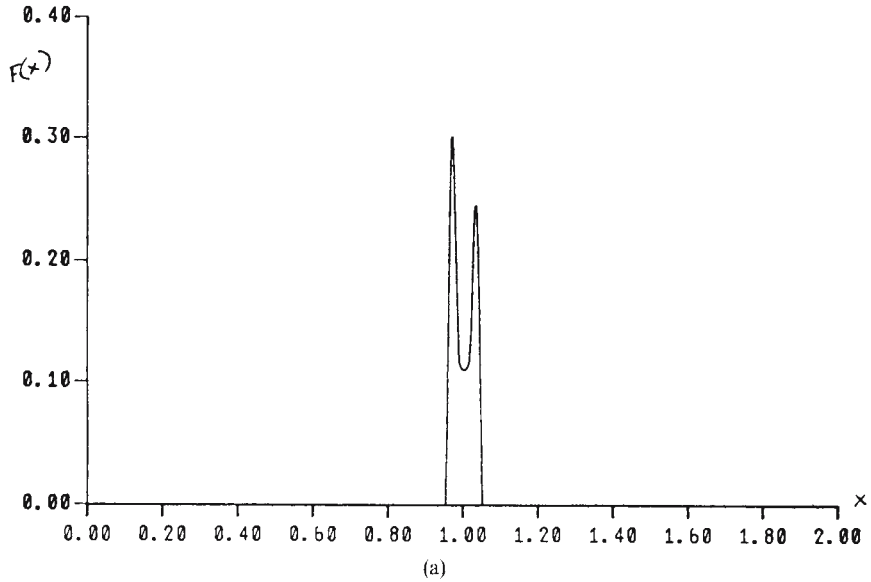


(a)

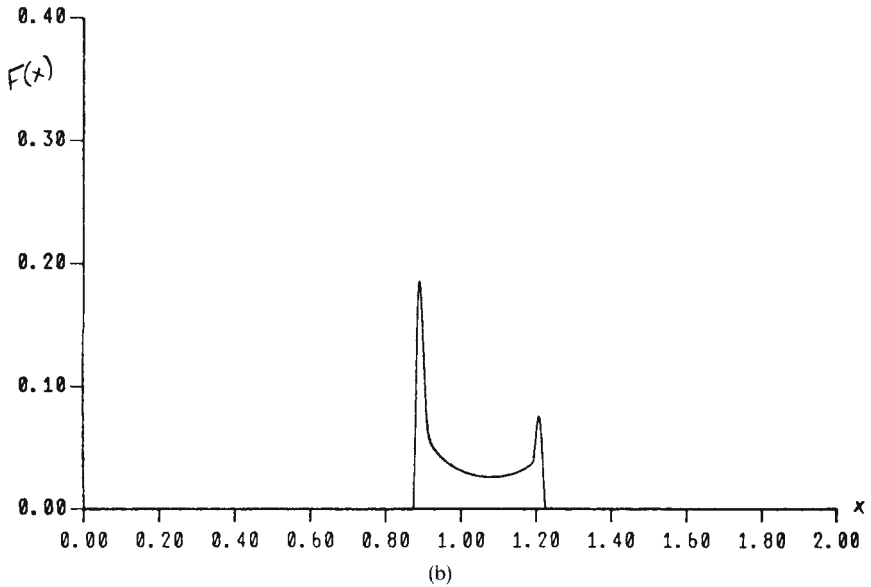


(b)

FIGURE 5.28. Fourier transform of the Young interferometer intensity distribution for a steepened SPM pulse as a function of $\chi$. (a) $\varepsilon V = 0.1$; (b) $\varepsilon V = 0.4$; (c) $\varepsilon V = 0.8$.

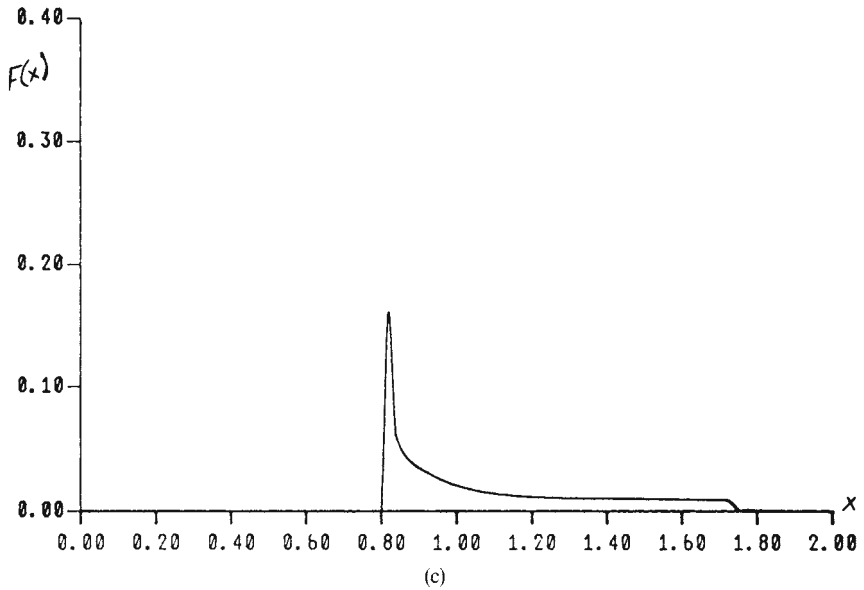


(c)

FIGURE 5.28. (*continued*)

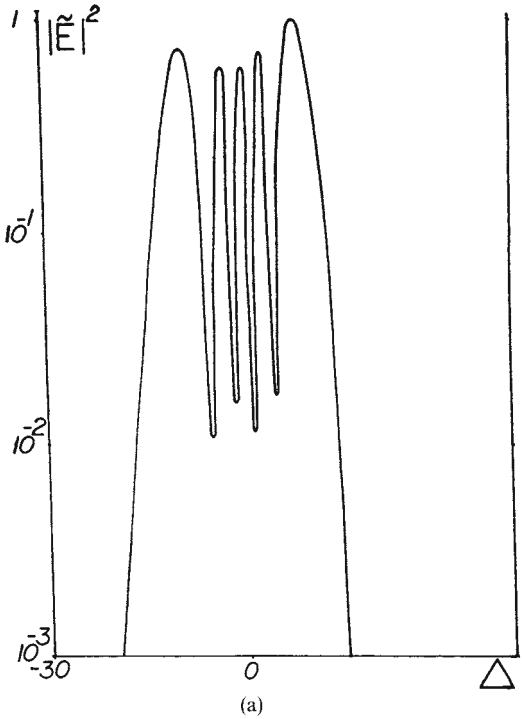


(a)

FIGURE 5.29. Normalized computed spectral distribution of the self-phase-modulated steepened pulse as a function of the frequency difference multiplied by the pulse duration. The pulse duration ~$10^{-13}$ *s* ($K = 300$). Left is anti-Stokes side. (a) $\varepsilon V = 0.1$; (b) $\varepsilon V = 0.4$; (c) $\varepsilon V = 0.8$.

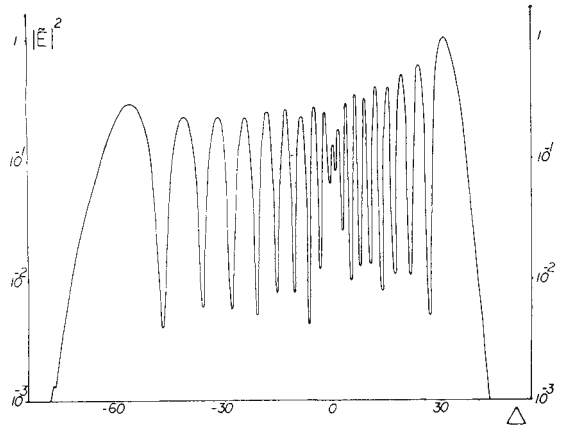


(b)

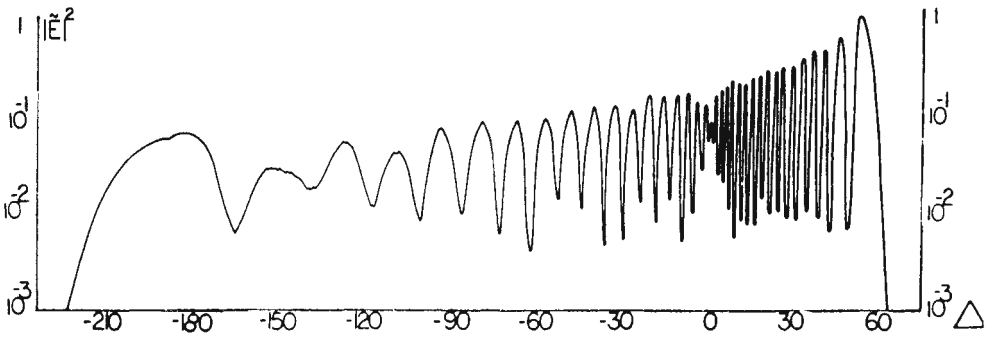


(c)

FIGURE 5.29. (*continued*)

2. The existence of two stationary points for all $\delta$ in the spectral distribution domain implies the existence of interference in the spectral intensity. $M$, the number of oscillations in the spectrum, is given by

$$M \approx \frac{\alpha^M}{\pi} \approx \frac{K\varepsilon V}{2\pi}, \tag{126}$$

where Eq. (104) has been used to derive the last relation. It is worth noting that $M$ increases with both $K$ (i.e., $\tau$) and $\varepsilon V$. The modulation frequency of these oscillations is approximately given by the frequency extent divided by the number of oscillations. Combining Eqs. (124), (125), and (126), we deduce that this quantity depends only on $\varepsilon V$ and is independent of $K$.

3. The envelope of the maxima of the spectral distribution is approximately given by

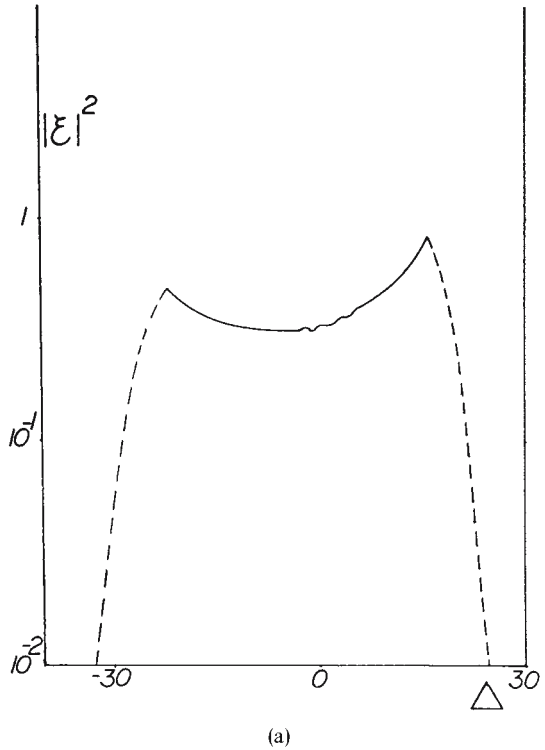


FIGURE 5.30. Approximate envelopes of the spectra of Figure 5.29 obtained by the method of the stationary phase approximation. (a) $\varepsilon V = 0.1$; (b) $\varepsilon V = 0.4$; (c) $\varepsilon V = 0.8$.

$$|\varepsilon|^2 \approx \frac{2\pi}{K}\left[\frac{a(U_1)}{\alpha''(U_1)^{1/2}} + \frac{a(U_2)}{|\alpha''(U_2)|^{1/2}}\right]^2. \tag{127}$$

In Figure 5.30 this approximate envelope is plotted for selected $\varepsilon V$. As can be observed, it mimics very well the exact envelope that can be deduced from Figure 5.29. The cutoff points for the envelope are, for $|\delta|$, equal to (max $\overline{\alpha}'$) and (min $\overline{\alpha}'$). This envelope maximum is in the shallow region of the $\alpha'$ curve. As can be observed from Figure 5.22, this is close to the region of (min $\alpha'$). Physically, this translates into the spectrum having a sharp band edge close to its Stokes maximum extent.

## 2.9 The SPM-Spectral Maximum Shift

In Figure 5.31 we plot the position of the spectral distribution maximum as function of $\varepsilon V$. We will refer to this displacement of the spectral maximum as the SPM-spectral maximum shift (Manassah and Mustafa, 1988a). For all practical purposes, the magnitude of this shift follows closely the Stokes

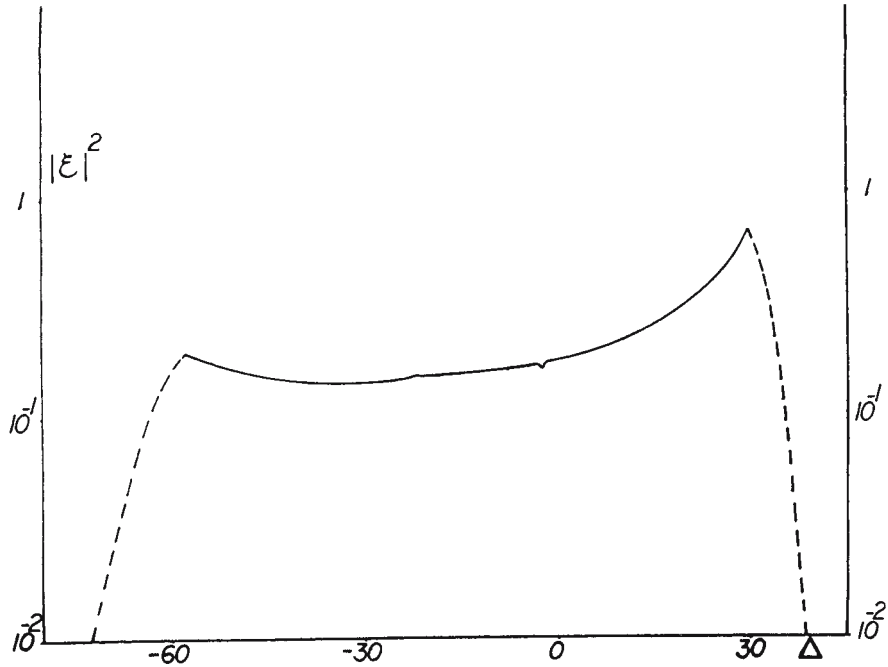


(b)

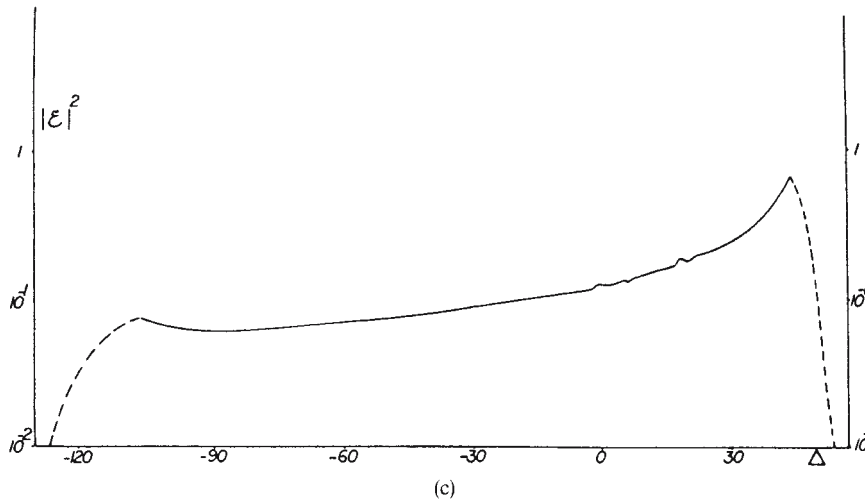


(c)

FIGURE 5.30. (*continued*)

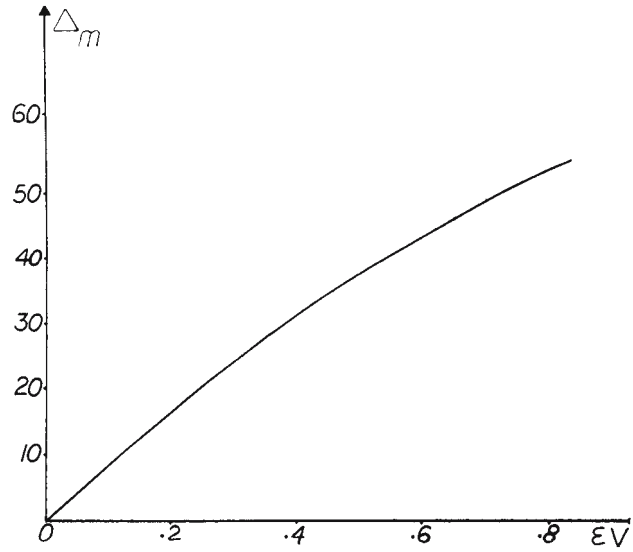


FIGURE 5.31. The SPM-spectral maximum shift, in the presence of pulse steepening, as a function of $\varepsilon V$. ($K = 300$.)

frequency extent to within half a modulation cycle. As will be seen in Section 4, this shift may also be observed in induced phase modulation (IPM) due to the similarity relations in the spectral distributions of SPM and IPM proved to exist under certain conditions (Manassah et al., 1985). This similarity-induced shift should be distinguished from the induced frequency shift (Manassah, 1987b) that will be shown to exist because of the group velocity dispersion between pump and probe. Also, the SPM-spectral maximum shift whose origin is the self-steepening of the pulse shape should be distinguished from the self-frequency shift (Gordon, 1986) whose origin is the nonzero relaxation time of the medium.

Physically, the SPM-spectral maximum shift can be understood simply by noting that the $\chi^{(3)}$ nonlinearity does not change the total number of photons in the pulse. Thus, since the spectral anti-Stokes extent is larger than the Stokes extent, in order to conserve energy it is necessary that the peak of the spectral intensity be shifted to the Stokes side. Mathematically the SPM-spectral maximum shift can be approximated as a function of $\varepsilon V$ by

$$\Delta_m / K \approx \varepsilon V / 4. \tag{128}$$

## 2.10 Filter Transform

In this section we compute the effects of amplitude filters on ultrafast self-phase-modulated pulses (Manassah, 1988c). We examine the dependence of

the outgoing signal shape (i.e., width, amplitude, structure, and maxima positions) on the self-phase modulation parameters and filter characteristics. In particular, we show that amplitude filters can be used, under certain conditions, to compress pulses. The physical setup we are examining consists of an SPM pulse passing through an amplitude filter.

The amplitude filter transfer function is assumed to be Gaussian and is given by

$$H(K') = \exp\left\{-\left[(K' - K_f)/2\Delta_f\tau\right]^2\right\}, \tag{129}$$

where $K = \omega\tau$ and $\Delta_f$ and $\omega_f$ are, respectively, the filter spectral half-width and center frequency. The outgoing field from the filter is related to the respective ingoing field by

$$\tilde{E}_{\text{out}}(K') = H(K')\tilde{E}_{\text{in}}(K'). \tag{130}$$

Expressed as a function of the amplitude and phase of the SPM ingoing field, $E_{\text{out}}(U)$ is given by (Manassah, 1986a)

$$\begin{aligned} E^{\text{out}}(U) = \frac{E_0(\Delta_f\tau)}{\sqrt{\pi}}\exp(iK_fU)\int_{-\infty}^{\infty} dU'a(U')\exp[i\alpha(U')] \\ \times\exp[i(K - K_f)U']\exp\left[-(U' - U)^2(\Delta_f\tau)^2\right]. \end{aligned} \tag{131}$$

In the case of very large $(\Delta_f\tau)$, specifically $(\Delta_f\tau)^2 >> K(\varepsilon V)$, and using the following representation of the Dirac delta function:

$$\delta(U - U') = \lim_{y\Rightarrow 0}\frac{1}{\gamma\sqrt{\pi}}\exp\left\{-\left[\frac{(U' - U)^2}{\gamma^2}\right]\right\}, \tag{132}$$

$E^{\text{out}} \Rightarrow E^{\text{in}}$. Physically, if the filter is transparent to all frequencies, there is no modification to the pulse.

On the other hand, if $1 << (\Delta_f\tau)^2 << K\varepsilon V$, we can evaluate Eq. (131) by the stationary phase method; specifically, we can approximate $E^{\text{out}}$ by

$$\begin{aligned} E^{\text{out}}(U) \approx E_0(\Delta_f\tau)\left(\frac{2}{K}\right)^{1/2}\left\{\frac{a(U')\exp[iK(\delta + \overline{\alpha}(U')) + i\pi/4]}{[\alpha''(U')]^{1/2}}\right\} \\ \times\exp\left[-(U' - U)^2(\Delta_f\tau)^2\right] + \exp\left[-(U'' - U)^2(\Delta_f\tau)^2\right] \\ \times\left\{\frac{a(U'')\exp[iK(\delta + \overline{\alpha}(U'')) - i\pi/4]}{|\alpha''(U'')|^{1/2}}\right\}, \end{aligned} \tag{133}$$

where $U'$ and $U''$ are the roots of

$$\delta_f + \overline{\alpha}'(U) = 0 \tag{134}$$

(i.e., the stationary points of the integral),

$$K - K_f \equiv \delta_f K, \tag{135}$$

$U'$ and $U''$ are chosen such that $\alpha''(U') > 0$ and $\alpha''(U'') < 0$. Two stationary points exist for any $(-\delta_f)$ in the interval spanning the values of $\alpha'$.

Examining Eq. (133), we notice that $E^{\text{out}}$ describes two pulses centered respectively at $U'$ and $U''$ and of width $(\Delta_f\tau)$. Because $(\Delta_f\tau) \ll K\varepsilon V$, the interference term in $|E^{\text{out}}|^2$ is negligible. In the case that $(-\delta_f)$ is close to the maximum or minimum of $\overline{\alpha}'$, the two stationary points are narrowly separated and the two pulses merge into one. This limit is referred to as the one-daughter-pulse regime. It should be noted that the above results differ qualitatively from those associated with chirped Gaussian (CG) pulses. To understand these differences, we note that although the phase function $\alpha$ for SPM and CG pulses coincides in the region around the maximum of $\alpha$, the respective derivative functions $\alpha'$ and $\alpha''$ are quiet distinct. For CG pulses, $\alpha'$ is linear in $U$ and its magnitude is symmetric with respect to an axis of symmetry and $\alpha''$ is constant. For SPM pulses, as we have seen, $\alpha'$ is asymmetric and is bounded; it has two extremes. Consequently, whereas approximating $\alpha$ for an SPM pulse by the CG pulse may be acceptable in the time domain in certain specific instances, it is nearly never so in the frequency domain. The transformation by a filter is essentially a frequency, domain calculation and therefore we should expect major qualitative differences in features between the SPM and CG pulses going through the amplitude filters, namely:

1. For CG pulses Eq. (135) has a single solution, whereas for SPM pulses the same equation admits two, one, or zero solutions depending on the value of $\delta_f$. Physically, this means that while the CG pulse produces only a single daughter pulse on passing through the filter, for an SPM pulse input, two pulses are the normal output from the filter. See Figure 5.32.
2. The outputs from two filters with center frequencies equidistant from the pulse center frequency have similar shapes for a CG input pulse; however, they do no for an SPM input pulse. This asymmetry is manifested through then amplitude, shape, and width of the outgoing pulses. Compare, for example, Figure 5.32 (iv) and (x).
3. In the CG case, the time of arrival of the pulse peak for different filter center frequencies is a linear function of the detuning with the pulse carrier frequency. For SPM pulses, this curve is given by the $\alpha'$ graph previously given (see Figure 5.22). In Figure 5.32, numerically evaluated values of $|E^{\text{out}}|^2$ for different values of the filter center frequency are shown. An efficient compression scheme will concentrate on values of $K_f$ where only one narrow daughter pulse is generated (i.e., near the frequency corresponding to the spectral maximum extent). The computed values for the position of the pulse maximum and width agree to better than 10% with the approximate values of the stationary phase approximation.

For estimation purposes, in the intermediate region (i.e., $(\Delta_f\tau)^2 \sim K(\varepsilon V)$) the stationary phase approximation should be replaced by the method of steepest descent, which is applicable in case the argument of the exponent in the integrand is complex and the exponent is multiplied by a large number, in this instance $K$.

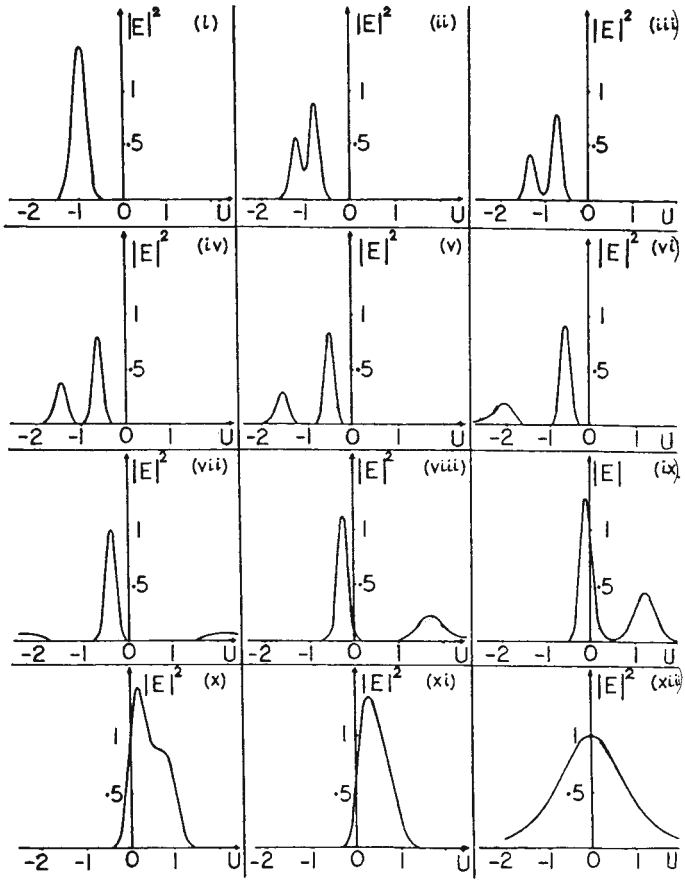


FIGURE 5.32. Field intensity outgoing from an amplitude filter, where the input is a steepened SPM signal ($K = 300$, $\varepsilon V = 0.4$, $\Delta_f \tau = 5$). All the intensities are normalized to the maximum value of the pulse resulting from a filter with the same center frequency as the incoming pulse. (i) $K - K_f = -60$; (ii) $K - K_f = -50$; (iii) $K - K_f = -40$; (iv) $K - K_f = -30$; (v) $K - K_f = -20$; (vi) $K - K_f = -10$; (vii) $K - K_f = 0$; (viii) $K - K_f = 10$; (ix) $K - K_f = 20$; (x) $K - K_f = 30$; (xi) $K - K_f = 34$; (xii) normalized $\text{sech}^2$ pulse.

In Figure 5.33 the computed magnitude of $|E^{(\text{out})}|^2$ and the compression ratio are plotted as functions of the parameter $(\Delta_f \tau)$ in the instance of optimal compression (i.e., one daughter pulse only). As can be observed, as the filter is broadened (more light passes through), the magnitude of $|E^{(\text{out})}|^2$ is increased. The compression ratio (the pulse width of $|E^{(\text{in})}|^2$ divided by the pulse width of $|E^{(\text{out})}|^2$) reaches a maximum as a function of $(\Delta_f \tau)$ and then decreases. As $(\Delta_f \tau)$ grows very large ($(\Delta_f \tau)^2 \gg K(\varepsilon V)$) the compression ratio approaches 1. An approximate value of the compression ratio can be estimated by the method of steepest descent, namely,

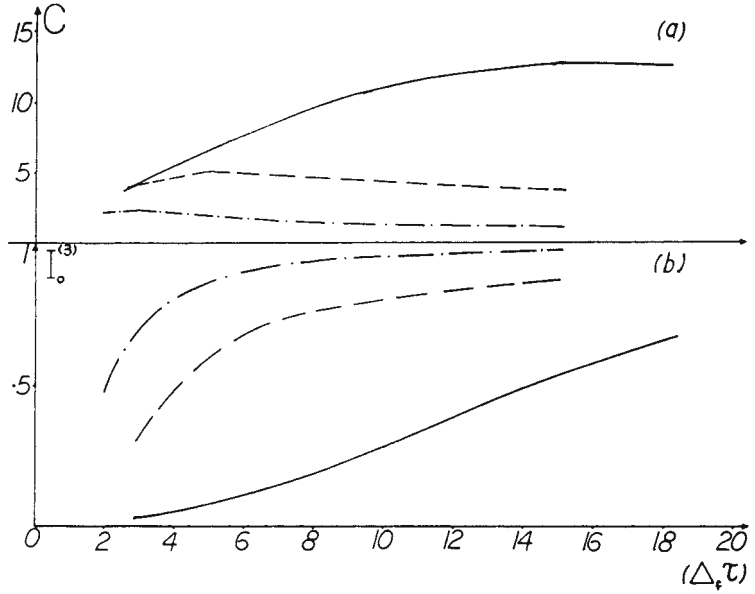


FIGURE 5.33. (a) Compression ratio and (b) intensity magnitude of the steepened SPM pulses outgoing from a filter as functions of $(\Delta_f\tau)$. (i) —$K$ = 300, $\varepsilon V$ = 0.4, $K - K_f = -60$; (ii) – · – · – $K$ = 30, $\varepsilon V$ = 0.4, $K - K_f = -6$; (iii) — —$K$ = 300, $\varepsilon V$ = 0.8, $K - K_f = -210$.

$$C^2 = (\Delta_f\tau)^2 - \frac{(\Delta_f\tau)^4\left[(\Delta_f\tau)^2 + 1\right]}{\left[(\Delta_f\tau)^2 + 1\right]^2 + g^2}, \tag{136}$$

where $g \approx Ka''(U_s)$, and $U_s$ is the average value of the two collapsing stationary points. Comparison of this estimate for $C$ with its computed values gives an error margin of less than 25% over the whole range of $(\Delta_f\tau)$.

Finally, we study the effect of laser source fluctuations on this compression scheme. In Figure 5.34 we show the effect of changing $\varepsilon V$ by ±25% which corresponds to ±25% in the ingoing laser intensity. While keeping $(\Delta_f\tau)$ constant, the effect of increasing $\varepsilon V$ is to create two daughter pulses. This can be understood by noting that the magnitude of the maximum of $\alpha'$ increases with $\varepsilon V$; therefore an increase of $\varepsilon V$ means the resurgence of two well-separated stationary points. On the other hand, a decrease in $\varepsilon V$ drastically reduces the magnitude of $E^{(\text{out})}$ but with only slight variations in the shape. Therefore, in designing a setup for pulse compression through the above scheme, the nonlinear parameters should be selected to overcompensate the positive fluctuation.

It should be emphasized that the above compression scheme produces ultrashort pulses but with center frequency different from that of the incom-

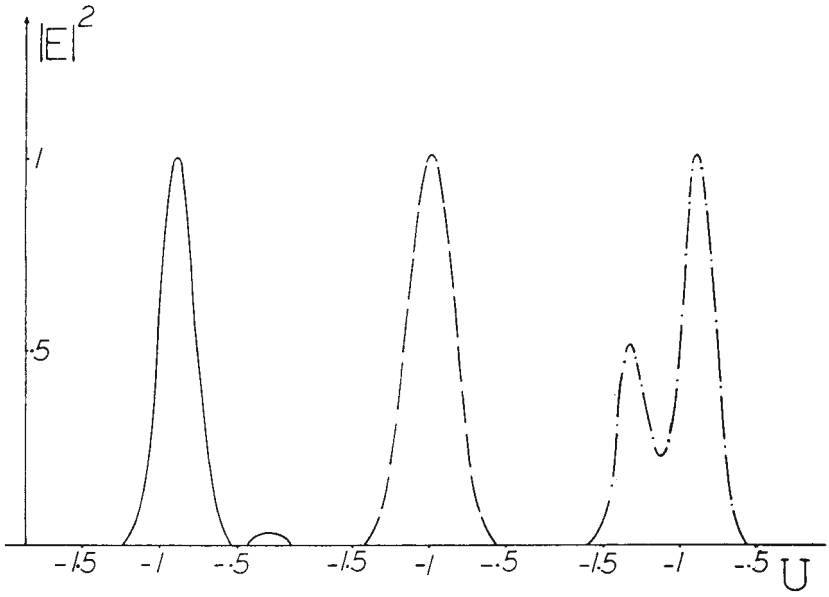


FIGURE 5.34. Effects of fluctuation in $\varepsilon V$ (i.e., laser intensity) on the shape of the filter output. ($K = 300$, $K - K_f = -60$, $\Delta_f \tau = 5$.) (i) ——$\varepsilon V = 0.3$; (ii) — — —$\varepsilon V = 0.4$; (iii) $- \cdot - \cdot - \varepsilon V = 0.5$. The peak intensities are, respectively $8.27 \times 10^{-3}$, $6.03 \times 10^{-1}$, and $2.54 \times 10^{-1}$.

ing laser signal. This scheme permits, inter alia, the generation of femtosecond pulses in new regions (such as the ultraviolet) of the spectral domain using a laser source, with center frequency in the visible.

## 3. $\chi^{(5)}$ Dispersionless Medium

So far, our calculations assumed a $\chi^{(3)}$ nonlinear medium. Higher-order leading linearity is possible; for example, in cases where the nonlinearity is due to two-quantum photogeneration of nonequilibrium carriers in certain semiconductors the medium will be a $\chi^{(5)}$ medium. In this section we treat such a case. As we will observe, all calculations made for the $\chi^{(3)}$ medium case can be repeated for the $\chi^{(5)}$ medium case. We restrict ourselves here to some illustrative examples.

### 3.1 Self-Focusing in $\chi^{(5)}$ Material

In this section we examine the combined effects of the $\chi^{(5)}$ nonlinearity and diffraction on the spatial properties of a Gaussian pulse propagating in a $\chi^{(5)}$ medium. We make the same assumptions as in Sections 1.3 and 1.4.

The envelope of the electric field obeys the equation

$$\nabla_T^2 \varepsilon - 2ik\varepsilon' + \frac{n_4 k^2}{n_0}|\varepsilon|^4 \varepsilon = 0, \tag{137}$$

where $\nabla_T^2$ is the transverse component of the Laplacian $\varepsilon' = \partial\varepsilon/\partial z$, $n_4$ is the quartic nonlinear index of refraction, and $n_0$ is the linear index of refraction of the medium.

We consider the initial condition

$$\varepsilon(r,0) = \varepsilon_0 \exp(-r^2/a^2); \tag{138}$$

that is, we are considering a CW Gaussian beam (the generalization to a Gaussian pulse can be performed using the same steps as in Sections 1.3 and 1.4). An approximate solution to Eq. (137) with the boundary condition (138), correct to order $r^2/a^2$, can be obtained through the trial solution

$$\varepsilon(r,z) = \frac{\varepsilon_0}{\bar{\omega}(z)} \exp\left[-\frac{r^2}{a^2\bar{\omega}^2(z)} - \frac{ik}{2}\rho(z)r^2 + ik\alpha(z)\right], \tag{139}$$

where the different functions have the same meaning as in Sections 1.3 and 1.4. The equations for $\bar{\omega}$, $\rho$ and $\alpha$ are given by

$$\rho = \bar{\omega}'/\bar{\omega}, \tag{140}$$

$$\alpha' = \frac{2}{k^2 a^2 \bar{\omega}^2} - \frac{n_4}{n_0} k^2 \frac{\varepsilon_0^4}{\bar{\omega}^4}, \tag{141}$$

$$\bar{\omega}'' - \frac{4}{a^4 k^2}\frac{1}{\bar{\omega}^3} + \frac{n_4}{n_0 a^2}\frac{4\varepsilon_0^4}{\bar{\omega}^5} = 0. \tag{142}$$

For the initial conditions $\bar{\omega}(z = 0) = 1$, and $\rho(z = 0) = 0$, the function $\bar{\omega}$ obeys the equation

$$\pm \int_1^{\bar{\omega}} \frac{\bar{\omega}^2 d\bar{\omega}}{\left[(1-\bar{\omega}^2)(\bar{\omega}^2 + F/2(D+\frac{1}{2}F))\right]^{1/2}\left[D+\frac{1}{2}F\right]^{1/2}} = z, \tag{143}$$

where

$$D = \frac{-4}{a^4 k^2} \quad \text{and} \quad F = \frac{4n_4}{n_0 a^2}\varepsilon_0^4. \tag{144}$$

The critical field is given by

$$\varepsilon_c = \left(\frac{2n_0}{a^2 k^2 n_4}\right)^{1/4}. \tag{145}$$

For $\varepsilon > \varepsilon_c$, the relation between $\bar{\omega}$ and $z$ is given by

$$y \equiv \frac{z}{L_d} = \frac{\sqrt{2}}{(s-1)}\left\{\frac{s}{2(s-\frac{1}{2})^{1/2}}\tilde{F}\left(\arcsin\bar{\omega}, \left(\frac{s-1}{2s-1}\right)^{1/2}\right)\right.$$
$$\left. - \left(s-\frac{1}{2}\right)^{1/2}\tilde{E}\left(\arcsin\bar{\omega}, \left(\frac{s-1}{2s-1}\right)^{1/2}\right)\right\}, \tag{146}$$

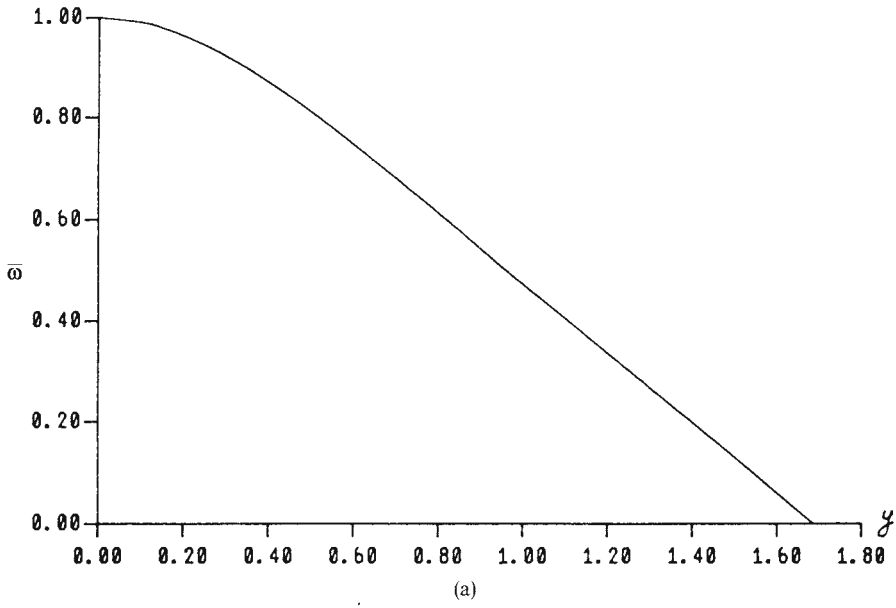


(a)

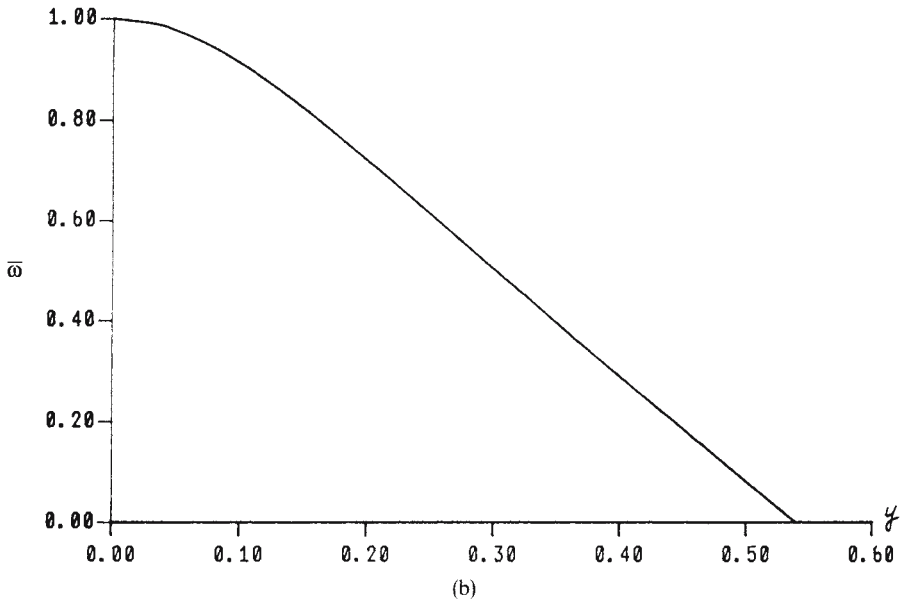


(b)

FIGURE 5.35. Normlized beam diameter of a pulse propagating in a dispersionless $\chi^{(5)}$ material, and with intensity larger than the critical intensity, plotted as a function of the distance expressed in units of the Rayleigh length. (a) $s = (1.1)^4$; (b) $s = 10$; (c) $s = (2)^4$.

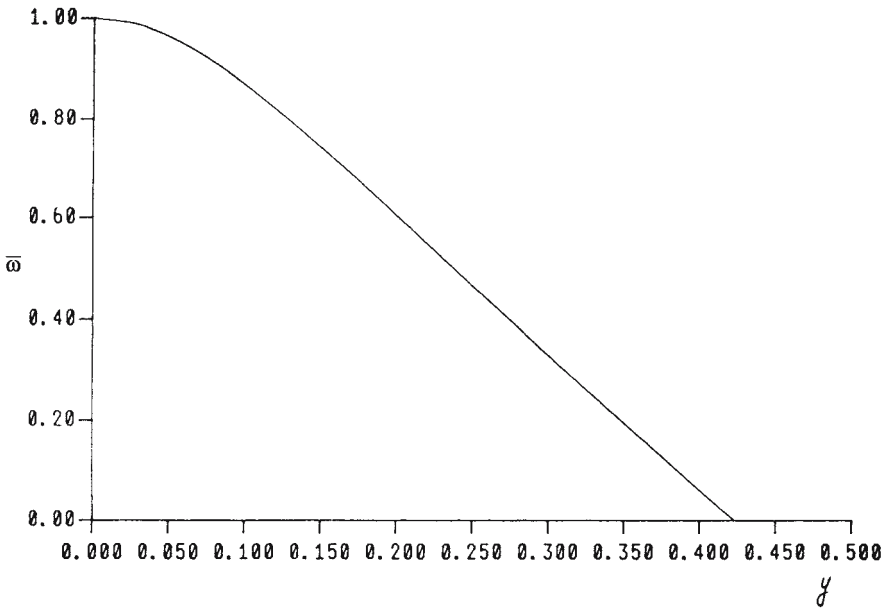


(c)

FIGURE 5.35. (*continued*)

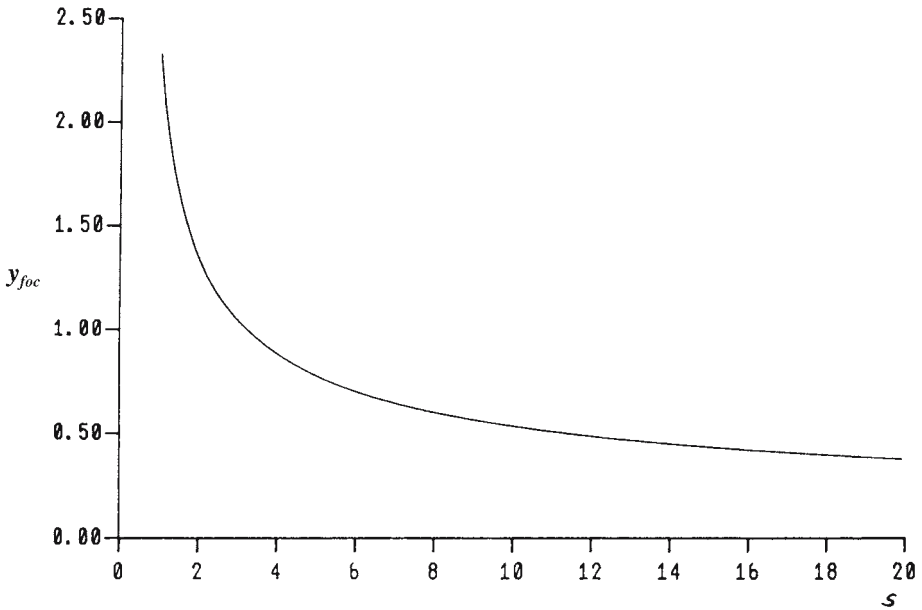


FIGURE 5.36. Normalized focusing distance in $\chi^{(5)}$ material as a function of the pulse (intensity)$^2$ measured in units of the (critical intensity)$^2$.

where $L_d$ is the Rayleigh diffraction length,

$$s = \varepsilon_0^4 / \varepsilon_c^4, \tag{147}$$

and $\tilde{F}$ and $\bar{E}$ are the elliptic integrals of the first and second kinds.

In Figure 5.35 the function $\bar{\omega}$ as a function of the normalized length $y$ is plotted for different values of $s$. In Figure 5.36 the normalized focusing distance as a function of $s$ is plotted. As can be observed, the focusing distance decreases as $s^{-1/2}$ for large $s$, that is, as the normalized (energy)$^{-1}$, whereas for a $\chi^{(3)}$ medium it decreases as (energy)$^{-1/2}$.

## 3.2 Self-Steepened Pulse in $\chi^{(5)}$ Dispersionless Medium: Plane Wave Approximation

In this section we investigate the amplitude, phase, and spectral distribution of a high-intensity pulse propagation in a $\chi^{(5)}$ dispersionless medium (Manassah and Mustafa, 1988d). We consider the case where diffraction can be neglected. Our treatment follows exactly the same steps as in Section 2.1; consequently, here we give only the results.

The Maxwell wave equation is given by

$$\nabla^2 \mathbf{E} - \frac{n_0^2}{c^2} \frac{\partial^2}{\partial t^2} \mathbf{E} = \frac{4 n_0 n_4}{c^2} \frac{\partial^2}{\partial t^2} \langle \mathbf{E} \cdot \mathbf{E} \rangle^2 \mathbf{E}, \tag{148}$$

where $n$ is the linear index of refraction and $n_4$ is the quartic nonlinear index of refraction. This wave equation can be simplified under the assumption that one component of $\mathbf{E}$ is present, the transvers variation of $\mathbf{E}$ is neglected (i.e., diffraction effects are neglected), and $\langle \mathbf{E} \cdot \mathbf{E} \rangle = |E|^2/2$. The dimensionless variables $\Phi$, $Z$, and $T$ are defined in the same manner as in Section 2, and the dimensionless nonlinear coupling constant $\varepsilon'$ is defined as

$$\varepsilon' = n_4 |E_0|^4 / n_0 \tag{149}$$

and the nonlinear wave equation form reduces to

$$\left( \frac{\partial^2}{\partial Z^2} - \frac{\partial^2}{\partial T^2} \right) \Phi = \varepsilon' \frac{\partial^2}{\partial T^2} |\Phi|^4 \Phi. \tag{150}$$

Using the variables $U$, $V$, and $K$ of Section 2 and the method of multiple scales, the quasi-linear partial differential equations for the amplitude $a$ and the phase $\alpha$ are given by

$$\frac{\partial a}{\partial V} - \frac{5}{2} \varepsilon' a^4 \frac{\partial a}{\partial U} = 0, \tag{151}$$

$$\frac{\partial \alpha}{\partial V} - \frac{\varepsilon'}{2} a^4 \frac{\partial \alpha}{\partial U} = \frac{K \varepsilon'}{2} a^4 - \frac{K \varepsilon'^2}{8} a^8. \tag{152}$$

For the initial boundary conditions

$$a(U,0) = \text{sech}(U), \tag{153}$$

$$\alpha(U,0) = 0, \tag{154}$$

the solution for the amplitude is given by

$$a^2 = \text{sech}^2\left(U + \tfrac{5}{2}\varepsilon' V a^4\right), \tag{155}$$

where $\varepsilon' V = n_4 |E_0|^{4*} z/c\tau$. The slope of the amplitude is given by

$$\frac{\partial a}{\partial U} = \frac{-a(1-a^2)^{1/2}}{10\varepsilon' V a^4 (1-a^2)^{1/2} \pm 1}, \tag{156}$$

where (–, +) corresponds respectively to $U$ (smaller, larger) than $-\frac{5}{2}\varepsilon' V$. Solution (155) derived for the amplitude under the condition of no dispersion and no absorption is valid for all values of $V < V_{\text{crit}}$, where $V_{\text{crit}}$ is the critical value of $V$ at which the optical amplitude shock develops (i.e., $\partial a/\partial U \Rightarrow \infty$). This solution is smoothed at the shock discontinuity by higher-order derivatives in Maxwell's equation. The value of $V_{\text{crit}}$ is given by

$$\varepsilon' V_{\text{erit}} = 5\sqrt{5}/32 \approx 0.349. \tag{157}$$

In Figures 5.37 and 5.38 the amplitude and its first derivative are plotted for selected $\varepsilon' V$. The self-steepening effect is as expected, more pronounced as

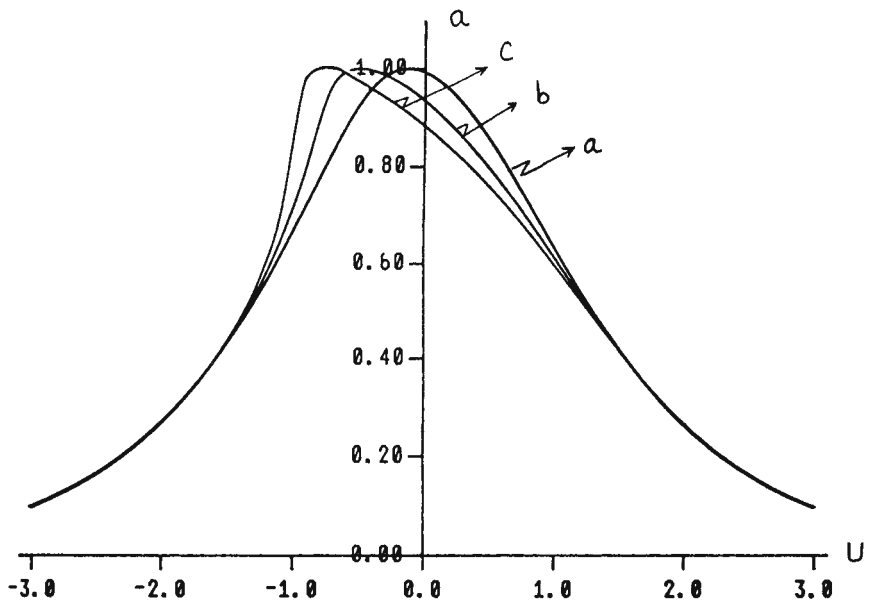


FIGURE 5.37. Steepened amplitude of a pulse propagating in dispersionless $\chi^{(5)}$ material as a function of $U$. (a) $\varepsilon' V = 0.05$; (b) $\varepsilon' V = 0.2$; (c) $\varepsilon' V = 0.34$.

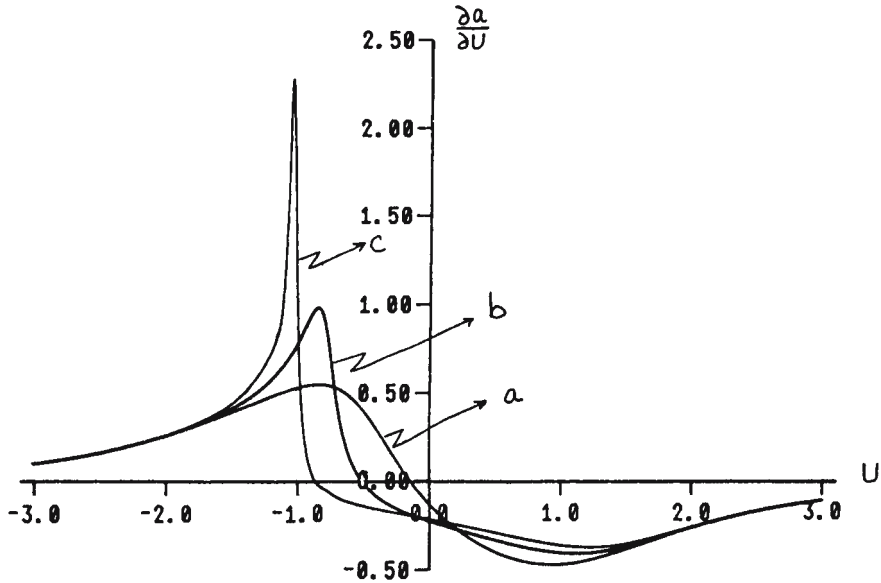


FIGURE 5.38. The $U$ partial derivative of the steepened amplitude of a pulse propagating in dispersionless $\chi^{(5)}$ material as a function of $U$. (a) $\varepsilon' V = 0.05$; (b) $\varepsilon' V = 0.2$; (c) $\varepsilon' V = 0.34$.

$\varepsilon' V$ increases, and so is the asymmetry. The position of the amplitude maximum, denoted by $U_a$, is at

$$U_a = -\tfrac{5}{2}\varepsilon' V. \tag{158}$$

The solution of the phase equation (152) obeying (158) the boundary condition of Eq. (154) is given by

$$\overline{\alpha} \equiv \frac{\alpha}{K} = -U - \frac{\varepsilon'}{2}\int_0^U a^4(p,V)dp - \frac{5\varepsilon'^2}{24}\int_0^V a^8(0,q)dq + \tanh^{-1}[\sin g(U,V)] + \frac{\varepsilon'}{6}\sin[g(U,V)] - \frac{\varepsilon'}{18}\sin^3[g(U,V)], \tag{159}$$

where

$$g(U,V) = \frac{\varepsilon'}{2}\int_0^V a^5(U,q)dq + \sin^{-1}(\tanh U). \tag{160}$$

The first partial derivative of $\alpha$ with respect to $U$ is given by

$$\frac{\partial \overline{\alpha}}{\partial U} = -1 - \frac{\varepsilon'}{6}a^4 + \frac{a}{\cos g} + \frac{\varepsilon'}{6}a(\cos g) - \frac{\varepsilon'}{6}a(\sin^2 g)(\cos g). \tag{161}$$

This quantity represents physically the normalized frequency sweep.

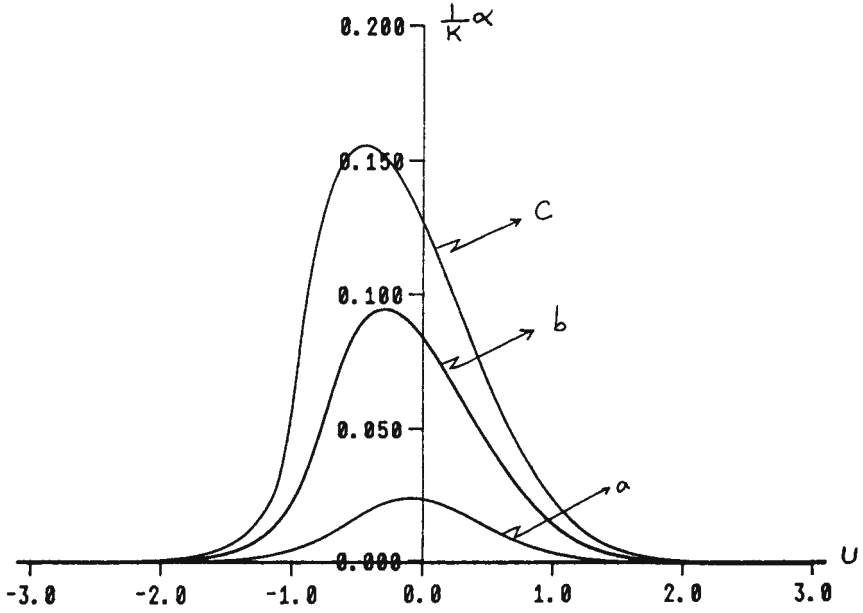


FIGURE 5.39. Normalized phase of a steepened pulse propagating in dispersionless $\chi^{(5)}$ material as a function of $U$. (a) $\varepsilon' V = 0.05$; (b) $\varepsilon' V = 0.2$; (c) $\varepsilon' V = 0.34$.

The second partial derivative of $\alpha$ with respect to $U$ is given by

$$\frac{\partial \bar{\alpha}}{\partial U} = \frac{\partial a}{\partial U}\left[-\frac{2\varepsilon'}{3}a^3 + \frac{1}{\cos g} + \frac{\varepsilon}{6}\cos g - \frac{\varepsilon'}{6}\sin^2 g \cos g\right] + a^2 \frac{\sin g}{\cos^2 g}$$
$$-\frac{\varepsilon}{6}a^2 \sin g + \frac{\varepsilon}{6}a^2 \sin^3 g - \frac{\varepsilon}{3}a^2 \sin g \cos^2 g. \tag{162}$$

In Figures 5.39, 5.40, and 5.41, respectively, are plotted the phase and its derivatives $\partial\bar{\alpha}/\partial U$ and $\partial^2\bar{\alpha}/\partial U^2$. We note the following:

1. The phase is asymmetric with respect to the $U$ axis. This is a result of the amplitude self-steepening.
2. The position and the value of the phase maximum, denoted respectively by $U_\alpha$ and $\alpha_M$, are given by

$$U_\alpha \approx -\tfrac{3}{2}\varepsilon' V, \tag{163}$$

$$\alpha_M \approx \frac{K}{2}\varepsilon' V. \tag{164}$$

3. The maxima of the amplitude and the phase, as can be deduced by comparing Eqs. (158) and (163), are shifted with respect to each other. This

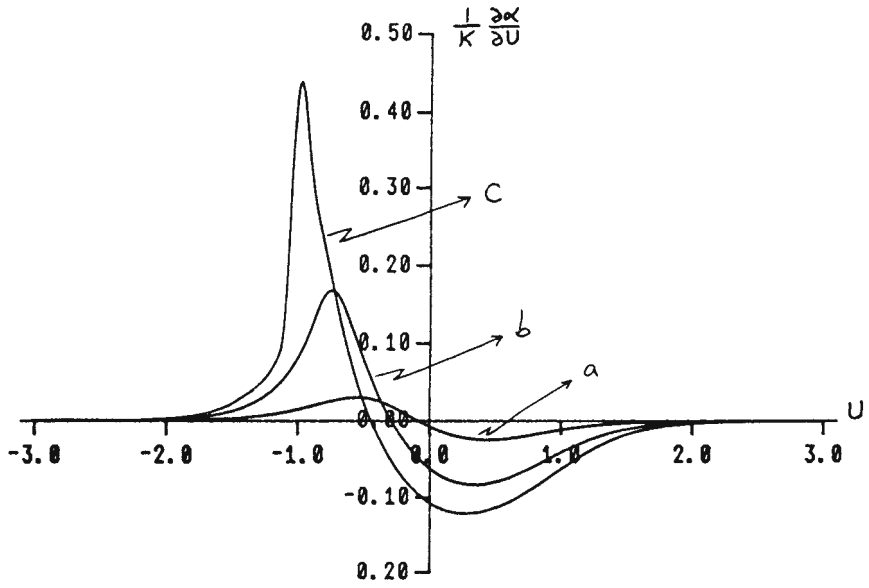


FIGURE 5.40. Normalized frequency sweep (slope of the phase) of a steepened pulse propagating in $\chi^{(5)}$ dispersionless medium as a function of $U$. (a) $\varepsilon' V = 0.05$; (b) $\varepsilon' V = 0.2$; (c) $\varepsilon' V = 0.34$.

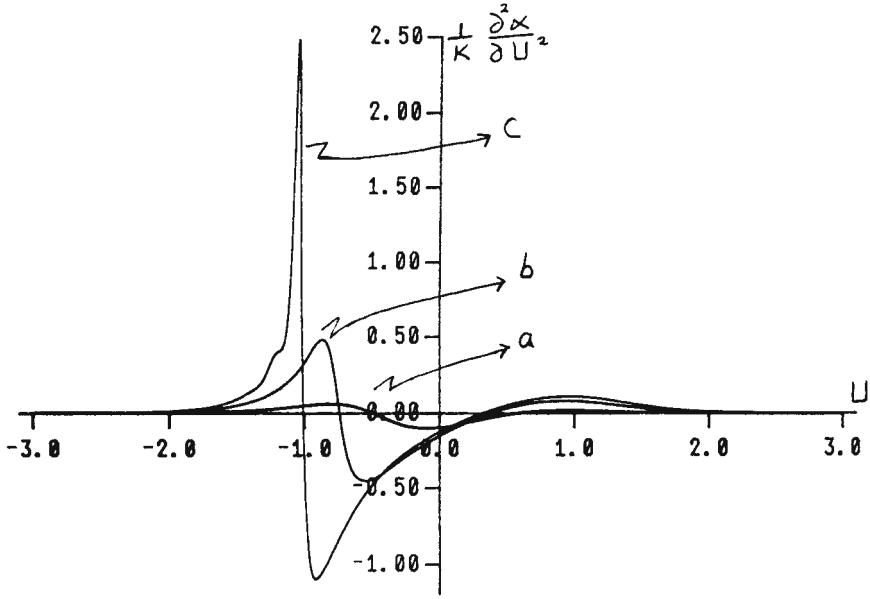


FIGURE 5.41. Normalized second partial derivative of the phase of a steepened pulse propagating in $\chi^{(5)}$ dispersionless medium as a function of $U$. (a) $\varepsilon' V = 0.05$; (b) $\varepsilon' V = 0.2$; (c) $\varepsilon' V = 0.34$.

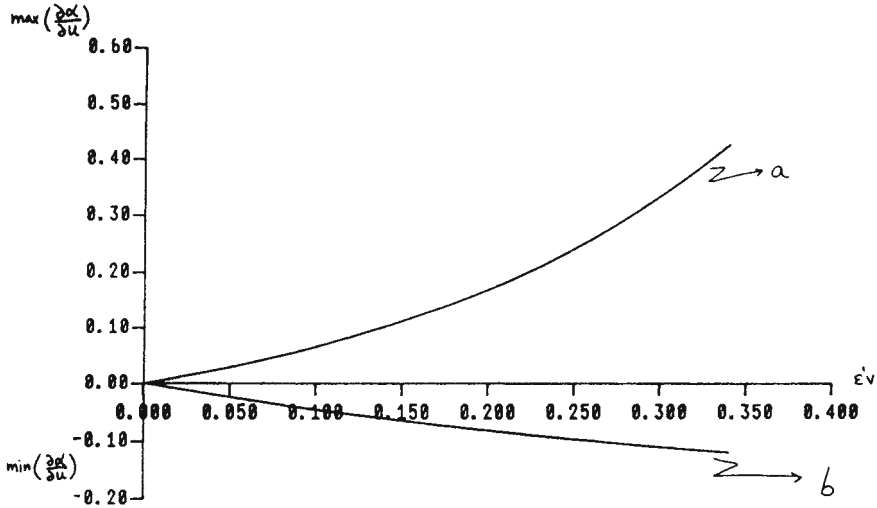


FIGURE 5.42. Extrema of the frequency sweep of a steepened pulse propagating in $\chi^{(5)}$ dispersionless medium as a function of $\varepsilon' V$. (a) Maxima; (b) minima.

results in a shift of the minima of the interference pattern as shown is Section 2.8.

4. The derivative of the phase is asymmetric with respect to the $U$ axis. This results in an asymmetry of the spectral distribution between the Stokes and anti-Stokes portions of the spectrum.
5. The absolute value of the maximum of $\partial\alpha/\partial U$ is always bigger than that corresponding to its minimum value; therefore the anti-Stokes extent is larger than the Stokes extent of the spectrum. This inequality also leads to having for $x > 0$ the left peak of the Fourier transform of the interference pattern closer (in the notation of Section 2.8) to $x = 1$ than the right peak.

In Figure 5.42 we plot the values of $\max(\partial\alpha/\partial U)$ and $\min(\partial\alpha/\partial U)$ as functions of $\varepsilon' V$. The asymmetry in their values for the same $(\text{intensity})^2$ is clear. In Figure 5.43 we plot the function $F(x)$ for this case; the asymmetry in the values of the extrema is again exhibited. Notice that a peak appears at $x = 1$. This peak is associated with the spectral peak at the center frequency, as will be seen later.

The spectral distributions of the resulting supercontinuum obtained by taking the amplitude squared of the Fourier transform of the electric field are shown in Figure 5.44. We note that:

1. The detailed features of the calculated spectral extents conform very well with the estimated values deduced from the values of $\max(\partial\alpha/\partial U)$ and $\min(\partial\alpha/\partial U)$.

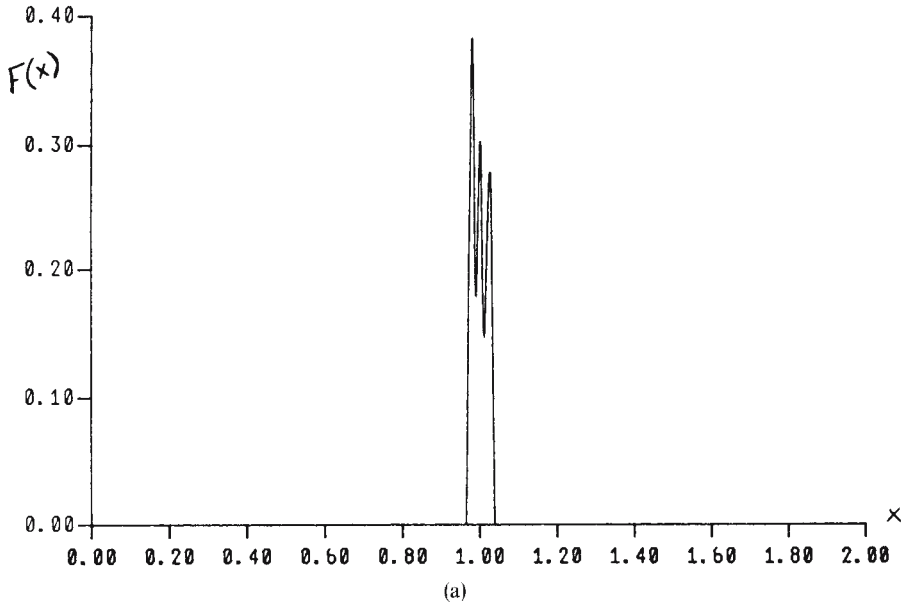


(a)

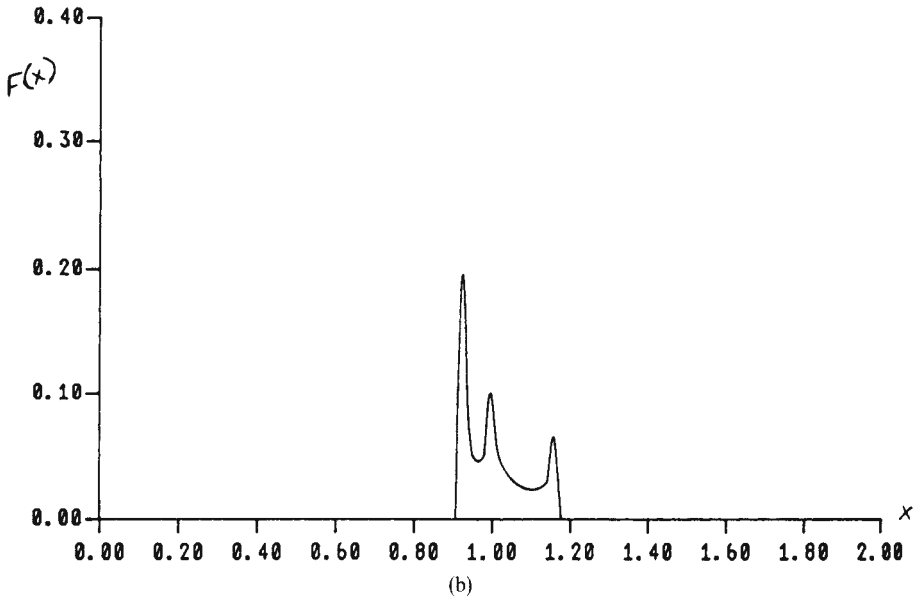


(b)

FIGURE 5.43. Envelope of the Fourier transform of the intensity distribution of a Young interferometer having as input a steepened pulse outgoing from a dispersionless $\chi^{(5)}$ material. (a) $\varepsilon' V = 0.05$; (b)$\varepsilon' V = 0.2$; (c) $\varepsilon' V = 0.34$.

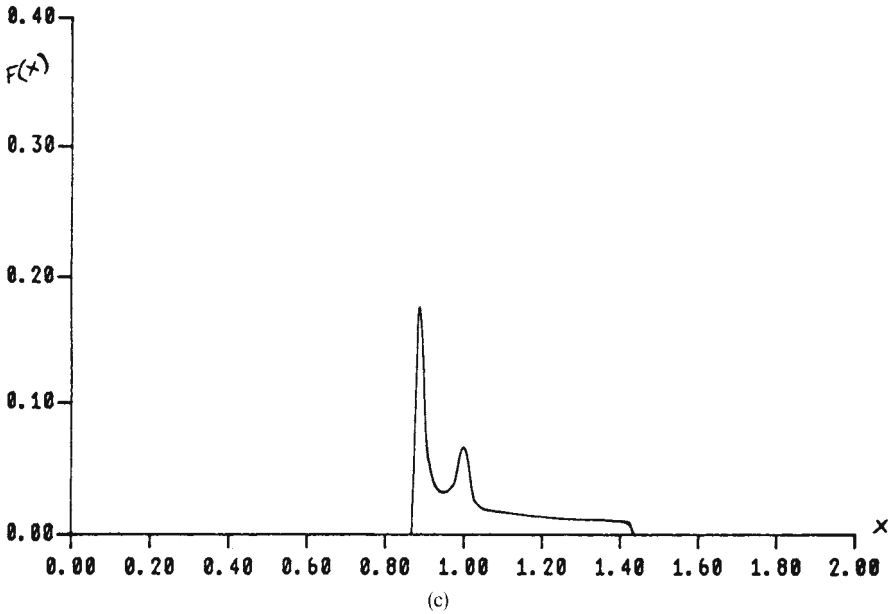


(c)

FIGURE 5.43. (*continued*)

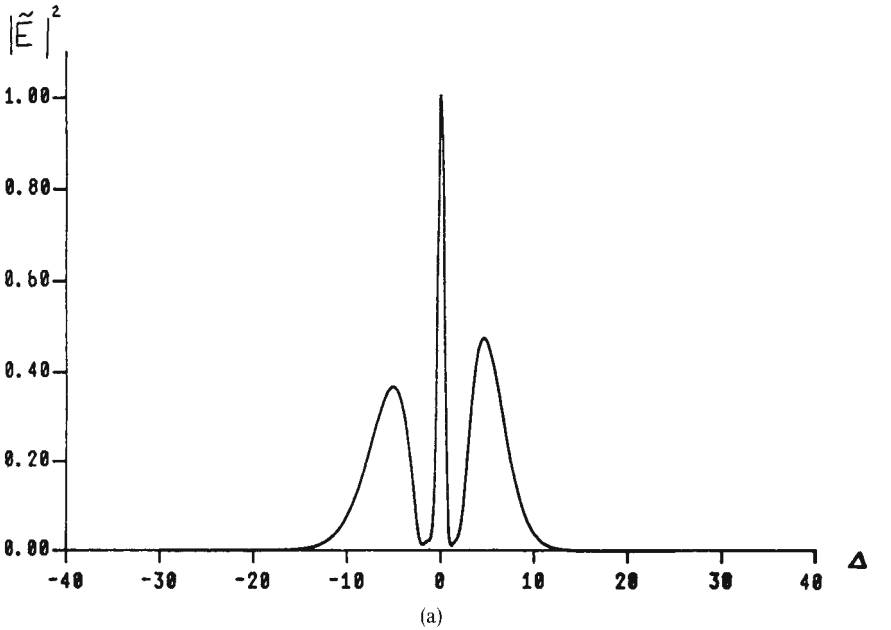


(a)

FIGURE 5.44. Spectral distribution of a steepened pulse outgoing from a dispersionless $\chi^{(5)}$ material. The zero of $\Delta$ is the center frequency of the original pulse. (a) $\varepsilon' V = 0.05$; (b) $\varepsilon' V = 0.2$; (c) $\varepsilon' V = 0.34$.

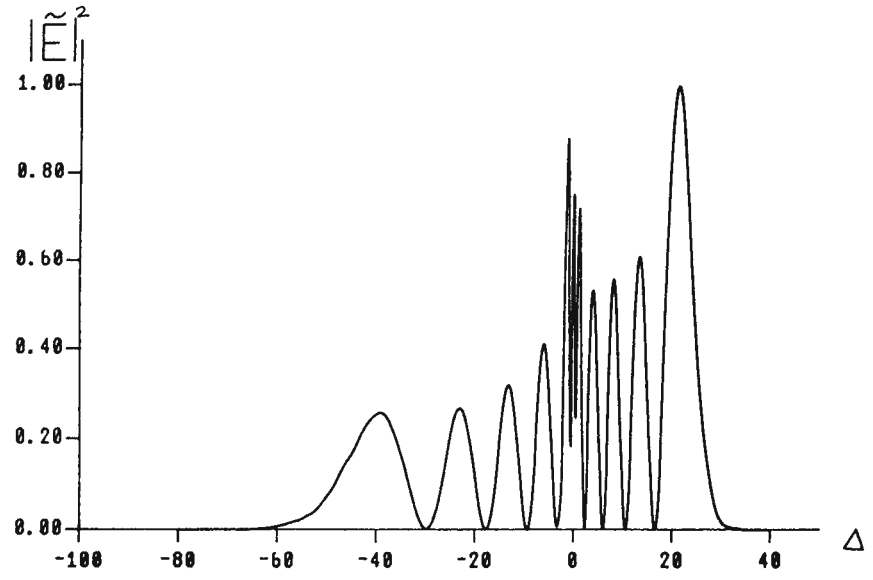


(b)

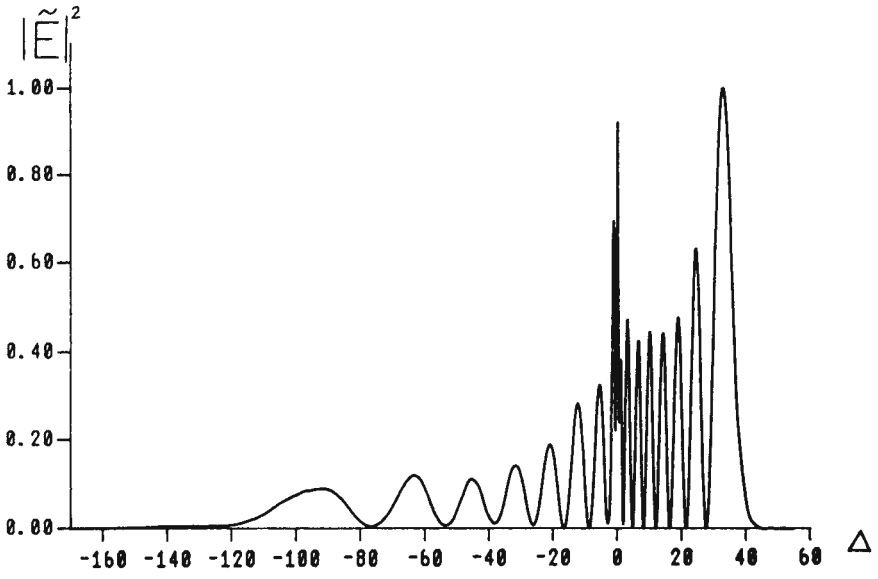


(c)

FIGURE 5.44. (*continued*)

2. The existence of a spectral peak on the edge of the Stokes portion of the spectrum is a result of the shallowness of the $\partial\alpha/\partial U$ curve near its minimum value.
3. The number of oscillations in the spectral distribution is estimated by the method of the stationary phase approximation to be given by

$$\alpha_M/\pi \approx K\varepsilon' V/2\pi \tag{165}$$

and is the close agreement with the numerically computed values.
4. The spectral shape has a peak at the center frequency, a new feature not present in the $\chi^{(3)}$ medium supercontinuum.

$\chi^{(5)}$ in the presence of self-steepening and material relaxation is treated in the appendix at the end of the chapter.

## 4. Induced Nonlinear Effects

In this section we study the geometric, time, and frequency domain effects on a pulse (probe) propagating in a $\chi^{(3)}$ medium due to the presence of a strong pump.

### 4.1 Induced-Phase Modulation

When a weak probe pulse is sent together with a pump, the phase of the probe pulse at different frequencies can be modulated by the time variation of the nonlinear index of refraction originating from the primary intense pulse (Manassah, 1987b). This process is defined as induced-phase modulation (IPM). If we denote by $A$ and $B$ the envelopes of the pump and probe, respectively, their differential equations are given for the lowest order of the quasi-linearized model (i.e., the pump shape distortion due to group velocity dispersion is neglected, higher derivatives beyond the first derivative of the index of refraction are neglected, the self-steepening effect is neglected, and the transverse variation of the envelope is neglected) by

$$\frac{\partial A}{\partial z} + \frac{1}{v_a}\frac{\partial A}{\partial t} = i\gamma_a\left[|A|^2 + 2|B|^2\right]A, \tag{166}$$

$$\frac{\partial B}{\partial z} + \frac{1}{v_b}\frac{\partial B}{\partial t} = i\gamma_b\left[|B|^2 + 2|A|^2\right]B, \tag{167}$$

where $\gamma_{a,b} = n_2 k_{a,b}/2n_0$, $n_0$ is the linear index of refraction, $n_2$ is the quadratic (Kerr) index of refraction, $\gamma_a$ is the conventional SPM coefficient (see Section 1.1), and $v_a$ and $v_b$ are respectively the group velocities of the pump and the probe in the medium. We assume that the probe and pump durations are given by $\tau_b$ and $\tau_a$ and we introduce the normalized probe comoving coordinate $\overline{U}$ defined by

$$\overline{U} = \frac{1}{\tau_a}\left(t - \frac{z}{v_b}\right), \tag{168}$$

where the normalization is with respect to the pump duration. Denoting by $F$ and $G$ the pulse shape functions for the pump and probe, the initial conditions for the amplitude and phase of each pulse are given by

$$a(0,t) = a_0 F[(t - t_0)/\tau_a], \tag{169}$$

$$\alpha(0,t) = 0, \tag{170}$$

$$b(0,t) = b_0 G(t/\tau_b), \tag{171}$$

$$\beta(0,t) = 0, \tag{172}$$

where $t_0$ is the initial displacement of maxima between the pump and probe. The solutions of Eqs. (166) and (167), in the case that $a \gg b$, obeying the boundary conditions (169) through (172) are given by

$$a(z,t) = a_0 F\left[\left(t - t_0 - \frac{z}{v_a}\right)\Big/ t_a\right], \tag{173}$$

$$\alpha(z,t) = \gamma_a a_0^2 F^2\left[\left(t - t_0 - \frac{z}{v_a}\right)\Big/ \tau_a\right] z, \tag{174}$$

$$b(z,t) = b_0 G\left[\left(t - \frac{z}{v_b}\right)\Big/ \tau_b\right], \tag{175}$$

$$\beta(z,t) = 2\gamma_b a_0^2 \psi(z,t), \tag{176}$$

where

$$\psi(z,t) = \int_0^z F^2\left\{\left[t - t_0 - \frac{z}{v_b} - z'\left(\frac{1}{v_a} - \frac{1}{v_b}\right)\right]\Big/ \tau_a\right\} dz'. \tag{177}$$

If the pump form function is hyperbolic secant, then

$$\psi = \frac{1}{\eta}\left[\tanh\left(\frac{t - t_0}{\tau_a} - \frac{z}{\tau_a v_b}\right) - \tanh\left(\frac{t - t_0}{\tau_a} - \frac{z}{\tau_a v_b} - \eta z\right)\right], \tag{178}$$

where

$$\eta = \left(\frac{1}{v_a} - \frac{1}{v_b}\right)\Big/ \tau_a. \tag{179}$$

$\eta$ is the inverse walk-off distance between the pump and probe over the duration of the pump pulse. In the $\bar{U}$ notation, the functions $a$, $\alpha$, $b$, and $\beta$ reduce to

$$a = a_0 \mathrm{sech}[\overline{\mathrm{U}} - \eta \mathrm{z} - \mathrm{T}_0], \tag{180}$$

$$\alpha = (\gamma_a a_0^2 z)\mathrm{sech}^2[\overline{U} - \eta z - T_0], \tag{181}$$

$$b = b_0 G(\sigma \overline{U}), \tag{182}$$

$$\beta = (2\gamma_b a_0^2 z)\psi = \frac{(2\gamma g_b a_0^2 z)}{\eta z}[\tanh(\overline{U} - T_0) - \tanh(\overline{U} - T_0 - \eta z)], \tag{183}$$

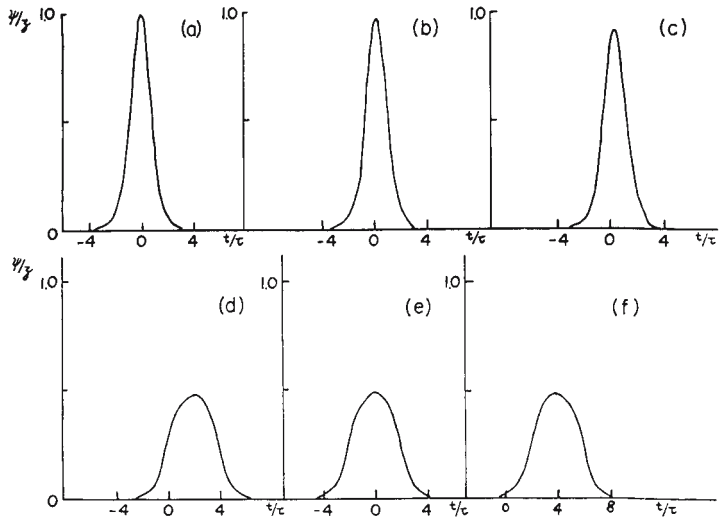


FIGURE 5.45. Induced phase function $\psi$. (a) $\eta = 0$, $T_0 = 0$; (b) $\eta z = 1/2$, $T_0 = 0$; (c) $\eta z = 1$, $T_0 = 0$; (d) $\eta z = 4$, $T_0 = 0$; (e) $\eta z = 4$, $T_0 = -2$; (f) $\eta z = 4$, $T_0 = 2$.

where $T_0 = t_0/\tau_a$ and $\tau_a \equiv \sigma\tau_b$. It is worth noting that in this model the pump only modulates the probe; that is, there is no energy transfer between the two pulses. In Figure 5.45 the phase function $\psi$ is plotted for different values of the parameters.

In the frequency domain, the electric field for the probe signal is proportional to

$$\tilde{E}_B(\Delta) = \frac{1}{2\pi}\int_{-\infty}^{\infty} b(\overline{U})\exp[i\beta(\overline{U}) + i\Delta\overline{U}]d\overline{U}, \tag{184}$$

where $\Delta = (\omega' - \omega)\tau_a$ and $\omega$ is the probe center frequency. The spectral intensity is proportional to $|\tilde{E}_B(\Delta)|^2$. In Figure 5.46 the spectral intensity of the probe is plotted for different values of the parameters $\eta Z$ and $T_0$ in the case that $\sigma = 1$.

The spectral extent of the probe due to IPM can be obtained by the stationary phase method; in essence:

$$\overline{\Delta} \approx \left(\frac{\partial\beta}{\partial\overline{U}}\right)_{\max} - \left(\frac{\partial\beta}{\partial\overline{U}}\right)_{\min}, \tag{185}$$

where

$$\overline{\Delta} = \Delta_1 - \Delta_2 \tag{186}$$

and the values of $\Delta_1$ and $\Delta_2$ are given by

$$\Delta_{1,2} = \frac{2\gamma_b a_0}{\eta}[\operatorname{sech}^2(\overline{U}_{1,2} - \eta l) - \operatorname{sech}^2(U_{1,2})], \tag{187}$$

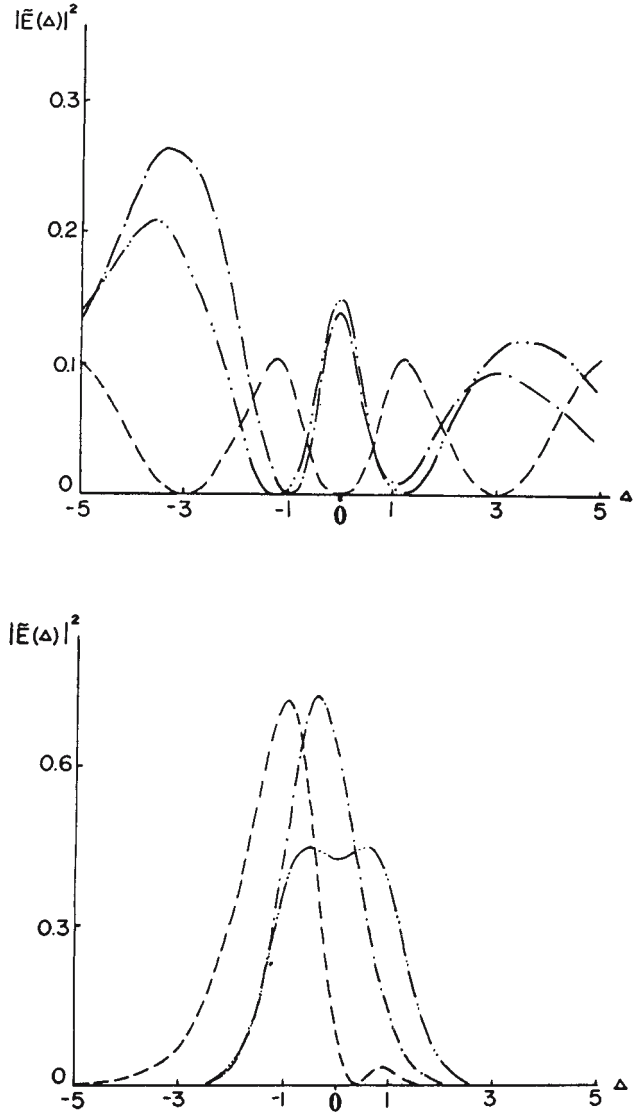


FIGURE 5.46. Spectral distribution of the probe. The probe and pump have the same initial width. *Top figure*: (a) – – $\eta z = 0$, $T_0 = 0$; (b) – · · – $\eta z = 1/2$, $T_0 = 0$; (c) – · – $\eta z = 1$, $T_0 = 0$; *Bottom figure*: (a) – – $\eta z = 4$, $T_0 = 0$; (b) – · · – $\eta z = 4$, $T_0 = -2$; (c) – · – $\eta z = 4$, $T_0 = 2$. [$a_0^2 \gamma z = 5\pi/2$.]

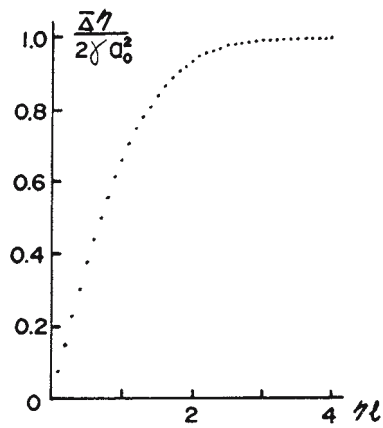


FIGURE 5.47. Induced frequency extent as a function of fiber length.

where $l$ is the length of the material and $\bar{U}_{1,2}$ are the roots of the transcendental equation

$$\frac{\sinh(\bar{U}-\eta l)}{\cosh^3(\bar{U}-\eta l)}=\frac{\sinh(\bar{U})}{\cosh^3(\bar{U})}. \tag{188}$$

In Figure 5.47 the spectral extents are plotted as functions of $\eta l$. We note that the spectral extent of the probe-induced broadening increases linearly with the length of the sample for small walk-off; however, it saturates for values of $\eta l > 2$. Physically, twice the walk-off distance measures the distance over which the pump and probe have some overlap; consequently it acts as a maximum effective length for material as far as induced-phase modulation is concerned.

In conclusion, the following features are observed in the induced supercontinuum spectrum, in the presence of walk-off between pump and probe:

1. There is asymmetry in the spectral distribution between the Stokes and anti-Stokes sides.
2. The spectral intensity maximum is shifted to the Stokes side of the probe center frequency for $\eta > 0$ and to the anti-Stokes side for $\eta < 0$. This effect is called induced frequency shift.
3. The spectral distributions for equal magnitude but opposite sign $\eta$ are symmetric with regard to the $\Delta$ axis.
4. The spectral distribution extent saturates for $l \gg \eta^{-1}$.

## 4.2 Raman Amplification and Induced-Phase Modulation

In optical fiber transmission one encounters the situation where Raman amplification and induced-phase modulation are simultaneously present (Manassah and Cockings, 1987a). In this section we study this combined effect to the lowest order approximation. The modifications to be made to Eqs. (166) and (167) are that an amplification term should be added to the

probe amplitude equation and the $\gamma$'s should be multiplied by 1/2 to take into account the value of the overlap integrals of the transverse distribution of the pump and signal over the fiber cross section. The differential equation for the probe amplitude is given by

$$\frac{\partial b}{\partial z} + \frac{1}{v_b}\frac{\partial b}{\partial t} = \frac{\delta}{2}a^2 b, \tag{189}$$

where $\delta$ is the Raman loss coefficient. The expressions for $a$, $\alpha$, and $\beta$ are the same as those given by Eqs. (180), (181), and (183) with $\gamma \Rightarrow \gamma/2$ and Eq. (182) is modified to read

$$b = b_0 G(\sigma \overline{U}) \exp\left[\frac{\delta a_0^2}{2}\psi\right]. \tag{190}$$

Here we treat the case $\sigma = 1$. The time of arrival of the peak of the pump at length $l$ of the fiber is denoted by $\overline{U}_1$ and is given by

$$\overline{U}_1 = T_0 + \eta l. \tag{191}$$

With no pump present, the time of arrival of the probe peak is denoted by $\overline{U}_2$ and is given by

$$\overline{U}_2' = 0. \tag{192}$$

In the presence of the pump, the coordinate of the probe peak, denoted by $\overline{U}_2$, is obtained by finding the maximum of $b$, which reduces to solving the transcendental equation

$$\tanh \overline{U} = \frac{\delta a_0^2}{2\eta}\left[\operatorname{sech}^2(\overline{U} - T_0) - \operatorname{sech}^2(\overline{U} - T_0 - \eta l)\right]. \tag{193}$$

We plot the values of $\overline{U}_1 - \overline{U}_2$ and of $b(\overline{U}_2)$ in the three following experimentally implementable cases:

1. $\eta l$ fixed, $T_0 = 0$, and $a_0^2$ (intensity of the pump) is changed—see Figure 5.48a.
2. $a_0^2$ fixed, $T_0 = 0$, and $l$ is changed—see Figure 5.48b.
3. $\eta l$ fixed, pump intensity fixed, and $T_0$ is varied. In Figure 5.49 the pulse shape and position and in Figure 5.50 the maximum magnitude of the probe are plotted for this case.

The outstanding features observed are

1. a pull between the pump and probe pulses, that is, $|\overline{U}_1 - \overline{U}_2| < |\overline{U}_1 - \overline{U}'_2|$;
2. a time ordering with the pump pulse out last at the exit, if the initial time delay between the two pulses is smaller than $t_{\text{correl}}$, where $t_0 < t_{\text{correl}}$, and $t_{\text{correl}}$ is the region of strong distortion of the signal;
3. a long time correlation (many pulse widths) in the pump-probe system;
4. an increase in the intensity of the pump increasing the pull;
5. the probe pulse perhaps splitting for $t_0 > t_{\text{correl}}$ and producing a daughter pulse, that is, a secondary pulse of weak amplitude;

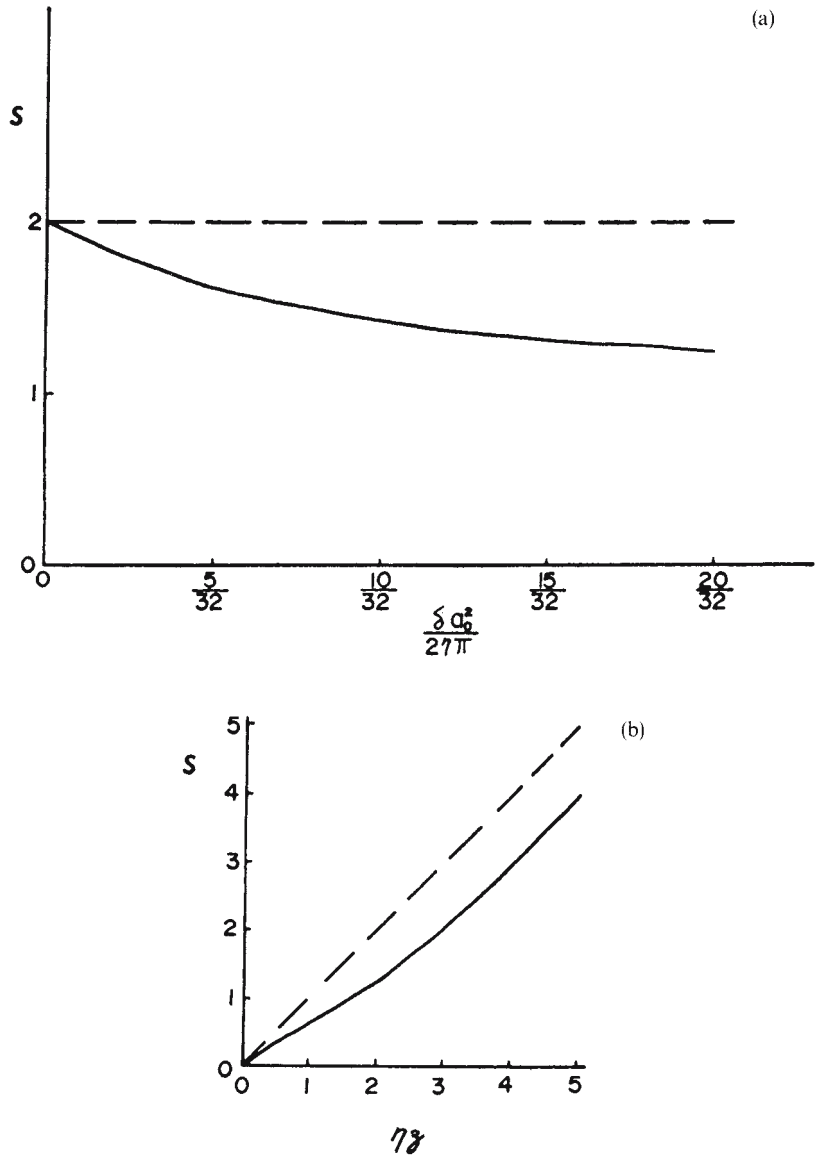


FIGURE 5.48. Time delay between pump and Raman pulses, at exit $S = \overline{U}_1 - \overline{U}_2$. (Solid line) Pump and signal system; (dashed line) noninteractive signal and pump. (a) $\eta z = 2$, $T_0 = 0$; (b) $\delta a_0/2\eta = (5\pi)/8$, $T_0 = 0$.

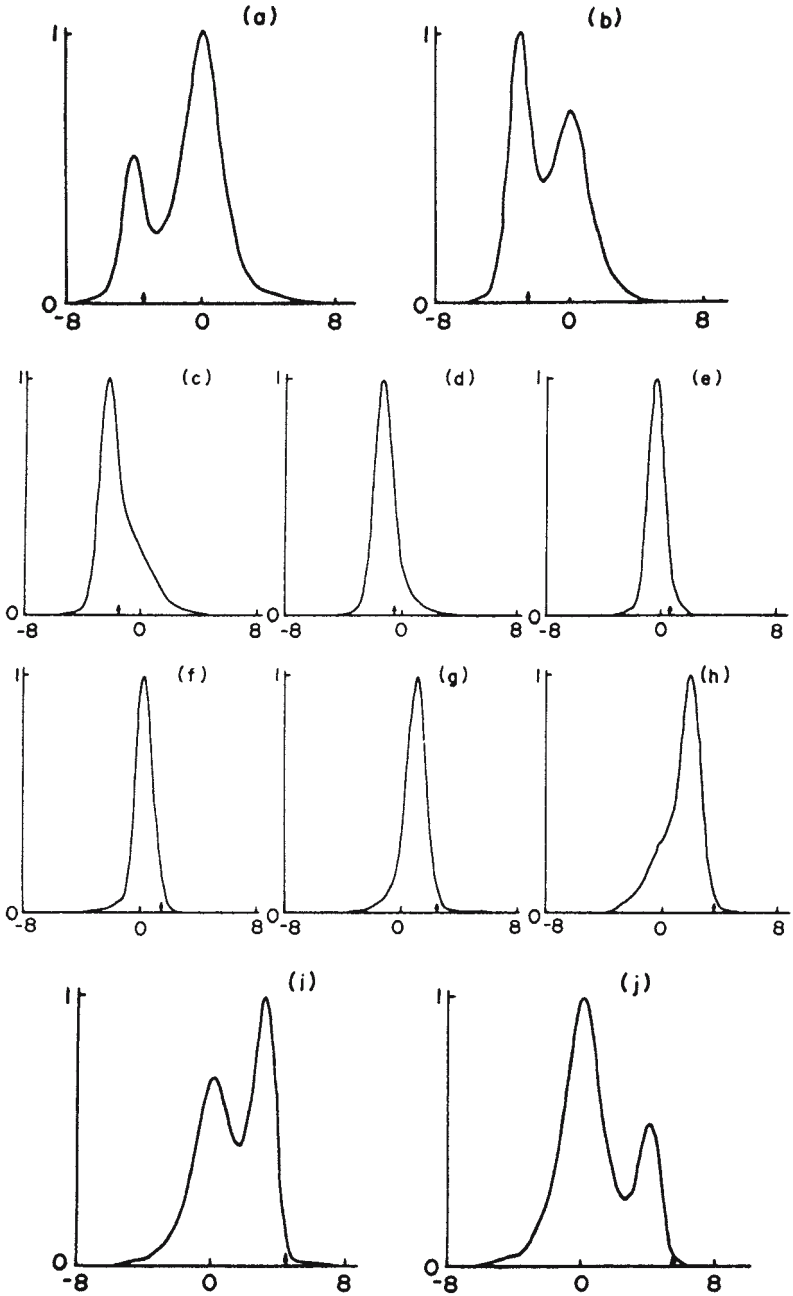


FIGURE 5.49. Normalized outgoing Raman probe amplitude ($b/b_{\max}$) for different initial delay times between probe and pump. The arrow indicates the position of the outgoing pump maximum. In the absence of a pump, the probe maximum would have been in all these graphs at $T = 0$. Parameters for all cases are $\eta z = 2$, $\delta a_0^2/2\eta = (5\pi)/8$. (a) $T_0 = -5.5$; (b) $T_0 = -4.5$; (c) $T_0 = -3.5$; (d) $T_0 = -2.5$; (e) $T_0 = -1.5$; (f) $T_0 = -0.5$; (g) $T_0 = 0.5$; (h) $T_0 = 1.5$; (i) $T_0 = 2.5$; (j) $T_0 = 3.5$.

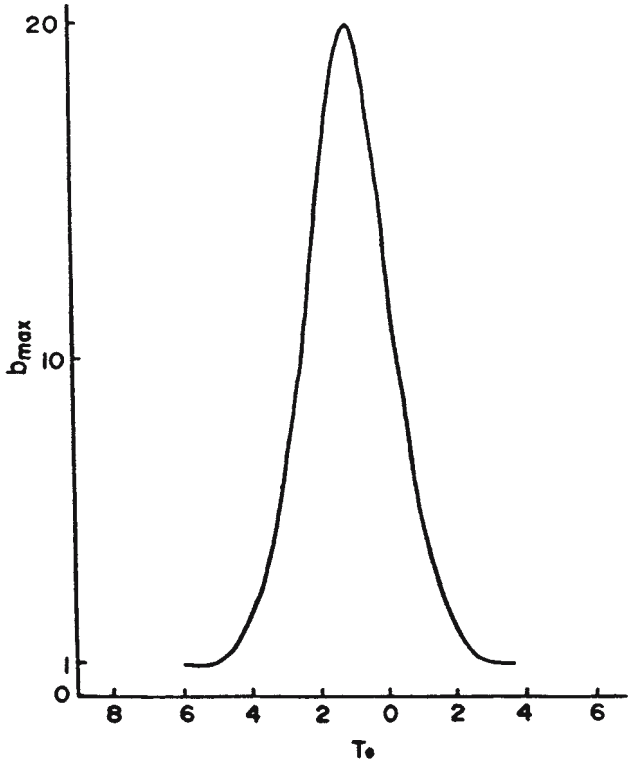


FIGURE 5.50. Maximum amplitude of the Raman signal as a function of initial delay time $T_0$. $\eta z = 2$, $\delta a_0^2/2\eta = 5\pi/8$.

6. the amplification curve being a narrow function of the initial time lag between pump and probe; and
7. the amplification saturating as the length of the fiber exceeds a few walk-off distances.

## 4.3 Induced Pulse Compression

In Section 1.2 we discussed the fiber-grating compressor. In this section we study the possibility of using induced-phase modulation as the source of the chirp (Manassah, 1988a, 1988b). Walk-off effects between pump and probe, discussed in Section 4.1, are incorporated in this analysis. For computational simplicity we assume that the probe and pump pulse shapes are given, respectively, by a Gaussian and a hyperbolic secant.

In Figure 5.51a the derivative of the probe normalized phase with respect to $\overline{U}$ is given for different values of $\eta z$. The values of the extrema of this function determine the induced spectral extent of the probe. As can be

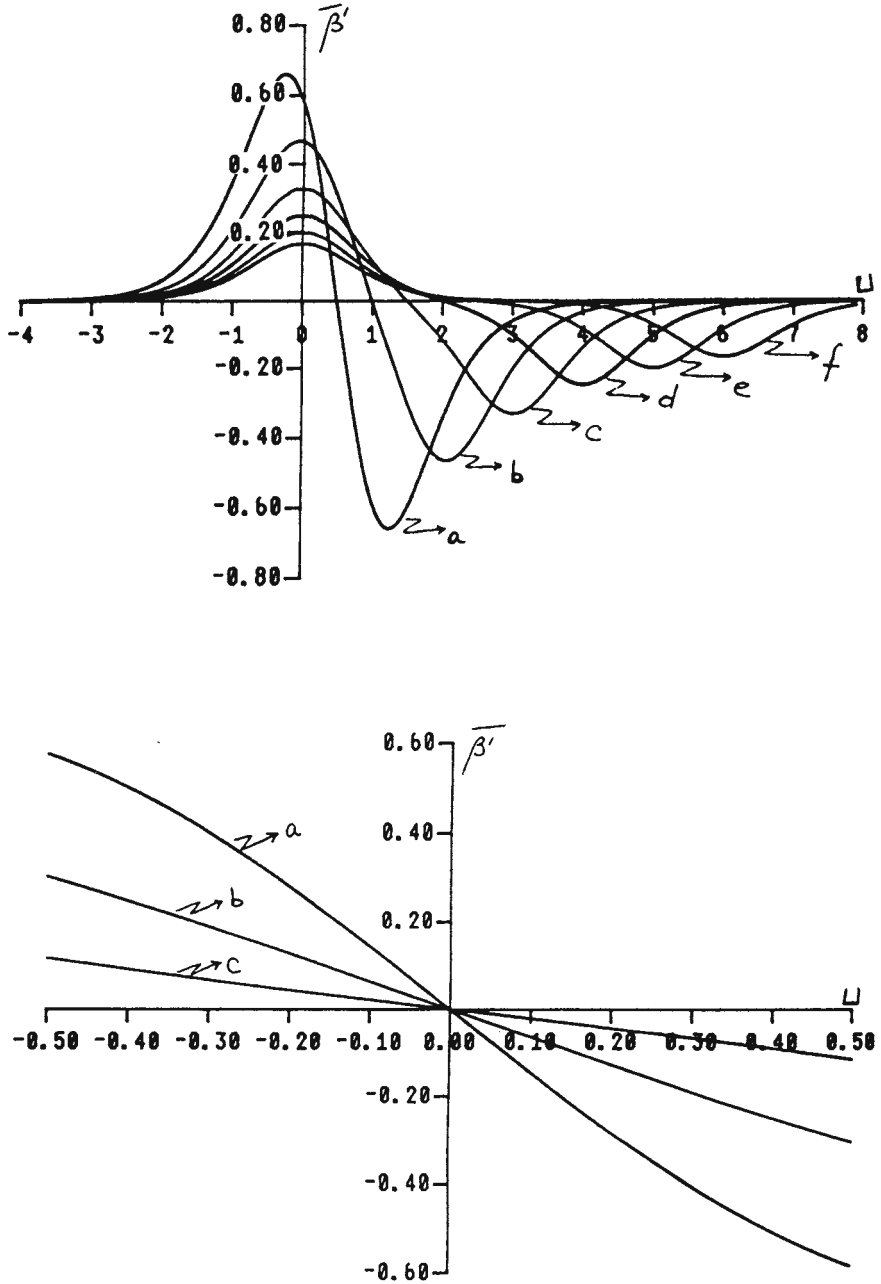


FIGURE 5.51. *Top*: Induced frequency sweep (i.e., derivative of the induced phase) for different $\eta z$ and $T_0 = 0$. (a) $\eta z = 1$; (b) $\eta z = 2$; (c) $\eta z = 3$; (e) $\eta z = 5$; (f) $\eta z = 6$. *Bottom*: Induced frequency sweep near $\overline{U} = 0$. (a) $\eta z = 1$; (b) $\eta z = 2$; (c) $\eta z = 3$. Best fits for the slopes are, respectively, –1.44, –0.64, and –0.22.

observed, for a specific material length $z$, the induced spectral extent decreases with increasing $\eta$. Physically, an increase in the value of $\eta$ corresponds to a shorter spatial overlap between probe and pulse and consequently to a smaller induced-phase modulation. It should also be noted that for $1 < \eta z < 3$ and for $T_0 = -\eta z/2$, $\psi'$ is linear in $\overline{U}$ in the region around $\overline{U} = 0$ and is symmetric with respect to this point. In Figure 5.51B $\psi'$ is plotted for such cases. Consequently, if the probe pulse duration is much shorter than the pump pulse duration (i.e., the probe amplitude range is entirely within the region of the linear chirp), it is reasonable to expect the induced-phase modulated probe pulse, under these conditions, to be efficiently compressed through the grating.

We assume that $T_0 = -\eta z/2$ and $\sigma \gg 1$ and we denote the induced phase by $p$, which is given by

$$|p| = (2\gamma_b a_0^2 z)\rho(\eta z), \tag{194}$$

where $\rho(\eta z)$ is a function of $\eta z$ equal to (0.72, 0.32, 0.11), respectively, for $\eta z = (1, 2, 3)$.

If the incoming probe pulse intensity is given by

$$I_{\text{in}}^{(b)}(\overline{U}) = b_0^2 \exp(-2\overline{U}^2), \tag{195}$$

then the outgoing probe pulse from a pump-fiber-grating compressor, under the optimal phase condition, is given by

$$I_{\text{out}}^{(b)}(\overline{U}) = (\xi b_0)^2 \exp(-2\lambda^2 \overline{U}^2), \tag{196}$$

where

$$\zeta^2 = (\sigma^4 + p^2)^{1/2} / \sigma^2, \tag{197}$$

$$\lambda^2 = (\sigma^4 + p^2)/\sigma^2, \tag{198}$$

and the optimal phase-matching condition is given by

$$g = p/4(\sigma^4 + p^2), \tag{199}$$

where the grating phase function is given by

$$\Phi_g = g(K' - K)^2, \tag{200}$$

where $K = \omega\tau_a$ is the probe central frequency normalized to the pump width.

In Figure 5.52 the numerically computed outgoing pulse intensity is plotted and is compared with the incoming pulse. The compression ratio agrees to better than 1% with the result of Eq. (198).

In Figure 5.53 the amplitude scale $\zeta$ and the relative with $\lambda$ of the probe are plotted as function of $p$. It should be noted that in the choice of $p$, values for the SPM coefficient should be smaller than those at which pump distortion sets in (i.e., in the notation of Section 2, $\varepsilon V \approx 0.2$). As can be observed, the parameter $\lambda$ is larger than $\sigma$; that is, the probe pulse is compressed even for large values of $\sigma$. Experimentally, for a 10-ps pump pulse, $\eta z = 3$; for $\gamma_a a_0^2 z = 1500$ (i.e., $\varepsilon V \approx 0.1$), $2\gamma_a = \gamma_b$, the value of $|p|$ is approximately 650.

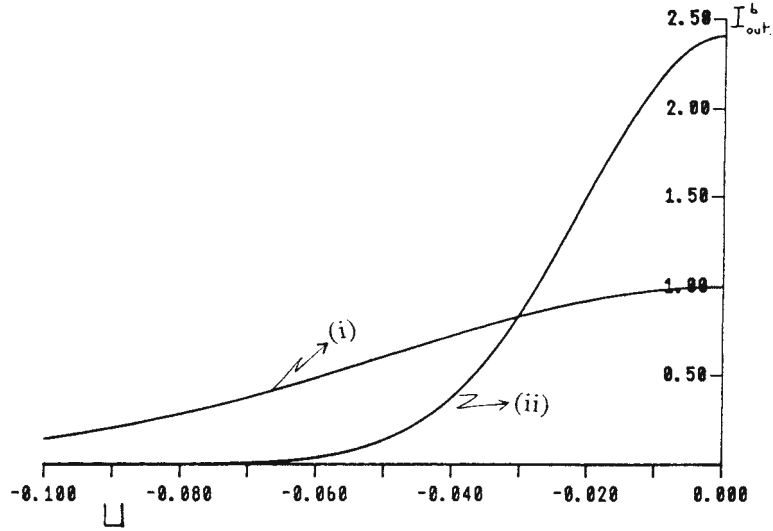


FIGURE 5.52. Induced-phase-modulated probe pulse at the input and output of the fiber-grating compressor as a function of $\overline{U}$. $\sigma = 10$; $\gamma_b a_0^2 z = 1000$; $\eta z = 3$. (i) Input; (ii) output.

Another method for pulse compression is through chirping-filtering, as discussed in Section 2.10. The disadvantage of this technique over the above one is the energy loss suffered by the probe in this process. The expression for the outgoing probe pulse, following its induced-phase modulation and filtering, is given by

$$E_{\text{out}}^{(b)}(\overline{U}) = \frac{[\Delta_f \tau_a]}{\sqrt{\pi}} \int_{-\infty}^{\infty} d\overline{U}' \exp[-\sigma^2 \overline{U}'^2] \times \exp\left\{ i(2\gamma_b a_0^2 z) \frac{1}{\eta z} \left( \tanh\left( \overline{U}' + \frac{\eta z}{2} \right) - \tanh\left( \overline{U}' - \frac{\eta z}{2} \right) \right) \right\} \times \exp[i(K_b - K_f)\overline{U}'] \exp\left[ -(\overline{U}' - \overline{U})^2 (\Delta_f \tau)^2 \right], \tag{201}$$

where we assumed that $T_0 = -\eta z/2$, $\Delta_f$ is the Gaussian filter width, $K_b = \omega_b \tau_a$, $K_f = \omega_f \tau_a$, and $\omega_f$ is the filter center frequency. The filter transform function is given by Eq. (129), and Eq. (201) can be analytically evaluated in the approximation of a linear chirp. The intensity of the outgoing pulse is then given by

$$I_{\text{out}}^{(b)}(\overline{U}) = (\xi b_0)^2 \exp[-2\chi^2 \overline{U}^2], \tag{202}$$

where

$$\xi^2 = \frac{\delta^2}{\left[ (\sigma^2 + \delta^2)^2 + p^2 \right]^{1/2}}, \tag{203}$$

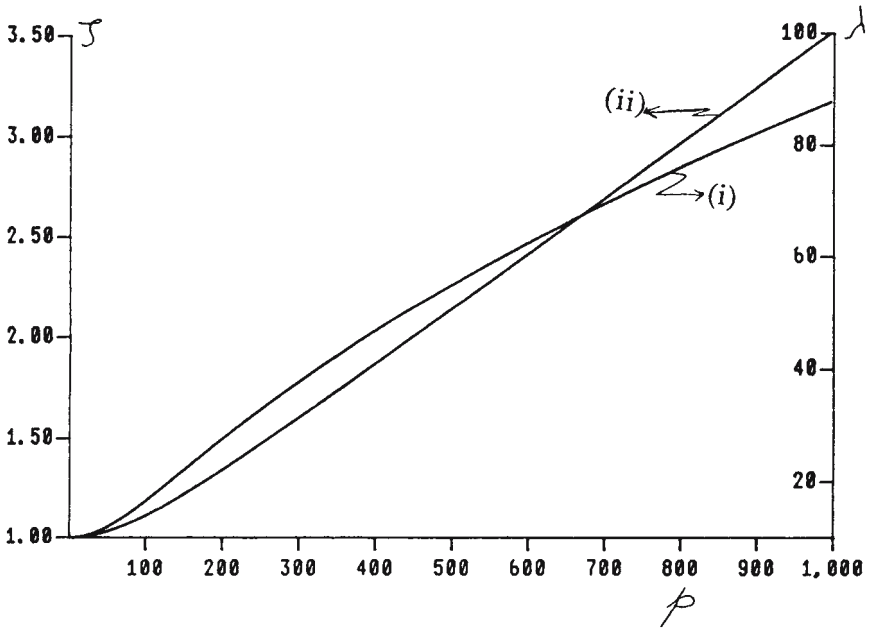


FIGURE 5.53. Fiber-grating outgoing induced-phase-modulated pulse's amplitude scale factor $\zeta$ and the pulse inverse width $\lambda$ as functions of the induced-phase modulation parameter $p$. $\sigma = 10$. (i) Amplitude scale factor; (ii) inverse width.

$$\chi^2 = \delta^2 - \frac{(\sigma^2 + \delta^2)\delta^4}{(\sigma^2 + \delta^2)^2 + p^2}, \tag{204}$$

and

$$\delta = (\Delta_f \tau_a). \tag{205}$$

In Figure 5.54 the parameter $\zeta$ and $\chi$ are plotted as functions of $\delta$ for a value of the SPM coefficient just smaller than that at which pulse distortion sets in. As can be observed, the parameter $\chi$ can be larger than $\sigma$; that is, the probe pulse is compressed even for relatively large value of $\sigma$.

In conclusion, through combination with either a grating or amplitude filter, induced-phase modulation can lead to pulse compression.

## 4.4 Induced Focusing

In this section we compute the induced focusing effects (Bladeck et al., 1987; Manassah, 1988c) generated by a strong pump on the propagation of a probe Gaussian pulse in a $\chi^{(3)}$ medium. The differential equations for the probe pulse diameter, radius of curvature, and phase are expressed as functions of the pump pulse characteristics. We prove that waveguiding or the probe by the pump is possible.

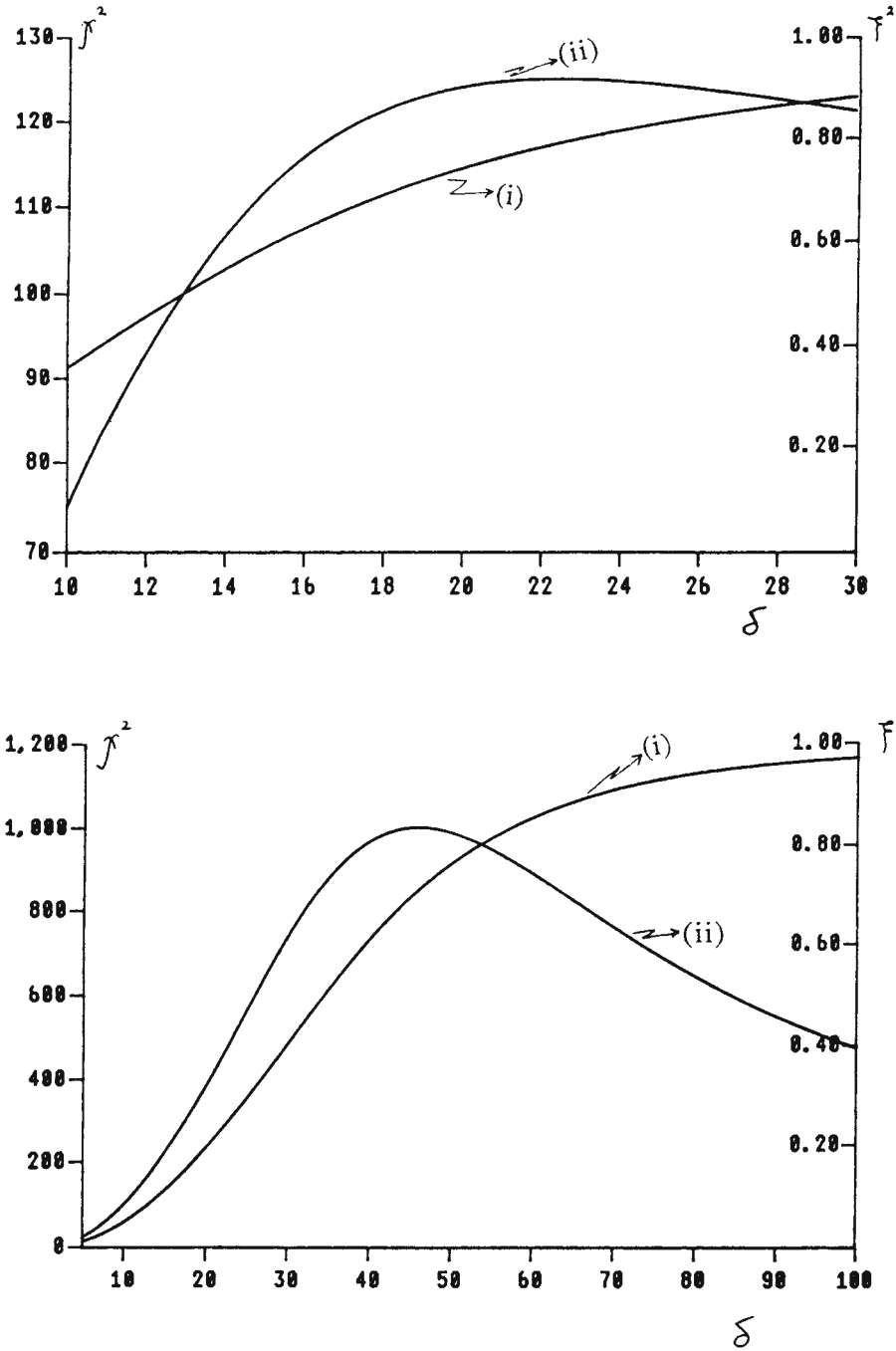


FIGURE 5.54. Fiber-filter outgoing induced-phase-modulated pulse's intensity amplitude scale factor and the pulse inverse width squared as functions of the normalized filter width ($\Delta_f \tau_a$). (i) Intensity scale factor; (ii) width squared (*top*) $\sigma = 10$, $p = 200$; (*bottom*) $\sigma = 10$, $p = 200$.

In the approximation where effects of group velocity dispersion and self-steepening are neglected and the general conditions for the slowly varying approximation are valid, the differential equations for the envelopes of the pump and probe pulses are given by

$$\nabla_T^2 A_1 - 2ik_1 A_1' + \frac{n_2}{n_0} k_1^2 \left[ |A_1|^2 A_1 + 2|A_2|^2 A_1 \right] = 0, \tag{206}$$

$$\nabla_T^2 A_2 - 2ik_2 A_2' + \frac{n_2}{n_0} k_2^2 \left[ |A_2|^2 A_2 + 2|A_1|^2 A_2 \right] = 0, \tag{207}$$

where $A_1$ and $A_2$ are respectively the pump and probe envelopes, $A' = \partial A/\partial z$, and $\nabla_T^2$ is the transverse component of the Laplacian.

If the initial conditions for the envelopes are written as

$$A_{1,2}(r,0,\bar{u}) = A_{1,2}^0 \exp\left(\frac{-r^2}{a_{1,2}^2}\right) \exp\left(\frac{-\bar{u}^2}{2\tau_{1,2}^2}\right), \tag{208}$$

that is, the initial pulses are assumed to be Gaussian both in the transverse plane and in the commoving coordinate system, $\bar{u} = (z/v_g - t)$ where $v_g$ is the group velocity, $a$ is the initial beam radius, $\tau$ is the pulse duration, $A^0$ is the magnitude of the pulse amplitude, and the subscripts (1, 2) refer respectively to the pump and probe.

In the following, the product $A^0 \exp(-\bar{u}^2/2\tau^2)$ is denoted by $\tilde{A}^0$. Furhtermore, we will solve Eqs. (206) and (207) in the limit $A_1^0 \gg A_2^0$, and $\tau_1 \gg \tau_2$. For practical purposes, we are assuming that the pump pulse duration is long enough that any walk-off between pulse and pump because of a difference in group velocity can be neglected. Approximate solutions to Eqs. (206) and (207), correct to order $r^2/a^2$, can be obtained through the trial solutions:

$$A_{1,2}(r,z,\bar{u}) = \frac{\tilde{A}_{1,2}^0}{\bar{\omega}_{1,2}(z,\bar{u})} \exp\left[ -\frac{r^2}{a_{1,2}^2 \bar{\omega}_{1,2}^2(z,\bar{u})} - \frac{ik_{1,2}}{2} \rho_{1,2}(z,\bar{u}) r^2 + ik_{1,2}\alpha_{1,2}(z,\bar{u}) \right], \tag{209}$$

where the different functions have the same meaning as in Section 1.3; specifically, $\bar{\omega}$ is the normalized beam radius, $\rho$ is the inverse of its radius of curvature, and $k\alpha$ is the longitudinal phase. The equations satisfied by these subsidiary functions are

$$\rho_{1,2} = \frac{1}{\bar{\omega}_{1,2}} \frac{\partial \omega_{1,2}}{\partial z}, \tag{210}$$

$$\frac{\partial \alpha_1}{\partial z} = \frac{a_1^2}{2\bar{\omega}_1^2} \left\{ \frac{4}{a_1^4 k_1^2} - \frac{n_2}{n} \frac{\left(\tilde{A}_1^0\right)^2}{a_1^2} \right\}, \tag{211}$$

$$\frac{\partial \alpha_2}{\partial z} = \frac{a_2^2}{2} \left\{ \frac{4}{a_2^4 k_2^2 \bar{\omega}_2^2} - \frac{2n_2}{n a_2^3} \frac{\left(\tilde{A}_1^0\right)^2}{\bar{\omega}_1^2} \right\}, \tag{212}$$

$$\frac{\partial^2 \overline{\omega}_1}{\partial z^2} = \left\{ \frac{4}{a_1^4 k_1^2 \overline{\omega}_1^3} - \frac{2n_2}{na_1^2} \frac{\left(\tilde{A}_1^0\right)^2}{\overline{\omega}_1^3} \right\}, \tag{213}$$

$$\frac{\partial^2 \overline{\omega}_2}{\partial z^2} = \left\{ \frac{4}{a_2^4 k_2^2 \overline{\omega}_2^3} - \frac{2n_2}{na_1^2} \frac{\left(\tilde{A}_1^0\right)^2 \overline{\omega}_2}{\overline{\omega}_1^4} \right\}. \tag{214}$$

Physically, the above factors are easily identifiable: $4/k^2a^4$ is the square of the inverse Rayleigh diffraction length (denoted $L$), and the Kerr phase for the pump pulse in the conventional SPM theory (see Section 1.1) is given by

$$\phi_{\text{SPM}} = -\frac{k_1 n_2 \left|\tilde{A}_1^0\right|^2 z}{2n}, \tag{215}$$

where $n = n_0$.

The solutions for the pump subsidiary functions are the same as those derived in Section 1.4, specifically,

$$\overline{\omega}_1 = \left[1 + y_1^2 (1 - p')\right]^{1/2}, \tag{216}$$

$$L_1 \rho_1 = \frac{y_1 [1 - p']}{\left[1 + y_1^2 (1 - p')\right]}, \tag{217}$$

$$k_1 \alpha_1 = \frac{\left[1 - \frac{1}{2} p'\right]}{\left[(1 - p')^{1/2}\right]} \operatorname{arctg}\left[(1 - p')^{1/2} y_1\right], \tag{218}$$

where

$$p' = p \exp\left[-\bar{u}^2 / \tau_1^2\right], \tag{219}$$

$$p = \left(A_1^0\right)^2 / \left(A_1^c\right)^2, \tag{220}$$

$$y_1 = z / L_1, \tag{221}$$

$$\left(A_1^c\right)^2 = na_1^2 / 2n_2 L_1^2. \tag{222}$$

$(A_1^c)^2$ is the critical field for self-focusing (i.e., the field for which the self-focusing distance is at $z = \infty$). In this notation, as noted in Section 1.4, the normalized self-focusing distance is $(y_1)_{\text{foc}} = 1/(p-1)^{\frac{1}{2}}$ for $p > 1$. Here we will solve only for the probe subsidiary functions $\overline{\omega}_2$, $\rho_2$, and $\alpha_2$ under the condition that $p \approx 1$ and that for the duration of the probe pulse we have $p \approx p'$. In this instance, $\overline{\omega}_1 = 1$ and the solutions of the probe subsidiary functions are given by

$$\overline{\omega}^2 = \left[\bar{\xi} \cos(\bar{\chi} z) + \bar{\eta}\right]^{1/2}, \tag{223}$$

$$\rho_2 = -\frac{1}{2} \frac{\bar{\xi} \bar{\chi} \sin(\bar{\chi} z)}{\left[\bar{\xi} \cos(\bar{\chi} z) + \eta\right]}, \tag{224}$$

$$\alpha_2 = \left\{ -\frac{a_1^2}{2L_1^2} z + \frac{a_2^2}{L_2^2} \frac{1}{\bar{\chi} \left(\bar{\eta} - \bar{\xi}\right)^{1/2}} \operatorname{arctg}\left[ \left(\bar{\eta} - \bar{\xi}\right)^{1/2} \tan \frac{\bar{\chi} z}{2} \right] \right\}, \tag{225}$$

where

$$\bar{\xi} = \tfrac{1}{4}[2 - L_1^2/L_2^2], \tag{226}$$

$$\bar{\eta} = \tfrac{1}{4}[2 + L_1^2/L_2^2], \tag{227}$$

$$\bar{\chi} = 2\sqrt{2}/L_1, \tag{228}$$

and the range $\bar{\omega}_2^2$ is between $L_1^2/2L_2^2$ and 1. In the same notation, the expressions for $\bar{\omega}_2$, $\rho_2$, and $\alpha_2$ in the absence of a pump (i.e., $A_1^0 = 0$) are given by

$$\bar{\omega}_2 = (1 + y_2)^{1/2}, \tag{229}$$

$$\rho_2 L_2 = y_2[(1 + y_2^2)]^{-1}, \tag{230}$$

$$k_2\alpha_2 = \text{arctg}(y_2), \tag{231}$$

where $y_2 = z/L_2$.

In the figures, we consider the easily achievable experimental setup of a probe with a central frequency at twice that of the pump (i.e., $\lambda_2 = \lambda_1/2$) and for $a_1 = a_2$. In this case $L_2 = 2L_1$. In Figure 5.55, $\bar{\omega}_2$ is plotted in the presence and absence of the pump field; in Figure 5.56, $\rho_2$ is plotted; and in Figure 5.57, the longitudinal phase $\alpha_2$ is plotted. The curves in the presence of the pump are reminiscent of those corresponding to the propagation of a

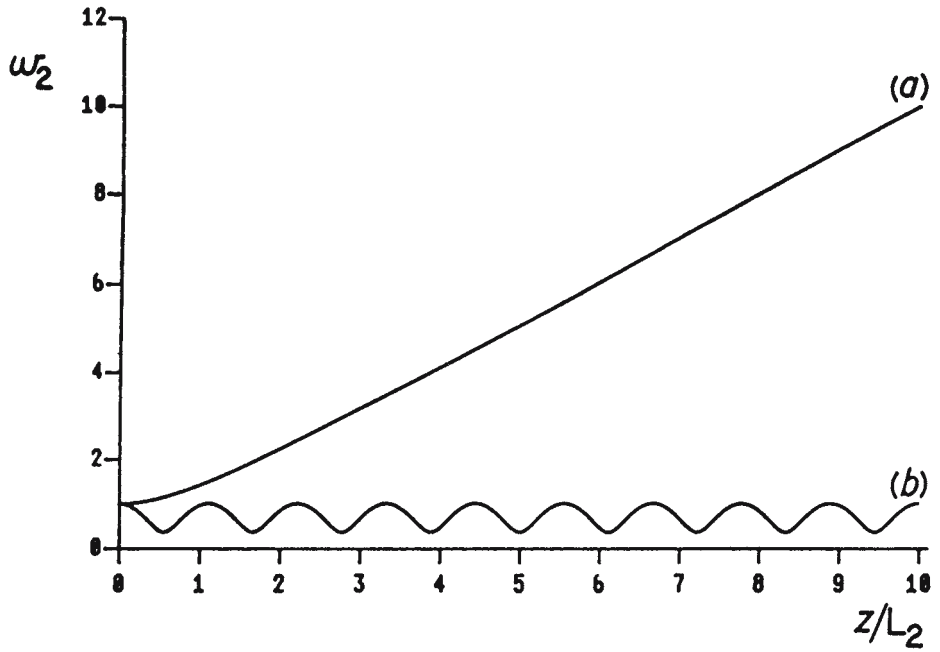


FIGURE 5.55. Normalized radius of an IPM probe as a function of distance. The pump intensity when present is at the self-focusing critical value. (a) No pump; (b) pump present.

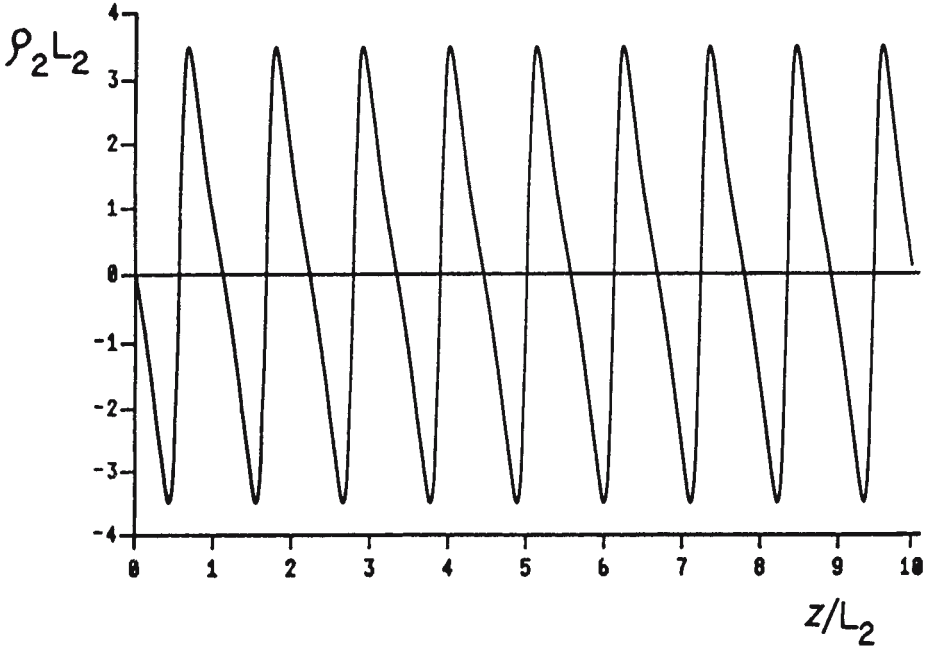


FIGURE 5.56. Inverse radius of curvature of an IPM probe as a function of distance. The pump intensity is at the self-focusing critical value.

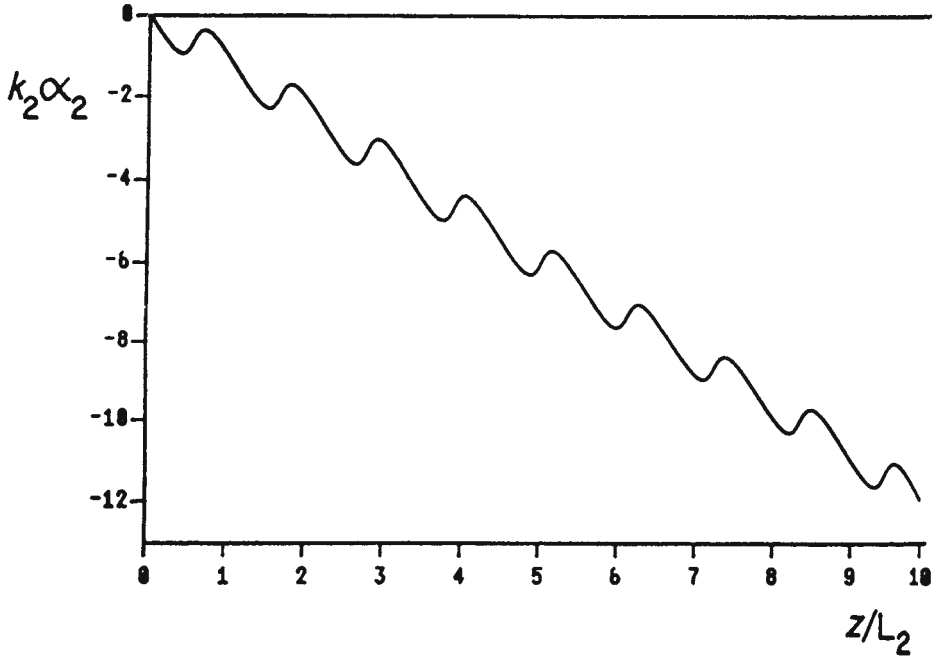


FIGURE 5.57. Longitudinal phase of an IPM probe as a function of distance. The pump intensity is at the self-focusing critical value.

Gaussian pulse in a quadratic graded-index material. This should come as no surprise, since Eq. (214) is equivalent to that case.

In conclusion, in this section we computed the geometric effects of induced-phase modulation of a pump on the propagation of a weak probe in a nonlinear $\chi^{(3)}$ material. We showed that, physically, the induced index of refraction can lead to a waveguiding of the probe. Furthermore the computed cumulative longitudinal phase [i.e., Eq. (225)] may lead to some interesting verification of the model through interference experiments.

## 4.5 Induced Self-Steepening

In this section we consider induced-phase modulation when the pump intensity produces self-steepening (Manassah et al., 1985). This case can be solved by the method of multiple scales used in Section 2. Using the notation of Section 2, for the case of the probe at the second harmonic frequency of the pump and assuming that the material has no $\chi^{(2)}$ (i.e., there is no conversion of two primary photons into a second harmonic photon) and that all conditions of Section 2.1 are satisfied, the total $\Phi_0$ can be written as

$$\Phi_0 = Ae^{iKU} + \delta Be^{i2KU}. \tag{232}$$

This equation should be compared with Eq. (76). A corresponds to the pump and $B$ to the probe and $\delta$ is the initial scaling factor between the probe and pump amplitudes. For the case of $\delta << 1$, that is, a weak probe, the equations that will correspond to Eqs. (84) and (85), for the nonlinear polarization $<|\Phi|^2>\Phi$, are

$$\frac{\partial a}{\partial V} - \frac{3}{2}\varepsilon a^2 \frac{\partial a}{\partial U} = 0, \tag{233}$$

$$\frac{\partial b}{\partial V} - \frac{\varepsilon}{2} a^2 \frac{\partial b}{\partial U} - \varepsilon ab \frac{\partial a}{\partial U} = 0, \tag{234}$$

$$\frac{\partial \alpha}{\partial V} - \frac{\varepsilon}{2} a^2 \frac{\partial \alpha}{\partial U} = \frac{K\varepsilon}{2} a^2 - \frac{K\varepsilon^2}{8} a^4, \tag{235}$$

$$\frac{\partial \beta}{\partial V} - \frac{\varepsilon}{2} a^2 \frac{\partial \beta}{\partial U} = K\varepsilon a^2 - \frac{K\varepsilon^2}{4} a^4. \tag{236}$$

This system of equations indicates that once the pump pulse shape function is determined, $b$, $\alpha$, and $\beta$ can be deduced as functions of it. For the initial conditions, that the pump and probe have hyperbolic secant shape with the same width, the solutions of $a$ and $\alpha$ are given by Eqs. (93) and (98), respectively, and those of $b$ and $\beta$ by

$$\beta = 2\alpha, \tag{237}$$

$$b = a. \tag{238}$$

Essentially the pump self-steepening is directly mirrored in the probe. The key results of the above analysis are as follows:

1. The ratio of the magnitudes of $a$ and $b$ is constant throughout the medium; that is, the ratio of the energy densities in the pump and the probe is preserved and thus the pump only modulates the probe.
2. For the case where the ratios of the pump and probe center frequencies are the same as the ratio of the phases ($\alpha$, $\beta$), the supercontinuum and the induced supercontinuum spectral distributions are geometrically similar. This could provide direct experimental verification of the model.

   The solutions of Eqs. (234) and (236), for pump and probe having the same initial shape and width, are given by Eqs. (237) and (238). The general solution for $b$ is given by

$$b = aL, \tag{239}$$

   where the function $L$ can be written as $L(l)$, the function $l$ satisfies the equation

$$\frac{\partial l}{\partial V} - \frac{\varepsilon}{2} a^2 \frac{\partial l}{\partial U} = 0, \tag{240}$$

   its solution is given by

$$l = \frac{\varepsilon}{2} \int_0^V a^3(U,q)dq + \int_0^U a(p,0)dp, \tag{241}$$

   and the particular solution of $L$ is then obtained by making it satisfy the initial condition. The $\beta$ solution is given by Eq. (237) as long as $\beta(U, 0) = 0$.

The treatment in this section has so far considered a nonlinear index of refraction that has been averaged over time (the light cycle). If, on the other hand, we consider the time-dependent nonlinear index of refraction (i.e., the polarization is proportional to $|\Phi|^2\Phi$), the equations of motion for the envelopes $A$ and $B$ are given by

$$\frac{\partial \alpha}{\partial V} - \frac{1}{2}\varepsilon\left[(3a^2 + 2\delta^2 b^2)\frac{\partial a}{\partial U} + 4\delta^2 ab \frac{\partial b}{\partial U}\right] = 0, \tag{242}$$

$$\frac{\partial a}{\partial V} - \frac{1}{2}\varepsilon(a^2 + 2\delta^2 b^2)\frac{\partial \alpha}{\partial U} = \frac{1}{2}K\varepsilon(a^2 + 2\delta^2 b^2) - \frac{1}{8}\varepsilon^2 K(a^2 + 2\delta^2 b^2)^2, \tag{243}$$

$$\frac{\partial b}{\partial V} - \frac{1}{2}\varepsilon\left[(2\delta^2 b^2 + 2a^2)\frac{\partial b}{\partial U} + 4ab \frac{\partial a}{\partial U}\right] = 0, \tag{244}$$

$$\frac{\partial \beta}{\partial V} - \frac{1}{2}\varepsilon(\delta^2 b^2 + 2a^2)\frac{\partial \beta}{\partial U} = K\varepsilon(2a^2 + \delta^2 b^2) - \frac{1}{4}\varepsilon^2 K(\delta^2 b^2 + 2a^2)^2. \tag{245}$$

In the limit considered earlier, $\delta^2 \ll 1$, the above equations reduce to

$$\frac{\partial a}{\partial V} - \frac{3}{2}\varepsilon a^2 \frac{\partial a}{\partial U} = 0, \tag{246}$$

$$\frac{\partial \alpha}{\partial V} - \frac{1}{2}\varepsilon a^2 \frac{\partial \alpha}{\partial U} = \frac{1}{2}K\varepsilon a^2 - \frac{1}{2}K\varepsilon^2 a^4, \tag{247}$$

$$\frac{\partial b}{\partial V} - \varepsilon a^2 \frac{\partial b}{\partial U} - 2\varepsilon ab \frac{\partial a}{\partial U} = 0, \tag{248}$$

$$\frac{\partial \beta}{\partial V} - \varepsilon a^2 \frac{\partial \beta}{\partial U} = 2K\varepsilon a^2 - \varepsilon^2 K a^4. \tag{249}$$

In this limit, the equations for $a$ and $\alpha$ reduce to those of the SPM theory of Section 2 and the solutions for $b$ and $\beta$ are, respectively, given by

$$b(U,V) = L_1(U,V)a^4(U,V), \tag{250}$$

$$\begin{aligned}\beta(U,V) = &-2KU + 4\varepsilon K \int_0^U a^2(p,V)dp \\ &+ 3K\varepsilon^2 \int_0^V a^4(0,q)dq + KL_2(U,V),\end{aligned} \tag{251}$$

where $L_1$ and $L_2$ satisfy the partial differential equation

$$\frac{\partial L_i}{\partial V} - \varepsilon a^2 \frac{\partial L_i}{\partial U} = 0. \tag{252}$$

The solution of Eq. (252) is given by

$$\begin{aligned}L(U,V) &= L\left(\varepsilon \int_0^V a^6(U,q)dq + \int_0^U a^4(p,0)dp\right) \\ &= L(r) \\ &= L\left(\varepsilon \int_0^V a^6(U,q)dq + \tanh U - \frac{1}{3}\tanh^3 U\right),\end{aligned} \tag{253}$$

where the initial pump pulse has been assumed to be given by sech $(U)$. If the probe pulse shape is also a sech function but of different width, that is, $b(U, 0) = \mathrm{sech}(nU)$ and $\beta(U, 0) = 0$, then the functions $L_1$ and $L_2$ are given by the following parametric representation (where $s$ is the parameter):

$$L_1(x) = (\cosh^4 s)\mathrm{sech}(ns), \tag{254}$$

$$L_2(x) = 2s - 4\varepsilon \tanh s, \tag{255}$$

$$x = \tanh s - \tfrac{1}{3}\tanh^3 s. \tag{256}$$

The frequency extent of the induced supercontinuum centered at the probe frequency (i.e., $2\omega$) is given by the maximum and minimum of $(1/2K)\partial\beta/\partial U$, where

$$\left(\frac{1}{2K}\frac{\partial \beta}{\partial U}\right) = 1 + 2\varepsilon a^2(U,V) + \frac{1}{2}\left[\frac{\partial L_2(r)}{\partial r}\right]a^4(U,V) \tag{257}$$

and the derivative of $L_2$ in parametric form is

$$\frac{\partial L_2}{\partial x} = \frac{2 - 4\varepsilon \mathrm{sech}^2 s}{\mathrm{sech}^2 s - (\tanh^2 s)(\mathrm{sech}^2 s)}. \tag{258}$$

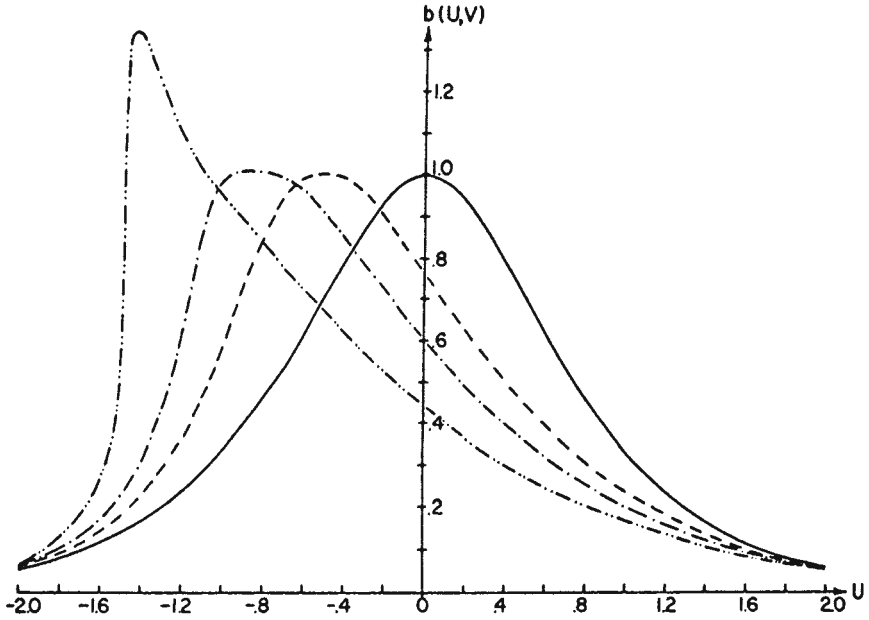


FIGURE 5.58. Amplitude of the induced-phase-modulated steepened second harmonic pulse in a dispersionless $\chi^{(3)}$ medium as a function of $U$. $\chi^{(2)} = 0$.—$\varepsilon V = 0.0$; — — —$\varepsilon V = 0.3$; — · —$\varepsilon V = 0.5$; — ·· —$\varepsilon V = 0.8$.

In Figure 5.58, $b(U, V)$ is plotted for different values of $\varepsilon V$ for $n = 1.7$ and in Figure 5.59 the induced supercontinuum frequency extents are plotted as functions of $\varepsilon V$. The induced supercontinuum frequency extents, as functions of $\varepsilon V$, grow faster than those corresponding to SPM.

## 4.6 Induced-Phase Modulation of a Generated Second Harmonic Pulse

In the previous sections we considered the induced-phase modulation on a probe by a pump when both were initially introduced in the system. In this section (Manassah and Cockings, 1987b) we examine the induced-phase modulation of a second harmonic signal generated by the pump; that is, we consider a medium with both $\chi^{(2)}$ and $\chi^{(3)}$ coefficients present (Alfano and Ho, 1986, 1988; Alfano et al., 1987).

To first order in the quadratic susceptibility [$\chi^{(2)}$] and the Kerr susceptibility, and neglecting all higher-order derivatives of the linear refractive index beyond the first derivative with respect to frequency, the quasi-linear partial differential equations describing the envelopes of the first and second harmonic pulses are given by

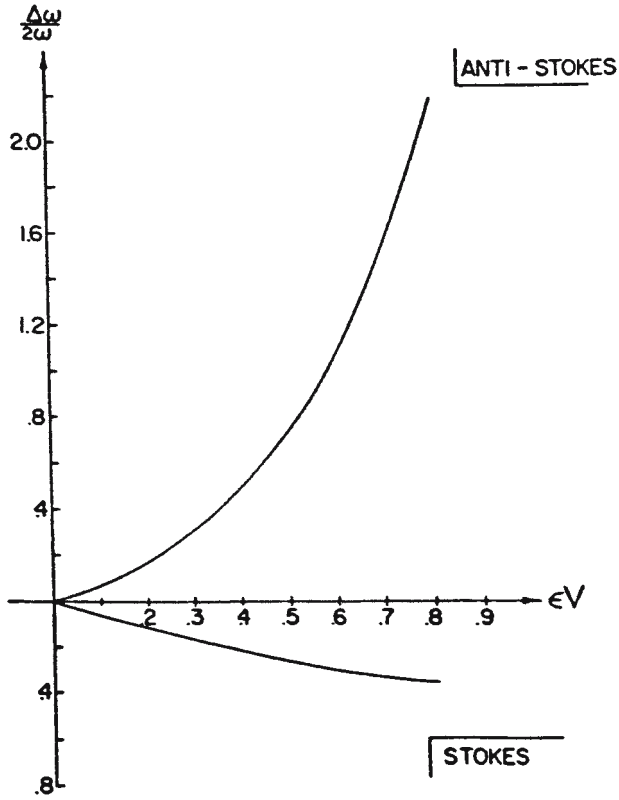


FIGURE 5.59. Induced frequency sweep extents (maxima and minima of the derivative of the induced phase) for a steepened second harmonic pulse in a dispersionless $\chi^{(3)}$ medium as a function of $\varepsilon V$. $\chi^{(2)} = 0$.

$$\frac{\partial A}{\partial z} + \frac{1}{v_1}\frac{\partial A}{\partial t} = i\varepsilon A^* B \exp[i(k_2 - 2k_1)z] + i\gamma_a\left(|A|^2 + 2|B|^2\right)A, \tag{259}$$

$$\frac{\partial B}{\partial z} + \frac{1}{v_2}\frac{\partial B}{\partial t} = i\varepsilon A^2 \exp[-i(k_2 - 2k_1)z] + i\gamma_b\left(|B|^2 + 2|A|^2\right)B - \alpha B, \tag{260}$$

where $\gamma$ was defined earlier, $\varepsilon$ is given by

$$\varepsilon = \mu_0 \omega_1 c d/2\,, \tag{261}$$

$\alpha$ is the absorption coefficient of the medium at $\omega_2$, $v_1$ and $v_2$ refer to the group velocities, respectively, at the primary and second harmonic frequencies, $k_1$ and $k_2$ are the corresponding wave vectors, and $d$ is the quadratic nonlinear optical coefficient ($P_{NL} = dE^2$ ). In the weak second harmonic signal limit (i.e., $|B| \ll |A|$ or no pump depletion), the solutions of the above equations reduce to

$$A = a_0 F\left[\left(t - \frac{z}{v_1}\right)\Big/\tau\right]\exp\{i\gamma_a a_0^2 F^2[(t - z/v_1)/\tau]z\}, \tag{262}$$

$$\begin{aligned} B = {} & i\varepsilon a_0^2 \exp\left[-\alpha z + i(2\gamma_b a_0^2)\int_0^z F^2(\overline{U} + \eta' z')dz'\right] \\ & \times \int_0^z dz' F^2(\overline{U} + \eta' z')\exp[i2\gamma_a a_0^2 F^2(\overline{U} + \eta' z')z' - i\zeta' z'] \\ & \times \exp\left[\alpha z' - i2\gamma_b a_0^2 \int_0^{z'} F^2(\overline{U} + \eta' z'')dz''\right], \end{aligned} \tag{263}$$

where

$$\overline{U} = (t - z/v_2)/\tau, \tag{264}$$

$$\eta' = \left(n_2^g - n_1^g\right)/c\tau, \tag{265}$$

$$\zeta' = (2\omega/c)\left(n_2^p - n_1^p\right), \tag{266}$$

$n_1$ and $n_2$ are the indices of refraction at $\omega$ and $2\omega$, ad the superscripts $p$ and $g$ refer, respectively, to the phase and group quantities. If the pulse form function is a hyperbolic secant, then the expressions for $A$ and $B$ can be written as

$$A = a_0 \mathrm{sech}[(t - z/v_1)/\tau]\exp\{i\gamma_a a_0^2 \mathrm{sech}^2[(t - z/v_1)/\tau]\}, \tag{267}$$

$$\begin{aligned} B = {} & i\varepsilon a_0^2 \exp\left[-\alpha z + \frac{i2\gamma_b a_0^2}{\eta'}\tanh(\overline{U} + \eta' z')\right] \\ & \times \int_0^z dz' \mathrm{sech}^2(\overline{U} + \eta' z')\exp\{(\alpha - i\zeta')z' + i2a_0^2 \\ & \times \left[(\gamma_a \mathrm{sech}^2(U + \eta' z'))z' - \frac{\gamma_b}{\eta'}\tanh(\overline{U} + n' z')\right]\Big\}. \end{aligned} \tag{268}$$

We note that $A$ includes self-phase modulation (SPM), and $B$ includes the SPM of $A$ through the $\chi^{(2)}$ term and its induced-phase modulation (IPM) by $A$ through the $\chi^{(3)}$ term. A convenient expression for $B$ suitable for numerical integration is

$$\begin{aligned} B = {} & \frac{i\varepsilon a_0^2}{\eta'}\exp\left\{-\alpha z + \frac{i2\gamma_b a_0^2}{\eta'}\tanh(\overline{U} + \eta' z)\right. \\ & \left. + i\frac{\zeta'}{\eta'}\overline{U} - \frac{\alpha}{\eta}U\right\}\int_{\overline{U}}^{\overline{U} + \eta' z} dy\,\mathrm{sech}^2(y) \\ & \times \exp\left\{\left(\frac{\alpha}{\eta'} - \frac{i\zeta'}{\eta'}\right)y + \frac{i2a_0^2}{\eta'}[\gamma_a(y - \overline{U})\mathrm{sech}^2(y) - \gamma_b \tanh y]\right\}. \end{aligned} \tag{269}$$

We note that

1. The modulation term inside the integral depends on $\zeta'/\eta' = 2\omega\tau(n_2^p - n_1^p)/(n_2^g - n_1^g)$ and on the phase term due to SPM of $A$ and IPM of $B$.

2. The dependence on the primary intensity in the integrand is multiplicative through $\chi^{(2)}$ and in the phase through $\chi^{(3)}$.
3. The upper limit of integration in $y$ differs from the lower limit by $\eta' z$, which represents the length of the sample in units of walk-off distance.
4. The above treatment for SPM assumes that we are in the regime where self-steepening is unimportant.

To gain a feeling for the different parameters of the present problem, consider ZnSe (Alfano and Ho, 1986, 1988; Alfano et al., 1987). This material was shown to have large values for both $\chi^{(2)}$ and $\chi^{(3)}$ and is therefore an excellent candidate for observing both the induced-phase modulation of a generated second harmonic signal and its time domain structure. The group indices of refraction for this material at the primary (1.06 $\mu$m) and second harmonic frequencies are, respectively $n_1^g = 2.62$ and $n_2^g = 3.44$; therefore, for a sample 2 cm long and a pulse of 10-ps duration, $\eta' z \approx 5$.

In Figure 5.60 the magnitude of $B = |B|$ is plotted. As observed, the time domain structure of $|B|$ exhibits two peaks (Manassah, 1988d), one located near $\overline{U} = -\eta' z$ and the other at $\overline{U} = 0$; these two positions correspond to the time of arrival of two weak pulses, at the primary frequency and at the socondary frequency, going through the linear medium [i.e., $\chi^{(2)} = \chi^{(3)} = 0$]. The appearance of the pump companion (i.e., at $\overline{U} \approx \eta' z$) results from the $\chi^{(2)}$ term; the $\chi^{(3)}$ term shifts slightly this pump companion forward.

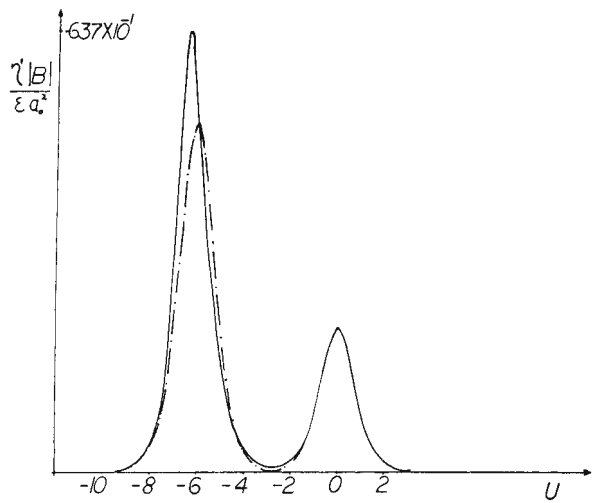


FIGURE 5.60. Magnitude of the generated second harmonic pulse envelope as a function of the normalized time (in units of primary pulse width), in the presence of SPM and IPM: $\eta' z = 6$, $\alpha z = 0.9$, $\zeta'/\eta' = 20$. (Dotted line) $\gamma = 0$; (full line) $\gamma_a = \gamma_b$ and $2\gamma a_0^2/\eta' = 0.5\pi$.

The magnitude of $B$ for weak phase modulation at the points $\overline{U} = \eta' z$ and $\overline{U} = 0$ is given by

$$|B(\overline{U} = -\eta' z)| \approx \varepsilon a_0^2 \frac{1}{(\alpha^2 + \zeta'^2)^{1/2}}, \tag{270}$$

$$|B(\overline{U} = 0)| \approx \varepsilon a_0^2 \exp(-\alpha z) \frac{1}{(\alpha^2 + \zeta'^2)^{1/2}}. \tag{271}$$

These magnitudes are not specific to the detailed pulse shape; for example, they will be the same if, instead of a sech pulse, a Gaussian pulse is used.

The shift and the magnitude value of the pump companion peak are shown in Figure 5.61. As the product of the Kerr constant by the primary intensity is increased (within the range of validity of the above weak phase-modulation equations), the magnitude of the pump companion peak compared with the magnitude of the other peak increases.

Next, we examine the spectral distribution of the second harmonic pulse. We compare the spectral distribution of the second harmonic signal in the absence of $\chi^{(3)}$ (i.e., $\gamma = 0$) with that in its presence (hereafter $\gamma_a = \gamma_b \neq 0$). Furthermore, we compare the phase-modulated primary pulse's spectral distribution with the corresponding incoming pulse's spectral distribution. [It is

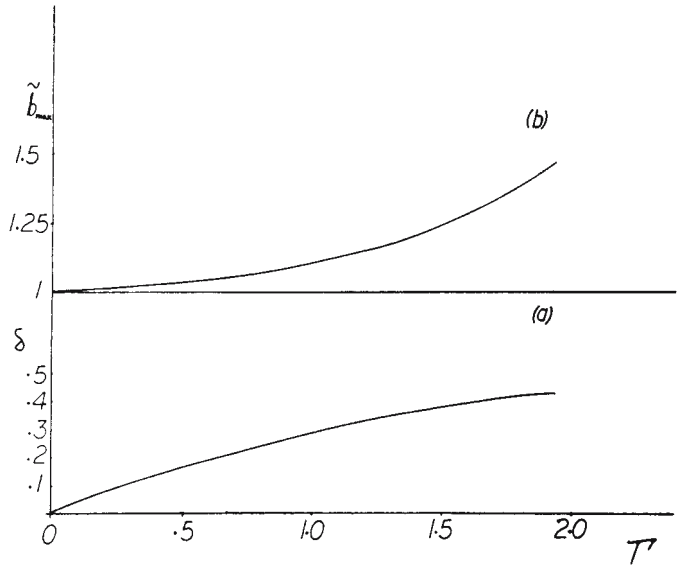


FIGURE 5.61. (a) Position shift, away from the pump, of the pump companion peak as a function of the product of the Kerr constant by the primary pulse intensity. (b) Magnitude of this peak normalized to $\Gamma = 0$ peak: $\zeta'/\eta' = 20$, $\eta' z = 6$, $\alpha z = 0.9$, $\Gamma = 2\gamma a_0^2/\eta'$.

obvious that the spectral distribution of the outgoing primary pulse will have the shape predicted by the conventional self-phase modulation theory.]

In the absence of self-phase modulation, the spectral distribution of the second harmonic signal will exhibit some modulation. Physically, this is a direct result of its two-peak structure. Interference terms will manifest themselves because of the phase difference due to the time separation between the two peaks. The Fourier transform of the second harmonic pulse in the absence of $\chi^{(3)}$ is given by

$$\tilde{B}(\Delta_2) = \int_{-\infty}^{\infty} \exp[i(\omega - \omega_2)t]B(t)dt$$

$$= -2\frac{(\varepsilon a_0^2 \tau)}{\eta'} \frac{[\Delta_2 \pi/2]}{\left[\dfrac{\zeta'}{\eta'} + \Delta_2 + \dfrac{i\alpha}{\eta'}\right]} \times \frac{\left\{\exp\left[-i\eta' z\left(\dfrac{\zeta'}{\eta'} + \Delta_2\right)\right] - \exp[-\alpha z]\right\}}{\sinh[\Delta_2 \pi/2]}. \tag{272}$$

Denote the normalized intensities of the primary and second harmonic, respectively, by $\tilde{I}_1$ and $\tilde{I}_2$. In Figures 5.62 and 5.63 these spectral distributions are plotted for specific parameters. The $\tilde{I}$ functions are defined by

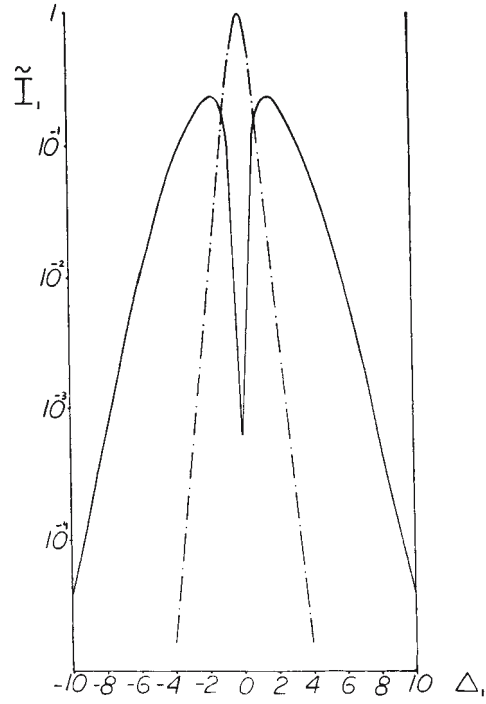


FIGURE 5.62. Normalized spectral distribution of the primary pulse as a function of the normalized frequency difference: $\alpha z = 0.9$, $\eta' z = 6$, $\zeta'/\eta' = 20$. (Dotted line) $\gamma = 0$; (full line) $2\gamma a_0^2/\eta' = 0.5\pi$.

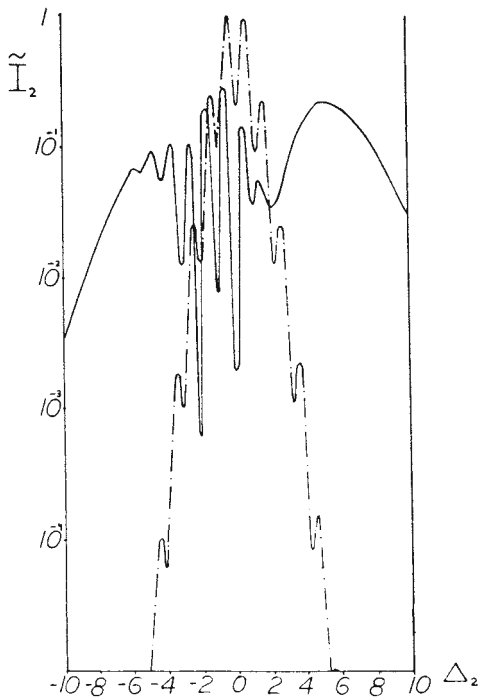


FIGURE 5.63. Normalized spectral distribution of the generated second harmonic signal as a function of the normalized frequency difference: $\eta' z = 6$, $\alpha z = 0.9$, $\zeta'/\eta' = 20$. (Dotted line) $\gamma = 0$; (full line) $2\gamma a_0^2/\eta' = 0.5\pi$.

$$\tilde{I}_1(\Delta_1\Gamma) = \frac{\left|\int_{-\infty}^{\infty} \exp(i\Delta_1 \overline{U}) A(\overline{U}, \Gamma) d\overline{U}\right|^2}{\left|\int_{-\infty}^{\infty} A(\overline{U}, 0) d\overline{U}\right|^2}, \tag{273}$$

$$\tilde{I}_2(\Delta_2\Gamma) = \frac{\left|\int_{-\infty}^{\infty} \exp(i\Delta_2 \overline{U}) B(\overline{U}, \Gamma) d\overline{U}\right|^2}{\left|\int_{-\infty}^{\infty} B(\overline{U}, 0) \exp(i\Delta_2 \overline{U}) d\overline{U}\right|^2_{\max}}, \tag{274}$$

where

$$\Gamma = 2\gamma a_0^2/\eta', \tag{275}$$

$$\Delta_1 = (\omega - \omega_1)\tau, \tag{276}$$

$$\Delta_2 = (\omega - \omega_2)\tau. \tag{277}$$

We note the following:

FIGURE 5.64. The (radiated intensity)$^{1/4}$ = $i$ as a function of $v = (\Delta\omega)\tau$ for $a = n/2$. (*Top*) Full line, $n = 1$; dotted line, $n = 5$. (*Bottom*) Full line, $n = 3$; dashed line, $n = 7$. The intensity curve reaches zero at the minima.

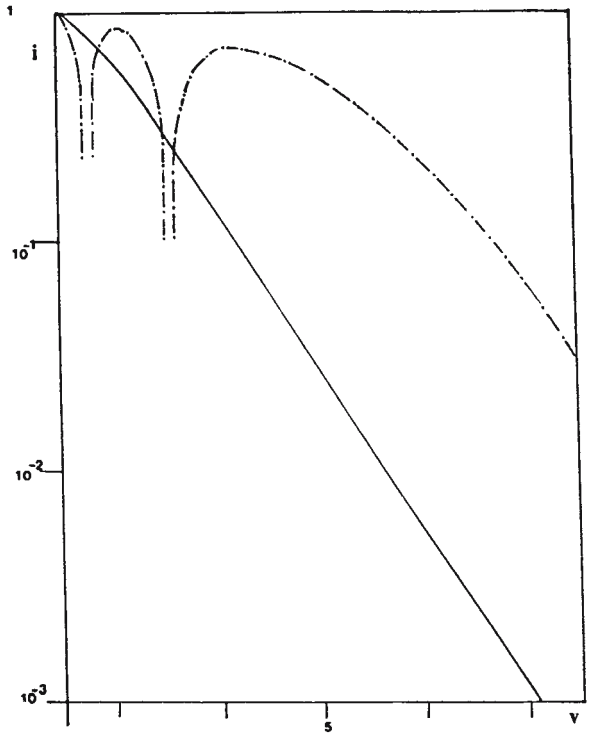
1
i
$10^{-1}$
$10^{-2}$
$10^{-3}$
5
V

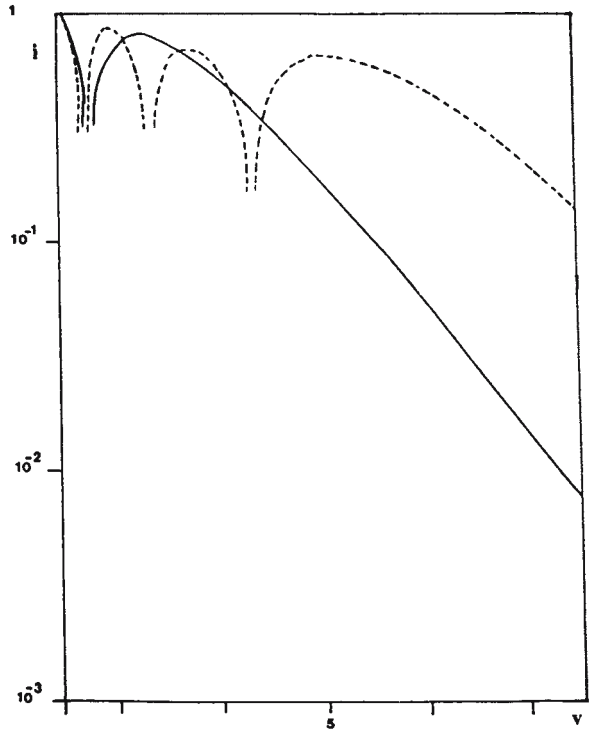
1
i
$10^{-1}$
$10^{-2}$
$10^{-3}$
5
V

1. $\tilde{I}_2$ is not symmetric in $\Delta_2$. This results from the asymmetry in the phase modulation exponents.
2. The frequency extents for the primary and secondary spectral distributions do not scale with $\gamma$. The second harmonic spectral distribution is affected by both SPM (through $A$) and IPM (because of $A$).

## 5. Quantum Mechanical Treatment of Supercontinuum Generated in a Thin Sample of Two-Level Resonant Atoms

The phenomenological theories of direct and induced supercontinuum have been developed in previous sections for a Kerr-like medium. In the phenomenological theory, the interaction term in Maxwell's equation is assumed to be instantaneous in the electric field. The microstructure of the nonlinear polarization constant is nowhere incorporated in the phenomenological model. This assumption is reasonable as long as the excitation laser frequency is far off any resonance line of the medium and the medium relaxation constants are short compared to the pulse duration. In this section we investigate the spectrum generated as a result of an incoming resonant ultra-short pulse impinging on a very thin sample of a system of two-level atoms (Manassah, 1986b). We emphasize in our analysis the case of large-amplitude pulses whose width is much shorter than the system inherent relaxation time constant (i.e., natural lifetime).

The model that we adopt for our analysis is Robiscoe's (1978) generalization of the model of Rosen and Zener (1932). In this model, a pulse with a secant hyperbole envelope is incident on a two-level atom system. The natural decay of the atom is incorporated in the Schrödinger equation through the Bethe-Lamb phenomenological prescription (Lamb and Retherford, 1950; Bethe and Salpeter, 1957). The wave function of a two-level atom can be represented by

$$\psi(r,t) = c_1(t)\exp(-i\omega_1 t)u_1 + c_2(t)\exp(-i\omega_1 t)u_2, \tag{278}$$

where $u_i$ and $\omega_i$ refer, respectively, to the eigenfunctions and eigenvalues of the unperturbed Hamiltonian. In the presence of an electromagnetic field, central frequency $v$, and envelope function $f(t)$, the differential equations for $c_1$ and $c_2$ are

$$\dot{c}_1 = [V_0 f(t)/i\hbar]e^{+i\omega t}c_2, \qquad \dot{c}_2 = -\tfrac{1}{2}\gamma c_2 + [V_0 f(t)/i\hbar]e^{-i\omega t}c_1, \tag{279}$$

where $\omega = \omega_2 - \omega_1 - v$ and level 1 is assumed to be long lived. If we define the new variables $C_1$ and $C_2$ by

$$C_1(t) = c_1(t) \quad \text{and} \quad C_2(t) = c_2(t)e^{\gamma t/2}, \tag{280}$$

the equations of motions reduce to

$$i\hbar\dot{C}_1 = V_0 f(t)C_2 e^{i\Omega t}, \qquad i\hbar\dot{C}_2 = V_0 f(t)C_1 e^{-i\Omega t}, \tag{281}$$

where $\Omega = \omega + \frac{1}{2}i\gamma$. The boundary conditions are assumed to be

$$C_1(t \Rightarrow -\infty) = 1, \qquad C_2(t \Rightarrow -\infty) = 0. \tag{282}$$

The decoupled equations for $C_1$ and $C_2$ are given by

$$\begin{aligned} \ddot{C}_1 - \left(\dot{f}/f + i\Omega\right)\dot{C}_1 + |V_0 f(t)/i\hbar|^2 C_1 = 0, \\ \ddot{C}_2 - \left(\dot{f}/f + i\Omega\right)\dot{C}_2 + |V_0 f(t)/i\hbar|^2 C_2 = 0 \end{aligned} \tag{283}$$

for

$$f(t) = \operatorname{sech}(t/\tau), \text{ and } z = \tfrac{1}{2}[\tanh(t/\tau) + 1]. \tag{284}$$

The solutions of (283), satisfying the boundary condition (282), were given by Robiscoe (1978) as

$$\begin{aligned} C_2(t) &= (a/|\phi|) z^{\phi} F(\phi + a, \phi - a; \phi + 1; z), \\ C_1(t) &= (i\phi/|\phi|) z^{\phi - 1/2} (1 - z)^{1/2} x F(\phi + a, \phi - a; \phi; z), \end{aligned} \tag{285}$$

where

$$\phi = \tfrac{1}{2} + \tfrac{1}{4}\gamma\tau - \tfrac{1}{2}i\omega\tau \text{ and } a = V_0\tau/\hbar.$$

In this section we concentrate henceforth on the physical conditions of on-resonance radiation and pulse duration much shorter than the atomic lifetime (if other relaxation times are present, the pulse duration is also assumed much shorter). The solutions for $C_1$ and $C_2$ reduce then to those obtained from Eq. (283) if $\gamma$ is zero, multiplied by the phenomenological decay function $e^{-\gamma t/2}$. Specifically,

$$\begin{aligned} C_2(t) &= 2az^{1/2} F(\tfrac{1}{2} + a, \tfrac{1}{2} - a; \tfrac{3}{2}; z), \\ C_1(t) &= i(1 - z)^{1/2} \exp[-(\gamma t/2)] F(\tfrac{1}{2} + a, \tfrac{1}{2} - a; \tfrac{1}{2}; z). \end{aligned} \tag{286}$$

The off-diagonal matrix element for the density matrix is given by

$$\rho_{12} = 2iaz^{1/2}(1 - z)^{1/2} F(\tfrac{1}{2} + a, \tfrac{1}{2} - a; \tfrac{3}{2}; z) F(\tfrac{1}{2} + a, \tfrac{1}{2} - a; \tfrac{1}{2}; z) e^{-\gamma t/2} e^{i\omega_0 t}, \tag{287}$$

where $\omega_0$ is the energy level difference.

If $a = n/2$ and the area of the pulse $A = n\pi$, the expression for the off-diagonal matrix element is

$$\rho_{12}^{(a=n/2)} = \tfrac{1}{2} i e^{-\gamma t/2} \sin(2n \arcsin\sqrt{z}) e^{i\omega_0 t}. \tag{288}$$

This density matrix element is proportional to the medium complex polarization. For a thin sample, the sheet source approximation, the radiated field is proportional to the polarization (Sargent et al., 1974); specifically,

$$E_R \propto \int P(x, t_r) \exp(i \mathbf{K}_R \cdot \chi) d^3x \propto CP(t_r), \tag{289}$$

where $t_r$ refers to the retarded time and $C$ is time independent.

Our next task is to study the radiated electric field in the time and frequency domains. The zeroes of the polarization in the time domain are located at

TABLE 5.3. The function $g_n$ for integers ($x = t/\tau$).

| $n$ | $g_{(n)}(x)$ |
|---|---|
| 1 | sech $x$ |
| 2 | 2 tanh $x$ sech $x$ |
| 3 | 3 sech $x$ – 4 sech$^3$ $x$ |
| 4 | tanh $x$ [4 sech $x$ – 8 sech$^3$ $x$] |
| 5 | 5 sech $x$ – 20 sech$^3$ $x$ + 16 sech$^5$ $x$ |
| 6 | tanh $x$ [6 sech $x$ – 32 sech$^3$ $x$ + 32 sech$^5$ $x$] |
| 7 | 7 sech $x$ – 56 sech$^3$ $x$ + 112 sech$^5$ $x$ – 64 sech$^7$ $x$ |

$$t = \tau \ln \tan(m\pi/2n), \tag{290}$$

where $m \le n$. Notice that $t = 0$ is a zero for even $n$. The specific forms for the polarization, expressed as direct functions of $t$, are given by

$$\rho_{12}^{(a=n/2)} = \tfrac{1}{2} i\left[e^{-\gamma t/2}\right] e^{i\omega_0 t} g_n(t/\tau) \tag{291}$$

where $g_n$ are given in Table 5.3. Notice that $g_n$ determines the asymptotic time dependence given that $\gamma\tau \ll 1$. The values of $g_n$ at $t = 0$ are 1 and 0, respectively, for odd and even $n$. Observe that as $n$ increases (i.e., the energy of the incoming pulse is increasing) the degree of the polynomial $g_n$ (in sech$x$) is increasing. The functions sech$^n x$ are narrower than (sech$x$) for $n > 1$, which physically implies that as $n$ increases the spectral extent of the radiated field increases. Specifically, the Fourier transform, for odd $n$, of $\rho$ is given by

$$\rho^{(a=n/2)}(\Delta\omega\tau) = \tfrac{1}{2} i\pi\tau \operatorname{sech}(\tfrac{1}{2}\Delta\omega\tau\pi) h_n(\Delta\omega\tau), \tag{292}$$

where $\Delta\omega$ is the frequency of the radiated field as measured from the center of the resonance line, and $h_n(\Delta\omega\tau)$ are polynomials given in Table 5.4. Notice that $h_n$ are even polynomials of degree $n - 1$. The coefficient of the leading power of this polynomial is given by

$$a_{n-1} = (-1)^{(n-1)/2} \frac{2^{n-1}}{(n-1)!}. \tag{293}$$

TABLE 5.4. The function $h_n(v)$ for small odd integers ($v = \Delta\omega\tau$).

| $n$ | $h_n(\omega)$ |
|---|---|
| 1 | 1 |
| 3 | $1 - 2v^2$ |
| 5 | $1 - \frac{10}{3} v^2 + \frac{2}{3} v^4$ |
| 7 | $1 - \frac{196}{45} v^2 + \frac{70}{45} v^4 - \frac{4}{45} v^6$ |

The behavior at the wings for the Fourier transform of the off-diagonal element of the density matrix is given (for $a = n/2$, $n$ odd) by

$$|\rho^{n/2}(v)| = \frac{1}{2}\pi\tau\frac{(2v)^{n-1}}{(n-1)!}e^{-v\pi/2}, \tag{294}$$

where $v = \Delta\omega\tau$.

Having found $\rho$ on this infinite set of discrete points to be equivalent to the solutions of (279) with $\gamma = 0$ and multiplied by $e^{-rt}$, and given that $\rho$ is an analytical function, then the solution for any arbitrary value of $a$ can similarly be found for the same conditions ($\gamma \ll \tau$, $u = \omega_0$), by

$$\rho^a(t) = \tfrac{1}{2}ie^{-\gamma t/2}e^{i\omega_0 t}\sin(a\pi + 2a\,\mathrm{gd}\,t/\tau), \tag{295}$$

where gd is the Gudermannian (hyperbolic amplitude), given by

$$\mathrm{gd}x = \int_0^x \frac{dt'}{\cosh t'}. \tag{296}$$

For example, $\rho^a$ is given for $a = \frac{1}{4}(2m + 1)$ by

$$\rho^{(a=(2m+1)/4)} = \tfrac{1}{2}ie^{-\gamma t/2}e^{i\omega_0 t}k_{2m+1}(X), \tag{297}$$

where $X = (1 + e^{-2x})^{-1/2}$, $x = t/\tau$, and $k_{2m+1}$ is a polynomial of order $2m + 1$. In Table 5.5, $k_{2m+1}$, for lowest-order values, is given. Notice that as $t \Rightarrow \infty$, $|\rho^a| \approx e^{-\gamma\pi t/2}$. The Fourier component for $\rho^{(a=(2m+1)/4)}$ is given by

$$\tilde{\rho}^{a=(2m+1)/4}(v) = \frac{1}{2}i\pi\tau\frac{1}{2\pi}\frac{\Gamma(s)\Gamma(\frac{1}{2}-s)}{\Gamma(\frac{1}{2})}l_m(s), \tag{298}$$

where $v = \Delta\omega\tau$, $s = \frac{1}{4}\gamma\tau + \frac{1}{2}iv$, and $l_m$ is a polynomial of order $m$. In Table 5.6, $l_m(s)$ is given for the lowest-order values of $m$. For $\Delta\omega \Rightarrow 0$,

$$|\tilde{\rho}^{a=(2m+1)/4}(0)| \approx \gamma^{-1}. \tag{299}$$

The long tail of $\rho(t)$ for $a = (2m + 1)/4$, at $t \Rightarrow \infty$, is responsible for this large value of $\tilde{\rho}$ at $\Delta\omega = 0$. For $v >> 1$,

$$\left|\tilde{\rho}^{a=2m+1/4}(v \Rightarrow \infty) \approx \frac{1}{2}\pi\tau\left(\frac{1}{v\sinh\pi v}\right)^{1/2}\frac{(4v)^m}{(2m-1)!!}\right. . \tag{300}$$

TABLE 5.5. The function $k_{2m+1}(X)$ for small odd integers $X = (1 + e^{-2x})^{-1/2}$, $x = t/\tau$.

| $2m + 1$ | $k_{2m+1}(X)$ |
|---|---|
| 1 | $X$ |
| 3 | $3X - 4X^3$ |
| 5 | $5X - 20X^3 + 16X^5$ |
| 7 | $7X - 56X^3 + 112X^5 - 64X^7$ |

TABLE 5.6. The function $l_m(s)$ for small odd integers $s = \frac{1}{2}\tau(i\Delta\omega + \gamma/2)$.

| $2m+1$ | $l_m(s)$ |
|---|---|
| 1 | 1 |
| 3 | $-1+8s$ |
| 5 | $1-\frac{8}{3}s+\frac{64}{3}s^2$ |
| 7 | $-1+\frac{144}{15}s-\frac{54}{15}s^2+\frac{512}{15}s^3$ |

The steep switch-on in the value of $\rho(t)$, in time of order $\tau$, determines this asymptotic behavior. From Eqs. (294) and (300) it can be observed that the asymptotic form of $\tilde{\rho}(v)$ can be written as

$$\tilde{p}(v) \Rightarrow f(a) v^{2a-1} \exp(-\tfrac{1}{2}\pi v) \quad \text{for} \quad v \gg 1, \tag{301}$$

where $f(a)$ is $v$ independent.

In conclusion, using the two-level atom as a model for the interaction of an ultrafast pulse with a resonant system, we exhibited the following features for the generated supercontinuum:

1. At a specific incoming pulse energy, the intensity oscillates as a function of $\omega$, the number of oscillations increasing linearly as a function of the incoming energy.
2. At a specific frequency, the intensity oscillates as a function of the incoming pulse amplitude.
3. On the wings of the line, the intensity is an exponentially decreasing function multiplied by a polynomial whose degree is proportional to the energy of the incoming pulse. Another feature that we found, but that we do not present here, is that if the excitation pulse center frequency is off-resonance, the spectrum of the produced radiation field is asymmetric. Experimentally, the above predictions can easily be tested using 30-fs pulses that have been amplified in a copper vapor laser.

Finally, we reemphasize that in the above analysis we assumed an optically thin sample. This implies that only a very small fraction of the pulse is absorbed by the medium, which in turn implies that the predicted supercontinuum sits on top of a large unaltered component. The portion of the pulse that is absorbed, and thus acts as a source for the supercontinuum, $I_s$, can be obtained from Beer's law

$$I_s = I(L) - I(0) \quad \text{and} \quad I(L)/I(0) = e^{-\alpha' L}, \tag{302}$$

where $I(0)$ is the incoming pulse intensity, $L$ is the thickness of the sample, $\alpha'$ is the transient effective absorption coefficient, $\alpha' \approx \alpha\tau/T$, $\alpha$ is the CW absorption coefficient, $\tau$ is the pulse width, and $T$ is the line width. In the

treatment of the optically thick sample case, the full-fledged Maxwell-Bloch equations (Bloch, 1946; Feynman et al., 1957) describing the electromagnetic field-two-level atom system should be used. Under such circumstances, effects such as self-induced transparency (McCall and Hahn, 1969) and superradiant damping (Friedberg and Hartmann, 1971) were shown to be present and are expected to influence the spectral shape of the emitted radiation.

## 6. Concluding Remarks

In this chapter, we had the opportunity to review some recent work on simple models of self-phase and induced-phase modulation that can be treated analytically or almost so. What we observe is that:

1. Despite the many simplifying assumptions required to obtain analytical solutions, important qualitatively new features are obtained. Thus, these models serve as all good models should, as theoretical laboratories to seek new effects.
2. The old myth about the existence of "standard supercontinuum characteristics" is as valid as that of any phenomenological categorization, that is, in very limited cases. A rich and diversified variety of supercontinuum structures is shown to exist for different experimental regimes.
3. The partial differential equations derived are amenable to standard numerical computations and approximate methods and would provide the means to the natural extension of the simple analytical cases presented.

This chapter did not treat the following important cases:

1. Instances where the group velocity dispersion effects are important. This precluded any discussion of solitons, an area of intense and extensive research effort.
2. The experimental case where the pump and probe in induced-phase modulation are of the same magnitude. [Our solutions are restricted to weak probes.]
3. The general transverse dependence for large $r$, that is, for values of $r$ comparable to the value of the pulse radius $a$. [Our finite beam solutions are restricted to small $r/a$.]
4. Saturable absorbers, where a full treatment of the Bloch-Maxwell equations is required. Such a treatment will lead to a rigorous inclusion of relaxation times and to the detailed study of frequency-dependent nonlinear indices of refraction.
5. Multimodes of the electromagnetic field and in general the noise problem.

We are actively pursuing work in all of the above areas and will report our results in the literature as they develop.

Finally, I would like to acknowledge the contributions of my coworkers R. Alfano, P. Baldeck, O. Cockings, P. Ho, and M.A. Mustafa, whose partici-

pation in the different portions of the work reported in this chapter made it possible. Victoria Okai deserves the credit for typing and producing the manuscript.

## References

Alfano, R.R. (1972) GTE Report, TR-72-230-1, April 1972.
Alfano, R.R. and P.P. Ho (1986) Induced phase modulation and induced spectral broadening of propagation laser pulses in condensed matter. *Proc. International Conference on Lasers '86.*
Alfano, R.R. and P.P. Ho (1988) IEEE J. Quantum Electron. **24**, 351.
Alfano, R.R. and S.L. Shapiro (1970) Phys. Rev. Lett. **24**, 592.
Alfano, R.R., Q.X. Li, T. Jimbo, J.T. Manassah, and P.P. Ho (1986) Opt. Lett. **11**, 626.
Alfano, R.R., Q.Z. Wang, T. Jimbo, P.P. Ho, R.N. Bhargava, and B.J. Fitzpatrick (1987) Phys. Rev. A **35**, 459.
Anderson, D. and M. Lisak (1983) Phys. Rev. A **27**, 1393.
Baldeck, P.L., F. Raccah, and R.R. Alfano (1987) Opt. Lett. **12**, 588.
Bethe, H.A. and E.E. Salpeter (1957) *Quantum Mechanics of One- and Two-Electron Atoms.* Academic Press, New York.
Bloch, F. (1946) Phys. Rev. **70**, 460.
Bloembergen, N. (1965) *Nonlinear Optics.* Benjamin, New York.
Born, M. and E. Wolf (1975) *Principles of Optics*, 5th ed. Pergamon, New York.
Dabby, F.W. and J.R. Whinnery (1968) Appl. Phys. Lett. **13**, 284.
De Martini, F., C.H. Townes, T.K. Gustafson, and P.L. Kelley (1967) Phys. Rev. **164**, 312.
Feynman, R.P., F.L. Vernon, Jr., and R.W. Hellwarth (1957) J. Appl. Phys. **28**, 49.
Fork, R.L., C.H. Brito-Cruz, P.C. Becker, and C.V. Shank (1987) Opt. Lett. **12**, 483.
Friedberg, R. and S. Hartmann (1971) Phys. Lett. A **37**, 285.
Gaskill, J.D. (1978) *Linear Systems, Fourier Transforms and Optics.* Wiley, New York.
Gordon, J.P. (1986) Opt. Lett. **11**, 662.
Gordon, J.P., R.C.C. Leite, R.S. Moore, S.P.S. Porto, and J.R. Whinnery (1965) J. Appl. Phys. **36**, 3.
Grischkowsky, D. and A. Balant (1986) Appl. Phys. Lett. **41**, 1.
Kelley, P.L. (1965) Phys. Rev. Lett. **15**, 1085.
Kogelnik, H. (1965) Appl. Opt. **4**, 1562.
Kogelnik, H. and T. Li (1966) Proc. IEEE **54**, 1312.
Lamb, W.E. Jr. and R.C. Retherford (1950) Phys. Rev. **79**, 549.
McCall, S.L. and E.L. Hahn (1969) Phys. Rev. **183**, 457.
Manassah, J.T. (1986a) Appl. Opt. **25**, 1737.
Manassah, J.T. (1986b) Phys. Lett. **117A**, 5.
Manassah, J.T. (1987a) Appl. Opt. **26**, 1972.
Manassah, J.T. (1987b) Appl. Opt. **26**, 3747.
Manassah, J.T. (1988a) Opt. Lett. **13**, 755.
Manassah, J.T. (1988b) Appl. Opt. **28**, 206.
Manassah, J.T. (1988c) Opt. Lett. April (1989).
Manassah, J.T. (1988d) Appl. Opt. **27**, 4635.
Manassah, J.T. and O. Cockings (1987a) Appl. Opt. **26**, 3749.
Manassah, J.T. and O. Cockings (1987b) Opt. Lett. **12**, 1005.

Manassah, J.T. and M.A. Mustafa (1988a) Phys. Lett. **A133**, 51.
Manassah, J.T. and M.A. Mustafa (1988b) Opt. Lett. **13**, 752.
Manassah, J.T. and M.A. Mustafa (1988c) Appl. Opt. **27**, 807.
Manassah, J.T. and M.A. Mustafa (1988d) The supercontinuum generated by six-photon mixing. Opt. Lett. **13**, 862.
Manassah, J.T., M.A. Mustafa R.R. Alfano, and P.P. Ho (1985) Phys. Lett. **113A**, 242.
Manassah, J.T., M.A. Mustafa R.R. Alfano, and P.P. Ho (1986) IEEE J. Quantum Electron. **QE-22**, 197.
Manassah, J.T., P.L. Baldeck, and R.R. Alfano (1988a) Opt. Lett. **13**, 589.
Manassah, J.T., P.L. Baldeck, and R.R. Alfano (1988b) Opt. Lett. **13**, 1090.
Manassah, J.T., P.L. Baldeck, and R.R. Alfano (1988c) Appl. Opt. **27**, 3586.
Marburger, J.H. (1975) Prog. Quantum Electron. **4**, 35.
Martinez, O.A., J.P. Gordon, and R.L. Fork (1984) J. Opt. Soc. Am. **A-1**, 1003.
Nayfeh, A.H. (1981) *Introduction to Perturbation Techniques.* Wiley, New York.
Robiscoe, R.T. (1978) Phys. Rev. **A-17**, 247.
Rosen, N. and C. Zener (1932) Phys. Rev. **40**, 502.
Rothenberg, J.E. and D. Grischkowsky (1987) Opt. Lett. **12**, 99.
Sargent, M., III, M.O. Scully, and W.E. Lamb, Jr. (1974) *Laser Physics.* Addison-Wesley, Reading, Massachusetts.
Thomas, D.G., L.K. Anderson, M.I. Cohen, E.I. Gordon, and P.K. Runge (1982) Lightwave communication. In *Innovations in Telecommunications*, J.T. Manassah, ed. Academic Press, New York.
Tien, P.K., J.P. Gordon, and J.R. Whinnery (1965) Proc. IEEE **53**, 129.
Tomlinson, W.J., R.H. Stolen, and C.V. Shank (1984) J. Opt. Soc. Am. **B1**, 139.
Treacy, E.B. (1969) IEEE J. Quantum Electron. **OE-5**, 454.
Tzoar, N. and M. Jain (1979) Propagation of nonlinear optical pulses in fibers. In *Fiber Optics*, B. Bendow and S. Mitra, eds. Plenum, New York.
Yang, G. and Y.R. Shen (1984) Opt. Lett. **9**, 510.

Note added in proof: We recently obtained the following new results:

1. An expression for the induced frequency shift of Section 4.1.
2. A scheme to balance Gordon's self-frequency shift by the induced frequency shift.
3. The general solution of the plane wave model for $\chi^{(3)}$ material with relaxation present.

Details of these calculations are given in:

Induced frequency modulation in a nonzero relaxation-time medium. JOSA **B6**, June 1989.

Analytical solution for a self-phase-modulated and self-steepened pulse in a nonlinear medium with material relaxation. JOSA **B6**, June 1989.

# Appendix: Analytical Solution for a Self-Phase Modulated and Self-Steepened Pulse Propagating in a $\chi^{(5)}$-Medium with Material Relaxation

In this appendix, we derive the analytical solution for a self-phase modulated pulse propagating in a nonlinear $\chi^{(5)}$-medium. The calculation is performed in the plane-wave approximation for dispersionless medium but with self-steepening and material relaxation present.

In the phenomenological model that we consider, the nonlinear source term for Maxwell's equation is taken as:

$$s = \frac{nn_4}{c^2}\frac{\partial^2}{\partial t^2}\left(|E|^4 E - c_1 E\frac{\partial}{\partial t}|E|^4\right). \tag{A.1}$$

That is, we are taking the first two terms of the noninstantaneous nonlinear polarization where $c_1$ is the first moment of the delayed response kernel is essentially equal to the material response time. Variable $n_4$ is the nonlinear Kerr coefficient, $n$ is the linear index of refraction of the material, and $c$ is the speed of light in vacuum. This phenomenological model is valid for a pulse duration longer than the material response time.

Maxwell's equation reduces to

$$\left(\frac{\partial^2}{\partial Z^2} - \frac{\partial^2}{\partial T^2}\right)\Phi = \varepsilon'\frac{\partial^2}{\partial T^2}\left(|\Phi|^4\Phi - \gamma'\Phi\frac{\partial}{\partial T}|\Phi|^4\right), \tag{A.2}$$

where the dimensional parameters $\varepsilon'$, was defined in Section 3, and $\gamma'$ is given by

$$\gamma' = \frac{c_1}{\tau}. \tag{A.3}$$

In the physical coordinates $U$ and $V$, as defined in Section 3, the amplitude $a$ and the phase $\alpha$ of $A$, then obey the following quasi-linearized partial differential equations:

$$\frac{\partial a}{\partial V} - \frac{5}{2}\varepsilon' a^4\frac{\partial a}{\partial U} = 0, \tag{A.4}$$

$$\frac{\partial \alpha}{\partial V} - \frac{\varepsilon'}{2}a^4\frac{\partial \alpha}{\partial U} = \frac{K}{2}\varepsilon' a^4 - \frac{K}{8}\varepsilon'^2 a^8 + 2K\gamma'\varepsilon' a^3\frac{\partial a}{\partial U}. \tag{A.5}$$

The $U$-partial derivatives, appearing on the left-hand side of Eqs. (A4) and (A5), are responsible for self-steepening and the term proportional to $\gamma'$ expresses the finite relaxation time of the medium. We notice that in this model the finite relaxation time does not alter the amplitude equation.

To discuss the impact of self-steepening and finite relaxation time, we shall index $a$ and $\alpha$ by two dummy indices where the first index refers to self-steepening and the second to finite relaxation time. Each index takes the value (0, 1) for the effect being (absent, present). (It is stressed that we can directly solve Eqs. (A4) and (A5) in the most general case, but we are going through these intermediate steps to clarify the role and meaning of the different terms in the equations.) We now write the solutions in the four cases, for an initial sech pulse with zero phase:

(i) $\gamma' = 0$, $\varepsilon' V \ll 1$

$$a_{0,0} = \operatorname{sech}(U) \tag{A.6}$$

$$\bar{\alpha}_{0,0} \equiv \frac{\alpha_{0,0}}{K} = \frac{\varepsilon' V}{2} \operatorname{sech}^4(U) \tag{A.7}$$

(ii) $\gamma' \neq 0$, $\varepsilon' V \ll 1$

$$a_{0,1} = \operatorname{sech}(U) = a_{0,0} \tag{A.8}$$

$$\bar{\alpha}_{0,1} = \frac{\varepsilon' V}{2} \operatorname{sech}^4(U) - 2\gamma' \varepsilon' V \operatorname{sech}^4(U) \tanh(U) \tag{A.9}$$

(iii) $\gamma' = 0$

$$a_{1,0}^2 = \operatorname{sech}^2\left(U + \tfrac{5}{2}\varepsilon' V a_{1,0}^4\right) \tag{A.10}$$

$$\begin{aligned}\bar{\alpha}_{1,0} = &-U - \frac{\varepsilon'}{6}\int_0^U a_{1,0}^4(p,V)\,dp - \frac{5}{24}\varepsilon'^2 \int_0^V a_{1,0}^8(0,q)\,dq \\ &+ \tanh^{-1}(\sin g(U,V)) + \frac{\varepsilon'}{6}\sin g(U,V) - \frac{\varepsilon'}{18}\sin^3(g(U,V)),\end{aligned} \tag{A.11}$$

where

$$g(U,V) = \frac{\varepsilon'}{2}\int_0^V a_{1,0}^5(U,q)\,dq + \sin^{-1}(\tanh U) \tag{A.12}$$

(iv) general case

$$a_{1,1}^2 = a_{1,0}^2 = \operatorname{sech}^2\left(U + \tfrac{5}{2}\varepsilon' V a_{1,1}^4\right) \tag{A.13}$$

$$\bar{\alpha}_{1,1} = \bar{\alpha}_{1,0} + \gamma' \ln(a_{1,1}) - \gamma' \ln[\operatorname{sech}[\tanh^{-1}(\sin g(u,v))]] \tag{A.14}$$

The foregoing general solution for the amplitude, derived under the condition of no dispersion, is valid for all values of $V < V_{\text{crit}}$, where $V_{\text{crit}}$ is the critical value of $V$.

In Figure A1, we plot $\bar{\alpha}_{0,1} - \bar{\alpha}_{0,0}$. This quantity, which represents the portion of the phase due to nonzero relaxation time for $\varepsilon' V \ll 1$, is

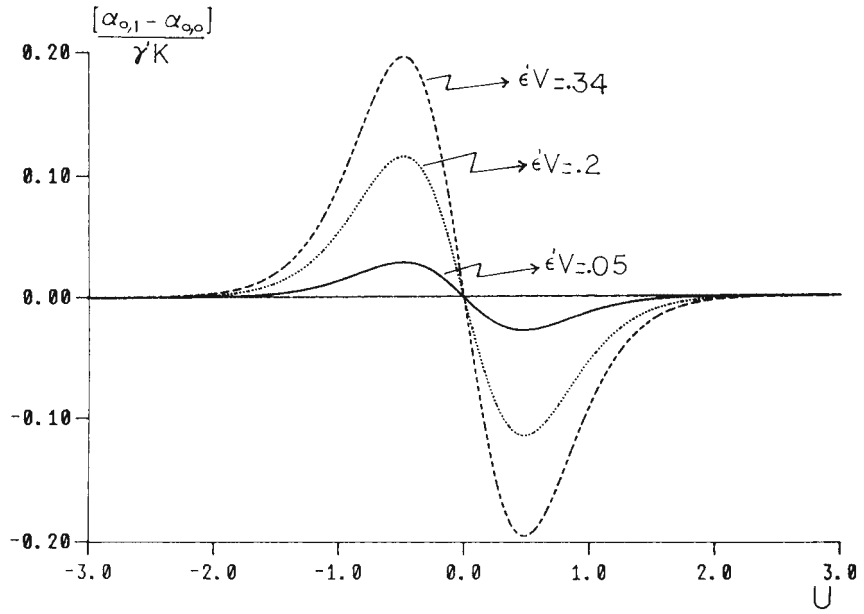


FIGURE A1. The phase portion due to nonzero relaxation time, in the absence of self-steepening, as function of $U$.

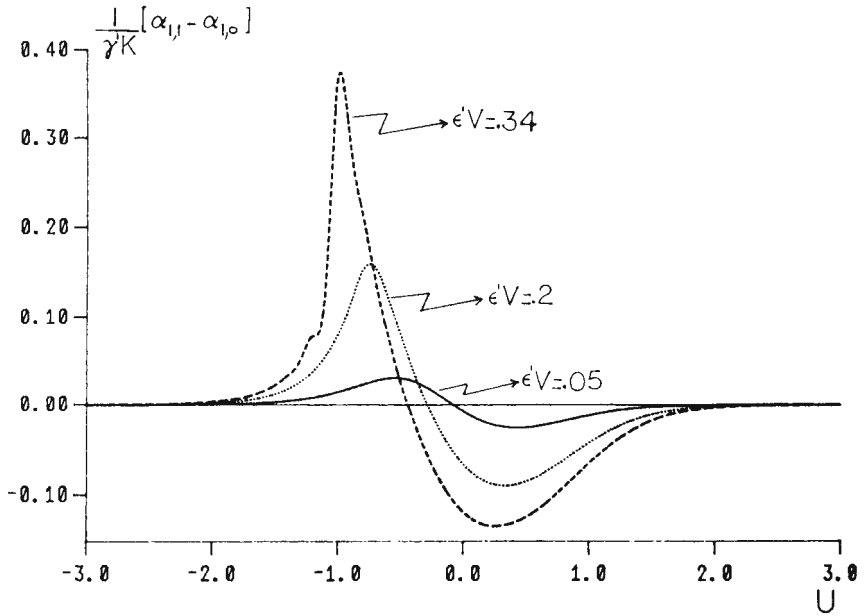


FIGURE A2. The phase portion due to nonzero relaxation time, in the presence of self-steepening, as function of $U$.

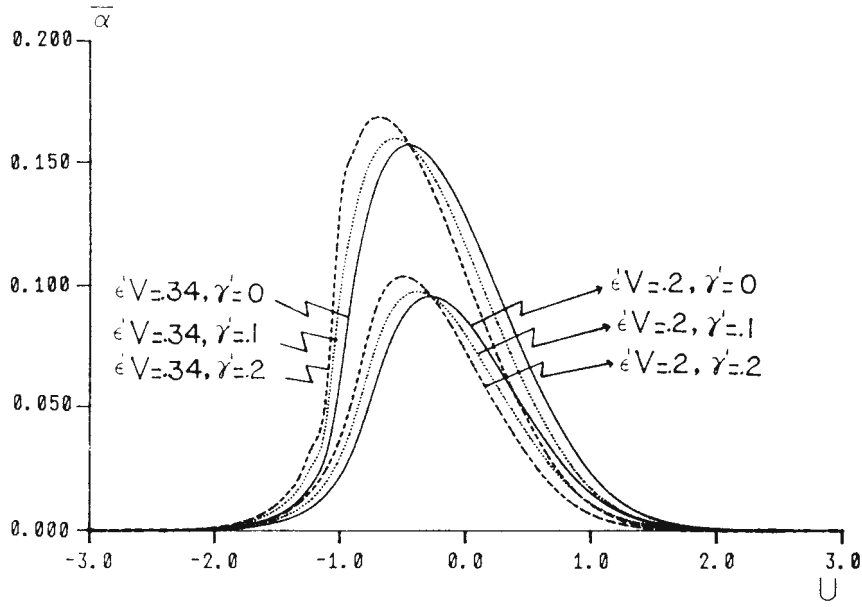


FIGURE A3. The pulse normalized total phase as function of $U$.

approximately linear in $U$ and has a negative slope, which translates into a Stokes shift in the instantaneous frequency. This shift is similar to Gordon's self-frequency shift, derived for $\chi^3$ material. In Figure A2, we plot $\bar{\alpha}_{0,1} - \bar{\alpha}_{0,0}$ for different values of $\varepsilon' V$ to qualitatively examine the effects of self-steepening on this Stokes shift.

In Figure A3, we are plotting $\bar{\alpha}_{1,1}$, the pulse total phase in the general case. (Henceforth, we will omit the subscripts to refer to the general case.) We note that the presence of the $\gamma'$-term and the self-steepening term shifts the position of the phase maximum from the $U = 0$ axis. Furthermore, the maximum of the pulse amplitude and that of the phase are shifted with respect to each other, which leads to a shift in the positions of the interference fringes of this pulse, for a Young set-up, from those of *cw* coherent light.

The normalized frequency sweep for this pulse, obtained by taking the $U$-partial derivative of $\bar{\alpha}$, is given, for the general case, by

$$\frac{\partial \bar{\alpha}}{\partial U} = -1 - \frac{\varepsilon'}{6} a^4 + \frac{a}{\cos g} + \frac{\varepsilon'}{6} a(\cos g) - \frac{\varepsilon'}{6} a(\sin^2 g)(\cos g) + \gamma' \left[ a(\tan g) + \frac{1}{a} \frac{\partial a}{\partial U} \right]. \tag{A.15}$$

In Figure A4, we are plotting this quantity. It should be remembered that the maximum of this curve determines in each case the spectral frequency extent on the anti-Stokes side, while its minimum determines the corresponding

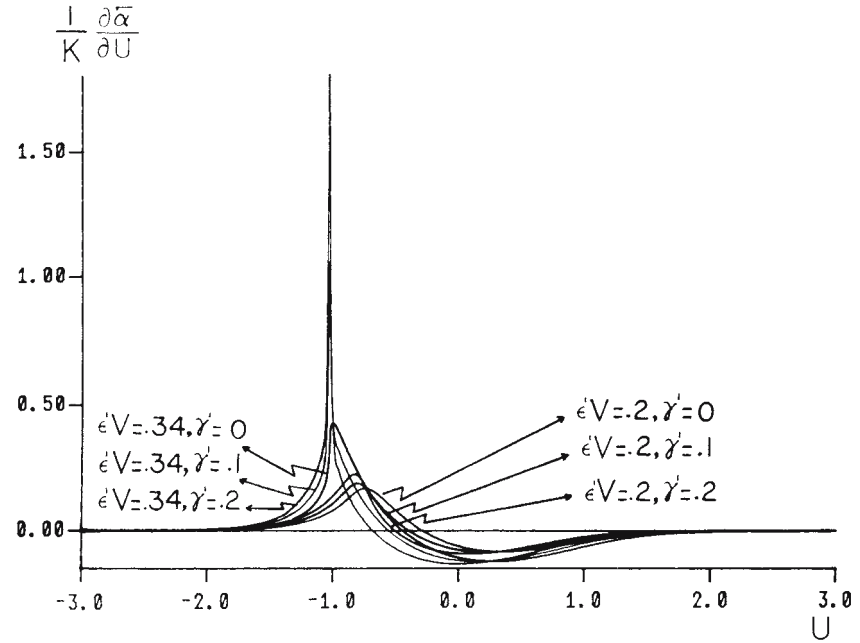


FIGURE A4. The pulse normalized instantaneous frequency sweep as function of $U$.

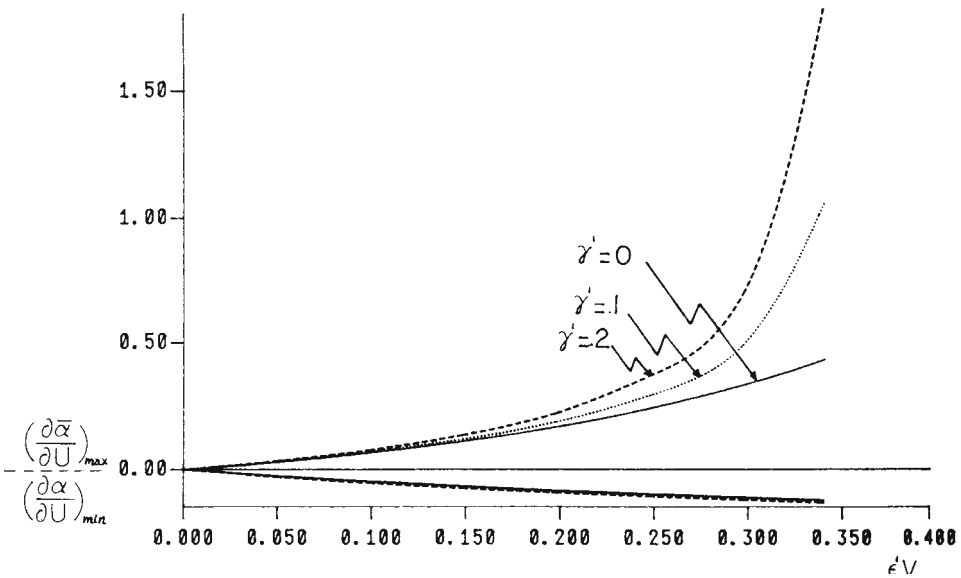


FIGURE A5. The Stokes and anti-Stokes spectral distribution extents as a function of $\varepsilon' V$.

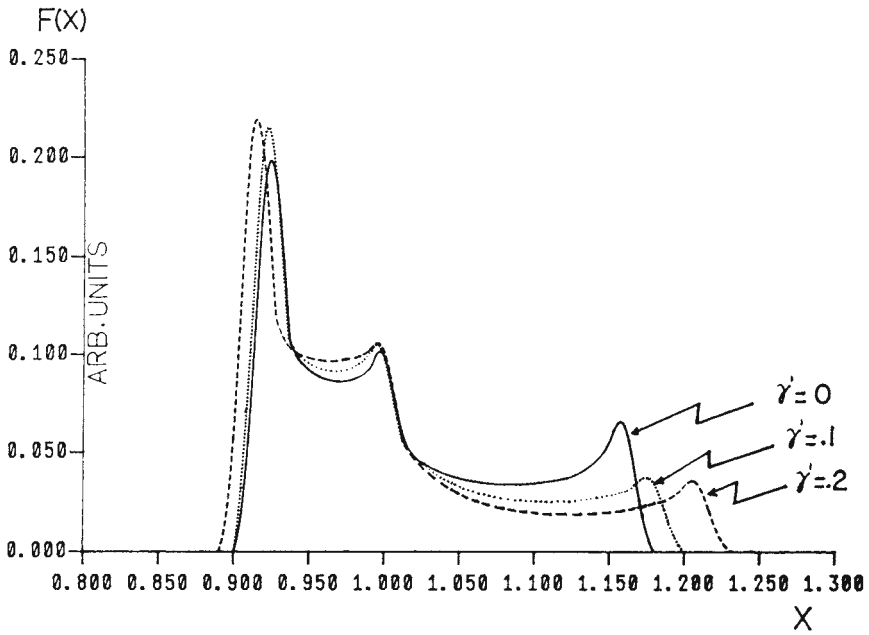


FIGURE A6. The envelope of the Fourier transform of the Young visibility function.

quantity on the Stokes side. As we can observe from the figure, the normalized frequency sweep is asymmetric with respect to the $U-0$ axis. This results in an asymmetry of the spectral distribution between the Stokes and anti-Stokes portion of the spectrum. Furthermore, the absolute value of the maximum of $\partial\overline{\alpha}/\partial U$ is always bigger than that corresponding to its minimum value, and therefore the anti-Stokes spectral extent is larger than the Stokes extent. In Figure A5, these extreme quantities are plotted as function of $\varepsilon' V$ for different $\gamma'$s. These extrema were also shown to determine the domain of $F(x)$, the Fourier transform of the visibility function of the Young intensity distribution with the general solution pulse as input. In Figure A6, we plot the envelopes of $F(x)$ for different cases. The domain for each case, as computed in Figure A6, agrees with the results of Figure A5.

The pulse spectral distribution is obtained by taking the absolute magnitude square of the Fourier transform of the pulse electric field. In Figure A7, the spectrum is shown for selected values of the parameters. The important features found in our calculations are the following:

1. As $\varepsilon' V$ increases, the spectrum is more asymmetric, and near the Stokes maximum extent the spectrum falls off rapidly.
2. As $\gamma'$ increases, the spectrum is further shifted to the Stokes side and the maximum frequency extents are consistent with the results of Figure A5.

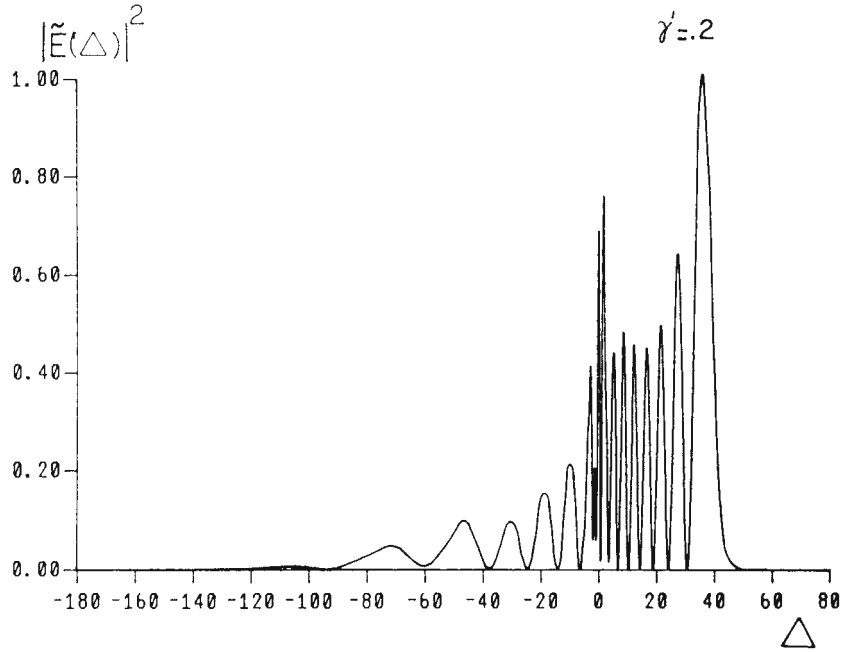


FIGURE A7. The pulse spectral distribution as function of the normalized frequency difference multiplied by the pulse duration. At left is the anti-Stokes side. Normalized center frequency $K = 300$; $\varepsilon' V = 0.2$.

To understand the role of the nonzero relaxation time in the Stokes shift, let us calculate the mean frequency of the pulse normalized to the original center frequency. The normalized first moment of the frequency can be written in the time domain representation as follows:

$$\frac{\overline{K}'}{K} = \frac{\int_{-\infty}^{\infty}\left(1+\frac{\partial\overline{\alpha}}{\partial U}\right)a^2 dU}{\int_{-\infty}^{\infty} a^2(U)dU} \tag{A.16}$$

for small $\varepsilon' V$, this quantity, for the $\gamma^{(5)}$ medium, is given by

$$\lim_{\varepsilon' V \ll 1} \frac{\overline{K}'}{K} \approx 1 - 0.3\gamma'(\varepsilon' V). \tag{A.17}$$

The second term on the right-hand side corresponds to the numerically computed Stokes shift. Note that this shift is linear in the thickness of the material, and in the relaxation time and is quadratic in the intensity.

# 6
# Self-Steepening of Optical Pulses

B.R. Suydam

Self-steepening of optical pulses has been well described in the literature (De Martini et al., 1967; Marburger, 1975) and has been invoked to explain certain cases of spectral superbroadening (Yang and Shen, 1984). For intense optical pulse the refractive index depends on the intensity. Thus, the peak of the pulse travels at a speed different from that of the leading and trailing edges, so that ultimately the pulse tries to form a shock at the trailing edge if $n_2$ is positive or on the leading edge if $n_2$ is negative. A very similar thing occurs in fluid mechanics. However, all fluids exhibit viscosity and heat flow and these effects combine to prevent the formation of a truly discontinuous shock; they give the final shock structure, which has finite thickness and a definite shape. In the optical case, dispersion will play an analogous role; it brings the process of self-steepening to an end before a true discontinuity can form. It is for this last reason that we feel it to be imperative to include the effects of dispersion in our present study of self-steepening.

## 1. Mathematical Formulation

For mathematical tractability, we restrict our discussion to that of a plane-polarized plane wave traveling in a uniform, isotropic, transparent medium. To arrive at manageable equations we have had to assume also the following:

1. dispersion, absorption, and nonlinearity of the medium are so weak that a light pulse changes shape but slowly as it propagates;
2. higher-order dispersion terms, which would be neglected in a slowly varying envelope theory, are required to take on a certain form; and
3. the nonlinearity develops instantaneously.

Note that we *do not* assume that the envelope varies slowly. Under the foregoing assumptions, if we set

$$E = \tfrac{1}{2} U \exp[i(kz' - \omega t)] + \text{c.c.}$$

into the wave equation for $E$, we can derive as a good approximation the equation

$$-i\frac{\partial U}{\partial z} = -a\frac{\partial^2 U}{\partial \tau^2} + \gamma |U|^2 U + i\varepsilon \frac{\partial}{\partial \tau}\left(|U|^2 U\right). \tag{1}$$

The derivation of this equation is given in Appendix A. In the process we have changed from laboratory coordinates $z'$, $t$ to coordinates $z$ and $\tau$ given by

$$\begin{aligned} z &= z', \\ \tau &= t - z/v, \end{aligned} \tag{2}$$

so that $\partial/\partial z$ is calculated in a frame moving with the pulse at the group velocity $v$.

The coefficients $a$ and $\gamma$ measure, respectively, the dispersion and the nonlinearity and are given by

$$a = \frac{\lambda^3}{2\pi c^2}\frac{d^2 n}{d\lambda^2} \quad \text{and} \quad \gamma = \frac{3\omega n_2}{4c},$$

where $n(\lambda)$ is the linear refractive index expressed as a function of the free space wavelength $\lambda \equiv 2\pi c/\omega$. Our derivation also yields

$$\varepsilon = \gamma/\omega = 3n_2/4c. \tag{3}$$

We keep the two symbols separate both to facilitate comparison with existing theories and to clarify the physical origin of the various effects we discuss.

In spite of its appearance, Eq. (1) is *not* the result of a slowly varying envelope theory. This is made clear in Appendix A. As a result we are able, without violating the conditions of our approximations, to study pulses of arbitrarily short rise times and of arbitrarily great bandwidths. Assumption (1) is well satisfied for pulses below the damage threshold and frequencies far from an absorption line or band. Assumption (2), spelled out in Appendix A, is automatically met for narrowband signals ($\Delta\omega \ll \omega$); for $\Delta\omega$ of order $\omega$ it imposes special, but not nonphysical, conditions on the behavior of $n(\lambda)$ near the band edges. Assumption (3) is not reasonable, but it is at present necessary. Certainly the linear part of the polarization does not respond instantaneously, as otherwise there would be no dispersion, and it would be unrealistic to expect the nonlinear part to respond faster than the linear part. Note also that we have neglected a small amount of absorption, which can be put back in as a perturbation once we have solved Eq. (1).

We shall wish to put numbers into some of our formulas. For this purpose we have chosen from the* *American Institute of Physics Handbook* (1963) and Boling et al. (1978)

$$\begin{aligned} &a = 2.5\times 10^{-27}(\text{s})^2(\text{cm})^{-1}, \qquad n_2 = 1.27\times 10^{-13}, \\ &\omega = 3.14\times 10^{15}(\lambda = 6000\,\text{Å}), \qquad n = 1.67, \\ &\gamma = 10^{-8}, \qquad \varepsilon = 3.2\times 10^{-24}, \end{aligned} \tag{4}$$

as typical. The number $a$ could vary by a factor 3 or so either way, and as $dn/d\lambda \propto \lambda^{-3}$ over the range considered $a$ scales roughly as $\lambda^{-1}$. The dispersion constant $a$ can be either positive for normal dispersion or negative for anomalous dispersion. On the other hand, $n_2$ can be negative only near to and on the high-frequency side of an absorption line or band, conditions that would strongly violate our assumptions of small dispersion and nearly negligible absorption. Consequently, we shall hereafter assume that $\gamma$ and $\varepsilon$ are positive.

Two special cases of our Eq. (1), both of which include dispersion, have been shown to be completely integrable. The case $\varepsilon \equiv 0$ (no self-steepening), known as the *nonlinear Schrödinger* (NS) equation, was completely solved by Zakharov and Shabat (1972). The case $\gamma \equiv 0$ and $\varepsilon \neq 0$, called by the authors a *derivative nonlinear Schrödinger* (DNS) equation, has been completely solved by Kaup and Newell (1978). In both cases an arbitrary initial pulse of finite energy per unit area will ultimately break up into a set of solitons plus "radiation" (hash that ultimately disperses away). In our case, with general $\gamma$ and $\varepsilon$, we also find solitary wave solutions, which we call "solitons," which are mathematically scarcely distinguishable from the solitons of the DNS equation and are a direct generalization of the solitons of the NS equation. As do the NS and DNS equations, our equation also admits "kink" or "dark soliton" solutions.

It is convenient for us to rewrite Eq. (1) in terms of a real amplitude $A$ and a real phase $\phi$; thus we set

$$U = A\exp(i\phi)$$

and obtain

$$\begin{aligned} A_z &= a[2A_\tau\phi_\tau + A\phi_{\tau\tau}] - 3\varepsilon A^2 A_\tau, \\ A\phi_z &= a\left[A(\phi_\tau)^2 - A_{\tau\tau}\right] + A^3(\gamma - \varepsilon\phi_\tau). \end{aligned} \tag{5}$$

The subscripts $z$ and $\tau$ denote partial derivatives. These equations describe how the amplitude and the phase evolve as the pulse propagates in $z$.

## 2. Early Self-Steepening

There are two ways in which an initially smooth pulse can develop features that sharpen as it propagates, namely by self-steepening and by growth of the modulational instability (longitudinal self-focusing). First let us consider self-steepening. The operator $\partial/\partial\tau$ is of order $\Omega$, which represents the bandwidth of the envelope function $U$. Thus the dispersion term is of order $a\Omega^2$, whereas the self-steepening term is of order $\varepsilon A^2\Omega$. For very smooth pulses $\Omega$ is small; if the power level is not too low we will have

$$\Omega << \varepsilon A^2/a \tag{6}$$

and under this condition we can neglect dispersion. In this limit Eqs. (5) reduce to

$$\begin{aligned} u_z + 3\varepsilon u u_\tau &= 0, \\ \phi_z + \varepsilon u \phi_\tau &= -\gamma u, \\ u &\equiv A^2. \end{aligned} \tag{7}$$

The first is well known (Whitham, 1974), and its general solution can be written in the form

$$u = f(\tau - 3\varepsilon u z). \tag{8}$$

Initially, that is to say at $z = 0$,* $u(\tau, 0) = f(\tau)$, so the form of the arbitrary function $f$ is determined by the pulse shape at $z = 0$. Equation (8) describes shock formation, which we can see as follows. Differentiating Eq. (8) yields

$$u_\tau = \frac{f'}{\Delta}, \qquad u_z = \frac{-3\varepsilon u f'}{\Delta}, \qquad \Delta \equiv 1 + 3\varepsilon z f'. \tag{9}$$

Clearly, these derivatives become infinite and a shock starts to form when $\Delta$ first vanishes, and as $\varepsilon$ is positive this occurs when $f'$ achieves its most negative value, say $f'_m$; clearly this occurs on the trailing edge.

The value of $z$ at which the shock first starts to form is clearly given by

$$z_s = -(3\varepsilon f'_m)^{-1}. \tag{10}$$

For a Gaussian pulse of width $2T$, we have

$$f(\tau) = A_0^2 \exp\left[-(\tau/T)^2\right].$$

Clearly $|f'|$ is maximum when $(\tau/T)^2 = \frac{1}{2}$, so for such a pulse

$$f'_m = -\left(\sqrt{2/e}\right) A_0^2/T = -0.85776\, A_0^2/T,$$

whence, for a Gaussian pulse in a medium of refractive index 1.67,

$$z_s = (0.3886T)/(\varepsilon A_0^2) = (71.42T)/\varepsilon I_0, \tag{11}$$

where $I_0$ is the peak intensity in watts/cm$^2$. As an example, for a 100-fs pulse we set $T = 5 \times 10^{-14}$ and with our typical value for $\varepsilon$ we would have

$$z_s(100\,\text{fs}) = (1.2 \times 10^{11})/I_0 \tag{12}$$

(i.e., a pulse of 1 TW/cm$^2$ would start to shock after about 12 mm of travel). We have seen that the distance for shock formation is proportional to the pulse width. Thus for a pulse of 10 ps width $z_s$ would be 100 times greater than that for a 100-fs pulse, that is, about 1.2 m for a 1 TW/cm$^2$ pulse and 1.2 km for a 1 GW/cm$^2$ pulse.

How a shock actually develops according to Eq. (8) is illustrated in Figure 6.1, in which we have depicted an initially Gaussian pulse, labeled $z = 0$, and

* Throughout this chapter we use the expression "initially" or "initial condition" in this sense (i.e., the condition at $z = 0$).

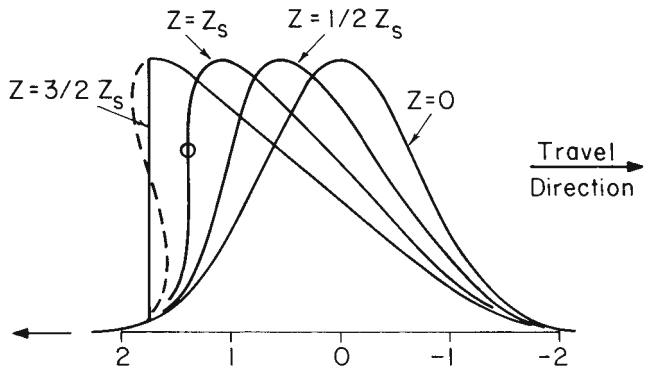
Z = Z_S
Z = 1/2 Z_S
Z = 3/2 Z_S
Z = 0
Travel
Direction
2
1
0
-1
-2
The horizontal axis is Proper Time T, normalized to pulse half width; the vertical axis is the Intensity, u from Eq. (8). Thus one can visualize the pulse as travelling from left to right.

FIGURE 6.1. Various states of self-steepening of an initially Gaussian pulse, according to Eq. (8). Shown are curves for $z = 0$, the initial pulse, $z = \frac{1}{2}z_s$, $z = z_s$, the beginning of shock formation, and $z = \frac{3}{2}z_s$, depicting a well-formed shock. On the $z = z_s$ curve, the circle indicates the point of infinite slope. The dashed curve and vertical shock for $z = \frac{3}{2}z_s$ are discussed in the text.

shown how it changes shape after propagating the distances $z = z_s/2$, $z = z_s$ (the distance for first shock formation), and $z = 3z_s/2$ when the shock is well developed. For $z > z_s$ we must use Eq. (8) with some care. In general, for $z > z_s$, Eq. (8) describes a breaking wave, indicated in our figure by the dashed lines for $z = 3z_s/2$. The intensity cannot, however, be three valued, so we must instead place a shock (i.e., a discontinuous jump) in this region. Equation (8) and, therefore, Eq. (7) also is satisfied on both sides of the jump. The location of the jump is determined by the condition that

$$W = \int_{-\infty}^{\infty} u(\tau, z)d\tau = \int_{-\infty}^{\infty} |U|^2 d\tau = \text{a constant},$$

that is, energy is conserved, as demanded by Eq. (1). We must remember that for $z \geq z_s$ our Figure 6.1 depicts the behavior of the solution of the first of Eqs. (7); in fact, before $z$ reaches $z_s$, the pulse bandwidth will have become large enough that dispersion can no longer be neglected. We shall now proceed to estimate at what point dispersion must be included.

Once $u$ has been determined, the equation for $\phi$ is linear and can be solved by the method of characteristics. In the special case of the DNS equation, $\gamma = 0$ and $\phi \equiv 0$ is a solution; in this case phase modulation does not grow as the pulse propagates.

To show more clearly how early self-steepening occurs I think it useful to resort to a simple model problem. To this end we choose the leading edge of

$f(\tau)$ to be anything that rises smoothly to a peak value $f_0$ at $\tau = 0$. The trailing edge, where the self-steepening occurs, we choose to be of the form

$$f(\tau) = \begin{cases} f_0(1-\tau/\tau_0) & \text{for } 0 < \tau < \tau_0, \\ 0 & \text{for } \tau > \tau_0. \end{cases} \tag{13}$$

Then by Eq. (8), for $\tau < 0$, $u$ will be some stretched-out version of the original pulse shape $f(\tau)$, and on the trailing edge

$$u = \begin{cases} f_0(1-\tau/\tau_0)/\Delta & \text{for } 3\varepsilon f_0 z < \tau < \tau_0, \\ 0 & \text{for } \tau > \tau_0. \end{cases} \tag{14}$$

and for this case our previously defined $\Delta$ becomes

$$\Delta = 1 - 3\varepsilon z f_0/\tau_0.$$

Setting this value of $u$ into the second of Eqs. (7), we can readily solve by the method of characteristics (in the trailing edge) and find

$$\phi = \begin{cases} \dfrac{\gamma}{\varepsilon}(\tau_0 - \tau)[1-\Delta^{-1/3}] + \phi_0(\tau_0 - (\tau_0 - \tau)\Delta^{-1/3}) & \text{for } 3\varepsilon f_0 z < \tau < \tau_0, \\ \phi_0(\tau_0) & \text{for } \tau > \tau_0, \end{cases} \tag{15}$$

where $\phi_0(\tau) = \phi(\tau, 0)$ is the initial phase. In the leading edge, $\tau < 3\varepsilon f_0 z$, the phase will build up in a way that depends on the choice of $f(\tau)$ in this region.

Consider now a pulse initially without phase modulation, so $\phi_0 \equiv 0$. We see $\phi$ reaches its maximum at $\tau = \tau_{\min} = 3\varepsilon f_0 z$ and it is zero at $\tau = \tau_0$. Thus over this period of duration

$$\tau = \tau_0 - 3\varepsilon f_0 z = \tau_0 \Delta$$

the phase swings by

$$\Delta\phi = \omega\tau_0\Delta[1-\Delta^{-1/3}]$$

so we can estimate the bandwidth induced solely by this phase modulation, $\Omega_\phi$, as

$$\Omega_\phi = \Delta\phi/\tau = \omega[1-\Delta^{-1/3}]. \tag{16}$$

If we insert this into (6) rewritten as an equality we obtain

$$\Delta = [1 + \gamma A_0^2/a\omega^2]^{-3}. \tag{17}$$

When this condition is satisfied dispersion has become just as important as self-steepening and Eqs. (7) have broken down as a decent approximation. For our typical numbers $\gamma A_0^2/a\omega^2 = 1$ implies a peak power level of $3 \times 10^{14}\,\mathrm{W/cm^2}$ ($A_0 = 4.7 \times 10^8\,\mathrm{V/cm}$). For peak power levels significantly lower than this,

$$z_0 = \tau_0/a\omega \tag{18}$$

is the distance at which this breakdown occurs. For our typical numbers and $\tau_0 = 50\,\mathrm{fs}$ (fall time), this gives $z_0 = 6.4 \times 10^{-3}\,\mathrm{cm}$, which is far less than the

distance for shock formation, $z_s$. For peak power notably less than $10^{14}\,\mathrm{W/cm^2}$ $\Delta$ is very nearly unity and the trailing edge has steepened very little. Thus, for such a pulse, self-steepening is of only minor importance during the initial phase; it is the buildup of phase modulation that forces one to include the effects of dispersion.

## 3. Modulational Instability

Another mechanism for the breakup of an initially smooth pulse is the modulational instability, which has also been called longitudinal self-focusing. This has been well discussed by Marburger (1975) in the case $\varepsilon = 0$. To illustrate how this comes about, let us consider the smoothest possible pulse, namely, an unmodulated wave train. Thus we set

$$\begin{aligned} &A = A_0 = \text{a constant} \quad \text{and} \\ &\phi = \phi_0 \equiv \text{a const} + \gamma A_0^2 z. \end{aligned} \tag{19}$$

These functions satisfy Eqs. (5). Now consider a small perturbation to this solution; namely, we set

$$\begin{aligned} &A = A_0(1+w), \\ &\phi = \phi_0 + \tilde{\phi} = \text{const} + \gamma A_0^2 z + \tilde{\phi}. \end{aligned} \tag{20}$$

Setting Eqs. (20) into Eqs. (5) yields equations for $w$ and $\tilde{\phi}$. If the perturbation is small enough, we can neglect squares and products of $w$, $\tilde{\phi}$, and their derivatives. The resulting linearized equations for the perturbations are

$$\begin{aligned} &w_z + 3\varepsilon A_0^2 w_\tau = a\tilde{\phi}_{\tau\tau}, \\ &\tilde{\phi}_z + \varepsilon A_0^2 \tilde{\phi}_\tau = -a w_{\tau\tau} + 2\gamma A_0^2 w \end{aligned} \tag{21}$$

and the question is, what happens to the perturbation as it propagates; does it grow?

We can readily reduce Eqs. (21) to a pair of first-order ordinary differential equations by Fourier analyzing in $\tau$, setting

$$\begin{aligned} &w(z,\tau) = u(z)\exp[i\Omega\tau], \\ &\tilde{\phi}(z,\tau) = q(z)\exp[i\Omega\tau] \end{aligned} \tag{22}$$

and thus eliminate one of the variables, say $q$, between the two resulting equations. The result is the second-order equation

$$u'' + 4i\varepsilon\Omega A_0^2 u' + \left[a\Omega^2\left(a\Omega^2 + 2\gamma A_0^2\right) - 3\varepsilon^2 A_0^4\right]u = 0. \tag{23}$$

This has the solutions

$$u_\pm(z) = \text{const.}\exp\left\{\left(-2i\varepsilon\Omega A_0^2 \pm \alpha\right)z\right\}, \tag{24}$$

where

$$\alpha = +\left[-a\Omega^2\left(a\Omega^2 + 2\gamma A_0^2\right) - \varepsilon^2 A_0^4\Omega^2\right]^{1/2}. \tag{25}$$

By hypothesis $\gamma$ is positive; if $\alpha$ is also positive then $\alpha$ is pure imaginary and both functions $u_+(z)$ and $u_-(z)$ simply oscillate as the pulse propagates, that is, as $z$ increases; the perturbation neither grows nor dampens.

Now suppose that the dispersion is anomolous, that is, that $a$ is negative. We set $b = -a$ = positive and obtain

$$a^2 = b\Omega^2(2\gamma A_0^2 - b\Omega^2) - \varepsilon^2 A_0^4 \Omega^2 \tag{26}$$

and this is maximized for

$$\Omega^2 = \Omega_M^2 \equiv (\gamma/b)A_0^2 - (\varepsilon^2/2b^2)A_0^4. \tag{27}$$

If we set this value into Eq. (26) we determine that the maximum value of $\alpha^2$ is

$$\alpha_M^2 = [\gamma A_0^2 - (\varepsilon^2/2b)A_0^4]^2. \tag{28}$$

Now if

$$A_0^2 < 2b\gamma/\varepsilon^2 \tag{29}$$

(which for our typical numbers means peak power less than $10^{15}$ W/cm$^2$), $\Omega_M^2$ and $\alpha_M^2$ are positive and $u_+(z)$ oscillates with an exponentially growing amplitude as the beam propagates. Thus, no matter how small the initial disturbance, the modulation of the beam will grow exponentially until it interacts nonlinearly with itself. This is the modulational instability. The reader may notice that had we set $\varepsilon = 0$ our analysis would have been identical to that of the self-focusing instability (Bespalov and Talanov, 1966; Suydam, 1973). One might therefore call the phenomenon longitudinal self-focusing rather than modulational instability; the two terms mean the same thing.

It is interesting to compare the effects of the modulational instability and of self-steepening. To this end we will consider a beam of a few terawatts power or less in a medium of anomalous dispersion. The inequality (29) is strongly satisfied, so the maximum growth rate is

$$\alpha_M = \gamma A_0^2$$

very nearly. Now multiply this by the shock formation distance $z_s$, given by Eq. (11); we get

$$\alpha_M z_s = 0.3886 T\omega = 2.44 N,$$

where $N$ is the half-width of the pulse measured in cycles of the carrier frequency $\omega$. In propagating over the shock-forming distance $z_s$ the modulational instability grows by a factor exp[2.44$N$], which amounts to a factor $10^5$ for $N$ = 4.7 cycles half-width. Clearly, unless we are dealing with pulses of less than 10 cycles full width, the modulational instability, if it occurs (i.e., if $a$ is negative), far outstrips self-steepening. Thus, for the exceptional case of anomalous dispersion, the breakup of a smooth pulse into nascent solitons does not involve self-steepening. However, as we shall see in the next section, the ultimate soliton (or solitons) possesses strong phase modulation, which

would have been absent were $\varepsilon = 0$. Thus even here the self-steepening term is very important in establishing the ultimate bandwidth of the pulse.

## 4. Solitonlike Solutions

When dispersion is normal, the only way a pulse can develop sharp features and undergo spectral broadening is through the processes of self-steepening and self-phase modulation. As we saw in Section 2 [see Eqs. (15) and (16)], self-steepening enhances the self-phase modulation. For the DNS equation self-steepening interacting with dispersion ultimately breaks the pulse up into a set of solitons plus, perhaps, some radiation. We therefore expect something similar to happen in our case, so we turn now to the study of the solitary wave solutions of Eq. (1).

For a traveling wave solution, the amplitude will be of the form

$$A = A(\tau - \eta z/v) \equiv A(\xi), \tag{30}$$

where $\eta$ is an as yet undetermined constant. With this ansatz the first of Eqs. (5) becomes

$$-(\eta/v)A' = a[2A'\phi_\tau + A\phi_{\tau\tau}] - 3\varepsilon A^2 A'. \tag{31}$$

This equation is solved identically in $A$ by the choice

$$\phi_\tau = -(\eta/2av) + (3\varepsilon/4a)A^2. \tag{32}$$

If we define a new function

$$H(\xi) = \int^{\xi} \left[A(\xi')^2\right] d\xi', \tag{33}$$

we can integrate Eq. (32), obtaining

$$\phi(z,\tau) = \phi_0(z) - (\eta\tau/2av) + (3\varepsilon/4a)H(\xi), \tag{34}$$

whence

$$\phi_z = \phi_0' - (3\varepsilon\eta/4av)A^2. \tag{35}$$

Setting Eqs. (32) and (35) into the second of Eqs. (5) yields

$$A'' - \left(\frac{\eta^2}{4a^2v^2} - \frac{b}{a}\right)A - \frac{1}{a}\left(\gamma + \frac{\varepsilon\eta}{2av}\right)A^3 + \frac{3\varepsilon^2}{16a^2}A^5 = 0. \tag{36}$$

We have set $\phi_0'(z) = b =$ constant, as is required by our insistence that $A$ depend only on $\xi \equiv \tau - \eta z/v$. Equation (36) has the first integral

$$(A')^2 = C + PA^2 - 2QA^4 - R^2A^6, \tag{37}$$

where $C$ is an arbitrary integration constant and we have set

$$P = \left(\frac{\eta}{2av}\right)^2 - \left(\frac{b}{a}\right), \qquad Q = -\frac{1}{4a}\left(\gamma + \frac{\varepsilon\eta}{2av}\right), \qquad R^2 = \frac{\varepsilon^2}{16a^2} \tag{38}$$

for short. If we set

$$u = A^2$$

into Eq. (37) we can write its solution as

$$\pm 2\xi = \int \frac{du}{\sqrt{Cu + Pu^2 - 2Qu^3 - R^2u^4}}. \tag{39}$$

For general values of $C$, this is an elliptic integral and the solution represents the anharmonic oscillations of a particle of mass 2 and total energy $C$ in the potential well

$$V = -PA^2 + 2QA^4 + R^2A^6.$$

In the special case $R = 0$, these are the so-called cniodal waves.

For two special choices of $C$ the integration becomes elementary. First, if we set $C = 0$, $u^2$ factors out of the radical so that we can carry out the integration and then solve for $u$, obtaining

$$u \equiv A^2 = \frac{A_0^2}{\cosh^2 \nu\xi + y^2 \sinh^2 \nu\xi}, \tag{40}$$

where

$$\begin{aligned} A_0^2 &= \frac{1}{R^2}\left[-Q + \sqrt{Q^2 + PR^2}\right], \\ \nu^2 &= P, \\ y^2 &= R^2A_0^4/\nu^2. \end{aligned} \tag{41}$$

This solution requires that $P$ be positive. The material constants $a$, $\gamma$, and $\varepsilon$ together with the two integration constants $b$ and $\eta$ determine $A_0$ and $\nu$. Alternatively, we could assign $A_0$ and $\nu$ and solve for the integration constants, obtaining

$$\begin{aligned} \eta &= \frac{4a^2\nu}{\varepsilon A_0^2}\left(R^2A_0^4 - \nu^2\right) - \frac{2a\nu\gamma}{\varepsilon}, \\ b &= \frac{1}{4a\nu^2}\left[\frac{4a^2\nu}{\varepsilon A_0^2}\left(R^2A_0^4 - \nu^2\right) - \frac{2a\nu\gamma}{\varepsilon}\right]^2 - a\nu^2. \end{aligned} \tag{42}$$

The quantities $\eta$ and $b$ can be viewed as nonlinear modifications of the group and phase velocities, respectively.

To complete our solution, we set Eq. (40) into Eq. (33) and obtain

$$H(\xi) = \frac{1}{R}\left\{\arctan y - \arctan\left[\frac{2y}{(1+y^2)\exp(\nu\xi) + (1-y^2)}\right]\right\}. \tag{43}$$

With this value of $H$ the phase function is

$$\phi(\tau, z) = bz - (\eta\tau/2a\nu) + (3\varepsilon/4a)H(\tau - \eta z/\nu). \tag{44}$$

Using the addition formula for the tangent, one sees that $H$ is odd, that is, $H(-\xi) = -H(\xi)$. Clearly

$$W \equiv \int_{-\infty}^{\infty} A^2 d\tau = (2/R)\arctan\, y. \tag{45}$$

The solutions we have found above we shall call solitons for short. They are the only traveling wave solutions for which $W$ is finite. Clearly $W$ is proportional to the total soliton energy per unit area; we shall simply call it the total energy for short.

Our solution goes to a perfectly regular limit as $P \to 0$, namely,

$$A = \pm A_0\left[1 + R^2 A_0^4 \xi^2\right]^{-1/2} \qquad (\nu = 0), \tag{46}$$

and

$$H(\xi) = \frac{1}{R}\arctan\left(RA_0^2\xi\right) \qquad (\nu = 0). \tag{47}$$

Both our general soliton and our limiting algebraic soliton are formally identical to those of the DNS equation (Kaup and Newell (1978)); our general solitons go over to the solitons of the NS equation in the limit $\varepsilon \to 0$.

Another traveling wave solution, known as a "kink" or as a "dark soliton," can be found as a special case of Eq. (39). As it contains infinite total energy in the sense that the integral of Eq. (45) diverges, it is not germane to our discussion. Nevertheless, the reader might find it interesting, so we give this solution in Appendix B.

As is seen, our solitons differ from those of Kaup and Newell (1978) only in the presence of the constant $\gamma$ in our Eqs. (42). Soliton solutions exist quite independently of the algebraic signs of the material constants $a$, $\gamma$, and $\varepsilon$. In both cases the phase $\phi$ is given by Eqs. (43) and (44), so with identical values of $\varepsilon$ the two show identical phase modulation. The solitons of the NS equation, for which $\varepsilon = 0$, are quite different. In this case Eqs. (40) and (44) become

$$A = \pm A_0\, \mathrm{sech}(\nu\xi),$$
$$\phi = bz - (\eta\tau/2a\nu),$$

so for this case there is no phase modulation. Equations (41) become

$$\nu^2 = P,$$
$$A_0^2 = P/2Q = -2(a/\gamma)\nu^2.$$

Thus such solitons can exist only if the dispersion is anomalous. Moreover, $A_0^2$ and $\nu^2$ are not independent so we cannot determine $\eta$ or $b$ but only the relationship between them:

$$\nu^2 = (\eta/2a\nu)^2 - (b/a).$$

Note also that Eq. (45) goes into

$$\int_{-\infty}^{\infty} A^2 d\tau = 2A_0\sqrt{-2a/\gamma}$$

so there is no upper limit to the total energy that an NS soliton may carry. The two constants that uniquely specify an NS soliton ($\varepsilon \equiv 0$) are its peak amplitude and its velocity; that is, $A_0$ and $\eta$ may be arbitrarily chosen.

It is useful to make estimates of the total bandwidth of one of our solitons. We can define the effective width of our soliton, $T_W$, as that of a square pulse with the same total energy and the same peak intensity as our soliton. Then clearly, from Eq. (45)

$$T_W = (2/RA_0^2)\arctan y. \tag{48}$$

We know the spectrum and can compute $T_W$ for a Gaussian pulse. If we define the spectral bandwidth $\Omega$ to be that of the interval (–$\Omega$/2, $\Omega$/2) that contains half the pulse energy, we find that a Gaussian pulse yields

$$\Omega_A = 0.8455RA_0^2/\arctan y. \tag{49}$$

The subscript $A$ means that this is the bandwidth arising solely from the temporal shape of the real amplitude.

In addition to $\Omega_A$, there is frequency modulation on the pulse. If we define the instantaneous frequency to be the time derivative of the total phase, we have seen that this frequency swings over a range ($\omega$, $\omega + 3RA_0^2$). Thus it seems reasonable to estimate the total bandwidth owing to phase modulation to be

$$\Omega_\phi = 3RA_0^2. \tag{50}$$

For our typical numbers $\Omega_\phi = \omega$ at a peak power of $6.5 \times 10^{14}$ W/cm$^2$. If instead we took $\Delta\phi = \phi(\infty) - \phi(-\infty)$ as given by Eq. (44) and estimated this bandwidth as $\Delta\phi/T_W$, we would exactly recover Eq. (50) above. The ratio of the phase-to-amplitude modulational bandwidths is

$$\Omega_\phi/\Omega_A = 3.55\arctan y. \tag{51}$$

If we define $W$ for the actual soliton by Eq. (45) and call $W_M$ its maximum possible energy, that is, that when $\nu \to 0$, $y \to \infty$, then Eq. (51) can also be written as

$$\Omega_\phi/\Omega_A = 5.57\,W/W_M. \tag{52}$$

When $W$ approaches $W_M$, the bandwidth of the soliton is dominated by phase modulation, whereas for $W \ll W_M$ the quantity $\nu$ becomes large, the soliton is very narrow, and this effect dominates the bandwidth. For our typical numbers $W_M$ corresponds to about 2 J/cm$^2$. In general,

$$W_M = \frac{\pi}{R} = \frac{16\pi|a|c}{3n_2}, \tag{53}$$

so it can readily vary a factor 3 or so either way from the figure quoted above.

Note that the frequency modulation disappears if we set $\varepsilon = 0$ into Eq. (44), so although self-phase modulation is a dominant contributor to the bandwidth of very energetic solitons ($W$ approximately $W_M$), it arises from the interaction of dispersion with the self-steepening term of Eq. (1) and is, in this sense, a self-steepening effect.

## 5. An Attempted Synthesis

We have seen that the trailing edge of an initially very smooth pulse will steepen and will develop phase modulation as it propagates. In the absence of dispersion, this process would continue until a discontinuous shock formed on the trailing edge and the phase modulational bandwidth would become infinite at the shock. We have further seen that when dispersion is taken into account there are traveling wave solutions, which we have called solitons, for which the self-steepening and the dispersion just balance. It seems very reasonable, then, to postulate that the self-steepening process is limited by soliton formation. In fact, for the DNS equation, our Eq. (1) with $\gamma \equiv 0$, this postulate is a rigorous result (Kaup and Newell, 1978).

According to the above ideas, I now describe my view of the development of an initially smooth pulse as it propagates. At first, dispersion is unimportant and the pulse gradually sharpens up on its trailing edge, and this self-steepening process is accompanied by the growth of self-phase modulation, all as described in Section 2. As we have seen, when the phase modulation during the self-steepening phase reaches a value

$$(\Omega_\phi)_{ss} = \gamma A_0^2 / a\omega \,, \tag{54}$$

Equations (7) break down as a model for the propagation because they ignored dispersion, which has a very important influence on the further development. Actually, dispersion starts to play an important part somewhat earlier, and by the time Eq. (54) is satisfied it will already have modified the trailing edge shape to somewhat resemble that of a soliton. In Section 4 we saw that the phase modulational contribution to the bandwidth of a soliton is

$$(\Omega_\phi)_{\text{sol}} = 3\gamma A_0^2 / 4a\omega. \tag{55}$$

The similarity of Eqs. (54) and (55) reinforces our belief that at this transitional stage the trailing edge of our steepened pulse somewhat resembles that of a soliton.

During the self-steepening phase the velocity of the trailing edge (actually of its peak) is given by

$$v_{ss} = v/(1 + 3\varepsilon u_0 v), \tag{56}$$

where $u_0$ is the peak value of $A^2$ for the initial pulse. A soliton propagates with velocity

$$\begin{aligned} v_{sol} &= v/(1+\eta), \\ \eta &= \tfrac{1}{4}\varepsilon A_0^2 v - 2av(\omega + 2av^2/\varepsilon A_0^2) \end{aligned} \tag{57}$$

so that $v_{\mathrm{sol}} > v_{ss}$. In fact, for our typical numbers $v_{\mathrm{sol}}$ exceeds group velocity unless the peak power exceeds $4 \times 10^{15}\,\mathrm{W/cm^2}$. The solitonlike trailing edge will therefore advance into the smooth leading section of the pulse. What subsequently happens depends on the total energy $W$ of the initial pulse.

If the initial pulse energy is

$$W \le W_M,$$

the nascent soliton can engulf the whole pulse and form a genuine soliton. Our parameter $y = RA_0^2/v$ will be determined by

$$y = \tan(\pi W/2W_M). \tag{58}$$

To estimate separately $A_0^2$ and $v$, we note that the trailing edge need not steepen beyond what it had reached at the end of the self-steepening stage, Eq. (17). Thus, this trailing edge advances until the pulse is symmetrical, and from this stage onward there are only detailed shape adjustments to arrive finally at the exact soliton form. Using as our model an initial triangular pulse with rise time $T_1$ and decay time $T_0$, we have clearly

$$W = \tfrac{1}{2} f_0(T_0 + T_1) = \tfrac{1}{2} A_i^2 (T_0 + T_1), \tag{59}$$

where $A_i$ denotes the peak value of $A$ in the initial pulse. As the pulse advances its decay time becomes $T = T_0\Delta$ and this continues until $\Delta$ reaches the value given by Eq. (17). From this time on, the decay time remains $T_0\Delta$ and the pulse compresses until the rise time is the same. Thus at the time of formation of the quasi-soliton

$$W = A_0^2 T_0 \Delta, \tag{60}$$

whence for the peak amplitude of the quasi-soliton we have

$$A_0^2 = (A_i)^2 (T_0 + T_1)/2\Delta T_0, \tag{61}$$

with $\Delta$ given by Eq. (17). As we saw in Section 2, unless we are dealing with initial pulses of peak power in excess of $10^{14}\,\mathrm{W/cm^2}$, $\Delta$ differs little from unity, so an initially symmetrical pulse would undergo little compression unless its peak intensity was very high.

If $W > W_M$ the situation is more complicated and our present understanding more conjectural. Again the trailing edge starts to eat up the smooth part of the pulse until it can swallow no more. Somewhere along this process the advancing "snowplow" must wrinkle the part of the pulse immediately ahead of itself, which can then proceed to self-steepen on its own and ultimately develop a new soliton. If $W$ exceeds $W_M$ by only a modest amount, an alternative to the formation of a new soliton is simply to throw the remain-

ing energy away as radiation. Something analogous to this is known to happen in self-focusing.

## 6. Conclusion

We conclude this chapter by examining the virtues and the weaknesses of what we have presented. The virtues are easily disposed of; there are two, namely:

1. we do not employ a slowly varying envelope approximation, and
2. we include linear dispersion in an approximation that is reasonably good for many common transparent media.

Our mathematical model contains three weaknesses. First, dispersion is always accompanied by some small absorption and this we have neglected. This is not a serious fault, as the effects of a small absorption can readily be estimated. The method is to start with Eqs. (40) and (44) for the amplitude and the phase. In these equations one now allows $A_0$ and $\nu$ to be slowly varying functions of $z$; they are determined by substituting the resulting expressions into Eqs. (5), to which a smll absorption term has been added. One then solves for $A_0(z)$, $\nu(z)$ by a "slowly varying $A_0$ and $\nu$ approximation." Normally such corrections are important only for fiber transmission lines.

The second fault of our mathematical model is that it is limited to plane waves, for which nothing varies in the $x$ or $y$ direction. We could extend our results to a nearly plane wave for which the beam diameter is so large that the $\Delta_\perp^2$ operator (missing from our Eq. (1)) is negligible compared to all the other operators in our equation. This seems to rule out any really practical application of our treatment to transmission in fibers.

The third fault is that we do not include nonlinear dispersion; that is, we postulate that the nonlinear response develops instantaneously. The linear part of the polarization does not respond instantaneously, as otherwise there would be no linear dispersion. Surely the nonlinear polarization cannot respond faster than does the linear. Thus, one really should write the nonlinear polarization in the form

$$\Pi_{NL} = \int_{-\infty}^{t} dt' \int_{-\infty}^{t'} dt'' \int_{-\infty}^{t''} G(t-t', t'-t'', t''-t''') E(t') E(t'') E(t''') dt''$$

in the cubic approximation. If we set

$$E = \tfrac{1}{2} U \exp[i(kz - \omega t)] + \text{cc}$$

in this, it becomes a three-dimensional generalization of our expression for the linear polarization in Appendix A. Assuming a very quick (but not instantaneous) response, one could expand as in Appendix A, obtaining something like

$$4\pi P_{NL} = \gamma |U|^2 U + i\left[\alpha |U|^2 U_\tau + \beta (U)^2 U_\tau^*\right],$$

and now $\gamma$, $\alpha$, $\beta$, etc. would all be complex. If their imaginary parts can be neglected, the first-order effect would seem to be to modify the constant we called $\varepsilon$. A guess as to what this might do is that, at least in some cases, we would have something very like Eq. (1) for which $\varepsilon$ is no longer $\gamma/\omega$ but instead rather larger, thus shortening the distance over which self-steepening effects develop.

A fourth fault, not with our model but with our mathematics, is the handwaving in Section 5 that replaces sound mathematics. This fault I do not know how to cure unless someone can show our Eq. (1), or an appropriate improvement, to be completely integrable. However, our estimate of the final bandwidth owing to phase modulation, Eq. (50), does not depend on this handwaving, but is based on balancing the self-steepening term against the dispersion term. Similarly, the estimate of the propagation distance at which this broadening has essentially developed, given by Eq. (17), depends on rather modest handwaving.

## References

*American Institute of Physics Handbook*, 2nd ed. (1963) McGraw-Hill, New York. See p. 6–13 for dispersion data.

Bespalov, V.I. and V.I. Talanov (1966) Zh. Eksp. Teor. Fiz. Pis'ma **3**, 307–310 (June 15).

Boling, N.J., A.J. Glass, and A. Owyoung (1978) IEEE Jour. Quant. Electronics **QE-14**, 601 (August).

DeMartini, F., C.H. Townes, T.K. Gustafson, and P.L. Kelley (1967) Phys. Rev. **164**, 312.

Hasegawa, A. and F. Tappert (1973) Appl. Phys. Lett. **23** (No. 4), 171 (August 15).

Kaup, D.J. and A.C. Newell (1978) J. Math. Phys. **19** (No. 4), 798 (April).

Marburger, J.H. (1975) In *Progress in Quantum Electronics*, J.H. Sanders and S. Stenholm, eds., vol. 4, part 1, p. 35. Pergamon, New York.

Suydam, B.R. (1973) Self focusing of very powerful laser beams. In *Laser Induced Damage in Optical Materials: 1973*, A.J. Glass and A.H. Guenther, eds. NBS Special Publication 387.

Whitham, G.B. (1974) *Linear and Nonlinear Waves*, chapters 1 and 3. Wiley, New York.

Yang, G. and Y.R. Shen (1984) Opt. Lett. **9**, 510.

Zakharov, V.E. and A.B. Shabat (1972) Sov. Phys. JETP **34** (No. 1), 62.

# Appendix A: Approximations Leading to the Extended Nonlinear Schrödinger Equation

Equation (1) of the main text forms the foundation of all of our discussion of self-steepening and of spectral broadening of short intense pulses. It is our purpose here to derive this as an approximation to the true wave equation without assuming the envelope to be slowly varying in comparison with the oscillating factor, $\exp[i(kz - \omega t)]$.

For strictly plane waves traveling in a dielectric medium Maxwell's equations reduce to the simple wave equation

$$\frac{\partial^2 E}{c^2 \partial t^2} - \frac{\partial^2 E}{\partial z^2} = -\frac{\partial^2}{c^2 \partial t^2}(4\pi\Pi), \tag{A.1}$$

where $E$ is the electric vector and $\Pi$ is the polarization vector. We assume our medium to be uniform and isotropic and the electric field to be plane polarized in the direction of the unit vector $e$; then $\Pi$ is also parallel to $e$ and we can factor this vector out. In the resulting scalar equation we set

$$\begin{aligned} E &= \tfrac{1}{2} U \exp[i(kz - \omega t)] + \text{cc}, \\ \Pi &= \tfrac{1}{2} P \exp[i(kz - \omega t)] + \text{cc}, \end{aligned} \tag{A.2}$$

and the result is the equation

$$\begin{aligned} (k^2 - \omega^2/c^2)U - \left( \frac{2i\omega}{c^2}\frac{\partial U}{\partial t} + 2ik\frac{\partial U}{\partial z} \right) + \frac{\partial^2 U}{c^2 \partial t^2} - \frac{\partial^2 U}{\partial z^2} \\ = \frac{4\pi\omega^2}{c^2}\left[ P + \frac{2i}{\omega}\frac{\partial P}{\partial t} - \frac{1}{\omega^2}\frac{\partial^2 P}{\partial t^2} \right]. \end{aligned} \tag{A.3}$$

In general, we can split the polarization into a linear and a nonlinear part

$$\Pi = \Pi_L + \Pi_{NL}; \qquad P = P_L + P_{NL}. \tag{A.4}$$

In Eq. (A.2) we have ignored the higher harmonic terms in $\Pi_{NL}$ because we are only calculating the propagation of the fundamental.

In general, in our uniform isotropic medium, the linear part of the polarization can be represented as

$$4\pi\Pi_L(t) = \int_{-\infty}^{t} K(t - t')E(t')dt',$$

which, using Eq. (A.2), translates as

$$4\pi P_L = \int_{-\infty}^{t} K(t - t')\exp[i\omega(t - t')]U(t')dt'. \tag{A.5}$$

As $\Pi_L$ and $E$ are real, so is $K$. We have suppressed the $z$ dependence of $P$ and of $U$; $K$ is independent of $z$.

Our first assumption is that the dispersion is small. If $K(t)$ were equal to $\kappa_0\delta(t)$ ($\kappa_0$ = a constant), we would have $4\pi P = \kappa_0 U$ and there would be no dispersion. Weak dispersion then must mean that $K(t)$ is very sharply spiked near $t = 0$; this will soon be made precise. The nature of $K$ described above suggests expansion of Eq. (A.5) by partial integration. To this end, we define a sequence of functions

$$\begin{aligned} H_0(t) &= K(t)\exp(i\omega t), \\ H_{n+1}(t) &= \int_t^{\infty} H_n(t')dt'; \qquad n = 0,1,2,\ldots. \end{aligned} \tag{A.6}$$

With the aid of these functions, successive partial integration of Eq. (A.5) yields

$$4\pi P_L(t) = H_1(0)U - H_2(0)\frac{\partial H}{\partial t} + H_3(0)\frac{\partial^2 U}{\partial t^2} - H_4(0)\frac{\partial^3 U}{\partial t^3} + \int_{-\infty}^{t} H_4(t-t')\left[\frac{d^4U(t')}{(dt')^4}\right]dt'. \tag{A.7}$$

This is still exact; our assumption of weak dispersion means that the series converges quickly, because the $H_n(0)$ rapidly decrease with increasing $n$, and that the integral remainder is small.

From the recursion relations, Eqs. (A.6), it readily follows that

$$H_{n+1}(t) = \frac{1}{n!}\int_t^{\infty} (t'-t)^n K(t')\exp(i\omega t')dt', \tag{A.8}$$

whence, if we define

$$\kappa(\omega) = \int_0^{\infty} K(t)\exp(i\omega t)dt, \tag{A.9}$$

then

$$H_{n+1}(0) = \frac{1}{n!}\left(\frac{-id}{d\omega}\right)^n \kappa(\omega) \tag{A.10}$$

and Eq. (A.7) is just the Fourier transform of the Tayler series expansion of $\kappa(\omega)$. If we now differentiate Eq. (A.7) an appropriate number of times we obtain

$$4\pi\left(P_L + \frac{2i}{\omega}\frac{\partial P_L}{\partial t} - \frac{1}{\omega^2}\frac{\partial^2 P_L}{\partial t^2}\right) = \kappa U + i[\kappa' + 2\kappa/\omega]\frac{\partial U}{\partial t} - \left[\tfrac{1}{2}\kappa'' + 2\kappa'/\omega + \kappa/\omega^2\right]\frac{\partial^2 U}{\partial t^2} - i\left[\tfrac{1}{6}\kappa''' + \kappa''/\omega + \kappa'/\omega^2\right]\frac{\partial^3 U}{\partial t^3} + R, \tag{A.11}$$

where $R$ is the remainder, given by

$$R = \int_{-\infty}^{t}\left[H_4(t-t') - \frac{2i}{\omega}H_3(t-t') - \frac{1}{\omega^2}H_2(t-t')\right]\left[\frac{d^4U(t')}{(dt')^4}\right]dt', \tag{A.12}$$

$\kappa$ is given by Eq. (A.9), and primes on $\kappa$ mean $d/d\omega$. From Eq. (A.9), as $K$ is real it follows that $\kappa(\omega)$ *cannot* be pure real unless $K$ is a $\delta$-function, and in fact the Kramers-Kronig relations follow from Eq. (A.9). Small dispersion implies very small absorption, which we ignore. Thus, from now on $\kappa$ is assumed to be real.

Our next step is to set Eq. (A.11) into the right-hand side of Eq. (A.3) and to combine the terms in $U$, $\partial U/\partial t$, and $\partial^2 U/\partial t^2$. The choice

$$k^2 = \left((\omega^2)/c^2\right)(1+\kappa) \equiv \omega^2 n^2/c^2 \tag{A.13}$$

makes the term $U$ vanish; the rest of the terms yield

$$-2ik\left[\frac{\partial U}{v\partial t}+\frac{\partial U}{\partial z}\right]+\frac{\partial^2 U}{v^2\partial t^2}-\frac{\partial^2 U}{\partial z^2}=-\alpha\frac{\partial^2 U}{\partial t^2}-i\beta\frac{\partial^3 U}{\partial t^3}+\frac{\omega^2}{c^2}R + \frac{4\pi\omega^2}{c^2}\left[P_{NL}+\frac{2i}{\omega}\frac{\partial P_{NL}}{\partial t}-\frac{1}{\omega^2}\frac{\partial^2 P_{NL}}{\partial t^2}\right], \tag{A.14}$$

where we have defined new constants

$$\begin{aligned} 1/v &= \left(1+\kappa+\tfrac{1}{2}\omega\kappa'\right)\Big/\left(c\sqrt{1+\kappa}\right)=\frac{\partial k}{\partial\omega},\\ \alpha &= \left[(1+\kappa)(\omega\kappa'+\tfrac{1}{2}\omega^2\kappa'')-\tfrac{1}{4}(\omega\kappa')^2\right]\Big/ c^2(1+\kappa)=k\frac{\partial^2 k}{\partial\omega^2},\\ \beta &= \left[\kappa'+\omega\kappa''+\tfrac{1}{6}\omega^2\kappa'''\right]/c^2, \end{aligned} \tag{A.15}$$

and $R$ is as defined by Eq. (A.12). Owing to our assumption of weak dispersion, the expansion of Eq. (A.7) is a rapidly converging one and $\alpha\,\partial^2 U/\partial t^2$, $\beta\,\partial^3 U/\partial t^3$, and $R$ are all small.

We are now ready for the main step in our approximation. Defining the two operators

$$D_\pm = \frac{\partial}{v\partial t}\pm\frac{\partial}{\partial z}, \tag{A.16}$$

we can write Eq. (A.14) as

$$\left(1+\frac{i}{2k}D_-\right)D_+U=\frac{i}{2k}X, \tag{A.17}$$

where $X$ represents the right-hand side of Eq. (A.14). We assume both the dispersion and the nonlinearity to be weak, so $X$ is small. If $X$ were zero, a solution would be $U = f(t - z/v)$, which yields $D_+ U = 0$. With $X$ small but not quite zero $D_+ U$ must be very small; that is, the operator $D_+$ is small. Now

$$D_- = \frac{2\partial}{v\partial t}-D_+ \tag{A.18}$$

or, as $D_+$ is small,

$$D_- = \frac{2\partial}{v\partial t} \tag{A.19}$$

very nearly. Again

$$\frac{i}{2k}D_- = \frac{i}{kv}\frac{\partial}{\partial t}=\frac{i}{\omega}\left(1+\frac{\omega\kappa'}{2(1+\kappa)}\right)\frac{\partial}{\partial t}. \tag{A.20}$$

For weak dispersion $\omega\kappa'/2(1+\kappa) \ll 1$, so finally

$$\frac{iD_-}{2k} = p \equiv \frac{i\partial}{\omega \partial t} \tag{A.21}$$

is a good approximation. Thus Eq. (A.17) can be written as

$$-iD_+U = \frac{1}{2k}(1+p)^{-1}X. \tag{A.22}$$

First note that the nonlinear part of $X$ can be written as

$$X_{NL} = \frac{4\pi\omega^2}{c^2}(1+p)^2 P_{NL}. \tag{A.23}$$

Whence we immediately get

$$(1+p)^{-1}X_{NL} = \frac{4\pi\omega^2}{c^2}(1+p)P_{NL} = \frac{4\pi\omega^2}{c^2}\left[P_{NL} + \frac{i}{\omega}\frac{\partial P_{NL}}{\partial t}\right]. \tag{A.24}$$

To carry out a similar trick on the linear part of $X$, which arises from dispersion, we must assume something special about the behavior of $\kappa(\omega)$ at frequencies far removed from the carrier. Thus we write

$$X_L = -(1+p)\left(\alpha\frac{\partial^2 U}{\partial t^2}\right) - i(\beta - \alpha/\omega)\frac{\partial^3 U}{\partial t^3} + \frac{\omega^2}{c^2}R, \tag{A.25}$$

and we assume that $\kappa(\omega)$ or $K(t)$ takes a special form such that the terms $(\beta - \alpha/\omega)\partial^3 U/\partial t^3$ and $(\omega^2/c^2)R$ either vanish identically or are at least negligibly small even for $U$ that are not slowly varying in time. Under this special assumption

$$(1+p)^{-1}X_L = -\alpha\frac{\partial^2 U}{\partial t^2}$$

is a good approximation and Eq. (A.22) becomes

$$-iD_+U = -a\frac{\partial^2 U}{\partial t^2} + \frac{2\pi\omega}{nc}\left[P_{NL} + \frac{i}{\omega}\frac{\partial P_{NL}}{\partial t}\right], \tag{A.26}$$

where

$$a = \alpha/2k = \frac{1}{2}\frac{\partial^2 k}{\partial \omega^2}, \qquad n = \sqrt{1+\kappa}. \tag{A.27}$$

It is convenient to express things in terms of the retarded time $\tau = t - z/v$ rather than the true time $t$. Thus we make the transformation of independent variables

$$\begin{aligned} z' &= z, \\ \tau &= t - z/v \end{aligned} \tag{A.28}$$

and Eq. (A.26) becomes

$$-i\frac{\partial U}{\partial z'} = -a\frac{\partial^2 U}{\partial \tau^2} + \frac{2\pi\omega}{nc}\left[P_{NL} + \frac{i}{\omega}\frac{\partial P_{NL}}{\partial \tau}\right]. \tag{A.29}$$

Our derivation of Eq. (A.29) assumes nothing about $P_{NL}$ except that it is small. Our assumption about the dispersion, however, makes this equation really a model rather than a description of a real material. The function $\kappa(\omega)$ can be expanded about a frequency $\omega_0$ as

$$\kappa(\omega) \equiv \kappa(\omega_0 + \Omega) = \kappa_0 + \kappa_0'\Omega + \tfrac{1}{2}\kappa_0''\Omega^2 + \tfrac{1}{6}\kappa_0'''\Omega^3 + \text{etc.},$$

where $\kappa_0'$ means $\kappa'$ at $\omega = \omega_0$ etc. Our dropping all the terms on the right-hand side of Eq. (A.25) except the first means that there are special relations for determining all the $\kappa_0'''$, $\kappa_0''''$, etc. from the first three $\kappa_0, \kappa_0'$, and $\kappa_0''$, or at least these relations must be satisfied to a good approximation. For narrow-band signals $\Omega$ remains small and the values of $\kappa_0'''$, etc. do not matter. If, however, the bandwidth becomes wide enough that these terms do matter, they must be such as to make $\beta - \alpha/\omega \approx 0$ and $R \approx 0$.

Another thing to note about our derivation is that it works only for a plane wave. For a general wave, Eq. (A.1) acquires two new terms on the left-hand side, namely,

$$-\nabla_\perp^2 E = -\left(\frac{\partial^2 E}{\partial x^2} + \frac{\partial^2 E}{\partial y^2}\right)$$

and

$$\nabla\nabla\cdot E = -4\pi\nabla\nabla\cdot\Pi,$$

and this latter, owing to the nonlinear part of $\Pi$, cannot vanish in general. Our above derivation would throw these two extra terms into the $X$ of Eq. (A.22) and the operator $(1 + p)^{-1}$ would make a mess of them. An additional idea is required to include diffraction in the model.

For our study we make the very simply choice

$$4\pi\Pi_{NL} = 2nn_2E^3,$$

which using Eq. (A.2) becomes

$$4\pi P_{NL} = \tfrac{3}{2}nn_2|U|^2U. \tag{A.30}$$

Thus we assume a nonlinearity that responds instantaneously. Equation (1) of the main text, with $\varepsilon = \gamma/\omega$, follows.

## Appendix B: The "Kink" or "Dark Soliton"

An interesting solitary wave solution known as a "kink" or as a "dark soliton" can also be found as a special case of Eq. (39). To find it we must postulate that $P$ and $Q$ areboth negative and moreover that

$$4Q^2 > -3PR^2. \tag{B.1}$$

Under these conditions if one defines

$$\begin{aligned} u_0 &\equiv \frac{1}{3R^2}\left[2Q + \sqrt{4Q^2 + 3PR^2}\right], \\ u_1 &\equiv \frac{2}{3u_0R^2}(Qu_0 - P) \end{aligned} \tag{B.2}$$

and chooses

$$C = R^2 u_1 u_0^2 = \tfrac{2}{3}(Qu_0 - P)u_0, \tag{B.3}$$

one finds that

$$Cu + Pu^2 - 2Qu^3 - R^2u^4 = R^2u(u - u_0)^2(u_1 - u) \tag{B.4}$$

and the integration of Eq. (39) becomes elementary. Carrying it out and solving the result for $u$ yields

$$A = \frac{A_0\sqrt{1+y^2}\,\sinh \nu\xi}{\sqrt{\cosh^2 \nu\xi + y^2 \sinh^2 \nu\xi}}, \tag{B.5}$$

where

$$\begin{aligned} A_0^2 &\equiv u_0^2 = -\frac{1}{3R^2}\left[2Q + \sqrt{4Q^2 + 3PR^2}\right], \\ \nu^2 &= -\frac{1}{3R^2}\left[4R^2 + 3PR^2 + 2Q\sqrt{4Q^2 + 3PR^2}\right], \\ y^2 &= R^2A_0^4/\nu^2. \end{aligned} \tag{B.6}$$

Note that condition (B.1) guarantees that both $A_0^2$ and $\nu^2$ are positive.

As before, we can express $\eta$ and $b$ in terms of $A_0^2$ and $\nu^2$, namely,

$$\begin{aligned} \eta &= \frac{2a\nu}{\varepsilon A_0^2}\left[2a\left(\nu^2 + 3R^2A_0^4\right) - \gamma A_0^2\right], \\ b &= a\left\{\frac{1}{\varepsilon^2 A_0^4}\left[2a\left(\nu^2 + 3R^2A_0^4\right) - \gamma A_0^2\right]^2 + 2\nu^2 + 3R^2A_0^4\right\}. \end{aligned} \tag{B.7}$$

It is interesting to note that this kink solution is, in a sense, complementary to our soliton. Writing $A_{\text{sol}}$ for the soliton and $A_k$ for the kink and choosing $A_0^2$ and $\nu^2$ identical for the two, we have

$$[A_{\text{sol}}(x)]^2 + [A_k(x)]^2 = A_0^2; \qquad x \equiv \nu\xi. \tag{B.8}$$

For this reason this kink solution has, in the case $\varepsilon = 0$, been called a dark soliton by Hasegawa and Tappert (1973). As the kink and the soliton have different velocities (different values of $\eta$), Eq. (B.8) can be true only instantaneously, e.g., at $z = 0$. However, it immediately follows that for the kink

$$H(\xi) = A_0^2\xi + \frac{1}{R}\left\{\arctan\, y - \arctan\left[\frac{2y}{(1+y^2)\exp(2\nu\xi)+(1-y^2)}\right]\right\}. \quad \text{(B.9)}$$

As does the soliton, the kink goes to a perfectly regular solution in the limit $\nu \to 0$, namely, the algebraic kink

$$\left\{\begin{array}{l} A = A_0\left(RA_0^2\xi\right)\left[1+R^2A_0^4\xi^2\right]^{-1/2} \\ H(\xi) = A_0^2\xi + \dfrac{1}{R}\arctan\left(RA_0^2\xi\right) \end{array}\right\} \quad \text{for } \nu = 0. \quad \text{(B.10)}$$

If one looks at the amplitude $A$ rather than the intensity $A^2$, these kinks are somewhat reminiscent of a plane hydrodynamic shock in which viscosity and heat conduction are taken into account. This kink solution is also a solution to the DNS equation and is mentioned, but not discussed, by Kaup and Newell (1978).

# 7
# Self-Focusing and Continuum Generation in Gases

Paul B. Corkum and Claude Rolland

## 1. Introduction

This book attests to the fact continuum generation has become both technically and conceptually important. Discovered in 1970 (Alfano and Shapiro, 1970a, 1970b), continuum generation is a ubiquitous response of transparent materials (liquids, solids, and gases) to high-power, ultrashort-pulse radiation. This chapter highlights some of these aspects while presenting the sometimes unique characteristics of continuum generation in gases. In addition, we introduce some related results that reflect on the light-atom interaction at high intensities.

Gases are ideal media in which to study nonlinear phenomena, such as continuum generation. The choice of low-density rare gases makes the nonlinearity simple since the susceptibility will be purely electronic in nature. Experimentally, the strength of the nonlinearity can be precisely controlled by varying the gas pressure. Gases are ideal in another way. There is a strong conceptual link between the susceptibility and the transition probability. Since there is a lot of emphasis, at present, on understanding multiphoton ionization in rare gases,* concepts being developed in this area can provide a framework for further advances of nonlinear optics in general and continuum generation in particular.

In gases, the lowest-order contribution to the nonlinear susceptibility is $\chi^{(3)}$. The magnitude of the nonresonant $\chi^{(3)}$ for the rare gases (Lehmeier et al., 1985) and for many molecular gases is well known. For xenon $\eta_2 = (3\chi^{(3)}_{1111}/\eta_0 = 2.4 \times 10^{-25} \mathrm{m^2/V^2 atm}$, where the refractive index $\eta$ is given by $\eta = \eta_0 + \eta_2 E^2 + \cdots$, $E$ being the rms electric field. $\chi^{(3)}$ is proportional to the gas pressure.

This chapter is organized around the pressure-dependent strength of the nonlinearity. Much of the content originates from six experimental papers (Corkum et al., 1986a, 1986b; Corkum and Rolland, 1987, 1988a, 1988b;

* See, for example, papers in *Multiphoton Ionization of Atoms* (S.L. Chin and P. Lambropoulos, eds.), Academic Press, New York (1984), and special issue on Multielectron Excitation of Atoms, J. Opt. Soc. Am. **B4**, no. 5 (1987).

Chin et al., 1988) describing related work at the National Research Council of Canada.

Section 2 discusses the aspects of the experiment that are common to all parts of the chapter.

Section 3 describes the interaction of ultrashort pulses with very low-pressure gases. Low pressure ensures that nonlinear optics plays no role in the interaction (Corkum and Rolland, 1988a; Chin et al., 1988). This allows the ionization properties of xenon to be established. We will see that relatively high intensities are required to ionize gases with ultrashort pulses (~100 fs). In this way, we establish an upper intensity limit for the nonlinear interaction in a purely atomic system.

Section 3 also introduces the concept of transient resonances. Although transient resonances are a characteristic of the interaction of ultrashort pulses with matter in the intensity and wavelength range discussed in this chapter, their role in multiphoton ionization depends on the pulse duration.

As the gas pressure is increased, we enter the traditional realm of nonlinear optics. If the intensity for the production of significant plasma is not exceeded, changes to the spectrum of the pulse can be investigated under conditions where self-phase modulation is the dominant mechanism. We will see in Section 4 that high-order nonlinear terms must contribute to the spectral bandwidth if the laser intensity reaches $10^{13}$ W/cm$^2$ or higher (Corkum and Rolland, 1988b).

A qualitative explanation of why high-order terms must contribute to self-phase modulation is given in Section 5.

At still higher pressures the region of continuum generation (Corkum et al., 1986a, 1986b) and self-focusing (Corkum and Rolland, 1988b) is reached. Section 6.1 describes the spectral aspects of continua in gases. In particular, it shows that the spectra are similar for condensed media and for gases.

The spatial characteristics of continuum generation are particularly striking (Corkum and Rolland, 1988b). These are described in Section 6.2 with special emphasis on the role of self-focusing in continuum generation. There is a wide range of conditions over which continua are produced with virtually the same beam divergence as the incident diffraction-limited beam (Corkum and Rolland, 1987, 1988b). As the intensity or the gas pressure is increased, conical emission is observed.

## 2. Experimental Aspects

Pulses of three different durations (22, ~90, and ~900 fs full width at half-maximum (FWHM)) were used in various parts of the experiment. This section discusses the experimental aspects that are common to all parts of the chapter. Each subsection includes experimental details of specific interest.

Laser pulses were produced by amplifying the output of either a spectrally filtered synchronously pumped dye laser (900 fs) or a colliding-pulse mode-

locked dye laser (90 fs). The temporal, spatial, and spectral characteristics of the pulses have been fully described (Corkum and Rolland, 1988a; Rolland and Corkum, 1986). The wavelength of the 900-fs pulse was centered at 616 nm and its bandwidth ($\Delta\nu$) was slightly greater than the transform limit ($\Delta t\,\Delta\nu = 0.52$; $\Delta t$ is the FWHM pulse duration). The 90-fs pulse was centered at 625 nm and had $\Delta t\,\Delta\nu = 0.5$. The pulse durations were measured by autocorrelation and fit by a $\text{sech}^2$ (90 and 22 fs) or to a Gaussian (900 fs) pulse shape. After amplification the 90- and 900-fs pulses were spatially filtered to ensure diffraction-limited beam profiles.

The 22-fs pulses were created from the 90-fs pulses using large-aperture pulse compression techniques (Rolland and Corkum, 1988). The resulting 100-$\mu$J pulses were diffraction limited with a signal-to-background power contrast ratio of approximately 30:1 (5:1 in energy). Compensation for the dispersion in all optical elements (lenses, windows, beam splitters, etc.) was accomplished by predispersing the pulse. Thus, the pulse measured 22 fs only in the target chamber and at the autocorrelation crystal. Since the 350-Å bandwidth of the 22-fs pulse gives rise to serious chromatic aberration in a single-element lens, an achromatic lens ($f = 14.3$ cm) was used to focus the pulses into the vacuum chamber (and onto the autocorrelation crystal).

All focal spot measurements were made by either scanning a pinhole (900 and 90 fs) through the focus or observing the portion of the energy transmitted through a pinhole (22 fs) of known diameter. Within the accuracy of the scans, the beam profiles were Gaussian.

## 3. Multiphoton Ionization

Some time ago it was proposed (Bloembergen, 1973) that ionization could play a major role in continuum generation though a time-dependent change in the plasma density. Plasma density changes impress a frequency chirp on a transmitted pulse. However, to influence continuum generation (Corkum et al., 1986a, 1986b) even to a small degree by plasma production there is a price to pay in energy absorption and in the distortion of the spatial beam profile (Corkum and Rolland, 1988b). Since we will show that these signatures of plasma production are not observed, we can conclude that ionization plays no role in gaseous continuum generation. The absence of ionization can be used to establish a maximum intensity in the laser focus where the continuum is being generated and hence the maximum value of $\eta_2 E^2$.

Continuum experiments were the first to indicate that it is difficult to ionize xenon and krypton with ultrashort pulses (Corkum et al., 1986a, 1986b) relative to extrapolations of 0.53 $\mu$m, 1.06 $\mu$m experiments (l'Huillier et al., 1983) (25 ps). Since the ionization threshold is a major uncertainty in continuum generation, we have performed two experiments (Corkum and Rolland, 1988a; Chin et al., 1988) whose specific aim was to study multiphoton ionization. The more recent and more quantitative of these is described in this section (Chin et al., 1988).

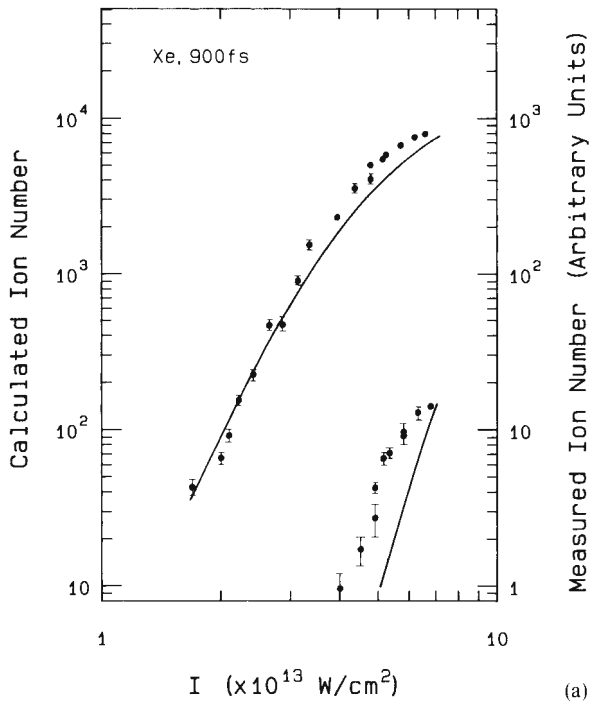


FIGURE 7.1. Ion yield of Xe for 900-, 90-, and 22-fs pulses. The solid curves are calculated from a modified Keldysh theory (Szöke, 1988). The calculations give an absolute number of ions for the measured focal geometry and the neutral gas density. The experimental number of ions is plotted in relative units. The data have been positioned on the graph so as to emphasize the agreement between experiment and theory. The error bars show the standard error of the experimental data.

Femtosecond pulses were focused into a vacuum cell filled with $\sim 4 \times 10^{-6}$ torr of xenon. Ions were extracted with an ~80 V/cm static field into a time-of-flight mass spectrometer. Data were obtained using a microcomputer, coupled to a boxcar integrator that was programmed to accept only laser pulses within a narrow energy range (±2.5%). The computer recorded and averaged the associated ion signals. The intensity in the vacuum chamber was varied by rotating a $\lambda/2$ plate placed in front of a polarizer (reflection from a Brewster's angle germanium plate was used as a dispersion-free polarization selector for the 22-fs pulse).

Figure 7.1 is a graph of the number of ions as a function of the peak laser intensity for both rare gases and all three laser pulse durations. (Higher ionization states were observed but not plotted since they were too weak.) The solid curves were obtained from a modified Keldysh theory (Szöke, 1988). Although we did not measure the absolute number of ions, we estimate the threshold sensitivity (the lowest ion signals in Figure 7.1) of our ion collector to be approximately 10 ions. The relative scaling between

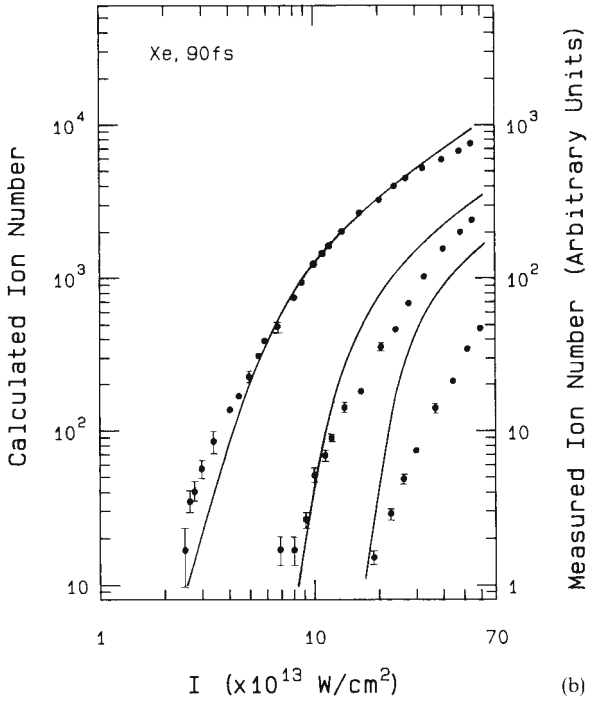


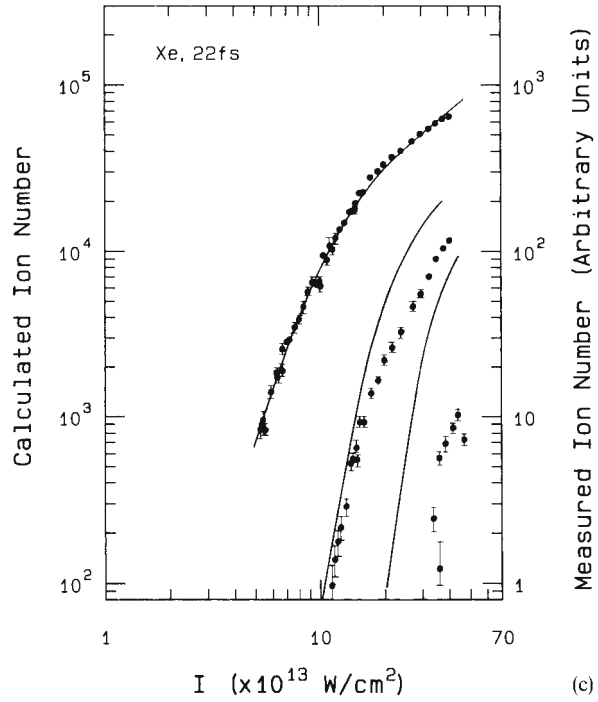


FIGURE 7.1. (*continued*)

experimental and calculated ion signals for Xe (Figure 7.1) is consistent with this estimate.

We performed this experiment to find the intensity at which ionization would need to be considered in nonlinear optics experiments. Not only does Figure 7.1 answer this question qualitatively, but the agreement between theory and experiment allows us to make quantitative predictions. However, the agreement raises an important issue. How can a Keldysh theory, which assumes that resonances are unimportant, be consistent with electron spectral measurements (Freeman et al., 1987) which indicate that resonances play a major role in ionization? Because of the importance of this issue for nonlinear optics, we discuss it below with respect to ionization and, in Section 5, with respect to high-order nonlinear optics.

An important feature of the high-power light-atom interactions is the ac Stark shift. At $I = 10^{13}$ W/cm$^2$, the laser field exceeds the atomic field (of hydrogen) for all radii greater than $R = 4$ Å. At this radius the atomic potential is 3.8 eV below the ionization potential. For $R > 4$ Å, it is appropriate to consider the electron oscillating in the laser field as the lowest-order solution and the atomic field as a perturbation. Nearly all excited states, therefore, have an energy of oscillations (ac Stark shift) approximately equal to the ponderomotive potential ($U_{\text{osc}} = (qE)^2/2m\omega^2$ where $q$ is the electronic charge, $\omega$ is the laser angular frequency, and $m$ is the electron mass). At $10^{13}$ W/cm$^2$ and 620 nm the ponderomotive potential is approximately 0.4 eV. Thus resonances are transiently produced and resonant enhancement of high-order terms in the susceptibility will occur.

In view of the transient resonance induced in the medium, we might expect resonances always to be important. However, small deviations from Keldysh models appear only at relatively low intensities. Transient resonances appear to play a significant role in the overall ionization rate over, at most, a limited intensity/time range. (Note that detailed electron spectral measurements have so far been performed only in the $1–3 \times 10^{13}$ W/cm$^2$ intensity range with ~500-fs pulses (Freeman et al., 1987).)

To understand why the contributions of transient resonances to ultrashort pulse ionization should be so small, consider just how transient these resonances can be. Assuming that all high-lying states move with the ponderomotive potential, we can write the maximum rate of change of the ponderomotive shift as $dU/dt)_{\max} = 2\sqrt{2}U_0\left(\ln(0.5)^{1/2}/\Delta t \exp(0.5)\right)$ where $U_0$ is the maximum value of the ponderomotive shift during the pulse and a Gaussian pulse shape has been assumed. In the case of the 90-fs pulse with a characteristic peak intensity of $10^{14}$ W/cm$^2$, $dU/dt)_{\max} = 0.1$ eV/optical cycle. In the even more extreme case of the 22-fs pulse, the same peak intensity gives $dU/dt)_{\max} = 0.4$ eV/optical cycle.

The significance of such large ponderomotive shifts can be seen by considering a two-level system. For a two-level system both the pulse duration dependence and the intensity dependence of the dephasing between the transition (transition frequency = $\omega_{ab}$) and the near-resonant harmonic of the

laser frequency can be estimated. For a constantly shifting transition, $\omega_{ab} + (dU/dt)t/h$, the dephasing time ($T$) is given by the condition that $\delta\phi \sim 2\pi$. That is, $T \sim (2h/dU/dt)^{1/2}$ where $dU/dt$ is assumed constant. For a 90-fs pulse at $10^{14}$ W/cm$^2$, $T \sim 13$ fs. At the same intensity $T \sim 6$ fs for a 22-fs pulse. Resonances that last only a few cycles are hardly resonances at all and can be expected to have only minor effects on the overall ionization rate. Only for relatively small $dU/dt$ can transient resonances play an important role. They may account for the deviations of the experimental and calculated curves observed in the 900-fs and low-power 90-fs xenon results.

The above discussion does not imply that transient resonances cannot lead to observable nonlinear optical consequences. In fact, nonlinear optics may provide one of the best methods of observing transient resonances.

In summary, these experiments show that ionization will be barely significant for 90-fs pulses at intensities of $10^{13}$ W/cm$^2$. In addition, the slopes of the ion curves in Figure 7.1 indicate that a lowest-order perturbation expansion for the transition rate (and, therefore, the susceptibility) will be incomplete for intensities greater than $\sim 3 \times 10^{13}$ W/cm$^2$ for 0.6-$\mu$m light. This intensity can be used to estimate the maximum value of $\eta_2 E^2$ that is experimentally accessible with 90-fs pulses.

## 4. Self-Phase Modulation

One of the most studied nonlinear processes with ultrashort pulses is self-phase modulation. It is the basis of optical pulse compression, which is widely used in femtosecond technology. In many cases continuum generation is believed to be an extreme version of self-phase modulation. Thus, it seems natural to adjust the strength of the nonlinearity by varying the gas pressure so that only modest self-phase modulation occurs. We can then follow the magnitude of the spectral broadening as the intensity or the nonlinearity is increased. Analogous experiments can be performed in fibers by increasing the length of the fiber.

Self-phase modulation is more complex in unbounded media than in fibers because, in unbounded media, self-phase modulation is inescapably related to self-focusing. (This relationship ensured that pulse compression based on self-phase modulation remained a curiosity until fiber compression became available.) It is possible to minimize the effects of self-focusing by keeping the medium shorter (Rolland and Corkum, 1988; Fork et al., 1983) than the self-focusing length. High-power pulse compression experiments use precisely this technique to control self-focusing (Rolland and Corkum, 1988). However, long before the self-phase modulation has become strong enough to generate continua, the beam propagation can no longer be controlled (Rolland and Corkum, 1988). In spite of this complexity, most continua are produced in long, unbounded media. Much of the remainder of the chapter

addresses some of the physics issues associated with continuum production in this kind of medium.

The self-phase modulation experiment (Corkum and Rolland, 1988b) was performed with the 90-fs, 625-nm pulse with a maximum energy of ~500 $\mu$J. A vacuum spatial filter with aperture diameter less than the diffraction limit of the incident beam produced an Airy pattern from which the central maximum was selected with an iris. The resulting diffraction-limited beam was focused into a gas cell that was filled to s maximum pressure of 40 atm. We report here mainly on the results obtained with xenon. However, where other gases have been investigated, we have found similar behavior.

As the gas pressure or laser power is increased, spectral broadening due to self-phase modulation is observed. In the $\eta_2$ limit (i.e., terms of higher order than $\eta_2 E^2$ are negligible) and neglecting dispersion, the spectral width depends only on the laser power

$$\delta\lambda)_{\max} \sim \frac{8\sqrt{2}\eta_2 P_0}{c^2 \varepsilon_0 \tau \exp(0.5)} + \delta\lambda)_{\text{init}}, \tag{1}$$

where the power in the pulse is given by $P = P_0 e^{-(t/\tau)^2}$ and $\delta\lambda)_{\max}$ and $\delta\lambda)_{\text{init}}$ are the maximum and initial bandwidth of the pulse, respectively. All other symbols have their conventional meaning. The factor exp(0.5) arises because the maximum broadening for a Gaussian pulse occurs at $t = \tau/\sqrt{2}$. It will be present in Eq. (2) for the same reason. We can evaluate* $\delta\lambda)_{\max}$ for $\eta_2 = 2.4 \times 10^{-25}\,\text{m}^2/\text{V}^2\,\text{atm}$ and obtain $\delta\lambda)_{\max} = 3.9 \times 10^{-7}\,\text{Å/W atm}$. Equation (1) is valid only below the self-focusing threshold.

Equation (1) shows that modifications of the nonlinearity can be observed through an intensity dependence of the spectral broadening. The results obtained with two different focusing lenses (*F*/70 and *F*/30) and a selection of pressures are presented in Figure 7.2. In all cases, the power was maintained below the self-focusing threshold. The solid lines are a fit to the experimental data using Eq. (2) and a saturation intensity of $I_{\text{sat}} = 10^{13}\,\text{W/cm}^2$.

$$\delta\lambda)_{\max} = \frac{8\sqrt{2}P_0}{(2.1)c^2\varepsilon_0\tau\exp(0.5)}\left[\frac{\eta_2}{1 + I/(I_{\text{sat}}\exp(0.5))}\right] + \delta\lambda_{\text{init}}. \tag{2}$$

In Figure 7.1, the saturation intensity of $10^{13}\,\text{W/cm}^2$ corresponds to a power of $1.5 \times 10^8$ W for the *F*/30 and $8 \times 10^8$ W for the *F*/70 lens. The dashed lines are obtained using Eq. (2) and $I_{\text{sat}} = \infty$. Compared to Eq. (1), a factor of 2.1 is required in the denomimator of Eq. (2) to fit the data. This factor is attributed to uncertainties in the input parameters such as the value of $\eta_2$, the pulse shape and duration (measured by autocorrelation), and approximations made in deriving Eq. (1).

---

* $\eta_2$ of xenon at atmospheric pressure was erroneously reported to be $\eta_2 = 4 \times 10^{-26}\,\text{m}_2/\text{V}_2$ in Corkum et al. (1986a, 1986b).

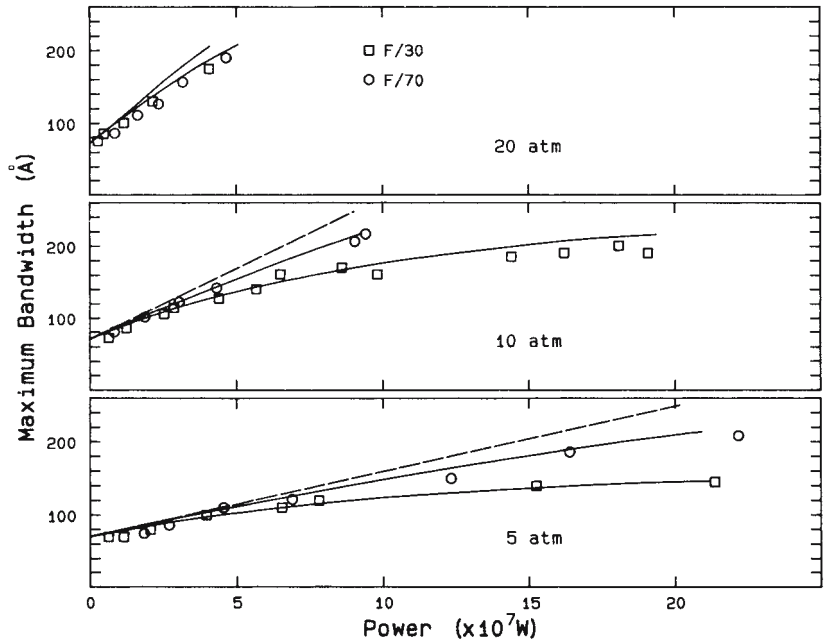


FIGURE 7.2. Spectral width of the radiation transmitted through a cell filled with 5, 10, and 20 atm of xenon as a function of the peak laser power. The circles and squares represent data obtained with an *F*/70 and an *F*/30 lens, respectively. The solid curves are plots of Eq. (2) with a saturation intensity of $10^{13}$ W/cm$^2$ corresponding to $1.5 \times 10^8$ W for the *F*/30 lens ($\omega_0 = 21\,\mu$m).

Saturationlike behavior of the nonlinearity could be caused by plasma produced by ionization (Corkum and Rolland, 1988b). There are four experimental reasons to believe that saturation is a fundamental phenomenon, not directly related to ionization:

1. At $10^{13}$ W/cm$^2$, sufficient ionization to modify the beam propagation by one diffraction-limited beam divergence, or to modify the spectrum measurably, would require ~25% of the beam energy. We measure an absorption of less than 3%.
2. Ionization would produce asymmetric self-phase modulation since the plasma would most affect the trailing region of the pulse. We observe a nearly symmetrical spectrum.
3. Figure 7.1 shows that insignificant plasma density is produced by $I < 3 \times 10^{13}$ W/cm$^2$.
4. Ionization would produce irreversible distortion of the transmitted beam profile. In fact, beam distortion is frequently used as a diagnostic of ionization (Corkum and Rolland, 1988a; Guha et al., 1985). We see little beam distortion.

## 5. Saturation of the Nonlinear Response in Gases

Since the nonlinear response is not modified by ionization, we must consider other explanations. For xenon and 0.6-$\mu$m light, the first excited state is 4.2 photon energies above the ground state. Any pulse duration or intensity-dependent changes must come from higher-order terms. In the absence of resonances, high-order terms should contribute to the nonlinear response approximately in the ratio $\chi^{(3)}E^2/\chi^{(1)}$. At $10^{13}$ W/cm$^2$ the ratio is ~0.04. To explain the observations in Figure 7.2, resonant enhancement is required and, as we have already indicated in Section 3, resonant enhancements are inevitable.

In discussing transient resonances, we have already pointed out that bound carriers in a high-lying resonant level respond as free electrons. It was just this fact that required that the ac Stark shift be equal to the ponderomotive potential. These bound electrons *must* reduce the refractive index as would truly free electrons. Since the high-lying states are only transiently resonant, they are only virtually occupied. Thus, aside from resonantly enhanced ionization, which is discussed below, the reduced refractive index need not be associated with net absorption from the beam. The change in refractive index due to bound electrons in high-lying levels is equivalent to $\eta_2 E^2$ when only $10^{-3}$ of the ground state population is in these levels. (It is interesting to note that the connection between the ac Stark shift and the susceptibility, implicit in this description, can also be shown for a weakly driven two-level system (Delone and Krainov, 1985).)

It is essential to consider whether a transiently resonant population of $10^{-3}$ is consistent with low ionization levels, since transiently resonant states in xenon lie within one or two photon energies of the continuum. Resonantly enhanced ionization of xenon has been observed in multiphoton ionization experiments with ~500-fs pulses (Freeman et al., 1987). If we assign a cross section (Mainfray and Manus, 1980) of $\sigma = 10^{-19}$ $(10^{-20})$ cm$^2$ to the single-photon ionization from a near-resonant state, we can calculate the ratio of resonantly excited electrons ($N_e$) to free electrons ($N_i$) at an intensity of $10^{13}$ W/cm$^2$ ($N_e/N_i = \hbar\omega/\sigma I\tau$). The ratio for a 90-fs pulse is ~3(30). Note the pulse duration scaling. Thus the resonant population can exceed the free-electron population for ultrashort pulses.

It may seem that the small cross section used above is in contrast to what would be calculated from Keldysh-type theories (Szöke, 1988; Keldysh, 1965) for $10^{13}$ W/cm$^2$, assuming an ionization potential of <1 eV. This apparent discrepancy is explained by the fact that a transiently resonant electron is only weakly bound. Since an unbound electron cannot absorb photons from a plane electromagnetic wave, as we cross the boundary between an unbound and a weakly bound electron we should not expect the electron to absorb photons readily. (In the long-wavelength limit this is no longer valid because of the Lorentz force contribution to ionization.)

Values for $\sigma$ are very poorly known experimentally, especially for levels near the continuum. Recent UV measurements (Landen et al., 1987) for the krypton $4p5d$ and $4p4d$ levels (1 and 1.7 eV below the continuum) yielded values of $\sigma = 3 \times 10^{-18}$ and $8 \times 10^{-18}\,\mathrm{cm}^{-2}$, respectively. These results satisfy the trend of decreasing $\sigma$ as the continuum is approached.

It is useful to reexpress the above discussion in more general terms. Many high-order nonlinear terms will be enhanced by transient resonance due to the dense packing of levels at high energies. Our qualitative description of the plasmalike response of the electron is equivalent to summing a series of nonlinear terms. It should be emphasized that transient resonances will influence all nonlinear processes in this intensity range. Their effects could well exceed the nonresonant contributions to the susceptibility. Note that enhancement of the nonlinear response is also observed in partially ionized plasma due to excited state population (Gladkov et al., 1987).

## 6. Self-Focusing: $\chi^{(3)}$ Becomes Large

The modification to the nonlinear response of the medium that we have described has important consequences for self-focusing. In Figure 7.2 the highest-intensity data points (for a given *F*-number and gas pressure) give approximately the threshold above which the nature of the spectral broadening changes nearly discontinuously. For *F*/70 optics this value is approximately a factor of 2 above the calculated self-focusing threshold. A factor of 2 discrepancy is consistent with the correction factor of 2.1 that we required to make Eq. (2) agree with experimental data. The critical power is clearly not a useful parameter if the intensity at the geometric focus exceeds $10^{13}\,\mathrm{W/cm}^2$.

To ensure that self-focusing will be initiated all remaining results are taken with large *F*-number optics (*F*/200).

### 6.1 Spectral Characteristics of Gaseous Continua

When the beam intensity is increased above that plotted in Figure 7.2, the wavelength scale of the spectral broadening increases dramatically. In Figure 7.3 typical multishot spectra are plotted for the 70-fs and 2-ps pulses (with characteristics similar to the 90- and 900-fs pulses described previously) transmitted through a gas cell filled with various gases. Shown in Figure 7.3a are spectra for 30 atm of xenon illuminated with 70-fs and 2-ps pulses, respectively. Figure 7.3b shows spectra for 40 atm of $N_2$ (2 ps) and 38 atm of $H_2$ (70 fs). The spectra in Figure 7.3 are typical of spectra obtained with all gases that we have investigated, provided only that the laser intensity was sufficient to exceed the critical power for self-focusing.

The similarity in the blue spectral component for all the curves in Figure 7.3 should be noted. In fact, the blue spectral component is nearly universal

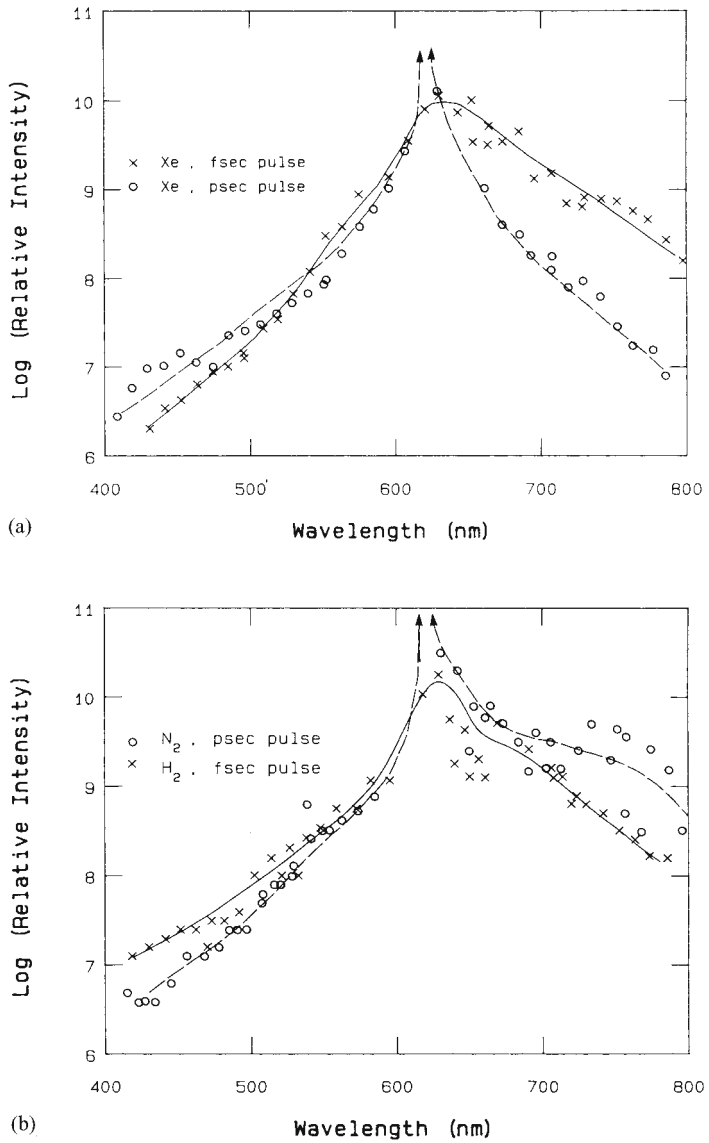


FIGURE 7.3. Continuum spectra. (a) In xenon: $P = 30\,\text{atm}$, $\Delta t = 70\,\text{fs}$ (crosses); $P = 15\,\text{atm}$, $\Delta t = 2\,\text{ps}$ (circles). (b) In $N_2$: $P = 40\,\text{atm}$, $\Delta t = 2\,\text{ps}$ (circles) in $H_2$: $P = 38\,\text{atm}$, $\Delta t = 70\,\text{fs}$ (crosses).

for all gases that produce continua regardless of the (above-threshold) intensity or pressure. (It is also typical of a chaotic spectrum (Ackerhalt et al., 1985).) The red component, however, varies with the laser and gas parameters. We have investigated the red cutoff only with $CO_2$ using femtosecond pulses. The maximum wavelength for 30 atm of $CO_2$ exceeded the 1.3-$\mu$m limit of our S1 photocathode. (Because of an orientational contribution to the non-linearity, continua can be produced at a particularly low threshold intensity with picosecond pulses in $CO_2$.)

Figure 7.4 shows that spectral modulation is another characteristic of the spectrum of gaseous continua. Modulation has been noted previously on the single-shot spectra of gases (Glownia et al., 1986). Spectral modulation is characteristic of continua from condensed media as well (Smith et al., 1977). Figure 7.4 illustrates the intensity and $\eta_2$ scaling of the spectral modulation of a xenon continuum as measured in the region of 450 nm. Figures 7.4a and 7.4b show that the modulation frequency is reproducible from shot to shot. The modulation depth is not always as great as shown in Figure 7.4. Figures 7.4c and 7.4d demonstrate that the modulation frequency varies with $\eta_2 E^2$ near the continuum threshold. However, in Figure 7.4e to 7.4g we see that the simple $\eta_2 E^2$ scaling is eventually lost at higher pressure-power products. In all cases, the modulation frequency increases further from the laser frequency. This behavior is in contrast with that expected for self-phase modulation (Smith et al., 1977).

The characteristics of gaseous continua described so far are similar to those of condensed-medium continua. However, the extra flexibility provided by pressure dependence of the nonlinearity allows issues like the $\eta_2 E^2$ dependence of the spectral modulation to be addressed. We will see that it also allows us to correlate self-focusing with continuum generation much more precisely than previously possible.

As already mentioned, continuum generation showed a sharp threshold, below which spectral broadening is described by Eq. (2) and above which full continua re produced. The threshold power for continuum generation equals the self-focusing threshold power to the accuracy to which the self-focusing threshold is known. The functional dependence of the continuum threshold on laser power, gas pressure, and the hyperpolarizability is also the same as that for self-focusing. This dependence is shown in Figure 7.5, where the product of the gas pressure and the laser power at threshold for all gases investigated with the femtosecond pulse is plotted as a function of the laser power. Comparing the pressure-power products for each gas, we find that they are inversely proportional to the hyperpolarizabilites. Similar data were obtained (but are not plotted) with the picosecond pulse. For the rare gases and $H_2$, the picosecond data would fit on their respective lines in Figure 7.5. Both $N_2$ and $CO_2$, however, have lower thresholds than would be indicated from their purely electronic nonlinearities. This is due to orientational effects that are important in both gases.

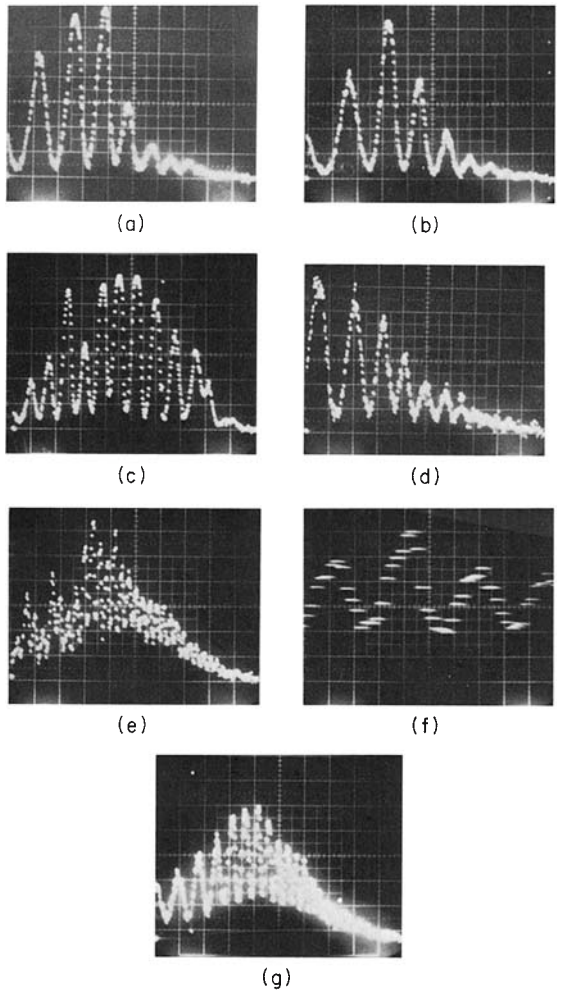


FIGURE 7.4. Details of the single-shot continuum spectrum centered near $\lambda = 450\,\text{nm}$ illustrating the spectral modulation on the continuum. (The horizontal scale for all traces except (f) is 137 Å/div.) (a) and (b) (7 atm pressure of xenon) show the reproducibility of the spectral modulation. (c) and (d) (14 atm pressure of xenon) show the $\eta_2 E^2$ scaling of the spectral modulation. (c) was taken with the same laser power as (a) and (b). (d) was taken with one-half the laser power of (a)–(c). (e) to (g) (21 atm pressure of xenon) show that the $\eta_2 E^2$ scaling is not valid well above the continuum threshold. (e) and (f) were taken with the same laser power as (a)–(c). The wavelength scale in (f) has been expanded by a factor of 10. (g) was taken with one-third of the laser power of (a)–(c).

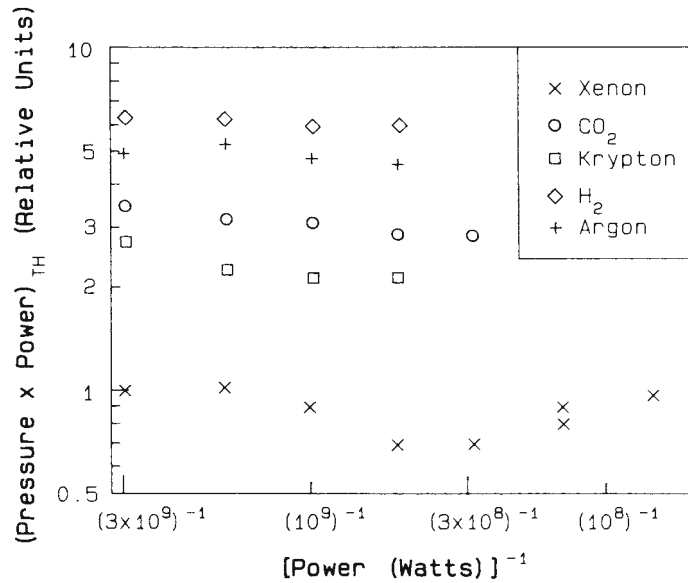


FIGURE 7.5. Laser power multiplied by the gas pressure at the continuum threshold, plotted as a function of the inverse of the laser power for different gases.

## 6.2 Spatial Characteristics of Gaseous Continua

One might expect that spatial changes in a beam that has experienced at least the onset of self-focusing would be severe. Considering that the spectrum of the beam is catastrophically modified, can we expect anything but a severely distorted transmitted beam?

Figure 7.6 shows the near-field and far-field distributions of the beam after passing through the gas cell. The first row is composed of reproductions of Polaroid photos of the near-field spatial distribution as viewed through an ~0.5-mm-wide slit and recorded on an optical multichannel analyzer (OMA). The second row shows far-field distributions recorded in a similar manner. From left to right are distributions taken through a filter that blocks all wavelengths $\lambda < 650$ nm (left column), with the gas cell evacuated (middle column), and through a filter that blocks $\lambda > 525$ nm (right column). The left- and right-hand columns were obtained with the gas cell filled with sufficient pressure to ensure that the laser peak power exceeded the continuum threshold. On the basis of the spatial profile alone, it is virtually impossible (with large $F$-number optics) to distinguish between the presence and absence of self-focusing and continuum generation for powers near the self-focusing threshold.

As the laser power is increased to approximately four times the continuum threshold, conical emission is observed. At first the ring structure is simple, but it becomes increasingly complex at higher powers. Figure 7.7 shows the

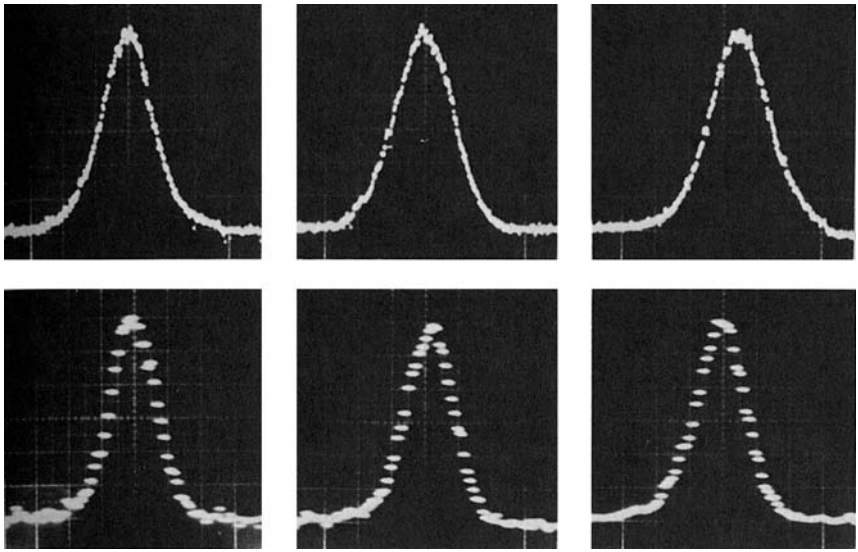

FIGURE 7.6. Near-field (top row) and far-field (bottom row) distributions of the beam after passing through the gas cell. From left to right are shown the red spectral component ($\lambda > 650\,\text{nm}$), the beam with the gas cell evacuated, and the blue spectral component ($\lambda < 525\,\text{nm}$).

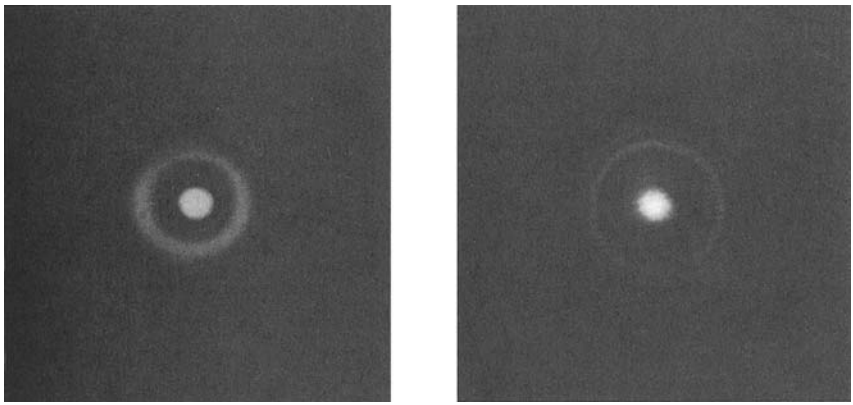

FIGURE 7.7. Conical emission as observed in the near field through the red ($\lambda > 650\,\text{nm}$, left image) and blue ($\lambda < 525\,\text{nm}$, right image) filters.

ring structure only slightly above the threshold for conical emission. Conical emission was previously observed in condensed-medium continuum generation (Smith et al., 1977; Alfano and Shapiro, 1970a).

Figure 7.6 indicates that the transverse beam distribution is almost totally reconstructed after self-focusing. The spatial reconstruction of the beam stands in stark contrast to the catastrophic change in the initial spectrum. With such beam reconstruction, it is natural to reexamine whether self-focusing was ever initiated. Several reasons to associate continuum generation with self-focusing in gases are listed below:

1. Conceptually, self-focusing is just the free-space spatial manifestation of self-phase modulation. Since Eq. (1) is valid for large *F*-number optics, $\eta_2$ must be the dominant nonlinearity, rendering self-focusing inevitable. Of course, when the intensity approaches $10^{13}$ W/cm$^2$, $\eta_2$ is no longer dominant.
2. The continuum threshold has approximately the same magnitude as the calculated self-focusing threshold. It also has the same functional dependence on the gas pressure, laser power, and hyperpolarizability.
3. Conical emission has been predicted by the moving-focus model of self-focusing (Shen, 1975). It is also a characteristic of a saturating nonlinearity (Marburger, 1975) and high-order nonlinear mixing processes. With large *F*-number optics, all of these potential explanations of conical emission require self-focusing to increase the peak intensity.
4. We have projected conical emission to its source and find that it originates from the prefocal region. This origin can be graphically illustrated by placing a 3-mm-diameter opaque disk at the geometric focus. Significant conical emission escapes around its side.
5. The $\eta_2 E^2$ dependence of the spectral modulation implies that $\eta_2$ plays at least a limited role in continuum generation.
6. In no case have we been able to observe continuum generation without the laser power exceeding the calculated self-focusing power.

## 6.3 Discussion

It is not possible to consider gaseous continuum generation as if it were produced by self-phase modulation in the $\eta_2$ limit alone. The conceptual link between self-phase modulation and self-focusing makes this approach unrealistic. The very small value of $\eta_2 E^2$, even at the ionization threshold (Corkum et al., 1986a, 1986b), gives additional evidence that continuum generation is not only an $\eta_2$ process.

There is a second conceptual problem. If plasma is not created (as we have shown experimentally), then high-order nonlinearities are required to stabilize self-focusing: consequently, $\eta_2$ is no longer the dominant nonlinear term. (It is interesting to note that nonlinear optics will be very different in the long-

wavelength limit, where the Lorentz force severely limits the lifetime of most high-lying states.)

Out of this apparent complexity, however, very simple and near-universal behavior emerges. This simple behavior will have to be explained by continuum theories. In particular, theory will have to explain the periodicity of the modulation, the spatial properties of the beam, conical emission, and the universality of the blue spectral component of the continuum.

## 7. Conclusions

With the recent development of ultrashort pulses, it is now possible to perform nonlinear optics experiments in new limits of intensity and pulse duration. Due to the sweep of the focus, earlier self-focusing experiments may already have explored this region, although unwittingly.

This chapter has described experiments explicitly performed to investigate subpicosecond nonlinear optics. It described the first high-intensity experiments performed with pulses as short as 22 fs and showed that ionization cannot be described by perturbation theory for pulse durations shorter than 1 ps. It also discussed the role of transient resonances in multiphoton ionization and in high-intensity self-phase modulation experiments. For ultrashort pulses, these transient resonances dominate the nonlinear optical response of gases in much the same way that high-lying resonances dominate in partially ionized plasmas (Gladkov et al., 1970.) (Presumably, the same is true in condensed media near the multiphoton ionization threshold).

Continuum generation in gases (and indeed all nonlinear optical phenomena in this intensity and pulse duration range) will be understood only in the context of transient resonances and limited convergence of perturbation theory.

In conclusion, it should be emphasized that the observations in this chapter are very much in keeping with the condensed-media results. The difference is only that gases show the properties of continua in such a dramatic form as to strongly challenge conventional ideas of continuum generation.

*Acknowledgments.* The author acknowledges important contributions to this work by Dr. S.L. Chin, during a five-month sabbatical at NRC. His experience with multiphoton ionization experiments was invaluable, as was his contribution to other concepts expressed in this chapter. Dr. T. Srinivasan-Rao's contributions are also acknowledged. Without her short visit to NRC we would never have begun this set of experiments. D.A. Joines has cheerfully provided technical support throughout all of the experiments. Our rapid progress would not have been possible without him. Discussion with many colleagues at NRC are gratefully acknowledged.

## References

Ackerhalt, J.R., P.W. Milonni, and M.-L. Shih (1985) Phys. Rep. **128**, 207.
Alfano, R.R. and S.L. Shapiro (1970a) Phys. Rev. Lett. **24**, 584.
Alfano, R.R. and S.L. Shapiro (1970b) Phys. Rev. Lett. **24**, 592.
Bloembergen, N. (1973) Opt. Commun. **8**, 285.
Chin, S.L., C. Rolland, P.B. Corkum, and P. Kelly (1988) Phys. Rev. Lett. **61**, 153.
Corkum, P.B. and C. Rolland (1987) Summary of postdeadline papers, XV International Quantum Electron. Conference, April, Baltimore, Maryland, Paper PD-21.
Corkum, P.B. and C. Rolland (1988a) In *NATO ASI Series—Physics B*, vol. 171, A. Bandrauk, ed., p. 157. Plenum, New York.
Corkum, P.B. and C. Rolland (1988b) unpublished.
Corkum, P.B., C. Rolland, and T. Srinivasan-Rao (1986a) Phys. Rev. Lett. **57**, 2268 (1986a).
Corkum, P.B. and C. Rolland, and T. Srinivasan-Rao (1986b) In *Ultrafast Phenomena V*, G.R. Fleming and A.E. Siegman, eds., p. 149. Springer-Verlag, New York.
Delone, N.B. and V.P. Krainov (1985) *Atoms in Strong Light Fields*, p. 174, Springer-Verlag, Berlin.
Fork, R.L., C.V. Shank, C. Hirliman, R. Yen, and W.J. Tomlinson (1983) Opt. Lett. **8**, 1.
Freeman, R.R., P.H. Bucksbaum, H. Milchberg, S. Darack, D. Schumacher, and M.E. Geusic (1987) Phys. Rev. Lett. **59**, 1092.
Gladkov, S.M., N.I. Koroteev, M.V. Ruchev, and A.B. Fedorov (1987) Sov. J. Quantum Electron. **17**, 687.
Glownia, J.H., J. Miswich, and P.P. Sorokin (1986) J. Opt. Soc. Am. **B3**, 1573.
Guha, S., E.W. Van Stryland, and M.J. Soileau (1985) Opt. Lett. **10**, 285.
l'Huillier, A., L.A. Lompre, G. Mainfray, and C. Manus (1983) Phys. Rev. A**27**, 2503.
Keldysh, L.V. (1965) JETP **20**, 1307.
Landen, O.L., M.D. Perry, and E.M. Campbell (1987) Phys. Rev. Lett **59**, 2558.
Lehmeier, H.J., W. Leupacher, and A. Penzkofer (1985) Opt. Commun. **56**, 67.
Mainfray, G. and C. Manus (1980) Appl. Opt. **19**, 3934.
Marburger, J.H. (1975) Prog. Quantum Electron **4**, 35.
Rolland, C. and P.B. Corkum (1986) Opt. Commun. **59**, 64.
Rolland, C. and P.B. Corkum (1988) J. Opt. Soc. Am. **B5**, 641.
Shen, Y.R. (1975) Prog. Quantum Electron **4**, 1.
Smith, W.L., P. Liu, and N. Bloembergen (1977) Phys. Rev. **A15**, 2396.
Szöke, A. (1988) *NATO ASI Series—Physics B*, vol. 171, A. Bandrauk, ed., p. 207. Plenum, New York.

# 8
# Utilization of UV and IR Supercontinua in Gas-Phase Subpicosecond Kinetic Spectroscopy

J.H. Glownia, J. Misewich, and P.P. Sorokin

## 1. Introduction

Through the work of photochemists extending over many decades, there now exists a wealth of information on the various reactions that photoexcited gas phase molecules undergo. Most of this information relates to the product molecules that are formed, either as the direct result of a primary photochemical act, such as photodissociation, or through subsequent secondary reactions, involving collisions with other molecules in the gas. Recently, there has been an extensive effort directed at determining the exact energy distributions of the primary products formed in photodissociation. With the use of nanosecond tunable-laser techniques, such as laser-induced fluorescence (LIF) and coherent anti-Stokes Raman spectroscopy (CARS), scientists have successfully determined the nascent electronic, vibrational, and rotational energy distributions of various diatomic fragments such as CN, OH, NO, and $O_2$ that are directly formed in the photodissociation of many kinds of molecules. The ready availability of high-quality, tunable, nanosecond lasers has made determination of the above-mentioned collisionless energy distributions a relatively straightforward process. The determination of product translational energies has long effectively been handled by angularly resolved time-of-flight (TOF) spectroscopy, or by sub-Doppler resolution spectroscopy, including a recently improved version of the latter, velocity-aligned Doppler spectroscopy (Xu et al., 1986).

Of great interest, but until recently unobtainable, is detailed knowledge of the time sequences of the various internal conversions, rearrangements, dissociations, etc. that molecules typically undergo upon photoexcitation. To illustrate this point, let us consider Figure 8.1, which depicts an alkyl azide analog of the Curtius rearrangement for an acyl azide molecule. It is known that the weakest bond in the covalently bonded azide group lies between the two nitrogen atoms closest to the carbon atom. This fact explains the finding that molecular nitrogen is invariably produced in the photolysis of covalently bonded azides. The existence of the stable methylenimine product in the case of Figure 8.1 implies a breaking of the C—H bond and forming of an

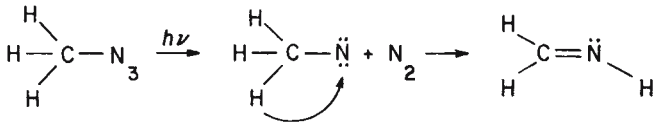

FIGURE 8.1. Rearrangement mechanism proposed for the photolysis of methyl azide.

N—H bond. However, as to whether the above reactions actually happen sequentially in the order described, or whether the whole sequence occurs in a simultaneous, concerted manner, the relevant literature is quite contentious. It would appear that an advanced technique of *kinetic spectroscopy*,* having a spectral range that includes portions of the infrared and having a subpicosecond time resolution, could provide direct answers in the above example, provided that the time to form the final methylenimine product is no less than several hundred femtoseconds. Experimentally, one would monitor the times for disappearance of the azide symmetric or antisymmetric stretches and compare these with the appearance time for the N—H stretch.

While time-resolved broadband infrared probing of the vibrational modes of photoexcited molecules should thus give easily interpretable results, it appears, unfortunately, to be a rather difficult technique to develop and to apply. In general, the optical absorbances associated with purely vibrational transitions are a few orders of magnitude weaker than those associated with electronic transitions. Thus, signal-to-noise considerations become of paramount importance. Aside from questions of sensitivity, there is also the problem that only a very limited spectral range has thus far been demonstrated for subpicosecond kinetic spectroscopy in the infrared. For many photoexcited molecules one can, of course, determine exact times of dissociation by observing the appearance times of products of the photodissociation. Here one can fortunately utilize as monitors electronic transitions with their intrinsically high molar absorbances. Examples are given further on in this chapter. Electronic transitions between excited states of a molecule can also be utilized to monitor the motion of a molecule along an excited state potential surface, tracking the times when the molecule internally converts or fragments. This is illustrated by another example, discussed further on, in which an infrared subpicosecond kinetic spectroscopy probe is actually utilized.

Of course, the problem of spectroscopically monitoring in real time the unimolecular reactions of a photoexcited molecule can also be attacked in ways other than through kinetic spectroscopy. A.W. Zewail's group uses a different time-resolved approach, which is illustrated by their recent study of

* The term "kinetic spectroscopy" was used by G. Porter, R. Norrish, and others, who pioneered the field of flash photolysis. Since the technique we describe in this chapter also relies on the use of a time-resolved, broadband, absorption spectroscopy probe, we choose to describe our work with the same term, with the addition, however, of the prefix "subpicosecond."

ICN photodissociation (Dantus et al., 1987). After a subpicosecond UV pump pulse has initiated ICN fragmentation, a tunable LIF subpicosecond probe pulse induces the CN fragments to fluoresce. They recorded the CN* excitation spectrum as a function of pump-probe delay, providing new information about the photodissociation dynamics.

We have tried briefly in the preceding paragraphs to stress the potential utility of a subpicosecond kinetic spectroscopy approach to the real-time study of intramolecular photoinitiated reactions of gas-phase molecules. As is well known, subpicosecond kinetic spectroscopy has already been employed successfully in the condensed phase by several research groups to elucidate the dynamics of biological processes, to follow the approach to equilibrium in photoexcited dyes, to study ultrafast processes in semiconductors, etc. However, such studies, almost without exception, have relied on the use of broadband time-resolved spectroscopic probes in the visible. Our group has recently started to make advances toward developing equipment capable of providing a wider subpicosecond spectral probing range. In recent papers (Glownia et al., 1986a, 1987a, 1987b) we have described an apparatus capable of simultaneously generating both intense subpicosecond UV (308, 248.5 nm) excitation pulses and subpicosecond continua for probing photoexcited molecules via broadband absorption spectroscopy. Both UV (230 to 450 nm) and IR (2.2 to 2.7 $\mu$m) continua have thus far been produced. A method of upconverting the latter to the visible for ease of detection has also been demonstrated. In the present chapter this apparatus is described in detail. Also given is an account of some of the first experiments performed using this equipment.

The organization of this chapter is as follows. Since the pulses in both excitation and probe channels are derived from subpicosecond UV pulses amplified in XeCl gain modules, we begin, in Section 2, with a description of the apparatus we have built for producing intense subpicosecond 308-nm pulses. In Section 3 we show how these 308-nm pulses can be used to generate ultrafast UV supercontinuum pulses and also how the latter can be used to seed an amplification process in a KrF excimer gain module in order to produce intense subpicosecond pulses at 248 nm. Section 4 describes our technique for producing an ultrafast IR continuum, as well as the method we use for upconverting it to the visible for ease of detection. Exactly how the UV and IR continua are utilized in subpicosecond kinetic spectroscopy experiments is shown in the examples discussed in the balance of the chapter. Section 5 describes an IR experiment we have performed, the measurement of the $\tilde{B} \rightarrow \tilde{A}$ internal conversion rate in 1,4-diazabicyclo[2.2.2]octane (DABCO) vapor, while Section 6 describes some preliminary results obtained in the case of two subpicosecond kinetic spectroscopy experiments recently attempted, photolysis of thallium halide vapors at 248 and 308 nm and photolysis of chlorine dioxide vapor at 308 nm. Section 7 concludes with a brief description of two promising directions than can now be taken in our approach to subpicosecond kinetic spectroscopy.

## 2. 160-fs XeCl Excimer Amplifier System

The suitability of commercially available excimer gain modules for amplification of ultrafast UV pulses has been apparent for many years. Around 1982, various groups (Corkum and Taylor, 1982; Egger et al., 1982; Bucksbaum et al., 1982; Szatmári and Schäfer, 1984a) successfully utilized discharge-pumped excimer gain modules for amplification of UV pulses having durations of a few picoseconds. However, it was well known (e.g., see Corkum and Taylor, 1982) that the gain bandwidth of these systems is such that amplification of much shorter pulses can also be accomplished. The first published accounts of subpicosecond pulse amplification in excimers were published some four years later (Glownia et al., 1986b; Schwarzenbach et al., 1986). Glownia et al. (1986b) used a pair of XeCl gain modules to amplify 350-fs, 308-nm pulses to ~10-mJ energies with <1-mJ amplified spontaneous emission (ASE) content. Seed pulses for the excimer amplifier were formed through the combined use of a synch-pumped mode-locked dye laser tuned to 616 nm, a single-mode fiber pulse compressor (Nakatsuka et al., 1981; Nikolaus and Grischkowsky, 1983), a four-stage $Nd^{3+}$ : YAG-laser-pumped dye amplifier, and, finally a KDP frequency-doubling crystal. Schwarzenbach et al. (1986) used generally similar methods to produce subpicosecond seed pulses suitable for amplification at 248.5 nm in KrF gain modules.

In 1987 further significant advances in excimer-based UV subpicosecond amplification were made. Szatmári et al. (1987a) reported the generation of 220-fs pulses at 308 nm from an XeCl amplifier. Shortly afterwards, the same Göttingen group (Szatmári et al., 1987b) reported having obtained 15-mJ, 80-fs, 248.5-nm pulses from a KrF amplifier and having then amplified these pulses to 900 GW peak power in a wide-aperture KrF discharge amplifier. A remarkable feature of the above work is that the seed pulses in each case were formed directly with nanosecond excimer-pumped dye laser sources. A novel method discovered earlier (Szatmári and Schäfer, 1983, 1984b) of generating single, picosecond pulses through the combined use of an excimer-pumped, quenched, dye laser and a distributed feedback dye laser (DFDL) was improved on by Szatmári et al. (1987a, 1987b) to the degree that subpicosecond pulses were produced. These pulses were amplified and then frequency doubled prior to final amplification in an excimer gain module. One of the many advantages of the technique employed by the Göttingen group is that, due to the wide wavelength range accessible with DFDLs, all of the known rare-gas halide wavelengths can be reached through frequency doubling or mixing. Possible disadvantages of the Göttingen technique center around the inherent difficulties in adjusting and stabilizing the DFDL. It will be interesting to follow the development of this unique approach and to see also if it eventually benefits from commercial product engineering.

In 1987 a full description was published (Glownia et al., 1987b) of the XeCl excimer-based system our group currently employs, which generates bandwidth-limited, 160-fs, 308-nm pulses at a 10-Hz rate. Subpicosecond

pulses at ~616 nm are formed in a colliding-pulse mode-locked (CPM) laser (Fork et al., 1981; Valdmanis et al., 1985), amplified in a four-stage $Nd^{3+}$:YAG laser-pumped amplifier chain, and then frequency doubled in a 1-mm-long KDP crystal, forming seed pulses at 308 nm for further amplification in the XeCl excimer gain module. Since this sytem is the heart of our subpicosecond pump-probe apparatus, we summarize its main features here.

The design of the CPM laser is generally similar to that of Valdmanis et al. (1985), incorporating four dispersion-compensating prisms in the seven-mirror ring cavity arrangement of Fork et al. (1981). The pulse repetition rate is 116 MHz. An 80-mm focal-length lens is used to focus the 514.5-nm CW $Ar^+$-ion laser pump beam into the Rhodamine 6G gain jet. Surprisingly, optimum mode locking at 616 nm, described below, requires only 1.4 W of pump power. Both the gain and DODCI absorber jets are standard Coherent dye laser nozzles (dye stream thickness ~100 $\mu$m). A relatively dilute concentration of DODCI (50 mg in 21 ethylene glycol) was found to be optimum for operation at 616 nm. The CPM output power is about 20 mW in each arm when the laser is optimized at this frequency.

We generally tune the intraprism path length for minimum amplified laser-pulse duration (see below) while maintaining the peak of the output spectrum near 616 nm. With this adjustment, the CPM pulse width is about 240 fs. However, when measured after the beam has propagated through an additional 5 cm of $H_2O$, the pulse width is 200 fs, showing that the laser operates with excess negative dispersion in the cavity. It should be noted that this CPM laser can readily produce much shorter pulse widths (~70 fs) at longer wavelengths. However, the spectrum of the amplified and frequency-doubled pulses cannot then properly match the XeCl gain profile. The first three stages of the dye amplifier are excited transversely; the fourth, longitudinally. Kiton Red 620 dye is used in the first stage; Sulforhodamine 640 in the last three stages. The solvent used in all stages is $H_2O$ + 4% Ammonyx LO. Malachite Green bleachable absorber dye jets are used between the first three amplifier stages to control amplified spontaneous emission. The small-signal attenuations of the absorber jets are roughly 10× and 200×. Pumping of the dye amplifier chain is accomplished with ~125 mJ of 532-nm light from a Quanta-Ray DCR-2A $Nd^{3+}$:YAG laser operating in the short pulse (2-ns central peak) mode. We typically measure a total amplified pulse energy of ~0.6 mJ. The autocorrelation trace of the amplified CPM dye laser pulses at full power indicates a pulse width of ~200 fs.

The ~200-fs amplified 616-nm pulses are spatially compressed to a beam diameter of ~2 mm, then frequency doubled in 1-mm-long KDP crystals to form seed pulses for amplification in the XeCl excimer gain module. In Glownia et al. (1987b) extensive frequency broadening of the second harmonic was noted when the size of the input beam in the KDP crystal was allowed to be less than 2 mm in diameter. This was attributed to self-phase modulation (SPM) occurring in the KDP crystals. Since the UV spectral width of the seed pulses was observed to be typically 10× the XeCl gain band-

width, it was argued by Glownia et al. (1987b) that the positive frequency sweep associated with the most intense part of the pulse would result in a nearly in-phase excitation of all the frequencies lying under the XeCl gain curve. This is an exact prescription for forming bandwidth-limited pulses. This argument was used to explain the observation (see below) that the UV pulses amplified by the XeCl gain module are bandwidth limited.

The UV seed pulses are amplified in a single pass through a Lambda-Physik EMG101-MSC excimer gain module (45-cm-long discharge). Provided that the seed pulse spectrum is relatively flat over the XeCl gain profile, the spectrum of the amplified 308-nm pulse appears as shown in Figure 8.2. Figure 8.3 displays a typical amplified 308-nm pulse autocorrelation trace. (Two-photon ionization in DABCO vapor is used for the 308-nm pulse autocorrelation measurements.) Measurements made on this system over a period

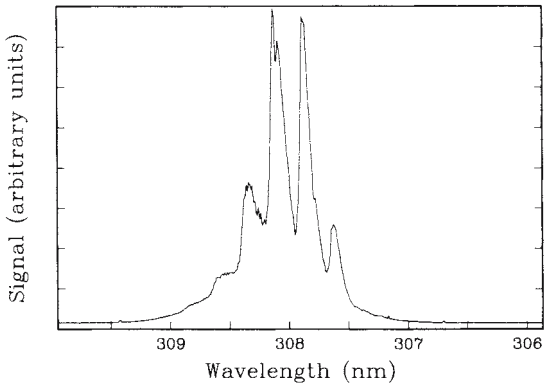


FIGURE 8.2. Spectrum of amplified 308-nm pulses.

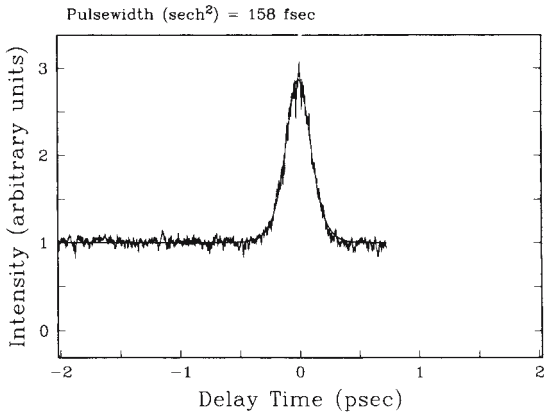


FIGURE 8.3. Autocorrelation trace of amplified 308-nm pulses.

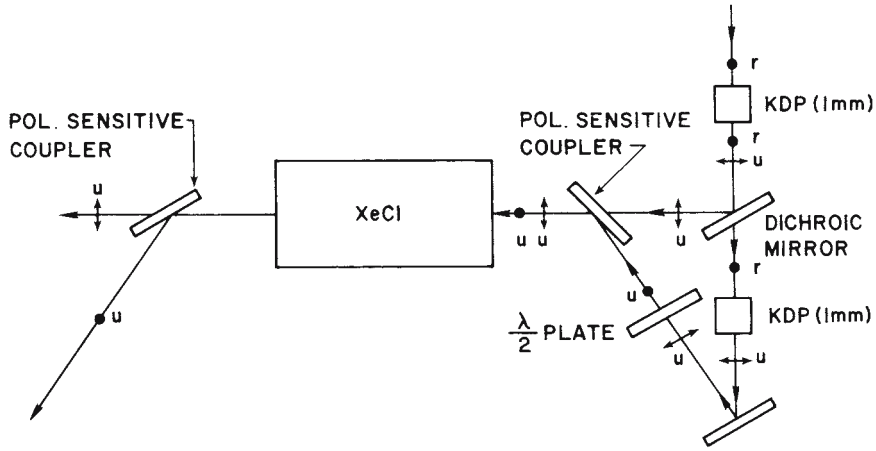


FIGURE 8.4. Scheme employed for multiplexing the 308-nm pulses (u, ultraviolet; r, red).

of more than one year have consistently shown the amplified 308-nm pulse width to be near 160 fs, a number very close to the bandwidth limit calculated (Glownia et al., 1987b) for the spectrum of Figure 8.2. This observed facile generation of bandwidth-limited UV pulses is rationalized by the argument mentioned in the preceding paragraph.

With the use of 1-mm-long KDP doubling crystals, pulse energies of 4 to 5 mJ are achieved in a single pass through the XeCl excimer gain module. With the scheme shown in Figure 8.4, however, a second UV pulse, having roughly the same energy, can be obtained during the same excimer discharge. Because the efficiency of second harmonic generation in the first 1-mm-long KDP crystal is only ~10%, enough 616-nm light remains to generate a second UV seed pulse having almost the same energy as the first. If the two UV seed pulses are spaced apart by 2 or 3 ns, there is sufficient time for repumping the XeCl B state, according to Corkum and Taylor (1982). Thus amplification in the XeCl gain module occurs in the form of pairs of orthogonally polarized pulses, each pulse 4 to 5 mJ in energy. The 160-fs amplified UV pulse pairs are then separated by a Brewster polarizer into pump and probe channels (see Figure 8.14).

## 3. Ultraviolet Supercontinuum Generation

It was noted by Glownia et al. (1986b) that gentle focussing in air of the XeCl-amplified subpicosecond pulses resulted in a spectral broadening of the pulses by roughly a factor ten. Figure 8.5 shows a typical single-shot spectrum of an amplified 308-nm, 160-fs pulse after it has been focused in the laboratory atmosphere with a 1-m lens. The spectrum is almost 100 $cm^{-1}$ wide,

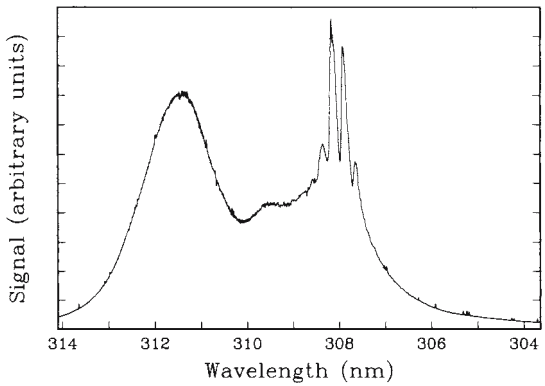


FIGURE 8.5. Single-shot spectrum of amplified 308-nm pulse, recorded after the latter was focused in air with a 1-m lens.

with the spectral enhancement being predominantly on the Stokes side. At the same time it was observed that the far-field pattern of the beam beyond the focal point of the 1-m lens usually contained bright spots in which the light was concentrated. These observations qualitatively suggested to us that SPM and self-focusing were involved in the above phenomena. However, due to the multimode spatial character of the beam, no direct steps were taken to verify these speculations. Instead, it was decided to experiment with a variety of gases (Ar, $H_2$, $N_2$, and $CO_2$) under high pressure to see if any differences in spectral broadening could be discerned between the various gases and also whether spectral continua with widths in excess of ~1000 $cm^{-1}$ could be produced by this method. The results of our measurements were reported in Glownia et al. (1986a, 1986c). The main features are summarized below. Independently of us, P. Corkum's group at National Research Council, Canada, observed the same basic phenomenon of supercontinuum generation from high-pressure gases (Corkum et al., 1986a, 1986b). In their case, both subpicosecond and picosecond amplified red pulses were successfully utilized as pump pulses. The basic physics of this newly discovered phenomenon is discussed by Corkum et al. (1986b). More recent observations and deductions about gas-phase supercontinuum generation are contained in Corkum and Rolland (Chapter 7 in the present volume).

Figure 8.6 displays the spectrum of the energetic UV supercontinuum beam that emerges from a high-pressure Ar cell when high-power subpicosecond UV (308 nm) pulses are focused into the cell. Consistent with the finding of Corkum et al. (1986b), we observe nearly full transmission (>80%) of energy through the pressurized cell, with no significant degradation of the beam profile. There is thus adequate probe energy to pass through a photoexcited sample on to a high-dispersion visible-UV spectrograph, to be then recorded on an unintensified silicon diode array. With the supercontinuum

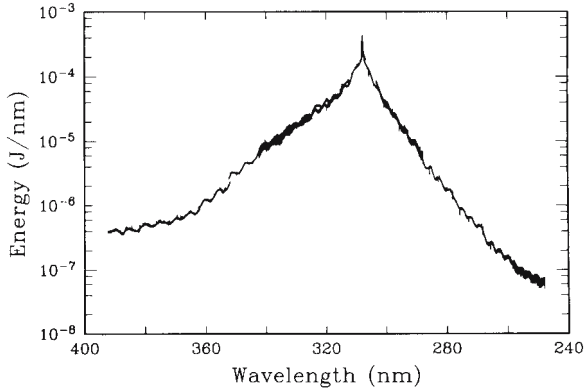


FIGURE 8.6. Spectrum of UV supercontinuum beam emerging from Ar cell, $p$ = 40 atm. Pump pulses (4 mJ, 308 nm, 160 fs) were focused into the middle of the 60-cm-long Ar cell with a 50-cm lens. Average of 64 shots.

source and spectrograph/detector system we normally employ, a spectral resolution of better than 0.3 Å is achieved. For probe continua at longer wavelengths, one must continue to rely on the various condensed-matter supercontinua (Alfano and Shapiro, 1970a, 1970b; Fork et al., 1982) or else on gas-phase supercontinua pumped by a red laser (Corkum et al., 1986a, 1986b), since all supercontinua peak at the pump wavelengths employed. It should be pointed out, however, that condensed-matter supercontinua peaking in the UV evidently cannot easily be generated. Our attempts to achieve this effect with the use of amplified subpicosecond 308-nm pulses as pump pulses were unsuccessful, possible due to nonlinear absorption in the various liquids tried.

Because of the large spectral extent of supercontinuum pulses, they are broadened in time by group velocity dispersion (GVD). For condensed-matter visible supercontinua, Li et al. (1986) have measured spectral delays with the use of a streak camera and filters. Utilizing a cross-correlation technique, Fork et al. (1983) have measured the sweep of a supercontinuum generated in an ethylene glycol jet. We have ultilized a novel method, based on time-resolved absorption spectroscopy, to measure with subpicosecond resolution the frequency sweep of the supercontinuum displayed in Figure 8.6. This method, in the form in which it was originally demonstrated (Misewich et al., 1988a), is now briefly described.

Thallium chloride molecules, contained in a vapor cell at 450°C, were irradiated by 250-fs, 248-nm pump pulses derived (by a method to be described below) from 160-fs, 308-nm pulses. Supercontinuum probe pulses were simultaneously obtained from the same apparatus by focusing 4-mJ, 160-fs, 308-nm pulses into 40-atm Ar with a 50-cm lens. The probe pulses were directed into the TlCl vapor colinearly with the pump pulses, then dispersed

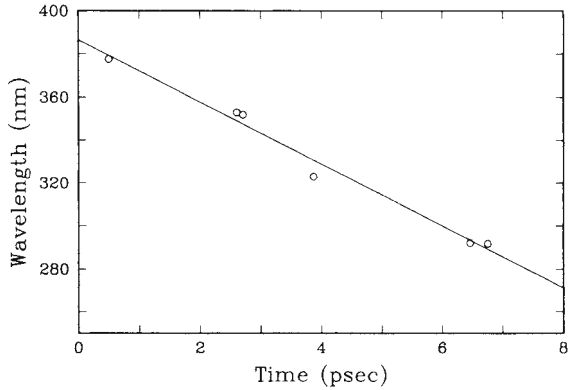


FIGURE 8.7. Frequency sweep of 40-atm Ar supercontinuum beam whose spectrum is shown in Figure 8.6. Data points correspond to Tl absorptive transitions whose onsets were measured.

in a spectrograph and recorded on an optical multichannel analyzer (OMA). Absorbances were computed by comparison of supercontinuum intensities recorded with and without the UV pump blocked.

Thallium chloride molecules irradiated at 248 nm undergo prompt dissociation into Tl and Cl atoms, with the former being distributed into ground $^2P_{1/2}$ and first-excited $^2P_{2/3}$ (7793 $cm^{-1}$) states in roughly a 30 : 70% ratio (van Veen et al., 1981). Several allowed transitions, spanning a wide range of frequencies, connect the two states with various higher excited states. By plotting the individual rise times of the above atomic transitions as a function of pump-probe delay, one obtains the plot in Figure 8.7, which shows that the 40-atm Ar supercontinuum is characterized by a positive chirp of approximately 1340 $cm^{-1}$/ps.

Our technique utilizing TlCl photodissociation to measured the UV supercontinuum frequency sweep has also revealed some interesting features of the photodissociation itself. We defer a discussion of the transient absorption spectra of photodissociating TlCl and TlI molecules until Section 6. From the results presented there, however, it can be stated that while the total duration of the gas-phase supercontinuum pulse emerging from the high-pressure cell is on the order of 10 ps, the effective time resolution is much better. As shown above, the probe continuum pulse has a fast red-to-blue linear sweep. Our spectral results (Section 6) indicate that the cross-correlation between the 160-fs, 308-nm pump pulse and a given wavelength interval of the swept probe pulse is stable to at least ±50 fs from shot to shot. It is this observed stability that gives the UV gas-phase supercontinuum pulse its good time resolution.

The UV supercontinuum pulses of Figure 8.6 can be directly used as seed pulses suitable for further amplification in KrF gain modules. From

Figure 8.6 one sees that there is roughly a microjoule of energy in the supercontinuum between 248 and 249 nm, the wavelength range over which KrF amplification occurs. With this amount of input energy one easily obtains 6-mJ output pulses through single-pass amplification in a KrF gain module with a 45-cm-long discharge region (Glownia et al., 1986a, 1986c, 1987c). In Glownia et al. (1986a), the high-pressure cell used to form the KrF seed pulses contained $H_2$ gas. We originally used hydrogen because of a coincidence between an anti-Stokes Raman wavelength and the wavelength at which maximum KrF gain occurs. Stimulated Raman scattering (SRS) occurs in high-pressure $H_2$ gas when 160-fs, 308-nm pump pulses are applied, but not without the simultaneous occurrence of UV continuum generation. In several other molecular gases we failed to observe SRS with our 308-nm, 160-fs pump source, but we do observe UV continuum generation. Since SRS is known to be a ubiquitous phenomenon when high-power pulses of a few picoseconds duration are applied to high-pressure molecular gases (Mack et al., 1970), once must conclude that the conditions for its occurrence are made far less favorable as one proceeds to the subpicosecond domain, while the occurrence of supercontinuum generation becomes much more likely.

## 4. Subpicosecond Time-Resolved Infrared Spectral Photography

Time-resolved infrared spectral photography (TRISP) (Avouris et al., 1981; Bethune et al., 1981, 1983; Glownia et al., 1985) is a nonlinear optical technique by which a broadband ($\Delta\nu \sim 1000\,\mathrm{cm}^{-1}$) infrared absorption spectrum can be recorded in a single shot of a few nanoseconds duration. The IR spectral range that has thus far been convered with this technique is 2 to 11 $\mu$m (Bethune et al., 1983). Recently, we reported a successful extension of the TRISP technique to the subpicosecond time domain (Glownia et al., 1987a). The IR spectral region that can be probed with our present ultrafast apparatus is only 2.2 to 2.7 $\mu$m, but extension of subpicosecond capability to other IR ranges seems possible.

In this section we present details of the 2.2–2.7-$\mu$m subpicosecond TRISP apparatus. In the following section we describe the actual measurement of a subpicosecond photophysical event with the use of this apparatus.

In a TRISP apparatus, means for generating a broadband infrared sample probing pulse are combined with a method for upconverting and detecting this signal in the visible. Our ultrafast TRISP apparatus combines a new subpicosecond IR continuum generator with a standard TRISP upconverter. We first discuss formation of an ultrashort IR continuum. Powerful subpicosecond IR pulses at ~2.4 $\mu$m are produced by stimulated electronic Raman scattering (SERS) in Ba vapor (Figure 8.8). The latter is contained at ~10 torr pressure inside an Inconel pipe heated to ~1050°C. The length of the heated

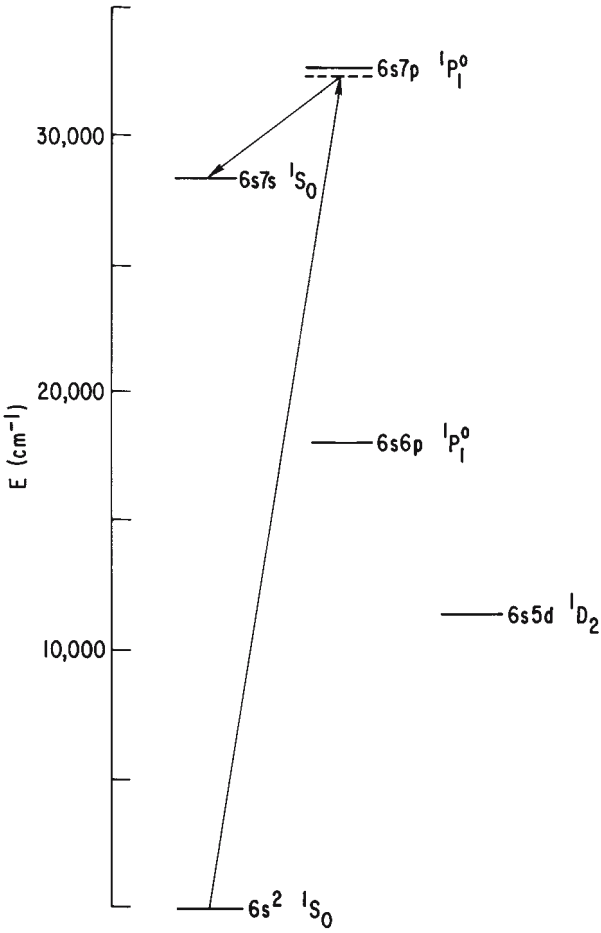


FIGURE 8.8. Diagram of the Ba SERS process.

region is ~0.5 m. As pump pulses we directly utilize amplified 308-nm, 160-fs pulses. Although application of ~20-ns XeCl laser pulses to Ba vapor is known (Burnham and Djeu, 1978; Cotter and Zapka, 1978) to produce SERS only on the $6s^2\ ^1S_0 \rightarrow 6s5d^1\ D_2$ transition, with a Stokes output near 475 nm, we find, by contrast, that with ultrashort 308-nm excitation SERS occurs only on the $6s^2\ ^1S_0 \rightarrow 6s7s^1\ S_0$ transition, with a Stokes output peaked near 2.4 $\mu$m. The 2.4-$\mu$m SERS output is highly photon efficient, with measured IR output pulse energies of ~0.4 mJ for ~5-mJ UV input pulses. The SERS threshold is lower than 1 mJ, even for an unfocused pump beam. Spectrally, the IR output is found to be a continuum, extending from 2.2 to 2.7 $\mu$m (Figure 8.9). Occurrence of the 2.4-$\mu$m SERS process is accompanied

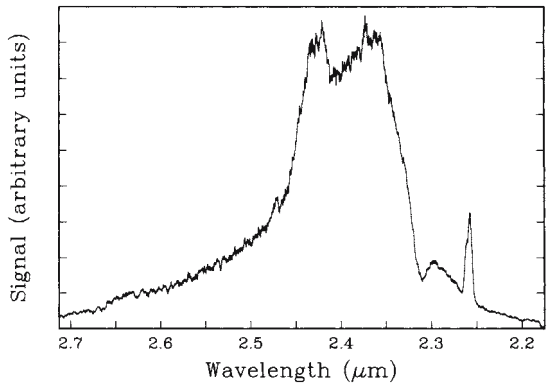


FIGURE 8.9. Spectrum of Raman Stokes light, recorded with the use of a scanning monochromator and PbS detector.

by the presence of a parametrically generated beam of light in the vicinity of the 535-nm Ba resonance line.

We have also measured the ~2.4-$\mu$m IR continuum pulse width by non-background-free autocorrelation, with the second harmonic being generated in a thin $LiIO_3$ crystal. For the 250-fs, 308-nm pump pulses that were applied (Glownia et al., 1986d), the IR pulse width was determined to be ~160 fs.

In Glownia et al. (1987a), a plausible argument was given to account for the switch of Stokes wavelength from 475 nm to 2.4 $\mu$m that occurs with ultrashort excitation. It was suggested that this switch could be attributed to the change in Raman gain regime (from stationary to transient) that occurs in going from ~20 ns to subpicosecond 308-nm excitation pulses. In the stationary regime ($t_p > T_2$), the intensity of the Stokes wave increases in accordance with the law

$$I_S(z) = K_0 \exp(\Gamma_0 z), \tag{1}$$

where $\Gamma_0$ is the static gain, inversely proportional to the Raman linewidth. In the transient regime, the intensity of the Stokes wave assumes (for a square input pulse) the value (Akhmanov et al., 1972; Carman et al., 1970)

$$I_S(z) \sim K_1 \exp\left[2(2\Gamma_0 t_p T_2^{-1} z)^{1/2}\right]. \tag{2}$$

Since $\Gamma_0$ is directly proportional to $T_2$, one sees that there is no dependence of Stokes gain on Raman linewidth in the transient regime. A possible explanation for the Stokes wavelength switch would thus be that the collisional linewidth of the $6s5d^1\ D_2$ state is sufficiently narrow compared with that of the $6s7s^1\ S_0$ state to favor Raman Stokes generation of 475 nm in the stationary case, even though the remaining factors in $\Gamma_0$ favor Stokes generation

at 2.4 $\mu$m. In the transient regime the gain is independent of $T_2$, and the above-mentioned remaining factors entirely determine the Stokes wavelength. No Ba linewidth data are available to support this contention. However, a crude calculation of the van der Waals interaction between a ground state Ba atom and a Ba atom in either the $6s7s^1\ S_0$ state or the $6s5d^1\ D_2$ state, with use of London's general formula (Margenau, 1939), indicates a larger width for the $6s7s$ state.

We now discuss upconversion of the IR. With the use of a polished Si wafer, the horizontally polarized ultrashort IR pulses ($\nu_{IR}$) are colinearly combined with the vertically polarized ~15-ns pulses ($\nu_L$) from a tunable narrowband furan 1 dye laser. With the timing between the two sources adjusted so that the subpicosecond IR pulses occur within the 15-ns-long dye laser pulses, both beams are sent into an Rb upconverter (Glownia et al., 1985) where the dye laser beam induces SERS on the Rb $5s \rightarrow 6s$ Stokes transition, producing a narrowband vertically polarized Stokes wave $\nu_S$. Horizontally polarized, visible continuum pulses at $\nu_L - \nu_S \pm \nu_{IR}$ are then observed to emerge from the Rb cell when $\nu_L$ is tuned to phase match either upconversion process.

Figure 8.10 shows a recording of the (lower-sideband) upconverted spectrum. In Figure 8.11 portions of two upconverted spectra are superimposed. In one case, the IR pulse was passed through an empty 20-cm cell; in the other case it was passed through the same cell filled with 200 torr of CO. The deduced absorbance is shown in Figure 8.12. A surprising finding is the observed increase in upconverted signal at the peaks of the CO 2–0 bands. This is explained as follows (Glownia et al., 1987a). Under the conditions of Figure 8.11 and 8.12, the upconverted signal was heavily saturated by the subpicosecond IR pulse; that is, too few photons at $\nu_L$ and $\nu_S$ were available

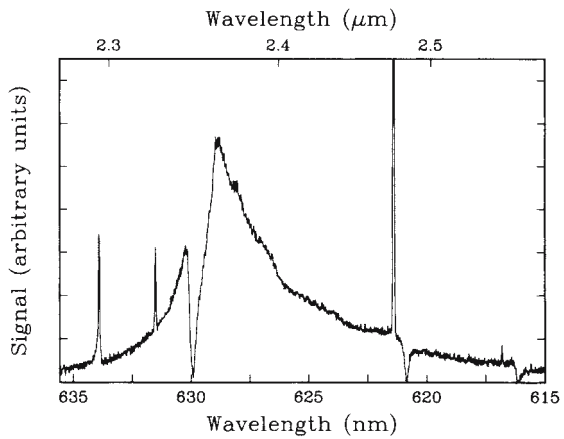


FIGURE 8.10. Upconverted TRISP spectrum (128-shot average, lower sideband). The spectrum is saturated (see text). The three absorptions are Rb excited state ($5p$) absorptions occurring at the visible wavelengths shown.

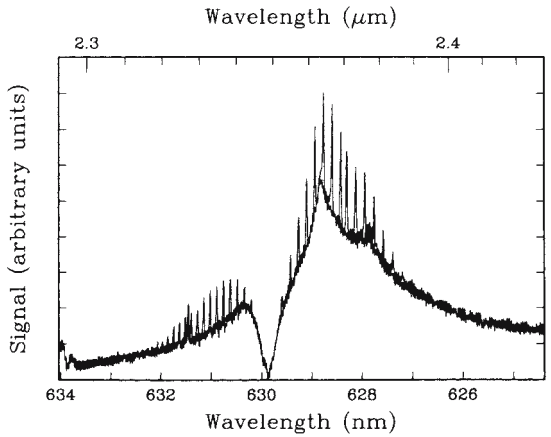


FIGURE 8.11. Superimposed upconverted spectra (cell empty and filled with 200-torr CO gas). Each spectrum is the average of 128 shots.

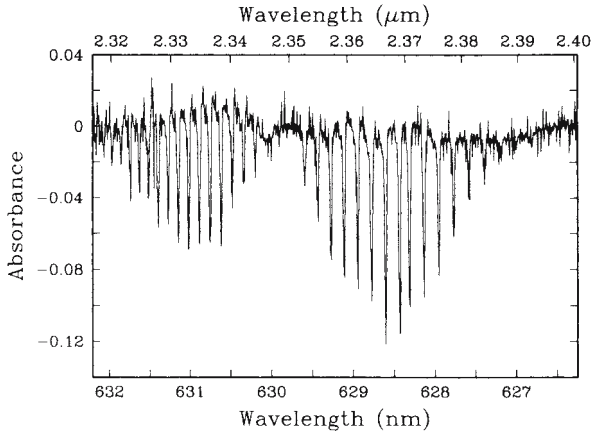


FIGURE 8.12. Absorbance formally deduced from Figure 8.11.

during the actual IR pulse to allow efficient upconversion of the latter. Therefore a decrease in transmitted light due to molecular resonance absorption during the IR pulse did not result in a measurable decrease in upconverted signal. However, the coherently reemitted light of the molecules (Hartmann and Laubereau, 1984), occurring for a time the order of $T_2$ after the IR pulse, when the upconverter is no longer saturated, was able to be efficiently upconverted, resulting in the observed peaks. Positive IR absorption is observed in the upconverted spectra when the subpicosecond IR probe beam is sufficiently attenuated.

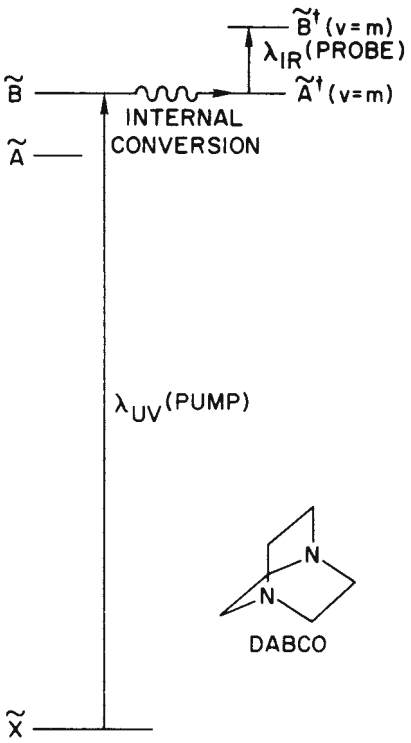


FIGURE 8.13. Diagram of photophysical processes involved in the subpicosecond DABCO experiment.

## 5. Application of Subpicosecond TRISP: Measurement of Internal Conversion Rates in DABCO Vapor

We recently reported (Glownia et al., 1987c) the first application of subpicosecond time-resolved IR absorption spectroscopy to measure an ultrafast molecular process. This experiment combined subpicosecond 248-nm excitation with subpicosecond IR continuum probing to measure the $\tilde{B} \rightarrow \tilde{A}$ internal conversion rate in DABCO vapor. A diagram of the photophysical processes involved is shown in Figure 8.13. The idea that the $\tilde{B} \rightarrow \tilde{A}$ internal conversion rate in DABCO might be high enough to require ultrafast techniques for its measurement is contained in an earlier study (Glownia et al., 1985), in which the population of the $\tilde{A}$ state was monitored following the application of a 30-ns, 248.5-nm KrF laser excitation pulse. A high $\tilde{B} \rightarrow \tilde{A}$ internal conversion rate for DABCO was also implied in a recent two-color laser photoionization spectroscopy study (Smith et al., 1984). In the abovementioned earlier study of DABCO by our group, nanosecond TRISP was used to monitor the $\tilde{A}$ state population. This was because the $\tilde{B} \leftarrow \tilde{A}$ transition (occurring at ~2.5 $\mu$m) was found to have a much higher oscillator strength than all other transitions connecting the $\tilde{A}$ state with higher elec-

tronic states (Glownia et al., 1985). Since the subpicosecond TRISP apparatus described in the last section monitors the region 2.2 to 2.7 $\mu$m, we decided to measure the DABCO $\tilde{B} \rightarrow \tilde{A}$ internal conversion with the greatly improved time resolution this apparatus offers.

Collimated 2-mJ, 250-fs, 248.5-nm pulses were sent unfocused (beam dimensions: 2 cm × 1 cm) into a 60-cm-long cell containing DABCO at its ambient vapor pressure (~0.3 torr) together with 100 torr of $H_2$. The linear absorption of the DABCO at 248.5 nm (40,229 $cm^{-1}$) was more than 50%, even though this wavelength lies near the point of minimum absorbance between the $v' = 0 \leftarrow v'' = 0$ (39,807 $cm^{-1}$) and next highest vibronic peaks of the lowest-energy, dipole-allowed, band (Halpern et al., 1968; Hamada et al., 1973).This band system has been assigned (Parker and Avouris, 1978, 1979) as $\tilde{B}^1E'[3p_{x,y}(+)] \leftarrow \tilde{X}^1A_1'[n(+)]$. Optical transitions from the ground state $\tilde{X}$ to the first excited state, the $\tilde{A}^1A_1'[3s(+)]$ (origin at 35,785 $cm^{-1}$), are one-photon forbidden, two-photon allowed (Parker and Avouris, 1978, 1979).

The 160-fs IR continuum pulses that probe the $\tilde{A}$ state population were directed through the vapor collinearly with the UV photoexcitation pulses, upconverted to the visible, and then dispersed in a spectrograph equipped with an unintensified OMA detection system. The pump-probe delay could be varied up to ±ns by means of an optical delay arm. Absorbances were computed by comparison of upconverted intensities recorded with and without the UV pump blocked.

A block diagram of the experiment is shown in Figure 8.14. As described in Section 2, subpicosecond pulses at ~616 nm formed in a CPM laser are amplified, then frequency doubled, forming seed pulses at ~308 nm for further amplification in the XeCl excimer gain module. Amplification of the UV

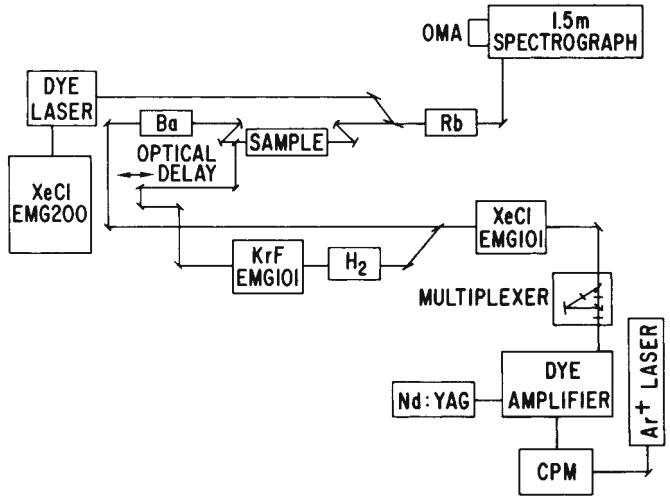


FIGURE 8.14. Diagram of experimental apparatus for the DABCO experiment.

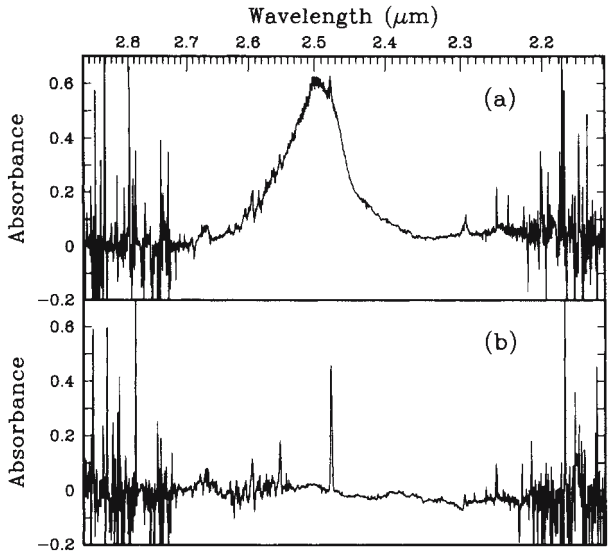


FIGURE 8.15. (a) Absorbance (base 10) with probe delayed ≈4 ps with respect to pump. (b) Absorbance with probe pulse preceding pump pulse.

pulses in the latter occurs in the form of pairs of orthogonally polarized pulses, spaced 2 to 3 ns apart, formed in the multiplexer described also in Section 2. The 160-fs amplified UV pulse pairs are separated by a polarization-sensitive coupler into pump and probe channels. The pump channel 308-nm pulses are focused into high-pressure gas to form seed pulses for amplification at 248.5 nm in a KrF module (see Section 3). The probe channel pulses are Raman shifted in Ba vapor to form IR probe continuum pulses (see Section 4). The narrowband pulsed dye laser drives the Rb upconverter (see Section 4).

Figure 8.15a shows the absorbance recorded when the probe is delayed ~4 ps with respect to the pump (point (a) in Figure 8.16), while Figure 8.15b displays the absorbance with the probe arriving just before the pump (point (b) in Figure 8.16). The absorbance recorded at 2.494 $\mu$m, as a function of probe delay, is shown in Figure 8.16. The large absorption band that develops represents transitions $\tilde{B}^{\dagger} \leftarrow \tilde{A}^{\dagger}$ of vibrationally excited $\tilde{A}$ state molecules, containing up to 4400 $cm^{-1}$ of vibrational energy. Since the $\tilde{B} \leftarrow \tilde{A}$ transition is one that occurs between Rydberg states, vertical ($\Delta v = 0$) transitions are expected. Thus it is not surprising that the peak of the band in Figure 8.15a appears very close to the $\tilde{B} \leftarrow \tilde{A}$ peak for vibrationally equilibrated $\tilde{A}$ state molecules, shown here in Figure 8.17 and described in detail in Glownia et al. (1985). However, the width of the $\tilde{B} \leftarrow \tilde{A}$ band is obviously greater in the vibrationally excited case.

The computer-generated curve in Figure 8.16 is a nonlinear least squares fit to the data. The fit indicates a rise time of ~500 fs. Although the infrared

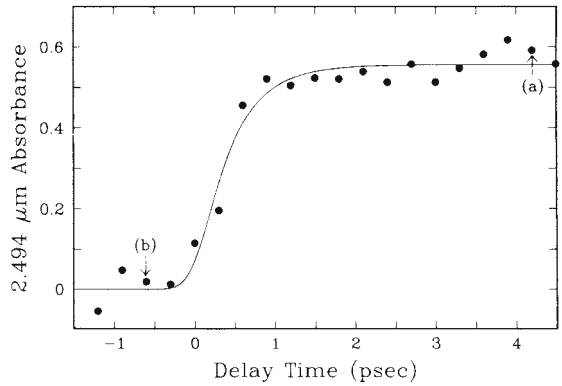


FIGURE 8.16. Peak $\tilde{B}^{\dagger} \leftarrow \tilde{A}^{\dagger}$ absorbance as a function of probe pulse delay time with respect to pump pulse.

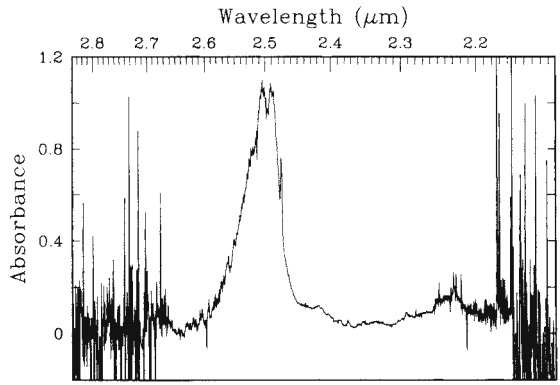


FIGURE 8.17. Absorbance measured with probe pulse delayed 75 ns with respect to pump pulse. The latter was an 8-mJ, 25-ns pulse obtained by operating the KrF gain module as a conventional laser. 60-cm DABCO cell, 3-atm $H_2$ pressure.

and ultraviolet pulse widths were determined by autocorrelation to be ~160 and ~250 fs, respectively, the cross-correlation between these pulses has not been measured. Thus, the rise time in our experiment could be limited by the laser system cross-correlation. In any case, the process converting DABCO states accessed by the subpicosecond 248.5-nm pump beam into vibrationally excited $\tilde{A}$ states is observed to occur on a time scale that is at least as fast as ~500 fs. That internal conversion to vibrationally excited $\tilde{A}$ state molecules is the dominant process for photoexcited DABCO molecules, even at UV pump intensities of ~4 GW/cm$^2$, is also underscored by the fact that there is no apparent decrease in the integrated intensity of the 2.5-$\mu$m absorption band induced at these pump intensities, as compared with the 2.5-$\mu$m integrated

intensity induced by 25-ns UV pulses at comparable fluence levels (compare Figures 8.15a and 8.17).

The DABCO experiment shows how subpicosecond TRISP can be used to monitor the internal conversion of photoexcited molecules in real time. In the sequence of spectra corresponding to the data points in Figure 8.16, it is clearly seen that the wavelength at which the peak absorbance occurs undergoes a definite blue-to-red shift as the magnitude of the absorbance grows in. It is tempting to attribute this to an intramolecular vibrational redistribution (IVR) process. However, heavy caution must be applied here, since the same apparent phenomenon could easily be induced by a red-to-blue sweep of the IR probe continuum. We have no information at present as to whether or not the IR continuum is swept.

## 6. Preliminary Results on the Application of the UV Supercontinuum Probe

In Section 3 we described a convenient method, based on photofragmentation of thallium halides, by which the sweep of the UV supercontinuum can be measured. In the process of measuring the rise times of the Tl absorption lines, we have consistently noted that the latter assume unusual line shapes, with enhanced integrated intensities, for a period lasting roughly a picosecond, beginning the moment the atomic absorption is first discerned and ending when the asymptotic, normal appearing, absorption line profile is finally attained. We present some of these preliminary spectral results in this section. These results are qualitatively discussed in terms of a model based on the transient behavior of the polarization induced by the subpicosecond swept UV continuum as the latter interacts with the time-varying population of two-level atoms produced by the photolysis pulse. A detailed description of our model will be presented elsewhere (Misewich et al., 1988b).

There has been broad interest for some time in the spectroscopy of the thallium halides. The ultraviolet absorption cross sections have been measured by Davidovits and Bellisio (1969). The UV absorption spectra comprise a number of well-defined bands whose conformity between the various halides is striking. In the most recent thallium halide photofragmentation study (van Veen et al., 1981), these bands are simply labeled A, B, C, and D. In that work, the time-of-flight spectra and angular distributions of photofragments were measured for the thallium halides at a variety of UV wavelengths, including 308 and 248 nm. We have now utilized subpicosecond pulses, at both 308 and 248 nm, to separately excite TlI and TlCl molecules. In the case of the former, 308 nm is very close to the peak of the C band, while 248 nm lies on the high-frequency side of the D band. For the latter, 308 nm is near the peak of the B band, while 248 nm excites the C band.

Figures 8.18, 8.19, and 8.20 show the appearance of time-resolved absorption spectra recorded in the vicinity of the 377.6-nm Tl $7S_{1/2} \leftarrow 6P_{1/2}$

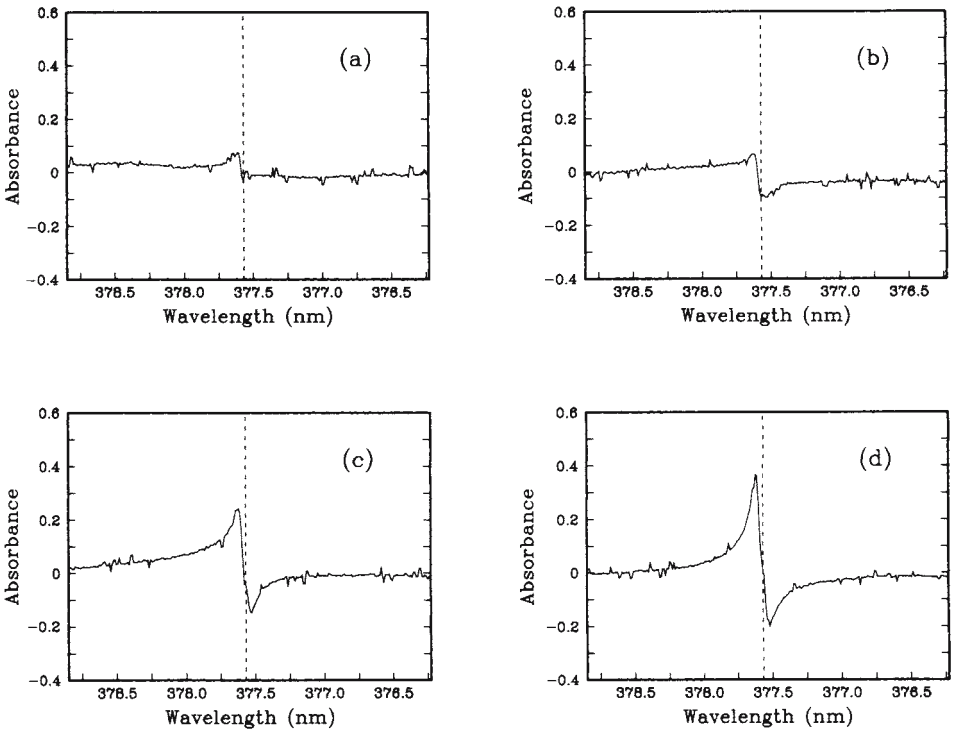


FIGURE 8.18. Time-resolved absorption spectra, recorded in the vicinity of the 377.6-nm Tl $7S_{1/2} \leftarrow 6P_{1/2}$ resonance line, following the application of 160-fs, 308-nm pulses to TlI vapor. Pump-probe separation increased by 100-fs between each spectrum shown. Each spectrum represents the average absorbance (base 10) deduced from dual 64-shot continuum accumulations, one with and one without the 308-nm pump blocked. The dashed line marks the position of the asymptotic resonance peak.

resonance line following the application of 160-fs, 308-nm pump pulses to TlI vapor. It is seen that roughly 1 ps elapses from the moment the atomic transition appears to the point at which no further changes in the appearance of the atomic resonance line occur. From the TOF data presented in van Veen et al. (1981), iodine atoms produced by 308-nm photolysis of TlI have a relatively broad distribution of translational velocities peaking at ~4.4 $\times 10^4$ cm/s. Hence the average Tl–I separation at large distances must increase as ~7.1 $\times 10^4$ cm/s. However, at smaller distances the average rate of increase of separation is much smaller, because the atoms are accelerated from rest. We have been unable to mark the exact time of occurrence of the 308-nm pump pulse with respect to the times shown in Figures 8.18 to 8.20. However, if one assumes the pump pulse occurs somewhere in the vicinity of Figures 8.18a and b, one deduces that the asymptotic line shape must be attained well before the Tl-I separation has increased by 7.1 Å.

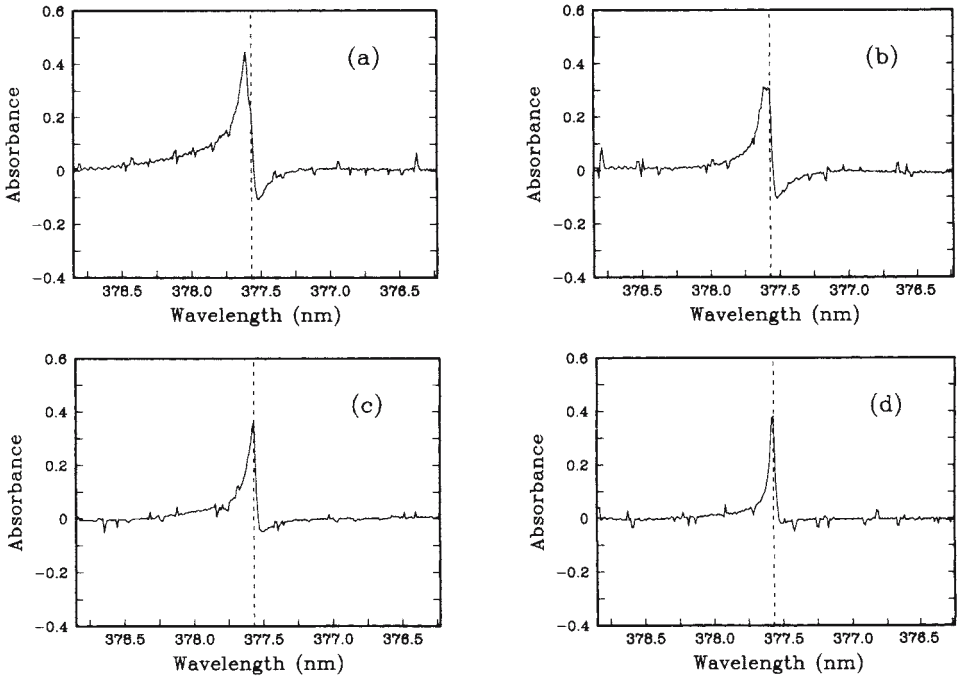


FIGURE 8.19. Continuation of Figure 8.18, with pump-probe separation in (a) increased by 100 fs over that in Figure 8.18 (d).

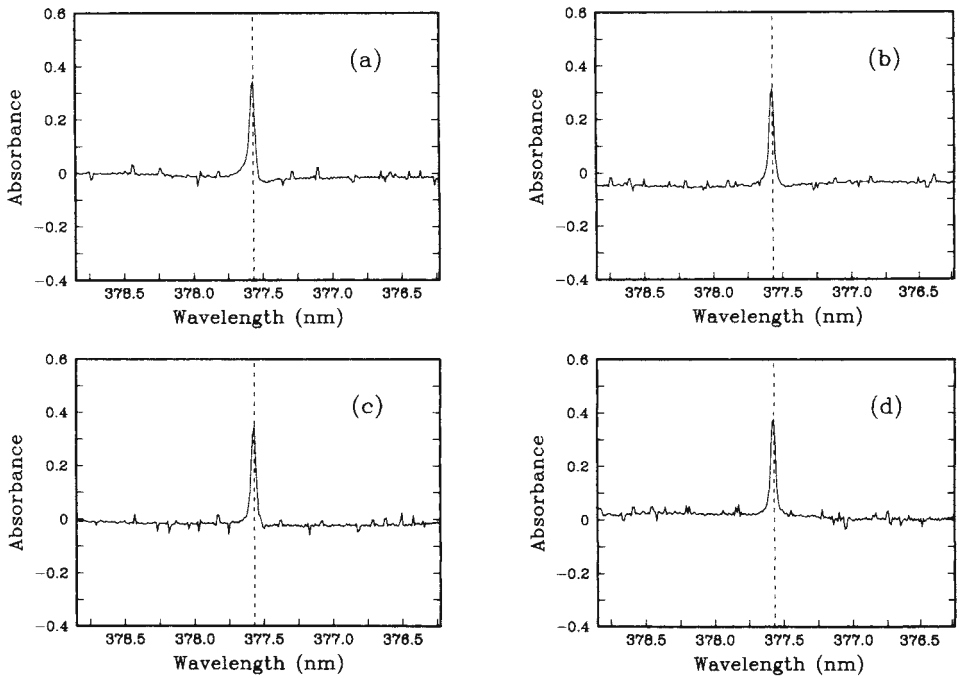


FIGURE 8.20. Continuation of Figure 8.19, with pump-probe separation in (a) increased by 100 fs over that in Figure 8.19 (d).

The most striking feature of Figures 8.18 to 8.20 is, of course, the dispersion-like appearance of the atomic absorption feature for the first 600 or 700 fs, with evidence of a spectral region in which apparent gain prevails. A superficially similar phenomenon was recently observed by Fluegel et al. (1987) in their femtosecond studies of coherent transients in semiconductors. However, in that work the dispersive structure observed in the normalized differential transmission spectra in the region of the excition resonance, when pump and probe pulses overlapped in time, was attributed to the frequency shift of the exciton resonance, i.e., the optical Stark shift. In the case of Figures 8.18 to 8.20 there is no preexisting absorption line to be shifted when the pump is applied.

The appearance of the absorption spectra when the 308-nm pump intensity is reduced by roughly a factor 3 (0.5 ND filter inserted in the pump arm) is shown in Figures 8.21 and 8.22. From the entire sequence of spectra constituting this particular experiment, we have selected the eight consecutive spectra that most closely correspond with Figures 8.18 and 8.19. (Exact

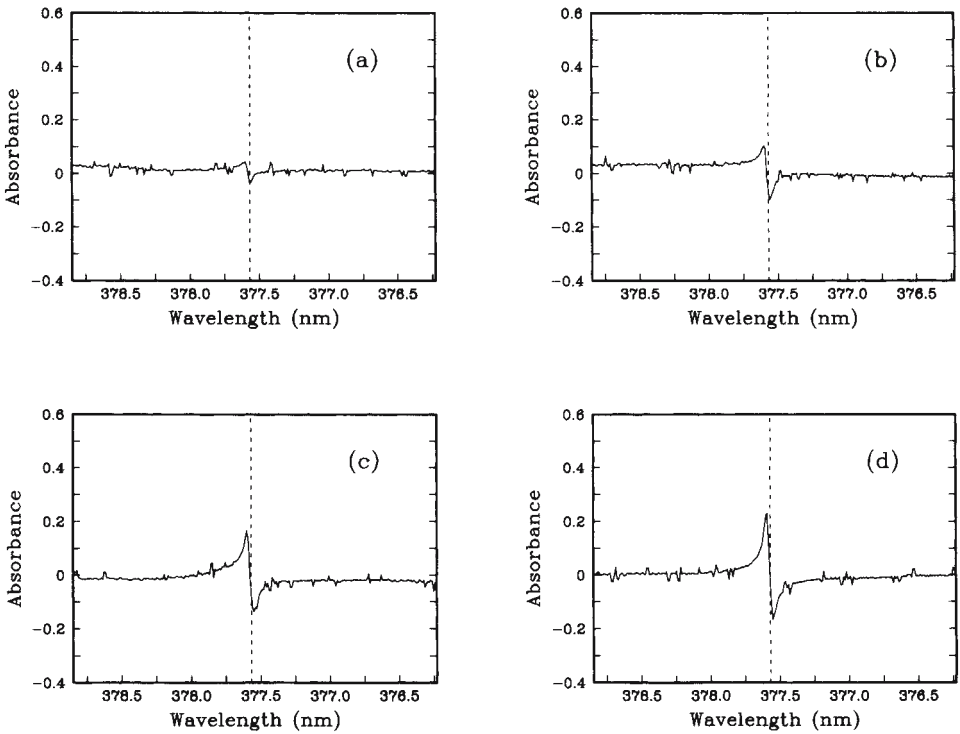


FIGURE 8.21. Time-resolved spectra taken from a sequence with conditions generally similar to those in Figures 8.18 to 8.20, except that the 308-nm pump intensity was reduced by a factor 3. Pump-probe separation increased by 100 fs between spectra.

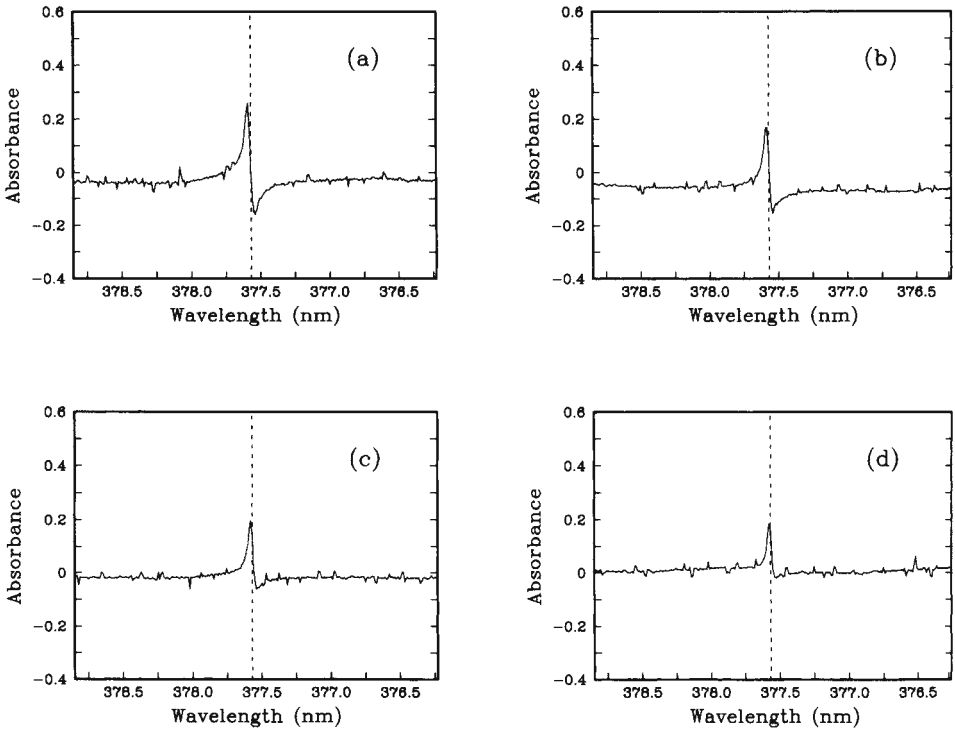


FIGURE 8.22. Continuation of Figure 8.21, with pump-probe separation in (a) increased by 100 fs over that in Figure 8.21 (d).

correspondence between the pump-probe delays of Figures 8.18 to 8.20 was not possible to maintain because of the insertion of the 0.5 ND filter in the pump arm.) The peak absorbances are clearly saturated. However, the integrated absorbances may not be so, since the spectra in Figures 8.21 and 8.22 are clearly narrower. This line broadening is a feature we have observed in all our Tl-halide spectra, with both 308- and 248-nm pumping and in both TlI and TlCl. Widths of all Tl absorption lines, even those measured at very long pump-probe separations, are dependent on the UV pump intensity applied. A reasonable explanation of this phenomenon is Stark broadening due to creation of ions or electrons in the vapor by the UV pump pulse.

Figures 8.23 to 8.26 show the appearance of the absorption spectra as a function of time in the vicinity of the 351.9-nm $6D_{5/2} \leftarrow 6P_{3/2}$ and 352.9-nm $6D_{3/2} \leftarrow 6P_{3/2}$ absorption lines, following application of a 308-nm, 160-fs excitation pulse to TlI vapor. These transitions thus monitor thallium atoms in the excited $6P_{3/2}$ state (7793 $cm^{-1}$). Note the absence of any evident spectral region with apparent gain during any part of the sequence. However, there are again strong transiently appearing asymmetries in the two line shapes.

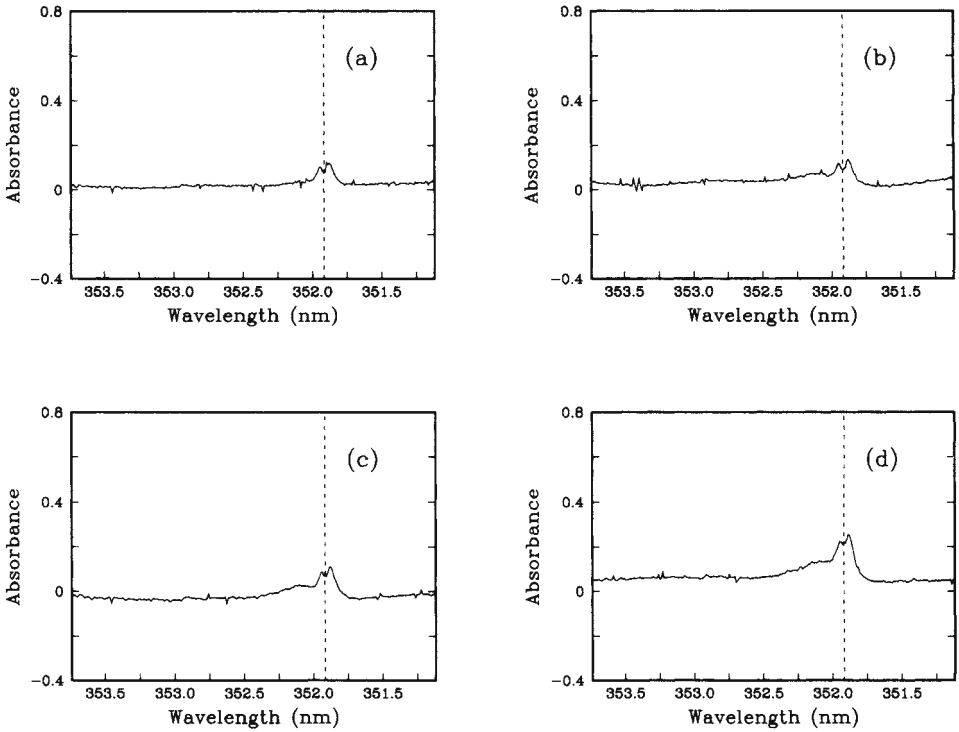


FIGURE 8.23. Time-resolved spectra, recorded in the vicinity of the 351.9-nm $6P_{5/2} \leftarrow 6P_{3/2}$ and 352.9-nm $6P_{3/2} \leftarrow 6P_{3/2}$ Tl absorption lines, following the application of 160-fs, 308-nm pulses to TlI vapor. Pump-probe separation increased by 100 fs between spectra.

Generally similar results were obtained in the case of 248-nm pump excitation of TlI, and with both 248- and 308-nm excitation of TlCl. In the case of TlI excited by a 248-nm pump, the time evolution of the line shapes of the two resonances near 352 and 353-nm is similar to that shown in Figures 8.23 to 8.26, with pronounced red wings during a period of again approximately a picosecond. The 377.6-nm line is much less intense and as a result comparatively difficult to minotor. These appears again to be a transiently appearing negative absorption on the high-frequency side of the line, but its magnitude is much less than the magnitude of the differential positive absorption appearing on the low-frequency side of the line. The latter absorbance monotonically grows to a final value of ~0.1 for the same UV pump powers for which the 353-nm absorbance (the weak line in Figures 8.23 to 8.26) almost attains the value 0.4. Clearly, a large inversion on the $6P_{3/2} - 6P_{1/2}$ transition is produced by 248-nm photolysis of TlI.

For the TlCl, with 248-nm excitation, the 352-nm absorption develops a pronounced *blue* wing, in contrast with the cases discussed above. This blue

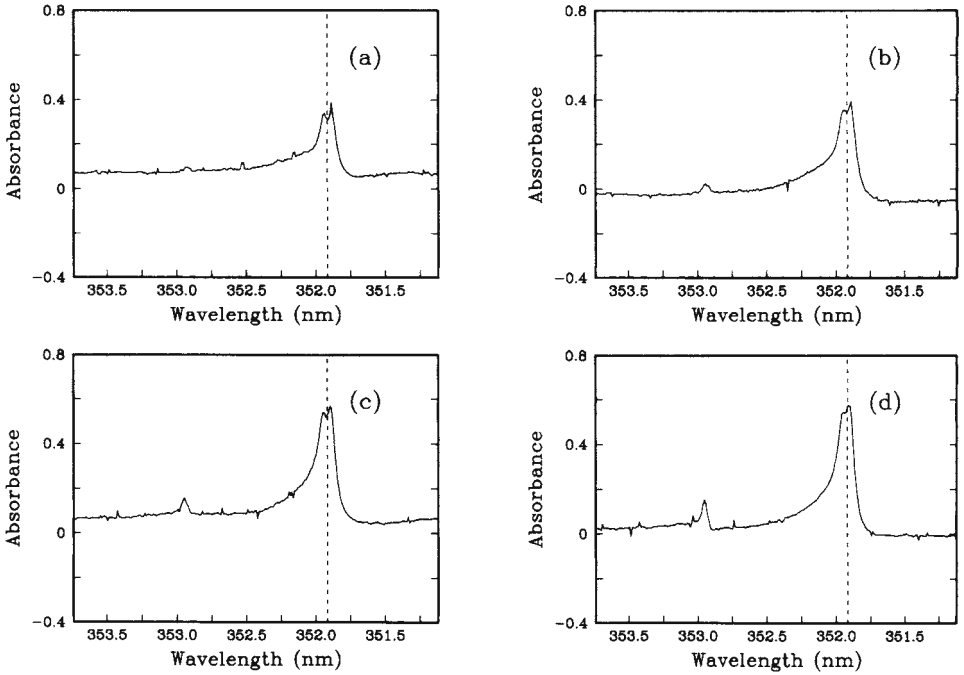


FIGURE 8.24. Continuation of Figure 8.23, with pump-probe separation in (a) increased by 100 fs over that in Figure 8.23 (d).

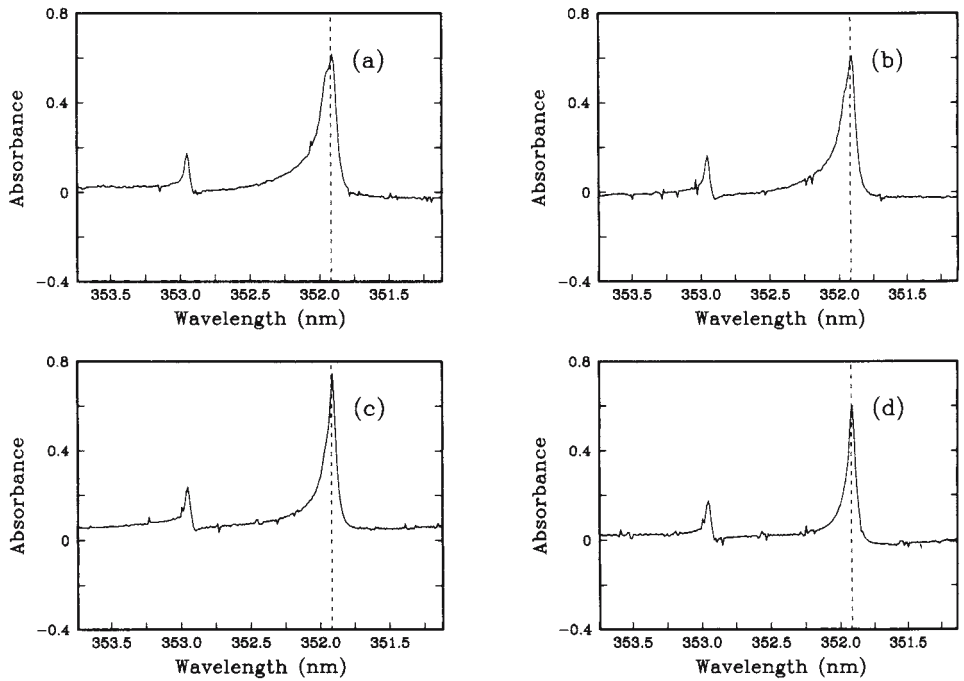


FIGURE 8.25. Continuation of Figure 8.24, with pump-probe separation in (a) increased by 100 fs over that in Figure 8.24 (d).

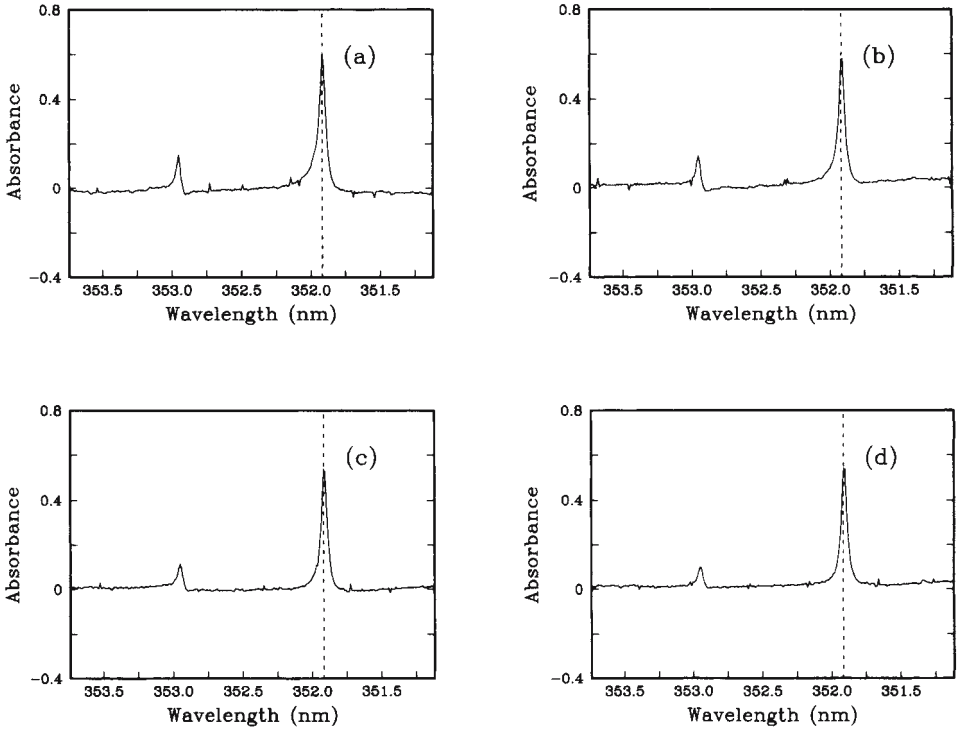


FIGURE 8.26. Continuation of Figure 8.25, with pump-probe separation in (a) increased by 100 fs over that in Figure 8.25 (d).

wing is evident for roughly 1.2 ps, then quickly disappears as the final line shape is assumed. During the 1.2-ps interval, the magnitude of the integrated absorption of the 352-nm line is enhanced by at least a factor 2, relative to that for the asymptotically attained line shape. The 377.6-nm line appears to grow monotonically to its asymptotic value, without noticeable line shape distortions other than a slight negative differential absorption on the high-frequency side of the line. For TlCl with 308-nm pumping, there is *no* observed 352- or 353-nm absorption feature, in agreement with the specific finding of van Veen et al. (1981) that only one dissociative channel (either Tl + Cl or Tl + Cl*) is active when TlCl is pumped at 308 nm. Since this should be the simplest situation to analyze, we present in Figures 8.27 to 8.29 some of the observed spectra for this specific case. A region of negative differential absorption is again clearly seen in some of the spectra (Figures 8.28a–d, Figure 8.29a).

We now present a qualitative explanation for the unusual spectral line shapes observed for the first picosecond following the photolysis pulse. Our model is based on the transient behavior of the polarization induced by the subpicosecond swept UV continuum pulse as the latter interacts with the

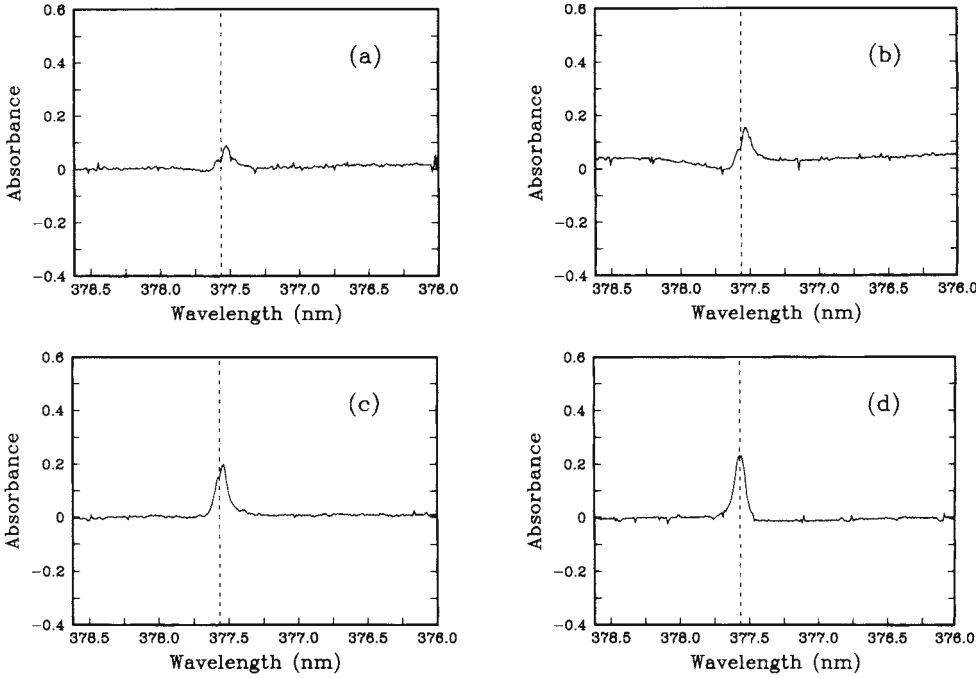


FIGURE 8.27. Time-resolved spectra, recorded near the 377.6-nm Tl line, following application of 160-fs, 308-nm pulses to TlCl vapor. 100-fs steps between successive spectra.

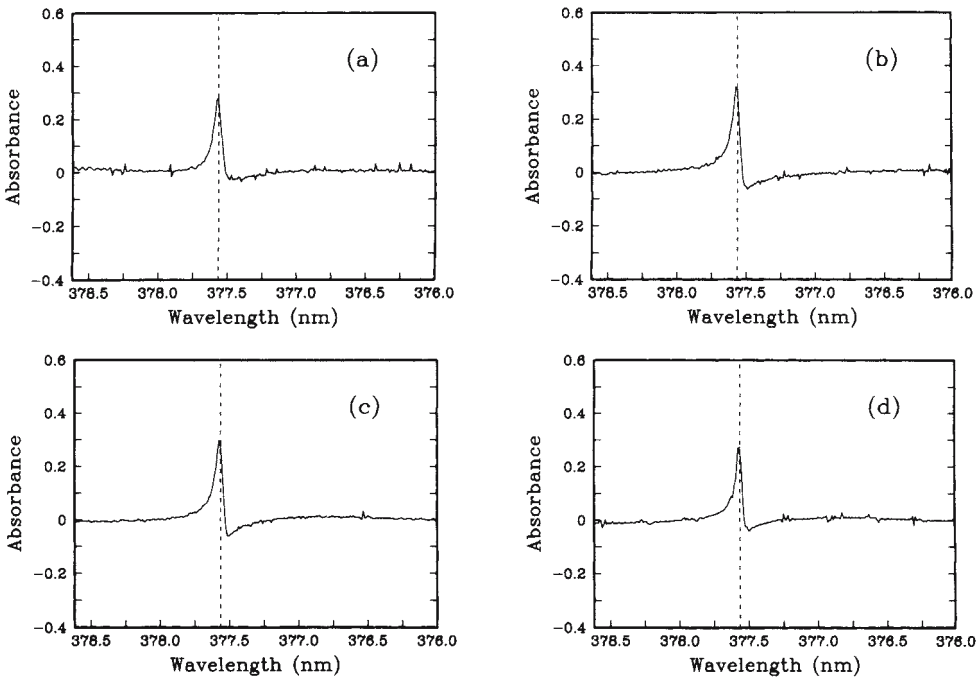


FIGURE 8.28. Continuation of Figure 8.27, with pump-probe separation in (a) increased by 100 fs over that in Figure 8.27 (d).

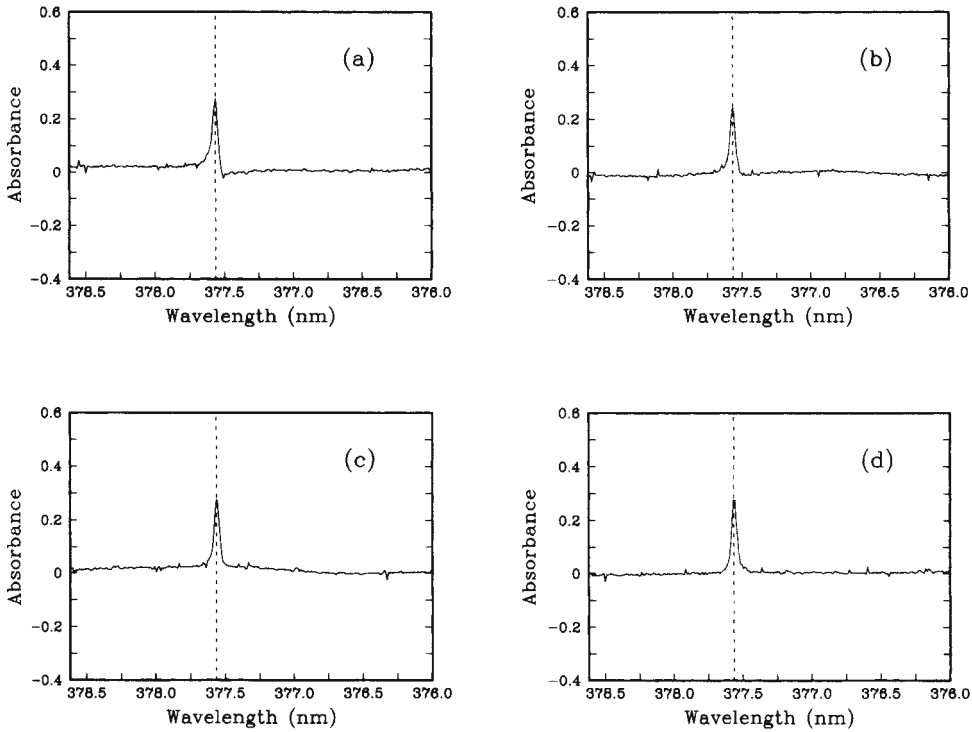


FIGURE 8.29. Continuation of Figure 8.28, with pump-probe separation in (a) increased by 100 fs over that in Figure 8.28 (d).

time-varying (growing) population of two-level atoms produced by the photolysis pulse. As we will show below, in order to get a reasonable correspondence of the line shapes calculated in this manner with the observed line shapes, especially with those possessing the most unusual feature (e.g., Figures 8.18 to 8.20), one has to allow the created atoms to undergo continuous frequency shifts in time for a period after the photolysis pulse.

The numerical calculations we have performed are basically straightforward. An optically thin sample is assumed. There are two contributions to the output field from the resonant vapor, i.e., $E_{\text{tot}}(t, z) = E_{\text{in}}(t, z) + E_{\text{rad}}(t, z)$, where $E_{\text{in}}(t, z)$ is the swept UV continuum and $E_{\text{rad}}(t, z)$ is the field radiated by the polarization it induces in the medium. Various contributions to the latter are numerically calculated, based on solutions of Schrödinger's equation for a two-level atom interacting with a swept continuum pulse

$$\dot{a}_1 = \left\{\frac{ier_{10}}{2\hbar}\mathscr{E}(t)\exp[i\omega_c z/c]\exp[-i(\omega_c - \omega_a)t]\right\}a_0 - \frac{\gamma}{2}a_1, \tag{3}$$

where $a_1$ and $a_0$ are the time-dependent amplitudes of the upper and lower atomic states, and $\omega_a$ is the atomic resonance frequency, equal to $\omega_1 - \omega_0$. The

rotating-wave approximation has been made in Eq. (3). We assume the swept continuum pulse to have the form

$$E_{\text{in}}(t,z) = \text{Re}\left\{\mathscr{E}(t)\exp\left[-i\omega_c\left(t-\frac{z}{c}\right)\right]\right\}, \tag{4}$$

with

$$\mathscr{E}(t) = \mathscr{E}_0(t)\exp(-ibt^2/2), \tag{5}$$

and

$$\mathscr{E}_0(t) = \mathscr{E}_0 t\left[\exp(-t^2/\Delta^2)\right]^{1/2}. \tag{6}$$

Equations (4) to (6) imply that the instantaneous frequency of the UV continuum sweeps across the frequency $\omega_c$ at time $t = 0$. The value of $b$ was taken to correspond with the value we measured for the supercontinuum sweep rate, 1340 $\text{cm}^{-1}$/ps. Equation (6) shows the form of the swept continuum pulse amplitude that we assumed in our numerical integrations. We generally specified a width $\Delta$ on the order of a picosecond. The wave function for the atom is

$$\psi = a_0 e^{i\omega_0 t}u_0 + a_1 e^{-i\omega_1 t}u_1, \tag{7}$$

and the polarization $P$ is generally expressed as

$$P = N\langle\psi|-er|\psi\rangle, \tag{8}$$

where $N$ is the atomic density.

We now outline the general procedure that was followed in obtaining numerical solutions. Let $a_0 = R(t - t_i)$ be the amplitude of the lower state for an atom created at time $t_i$. The solution to Eq. (3) can be formally expressed as

$$a_1(t) = \frac{ier_{10}}{2\hbar}e^{-\gamma t/2}\int_{-\infty}^{t}\mathscr{E}(t')\exp[i\omega_c z/c]\exp[-i(\omega_c-\omega_a)t']e^{\gamma t'/2}R(t'-t_i)dt'. \tag{9}$$

The contribution to the polarization (per atom) is

$$p(t,t_i) = -2e\,\text{Re}\{r_{01}a_0^* a_1 e^{i\omega t}\}. \tag{10}$$

Equation (9) was numerically integrated with the use of a specific rise function

$$R(t'-t_i) = \frac{1}{2}\left[1+\tanh\left(\frac{t'-t_i}{\text{WTANH}}\right)\right]. \tag{11}$$

The numerical integration in Eq. (9) was combined with an additional integration over another distribution function: $D(t) = dN(t)/dt$, where $N(t)$ represents the atomic population. We specified $D(t)$ to be proportional to the quantity $\text{sech}^2$ [$(t$ – TSECH2)/WSECH2]. Here the quantity TSECH2 marks the time at which the growth rate of $N(t)$ achieves its maximum, and WSECH2 characterizes the width of the growth period. Thus the total polarization $P$ is given by

$$P(z,t)=\int_{-\infty}^{\infty} p(t,t_i)D(t_i)dt_i. \tag{12}$$

We are modeling the dissociation of a diatomic molecule to create two atoms. At early times in the dissociation, when the two atoms are close to one another, the atomic transition frequencies are perturbed by the bending of the potential surfaces. We allowed for the existence of a continuous red (or blue) shift of the atomic transition frequency by making $\omega_a$ in the above equations a function of time relative to the creation of the atom:

$$\omega_a(t,t_i)=\omega_a^0-\mathrm{RMAX}\left[\exp\left(-\frac{t-t_i}{\mathrm{RTAU}}\right)\right], \tag{13}$$

where $\omega_a^0$ is the unperturbed atomic transition frequency.

In the slowly varying envelope approximation (SVEA), it is assumed that the total field $E_{\mathrm{tot}}(t, z)$ and polarization $P(t, z)$ can be written in the following forms:

$$E_{\mathrm{tot}}(t,z)=\mathrm{Re}\left\{\mathscr{E}(t,z)\exp\left[-i\omega_c\left(t-\frac{z}{c}\right)\right]\right\} \tag{14}$$

and

$$P(t,z)=\mathrm{Re}\left\{\mathscr{P}(t,z)\exp\left[-i\omega_c\left(t-\frac{z}{c}\right)\right]\right\}, \tag{15}$$

where $\mathscr{E}(t, z)$ and $\mathscr{P}(z, t)$ are complex functions of $z$ and $t$ that vary little in an optical period or wavelength. Following the usual procedure of neglecting second derivatives of the slowly varying quantities $\mathscr{E}(t, z)$ and $\mathscr{P}(t, z)$, one obtains on substitution of (14) and (15) into the wave equation the well-known complex field self-consistency equation

$$\frac{\partial\mathscr{E}(z,t)}{\partial z}+\frac{1}{c}\frac{\partial\mathscr{E}(z,t)}{\partial t}=\frac{i\omega_c}{2c\varepsilon_0}\mathscr{P}(z,t). \tag{16}$$

If one defines a retarded time $\tau = t - z/c$, one can rewrite Eq. (16) as

$$\frac{\partial\mathscr{E}(z,\tau)}{\partial z}=\frac{i\omega_c}{2c\varepsilon_0}\mathscr{P}(z,\tau). \tag{17}$$

From Eqs. (9), (10), (12), and (15), $\mathscr{P}(z, \tau)$ is seen to have no explicit dependence on $z$: $\mathscr{P}(z, \tau) = \mathscr{P}(\tau)$. Thus we can integrate Eq. (17) to obtain

$$\mathscr{E}(z,\tau)=\mathscr{E}(0,\tau)+\frac{i\omega_c}{2c\varepsilon_0}\mathscr{P}(\tau)z. \tag{18}$$

Hence, in general,

$$E_{\mathrm{tot}}(z,t)=E_{\mathrm{in}}(z,t)+\frac{i\omega_c z}{2c\varepsilon_0}P(z,t), \tag{19}$$

with the last term of Eq. (19) representing the field $E_{rad}(z, t)$ radiated by the polarization induced in the medium by $E_{in}(z, t)$. The spectral dependence of the total field $E_{tot}(z, t)$ is given by the sum of the Fourier transforms $\tilde{\mathscr{E}}_{in}(\omega)$ and $\tilde{\mathscr{E}}_{rad}(\omega)$, and the spectral dependence of the collected intensity at the end of the vapor cell is given by

$$L_{out}(\omega) = \left|\tilde{\mathscr{E}}_{in}(\omega)\right|^2 + \left|\tilde{\mathscr{E}}_{rad}(\omega)\right|^2 + 2\,\mathrm{Re}\left\{\tilde{\mathscr{E}}^*_{in}(\omega)\tilde{\mathscr{E}}_{rad}(\omega)\right\}. \tag{20}$$

With the use of fast Fourier transform numerical computation techniques, and with the quantity $\omega_c$ in Eq. (9) set equal to $\omega_a^0$, we obtained computer plots of the quantity $\log_{10}[I_{out}(\omega)/|\tilde{\mathscr{E}}_{in}(\omega)|^2]$ for various choices of the parameters introduced above.

An example of a sequence of calculated spectra is shown in Figures 8.30 to 8.32. The parameters used here were chosen in an attempt to approximate the shape of the observed spectra shown in Figures 8.18 to 8.20. It is seen that a qualitative agreement exists between theory and experiment, with the particular observed feature of a transient spectral region of negative

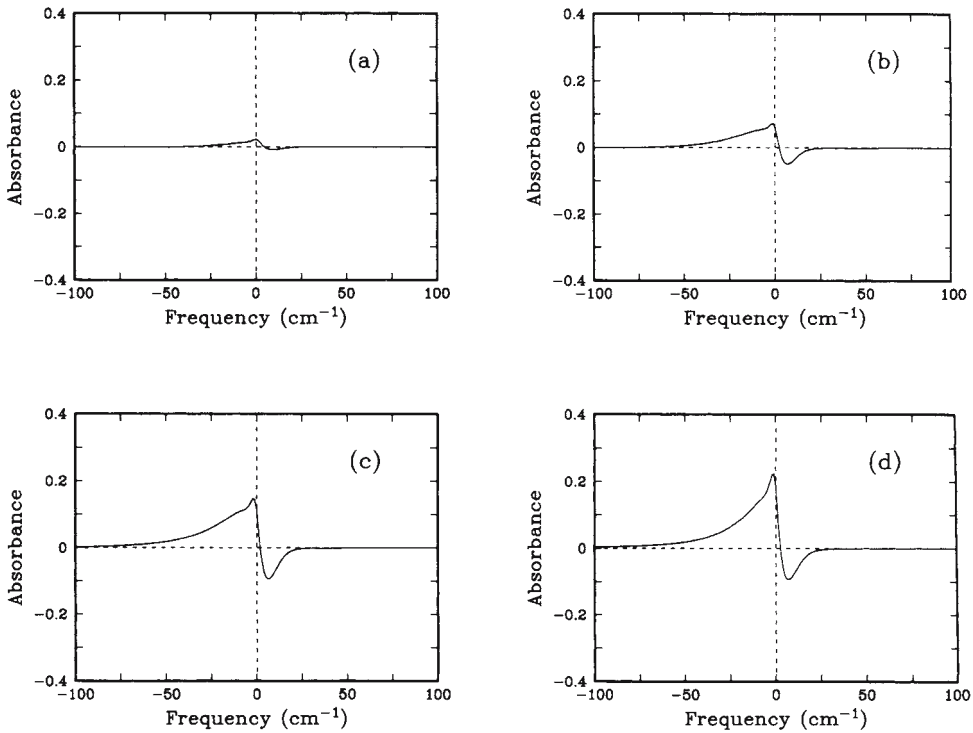


FIGURE 8.30. Calculated transient absorption spectra for a sequence of pump-probe separations increasing by 100 fs between successive spectra. The following parameter values were used: $\gamma = 0.0015\,\mathrm{fs}^{-1}$, WSECH2 = 150 fs, WTANH = 50 fs, RMAX = $40\,\mathrm{cm}^{-1}$, RTAU = 600 fs.

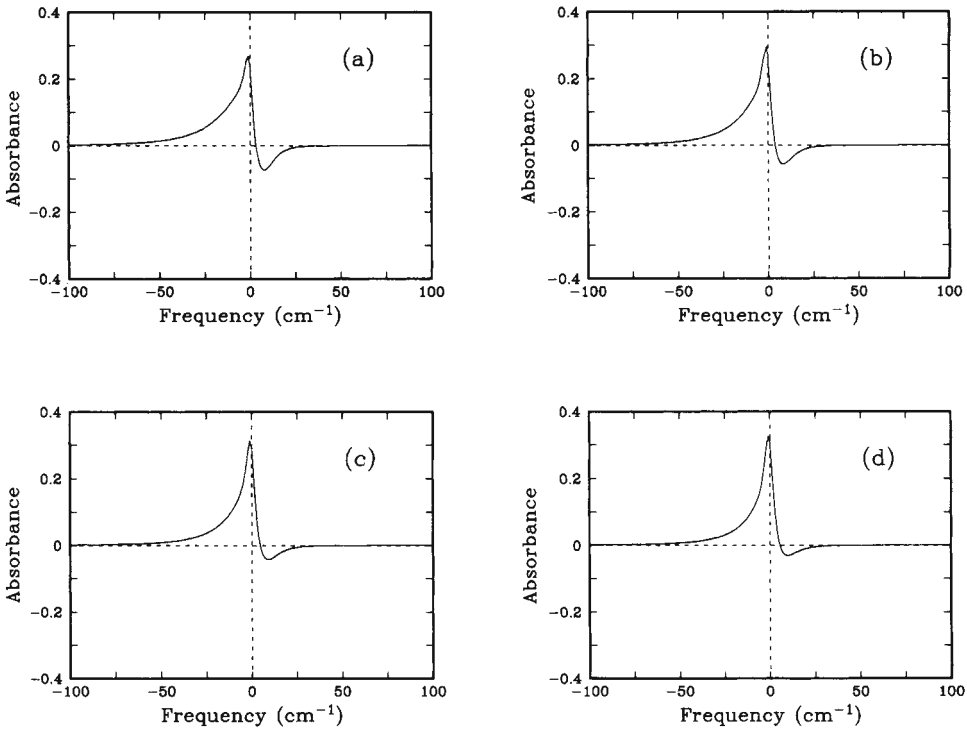


FIGURE 8.31. Continuation of Figure 8.30, with pump-probe separation in (a) increased by 100 fs over that in Figure 8.30 (d).

absorbance clearly captured in the calculated spectra. In Figures 8.30 to 8.32, the quantity $\gamma$ was chosen to correspond to a polarization dephasing time of $T_2$ = 1.3 ps. This value results in an asymptotic atomic linewidth (~6 cm$^{-1}$ FWHM) that closely approximates the measured value.

Several general conclusions can be drawn by examining the shapes of the various calculated spectra. Most important, *without the inclusion of a red shift RMAX very little asymmetry appears in the spectra, and there is no significant negative absorption.*

The rise time of the absorption seems to be simply related to the quantity WSECH2, for all values of RMAX.

For a given $T_2$, even for a relatively large RMAX (e.g., 60 cm$^{-1}$), decreasing RTAU below $T_2$/10 has the effect of reducing the height of the transiently appearing wings, so that the spectra are dominated at all times by a symmetric peak centered at $\omega_a^0$. To get more pronounced wings and a greater asymmetry for a given RMAX, one has to increase RTAU. However, if RTAU becomes comparable to $T_2$, additional oscillatory half-cycles of absorption and gain begin to appear in the absorption spectrum. For RTAU >> $T_2$, a simple growth of the absorption line at a frequency $\omega_a^0$ – RMAX is observed.

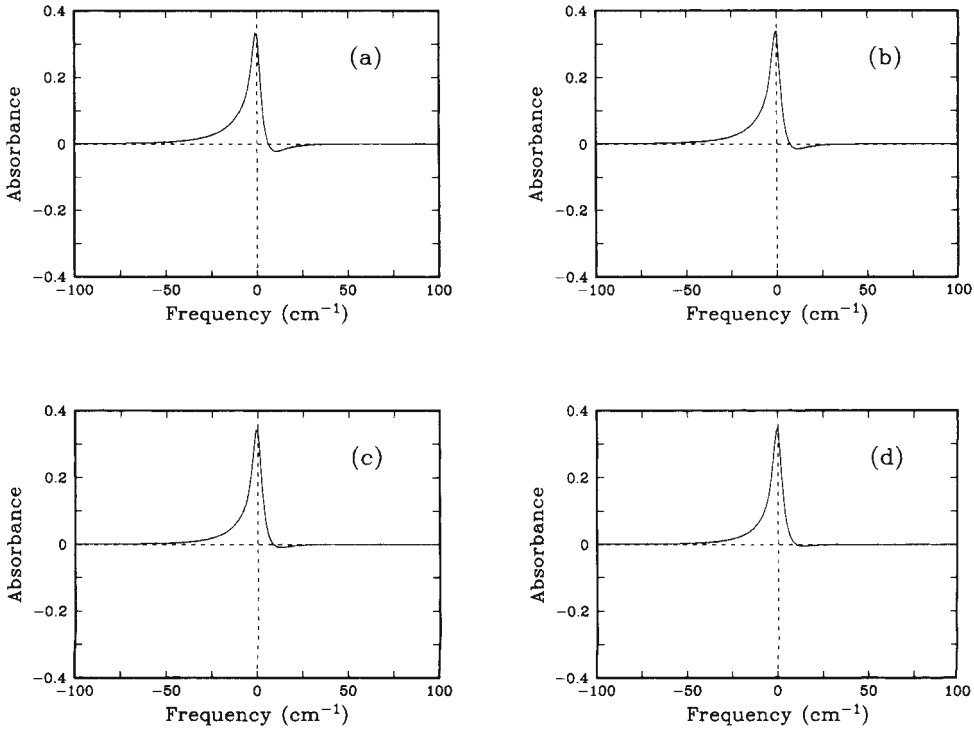


FIGURE 8.32. Continuation of Figure 8.31, with pump-probe separation in (a) increased by 100 fs over that in Figure 8.31 (d).

A blue atomic resonance frequency shift reverses the asymmetry, producing transient negative absorption in the region $\omega < \omega_a^0$. Changing the direction of the probe continuum sweep, however, does not appear to affect the appearance of the absorption spectrum, at least with the use of the $b$ value appropriate for our case.

We generally used a single value (50 fs) for WTANH. The spectra were seen to be generally insensitive to the choice of this parameter, provided it was taken to be short enough.

To summarize very briefly, it appears that the transient absorption spectra we have obtained of photolytically produced atoms contain qualitative information regarding the "transition state" that occurs between the time a molecule has absorbed a UV photon and the time its constituent atoms have fully separated. Specifically, information can be obtained about the rise time of the atomic population and the frequency shift that the atom undergoes during dissociation. However, information about the latter tends to be diluted by the polarization dephasing time $T_2$ of the separating atoms.

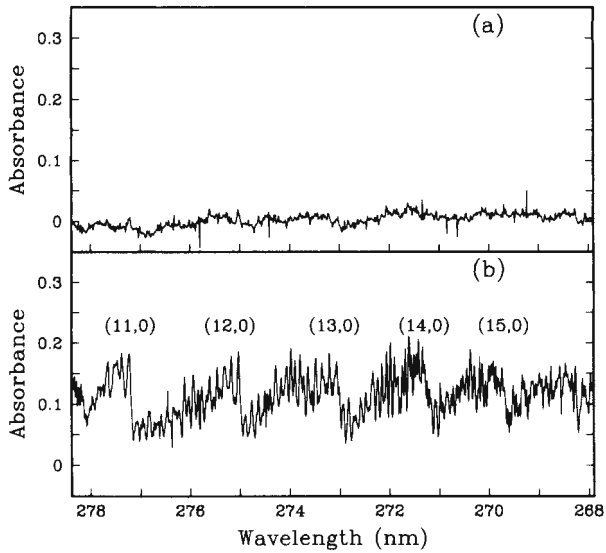


FIGURE 8.33. (a) Single-pass absorbance spectrum recorded through a 10-cm cell filled with 5-torr OClO with probe pulse occurring at the end of a 25-ns, 308-nm photolysis pulse. Pump energy of 3 mJ was sent through a 3-nm aperture. (b) Same as (a) but recorded 900 ns after the photolysis pulse.

We now describe a brief result obtained by applying the UV supercontinuum to the gas-phase molecule chlorine dioxide, OClO. For several decades it has been assumed that the sole result of applying light to the structured OClO ($\tilde{A}^2A_2 \leftarrow \tilde{X}^2B_1$) band system, which extends from ~460 to 280 nm, is the photolytic production of ClO + O (Bethune et al., 1983). From OClO absorption spectra taken at very high spectral resolution, in which the widths of individual vibronic lines could be measured, it was inferred that OClO predissociates at a rate strongly dependent on how far above the origin one photoexcites the molecule (Michielson et al., 1981).

As an initial test and possible calibration of the UV gas-phase supercontinuum, we attempted an experiment to photolyze OClO with a 160-fs, 308-nm UV pulse and then probe the appearance of the ClO radical with the UV supercontinuum pulse. The ClO radical strongly absorbs from ~310 to 250 nm, a region largely nonoverlapping with the OClO absorption band. With 308-nm excitation, subpicosecond predissociation rates for OClO were expected.

When the above spectral region was probed, no ClO was detected, with pump-probe delays of up to a nanosecond tried. The 160-fs, 308-nm excitation pulse was then replaced by a standard 25-ns, 308-nm pulse with the same 0.04 J/cm$^2$ fluence. (We sent 3 mJ through a 3-nm aperture into a 10-nm cell containing 5 torr OClO.) Again, no significant absorption was detected at relatively short delays (Figure 8.33a). However, if the probe was delayed by

several hundred nanoseconds, the fully developed ClO spectrum was easily observed (Figure 8.33b). We thus conclude that 308-nm photolysis of OClO produces $Cl + O_2^*$, with $O_2^*$ most likely being in high vibrational levels of the $^1\Sigma_g^+$ state. The observed slow appearance of ClO results from the combination of Cl atoms with unphotolyzed parent OClO molecules

$$Cl + OClO \rightarrow 2ClO. \tag{21}$$

For 5 torr of unphotolyzed OClO present in the cell and with use of the known 300 K rate constant for (21), $6 \times 10^{-11}$ cm$^3$ molec$^{-1}$ s$^{-1}$, one predicts the ClO would appear in ~100 ns, approximately what was observed. This OClO result should have a large impact on further understanding the interesting sequence of chemical reactions initiated by photolysis of OClO (Bethune et al., 1983).

## 7. Promising Directions for Subpicosecond Kinetic Spectroscopy

In the Introduction we presented an example of a unimolecular photochemical reaction, the rearrangement of methyl azide (Figure 8.1). The example was primarily meant to be illustrative. The IR subpicosecond continua required to probe the most relevant vibrational transitions have not yet been developed. However, through the use of the UV subpicosecond gas-phase continuum discussed in the preceding sections, an alternative method of attacking this problem, and many similar problems, now appears to be possible. Specifically, it should now be possible to observe momentarily in the UV the singlet spectrum of methylnitrene ($CH_3N$) and then to watch it disappear as the molecule isomerizes to singlet methylenimine ($CH_2NH$). Demuynck et al. (1980) have predicted little or no barrier for isomerization from singlet $CH_3N$ to singlet $CH_2NH$, but they also predict a sizable barrier (53 kcal/mol) for isomerization of triplet $CH_3N$. In recent years, searches for optical spectra of $CH_3N$ were made in several photolysis and pyrolysis studies, but no $CH_3N$ was ever observed in any of these studies, most likely because of rapid isomerization of singlet $CH_3N$ to $CH_2NH$. (By the spin conservation selection rule, photolysis of methyl azide has to produce singlet nitrene, since the ground state of $N_2$ is a singlet.) Recently, the $\tilde{A}^3E - \tilde{X}^3A_2$ ultraviolet emission spectrum of triplet $CH_3N$ was observed (Carrick and Engelking, 1984; Franken et al., 1970) by reacting methyl azide with metastable ($A^3\Sigma_u^+$) $N_2$ in a flowing afterglow. This result qualitatively confirms the prediction of a high triplet isomerization barrier height made by Demuynck et al. (1980). The triplet $CH_3N$ (0, 0) band occurs at 314.3 nm, not too distant from the 336-nm origin of the $A^3\Pi - X^3\Sigma^-$ band system of the isoelectronic radical NH. Since NH has also an allowed singlet system ($c^1\Pi - a^1\Delta$), with origin at 324 nm, one should expect an analogous singlet $CH_3N$ system to exist, with an origin somewhere in the region of 300 nm.

Methyl azide can be photolyzed at either 248 or 308 nm. With the effective good time resolution of the swept UV supercontinuum demonstrated in Section 6, one should be able to observe the transient singlet band system of $CH_3N$, even if the latter isomerizes in a time of half a picosecond.

We conclude by mentioning one improvement in the subpicosecond kinetic spectroscopy technique we employ that is scheduled to be tried soon. This is the incorporation of a reference arm for improved sensitivity. With the use of two matched spectrograph-OMA systems, it should be possible to cancel in every shot the effect of random spectral variations in the supercontinuum intensity. At present, we require two independent accumulations of several tens of shots, one with the pump blocked and one with the pump unblocked, from which the spectral variation of absorbance is electronically calculated. Incorporation of such a reference arm is, of course, simpler with the UV supercontinuum than in the case of the IR continua, due to the need to upconvert the latter. It will be interesting to see how much subpicosecond kinetic spectroscopy can benefit from such an improvement once it is implemented.

*Acknowledgments*. We are indebted to J.E. Rothenberg for suggesting to us an initial conceptual framework for the calculations. We also thank M.M.T. Loy and D. Grischkowsky for helpful discussions. L. Manganaro assisted us with some of the instrumentation. This research was sponsored in part by the U.S. Army Research Office.

## References

Akhmanov, S.A., K.N. Drabovich, A.P. Sukhorukov, and A.K. Shchednova (1972) Combined effects of molecular relaxation and medium dispersion in stimulated Raman scattering of ultrashort light pulses. Sov. Phys. JETP **35**, 279–286.

Alfano, R.R. and S.L. Shapiro (1970a) Emission in the region 4000 to 7000 Å via four-photon coupling in glass. Phys. Rev. Lett. **24**, 584–587.

Alfano, R.R. and S.L. Shapiro (1970b) Observation of self-phase modulation and small scale filaments in crystals and glasses. Phys. Rev. Lett. **24**, 592–594.

Avouris, Ph., D.S. Bethune, J.R. Lankard, J.A. Ors, and P.P. Sorokin (1981) Time-resolved infrared spectral photography: study of laser-initiated explosions in $HN_3$. J. Chem. Phys. **74**, 2304–2312.

Bethune, D.S., J.R. Lankard, P.P. Sorokin, R.M. Plecenik, and Ph. Avouris (1981) Time-resovled infrared study of bimolecular reactions between *tert*-butyl radicals. J. Chem. Phys. **75**, 2231–2236.

Bethune, D.S., A.J. Schell-Sorokin, J.R. Lankard, M.M.T. Loy, and P.P. Sorokin (1983) Time-resolved study of photo-induced reactions of chlorine dioxide. In B.A. Garetz and J.R. Lombardi (eds.), *Advances in Laser Spectroscopy*, vol. 2, pp. 1–43. Wiley, New York.

Burksbaum, P.A., J. Bokor, R.H. Storz, and J.C. White (1982) Amplification of ultra-short pulses in krypton fluoride at 248 nm. Opt. Lett. **7**, 399–401.

Burnham, R. and N. Djeu (1978) Efficient Raman conversion of XeCl-laser radiation in metal vapors. Opt. Lett. **3**, 215–217.

Carman, R.L., F. Shimizu, C.S. Wang, and N. Bloembergen (1970) Theory of Stokes pulse shapes in transient stimulated Raman scattering. Phys. Rev. A **2**, 60–72.

Carrick, P.G. and P.C. Engelking (1984) The electronic emission spectrum of methylnitrene. J. Chem. Phys. **81**, 1661–1665.

Corkum, P.B. and R.S. Taylor (1982) Picosecond amplification and kinetic studies of XeCl. IEEE J. Quantum Electron. **QE-18**, 1962–1975.

Corkum, P.B., C. Rolland, and T. Srinivasan-Rao (1986a) Supercontinuum generation in gases: a high order nonlinear optics phenomenon. In G.R. Fleming and A.E. Siegman (eds.), *Ultrafast Phenomena V*, pp. 149–152. Springer-Verlag, New York.

Corkum, P.B., C. Rolland, and T. Srinivasan-Rao (1986b) Supercontinuum generation in gases. Phys. Rev. Lett. **57**, 2268–2271.

Cotter, D. and W. Zapka (1978) Efficient Raman conversion of XeCl excimer laser radiation in Ba vapour. Opt. Commun. **26**, 251–255.

Dantus, M., M.J. Rosker, and A.H. Zewail (1987) Real-time femtosecond probing of "transition states" in chemical reactions. J. Chem. Phys. **87**, 2395–2397.

Davidovits, P. and J.A. Bellisio (1969) Ultraviolet absorption cross sections for the thallium halide and silver halide vapors. J. Chem. Phys. **50**, 3560–3567.

Demuynck, J., D.J. Fox, Y. Yamaguchi, and H.F. Schaefer III (1980) Triplet methyl nitrene: an indefinitely stable species in the absence of collisions. J. Am. Chem. Soc. **102**, 6204–6207.

Egger, H., T.S. Luk, K. Boyer, D.F. Muller, H. Pummer, T. Srinivasan, and C.K. Rhodes (1982) Picosecond, tunable ArF* excimer laser source. Appl. Phys. Lett. **41**, 1032–1034.

Fluegel, B., N. Peyghambarian, G. Olbright, M. Lindberg, S.W. Koch, M. Joffre, D. Hulin, A. Migus, and A. Antonetti (1987) Femtosecond studies of coherent transients in semiconductors. Phys. Rev. Lett. **59**, 2588–2591.

Fork, R.L., B.I. Greene, and C.V. Shank (1981) Generation of optical pulses shorter than 0.1 psec by colliding pulse mode locking. Appl. Phys. Lett. **38**, 671–672.

Fork, R.L., C.V. Shank, R.T. Yen, and C. Hirlimann (1982) Femtosecond continuum generation. In K.B. Eisenthal, R.M. Hochstrasser, W. Kaiser, and A. Laubereau (eds.), *Picosecond Phenomena III*, pp. 10–13. Springer-Verlag, New York.

Fork, R.L., C.V. Shank, C. Hirlimann, R. Yen, and W.J. Tomlinson (1983) Femtosecond white-light continuum pulses. Opt. Lett. **8**, 1–3.

Franken, Th., D. Perner, and M.W. Bosnali (1970) UV-absorptionsspektren von methyl- und äthylnitren mittels pulsradiolyse in der gasphase. Z. Naturforsch. A **25**, 151–152.

Glownia, J.H., G. Arjavalingam, and P.P. Sorokin (1985) The potential of DABCO for two-photon amplification. J. Chem. Phys. **82**, 4086–4101.

Glownia, J.H., J. Misewich, and P.P. Sorokin (1986a) Ultrafast ultraviolet pump-probe apparatus. J. Opt. Soc. Am. B **3**, 1573–1579.

Glownia, J.H., G. Arjavalingam, P.P. Sorokin, and J.E. Rothenberg (1986b) Amplification of 350-fsec pulses in XeCl excimer gain modules. Opt. Lett. **11**, 79–81.

Glownia, J.H., J. Misewich, and P.P. Sorokin (1986c) New excitation and probe continuum sources for subpicosecond absorption spectroscopy. In G.R. Fleming and A.E. Siegman (eds.), *Ultrafast Phenomena V*, pp. 153–156. Springer-Verlag, New York.

Glownia, J.H., J. Misewich, and P.P. Sorokin (1986d) Amplification in a XeCl excimer gain module of 200-fsec UV pulses derived from a colliding pulse mode locked (CPM) laser system. Proc. Soc. Photo-Opt. Instrum. Eng. **710**, 92–98.

Glownia J.H., J. Misewich, and P.P. Sorokin (1987a) Subpicosecond time-resolved infrared spectral photography. Opt. Lett. **12**, 19–21.

Glownia, J.H., J. Misewich, and P.P. Sorokin (1987b) 160-fsec XeCl excimer amplification system. J. Opt. Soc. Am. B **4**, 1061–1065.

Glownia, J.H., J. Misewich, and P.P. Sorokin (1987c) Subpicosecond IR transient absorption spectroscopy: measurement of internal conversion rates in DABCO vapor. Chem. Phys. Lett. **139**, 491–495.

Halpern, A.M., J.L. Roebber, and K. Weiss (1968) Electronic structure of cage amines: absorption spectra of triethylenediamine and quinuclidine. J. Chem. Phys. **49**, 1348–1357.

Hamada, Y., A.Y. Hirikawa, and M. Tsuboi (1973) The structure of the triethylenediamine molecule in an excited electronic state. J. Mol. Spectrosc. **47**, 440–456.

Hartmann, H.-J. and A. Laubereau (1984) Transient infrared spectroscopy on the picosecond time-scale by coherent pulse propagation. J. Chem. Phys. **80**, 4663–4670.

Li, Q.X., T. Jimbo, P.P. Ho, and R.R. Alfano (1986) Temporal distribution of picosecond super-continuum generated in a liquid measured by a streak camera. Appl. Opt. **25**, 1869–1871.

Mack, M.E., R.L. Carman, J. Reintjes, and N. Bloembergen (1970) Transient stimulated rotational and vibrational Raman scattering in gases. Appl. Phys. Lett. **16**, 209–211.

Margenau, H. (1939) Van der Waals forces. Rev. Mod. Phys. **11**, 1–35.

Michielson, S., A.J. Merer, S.A. Rice, F.A. Novak, K.F. Freed, and Y. Hamada (1981) A study of the rotational state dependence of predissociation of a polyatomic molecule: the case of $ClO_2$. J. Chem. Phys. **74**, 3089–3101.

Misewich, J., J.H. Glownia, and P.P. Sorokin (1988a) Measurement with subpicosecond resolution of the frequency sweep of an ultrashort supercontinuum. In *Conference on Lasers and Electro-Optics Technical Digest Series 1988*, vol. 7, pp. 420–421. Optical Society of America. Washington, D.C.

Misewich, J., J.H. Glownia, J.E. Rothenberg, and P.P. Sorokin (1988b) Subpicosecond UV kinetic spectroscopy; Photolysis of thallium halide vapors. Chem. Phys. Lett. **150**, 374–379.

Nakatsuka, H., D. Grischkowsky, and A.C. Balant (1981) Nonlinear picosecond-pulse propagation through optical fibers with positive group velocity dispersion. Phys. Rev. Lett. **47**, 910–913.

Nikolaus, B. and D. Grischkowsky (1983) 90-fsec tunable optical pulses obtained by two-stage pulse compression. Appl. Phys. Lett. **43**, 228–230.

Parker, D.H. and Ph. Avouris (1978) Multiphoton ionization spectra of two caged amines. Chem. Phys. Lett. **53**, 515–520.

Parker, D.H. and Ph. Avouris (1979) Multiphoton ionization and two-photon fluorescence excitation spectroscopy of triethylenediamine. J. Chem. Phys. **71**, 1241–1246.

Schwarzenbach, A.P., T.S. Luk, I.A. McIntyre, V. Johann, A. McPherson, K. Boyer, and C.K. Rhodes (1986) Subpicosecond KrF* excimer-laser source. Opt. Lett. **11**, 499–501.

Smith, M.A., J.W. Hager, and S.C. Wallace (1984) Two-color laser photoionization spectroscopy in a collisionless free-jet expansion: spectroscopy and excited-state dynamics of diazabicyclooctane. J. Phys. Chem. **88**, 2250–2255.

Szatmári, S. and F.P. Schäfer (1983) Simple generation of high-power, picosecond, tunable excimer laser pulses. Opt. Commun. **48**, 279–283.

Szatmári, S. and F.P. Schäfer (1984a) Generation of intense, tunable ultrashort pulses in the ultraviolet using a single excimer pump laser. In D.H. Auston and K.B. Eisenthal (eds.), *Ultrafast Phenomena IV*, pp. 56–59. Springer-Verlag, New York.

Szatmári, S. and F.P. Schäfer (1984b) Excimer-laser-pumped psec-dye laser. Appl. Phys. B **33**, 95–98.

Szatmári, S., B. Racz, and F.P. Schäfer (1987a) Bandwidth limited amplification of 220 fs pulses in XeCl. Opt. Commun. **62**, 271–276.

Szatmári, S., F.P. Schäfer, E. Müller-Horsche, and W. Mükenheim (1987b) Hybrid dye-excimer laser system for the generation of 80 fs, 900 GW pulses at 248 nm. Opt. Commun. **63**, 305–309.

Valdmanis, J.A., R.L. Fork, and J.P. Gordon (1985) Generation of optical pulses as short as 27 femtoseconds directly from a laser balancing self-phase modulation, group-velocity dispersion, saturable absorption, and saturable gain. Opt. Lett. **10**, 131–133.

van Veen, N.J.A., M.S. deVries, T. Beller, and A.E. deVries (1981) Photofragmentation of thallium halides. Chem. Phys. **55**, 371–384.

Xu, Z., B. Koplitz, S. Buelow, D. Bauch, and C. Wittig (1986) High-resolution kinetic energy distributions via Doppler shift measurements. Chem. Phys. Lett. **127**, 534–540.

# 9
# Applications of Supercontinuum: Present and Future

R. Dorsinville, P.P. Ho, J.T. Manassah, and R.R. Alfano

## 1. Introduction

Over the past two decades, the supercontinuum light source has been extensively used in laser spectroscopy research such as inverse Raman scattering (Alfano and Shapiro, 1971), time-resolved induced absorption in liquids and solids (Alfano and Shapiro, 1971; Greene et al., 1978), primary vision processes (Doukas et al., 1980), energy transfer mechanisms in photosynthesis (Searle et al., 1978; hot carrier and exciton relaxation processes in semiconductors (von der Linde and Lambrich, 1979; Shank et al., 1982), and time-resolved multiplex coherent anti-Stokes Raman scattering (Goldberg, 1982), to name a few.

In this chapter, we review some of the applications in time-resolved absorption and excitation spectroscopy and pulse compression and propose several new possible applications using supercontinuum light for ranging, imaging, remote sensing, and computation. It is impossible to review all the research involved using the supercontinuum. Only a small sample was selected, reflecting the interests of the authors. We apologize in advance to those whose work is not mentioned.

## 2. Time-Resolved Absorption Spectroscopy

The ultrafast supercontinuum pump-and-probe absorption technique has been used to study ultrafast relaxation processes in solid-state physics, chemistry, and biological systems. An intense pulse photoexcites the sample into an excited state. The dynamics of the excited state is followed using the white light supercontinuum at subsequent delay times. Optically thin samples are usually pumped by a pulse $I(t)$ at wavelength $\lambda$, and the induced transient optical density is observed at various wavelengths at time $\tau$ (delay time between pump and probe pulses). The OD can be written (Greene et al., 1978; Gayen et al., 1987) as

$$\mathrm{OD}(\tau,\lambda) = -\ln\left\{\int I(t-\tau)\exp[-\sigma L N_1(t)]dt \Big/ \int I(t)dt\right\}, \tag{1}$$

where $\sigma$ is the excited state absorption cross section at $\lambda$, $L$ is the sample thickness, and $N_1(t)$ is the instantaneous population density in the probing lower-lying energy level. Polarization selection in time can be investigated using polarized pump and probe pulses.

A typical experimental setup for the pump and probe is shown in Figure 9.1. The arrival time of the pump pulse to the sample can be adjusted with an optical delay line. Transient absorption change in the sample at various wavelengths are measured and processed with a spectrograph and an optical

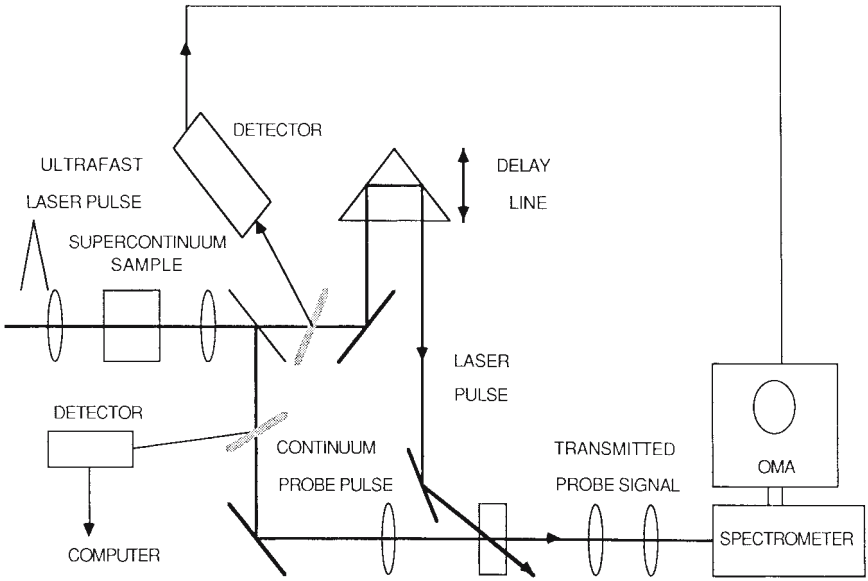


FIGURE 9.1. Schematic of an experimental setup for measuring ultrafast relaxation kinetics using the supercontinuum.

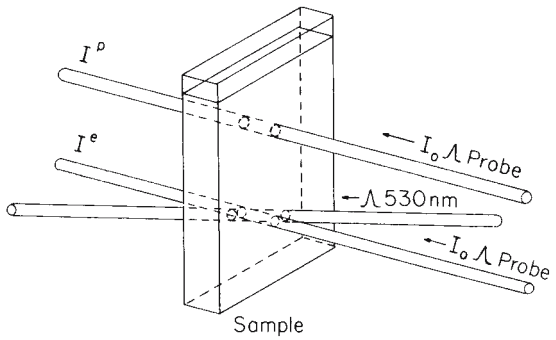


FIGURE 9.2. Geometry of the optical excitation and probing beams at the sample site.

multichannel analyzer. The supercontinuum probing pulse is usually separated into two beams at the sample site as shown in Figure 9.2. Accuracy of the measured induced OD change in the order of OD 0.005 can be achieved. By coupling a dispersion-corrected spectrometer to a streak camera (Masuhara, 1983), it is possible to measure simultaneously the temporal and spectral information of the sample. To give the reader a feeling for what is going on in the field, several experiments are reviewed using the supercontinuum induced absorption technique. The next section gives typical examples in the fields of solid-state physics, chemistry, and biology.

## 2.1 Solid-State Physics

### 2.1.1 Supercontinuum Spectroscopy of Semiconductor Microstructures

Carrier and elementary excitation relaxation, intervalley scattering, and phonon-carrier dynamics in very thin (50 to 200 Å) GaAs-AlGaAs semiconductor microstructures and bulk GaAs have been characterized using supercontinuum picosecond and femtosecond probe pulses. The optical density change of a 205-Å-thick GaAs layer sample is plotted in Figure 9.3 at three different probing times (Fork et al., 1980). Information on the induced bleaching of exciton absorption peaks at each of the 2-dimensional ($n$ = 1, 2, 3) band edges can be clearly identified. Ionization dynamics of excitons were also followed using femtosecond interactions. These techniques have effectively probed the carrier and excitation dynamics in quantum wells. A similar experiment has been applied in the understanding of subpicosecond optical nonlinearities in GaAs multiple-quantum-well structures (Hulin et al.,

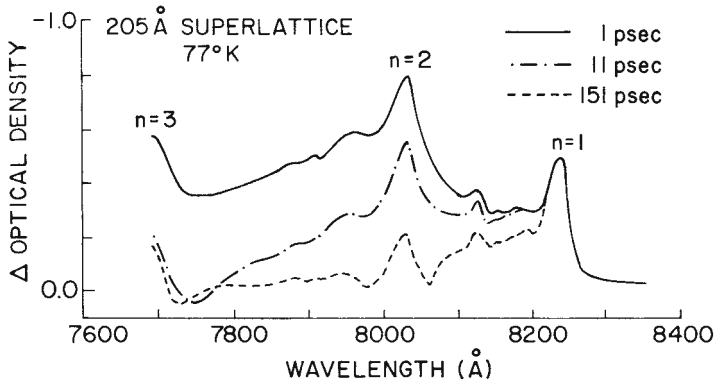


Figure 9.3. Optical density change in a superlattice optically pumped by a 625-nm femtosecond beam and probed by the supercontinuum at different delay times (1, 11, and 151 ps).

1986). Nonlinearities based on the optical Stark effect can be a potential application for the ultrafast optical logic gates and switches.

#### 2.1.2 Nonequilibrium Electron Processes in Metals

Nonequilibrium electron heating in gold films has been measured using an amplified 65-fs colliding-pulse mode-locked (CPM) laser pulse pump at 625 nm and supercontinuum probe technique (Schoenlein et al., 1986). Time-resolved reflectivity allows a characterization of both the excited electron thermal distribution and its cooling dynamics. Differential measurements of transient reflectivity can be obtained by monitoring the sample-reflected signal along with a reference signal from the continuum. Transient reflectivity was found to depend on the conduction band energy being probed and on the incident fluence. This technique allows the separation of electronic from phonon processes.

#### 2.1.3 Transient Lattice Defects in Alkali Halide Crystals

Dynamics of self-trapped exciton, F, and F-like species in semiconducting or insulating crystals by two 266-nm photons (Willians et al., 1984) were studied using supercontinuum absorption spectroscopy with 3-ps pulses. Kinetics from the NaCl measurements pertain to thermally activated defect formation from relaxed self-trapped excitons. Photochemical defect production follows promotion to a potential sheet on which the barriers to halogen diffusion are small.

### 2.2 Chemistry

#### 2.2.1 Iodine Photodissociation in Solution

Supercontinuum absorption spectroscopy (Berg et al., 1984) has identified the excited states of $I_2$ molecules using a 2-ps, 590-nm pump laser pulse. There is a fast predissociation in 5 to 10 ps with rapid partitioning between separated species excited state molecules and vibrationally excited ground state atoms. This is followed by a slower relaxation process that involves the transition from the excited electronic state to ground state vibrational relaxation. This study can help to understand the early partitioning among various intermediate states following photodissociation.

#### 2.2.2 Photoinduced Electron Transfer in Porphyrin-Quinone

A way to avoid the ultrafast deactivation of the porphyrin-quinone photoinduced electron transfer is to construct intramolecular exciplex-type compounds where porphyrin and quinone are combined by methylene chains. These chain will weaken the chromophore interactions and prevent the strong solvation by intervening chains. The transient absorption spectra (Hirata

et al., 1983) indicate a considerable contribution from the $S_1$ state at a short decay time. The long decay component of a few hundred picoseconds has demonstrated the characteristic of the electron transfer state. This information can be used to design a biomimetic photosynthetic system.

## 2.3 Biology

### 2.3.1 Photosynthesis

The present understanding of oxygen-evolving photosynthesis is that the process is driven by two light reactions (Wong, 1982). Associated with each photoreaction is a reaction center that utilizes the energy of a captured photon to promote an electron to a state of higher reduction potential.

Using supercontinuum induced-absorption spectroscopy, green plant photosystem I reaction centers, isolated from pea chloroplasts, have been measured (Gore et al., 1986). Transient absorption spectra of photosystem I reaction centers spanning supercontinuum wavelengths from 625 to 765 nm are displayed in Figure 9.4 at different delay times. In the samples containing chemically reduced P700, there is a significant delay between the grow-in of the excited antenna chlorophyll signal and the signal due to the excitation of P700. The 15- to 20-ps energy transfer time is consistent with the antenna chlorophyll lifetime.

Matveetz et al. (1985) have applied 300-fs pulses to study the transient differential absorption spectra of reaction centers of *Rhodopseudomonas viridis*. Kobayashi and Iwai (1984) have investigated the primary process in the photoconversion of protochlorophyllide to chlorophyllide a. This reveals the reduction of the precursor protochlorophyllide into chlorophyllide in the development of chloroplasts in higher plants.

### 2.3.2 Vision

Energy of absorbed photons in visual pigments is converted to a change in electrical potential across the photoreceptor cells, which is transmitted to the nervous system through standard synaptic processes. The first intermediate process in the photoreaction of rhodopsin is formed in subpicoseconds. Lippitsch et al. (1982a) have applied the supercontinuum from 340 to 460 nm in linear dichroism spectroscopy to study the primary processes in retinal. Conformational changes of retinal following excitation have been studied. Doukas et al. (1980) and Monger et al. (1979) studied laser-induced absorbance changes as a function of time in squid and bovine rhodopsin using a supercontinuum generated by the 7-ps, 530-nm second harmonic pulse from an Nd:glass laser. Their data show that bathorhodopsin formation is complete within 3 ps, supporting the cis-trans isomerization model of the primary event in vision. Kobayashi et al. (1984) used the 500 to 700-nm supercontinuum to probe the primary process in the photocycles of the

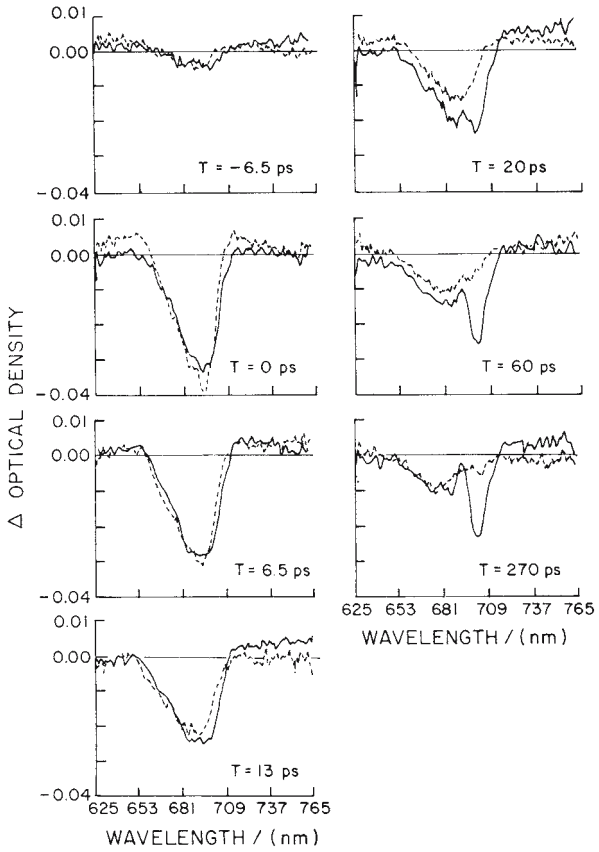


FIGURE 9.4. Transient absorption spectra of PS I reaction centers (——) P700 chemically reduced; (. . . . . .) P700 chemically oxidized.

purple membrane bacteriorhodopsin. They claimed a pH-dependent fast relaxation process for the change in structures of chromophore and near residues. These and similar studies should be able to establish the sequence and dynamics of the events initiating the visual process and the structural information.

### 2.3.3 HEMOPROTEINS

Hemoproteins contain one or more heme groups embedded as active centers in the folded polypeptide chain. They occur in all aerobic and many anaerobic cells and perform oxygen storage and transport, electron transfer, and catallysis (Eisenstein and Frauenfelder, 1982). Martin et al. (1984) have used a 100-fs supercontinuum from 390 to 500 nm to probe a photodissociation process of hemoproteins and protoheme with a lifetime of 350 fs. Informa-

tion or the primary events of local motions inside the heme pocket following ligand detachment can be obtained. Cornelius and Hochstrasser (1982) have examined the supercontinuum difference spectra from 400 to 480 nm of myoglobins with ligands of $O_2$ and CO pumped by 350 and 530 nm. No subnanosecond geminate recombination occurs in either case. Both species are efficiently photolyzed with the 350-nm pump. Details of spectral shape dynamics are useful for understanding some of the energy transfer mechanisms.

In addition, Lippitsch et al. (1982b) have found that biliverdin plays an important role in photobiological processes. Supercontinuum absorption spectroscopy from 400 to 650 nm suggested that the predominant relaxation mechanism is single-bond rotation after internal conversion.

## 3. Time-Resolved Excitation Spectroscopy

Several ultrafast excitation spectroscopy techniques using the continuum have been developed and successfully used. These are near-IR excitation and probing techniques, coherent anti-Stokes Raman scattering, and Raman induced-phase conjugation. In this section we present a brief description of these techniques and a short review of the use of the supercontinuum for optical pulse compression. A detailed discussion of pulse compression is given in Chapter 10 by Johnson and Shank.

### 3.1 Generation of Subpicosecond IR Laser Pulses

Picosecond IR pulses can be generated by difference frequency mixing a strong monochromatic picosecond pulse with a white light continuum, as recently shown by Jedju and Rothberg (1987). The apparatus is depicted in Figure 9.5. A CW mode-locked $Nd^{3+}$:YAG laser is used to pump synchronously a Rhodamine-6G-based dye laser to obtain 5-ps nearly transform-limited pulses of 1 nJ each at a repetition rate of 82 MHz. After amplification, 1-mJ pulses at 580 nm are obtained. Half of this energy is focused by a 15-cm lens into a 3-cm cell containing a liquid to generate a white continuum extending from 300 to 900 nm. The generated continuum and the other half of the laser pulse are loosely focused into an $LiIO_3$ crystal to generate the IR pulses. The wavelength of the output pulse is determined by the frequency within the continuum that is phase matched at the given crystal angle. The authors report a photon conversion efficiency of about $5 \times 10^{-3}$, 40 nJ maximum energy per pulse, 4 to 5 ps pulse duration, and tunability from 2 to 5 $\mu$m. The generated pulses were used to study transient absorption of photogenerated charged solitons in polyacetylene (Rothberg et al., 1986). In a similar arrangement, Moore and Schmidt (1987) have used the 25-$\mu$J output of an amplified CPM laser to generate 2-nJ, 0.2-ps pulses tunable from 1.7 to 4.0 $\mu$m.

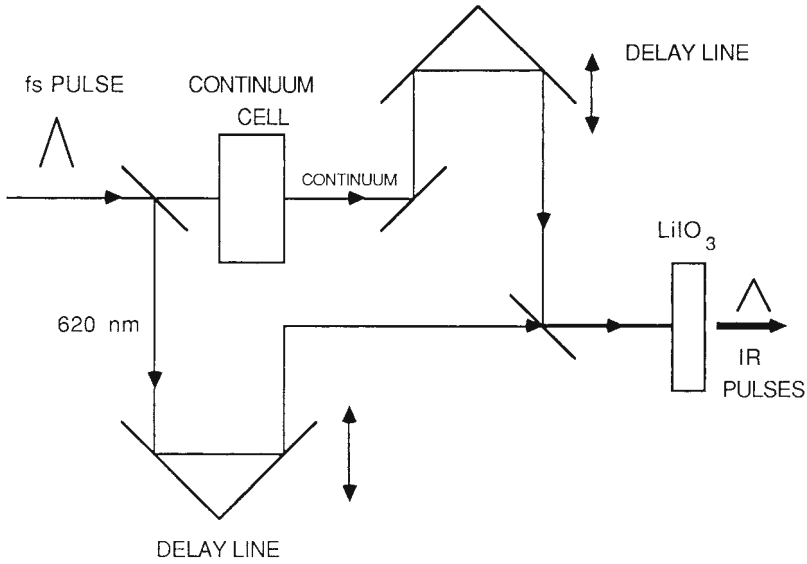


FIGURE 9.5. Experimental arrangement for generating subpicosecond near-IR pulses by difference mixing a strong monochromatic picosecond pulse with the supercontinuum.

## 3.2 Coherent Anti-Stokes Raman Scattering (CARS)

Coherent anti-Stokes Raman scattering (CARS) spectroscopy uses two electromagnetic fields, $E_1$ and $E_s$, with wave vectors $k_1$ and $k_s$ and photon frequencies $\omega_1$ and $\omega_s$, where $\omega_p = \omega_1 - \omega_s$ is the frequency of a Raman-active vibrational mode in the system under consideration. The interaction through the vibrational resonance components of the third-order nonlinear coefficient $\chi^3$ generates strong anti-Stokes signals at the frequency $\omega_{as} = 2\omega_1 - \omega_s$. Picosecond white light continuum can be used as the Stokes pulse $E_s$ and enables an extensive anti-Stokes spectrum to be obtained in a single ultrafast laser pulse. The method was first used by Goldberg (1982) to obtain transient CARS spectra of benzene and toluene vapors. The picosecond pulse continuum, extending throughout the visible and near-infrared spectrum, was produced by focusing the 25-mJ, 5-ps, 1054-nm fundamental from a mode-locked Nd : phosphate glass laser system into a 5-cm liquid $D_2O$ cell. The continuum beam was then collimated and filtered to pass wavelengths >530 nm, providing a broad band of light at Stokes frequencies. The second harmonic at 530 nm was used as the second beam, $E_1$. For photolysis purposes a third beam, the fourth harmonic at 264 nm, was sent through an independent delay path, recombined with the other two beams, and focused into the sample cell. The CARS spectrum was recorded using a grating spectrograph and a vidicon system. The sample was probed about 200 ps after arrival of the UV pulse.

The author observed a complex spectrum, which was attributed to the formation of a $C_2$ diradical.

### 3.3 Raman-Induced Phase Conjugation (RIPC)

Phase conjugation allows the generation of a time-reversed replica of an optical wave front using nonlinear optical effects. Saha and Hellwarth (1983) have used the phase conjugation geometry in conjunction with coherent Raman spectroscopy techniques to obtain vibrational spectra in liquids. In this Raman induced phase conjugation technique, two nanosecond singlepulse laser beams at $\omega$ and $\omega - \Omega$ or $(\omega + \Omega)$ (where $\Omega$ corresponds to a vibrational frequency in a nonlinear medium) mix with a third laser beam to generate a fourth beam at $\omega - \Omega$ or $(\omega + \Omega)$, nearly phase conjugate to one of the beams at $\omega$. The resonance enhancement of the $\chi^3$ nonlinear coefficient generates the signals at the Stokes and anti-Stokes frequencies. The main characteristics of this technique are a wide frequency range (thousands of $cm^{-1}$) and a broad acceptance angle for phase matching (40 mrad). For example, under identical conditions, the phase-matching limited frequency range for RIPC is one to two orders of magnitude larger than the frequency range in CARS spectroscopy. Dorsinville et al. (1987) later extended the RIPC technique to the picosecond regime by using a mode-locked YAG laser as the laser source at $\omega$ and a picosecond continuum as the $\omega \pm \Omega$ beam. Picosecond RIPC spectra covering a 2000-$cm^{-1}$ range were obtained for different liquids and solids. By delaying one of the interacting beams relative to the other two beams, vibrational lifetimes could be determined. The kinetic information on a picosecond time scale is obtained using a slow detector from the convolution of the probe pulse shape with the response function of the material. Delfyett et al. (1987) have shown that by combining the RIPC geometry with streak camera techniques, phonon and vibrational lifetimes can be measured in *real time*. In this method, the generated phase conjugate pulse using RIPC is passed into a streak camera and a video computer system to record its time profile. The rise and decay times of the generated pulse are directly related to the phonon formation and decay times. The technique was used to detemine phonon and vibrational lifetimes of solids and liquids in different organic liquids and solids.

## 4. Optical Pulse Compression

Pulse compression techniques have been used to generate optical pulses of few femtoseconds (Knox et al., 1985) from CPM dye lasers and to generate 2-ps pulses from a 35-ps Nd : YAG pulse (Kafka et al., 1984). Details of pulse compression are given in Chapter 10 by Johnson and Shank.

The fundamental limit on the shortness of the temporal duration of an ultrafast pulse can be determined by the uncertainty relation ($\Delta v\ \Delta t = K$;

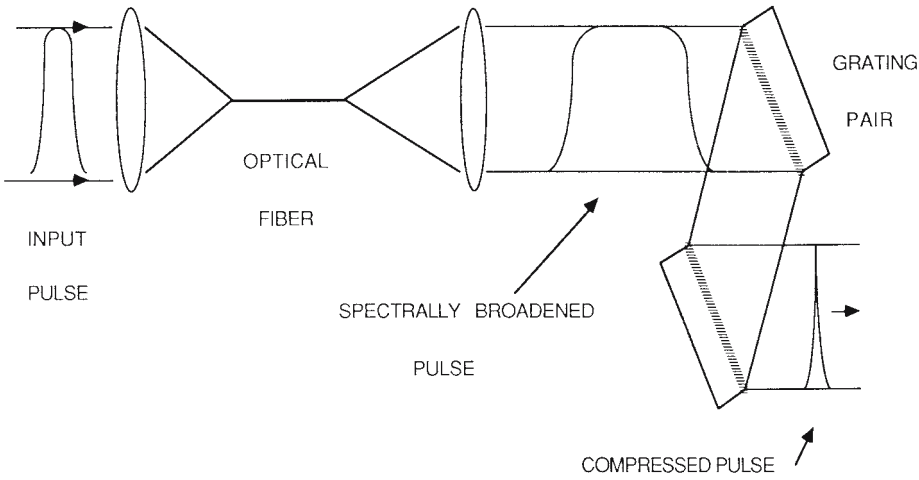


FIGURE 9.6. Experimental arrangement for compressing a laser pulse using an optical fiber and a grating pair.

$K = 0.44$ for a Gaussian pulse). This suggests that the first condition for obtaining a short pulse is a broad bandwidth. This can be achieved by self-phase modulation (SPM). The SPM-generated continuum pulse is chirped (has a time-dependent frequency shift). The lower frequencies are produced at the leading edge of the pulse, the higher frequencies at the trailing edge. If this positive chirp is linear and the chirped pulse is allowed to traverse a medium with negative linear dispersion, the pulse can be compressed to a temporal duration close to that allowed by the uncertainty principle.

Figure 9.6 shows a typical pulse compression setup consisting of an optical fiber and a grating pair. An ultrashort laser pulse is focused into the optical fiber. The pulse is spectrally broadened by SPM and acquires a positive linear chirp, i.e., $\phi = \omega_0 t + Bt^2$ and $\omega(t) = \omega_0 + 2Bt$. A positively chirped frequency increases in time from the leading edge to the trailing edge. That is, the pulse is blue in the rear and red in the front. Group velocity dispersion (GVD) temporally broadens the pulse. The graiting pair acts as the negative dispersive element by forcing the lower frequencies (red) to travel a longer optical path than the higher frequencies (blue) (Treacy, 1969). The higher frequencies of the trailing edge of the pulse catch up with the leading edge, resulting in a compressed pulse (Treacy, 1969; Shank et al., 1982).

Single-mode fibers have several advantages over bulk materials for pulse compression applications:

- There are no complications from other nonlinear processes, such as self-focusing. This is due to the relatively low light intensity inside the fiber.
- The chirp is independent of transverse position on the output beam.

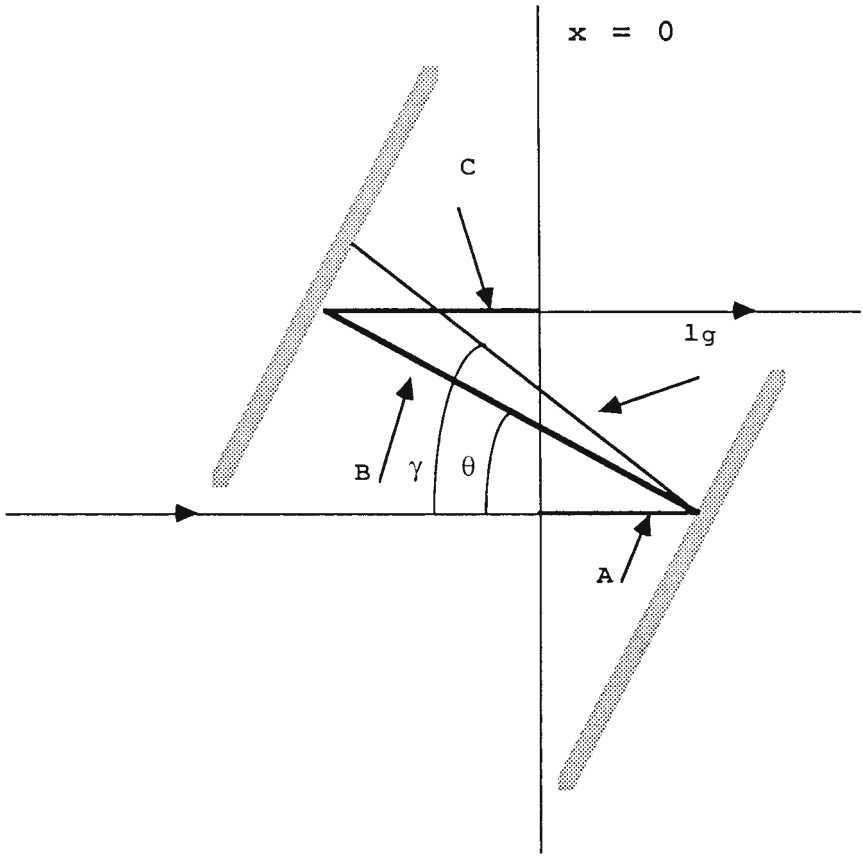


FIGURE 9.7. Ray path of a monochromatic wave through a pair of gratings used for pulse compression.

- The path length in fibers is usually longer than in bulk media and group velocity dispersion plays a more important role. GVD acts to linearize the chirp over most of the length of the pulse.

All these characteristics act to produce stable, reproducible, self-phase-modulated and positively linearly chirped pulse (Grischkowsky and Balant, 1982).

Figure 9.7 illustrates the ray path of a monochromatic wave through a pair of gratings used for pulse compression. Here $\theta$ is the angle between incident and diffracted rays, $\gamma$ is the angle of incidence, $l_g$ is the distance between the two gratings, and the relation between $\gamma$ and $\theta$ for first-order diffraction is given by $\sin(\gamma - \theta) = (\lambda/d) - \sin\gamma$, with $d$ being the groove spacing. The line $x = 0$ represents a reference plane between the two gratings.

The ray path length $p(\omega)$ is the sum of the paths $A$, $B$, and $C$ and is given by (see Figure 9.7)

$$p(\omega) = A + B + C = l_g \frac{1+\cos\theta}{\cos(\gamma-\theta)}. \tag{2}$$

The resulting frequency-dependent phase is given by

$$\Phi(\omega) = \omega \frac{p(\omega)}{c} + R(\omega), \tag{3}$$

where $R$ is a complex geometric function specific to the grating pair (Treacy, 1969) and $c$ is the velocity of light.

For pulse compression purposes, the important characteristic of a grating pair is the variation of group delay time $\tau(\omega)$ with frequency. This characteristic determines whether the grating pair can compensate for the linear chirp introduced by SPM and the fiber GVD. $\tau(\omega)$ is defined as follows:

$$\tau = \frac{\delta\Phi}{\delta\omega} = \frac{p(\omega)}{c} + \frac{\omega dp(\omega)}{cd\omega} + \frac{dR(\omega)}{d\omega}. \tag{4}$$

For gratings the last two terms cancel and $\tau(\omega) = p(\omega)/c$.

The group delay time can also be expressed as

$$\tau = \tau_0 + \frac{\delta\tau(d\omega)}{\delta\omega} + \frac{\delta^2\tau}{\delta\omega^2}(d\omega)^2 + \cdots. \tag{5}$$

Keeping only the linear term and taking into account that $\theta$ is frequency dependent (formula 2), an analytical approximation of the variation of the group delay with frequency can be derived by differentiating $p(\omega)/c$ with respect to $\omega$:

$$d\tau = \frac{\delta\tau}{\delta\omega}d\omega = \frac{\delta^2\Phi}{\delta\omega^2}d\omega = -4p^2 c l_g\, d\omega \Big/ \left(\cos(\gamma-\theta)\omega^3 d^2\left\{1-[(2pc/\omega d)-\sin\gamma]^2\right\}\right). \tag{6}$$

This formula gives the time separation $\Delta\tau$ introduced by a grating pair for a spectral separation $\Delta\omega$. For example, for $d^{-1} = 1200$ lines/mm, $\lambda = 1.06\,\mu$m, and $\gamma = 60°$, formula (6) gives a relative time separation of 0.6 ps per centimeter of grating spacing $l_g$ for two wavelength components differing by 100 Å.

Grating pairs also introduce nonlinear terms such as the quadratic term in Eq. (5). This term is positive and proportional to the second derivative of the group delay ($\delta^2\tau/\delta\omega^2$) or the third derivative of the phase ($\delta^3\Phi/\delta\omega^3$). At large bandwidth and pulse durations in the order of 10 fs, this introduces undesirable phase distortions that prevent further compression.

A prism-grating combination substantially reduces the phase distortion (Brito Cruz et al., 1988). Figure 9.8 shows the propagation of an optical pulse through the prism sequence. The optical path variation with frequency is caused by the refracted rays leaving the first prism at different angles for different wavelengths. In the case of normal dispersion, the low frequencies will be less refracted and reach the second prism earlier than the high frequencies, causing a path difference in air. An additional path variation is caused

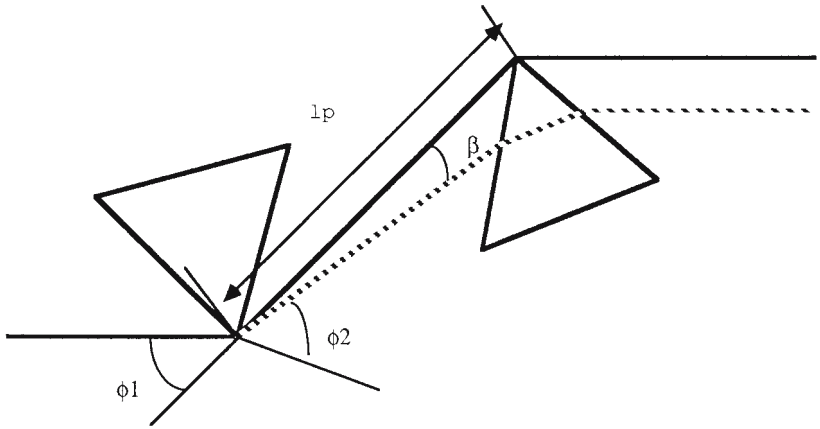


FIGURE 9.8. Propagation of the optical pulse through a prism pair. $\phi_1$ is the angle of incidence at the entrance face of the first prism, $\phi_2$ is the angle with respect to the normal to the exit face, $\beta$ is the angle between a line drawn between prism apices and the direction of a ray leaving the prism at $\phi_2$; and $l_p$ is the distance between prism apices.

by the difference in travel inside the two prisms. By changing the distance $l_p$ between the two prisms, the group delay time can be widely adjusted. The phase shift is given by (Fork et al., 1984):

$$\Phi_p = \frac{\omega l_p}{c}\cos\beta,$$

where $\beta$ is the angle between a line drawn between prism apices and the direction of a ray leaving the first prism. Prism pairs provide adjustable second- and third-order phase corrections (Fork et al., 1984) that can be either positive or negative. The prisms can be adjusted to cancel the third derivative of the phase introduced by the grating pair.

In general, for pulse compression, group delay times should satisfy the condition

$$\Delta\tau_g + \Delta\tau_p = -\Delta\tau, \tag{7}$$

where $\Delta\tau$ is the group delay time difference before the prism-grating compressor and the subscripts $g$ and $p$ refer to prism and grating group delay times, respectively.

Using the Taylor expansion for the group delay time (5), condition (7) gives

$$\begin{aligned}\frac{\delta^2\Phi_g}{\delta\omega^2} + \frac{\delta^2\Phi_p}{\delta\omega^2} &= \frac{\delta^2\Phi}{\delta\omega^2},\\ \frac{\delta^3\Phi_g}{\delta\omega^3} + \frac{\delta^3\Phi_p}{\delta\omega^3} &= \frac{\delta^3\Phi}{\delta\omega^3},\end{aligned} \tag{8}$$

Table 9.1. Second and third derivatives of the phase with respect to frequency for a double prism pair and double grating pair.[a]

| Derivative | Prisms | Gratings | Material |
|---|---|---|---|
| $\frac{d^2\Phi}{d\omega^2}(fs^2)$ | $+648 - 32(l_p)$ | $-3640(l_g)$ | $+2900(l_m)$ |
| $\frac{d^3\Phi}{d\omega^3}(fs^3)$ | $+277 - 49(l_p)$ | $+3120(l_g)$ | $+1620(l_m)$ |

[a] $l_g$ is the grating spacing, $l_p$ the prism spacing, and $l_m$ the material length.

where $\Phi$ is the phase before the prism-grating compressor and $\Phi_g$, $\Phi_p$ are the contributions to the phase due to the gratings and prisms, respectively.

A short transform-limited pulse is obtained if the different phase derivatives can be adjusted to satisfy (8), by choosing the gratings and prisms with the correct parameters and adjusting the angle and the separation between the two gratings and the two prisms forming the compressor pairs (Brito Cruz et al., 1988). This is illustrated in Table 9.1, which gives the second and third derivatives of the phase with respect to frequency for a double prism pair and double grating pair described by Fork et al. (1988). The expressions for the second and third derivatives of the phase for the prism pairs can be positive or negative depending on the prism separation $l_p$. The lengths $l_p$, $l_g$ (the grating separation), and $l_m$ (the length of material other than the minimum material path contributed by the prisms) can be adjusted to satisfy Eq. (8).

For example, using a value of $+700\,\text{fs}^2$ for the quadratic phase distortion (linear chirp) for the pulse emerging from the optical fiber and using the experimentally determined value for the grating spacing, the values of the prism spacing and material length can be calculated from the expressions in Table 9.1 to obtain a quadratic phase distortion of $-700\,\text{fs}$ and a net cubic phase distortion of zero. For this particular case, $l_g = 0.5\,\text{cm}$, $l_p = 68\,\text{cm}$, and $l_m = 1.0\,\text{cm}$, in good agreement with the experimental values (Fork et al., 1987).

The compression techniques we have described were used to obtain picosecond and femtosecond pulses from different laser systems. Table 9.2 reviews the pulse compression characteristics obtained from different laser systems.

Substantial pulse compression can also be obtained without gratings or prisms. As a result of the SPM process, the Stokes and anti-Stokes shifts are proportional to the intensity gradients on the sides of the pulse. Therefore, a pulse obtained by passing the SPM beam through a narrow spectral window could be shorter than the original beam (Masuhara et al., 1983). Gomes et al. (1986) demonstrated a pulse compression technique where a spectral window within the broadened spectral profile eliminates the wings of the

TABLE 9.2. Pulse compression performances of different laser systems.

| References | Pulse duration | | Repetition rate | Wavelength (nm) |
|---|---|---|---|---|
| | Before | After | | |
| Gomes et al., 1985 | 85 ps | 2.9 ps | 500 Hz | 1064 |
| Zysset et al., 1986 | 90 ps | 200 fs | 82 MHz | 1064 |
| Johnson and Simpson, 1986 | 33 ps | 410 fs | 100 MHz | 532 |
| Shank et al., 1982 | 90 fs | 30 fs | 20 Hz | 620 |
| Knox et al., 1985 | 40 fs | 8 fs | 5 kHz | 620 |
| Palfrey and Grischkowsky, 1985 | 5.4 ps | 16 fs | 200 Hz | 587 |
| Fork et al., 1987 | 30 fs | 7 fs | 8 kHz | 620 |

SPM-generated pulse where the high- and low-frequency components are located. They obtained a 3-fold shortening of 80-ps pulses from an Nd:YAG laser. The pulses were broadened from 0.3 to 4 Å after propagation through 125 m of optical fiber. A monochromator was used as a spectral window. Dorsinville et al. (1988) generated pulses down to 3 ps using a continuum generated in a 5-cm $D_2O$ cell by an intense 25-ps Nd:YAG second harmonic laser pulse and narrowband filters for spectral selection. The pulse duration was measured by a 2-ps time resolution streak camera. More details on pulse compression are given in Chapter 10.

## 5. Exploration of Future Applications

The supercontinuum can have a number of new applications in instances where knowledge is needed on specified phase and intensity for well-separated wavelengths (Manassah et al., 1984). Specifically, time delay and relative intensity measurements for different wavelengths become simple.

### 5.1 Ranging

The main limitation on accurate determination of optical lengths through the uncontrolled atmosphere is the uncertainty in the average refractive index over the optical path due to the nonuniformity and turbulence of the atmosphere. Simultaneous measurements over the same path using two or more different wavelengths of light could be used to provide the base values. The dispersive delays between any two wavelengths can be calculated using the expressions of Owens (1967) and Topp and Orner (1975) for the optical refractive index of air as a function of the ambient pressure, temperature, and composition. For path lengths of a few tens of meters, Erickson (1962) proposed the use of direct interferometry for the dispersive delay measurements. In effect, his system consists of an automatic fringe-counting Michelson interferometer. For lengths greater than 100 m, the method of direct interferometry is impractical. A system using a pulsed subpicosecond

single-wavelength laser source and a synchroscan streak camera with a time resolution of 3 ps as a detector can measure distances of a few kilometers to an accuracy of 1 mm if the index of refraction of ambient air is known to an accuracy of 0.1 ppm; however, the index of refraction of air varies by as much as 100 ppm over the operational range of such range finders and the measurement accuracy is thus reduced to ±1 m. (The time delay between two signals in different media is $\Delta\tau = (L/c\delta n)$.) On the other hand, if a system consists of a multiwavelength source, such as the supercontinuum, with a multichannel synchroscan streak camera (Tsuchiya, 1983) in the receiver, the arrival time data for the different wavelengths determine the parameters in the Owens index of refraction formula (wavelength, temperature, pressure, and relative humidity dependence) to an accuracy of 0.4 ppm, and consequently the accuracy of distance measurements is restored to the ±0.4-cm range. Simultaneously, the pressure can be determined to an accuracy of 1.5 mbar and temperature to ±1/2 K. Furthermore, the wide frequency band of the continuum source allows for selective tuning and encoding (for example, the addition of a constant phase) of the different emitted lines, thus providing the added feature of system integrity under adverse field conditions (jamming, interference, etc.).

## 5.2 3-D Imaging

Direct nondestructive in situ measurement of the contour of surface, as well as the internal structure of an object, with an accuracy of 30 $\mu$m can be accomplished using 100-fs laser pulses derived from the supercontinuum.

The reflection of an incoming signal from surface imperfections will be delayed in time, with respect to other points on the surface, arrival at the detector. Experimentally, these measurements are carried out by modulating the arrival times to the target using an oscillating delay prism and passing the reflected signal together with a reference signal into a second harmonic correlation crystal. The convoluted harmonic signal is then detected by a video system in synchronism with the modulation frequency. Using three different optical frequencies from the supercontinuum and collimating the corresponding beams in a three-dimensional orthogonal configuration, a 3-D image of the imperfection can be directly deduced. The $S/N$ ratios for each frequency channel and interchannels are excellent. This technique can, for example, measure the defects and wear on the ball bearings in delicate equipment, semiconductor surfaces, and tissue topography.

For the diagnostics of an object inside a material, the different reflection and absorption coefficients for the different optical frequencies at the interfaces and in the materials can be used to measure the location and contour of cracks or impurities inside a sample. It is to be noted that the accuracy of the measurement can be further enhanced from ±30 $\mu$m by selecting one of the frequencies to be close to a resonance line, thus endowing it with a large optical path in the medium and resulting in longer time delays and more accurate spatial measurements. These techniques can, for example, measure loca-

tions of impurities inside Si and GaAs. Measurements in biological and medical samples are possible.

## 5.3 Induced-Phase Modulation Based Optical Computational Switches

The development of optical systems for ultrafast signal processing, communication, and computation has been a very active area of research. The use of nonlinear properties of materials for implementing this program has received considerable attention. Using induced-phase modulation, it is possible to configure canonical logical elements (Lattes et al., 1983; Manassah and Cockings, 1987) for computation. The configurations of XOR (exclusive OR) and NOT gates presented here are only for illustrative purposes. We refer the reader to Section 4.2 of the Manassah (Chapter 5) for the underlying models and to Section 9 of Baldeck et al. (Chapter 4) for additional applications using cross-phase modulation.

In Figure 9.9, possible gates are displayed. The input signals and seed center frequencies are $\omega_2$ and the pump center frequency is $\omega_1$. The Kerr phase shifter(s) (KPS) is in the path of the seed signal. The seed, following its passage through the KPS, is multiplexed with the pump and both are fed into a fiber (or waveguide) with molecular vibration (phonon) energy equal to $\hbar(\omega_1 - \omega_2)$; that is, under proper time delays between the seed and pump the seed can be Raman amplified or left unchanged. The amplification factor can easily change by two orders of magnitude over a few pulse widths (Chapter 4). Denote this phase shift by $\Phi$. At the end of the fiber a filter allows only the seed to pass through to the next space.

The NOT gate pump arm and seed arm are chosen such that in the absence of an input signal the phase between the seed and pump corresponds to the maximum of the amplification curve, while in the presence of an input signal the KPS introduces in the seed phase a shift equal to $\Phi_0$.

The XOR gate seed arm and pump arm differ in the absence of any input by a phase $-\Phi_0$ from the maximum and amplification position. In the presence of either input the seed is amplified, while in the presence of both inputs the phase is $+\Phi_0$ from the maximum position and the seed is not amplified.

Other configurations that are more energy efficient and have fewer ports are possible but are not covered here.

## 5.4 Atmospheric Remote Sensing

The use of differential absorption lidar for remote sensing of atmospheric species is a viable experimental technique for the detection and identification of a wide range of molecular constituents. The lidar equation is given by

$$\frac{P_r}{P_t} = \frac{K\rho A}{\pi R^2} \exp[-2(\sigma_a(\lambda)N_a + \alpha(\lambda))R], \tag{9}$$

where $P_r$ and $P_t$ are, respectively, the received and transmitted powers, $K$ is the overall system efficiency, $\rho$ is the target reflectivity, $A$ is the receiving tele-

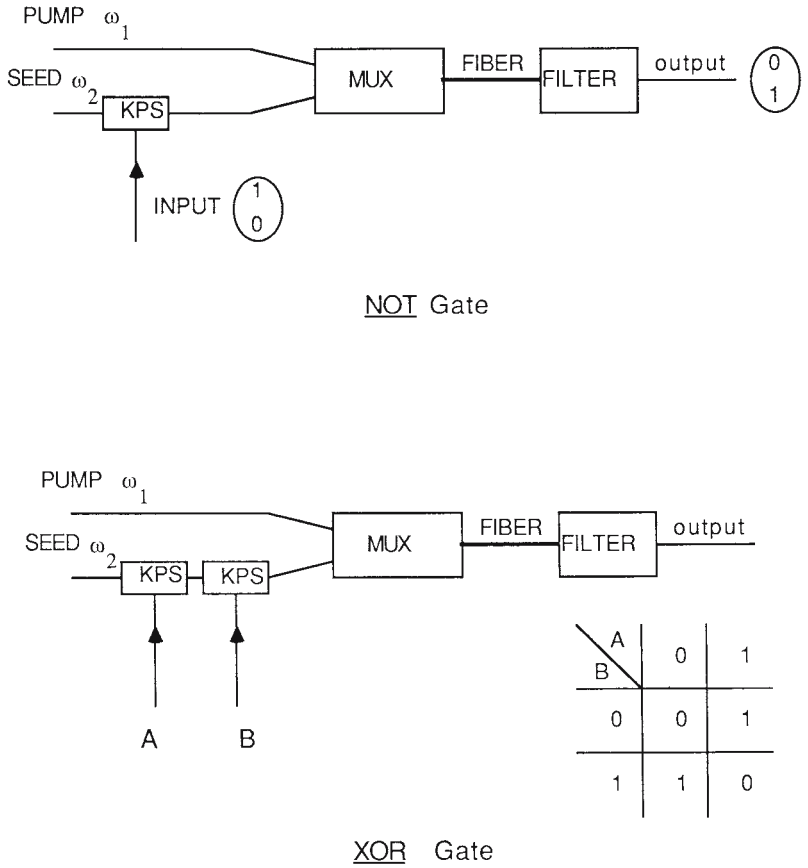


FIGURE 9.9. (*Top*) NOT gate and (*bottom*) XOR gate.

scope area, $\sigma_a$ is the absorption cross section of the absorbing molecule $a$, $R$ is the range, and $\alpha$ is the background extinction coefficient of the atmosphere. A measurement of $N_a$ based on a single wavelength requires an accurate knowledge of $K$, $\rho$, $\alpha$, and $\sigma_a$. However, $K$, $\rho$ and $\alpha$ are generally known with poor accuracy. The differential absorption lidar (Tsuchiya, 1983) approach attempts to overcome some of these difficulties by performing the lidar experiment with two or more frequencies. For a dual-wavelength source (with frequencies $\nu^1$ and $\nu^2$),

$$N_a = \frac{1}{2(\sigma_a^2 - \sigma_a^1)R}\left[\ln\left(\frac{P_a^1}{P_a^2}\right) - \ln\left(\frac{\rho^2}{\rho^1}\right) - 2(\alpha^1 - \alpha^2)R\right], \tag{10}$$

where $P_a = P_r/P_t$, and the superscript refers to the wavelength. A multiwavelength source such as the supercontinuum, with an inbuilt calibrated power

spectrum, provides the possibility for a more accurate determination of $N_a$. The differential spectral reflectance (DSR) error can be reduced significantly by using three or more frequencies because the DSR Taylor's expansion terms can be directly determined from the ratios of $P_a^{(i)}$ and $P_a^{(j)}$ for $i$ and $j$ off the molecular absorption line. Furthermore, the background extinction coefficient can be factored out and the water vapor absorption tail contribution can be Taylor expanded around the molecular absorption line. Another advantage of the supercontinuum is the virtual elimination of time interval (1 ns) between the different probing wavelengths. This interval should be less than $10^{-2}$ s to neglect temporal fluctuations in the atmospheric parameters.

## 5.5 Optical Fiber Measurements

Signal attenuation and pulse spreading are the two characteristics that determine the suitability of a particular optical fiber for communication use. Signal attenuation determines the distance between repeaters and pulse spreading determines the maximum bit rate over a channel (channel capacity). In an optical fiber, three sources of attenuation are present: Mie scattering (wavelength independent), Rayleigh scattering ($\lambda^{-4}$ law), and molecular absorption. The fiber loss is written as

$$\alpha = \frac{A}{\lambda^4} + B + C(\lambda), \tag{11}$$

where $C(\lambda)$ includes impurity absorption and other wavelength-dependent phenomena and $B$ includes Mie scattering and losses introduced by microbending or coating defects. The molecular absorption is a function of the impurities present in the raw material or introduced in the manufacturing process. Quality control and component specifications are achieved through a measurement of attenuation as a function of wavelength. Present techniques use near-IR fiber Raman laser to perform these measurements for discret points in the wavelength region 1.1 to 1.6 $\mu$m (pulse duration ~100 ps).

The supercontinuum in the IR band allows the measurement of a normalized attenuation profile for all points in the band 0.7 to 2 $\mu$m and with the option of reducing the pulse duration to 100 fs. This data can further provide the needed parameters for the design of wavelength division multiplexing (WDM) systems. Furthermore, the SPM source can actually be used in situ to calibrate existing network losses for the different wavelengths and assess their suitability for WDM upgrading.

Pulse spreading in fibers is dominated by the material dispersion term ($dn/d\omega$). The supercontinuum provides an experimental tool for measuring pulse spreading at different wavelengths and meaningfully comparing the results for WDM applications. Furthermore, this experimental technique is useful in exploring the inherent lower limits on the duration of a pulse that is suitable for optical communication.

### 5.6 Kinetics of Optical Nonlinearities

Spectral and temporal information on nonlinear optical susceptibilities is important for the design and application of future optoelectronic devices. Using the pump-and-probe technique to determine ultrafast temporal responses of nonlinear processes requires a great number of successive shots to obtain all the information. Based on the techniques of single-shot Kerr gate (Ho, 1984) and real-time picosecond oscilloscopes (Valdmanis, 1986), a single-short supercontinuum Kerr method can be developed to probe for complete information on nonlinearities with single-shot excitation (Saux et al., 1988). A long chirped probe pulse from a supercontinuum is used to transform a temporal modulation into a spectral modulation. A spectrograph then converts the wavelength-encoded temporal information to the spatial domain for readout. The chirp of the supercontinuum is created mainly by the group velocity dispersion in the generation sample. Subpicosecond temporal resolution of optical nonlinearity measurements of glasses has been demonstrated.

## 6. Conclusion

We have reviewed some of the applications of the continuum in ultrafast spectroscopy and nonlinear optics and suggested some future applications including ranging, imaging, and remote sensing. The supercontinuum source can be directly applied in many other areas of solid-state physics, biology, chemistry, and medicine. Exciting and far-reaching future applications are expected to be related to the possibility of producing femtosecond pulses using SPM. Ultrashort pulses are expected to lead to breakthroughs in communication and optical computing. Data transmission rates may be increased three or more orders of magnitude. Optical computing based on ultrafast logic units has the potential for revolutionizing the field of computers.

### References

Ahmed, S. (1973) Appl. Opt. **12**, 901.
Alfano, R.R. and S.L. Shapiro (1971) Chem. Phys. Lett. **8**, 631.
Berg, M., A.L. Harris, J.K. Brown, and C.B. Harris (1984) Opt. Lett. **9**, 50.
Brito Cruz, C.H., P.C. Becker, R.L. Fork, and C.V. Chank (1988) Opt. Lett. **13**, 123.
Cornelius, P.A. and R.M. Hochstrasser (1982) In *Picosecond Phenomena III*, Eisenthal et al., eds., p. 288. Springer-Verlag, New York.
Delfyett, P.J., R. Dorsinville, and R.R. Alfano (1987) Opt. Lett. **12**, 1002.
Dorsinville, R., P.J. Delfyett, and R.R. Alfano (1987) Appl. Opt. **26**, 3655.
Dorsinville, R., P.J. Delfyett, and R.R. Alfano (1988) Appl. Opt. **27**, 16.
Doukas, A.G., V. Stefancic, T. Suzuki, R.H. Callender, and R.R. Alfano (1980) Photobiochemistry and Photobiophysics **1**, 305.
Eisenstein, L. and Frauenfelder (1982) In *Biological Events Probed by Ultrafast Laser Spectroscopy*, R.R. Alfano, ed., chapter 14. Academic Press, New York.
Erickson, K.E. (1962) J. Opt. Soc. Am. **52**, 777.

Fork, R.L., C.V. Shank, and B.I. Greene (1980) In *Picosecond Phenomena II*, R.M. Hochrasser et al., eds. Springer-Verlag, New York.
Fork, R.L., O.E. Martinez, and J.P. Gordon (1984) Opt. Lett. **9**, 150.
Fork, R.L., C.H. Brito Cruz, P.C. Becker, and C.V. Shank (1987) Opt. Lett. **12**, 483.
Gayen, S.K., W.B. Wang, V. Petricevic, K.M. Yoo, and R.R. Alfano (1987) Appl. Phys. Lett. **50**, 1494.
Goldberg, L.S. (1982) In Proceedings of the Third International Conference on Picosecond Phenomena, *Picosecond Phenomena III*, p. 94. Springer-Verlag, New York.
Gomes, A.S.L., W. Sibbet, and J.R. Taylor (1985) IEEE J. Quantum Electron. **QE-21**, 1157.
Gomes, A.S.L., A.S. Gouveia-Neto, J.R. Taylor, H. Avramopoulos, and G.H.C. New (1986) Opt. Commun. **59**, 399.
Gore, B.L., L.B. Giorgi, and G. Porter (1986) In *Picosecond Phenomena V*, G.R. Fleming and A.E. Seigman, eds., 298. Springer-Verlag, New York.
Greene, B.I., R.M. Hochstrasser, and R.B. Weisman (1978) In *Picosecond Phenomena I*, p. 12. Springer-Verlag, New York.
Grischkowsky, D. and A.C. Balant (1982) Appl. Phys. Lett. **41**, 1.
Hirata, Y., Y. Kanda, and N. Mataga (1983) J. Phys. Chem. **87**, 1659.
Ho, P.P. (1984) In *Semiconductors Probed by Ultrafast Spectroscopy*" R.R. Alfano, ed., Chapter 25. Academic Press, New York.
Hulin, D., A. Mysyrowicz, A. Antonetti, A. Migus, W.T. Masselink, H. Morkoc, H.M. Gibbs, and N. Peyghambarian (1986) Phys. Rev. B 33, 4389.
Inada, K. (1976) Opt. Commun. **19**, 436.
Jedju, T.M. and L. Roghberg (1987) Appl. Opt. **26**, 2877.
Johnson, A.M. and M. Simpson (1986) IEEE J. Quantum Electron. **QE-22**, 133.
Kafka, J.D., B.H. Kolner, T. Baer, and D.M. Bloom (1984) Opt. Lett. **9**, 505.
Knox, W.H., R.L. Fork, M.C. Downer, R.H. Stolen, and C.V. Shank (1985) Appl. Phys. Lett. **46**, 1120.
Kobayashi, T. and J. Iwai (1984) In *Picosecond Phenomena IV*, D.H. Auston and K.B. Eisenthal, eds., p. 484. Springer-Verlag, New York.
Kobayashi, T., H. Ohtani, and J. Iwai (1984) In *Picosecond Phenomena IV*, D.H. Auston and K.B. Eisenthal, eds., p. 481. Springer-Verlag, New York.
Lattes, A., H.A. Haus, F.J. Leonberger, and E.P. Ippen (1983) IEEE J. Quantum Electron. **QE-19**, 1718.
Lippitsch, M.E., M. Rieger, F.R. Aussenegg, L. Margulies, and Y. Mazur (1982a) In *Picosecond Phenomena III*, K.B. Eisenthal et al., eds., p. 319. Springer-Verlag, New York.
Lippitsch, M.E., M. Riegler, A. Leitner, and F.R. Aussengg (1982b) In *Picosecond Phenomena III*, K.B. Eisenthal et al., eds., p. 323. Springer-Verlag, New York.
Manassah, J.T. (1986) Appl. Opt. **25**, 3979.
Manassah, J.T. and O. Cockings (1987) Appl. Opt. **26**, 3749.
Manassah, J.T., P.P. Ho, A. Katz, and R.R. Alfano (1984) Photonics Spectra, November issue.
Martin, J.L., A. Migus, C. Poyart, Y. Lecarpentier, A. Astier, and A. Antonetti (1984) In *Picosecond Phenomena IV*, D.H. Auston and K.B. Eisenthal, eds., p. 447. Springer-Verlag, New York.
Masuhara, H., H. Miyasaka, A. Karen, T. Uemiya, N. Mataga, and M. Koishi (1983) Opt. Commun. **44**, 426.

Matveetz, Yu. A., S.V. Chekalin, and A.V. Sharkov (1985) J. Opt. Soc. Am. **B 2**, 634.
Menyuk, N. and D.K. Killinger (1983) Appl. Opt. **22**, 2690.
Monger, T.G., R.R. Alfano, and R.H. Callender (1979) Biophys. J. **27**, 105.
Moore, D.S. and S.C. Schmidt (1987) Opt. Lett. **12**, 480.
Owens, J.C. (1967) Appl. Opt. **6**, 51; and Topp, M. and G. Orner (1975) Opt. Commun. **13**, 276.
Palfrey, S.L. and D. Grischkowsky (1985) Opt. Lett. **10**, 562.
Rothberg, L., T.M. Jedju, S. Etemad, and G.L. Baker (1986) Phys Rev. Lett. **57**, 3229.
Saha, S.K. and R.W. Hellwarth (1983) Phys. Rev. A **27**, 919.
Saux, G. Le, F. Salin, P. Georges, G. Roger, and A. Brun (1988) Appl. Opt. **27**, 777.
Schoenlein, R.W., W.Z. Lin, J.G. Fujimoto, and G.L. Eesley (1986) In *Ultrafast Phenomena V*, G.R. Fleming and A.E. Siegman, eds., p. 260. Springer-Verlag, New York.
Shank, C.V., R.L. Fork, R.T. Yen, R.J. Stolen, and W.J. Tomlinson (1982) Appl. Phys. Lett. **40**, 761.
Searle, G.F.W., J. Barbet, G. Porter, and C.J. Tredwell (1978) Biochim. Biophys. Acta **501**, 246–256.
Singer, S.S. (1969) Appl. Opt. **7**, 1125.
Thomas, D.G., L.K. Anderson, M.I. Cohen, E.I. Gordon, and P.K. Runge (1982) In *Innovations in Telecommunications*, J.T. Manassah. ed., Academic Press, New York.
Tomlinson, W.J., R.H. Stolen, and C.V. Shank (1984) J. Opt. Soc. Am. **B 1**, 139.
Treacy, E.B. (1969) IEEE J. Quantum Electron. **QE-5**, 454.
Tsuchiya, Y. (1983) "Picosecond streak camera and its applications," Hamamatsu Tech. Bull. **14**, June; C.S. Gardner, B.M. Tsai, and K.F. Im (1983) Appl. Opt. **22**, 2571; Abshire, J.B. and G.E. Kalshoven (1983) Appl. Opt. **22**, 2578.
Valdmanis, J.A. (1986) In *Ultrafast Phenomena V*, Fleming and Siegman, eds., p. 82.
von der Linde, D., and R. Lambrich (1979) Phys. Lett. **42**, 1090.
Williams, R.T., B.B. Craig, and W.L. Faust (1984) Phys. Rev. Lett. **52**, 1709.
Wong, D. (1982) In *Biological Events Probed by Ultrafast Laser Spectroscopy*, R.R. Alfano, ed., chapter 1, Academic Press, New York.
Zysset, B., W. Hodel, P. Beaud, and H.P. Weber (1986) Opt. Lett. **11**, 156.

# 10
# Pulse Compression in Single-Mode Fibers: Picoseconds to Femtoseconds

A.M. Johnson and C.V. Shank

## 1. Introduction

The compression of frequency swept (in time) or "chirped" optical pulses was independently proposed by Gires and Tournois (1964) and Giordmaine et al. (1968). Optical pulse compression is the optical analog of microwave pulse compression or chirp radar developed by Klauder et al. (1960). The compression is accomplished in two steps. First, an optical frequency sweep is impressed on the pulse. The next step is the compensation of this frequency sweep by using a dispersive delay line, where the group velocity or group delay varies with optical frequency. Ideally, the dispersive delay line would impress the opposite chirp on the pulse, resulting in the compression of the pulse to its minimum width, $\sim 1/\Delta\omega$, where $\Delta\omega$ is the frequency sweep. Treacy (1968, 1969) was the first to recognize that a pair of diffraction gratings was a suitable dispersive delay line for a linearly chirped pulse; he used gratings to compress the inherently chirped output of a mode-locked Nd : glass laser. Similar experiments were later performed by Bradley et al. (1970). Duguay and Hansen (1969) used an $LiNbO_3$ phase modulator and Gire-Tournois interferometer to compress pulses from a mode-locked He-Ne laser.

A chirp can be impressed on a intense optical pulse as it passes through a medium with an intensity-dependent refractive index, i.e., an optical Kerr medium. The phase of the intense optical pulse is modulated by the nonlinear refractive index. Extreme small spectral broadening of optical pulses in optical Kerr liquids was first observed in self-focused filaments by Bloembergen and Lallemand (1966), Brewer (1967), and Ueda and Shimoda (1967). The weak spectral broadening was first explained by Shimizu (1967) as due to a rapid time-varying phase shift arising from the nonlinear refractive index. Gustafson et al. (1969) further elaborated on Shimizu's explanation with detailed numerical calculations of the spectra of self-phase-modulated pulses, including the effects of dispersion and relaxation of the nonlinearity. Alfano and Shapiro (1970) made the first measurements of self-phase modulation (SPM) in crystals, liquids, and glasses (see Chapter 2). Spectral broadening data in glasses were also obtained by Bondarenko et al. (1970).

Fisher et al. (1969) suggested that optical pulses in the range $10^{-13}$ to $10^{-14}$ s could be achieved as a result of the SPM obtained by passing a short pulse through an optical Kerr liquid followed by a dispersive delay line. Laubereau (1969) used several cells of the optical Kerr liquid $CS_2$ and a pair of diffraction gratings to compress 20-ps-duration pulses from a mode-locked Nd : glass laser by 10×. Zel'dovich and Sobel'man (1971) proposed the possibility of using alkali metal vapors to both spectrally broaden optical pulses by SPM and compress the pulses by the strong dispersion of the group velocity near the atomic resonance. Lehmberg and McMahon (1976) compressed 100-ps-duration pulses from a mode-locked and amplified Nd : YAG laser by 14×, using a series of liquid $CS_2$ cells and diffraction gratings separated by 23 m. Spectral broadening of picosecond pulses from a flashlamp-pumped, passively mode-locked Rhodamine 6G dye laser was reported by Arthurs et al. (1971) and was attributed to SPM. Ippen and Shank (1975b) compressed 1-ps-duration pulses from a CW pumped, passively mode-locked Rhodamine 6G dye laser by 3× to a duration of 0.3 ps using diffraction gratings separated by 10 cm.

The early measurements of SPM (Bloembergen and Lallemand, 1966; Brewer, 1967; Ueda and Shimoda, 1967; Shimizu, 1967; Gustafson et al., 1969; Alfano and Shapiro, 1970; Bondarenko et al., 1970) occurred in self-focused filaments, where the intensity was high and there were problems with competing nonlinear effects and uncertainties concerning the filament size (see Chapter 2). Ippen et al. (1974) reported the first measurement of SPM in the absence of self-trapping or self-focusing with the use of a guiding multi-mode optical fiber filled with liquid $CS_2$. Stolen and Lin (1978) reported measurements of SPM is single-mode silica core fibers. In fibers, any additional confinement caused by self-focusing is negligible. An additional advantage of this guiding structure over bulk crystals or liquid cells is that the modulation can be imposed over the entire transverse spatial extent of the beam, and the problem of unmodulated light in the wings of the beam is eliminated (Ippen et al., 1974). Perhaps the most important feature of SPM in optical fibers is that significant spectral broadening can be achieved at power levels much lower than those required in bulk media.

The first fiber pulse compression experiments utilized the fiber as a dispersive delay line to compress chirped optical pulses. Suzuki and Fukumoto (1976) used an $LiNbO_3$ phase modulator to chirp 1-$\mu$m laser pulses, which were subsequently compressed by the normal or positive group velocity dispersion (GVD) (red frequencies lead blue) of a silica optical fiber. Wright and Nelson (1977) compressed the chirped output of a GaAs semiconductor laser operating at 0.894 $\mu$m using a positive GVD optical fiber delay line. Iwashita et al. (1982) demonstrated 5× compression of 1.7-ns, 1.54-$\mu$m pulses from a chirped InGaAsP injection laser using a 104-km negative GVD fiber delay line. Mollenauer et al. (1980) performed the first pulse compression experiments using optical fibers as a Kerr medium, in their work on soliton compression of pulses from a color center laser. In these experiments, the laser

wavelength ($\lambda = 1.55\,\mu$m) was in the anomalous or negative GVD (blue frequencies lead red) region for silica and did not require a separate dispersive delay line. In this instance, the fiber material forms an integrated dispersive delay line and self-compresses the pulse. Using soliton compression, Mollenauer et al. (1983) compressed 7-ps-duration pulses by 27× to a duration of 0.26 ps with a 100-m length of single-mode fiber. This compression was achieved with only 200 W of peak power at the fiber input, thus further attesting the low power requirements of nonlinear effects in optical fibers. It is beyond the scope of this chapter to consider soliton compression in optical fibers. Further information on soliton compression and its applications can be found, for example, in excellent discussions by Mollenauer and co-workers (Mollenauer and Stolen, 1982; Mollenauer, 1985; Mollenauer et al., 1986). This chapter is limited to pulse compression, in silica core fibers, in the normal or positive GVD region ($\lambda \leq 1.3\,\mu$m), where a separate dispersive delay line is necessary. The compression of positively chirped optical pulses passing through a dispersive medium possessing negative GVD is schematically illustrated in Figure 10.1.

Nakatsuka and Grischkowsky (1981) demonstrated distortion-free pulse propagation of synchronously mode-locked dye laser pulses by using the positive GVD of fibers to chirp the pulses. In this experiment, low-power (to avoid SPM) 3.3-ps dye laser pulses were chirped and temporally broadened to 13 ps and recompressed back to 3.3 ps by the negative GVD of a near-resonant atomic Na-vapor delay line. Subsequently, Nakatsuka et al. (1981) performed the first pulse compression experiment using fibers as a Kerr medium in the positive GVD region. This experiment utilized both the

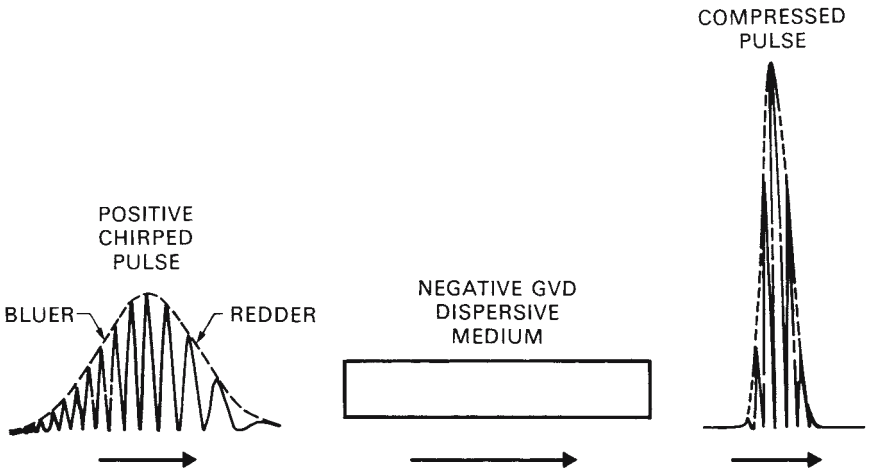


FIGURE 10.1. Compression of positively chirped optical pulses (red frequencies leading blue) using a dispersive medium possessing negative group velocity dispersion (GVD). Negative GVD: Red frequencies delayed with respect to blue.

positive GVD and SPM to temporally and spectrally broaden 5.5-ps dye laser pulses with subsequent compression by >3× to 1.5 ps by passage through a near-resonant atomic Na-vapor delay link. Shank et al. (1982) replaced the atomic vapor delay line with a Treacy (1968; 1969) grating pair to compress the 90-fs amplified output of a colliding-pulse mode-locked (CPM) dye laser by 3× to a duration of 30 fs, using a 15-cm fiber. Subsequently, Nikolaus and Grischkowsky (1983a) compressed the 5.4-ps output of a synchronously mode-locked and cavity-dumped dye laser by 12× to a duration of 450 fs, using a grating-based dispersive delay line and a 30-m fiber. Using two stages of fiber-grating compression, Nikolaus and Grischkowsky (1983b) compressed 5.9-ps pulses from the aforementioned dye laser by 65× to a duration of 90 fs. In the technological push to generate optical pulses of less than 10-fs duration, amplified CPM dye laser pulses were next compressed to 16 fs by Fujimoto et al. (1984). Compression to 12 fs by Halbout and Grischkowsky (1984) was soon followed by compression to 8 fs by Knox et al. (1985). Each of these compression achievements occurred with an important concomitant increase in repetition rate. Recently, Fork et al. (1987) achieve compression to 6 fs, the shortest to date, by using a grating pair followed by a prism sequence in order to compensate the cubic phase distortion of these large-bandwidth pulses by the grating pair.

Optical fiber compression of "long" duration picosecond pulses from CW mode-locked (CWML) Nd : YAG-based systems has also been achieved. Subpicosecond pulses can be generated with these sources without the use of a mode-locked dye laser. In addition, compressed CWML Nd : YAG-based systems can be used as pump sources for synchronously mode-lock dye lasers. Johnson et al. (1984a, 1984b) performed the first "long" pulse fiber compression experiments in a system other than a dye laser. In these experiments, 33-ps pulses at 0.532 $\mu$m from a CWML and frequency-doubled Nd : YAG laser were compressed 80× to a duration of 410 fs, using a 105-m fiber and a grating pair. Shortly thereafter, Dianov et al. (1984a) compressed 60-ps pulses, at 1.064 $\mu$m from a CWML and $Q$-switched Nd : YAG laser (1 kHz repetition rate), by 15× to a duration of 4 ps using a 10-m fiber and a grating-based delay line. The compression of 1.064-$\mu$m pulses from a CWML Nd : YAG laser was laser performed independently by Kafka et al. (1984) and Heritage et al. (1984). Kafka et al. (1984) demonstrated the compression of 80-ps pulses by 45× to a duration of 1.8 ps, while Heritage et al. (1984) compressed 90-ps pulses by 30× to a duration of 3 ps. Dupuy and Bado (1984) reported the compression of 110-ps pulses from a CWML argon-ion laser by 5×. Further studies of the compression of 1.064-$\mu$m pulses from CWML Nd : YAG laser were reported by Heritage et al. (1985a), Kafka and Baer (1985), and Gomes et al. (1985a). Using two stages of fiber-grating compression, Gomes et al. (1985b) compressed 85-ps pulses, at 1.064 $\mu$m, from a CWML Nd : YAG laser by 113× to a duration of 750 fs. Damm et al. (1985) reported on the use of large-core (50 $\mu$m) graded-index fiber to compress 5-ps pulses at 1.054 $\mu$m from a mode-locked Nd : phosphate glass laser by 7×

to a duration of 700 fs. CWML and $Q$-switched Nd : YAG laser pulses at 1.064 $\mu$m were compressed 29× to a duration of 2.9 ps by Gomes et al. (1985c) in a manner similar to that reported by Dianov et al. (1984). Blow et al. (1985) reported on all-fiber compression of a CWML Nd : YAG laser at 1.32 $\mu$m by adjusting the waveguide dispersion of two lengths of fiber. In this experiment, 130-ps pulses were compressed to a photodiode limit of 70 ps by using a dispersion-shifted positive GVD fiber followed by a negative GVD fiber. Kai and Tomita (1986a) reported the compression of 100-ps pulses at 1.32 $\mu$m from a CWML Nd : YAG laser by 50× to a duration of 2 ps using 2 km of dispersion-shifted fiber and a grating pair. Using two stages of fiber-grating compression, Zysset et al. (1986) compressed 90-ps pulses, at 1.064 $\mu$m, from a CWML Nd : YAG laser by 450× to a duration of 200 fs. Kai and Tomita (1986b) demonstrated the compression of 100-ps, 1.32-$\mu$m pulses from a CWML Nd : YAG laser by 1100× to a duration of 90 fs by using one stage of fiber-grating compression (dispersion-shifted fiber) followed by soliton compression in a length of negative GVD fiber.

In Section 2 we present results for picosecond fiber-grating compression in a normalized form, from which one can calculate the optimum fiber length, the achievable compression, and the proper grating separation for a given input pulse and fiber. Section 3 deals with the subtleties and nuances of femtosecond fiber pulse compression, that is, higher order dispersion compensation of very large bandwidth pulses.

## 2. Picosecond Pulse Compression

### 2.1 Optical Kerr Medium

Optical fibers are usually considered to be linear media; that is, as the input power is increased, one expects only a proportional increase in output power (Stolen, 1979b). However, dramatic nonlinear effects can occur that can cause strong frequency conversion, optical gain, and many other effects generally associated with very intense optical pulses and highly nonlinear optical materials. These nonlinear processes depend on the interaction length as well as the optical intensity. In small-core fibers high intensities can be maintained over kilometer lengths. If this length is compared with the focal region of a Gaussian beam of comparable spot size, enhancements of $10^5$ to $10^8$ are possible using fibers. This enhancement lowers the threshold power for nonlinear processes—in some cases to less than 100 mW (Stolen, 1979b). For example, single-mode fibers with core diameters less than 10 $\mu$m possess core areas of $<10^{-6}$ cm$^2$, which serves to translate powers in watts to intensities of MW/cm$^2$. An intensity-dependent refractive index leads to SPM and self-focusing within a single optical pulse. In fibers, however, any additional confinement caused by self-focusing is negligible (Stolen and Lin, 1978). Recently, Baldeck et al. (1987) reported on the observation of self-focusing in optical fibers with

25-ps pulses from an active-passive mode-locked and frequency-doubled Nd : YAG laser (see Chapter 4). There are several caveats to this observation of self-focusing: (1) self-focussing occurred with pulse energies greater than 10 nJ, in a multimode fiber with a core diameter of 100 $\mu$m; (2) self-focusing appeared primarily at Stokes-shifted stimulated Raman frequencies, for which the effect of the nonlinear refractive index is enhanced by cross-phase modulation; (3) self-focusing occurred at stimulated Raman conversion efficiencies of approximately 50%. The experimental conditions under which Baldeck et al. (1987) were able to observe self-focusing lend further substantial support to the claim that self-focusing is negligible under the standard experimental conditions for pulse compression in single-mode fibers. Hence single-mode fibers represent a nearly ideal nonlinear Kerr medium for the generation of the SPM necessary for pulse compression.

Fisher et al. (1969) suggested that picosecond pulses could be compressed to femtosecond durations by employing the large positive chirp obtainable near the center of a short pulse as a result of SPM in optical Kerr liquids. SPM results from the passage of an intense pulse through a medium with an intensity-dependent refractive index. When the relaxation time of the nonlinearity is much less than the input pulse duration, the region where the positive chirp is largest and least dependent on time occurs at about the peak of the pulse and large compression ratios are possible. For longer relaxation times, this region is delayed with respect to the peak of the pulse. Compression is diminished by the influence of relaxation, which not only delays the maximum chirp but also decreases the linear chirp in magnitude and extent. In the limit of the input pulse duration being much shorter than the relaxation time, the resultant chirp would be nonzero only on the wings of the pulse. In fact, if such a pulse were passed through the dispersive delay line, the most intense portion would remain uncompressed. Consequently, Fisher et al. (1969) limited their discussion to picosecond (>5 ps) pulses incident on Kerr liquid $CS_2$. The dominant contribution to the optical Kerr effect in $CS_2$ is molecular orientation, with a relaxation time of ~2 ps (Shapiro and Broida, 1967; Ippen and Shank, 1975a). In the optical Kerr gate experiments of Ippen and Shank (1975a) utilizing subpicosecond pulses incident on $CS_2$, the asymmetries in the transmission of the optical gate have been attributed to the relatively long relaxation time. In the case of fused silica, the dominant contribution to the Kerr coefficient is the optically induced distortion of the electronic charge distribution and is expected to have a relaxation time of $\sim 10^{-15}$ s (Alfano and Shapiro, 1970; Owyoung et al., 1972; Duguay, 1976). Thus, relaxation time effects should be negligible, even for the case of femtosecond duration input pulses, for compression in silica fibers.

In general, when an intense optical pulse passes through a nonlinear medium, the refractive index $n$ is modified by the electric field $E$,

$$n = n_0 + n_2 \langle E^2(t) \rangle + \cdots, \tag{1}$$

where $n_0$ is the refractive index at arbitrarily low intensity and $n_2$ is the optical Kerr coefficient (see Chapters 1 and 2). The time-dependent portion of the

refractive index modulates the phase of the pulse as it propagates through the medium. A phase change $\delta\phi(t)$ is therefore impressed on the propagating pulse:

$$\delta\phi(t) = n_2 \langle E^2(t) \rangle \frac{\omega z}{c}, \tag{2}$$

where $\omega$ is the optical frequency, $z$ is the distance traveled in the Kerr medium, and $c$ is the velocity of light. When relaxation time effects can be neglected, according to Shimizu (1967) and DeMartini et al. (1967), the approximate frequency shift at any retarded time ($t$) is given by the time derivative of the phase perturbation, which is therefore proportional to the time derivative of the pulse intensity

$$\delta\omega(t) = -\frac{d}{dt}\delta\phi(t) = -\frac{\omega z}{c} n_2 \frac{d}{dt}\langle E^2(t) \rangle. \tag{3}$$

The instantaneous frequency $\omega(t)$ will shift from the input optical frequency $\omega_0$ by an amount that depends on the intensity profile

$$\omega(t) = \omega_0 \left[ 1 - \frac{z}{c} n_2 \frac{d}{dt}\langle E^2(t) \rangle \right]. \tag{4}$$

A positive value of $n_2$ for silica implies that the increasing intensity in the leading edge of a short pulse results in an increasing refractive index, or a decreasing wave velocity. As a result of the negative sign in Eq. (4), the instantaneous frequency of the leading edge of the pulse will decrease with respect to $\omega_0$. This time-dependent slowing of the wave reduces the rate at which the wave fronts pass a given point in the fiber, thus reducing the optical frequency. The leading edge of the pulse is therefore red-shifted. On the trailing edge of the pulse there is a corresponding frequency increase, or blue shift, resulting in an increase in the spectral bandwidth of the pulse.

For the propagation of low-intensity optical pulses the input and output frequency spectra would be the same (Ippen et al., 1974). As the intensity increases, the transmitted spectrum is broadened and spectral interference maxima and minima appear as the peak phase shift passes through multiples of $\pi$. As discussed in the next section, the peaks in the self-phase-modulated spectrum can be washed out or filled in by the presence of GVD.

The spectral broadening of an optical pulse is much easier to treat in the time domain than in the frequency domain (Stolen and Lin, 1978). In the time domain the intensity-dependent refractive index causes a phase shift of the center of the pulse with respect to the wings. A phase modulation introduces sidebands on the frequency spectrum. In the absence of GVD, the shape of the pulse does not change with distance along the fiber and the instantaneous phase depends on the pulse intensity. A phase-modulated or chirped pulse is illustrated in Figure 10.2a, indicating that the instantaneous frequency is lower in the leading half of the pulse and higher, than the carrier frequency, in the trailing half of the pulse. The magnitude of this frequency

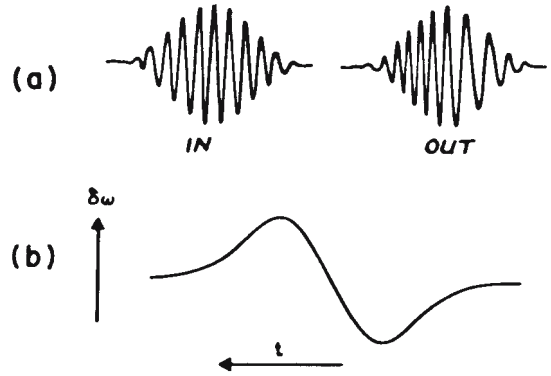


FIGURE 10.2. Effect of an intensity-dependent refractive index on the phase and instantaneous frequency of an optical pulse after propagation down a single-mode fiber.

chirp, in the absence of pulse-shaping effects, builds up in direct proportion to the length of fiber traversed. As illustrated in Figure 10.2b, there is a nearly linear chirp through the central part of the pulse. This region of linear chirp (positive) can be compressed by the linear dispersion (negative) of a grating-pair delay line, by reassembling its frequency components. Treacy (1978, 1979) showed that when two wavelength components, $\lambda$ and $\lambda'$ are incident on a grating pair, the longer wavelength experiences a greater group delay. This group delay is determined by the optical path length traversed. With reference to Figure 10.3a, the relationship between the first-order diffraction angles is

$$\sin(\gamma - \theta) = \frac{\lambda}{d} - \sin\gamma,$$

where $d$ is the grating ruling spacing, $\theta$ is the acute angle between incident and diffracted rays, and $\gamma$ is the angle of incidence measured with respect to the grating normal. The slant distance $AB$ between the gratings is $b$, which equals $G\sec(\gamma - \theta)$ where $G$ is defined as the perpendicular distance between the gratings. The ray path length $PABQ$ (see Figure 10.3a) is given by

$$p = b(1 + \cos\theta) = c\tau,$$

where $\tau$ is the group delay. After considerable algebraic manipulation, the variation of the group delay with wavelength, for various ray path lengths, is found by differentiating $p/c$ with respect to $\lambda$ leading to

$$\frac{\partial\tau}{\partial\lambda} = \left(\frac{b}{d}\right)\left(\frac{\lambda}{d}\right)\frac{1}{c\left[1 - (\lambda/d - \sin\gamma)^2\right]}$$

(see also Chapter 9).

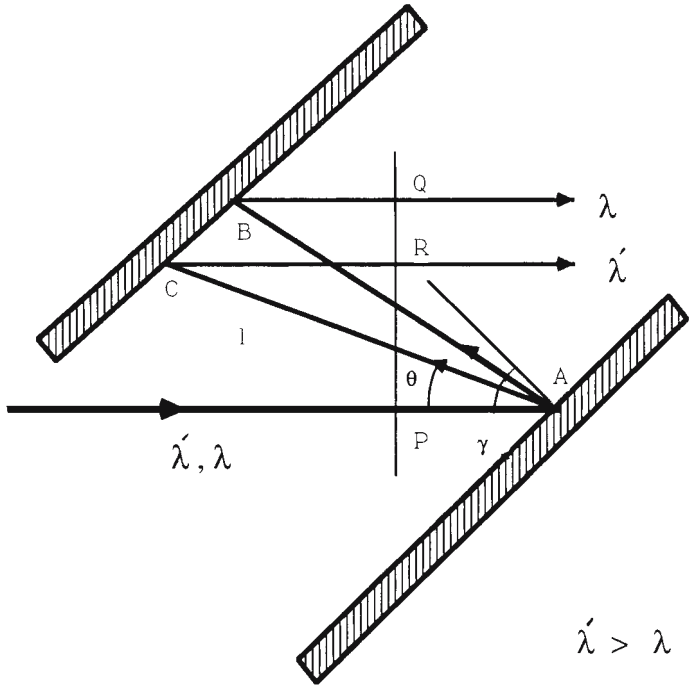


(a)

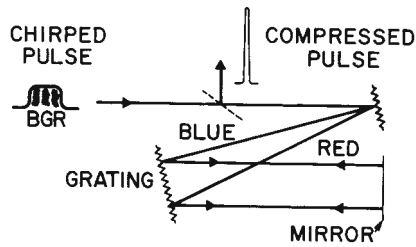


(b)

FIGURE 10.3. (a) Treacy (1978, 1979) "single-pass" geometrical arrangement of diffraction gratings used for pulse compression. The angle of incidence with respect to the grating normal is $\gamma$, and $\theta$ is the acute angle between the incident and diffracted rays. The ray paths are shown for two wavelength components with $\lambda' > \lambda$. Since the path length for $\lambda'$ is greater than that for $\lambda$, longer wavelength components experience a greater group delay. (b) A positively chirped optical pulse with red (R) frequencies leading the blue (B) incident on typical "double-pass" grating-pair compressor.

A typical "double-pass" (Johnson et al., 1984a, 1984b) grating-pair dispersive delay line is illustrated in Figure 10.3. Here the first grating disperses the beam and the second grating makes the spectral components parallel. The path for the red-shifted light is longer than that for the blue, so if the spacing is chosen correctly all the spectral components will be lined up after the second grating. However, the spectral components will not be together spatially and the output beam looks like an ellipse with red on one side and blue on the other. This is corrected by reflecting the beam back through the grating pair, and hence "double-pass," which puts the spectral components back together and doubles the dispersive delay; that is, the rays (blue and red) undergo double delay or retrace. Johnson et al. (1984a, 1984b) revived the use of the "double-pass" grating-pair delay line, introduced by Desbois et al. (1973) and Agostinelli et al. (1979), for the temporal expansion (picoseconds to nanoseconds) and shaping of mode-locked Nd : glass and Nd : YAG laser pulses. In large-compression-ratio experiments, the double-pass delay line cancels the large transverse displacement of the spatially dispersed spectral components of the output beam evident in Treacy's (1968, 1969) "single-pass" grating-pair delay line. The first compressor application of the double-pass delay line was in the 80× compression of mode-locked and frequency-doubled Nd : YAG laser pulses by Johnson et al. (1984a, 1984b).

In the next section the parameters necessary for constructing an optical pulse compressor based on a single-mode fiber and grating pair are described.

## 2.2 Nonlinear Pulse Propagation and Grating Compression

Tomlinson et al. (1984) and Stolen et al. (1984c) have shown, over a fairly broad range of experimental parameters, that the propagation of short, high-intensity pulses in a single-mode fiber can be accurately described by a model that includes only the lowest-order terms in GVD (positive) and SPM. The pulse propagation is modeled by the dimensionless nonlinear wave (Schrödinger) equation:

$$\frac{\partial \mathscr{E}}{\partial (z/z_0)} = -i\frac{\pi}{4}\left[\frac{\partial^2 \mathscr{E}}{\partial (t/t_0)^2} - 2|\mathscr{E}|^2\mathscr{E}\right], \tag{5}$$

where $\mathscr{E}$ is the (complex) amplitude envelope of the pulse. (For a derivation of the nonlinear wave equation see Chapter 3). The time variable $t$ is a retarded time and is defined such that for any distance $z$ along the fiber, the center of the pulse is at $t = 0$, and we assume an input pulse envelope of the form

$$\mathscr{E}(z = 0, t) = A\,\mathrm{sech}(t/t_0). \tag{6}$$

The normalized length $z_0$ and the peak amplitude $A$ are defined by

$$z_0 = 0.322\frac{\pi^2 c^2 \tau_0^2}{|D(\lambda)|\lambda} = 0.322\frac{\pi^2 c \tau_0^2}{|D|\lambda^2} \tag{7}$$

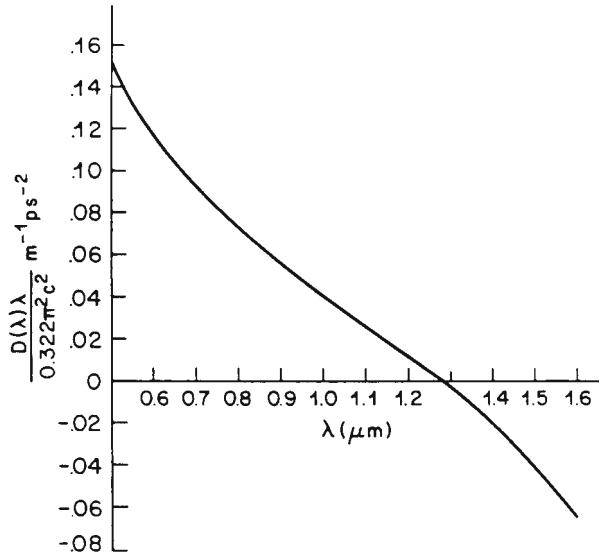


FIGURE 10.4. Plot of the normalized group velocity dispersion for a silica-core fiber. The normalized $z_0$ is obtained in meters by dividing the square of the input pulse width in picoseconds by the value from the plot.

and

$$A = \sqrt{P/P_1}, \tag{8}$$

where

$$P_1 = \frac{nc\lambda A_{\text{eff}}}{16\pi z_0 n_2} \times 10^{-7}\,\text{W}, \tag{9}$$

$\tau_0$ is the pulse width (full width at half-maximum) of the input pulse ($\tau_0 = 1.76t_0$), $D(\lambda)$ or $D$ is the GVD, $D(\lambda)$ in dimensionless units or $D$ in ps-nm/km, $n$ is the refractive index of the core material and $n_2$ is its nonlinear Kerr coefficient in electrostatic units ($1.1 \times 10^{-13}$ esu for silica), $c$ is the velocity of light (cm/s), and $\lambda$ is the vacuum wavelength (cm). Figure 10.4 is a plot of the normalized GVD for a silica-core fiber, based on values of $D(\lambda)$ derived from Gloge (1971) and Payne and Gambling (1975). The peak power of the input pulse is given by $P$, and the quantity $A_{\text{eff}}$ is an effective core area ($\text{cm}^2$), which for typical fiber parameters is fairly close to the actual core area. These normalized parameters come out of the theory for optical solitons in fibers (*negative* GVD), where $z_0$ is the soliton period and $P_1$ is the peak power of the fundamental soliton (Mollenauer et al., 1980). In the present regime of *positive* GVD there are no solitons, but these parameters are still useful because $z_0$ is actually the length of fiber required for GVD to approximately double the width of the input pulse (in the *absence* of SPM), and $P_1$ is the peak

power required for SPM to approximately double the spectral width of the input pulse in a fiber of length $z_0$ (in the *absence* of GVD).

As discussed earlier, an intense optical pulse will be spectrally broadened and frequency chirped on exiting the fiber. The next step of the pulse compression process is to reassemble the chirped pulse with a compressor. The action of the compressor is most easily described in the frequency domain since it is simply a frequency-dependent time delay. The Fourier transform of the pulse can be expressed in the form

$$\delta(z,\omega) = A(\omega)e^{i\phi(\omega)}, \tag{10}$$

where $A(\omega)$ and $\phi(\omega)$ are the amplitude and phase (for simplicity we do not indicate their $z$ dependence explicitly). The effect of the compressor can be described by a phase function $\phi_c(\omega)$, so that the Fourier transform of the compressed pulse is given by

$$\mathscr{E}_c(z,\omega) = A(\omega)\exp\{i[\phi(\omega)+\phi_c(\omega)]\}. \tag{11}$$

If $\phi_c(\omega) = -\phi(\omega)$, then at $t = 0$ all the frequency components of the pulse will be in phase and will thus create the pulse with the maximum peak amplitude. We assume that it is also the shortest possible compressed pulse or close to it. We define this compressor as *ideal*.

One of the most useful types of compressors is the Treacy (1968, 1969) grating-pair compressor. A grating-pair compressor has a delay function that is approximately of the form

$$\phi_c(\omega) = \phi_0 - a_0\omega^2. \tag{12}$$

The compressor constant $a_0$ can easily be adjusted by varying the grating separation and is thus a directly accessible experimental parameter. We use the term *quadratic* compressor to refer to a compressor with a response function of the form of Eq. (12). It can be shown that the Fourier transform of a pulse with a linear frequency chirp, which means that the temporal phase is proportional to $t^2$, has a phase that is proportional to $\omega^2$, so that, for a linearly chirped pulse, a quadratic compressor is the *ideal* compressor. To the extent that the frequency chirp on a pulse is nonlinear, a quadratic compressor is not the ideal compressor for that pulse, but if the departure is not too large, a quadratic compressor can still give reasonably good compression. The expression for the grating constant is

$$a_0 = \frac{b\lambda^3}{4\pi c^2 d^2 \cos^2\gamma'}, \tag{13}$$

where $b$ is the center-to-center distance between the two gratings, $d$ is their groove spacing, $\lambda$ is the center wavelength of the pulse, and $\gamma'$ is the angle between the normal to the input grating and the diffracted beam at $\lambda$. From the numerical solutions of Eq. (5), which includes GVD, Tomlinson et al. (1984) and Stolen et al. (1984c) were able to derive an expression for the grating constant in terms of the input pulse duration and peak amplitude,

$$a_0/t_0^2 \approx \tau/\tau_0 \approx 1.6/A \tag{14}$$

or

$$a_0 \approx 0.52\,\tau_0^2/A. \tag{15}$$

An expression for the grating separation can also be generated in terms of these experimental parameters by combining Eqs. (13) and (15):

$$b \approx \frac{2.08\pi c^2 d^2 \cos^2\gamma'}{\lambda^3}\left(\frac{\tau_0^2}{A}\right). \tag{16}$$

For the limiting case of zero GVD, the numerical results for the optimum quadratic compressor lead to

$$a_0/t_0^2 \approx 0.25\left(A^2 z/z_0\right)^{-1}. \tag{17}$$

Using Eqs. (13) and (17) as well as the pulse length normalization ($\tau_0 = 1.76t_0$), the grating separation in the absence of GVD is given by

$$b \approx \frac{0.323\pi c^2 d^2 \cos^2\gamma'}{\lambda^3}\left(\frac{\tau_0^2}{A^2 z/z_0}\right). \tag{18}$$

It is interesting to discuss the role GVD plays in the pulse compression process. In simulating the compression of picosecond pulses chirped by propagating in the nonlinear Kerr liquid $CS_2$, Fisher and Bischel (1975) concluded that GVD would have the influence of expanding the temporal region over which the chirp was relatively linear, resulting in optimum compression. Grischkowsky and Balant (1982a, 1982b) were the first to realize the significance of GVD in fiber-grating compression. During passage through the fiber, both the pulse shape and the frequency bandwidth are broadened by the combined action of SPM and positive GVD. Thus, the red-shifted light generated at the leading edge of the pulse travels faster than the blue-shifted light generated at the trailing edge, and this leads to pulse spreading and rectangular pulse shapes. Because the new frequencies are generated primarily at the leading and trailing edges, which gradually move apart in time, the pulse develops a linear frequency chirp over most of the pulse length. These "enhanced frequency chirped" (Grischkowsky and Balant, 1984a, 1984b) pulses can lead to almost ideal compression by a grating pair. Negligible GVD, on the other hand, can lead to large deviations from linearity of the chirp, which can result in substantial wings or sidelobes on the compressed pulse.

Optimum fiber-grating compression requires the appropriate choice of the fiber length and grating spacing for optimum chirp and chirp compensation, respectively. These length scales can vary over an enormous range. For example, Knox et al. (1985) compressed 40-fs pulses to a duration of 8 fs using 7 mm of fiber and a grating separation of approximately 1 cm. On the other extreme, Johnson et al. (1984a, 1984b) compressed 33-ps pulses to a duration of 410 fs using 105 m of fiber and a grating separation of 7.2 m. For

a particular input pulse width, peak power, wavelength, and fiber core area, the optimal chirp occurs for a single fiber length. The optimal fiber length varies as

$$z_{\text{opt}} \propto \tau_0^2/\sqrt{P}. \tag{19}$$

Not unexpectedly, the grating separation has the same dependence on input pulse width and peak power (see Eqs. (8) and (16)).

Two limiting fiber length regimes of practical interest can be identified (Tomlinson et al., 1984; Stolen et al., 1984). The first is that of a fiber of optimum length to provide the best linear chirp (Grischkowsky and Balant, 1982a, 1982b). The second regime is that for which the length is much less than optimal and the effects of GVD can be neglected. Some of the properties of the chirp and compression in these two limiting regimes are illustrated in Figure 10.5, where the compression factor is about 12.5× in each case. Displayed in Figure 10.5 are the pulse shape exiting the fiber, the frequency spectrum, the chirp, and the compressed pulse for both optimum quadratic and ideal compressors. If GVD is negligible, the fiber output pulse will have the same shape and intensity as the input pulse, while in a fiber of optimum length GVD will broaden the output pulse by about a factor of 3×. As pointed out by Grischkowsky and Balant (1982a, 1982b), a "squared" or

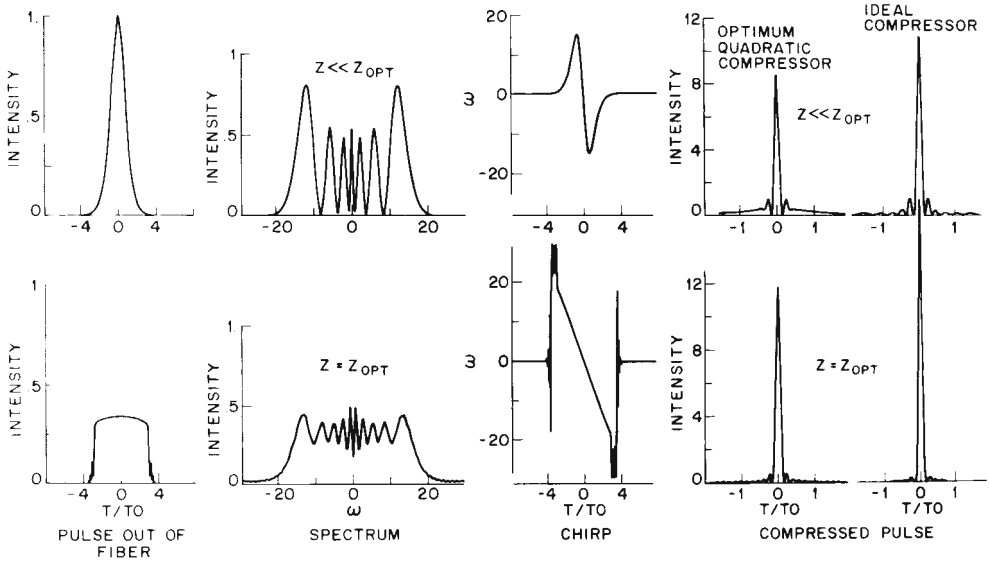


FIGURE 10.5. Pulse shapes before and after grating compression, frequency spectra, and chirp for the limiting regimes of optimal fiber length and of negligible group velocity dispersion. The upper curves are for the case of negligible GVD and an intensity-length product $A^2z/z_0 = 12.5$. The lower curves are for $A = 20$ and the corresponding optimum fiber length of $z_{\text{opt}} = 0.075z_0$. To compare the quality of compression in the two regimes, a common compression factor of approximately 12.5× was chosen in each case.

TABLE 10.1. Fiber-grating compressor parameters.[a]

$$C_1 = \frac{D(\lambda)\lambda}{0.322\pi^2 c^2} = \begin{cases} 0.144 & (\lambda = 0.5145\,\mu\text{m}) \\ 0.138\,\text{m}^{-1}\text{ps}^2 & (\lambda = 0.532\,\mu\text{m}) \\ 0.117 & (\lambda = 0.600\,\mu\text{m}) \\ 0.031 & (\lambda = 1.064\,\mu\text{m}) \end{cases}$$

$$P_1 = \frac{nc\lambda A_{\text{eff}}}{16\pi z_0 n_2} = 7.92\left[\frac{\lambda(\text{cm})A_{\text{eff}}(\text{cm})^2}{z_0(\text{cm})}\right] \times 10^{14}\,\text{W}$$

| $z = z_{\text{opt}}$ | $z << z_{\text{opt}}$ |
|---|---|
| $\tau_0/\tau \approx 0.63A$ | $\tau_0/\tau \approx 1 + 0.9[A^2 z/z_0]$ |
| $z_{\text{opt}}/z_0 \approx 1.6/A$ | — |
| $b \approx 84C_2 \dfrac{\text{cm}}{\text{ps}^2}\left[\dfrac{\tau_0^2}{A}\right]$ | $b \approx 13C_2 \dfrac{\text{cm}}{\text{ps}^2}\left[\dfrac{\tau_0^2}{A^2 z/z_0}\right]$ |

$$C_2 = \left[\frac{d(\text{cm})}{5.56 \times 10^{-5}}\right]^2 \left[\frac{600}{\lambda(\text{nm})}\right]^3 \cos^2\gamma'$$

[a] $z_0 = \tau_0^2/C_1$; $A = \sqrt{P/P_1}$; $\tau_0 = 1.76\tau_0$.

"rectangular" fiber output pulse will have a linear frequency chirp over most of the length of that pulse. The overall width of the frequency spectrum is about the same in the two cases, but GVD acts to fill in the spectrum. For each length, the grating separation was optimized to give the maximum peak intensity. The optimum fiber length was chosen to maximize the energy in the compressed pulse. In Figure 10.5 it is interesting to note that when the fiber length and grating separation are optimized, the quality of the compressed pulse (optimum quadratic compressor) is better than that with the ideal compressor in the absence of GVD.

The procedure of Tomlinson et al. (1984) and Stolen et al. (1984c) for calculating the compression, the optimal fiber length, and the grating separation is presented in Table 10.1. There are two important normalized parameters. The first is the normalizing length $z_0$ defined Eq. (7), and the second is the normalized amplitude $A$ defined in Eq. (8). For a silica-core fiber the GVD parameter $C_1$ has been given for several common laser wavelengths but can also be read directly from Figure 10.4 for an arbitrary wavelength. Table 10.1 also gives approximate expressions for the compression factor $\tau_0/\tau$, the optimum fiber length $z_{\text{opt}}$, and the grating separation $b$ in both limits of fiber length (see Eqs. (16) and (18)). These expressions are supported by a recent approximate analytical theory of the compression process reported by Meinel (1983). The angle $\gamma'$ is between the normal to the grating and the diffracted beam. For $A \leq 3$, the compression and pulse quality are not strong functions of fiber length, so there is no clear optimum length. This fact is consistent with the results of Shank et al. (1982) in which 90-fs pulses were compressed with fiber lengths between 4 and 20 cm and produced the same factor of 30× compression.

Johnson et al. (1984a, 1984b) used these numerical calculations to design the first "long" pulse fiber-grating compressor for 33-ps pulses (0.532 $\mu$m)

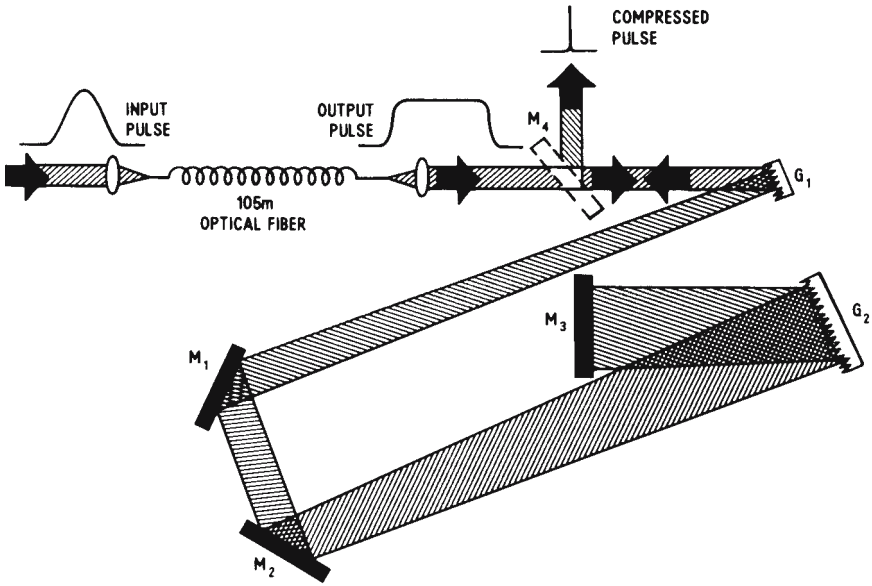


FIGURE 10.6. Schematic drawing of the "double-pass" fiber-grating pulse compressor used for the 80× compression of 0.532-$\mu$m pulses. The dispersive delay line consists of gratings $G_1$ and $G_1$ (1800 grooves/mm) and mirrors $M_1$, $M_2$, and $M_3$. Mirror $M_4$ is cut in half to allow the fiber output pulse to pass over it. $M_3$ is slightly tilted downward to allow the output beam to be reflected by $M_4$ out of the compressor. The round-trip distance between the gratings was 724 cm.

from a frequency-double Nd:YAG laser. The calculation deduced an optimum fiber length $z_{opt}$ = 83 m, a grating separation $b$ = 606 cm (1800 grooves/mm), and a compressed pulse width $\tau$ = 350 fs. The experiment consisted of coupling 240-W pulses into a 105-m single-mode polarization-preserving fiber (Stolen et al., 1978) with a core diameter of 3.8 $\mu$m. A schematic drawing of the fiber-grating compressor is displayed Figure 10.6. Compressed pulses as short as 410 fs or a compression of 80× was obtained with a grating separation of 724 cm. The fiber input pulse and the compressed pulse are displayed together in Figure 10.7. The agreement between calculation and experiment was quite remarkable in light of the fact that the calculations were for normalized amplitudes $A \leq 20$. The compression experiments had normalized amplitudes of $A > 150$.

As a result of the limited availability of high-reflectivity gratings at 0.532 $\mu$m with greater groove densities than 1800 grooves/mm it was important to keep the input pulse width as short as possible to avoid an unreasonable grating separation. The grating separation varies as the square of the input pulse width (see Eq. (16)). This is not as serious a problem at 1.064 $\mu$m, where the cubic wavelength dependence is quite helpful in keeping the grating

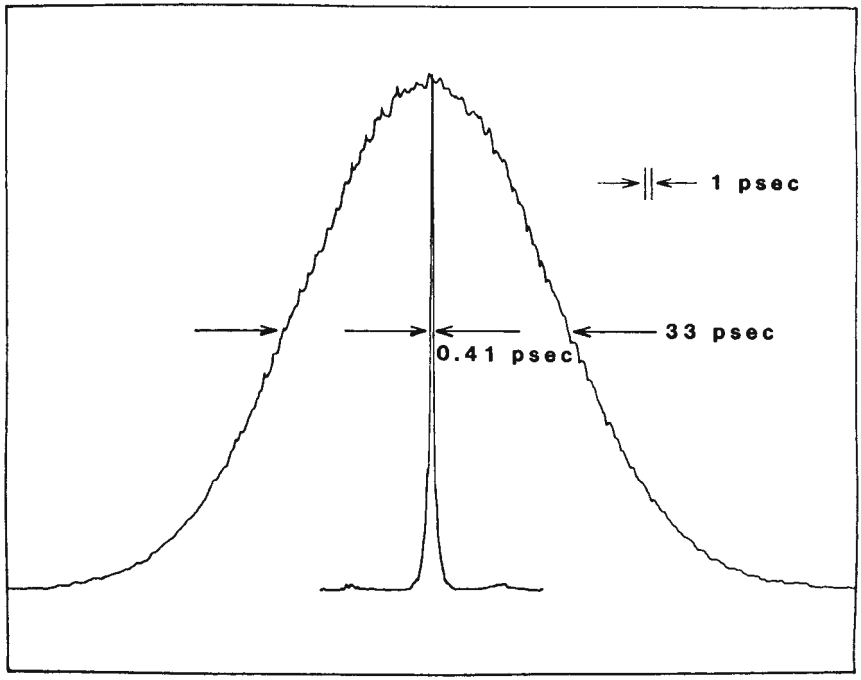


FIGURE 10.7. 80× compression of 33-ps, 0.532-$\mu$m pulses. Standard background-free autocorrelation of the input and compressed pulses displayed on the same scale. (Input: Gaussian pulse shape. Compressed pulse: $\text{sech}^2$ pulse shape.)

separation reasonable. The 33-ps fiber input pulses were obtained by frequency doubling a harmonically mode-locked CW Nd:YAG laser (Johnson and Simpson, 1983, 1985a; Keller et al., 1988). As opposed to fundamental mode locking, typical harmonic mode-locked pulse widths are 50 ps at 1.064 $\mu$m (Johnson and Simpson, 1985a) (see Figure 10.8). If 50- to 60-ps fiber input pulses (0.532 $\mu$m) from a standard fundamentally mode-locked laser were used, a grating separation of greater than 14 m would have been needed.

At this point it is useful to give a pulse compression example replete with experimental parameters, numerical calculation parameters, and the resultant numerical simulation of the compression process. This next example of 0.532 $\mu$m pulse compression was performed using a separate, larger-core fiber distinct from that discussed earlier in Johnson et al. (1984a, 1984b). A "flat" polarization-preserving fiber made by preform deformation (Stolen et al., 1984b) with a 4.1-$\mu$m silica-core diameter. A micrograph of the fiber is shown in Figure 10.9. The birefringence resulting from the stress cladding lifts the degeneracy of the two orthogonal modes of propagation. Thus linearly polarized light propagating along the well-defined principal fiber axis will be

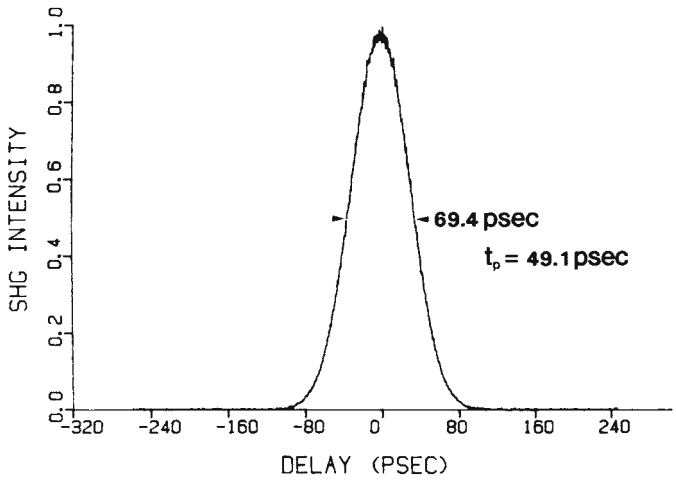


FIGURE 10.8. Background-free autocorrelation of the 1.064-$\mu$m output of a harmonically mode-locked CW Nd:YAG laser (Gaussian pulse shape). These pulses are frequency doubled in $KTiOPO_4$ (KTP) to yield pulses of 33 to 35 ps duration at 0.532 $\mu$m.

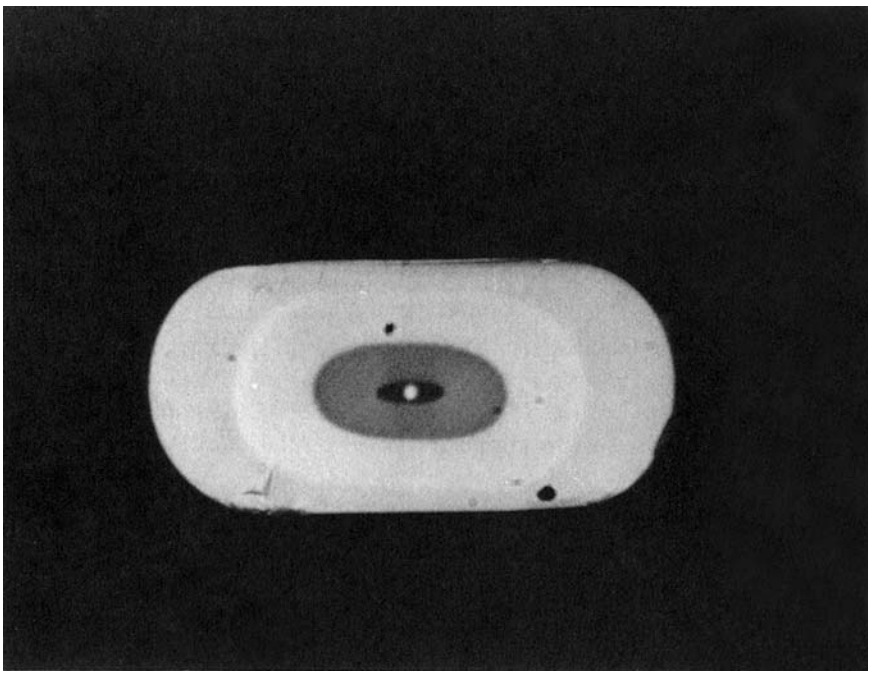

FIGURE 10.9. "Flat" polarization-preserving fiber made by perform deformation. The 4.1-$\mu$m pure silica core is surrounded by a B:Ge: $SiO_2$ stress cladding, an F:$SiO_2$ outer cladding, followed by a pure silica support cladding. The "rectangular" fiber has overall dimensions of $100 \times 200\,\mu$m.

preserved. The diffraction efficiency of the gratings is a very sensitive function of the polarization of the fiber output. Thus, polarization-preserving fiber is extremely useful in reducing amplitude fluctuations in the compressed output due to polarization "scrambling" effects in fibers. One disadvantage of using polarization-preserving fibers is that the threshold for stimulated Raman scattering (SRS) is reduced by a factor of 2 in fibers maintaining linear polarization (Stolen, 1979a). Experimentally, it was found that the reduced SRS threshold was a small price to pay for the increased amplitude stability afforded by polarization-preserving fiber. The effects of SRS on compression are discussed in the next section.

For comparable compression, this larger core diameter fiber resulted in the reduction of SRS by about a factor of 2. The fiber length was 93.5 m and had a loss of 16 db/km at 0.532 $\mu$m. At the input lens (10× objective) the peak power was 235 W (820 MW average, 100 MHz repetition rate). However, this is not the best estimate of the peak power actually coupled into the fiber. The best approach is to measure the light coupled out of the fiber and correct for the transmission of the output lens and the known loss in the given length of fiber. This approach corrects for the loss in the input lens, mode-matching effects, light coupled into the cladding, and the reflection loss on the fiber input face. In this instance the peak power actually coupled into the fiber is closer to 172 W. The fiber-grating compressor parameters given in Table 10.1 can be calculated with the following information: $P = 172$ W, $\tau_0 = 35$ ps, $n = 1.46$, $A_{\text{eff}} = 0.92A_{\text{core}} = 1.21 \times 10^{-7}$ cm$^2$, $n_2 = 1.1 \times 10^{-13}$ esu, $P_1 = 5.74$ mW, $A = 173$, $z_0 = 8.88$ km, $d = 5.56 \times 10^{-5}$ cm, and $\gamma' = 32.5°$. The calculations indicate an optimum fiber length $z_{\text{opt}} = 82$ m, a grating separation of 603 cm, and a compressed pulse width of 320 fs. With this fiber, pulses have been compressed to durations as short as 430 fs (80× compression). The typical day-to-day duration of the compressed pulses falls in the range 460 to 470 fs (Johnson and Simpson, 1985a, 1986). The actual grating separation used to generate the 460-fs pulse displayed in Figure 10.10 was 698 cm.

What actually happened to the 35-ps, 235-W pulse as it propagated through the fiber-grating compressor to produce the clean 460-fs pulses at the output? The spectral width of the fiber input pulses was measured to be 0.27 Å and was limited by the slits on the spectrometer. The self-phase-modulated spectrum of the output pulse was broadened to 17.2 Å and is displayed in Figure 10.11. GVD acted to fill in the self-phase-modulated spectrum, resulting in a flattened spectrum. The fiber output pulse was substantially broadened to a duration of 142 ps and is displayed in Figure 10.12. The triangular autocorrelation function is indicative of a rectangular intensity profile. As pointed out by Grischkowsky and Balant (1982a, 1982b), a rectangular fiber output pulse will have linear frequency chirp over most of its length and result in optimum compression by a grating pair.

The two symmetrically located sidelobes on the fiber output frequency spectrum in Figure 10.11 are not expected from pure SPM. To determine the origin of these sidelobes Tomlinson et al. (1985) performed numerical

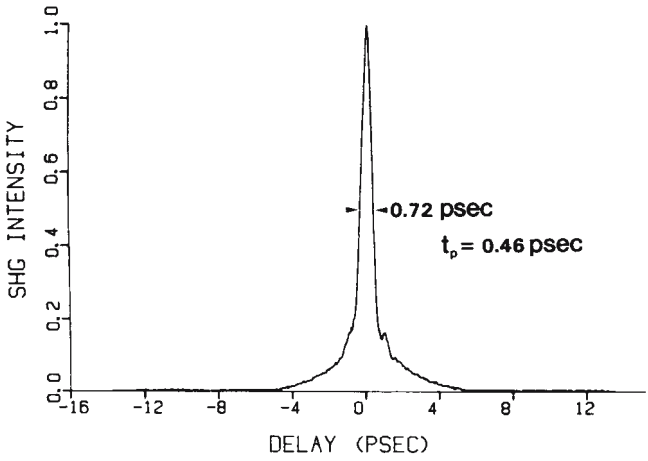


FIGURE 10.10. Typical autocorrelation of the compressed 0.532-$\mu$m pulses using a 93.5-m length of the "flat" polarization-preserving fiber displayed in Figure 10.9. Typical day-to-day pulses fall into the range of 460 to 470 fs.

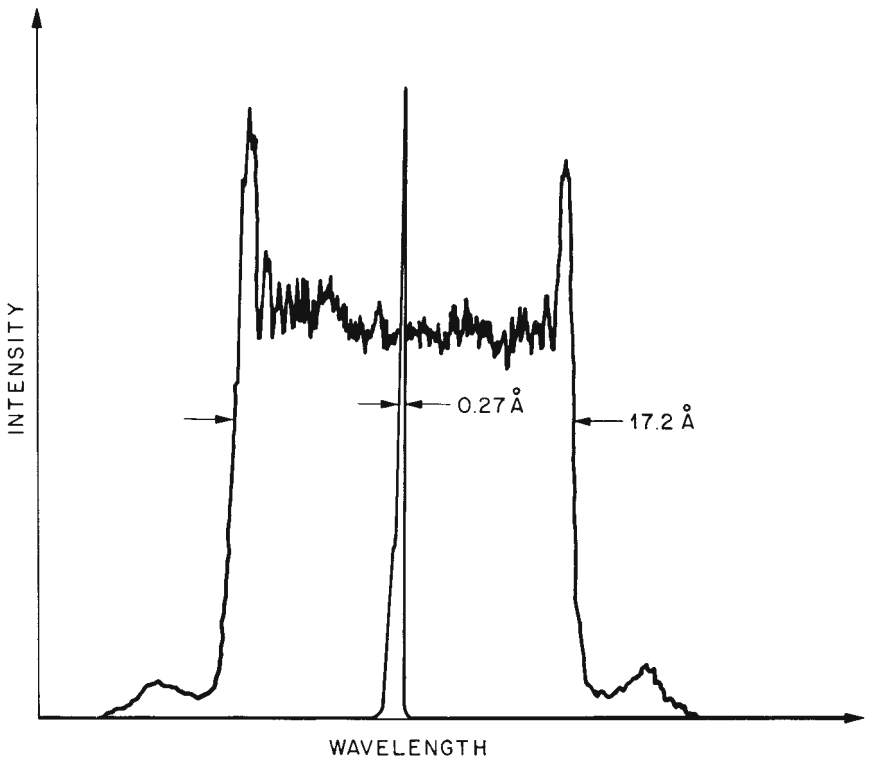


FIGURE 10.11. Spectral width of the 35-ps, 235-W, 0.532-$\mu$m fiber input pulses and the spectrally broadened (by SPM) output pulses after propagation down a 93.5-m length of the 4.1-$\mu$m core diameter polarization-preserving fiber.

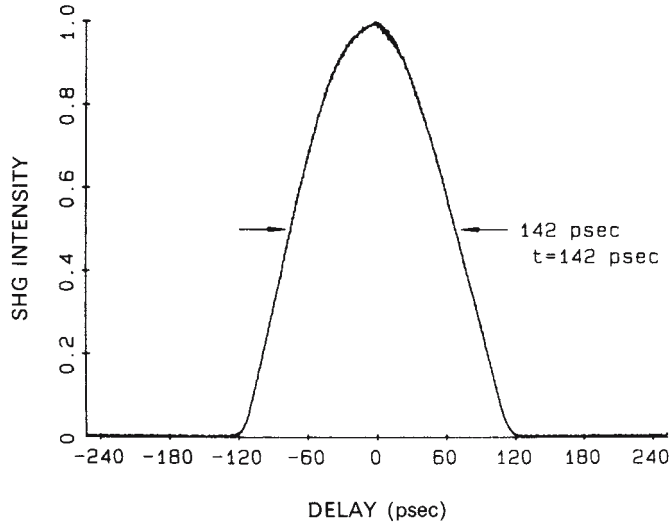


FIGURE 10.12. Autocorrelation of the fiber output pulse broadened by GVD. A triangular atuocorrelation function is indicative of a rectangular intensity profile that has a deconvolution factor of unity.

simulations of the nonlinear pulse propagation using the experimental and calculated numerical parameters given previously. The results of several of the numerical calculations are given in Figure 10.13. This figure presents the nonlinear pulse propagation as a function of fiber length $z/z_0$. In Figure 10.13a, at $z/z_0 = 0.0020$ ($z = 18\,\text{m}$), the temporal shape of the pulse is only slightly broadened (the input pulse width is $1.76t_0$), and the instantaneous frequency function and spectrum are characteristic of pure SPM. Recall that the calculated optimum fiber length is $z_{\text{opt}} = 82\,\text{m}$. In Figure 10.13b, at $z/z_0 = 0.0054$ ($z = 48\,\text{m}$), the temporal shape has become more "rectangular" as a result of the influence of GVD. The instantaneous frequency function indicates a nearly linear frequency chirp over a significant portion of the pulse width. In Figure 10.13c, at $z/z_0 = 0.0060$ ($z = 53\,\text{m}$), as the fiber length approaches $z_{\text{opt}}$ the chirp "linearization" proceeds as a result of the concomitant pulse broadening.

Figure 10.14 displays the instantaneous frequency function, the temporal pulse shape, and its frequency spectrum, for a length at $z/z_0 = 0.01$ ($z = 89\,\text{m}$), for a lossless fiber and for a fiber with a loss of 16 db/km (normalized loss parameter $\alpha = 16.36$). The nonlinear Schrödinger equation (Eq. (5)) with the inclusion of a normalized linear loss parameter $\alpha$ is given by

$$\frac{\partial \mathscr{E}}{\partial (z/z_0)} = -i\frac{\pi}{4}\left[\frac{\partial^2 \mathscr{E}}{\partial (t/t_0^2)} - 2|\mathscr{E}|^2 \mathscr{E}\right] - \alpha \mathscr{E}. \tag{20}$$

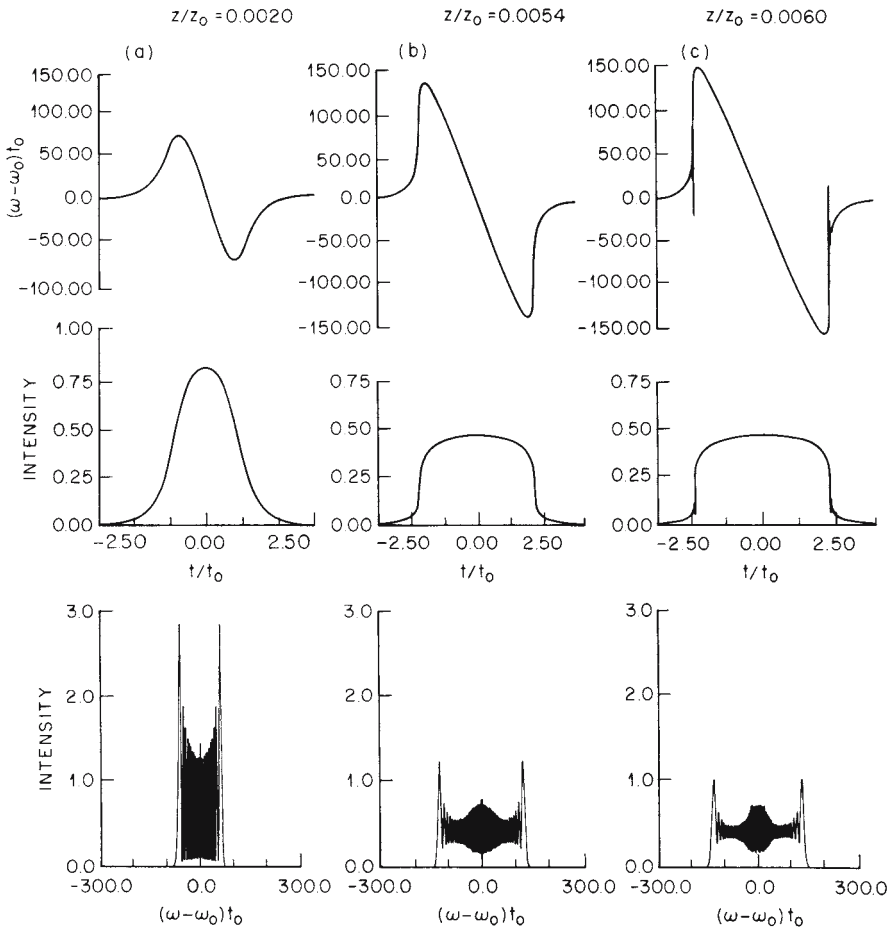


FIGURE 10.13. Numerical simulations of the nonlinear pulse propagation of 34.4-ps pulses ($t_0 = 19.5$ ps) at 0.532 $\mu$m with a normalized input amplitude of $A = 173$ and normalizing fiber length of $z_0 = 8.88$ km displayed as a function of fiber length $z/z_0$. The upper curves show the instantaneous frequency as a function of time, the middle curves show the intensity as a function of time, and the lower curves show the frequency spectra of the pulses. For the 93.5-m fiber used the normalized length was $z/z_0 = 0.0105$.

In Figure 10.14a and b the resulting pulse shape shows well-development interference fringes on the leading and trailing edges. The frequency spectra clearly display the symmetrically located sidelobes. The spectrum for the fiber with loss (Figure 10.14b) is in excellent agreement with the experimental spectrum of Figure 10.11. (Since the experimental spectrum is an average over many pulses, we do not expect to see the fine structure displayed in the calculated spectrum.) Simulations of the effect of a grating-pair compressor on these fiber output pulses gave a compression of 98× for the lossless fiber and

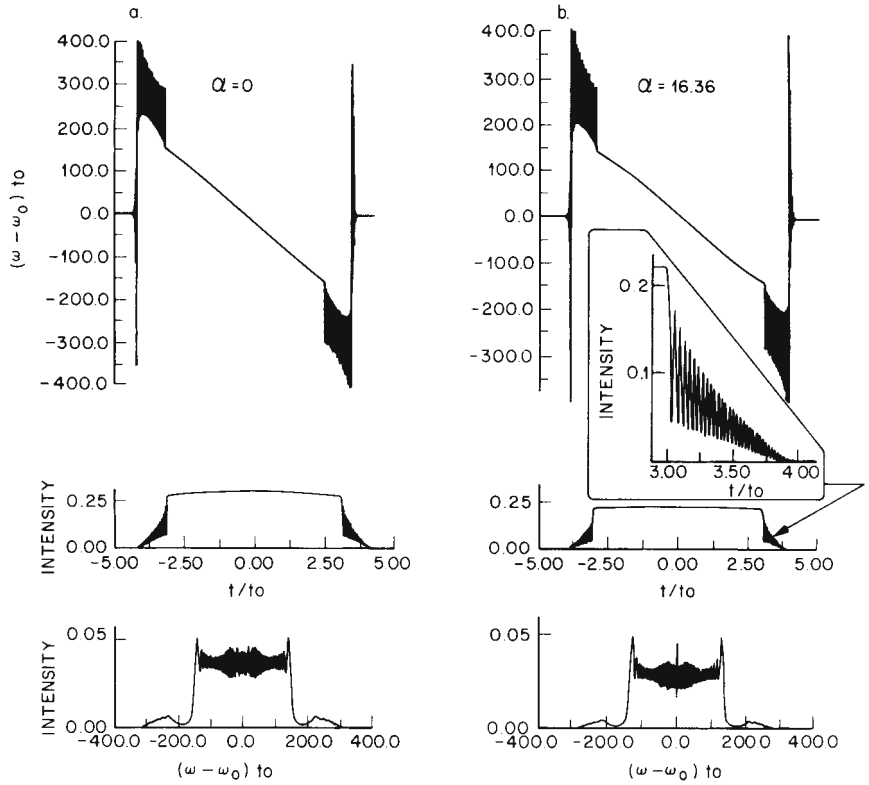


FIGURE 10.14. Numerical simulations of nonlinear pulse propagation for $A = 173$ and a fiber length of $z/z_0 = 0.01$ for (a) a lossless fiber and (b) a fiber with a normalized loss parameter $\alpha = 16.36$ (16 db/km). The upper curves are the instantaneous frequency, the middle curves are the temporal shape of the output pulse, and the lower curves show the frequency spectra of the output pulses. The inset in (b) displays a detail of the interference region (optical wave-breaking) on the edge of the pulse.

of 84× for the fiber with loss. Thus by including the fiber loss in the nonlinear Schrödinger equation, numerical solutions of Eq. (20) are in excellent agreement with the experimentally observed 80× compression.

The origin of the sidelobes in the frequency spectrum of the fiber output pulses on Figures 10.11 and 10.14 has been attributed to a phenomenon that Tomlinson et al. (1985) dubbed "optical wave-breaking." Briefly, when an intense pulse propagates down an optical fiber, the leading edge of the pulse experiences a frequency decrease or red shift, while the trailing edge experiences a blue shift. For large-compression experiments (large values of the normalized amplitude $A$) in the presence of GVD, the red-shifted light near the leading edge of the pulse travels faster than, and overtakes, the unshifted light in the forward tails of the pulse (and vice versa on the trailing edge). Therefore, the leading and trailing regions of the pulse will contain light at two dif-

ferent frequencies, which will interfere and generate new frequencies. These new frequencies appear as the sidelobes on the fiber output spectrum and result in a small increase in the background on the compressed pulse. This phenomenon is somewhat analogous to the "breaking" of water wave and has been described as optical wave-breaking. Optical wave-breaking can also occur in small-compression-ratio experiments (small values of $A$) if the fiber is longer than the optimum fiber length, so that there is sufficient GVD to mediate the interference process. The interference fringes resulting from the optical wave-breaking are prominent in the calculated temporal pulse shapes (see inset of Figure 10.14b). Since the spectral bandwidth that contributes to the compressed pulse is approximately twice the frequency difference involved in the wave-breaking interference, the period of the interference fringes is approximately twice the width of the compressed pulse. Additional evidence for optical wave-breaking has appeared in the numerical studies of nonlinear pulse propagation by Lassen et al. (1985).*

These experiments and numerical simulations demonstrate the enormous range of applicability of the nonlinear Schrödinger equation (Eq. (20)) for describing nonlinear pulse propagation in single-mode fibers. Each of the various terms in Eq. (20) represents the lowest-order approximation to the phenomenon that it is describing, and it is assumed that the higher-order terms will be significant for very high compression ratios and/or very short input pulses. The present results indicate that large compression ratios of 80× can accurately be described by Eq. (20) without invoking any higher-order terms. The limits of this fiber-grating compression approach have recently been studied by Bourkoff et al. (1987a, 1987b), Tomlinson and Knox (1987), and Golovchenko et al. (1988).

## 2.3 Stimulated Raman Scattering and Pulse Compression

The interplay between optical fiber pulse compression ($\lambda = 1.3\,\mu$m) and stimulated Raman scattering, or more appropriately the interplay between SPM, SRS, and GVD, could easily fill a book chapter. It is much beyond the scope of this chapter to discuss the role of SRS in great detail. Instead, the reader is referred to a number of excellent articles on SRS and nonlinear pulse propagation in fibers in the region of positive GVD: Auyeung and Yariv, 1978; Butylkin et al., 1979; Dianov et al., 1984b, 1985, 1986a, 1987; Gomes et al., 1986a, 1986b, 1988a; Heritage et al., 1988; Hian-Hua et al., 1985; Johnson et al., 1986; Kuckartz et al., 1987, 1988; Lin et al., 1977; Nakashima et al., 1987; Ohmori et al., 1983; Roskos et al., 1987; Schadt et al., 1986, 1987; Smith, 1972; Stolen and Ippen, 1973; Stolen and Johnson, 1986; Stolen et al., 1984a, 1972; Stolz et al., 1986; Valk et al., 1984, 1985; Weiner et al., 1988. Several of the salient features of SRS are briefly discussed in this section.

---

* Note added in proof: Optical wave-breaking was recently observed (temporally) by Rothenberg and Grischkowsky (1989).

The maximum power of an optical pulse in a fiber is usually limited by SRS. In the region of positive GVD, a Raman Stokes pulse will travel faster than the pump pulse. Thus the role of GVD is important in determining the limitations of SRS on the self-phase-modulated pump pulse. Stolen and Johnson (1986) discussed a simple picture of the SRS process that assumes that the Stokes power builds up from a weak injected signal rather than from spontaneous scattering. This follows the approach of Smith (1972) for CW Raman generation, in which the integrated spontaneous Raman scattering along the fiber can be replaced by a weak effective Stokes input power. At the top of Figure 10.15, a portion of the injected CW Raman signal enters the fiber along with the leading edge of the pump pulse. Because of GVD, this part of the signal will travel faster than the pump and never experience Raman amplification. In the second line of Figure 10.15, a portion of the signal enters the fiber along with the peak of the pump pulse. As the pump pulse travels along the fiber with velocity $V_p$, the faster-traveling Stokes signal ($V_s$) is amplified by extracting energy from the pump. Amplification ceases when the signal has passed through the pump pulse. Maximum amplification will occur for a stokes signal that passes through the entire pump pulse, and this is the portion of the CW signal that enters the fiber along with the trailing edge of the pump pulse (third line of Figure 10.15). If a significant part of the pump energy has been shifted to the Stokes frequency (pump depletion), subsequent portions of the CW signal (fourth and fifth lines of Figure 10.15) will see a much reduced amplification.

The net result is that the amplification of the injected CW signal by the pump pulse has produced a Stokes pulse with a peak that is ahead of the pump pulse by about one pump pulse length (line 7 of Figure 10.15). If we define a walk-off length $l_w$,

$$l_w = \left( \frac{V_s V_p}{V_s - V_p} \right) \tau_0, \tag{21}$$

as the distance in which the Stokes signal passes through one pump pulse width $\tau_0$ the Stokes maximum will be produced about two walk-off lengths into the fiber. All of the Stokes conversion will occur within about four walk-off lengths.

The signal gain depends on distance ($L$) along the fiber, and the net amplification involves an integral over the region where the Stokes and pump pulses interact. In the limit where the Stokes signal sees the entire pump pulse the gain becomes

$$P(L) = P(0)e^G, \tag{22a}$$

$$G \to \frac{g_0 P_0}{A_{\text{eff}}} \int dz \exp\left[ \frac{-1.67z}{l_w} \right]^2 = 1.06 \frac{g_0 P_0 l_w}{A_{\text{eff}}}, \tag{22b}$$

where $g_0$ is the peak Raman gain coefficient, $A_{\text{eff}}$ is the effective core area, and $P_0$ is the peak pump power. Thus, the maximum gain is approximately the

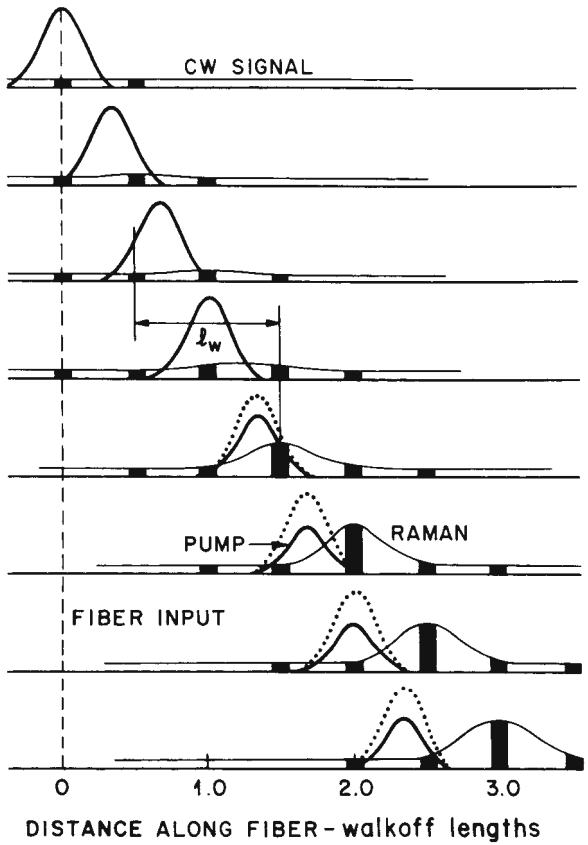


FIGURE 10.15. Schematic representation of a CW Stokes signal amplified as it passes through a pump pulse because of GVD. Portions of the CW signal are separately identified to illustrate that maximum amplification occurs for the part of the CW signal that enters the fiber with the trailing edge of the pump pulse. Earlier portions of the CW signal see reduced gain because they do not pass through the entire pump pulse, and later portions of the signal see reduced gain because the pump pulse has been depleted by earlier Raman conversion. The dotted curve represents the propagation of the pump pulse in the absence of Raman conversion.

peak power times the walk-off length. Typical values of $G$ will be around 16 but can go as high as 20 for significant Raman conversion and small walk-off or interaction lengths. For example, Stolen and Johnson (1986) estimated a value of $G = 19.7$, for 20% Raman conversion of 35-ps, 0.532-$\mu$m pulses, and a walk-off length of 6.2 m.

An estimate of the critical pump power $P_p = P_c$ entering the fiber, for which the intensities of the first Stokes component of SRS and of the pump were equal at the fiber output, was derived for the case of CW SRS by Smith (1972). This approach has proved to be fairly reliable even in the pulsed case.

For the case of *polarization-preserving* fiber, the critical pump power is estimated to be

$$P_c \approx \frac{GA_{\text{eff}}}{g_0 l_w}, \tag{23}$$

and for *non-polarization-preserving* fiber the critical pump power is

$$P_c \approx 2\frac{GA_{\text{eff}}}{g_0 l_w}. \tag{24}$$

The Raman gain in fibers is a factor of 2 higher if linear polarization is maintained (Stolen, 1979) and accounts for the factor of 2 in Eqs. (23) and (24). The peak Raman gain coefficient $g_0$ at a pump wavelength of 0.526 $\mu$m is $1.86 \times 10^{-11}$ cm/W (Stolen and Ippen, 1973). The Raman gain varies linearly with pump frequency and the peak coefficient for a 1.064-$\mu$m pump is $g_0 = 0.92 \times 10^{-11}$ cm/W (Lin et al., 1977).

Fiber-grating compression of optical pulses can be strongly affected by SRS, which at high intensities will distort the pulse profile and consequently the chirp on the pulse. SRS limit the power available in the compressed pulse. Above the Raman threshold, further increases in pump power result only in increased Raman conversion. SRS does not seem to have a major effect on the compression of femtosecond pulses, and this can be attributed to the very short walk-off lengths involved (see Eqs. (21), (23), and (24)). Longer pulses translate into longer walk-off lengths and lower critical powers for the onset of SRS. The compression of the fundamental and the second harmonic of mode-locked Nd : YAG laser falls squarely into this region of competition between SRS, SPM, and GVD. Under conditions of walk-off of the generated Stokes pulse, intense SRS will preferentially deplete the leading edge of the pump pulse and steepen its rising edge. SPM of the reshaped pump pulse causes nonsymmetric spectral broadening and a nonlinear chirp. An example of the distortion of the self-phase-modulated pump spectrum by the presence of 20% Roman conversion (Stolen and Johnson, 1986) is displayed in Figure 10.16. This figure shows the Stokes and pump spectra for 35-ps, 0.532-$\mu$m pump pulses after propagation down 101 m of single-mode polarization-preserving fiber (walk-off length = 6.2 m). The long-wavelength component, or red-shifted frequency component, shows signs of depletion. The resultant nonlinear chirp, of course, leads to very poor fiber-grating compression.

In general, compression in the presence of strong SRS using fiber lengths less than $z_{\text{opt}}$ (i.e., negligible GVD) results in compressed pulses accompanied by broad wings. In addition, the spectral fluctuations lead to severe fluctuations in compressed pulse amplitude and shape. Recently, Weiner et al. (1988) demonstrated that high-quality stabilized compression could be achieved, under these circumstances, only by utilizing an asymmetric spectral window (Heritage et al., 1985a) to select out a linearly chirped portion of the broadened spectrum.

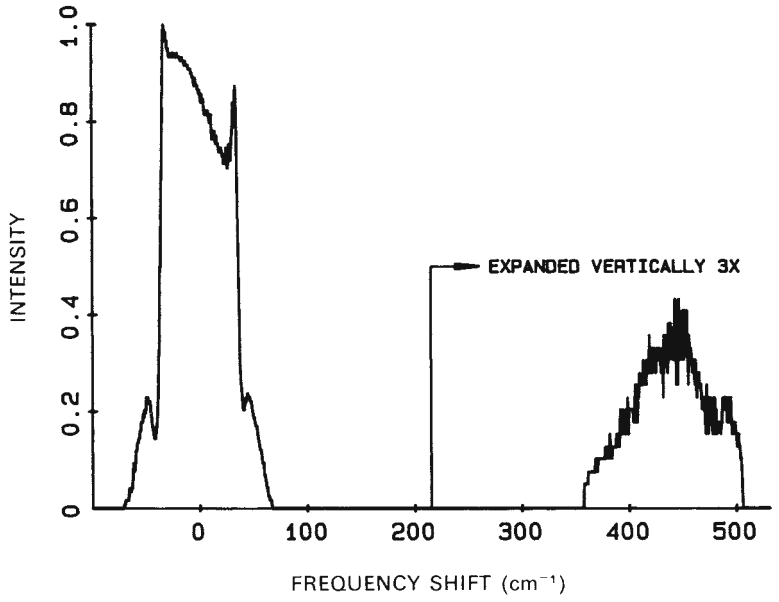


FIGURE 10.16. Raman and pump spectra of 35-ps, 0.532-$\mu$m pulses as measured from a 101-m fiber at about 20% Raman conversion. The self-phase-modulated pump spectrum shows signs of depletion of the long-wavelength or red-shifted frequency components by SRS leading to a nonlinear chirp. (Walk-off length = 6.2 m.)

Another approach to obtaining high-quality stable pulse compression is to avoid or severely limit SRS and use fibers of length $z_{opt}$ to obtain the necessary linear chirp. Johnson et al. (1984a, 1984b) generated high-quality 410-fs pulses (80× compression) at 0.532 $\mu$m with a fiber length greater than $z_{opt}$ and less than 5% Raman conversion. Using fibers of nearly optimum length and operating below the Raman threshold, Roskos et al. (1987) and Dianov et al. (1987) generated high-quality pulses as short as 550 fs (110× compression) at 1.064 $\mu$m.

Earlier pulse compression calculations for shorter fiber lengths clearly indicated that the chirp would be severely distorted and asymmetric as a result of strong SRS (Schadt et al., 1986; Schadt and Jaskorzynska, 1987; Kuckartz et al., 1987). However, Kuckartz et al. (1988) recently demonstrated that in sufficiently long fibers the combined action of GVD and SPM could cause a further reshaping and linearization of the chirp, which then could be efficiently compressed by a grating pair. High-quality pulses with comparatively low substructure as short as 540 fs (130× compression) at 1.064 $\mu$m using 120 m of polarization-preserving fiber were obtained in the presence of strong SRS (Kuckartz et al., 1988). Heritage et al. (1988) recently demonstrated that with a 400-m length of polarization-preserving fiber, significant *third* Raman

Stokes generation, and an asymmetric spectral window (Heritage et al., 1985a), high-quality ultrastable compressed pulses as short as 550 fs (130× compression) at 1.064 $\mu$m could be obtained. They found that most of the pump spectrum was linearly chirped by the strong reshaping due to strong SRS, SPM, and GVD.

Several review and extended-length articles on nonlinear pulse propagation, pulse shaping, and compression in fibers have recently been published: Alfano and Ho, 1988; Dianov et al., 1988; Golovchenko et al., 1988; Gomes et al., 1988b; Kafka and Baer, 1988; Thurston et al., 1986; Zhao and Bourkoff, 1988. (See Chapter 3.) This list of articles is by no means complete and furthermore is limited to discussions in the region of positive GVD.

Thus far, this chapter has dealt with negative dispersive delay lines consisting of Treacy, (1968, 1969) grating pairs in reflection mode. Several alternatives to this approach deserve mentioning. Yang et al. (1985) demonstrated femtosecond optical fiber pulse compression using a holographic volume phase transmission grating pair. Prisms were used as negative dispersive delay lines by Fork et al. (1984), Martinez et al. (1984), and Bor and Racz (1985) and were used in femtosecond optical fiber pulse compression by Kafka and

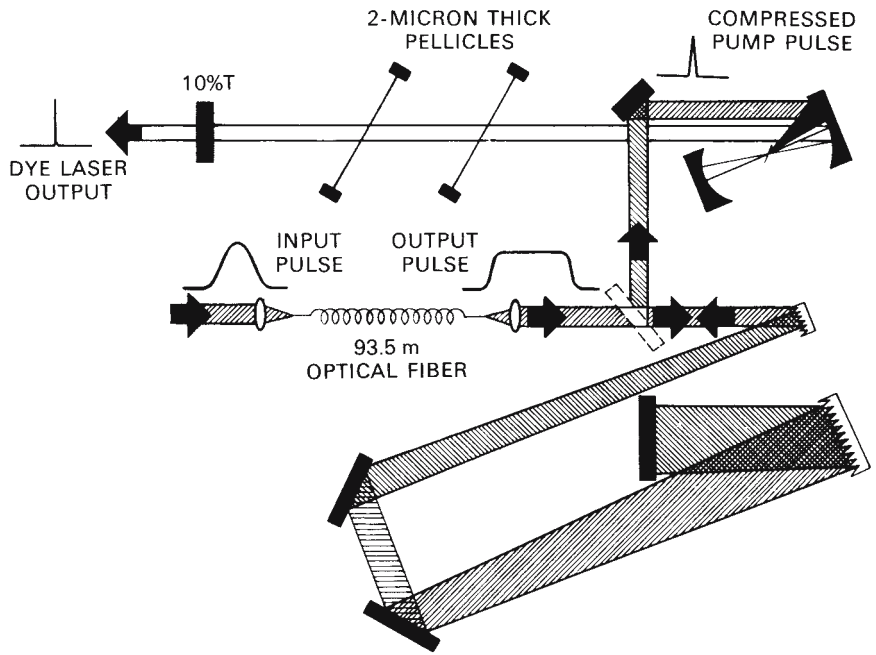


FIGURE 10.17. Schematic of a synchronously mode-locked Rhodamine 6G dye laser pumped by fiber-grating compressed 0.532-$\mu$m pulses. A pair of 2-$\mu$m-thick pellicles or a single-plate birefringent filter was used for wavelength tuning and bandwidth control.

Baer (1987). In another variation, Nakazawa et al. (1988) used a $TeO_2$ acousto-optic light deflector and corner cube combination as a negative dispersive delay to demonstrate femtosecond optical fiber pulse compression.

One of the first applications of "long" fiber-grating compressed pulses was their use by Johnson et al. (1984b), Johnson and Simpson (1985a, 1985b, 1986), Kafka and Baer (1985, 1986), and Beaud et al. (1986) as a source of ultrashort pump pulses for wavelength-tunable femtosecond dye lasers. A schematic of a Rhodamine 6G synchronously mode-locked dye laser pumped by compressed 0.532-$\mu$m pulses is displayed in Figure 10.17. Wavelength-tunable pulses as short as 180 fs (Johnson and Simpson, 1986) were obtained from the dye laser synchronously pumped with 470-fs-duration 0.532-$\mu$m pulses (see Figure 10.18).

Johnson et al. (1984a, 1984b) reported that the duration and functional form of the compressed 0.532-$\mu$m pulses were extremely sensitive to the grating separation (for constant fiber input power). As the grating separation was decreased from its optimum, the compressed pulse would broaden smoothly. Compressed pulses of 460 to 470 fs (Johnson and Simpson, 1985a) duration were obtained with a grating separation of 698 cm (see Figure 10.10). By decreasing the grating separation by 4.2, 15.6, and 27% the compressed pulses were broadened to 920 fs, 12.3 ps, and 22 ps, respectively (see Figure 10.19). Thus a *temporally* tunable source of ultrashort pulses was

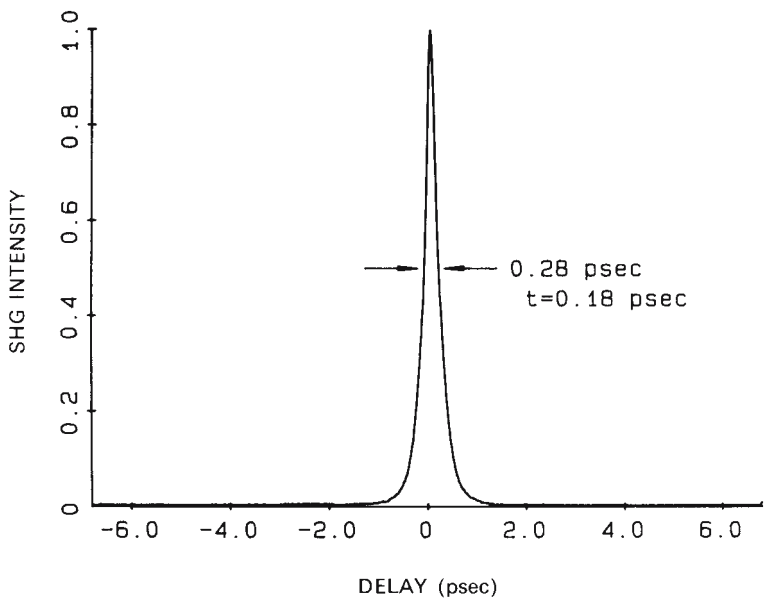


FIGURE 10.18. Autocorrelation function of the pellicle-tuned dye laser synchronously pumped by 470-fs-duration 0.532-$\mu$m pulses, tuned to a wavelength of 0.592 $\mu$m ($sech^2$ pulse shape assumed).

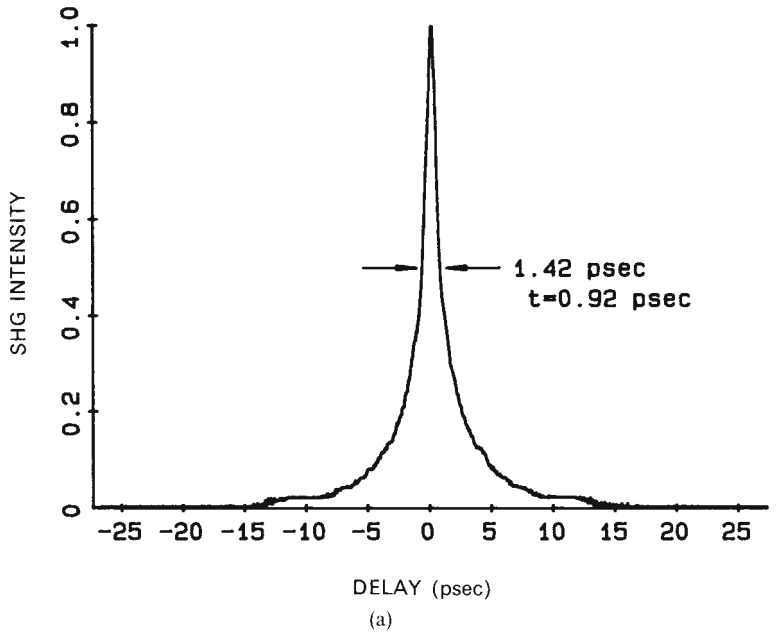


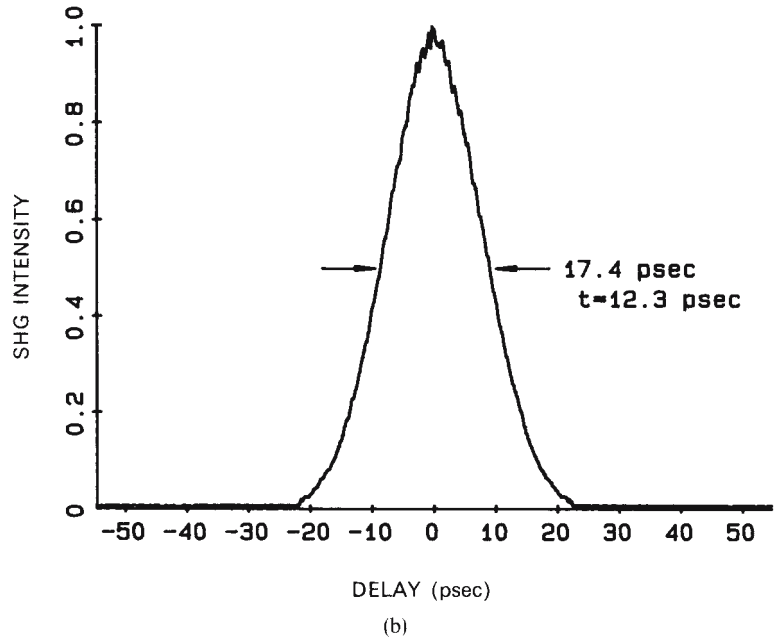


FIGURE 10.19. *Temporal* tuning of compressed 0.532-$\mu$m pulses with decreasing grating separation from the optimum (see Figure 10.10). The grating separation was reduced from the optimum of 698 cm by (a) 4.2% ($\text{sech}^2$ pulse shape), (b) 15.6% (Gaussian pulse shape, and (c) 27% (Gaussian pulse shape).

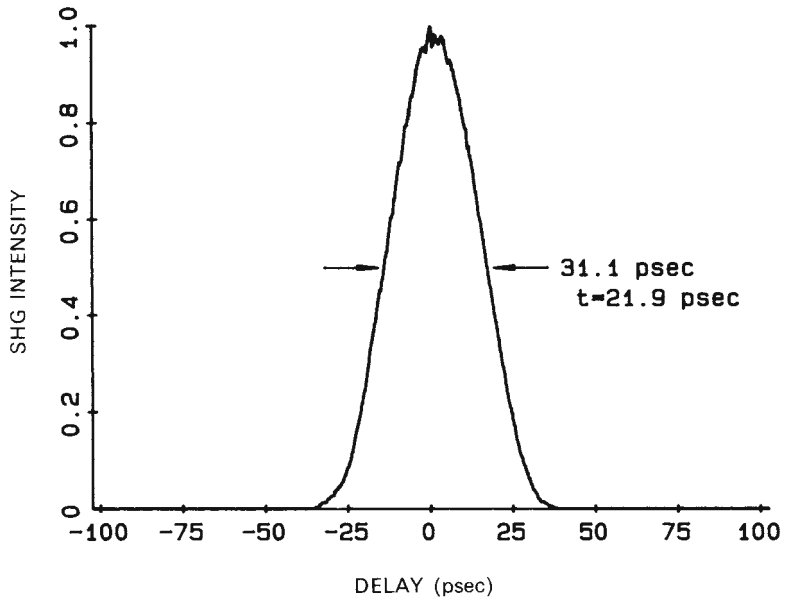


(c)

FIGURE 10.19. (*continued*)

demonstrated. With this source of temporally tunable pump pulses, the first reported investigation of the dynamics of synchronous mode locking as a function of pump pulse duration was made by Johnson and Simpson (1985a). The experimental variation of the dye laser pulse width as a function of the pump pulse width (see Figure 10.20) was

$$t_{\text{dye}} \sim t_{\text{pump}}^{0.52}, \tag{25}$$

in excellent agreement with the square root dependence predicted by Ausschnitt and Jain (1978) and Ausschnitt et al. (1979).

Palfrey and Grischkowsky (1985) generated 16-fs frequency-tunable pulses by using a two-stage fiber pulse compressor together with an optical amplifier. Ishida and Yajima (1986) generated pulses of less than 100 fs tunable over 0.597 to 0.615 $\mu$m by taking the output from a cavity-dumped, hybridly mode-locked CW dye laser and coupling it to a single-stage fiber compressor. Damen and Shah (1988) reported on femtosecond luminescence spectroscopy of III–V semiconductors with 60-fs compressed pulses. The 60-fs pulses were derived from a compressed pulse-pumped synchronously mode-locked dye laser that was further compressed by a fiber-prism pulse compressor.

Applications of fiber-grating compressed pulses include picosecond photoconductive sampling characterization of semiconductor epitaxial films

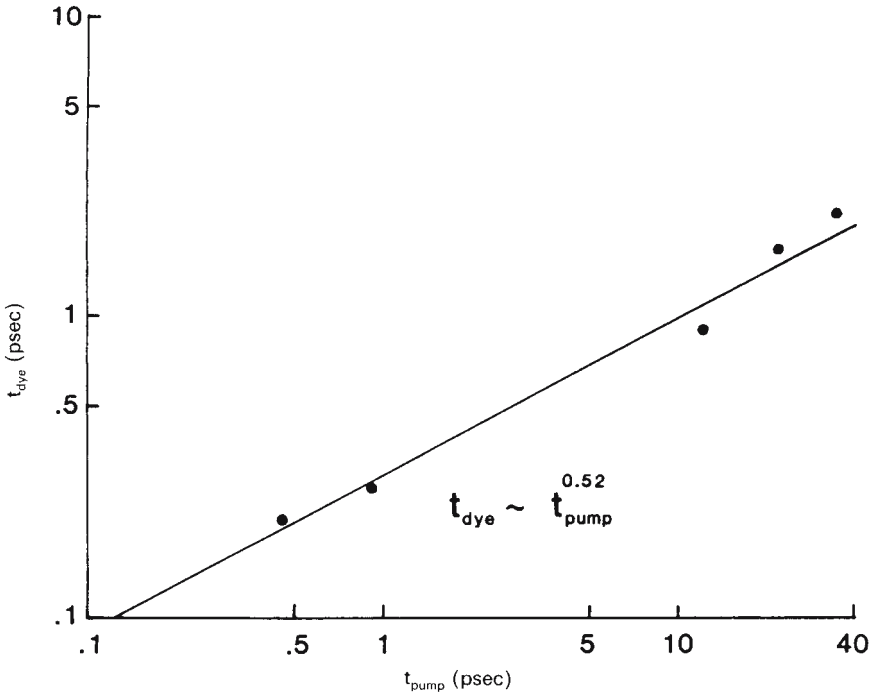


FIGURE 10.20. Temporal dynamics of the synchronous mode locking of the pellicle-tuned Rhodamine 6G dye laser as a function of the pump pulse duration, with the dye laser tuned to 0.595 $\mu$m.

deposited on lattice-mismatched substrates (Johnson et al., 1985, 1987; Feldman et al., 1988), picosecond electro-optic sampling of GaAs integrated circuits (Kolner and Bloom, 1984, 1986; Weingarten et al., 1988), picosecond photoemission sampling of integrated circuits (Bokor et al., 1986; May et al., 1987, 1988) picosecond vacuum photodiode (Bokor et al., 1988), picosecond optical pulse shaping and spectral filtering (Dianov et al., 1985, 1986b; Haner and Warren, 1987; Heritage et al., 1985a, 1985b; Weiner et al., 1986), and the demonstration of an ultrafast light-controlled optical fiber modulator (Halas et al., 1987) and its use in the first experimental investigation of dark-soliton propagation in optical fibers (Krokel et al., 1988).

Recently, pulse compression techniques have been applied to the amplification of high-energy 1.06-$\mu$m pulses. The onset of self-focusing limits the amplification of ultrashort optical pulses. Fisher and Bischel (1974) proposed avoiding self-focusing in Nd : glass amplifiers by temporally broadening the input pulse to lower the pulse intensity. They noted that under certain circumstances, the glass nonlinearity would impress a chirp on the pulse that could subsequently be compressed by a dispersive delay line. Strickland and

Mourou (1985) and Maine et al. (1988) used an optical fiber to stretch a short optical pulse, amplify, and then recompress using a grating pair. Since the stretched pulse is amplified, the energy density can be increased, thereby more efficiently extracting the stored energy in the amplifier.

## 3. Femtosecond Pulse Compression

### 3.1 Theory

Remarkable progress has taken place in the compression of optical pulses. The theoretical limit in the visible spectrum is just a few femtoseconds. Already optical pulses as short as 6 fs have been generated and used in experiments (Fork et al., 1987; Brito Cruz et al., 1986). Such a pulse contains spectral components covering nearly the entire visible and near-infrared region of the spectrum. The short pulse itself is nearly an ideal continuum source.

It is useful to explore the limits of pulse compression in order to understand and appreciate the processes involved in compressing optical pulses in the femtosecond time regime. Attacking the limits provides a pathway for both utilizing and generating ever shorter optical pulses.

When an optical pulse propagates through any dielectric medium, group velocity dispersion broadens the pulse. For example, an 8-fs pulse will have its width doubled by passage through ~1 mm of glass or ~3 m of air. These linear propagation effects are not fundamental and can in principle be corrected by a linear compensation scheme.

One of the most useful pulse compressors, the grating-pair compressor devised by Treacy (1969) has been discussed earlier in this chapter. In his original paper, Treacy pointed out some of the limitations of this compressor for very short optical pulses having a large bandwidth. A grating pair induces a phase distortion on an optical pulse that becomes more severe as the ratio of the pulse bandwidth to the carrier frequency begins to approach unity.

The problem of generating ultrashort optical pulses reduces to minimizing the phase distortion. A useful way to discuss this problem is in terms of the Taylor series expansion of the phase:

$$\phi(\omega) = \phi(\omega_0) + \left(\frac{d\phi}{d\omega}\right)_{\omega_0}(\omega-\omega_0) + \frac{1}{2}\left(\frac{d^2\phi}{d\omega^2}\right)_{\omega_0}(\omega-\omega_0)^2 + \frac{1}{6}\left(\frac{d^3\phi}{d\omega^3}\right)_{\omega_0}(\omega-\omega_0)^3, \tag{26}$$

which is made around the central frequency, $\omega_0$, of the pulse spectrum. Treacy has shown that a pair of diffraction gratings can be used to compensate for the quadratic phase distortion, $(d^2\phi/d\omega^2)_{\omega_0}$, of a frequency-broadened optical pulse. He pointed out in the same paper that the principal remaining problem in pulse compression of large-bandwidth signals using gratings is uncom-

TABLE 10.2. Second and third derivatives of phase with respect to frequency for a double prism pair, a double grating pair, and material.

| Prism | Grating | Material |
|---|---|---|
| $\frac{d^2\phi_p}{d\omega^2} = \frac{\lambda^3}{2\pi^2 c^2}\frac{d^2P}{d\lambda^2}$ | $\frac{d^2\phi_g}{d\omega^2} = \frac{\lambda^3 l_g}{\pi c^2 d^2}\left[1-\left(\frac{\lambda}{d}-\sin\gamma\right)^2\right]^{-3/2}$ | $\frac{d^2\phi_m}{d\omega^2} = \frac{\lambda^3 l_m}{2\pi c^2}\frac{d^2 n_m}{d\lambda^2}$ |
| $\frac{d^3\phi_p}{d\omega^3} = \frac{-\lambda^4}{4\pi^2 c^3}\left(3\frac{d^2P}{d\lambda^2}+\lambda\frac{d^3P}{d\lambda^3}\right)$ | $\frac{d^3\phi_g}{d\omega^3} = \frac{-d^2\phi_g}{d\omega^2}\frac{6\pi\lambda}{c} \times \frac{\left(1+\frac{\lambda}{d}\sin\gamma-\sin^2\gamma\right)}{\left[1-\left(\frac{\lambda}{d}-\sin\gamma\right)^2\right]}$ | $\frac{d^3\phi_m}{d\omega^3} = \frac{-\lambda^4 l_m}{4\pi^2 c^3}\left(\frac{3d^2 n_m}{d\lambda^2}+\frac{\lambda d^3 n_m}{d\lambda^3}\right)$ |

Derivatives of the path $P$ in the prism sequence with respect to wavelength

$$\frac{d^2P}{d\lambda^2} = 4\left[\frac{d^2n}{d\lambda^2}+(2n-n^{-3})\left(\frac{dn}{d\lambda}\right)^2\right]l_p\sin\beta - 8\left(\frac{dn}{d\lambda}\right)^2 l_p\cos\beta$$

$$\frac{d^3P}{d\lambda^3} = 4\frac{d^3n}{d\lambda^3}l_p\sin\beta - 24\frac{dn}{d\lambda}\frac{d^2n}{d\lambda^2}l_p\cos\beta$$

TABLE 10.3. Second and third derivatives of phase with respect to frequency for the double prism pair and double grating pair described in the text.[a]

| Derivative | Prisms | Gratings | Material |
|---|---|---|---|
| $\frac{d^2\phi}{d\omega^2}(\mathrm{fs}^2)$ | $+648-32l_p$ | $-3640l_g$ | $+2900l_m$ |
| $\frac{d^3\phi}{d\omega^3}(\mathrm{fs}^3)$ | $+277-49l_p$ | $-3120l_g$ | $+1620l_m$ |

[a] Lengths are in centimeters.

pensated cubic phase distortion, $(d^3\phi/d\omega^3)_{\omega_0}$. Christov and Tomov (1986) also recognized this problem in a recent publication on optical fiber-grating compressors Tables 10.2 and 10.3 show phase derivatives for prisms and gratings.

To overcome the problem of unwanted cubic phase distortion an elegant solution has been devised. Both a grating pair and a prism pair induce a cubic phase distortion. We can take advantage of the fact that the cubic phase distortion for gratings and prisms is of the opposite sign by using a configuration where the compressed pulse is passed sequentially through a pair of gratings and a pair of prisms. In this manner it is possible to cancel the cubic phase distortion (Treacy, 1969).

The effect of a combination of prisms, gratings, and material on a pulse is described by a total phase shift

$$\phi_T(\omega) = \phi_p(\omega) + \phi_g(\omega) + \phi_m(\omega), \tag{27}$$

where the subscripts $p$, $g$, and $m$ refer to prisms, gratings, and material, respectively. The material of length $l_m$ contributes a phase shift

$$\phi_m(\omega) = \frac{\omega l_m}{c} n_m(\omega), \tag{28}$$

where $c$ is the speed of light and $n_m(\omega)$ the refractive index. For the prism-and-grating pair we follow the method described by Martinez et al. (1984). A grating pair in a double-pass configuration causes a phase shift

$$\phi_g(\omega) = \frac{2\omega l_g}{c}\left[1 - \left(\frac{2\pi c}{\omega d} - \sin\gamma\right)^2\right]^{1/2}, \tag{29}$$

where $l_g$ is the grating spacing, $d$ is the groove spacing, and $\gamma$ is the angle of incidence.

For a double prism pair the phase shift is

$$\phi_p(\omega) = \frac{2\omega l_p}{c}\cos[\beta(\omega)], \tag{30}$$

where $l_p$ is the distance between prism apices and $\beta(\omega)$ is the angle between the refracted ray at frequency $\omega$ and the line joining the two apices (Figure 10.21). For prisms with apex angle $\alpha$ and refractive index $n_p(\omega)$ the angle $\psi_2(\omega)$ at which the refracted ray leaves the first prism can be calculated by a straightforward application of Snell's law as a function of the angle of incidence $\psi_1$.

We define $\psi_{2\max}$ as the maximum angle at which a ray can leave the first prism and still intersect the apex of the second prism. Equation (30) can then be rewritten as

$$\phi_p(\omega) = \frac{2\omega l_p}{c}\cos[\psi_{2\max} - \psi_2(\omega)]. \tag{31}$$

Typical experimental values are $\alpha = 60°$, $\psi_1 = 47°$ (minimum deviation), $n_p(\omega_0) = 1.457$ (quartz prisms) at $\omega_0 = 3.1$ rad/fs ($\lambda_0 = 615\,\text{mm}$), and $\psi_{2\max} = 49°$.

The total phase shift $\phi_T(\omega)$ can be calculated numerically for conditions typical of recent ultrashort-pulse-compression experiments by using Eqs. (28), (29), and (31) to provide a group delay dispersion $d^2\phi_T/d\omega^2|_{\omega_0}$ of $-700$ fs$^2$ and to cause the derivative of the group delay dispersion, $d^3\phi_T/d\omega^3$, to be zero at the center frequency of the pulse. The value of $d^2\phi_T/d\omega^2$ is such as to compensate the linear frequency sweep generated on a 60-fs, 200-kW pulse propagated through a 0.9-cm quartz fiber with a 4-$\mu$m core diameter. The prism spacing, grating spacing, and material length used in the numerical calculations are $l_p = 74\,\text{cm}$, $l_g = 0.7\,\text{cm}$, and $l_m = 0.5\,\text{cm}$ of quartz, respectively. The angle of incidence at the first grating was 45°, and the number of grooves per millimeter was 600.

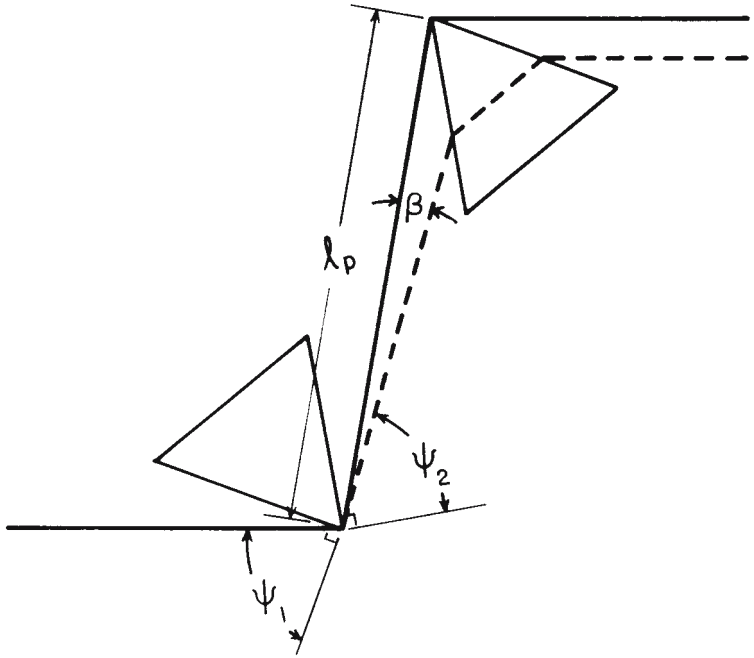


FIGURE 10.21. Parameters used in describing propagation of the optical pulse through the prism sequence. The angle of incidence at the face of the first prism is $\psi_1$ and the angle with respect to the normal to the exit face is $\psi_2$. The angle between a line drawn between prism apices and the direction of a ray exiting the first prism at $\psi_2$ is denoted by $\beta$. The distance between prism apices is $l_p$.

The departure of this compressor based on prisms and gratings from an ideal quadratic compressor can be evaluated by examining the variation of the group delay dispersion, $d^2\phi_T(\omega)/d\omega^2$, with frequency (Figure 10.22). One sees that this combination of prisms, gratings, and material provides the value of group delay dispersion required to compensate for the linear chirp in the pulse. At the same time, this combination of prisms, gratings, and material makes the derivative of the group delay dispersion zero at the center frequency of the pulse. This minimizes the cubic distortion and leaves as the main contribution to the phase that which is due to the curvature of the group delay dispersion ($d^4\phi/d\omega^4 \neq 0$) across the spectral range of the pulse.

The consequence of the departure of these actual compressors from an ideal quadratic compressor can be examined by calculating the temporal profile of the compressed pulse given a hypothetical incident pulse with an ideal quadratic phase distortion. In particular, we compare a compressor using prisms and gratings with a compressor using the gratings alone. Figure 10.23 shows the calculated intensity profile for the case when prisms, gratings, and material are used with the same parameters as in Figure 10.22. The

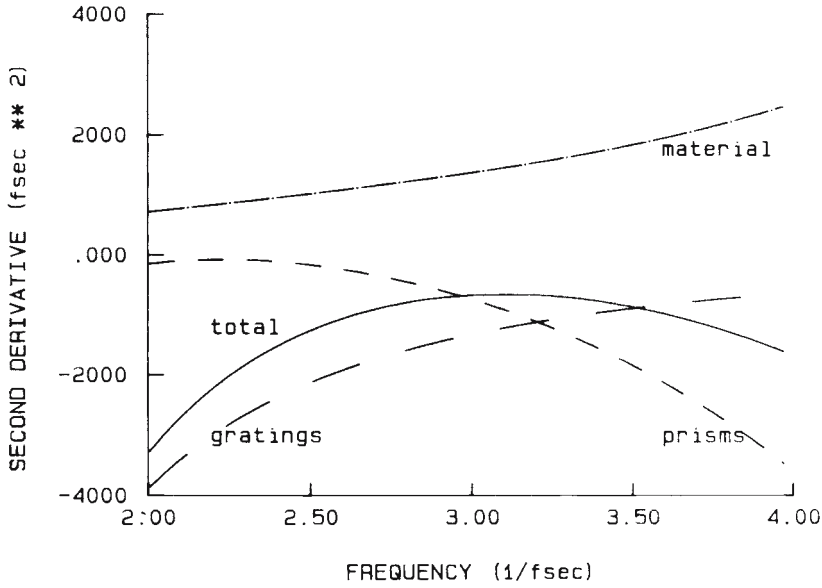


FIGURE 10.22. Plot of the second derivative of phase with respect to frequency for the prisms (short dash), gratings (long dash), and material (dash-dot) and for the total phase shift (solid).

bandwidth of the incoming pulse was chosen to be 0.5 rad/fs, which corresponds to a transform-limited pulse duration of 4 fs. In both Figures 10.23a and 10.23b the linear frequency sweep has been compensated for, but only in the case of the compressor with prism pair, grating pair, and dispersive material (Figure 10.23b) was it possible to compensate for the parabolic frequency sweep by setting the cubic phase distortion to zero.

The oscillatory trailing edge on the pulse shown in Figure 10.23a is due to the uncompensated cubic distortion, which causes the high- and low-frequency edges of the pulse spectrum to lag with respect to the center frequency. These delayed frequency components beat with each other to create an oscillatory trailing edge on the pulse. If prisms are used alone, the compressed pulse is similar to that shown in Figure 10.23a but with the time axis reversed; that is, the oscillatory trailing edge becomes an oscillatory leading edge.

The dominant residual distortion of the phase-corrected pulse is that which is due to the uncorrected negative curvature of the group velocity dispersion $d^4\phi/d\omega^4 < 0$. The effect is to leave small oscillatory wings on the leading and trailing edges of the pulse, as is evident from Figure 10.23b, and to broaden the main peak slightly. The lower limit on the duration of pulses compressed in this manner depends on the specific shape of the input-pulse spectrum and its precise distortions. For the ideal secant hyperbolic shape input pulse

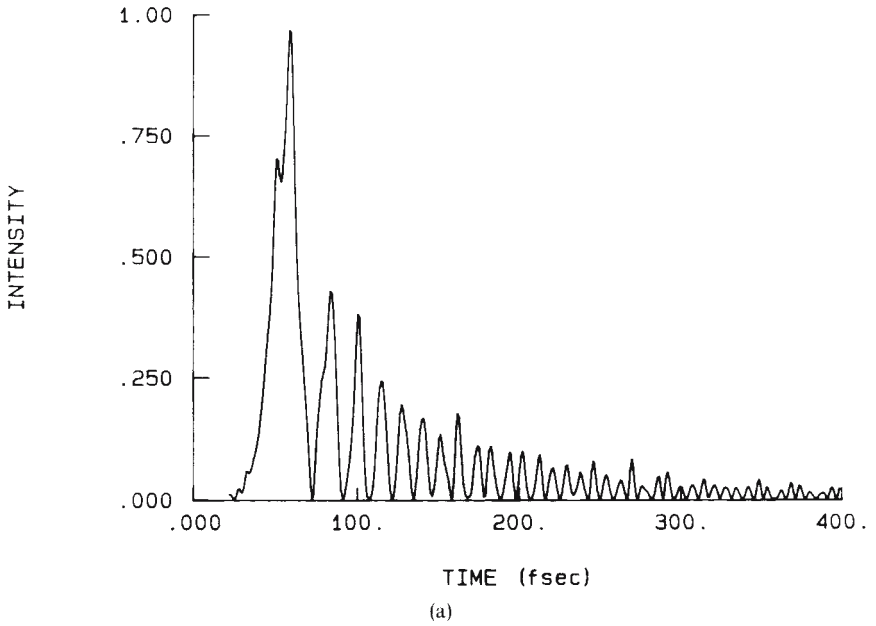


(a)

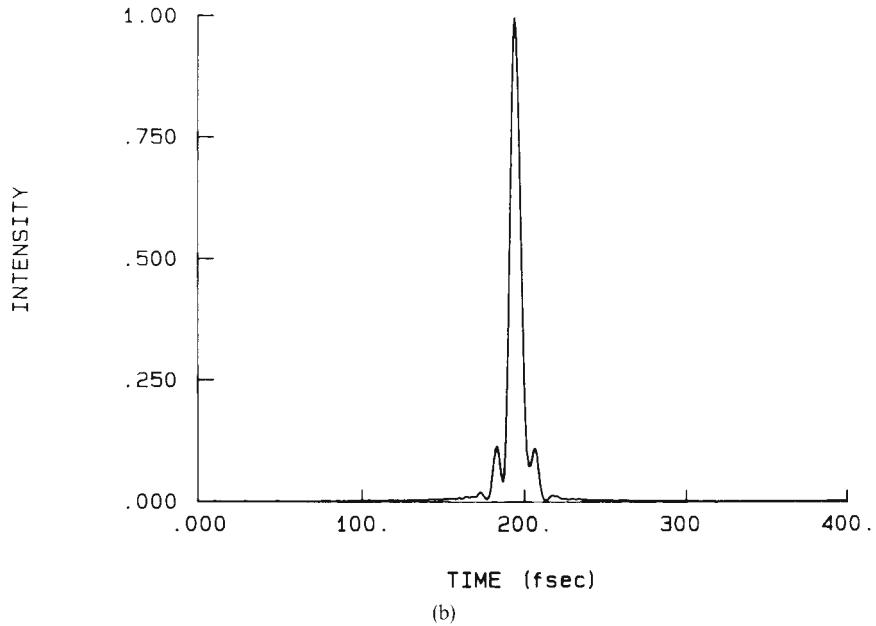


(b)

FIGURE 10.23. Calculated pulse intensity vs. time for the case of compression using only gratings and material dispersion (a) and for the case of compression using a combination of prisms, gratings, and material dispersion (b).

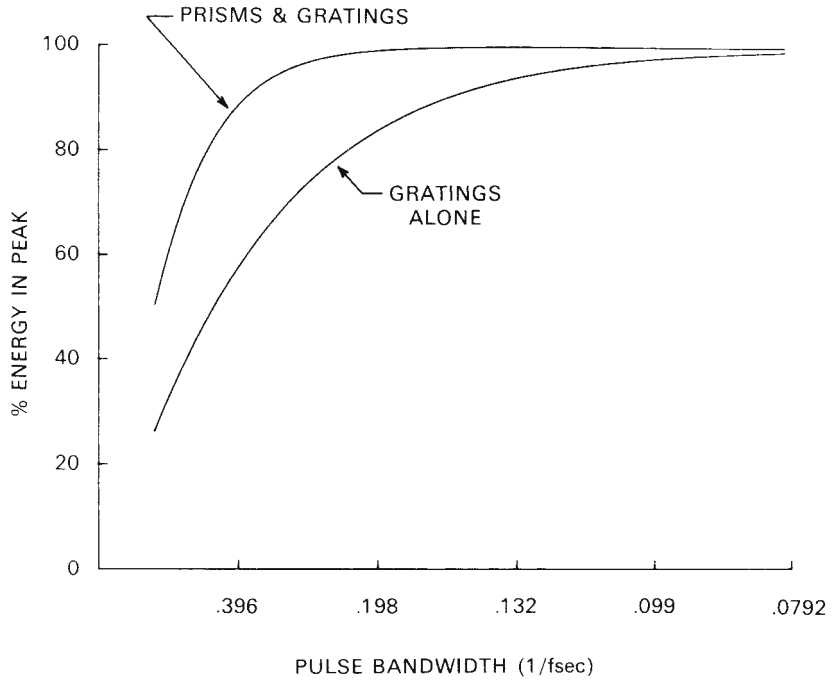


FIGURE 10.24. Plot of energy in the main peak of the compressed pulse for the case of combined prisms and gratings and for the case of gratings alone.

assumed above, the minimum compressed pulse width is between 6 and 7 fs, which is in approximate agreement with recently observed pulses compressed with grating and prism pairs (Fork et al., 1987). In Figure 10.24 the energy in the pulse peak is plotted versus pulse bandwidth for the case of gratings alone and the grating-prism pair combination.

## 3.2 Experiment

The arrangement of gratings and prisms for pulse compression is illustrated in Figure 10.25. The experimental study was carried out using optical pulses generated in a colliding-pulse mode-locked laser that contained an intracavity prism sequence identical to the four-prism set shown in Figure 10.25. These pulses were amplified at a repetition rate of 8 kHz in a copper-vapor laser-pumped amplifier to energies of ~1 $\mu$J. The amplified pulses had durations of 50 fs and a spectrum centered at 620 nm. A fraction of the amplified pulse energy was coupled into a polarization-preserving quartz fiber with core dimensions of ~4 $\mu$m and a length of 0.9 cm. The optical intensity in the fiber was $1–2 \times 10^{12}$ W/cm.

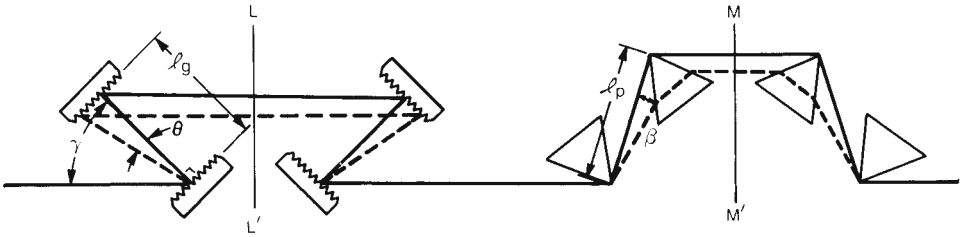


FIGURE 10.25. Combined grating and prism sequence used to remove both quadratic and cubic phase distortion. The solid line is a reference line. The dashed line is the path of a plane wave that propagates between the gratings at an angle $\theta$ with respect to the normal to the grating faces and between the prism pairs at an angle $\beta$ with respect to a line drawn between the prism apices. The plane $LL'$ is a plane of symmetry for the grating sequence, and the plane $MM'$ is a plane of symmetry for the prism sequence.

A four-prism sequence was then introduced, so the combined prism and grating sequence was equivalent to that shown in Figure 10.25. It was then possible to adjust the spacing of the prism and grating pairs so the maxima of the six different upconverted intensity traces all occurred at the same phase delay. Subsequent optimization was done by monitoring the interferometric autocorrelation (Diels et al., 1978, 1985) trace of the compressed pulse while adjusting the prism spacing $l_p$ and the grating spacing $l_g$. It is not possible to use the more conventional background-free autocorrelation technique for pulses this short since even a small relative angle between wave vectors of the interacting beams introduces measurable error. It was also necessary to use an extremely thin (32-$\mu$m) KDP crystal to double the compressed pulse so as to minimize distortion by group velocity dispersion within the doubling crystal.

The interferometric autocorrelation trace obtained on optimizing $l_p$ and $l_g$ is shown in Figure 10.26. The prism spacing for this trace was $l_p = 71$ cm, and the grating spacing was $l_g = 0.5$ cm. For purposes of comparison we have used crosses to indicate the calculated maxima and minima for an interferometric autocorrelation trace of a hyperbolic-secant-squared pulse having zero phase distortion and a full width at half-maximum of 6 fs. The close fit between the calculated and experimental interferometric autocorrelation functions indicates an absence of significant phase distortion over the bandwidth of the pulse. The well-resolved interference maxima also provide a rigorous calibration of the relative delay.

## 3.3 Applications

The success in generating optical pulses as short as 6 fs opens up the domain of physical processes that take place in a few femtoseconds to study. A pulse

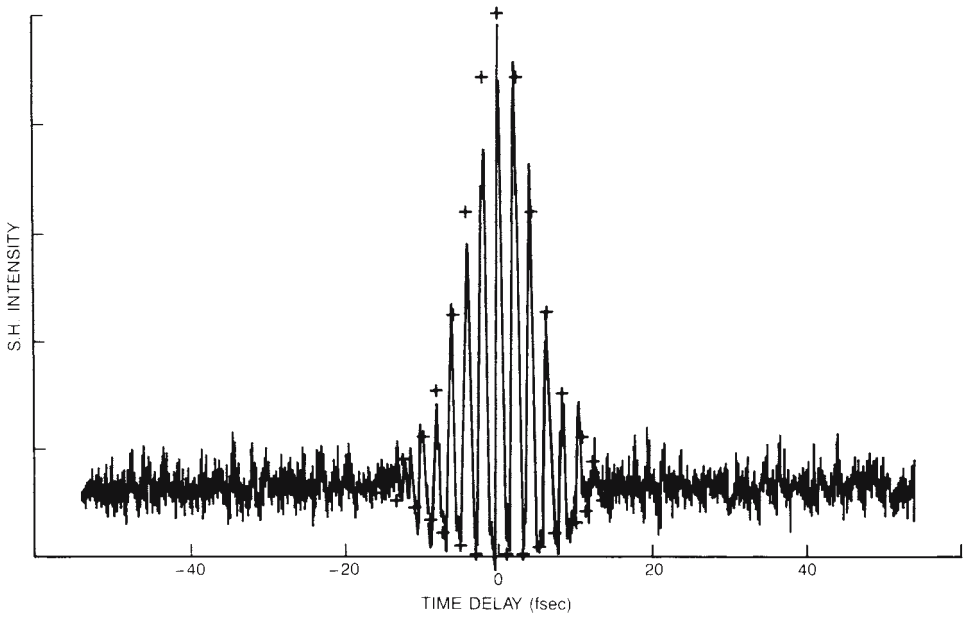


FIGURE 10.26. Experimental interferometric autocorrelation trace for a compressed pulse for $l_p = 71\,\text{cm}$ and $l_g = 0.5\,\text{cm}$. The interference maxima and minima calculated for the interferometric autocorrelation trace for a hyperbolic-secant-squared pulse of 6-fs duration are indicated by crosses. The close agreement between experiment and theory demonstrates absence of significant phase distortion in the compressed pulse.

that is so short contains frequency components from almost the entire visible region of the spectrum. Such a pulse is a nearly ideal continuum source. The well-defined temporal and spectral character of the pulse makes it quite useful for time-resolved spectroscopic problems.

Ultrashort optical pulse techniques provide a unique means for investigating nonequilibrium energy redistribution among vibronic levels in large organic molecules in solution. Previously, the dynamics of induced absorbance changes have been measured using pump and probe pulses having the same frequency spectrum. In the experiments described here induced absorption changes of optically excited molecules over a broad spectral range of $2400\,\text{cm}^{-1}$ centered at the energy of the excitation pulse were measured while maintaining a 10-fs time resolution. These experiments permit the observation of time-resolved hole burning and the process of equilibration to a thermalized population distribution on a femtosecond time sale (Brito Cruz et al., 1986, 1988b).

The absorption spectrum of a large dye molecule is dominated by vibronic transitions from a thermalized group state. Typically, these large molecules, which have a molecular weight of 400 or more, have a large number of degrees of freedom. The optical absorption coefficient may be written as a sum over

transitions from occupied vibrational levels in the ground state to vibrational levels in the excited state. The absorption coefficient is given by

$$\alpha(\nu) = C \sum_{if} P_i M^2 \chi_{if} \nu g(\nu - \nu_{if}), \tag{7}$$

where $C$ is a constant, $P_i$ is the thermal occupation probability of the initial state, $M$ is the dipole moment of the electronic transition, $\chi_{if}$ is the Franck-Condon factor, and $g$ is the line shape profile for each transition. The above expression describes the molecular system in thermal equilibrium. With a short optical pulse it is possible to excite a band of states that are resonant with the pumping energy. Before the molecular system comes into equilibrium, bleaching is observed in a spectral range determined by the convolution of the pump spectrum with the line shape profile of the individual transitions. As time progresses, the system relaxes to thermal equilibrium due to interaction with the thermal bath. The thermal bath couples to the vibronic levels by both intramolecular and intermolecular processes. The large number of degrees of freedom in the molecular backbone can form a thermal bath within the molecule itself. It is also possible for intermolecular energy transfer to take place on a somewhat longer time scale by collisions, dipole-dipole interaction, etc.

The experimental apparatus is arranged to perform a pump-probe type of experiment with one important modification over previous experiments. The probe pulse is approximately 10 fs in duration and has a significantly broader bandwidth than the 60-fs pump pulse. The pumping and probing pulses are derived from the same initial amplified 60-fs optical pulse having an energy of 1 $\mu$J with a center frequency at 618 nm. The probe pulse is formed by passing a portion of the initial pulse through a 12-nm length of optical fiber followed by a grating-pair compressor. The shorter pulse is then used to probe the absorption spectrum by passing through the excited sample into a spectro-meter and diode array. Care is taken to compensate for group velocity dispersion in the probe optical path. The experiments are performed at a repetition rate of 8 kHz.

The dyes are dissolved in ethylene glycol at concentrations that yield optical attenuations of less than $1/e$ when the dye solution is flowed through a jet with a thickness of 100 to 300 $\mu$m. The pump pulses are attenuated to levels that induce absorption changes of a few percent or less.

The data are collected by a differential measuring technique. The pump beam is periodically blocked by a shutter at a frequency of 10 Hz and the transmitted spectra are recorded in the computer memory in phase with the chopped pumping beam. Spectra are recorded at different time delays as determined by the optical path delay, which is controlled by a stepping motor translation stage. Integration time for a single spectrum is typically 30 s.

In Figure 10.27 the absorption spectrum for cresyl violet is plotted before and after excitation with a 60-fs optical pulse at 618 nm for zero relative time delay. A decrease in absorption is clearly observed in the spectral region close

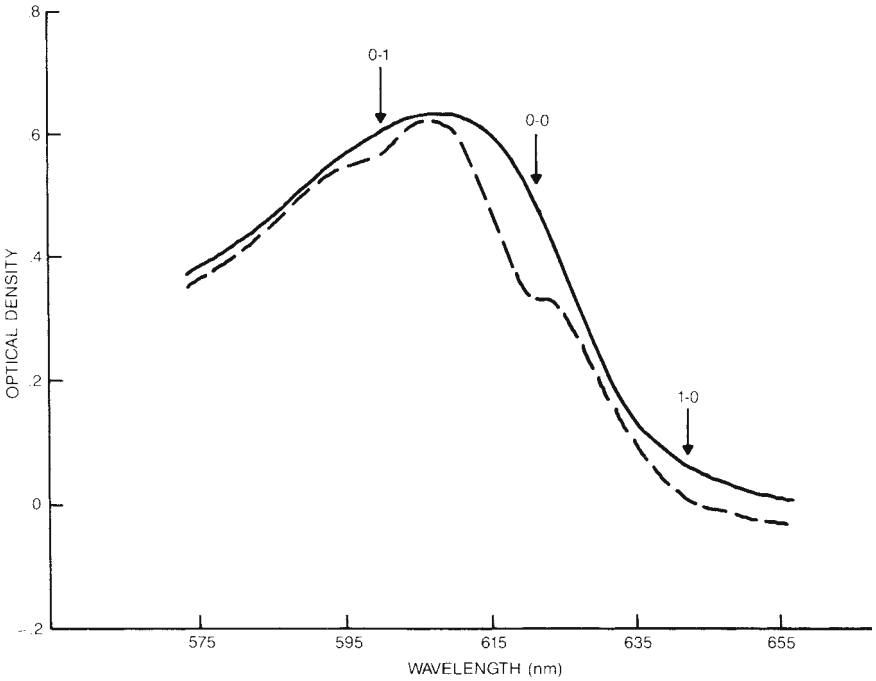


FIGURE 10.27. Plot of the absorbance spectrum of the molecule cresyl violet near zero time delay before (solid line) and after (dashed line) excitation with a 60-fs optical pulse.

to the pumping wavelength. In addition, replica holes are seen approximately 600 $cm^{-1}$ above and below the excitation energy. In Figure 10.28 the time-resolved differential spectra are plotted for cresyl violet. The time delay between spectra is 25 fs. The central hole and the two adjacent replica holes are seen to broaden and form a thermalized spectrum in the first few hundred femtoseconds following excitation.

The mechanism for the formation of the replica holes is readily understood. Measurements of the Raman spectra of cresyl violet reveal the presence of a strong mode at 590 $cm^{-1}$. In a large molecule with a large number of degrees of freedom a correspondingly large number of modes can contribute to the absorption spectrum, as illustrated with Figure 10.27. Usually only a few modes with energies larger than $kT$ change their occupation number during the optical transition to the excited state. These modes are called active or system modes and have large Franck-Condon factors. The strength of the absorption is determined by the Franck-Condon factor $\chi_{if}$. The 598-$cm^{-1}$ mode appears to be the dominant mode in the absorption spectrum as evidenced by bleaching both at the 0–0 transition, which is at the excitation energy, and at the 0–1 and 1–0 positions of the Franck-Condon progression.

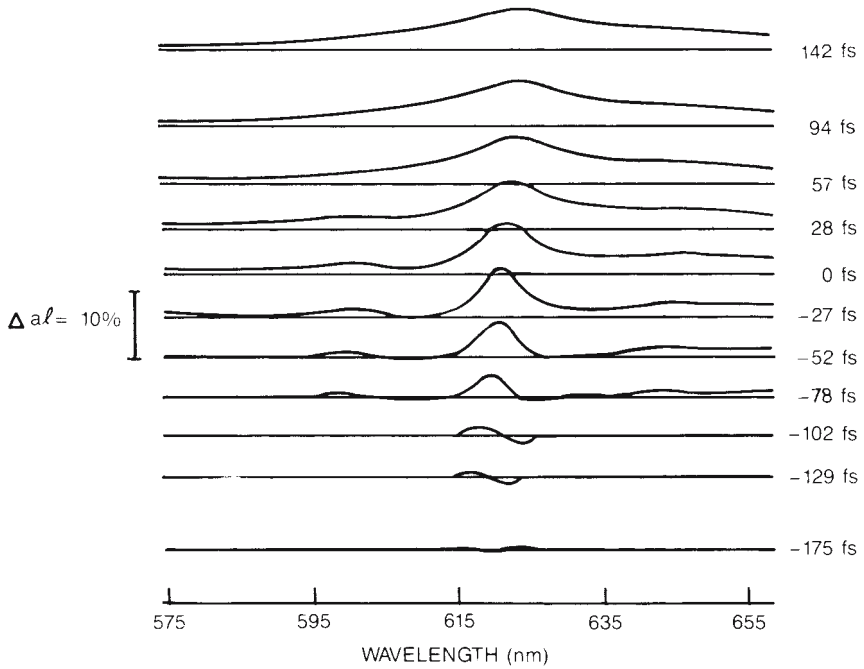


FIGURE 10.28. Differential absorbance spectra plotted as a function of relative time delay following excitation with a 60-fs optical pulse at 618 nm for the molecule cresyl violet.

The relative strengths of the bleaching at the central hole and at the replica holes can be determined by estimating the Franck-Condon factors in the harmonic approximation. We calculate $\chi_{00}/\chi_{01,10} = 0.26$, which is consistent with the experimental observation value.

The hole observed in Figure 10.28 broadens and relaxes to the quasi-equilibrium spectrum within the first few hundred femtoseconds. If we assume that the inhomogeneous linewidth is much larger than the homogeneous linewidth, we can estimate the polarization dephasing time $T_2$ from the width of the hole burned in the spectrum. For the case of a Lorentzian profile, where $\Delta\lambda$ is the half-width of the hole, the expression for $T_2$ is given by $T_2 = 2\lambda^2/\pi c\Delta\lambda$. Using the above expression we determine $T_2$ to be 75 fs for cresyl violet.

Some insight into the energy relaxation of the excited molecules can be obtained by looking at the time evolution of the differential absorption at different spectral regions within our range of observation. In Figure 10.29 we plot this evolution for a region 7 nm wide around 587, 625, and 654 nm. The curve for 625 nm shows the evolution of the population in levels that are very close in energy to the levels excited by the pump. In this spectral region an overshoot in the bleaching occurs as a consequence of the spectral hole

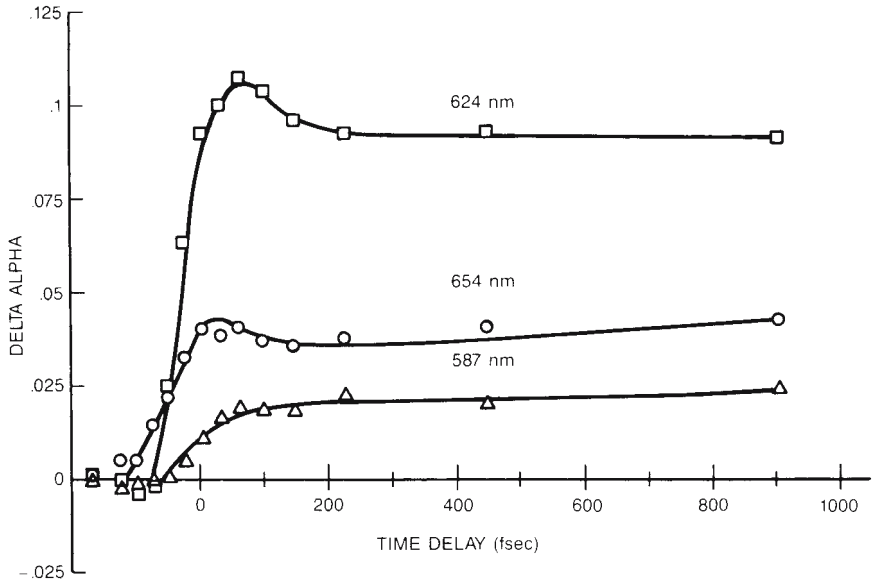


FIGURE 10.29. Plot of the differential absorption spectrum in time for three selected wavelengths for the molecule cresyl violet. (The lines are to guide the eye.)

burning and a rapid recovery on the order of 50 fs is observed as the ground and excited states become thermalized. The bleaching at 654 nm also shows a small overshoot, which recovers as the nonequilibrium distribution transits to a thermalized distribution in the first few hundred picoseconds. On the high-energy side at 587 nm a slower rise is observed as the molecular distribution thermalizes.

## References

Agostinelli, J., G. Harvey, T. Stone, and C. Gabel (1979) Appl. Opt. **18**, 2500.
Alfano, R.R. and P.P. Ho (1988) IEEE J. Quantum Electron. **QE-24**, 351.
Alfano, R.R. and S.L. Shapiro (1970) Phys. Rev. Lett. **24**, 592.
Arthurs, E.G., D.J. Bradley, and A.G. Roddie (1971) Appl. Phys. Lett. **19**, 480.
Ausschnitt, C.P. and R.K. Jain (1978) Appl. Phys. Lett. **32**, 727.
Ausschnitt, C.P., R.K. Jain, and J.P. Heritage (1979) IEEE J. Quantum Electron. **QE-15**, 912.
Auyeung, J. and A. Yariv (1978) IEEE J. Quantum Electron. **QE-14**, 347.
Baldeck, P.L., F. Raccah, and R.R. Alfano (1987) Opt. Lett. **12**, 588.
Beaud, P., B. Zysset, A.P. Schwarzenbach, and H.P. Weber (1986) Opt. Lett. **11**, 24.
Bloembergen, N. and P. Lallemand (1966) Phys. Rev. Lett. **16**, 81.
Blow, K.J., N.J. Doran, and B.P. Nelson (1985) Opt. Lett. **10**, 393.
Bokor, J., A.M. Johnson, R.H. Storz, and W.M. Simpson (1986) Appl. Phys. Lett. **49**, 226.

Bokor, J., A.M. Johnson, W.M. Simpson, R.H. Storz, and P.R. Smith (1988) Appl. Phys. Lett. **53**, 2599.
Bondarenko, N.G., I.V. Eremina, and V.I. Talanov (1970) JETP Lett. **12**, 85.
Bor, Z. and B. Racz (1985) Opt. Commun. **54**, 165.
Bourkoff, E., W. Zhao, R.I. Joseph, and D.N. Christodoulides (1987a) Opt. Lett. **12**, 272.
Bourkoff, E., W. Zhao, R.I. Joseph, and D.N. Christodoulides (1987b) Opt. Commun. **62**, 284.
Bradley, D.J., G.H.C. New, and S.J. Caughey (1970) Phys. Lett. **32A**, 313.
Brewer, R.G. (1967) Phys. Rev. Lett. **19**, 8.
Brito Cruz, C.H., R.L. Fork, W.H. Knox, and C.V. Shank (1986) Chem. Phys. Lett. **132**, 341.
Brito Cruz, C.H., P.C. Becker, R.L. Fork, and C.V. Shank (1988a) Opt. Lett. **13**, 123.
Brito Cruz, C.H., J.P. Gordon, P.C. Becker, R.L. Fork, and C.V. Shank (1988b) IEEE J. Quantum Electron. **24**, 261.
Butylkin, V.S., V.V. Grigoryants, and V.I. Smirnov (1979) Opt. Quantum Electron. **11**, 141.
Christov, I.P. and I.V. Tomov (1986) Opt. Commun. **58**, 338.
Damen, T.C., and J. Shah (1988) Appl. Phys. Lett. **52**, 1291.
Damm, T., M. Kaschke, F. Noack, and B. Wilhelmi (1985) Opt. Lett. **10**, 176.
DeMartini, F., C.H. Townes, T.K. Gustafson, and P.L. Kelley (1967) Phys. Rev. **164**, 312.
Desbois, J., F. Gires, and P. Tournois (1973) IEEE J. Quantum Electron. **QE-9**, 213.
Dianov, E.M., A. Ya. Karasik, P.V. Mamyshev, G.I. Onishchukov, A.M. Prokhorov, M.F. Stel'makh, and A.A. Fomichev (1984a) Sov. J. Quantum Electron. **14**, 726.
Dianov, E.M., A.Y. Karasik, P.V. Mamyshev, G.I. Onishchukov, A.M. Prokhorov, M.F. Stel'makh, and A.A. Fomichev (1984b) JETP Lett. **39**, 691.
Dianov, E.M., A.Y. Karasik, P.G. Mamyshev, A.M. Prokhorov, and V.N. Serkin (1985) Sov. Phys. JETP **62**, 448.
Dianov, E.M., L.M. Ivanov, A.Y. Karasik, P.V. Mamyshev, and A.M. Prokhorov (1986a) Sov. Phys. JETP **64**, 1205.
Dianov, E.M., L.M. Ivanov, A.Y. Karasik, P.V. Mamyshev, and A.M. Prokhorov (1986b) JETP Lett. **44**, 156.
Dianov, E.M., A.Y. Karasik, P.V. Mamyshev, A.M. Prokhorov, and D.G. Fursa (1987) Sov. J. Quantum Electron. **17**, 415.
Dianov, E.M., P.V. Mamyshev, and A.M. Prokhorov (1988) Sov. J. Quantum Electron. **18**, 1.
Diels, J.-C., E.W. Stryland, and D. Gold (1978) In *Proceedings of the First International Conference on Picosecond Phenomena*, p. 117. Springer-Verlag, Berlin.
Diels, J.-C., J.J. Fontaine, I.C. McMichael, and F. Simoni (1985) Appl. Opt. **24**, 1270.
Duguay, M.A. (1976) The ultrafast optical Kerr shutter. In *Progress in Optics XIV*, E. Wolf, ed., p. 161. North-Holland, Amsterdam.
Duguay, M.A. and J.W. Hansen (1969) Appl. Phys. Lett. **14**, 14.
Dupuy, C.G. and P. Bado (1984) Dig. Conf. Lasers and Electro-Opt., Anaheim, Calif., paper TUE2, 58.
Feldman, R.D., R.F. Austin, P.M. Bridenbaugh, A.M. Johnson, W.M. Simpson, B.A. Wilson, and C.E. Bonner (1988) J. Appl. Phys. **64**, 1191.
Fisher, R.A. and W.K. Bischel (1974) Appl. Phys. Lett. **24**, 468.
Fisher, R.A. and W.K. Bischel (1975) J. Appl. Phys. **46**, 4921.

Fisher, R.A., P.L. Kelley, and T.K. Gustafson (1969) Appl. Phys. Lett. **14**, 140.
Fork, R.L., O.E. Martinez, and J.P. Gordon (1984) Opt. Lett. **9**, 150.
Fork, R.L., C.H. Brito Cruz, P.C. Becker, and C.V. Shank (1987) Opt. Lett. **12**, 483.
Fujimoto, J.G., A.M. Weiner, and E.P. Ippen (1984) Appl. Phys. Lett. **44**, 832.
Giordmaine, J.A., M.A. Duguay, and J.W. Hansen (1968) IEEE J. Quantum Electron. **QE-4**, 252.
Gires, F. and P. Tournois (1964) C.R. Acad. Sci. (Paris) **258**, 6112.
Gloge, D. (1971) Appl. Opt. **10**, 2252.
Golovchenko, E.A., E.M. Dianov, P.V. Mamyshev, and A.M. Prokhorov (1988) Opt. Quantum Electron. **20**, 343.
Gomes, A.S., U. Osterberg, W. Sibbett, and J.R. Taylor (1985a) Opt. Commun. **54**, 377.
Gomes, A.S., W. Sibbett, and J.R. Taylor (1985b) Opt. Lett. **10**, 338.
Gomes, A.S., W. Sibbett, and J.R. Taylor (1985c) IEEE J. Quantum Electron. **QE-21**, 1157.
Gomes, A.S.L., W. Sibbett, and J.R. Taylor (1986a) Appl. Phys. B **39**, 43.
Gomes, A.S.L., W.E. Sleat, W. Sibbett, and J.R. Taylor (1986b) Opt. Commun. **57**, 257.
Gomes, A.S.L., V.L. da Silva, and J.R. Taylor (1988a) J. Opt. Soc. Am. B **5**, 373.
Gomes, A.S.L., A.S. Gouveia-Neto, and J.R. Taylor (1988b) Opt. Quantum Electron. **20**, 95.
Grischkowsky, D. and A.C. Balant (1982a) Appl. Phys. Lett. **41**, 1.
Grischkowsky, D. and A.C. Balant (1982b) Optical pulse compression with reduced wings. In *Picosecond Phenomena III*, K.B. Eisenthal, R.M. Hochstrasser, W. Kaiser, and A. Laubereau, eds., p. 123. Springer-Verlag, Berlin.
Gustafson, T.K., J.P. Taran, H.A. Haus, J.R. Lifsitz, and P.L. Kelley (1969) Phys. Rev. **177**, 306.
Halas, N.J., D. Krokel, and D. Grischkowsky (1987) Appl. Phys. Lett. **50**, 886.
Halbout, J.-M. and D. Grischkowsky (1984) Appl. Phys. Lett. **45**, 1281.
Haner, M. and W.S. Warren (1987) Opt. Lett. **12**, 398.
Heritage, J.P., R.N. Thurston, W.J. Tomlinson, A.M. Weiner, and R.H. Stolen (1984) J. Opt. Soc. Am. A **1**, 1288A.
Heritage, J.P., R.N. Thurston, W.J. Tomlinson, A.M. Weiner, and R.H. Stolen (1985a) Appl. Phys. Lett. **47**, 87.
Heritage, J.P., A.M. Weiner, and R.N. Thurston (1985b) Opt. Lett. **10**, 609.
Heritage, J.P., A.M. Weiner, R.J. Hawkins, and O.E. Martinez (1988) Opt. Commun. **67**, 367.
Hian-Hua, L., L. Yu-Lin, and J. Jia-Lin (1985) Opt. Quantum Electron. **17**, 187.
Ippen, E.P. and C.V. Shank (1975a) Appl. Phys. Lett. **26**, 92.
Ippen, E.P. and C.V. Shank (1975b) Appl. Phys. Lett. **27**, 488.
Ippen, E.P., C.V. Shank, and T.K. Gustafson (1974) Appl. Phys. Lett. **24**, 190.
Ishida, Y. and T. Yajima (1986) Opt. Commun. **58**, 355.
Iwashita, K., K. Nakagawa, Y. Nakano, and Y. Suzuki (1982) Electron. Lett. **18**, 873.
Johnson, A.M. and W.M. Simpson (1983) Opt. Lett. **8**, 554.
Johnson, A.M. and W.M. Simpson (1985a) J. Opt. Soc. Am. B **2**, 619.
Johnson, A.M. and W.M. Simpson (1985b) Proc. SPIE **533**, 52.
Johnson, A.M. and W.M. Simpson (1986) IEEE J. Quantum Electron. **QE-22**, 133.
Johnson, A.M., R.H. Stolen, and W.M. Simpson (1984a) Appl. Phys. Lett. **44**, 729.
Johnson, A.M., R.H. Stolen, and W.M. Simpson (1984b) Generation of 0.41-picosecond pulses by the single-state compression of frequency doubled Nd:YAG

laser pulses. In *Ultrafast Phenomena IV*, D.H. Auston and K.B. Eisenthal, eds., p. 16. Springer-Verlag, Berlin.
Johnson, A.M., D.W. Kisker, W.M. Simpson, and R.D. Feldman (1985) Picosecond photoconductivity in polycrystalline CdTe films prepared by UV-enhanced OMCVD. In *Picosecond Electronics and Optoelectronics*, G.A. Mourou, D.M. Bloom, and C.-H. Lee, eds., p. 188. Springer-Verlag, Berlin.
Johnson, A.M., R.H. Stolen, and W.M. Simpson (1986) The observation of chirped stimulated Raman scattered light in fibers. In *Ultrafast Phenomena V*, G.R. Fleming and A.E. Siegman, eds., p. 160. Springer-Verlag, Berlin.
Johnson, A.M., R.M. Lum, W.M. Simpson, and J. Klingert (1987) IEEE J. Quantum Electron. **QE-23**, 1180.
Kafka, J.D. and T. Baer (1985) Proc. SPIE **533**, 38.
Kafka, J.D. and T. Baer (1986) Proc. SPIE **610**, 2.
Kafka, J.D. and T. Baer (1987) Opt. Lett. **12**, 401.
Kafka, J.D. and T.M. Baer (1988) IEEE J. Quantum Electron. **QE-24**, 341.
Kafka, J.D., B.H. Kolner, T. Baer, and D.M. Bloom (1984) Opt. Lett. **9**, 505.
Keller, U., J.A. Valdmanis, M.C. Nuss, and A.M. Johnson (1988) IEEE J. Quantum Electron. **QE-24**, 427.
Klauder, J.R., A.C. Price, S. Darlington, and W.J. Albersheim (1960) Bell System Tech. J. **39**, 745.
Knox, W.H., R.L. Fork, M.C. Downer, R.H. Stolen, C.V. Shank, and J.A. Valdmanis (1985) Appl. Phys. Lett. **46**, 1120.
Kolner, B.H. and D.M. Bloom (1984) Electron. Lett. **20**, 818.
Kolner, B.H. and D.M. Bloom (1986) IEEE J. Quantum ELectron. **QE-22**, 79.
Krokel, D., N.J. Halas, G. Giulinai, and D. Grishckowsky (1988) Phys. Rev. Lett. **60**, 29.
Kuckartz, M., R. Schulz, and H. Harde (1987) Opt. Quantum Electron. **19**, 237.
Kuckartz, M., R. Schulz, and H. Harde (1988) J. Opt. Soc. Am. B **5**, 1353.
Lassen, H.E., F. Mengel, B. Tromborg, N.C. Albertsen, and P.L. Christiansen (1985) Opt. Lett. **10**, 34.
Laubereau, A. (1969) Phys. Lett. **29A**, 539.
Lehmberg, R.H. and J.M. McMahon (1976) Appl. Phys. Lett. **28**, 204.
Lin, C., L.G. Cohen, R.H. Stolen, G.W. Tasker, and W.G. French (1977) Opt. Commun. **20**, 426.
Maine, P., D. Strickland, P. Bado, M. Pessot, and G. Mourou (1988) IEEE J. Quantum Electron. **24**, 398.
Martinez, O.E., J.P. Gordon, and R.L. Fork (1984) J. Opt. Soc. AM. A **1**, 1003.
May, P., J.-M. Halbout, and G. Chiu (1987) Appl. Phys. Lett. **51**, 145.
May, P., J.-M. Halbout, and G. Chiu (1988) IEEE J. Quantum Electron. **QE-24**, 234.
Meinel, R. (1983) Opt. Commun. **47**, 343.
Mollenauer, L.F. (1985) Philos. Trans. R. Soc. London A **315**, 437.
Mollenauer, L.F. and R.H. Stolen (1982) Laser Focus **18(4)**, 193.
Mollenauer, L.F., R.H. Stolen, and J.P. Gordon (1980) Phys. Rev. Lett. **45**, 1095.
Mollenauer, L.F., R.H. Stolen, J.P. Gordon, and W.J. Tomlinson (1983) Opt. Lett. **8**, 289.
Mollenauer, L.F., J.P. Gordon, and M.N. Islam (1986) IEEE J. Quantum Electron. **QE-22**, 157.
Nakashima, T., M. Nakazawa, K. Nishi, and H. Kubota (1987) Opt. Lett. **12**, 404.
Nakatsuka, H. and D. Grischkowsky (1981) Opt. Lett. **6**, 13.
Nakatsuka, H., D. Grischkowsky, and A.C. Balant (1981) Phys. Rev. Lett. **47**, 910.

Nakazawa, M., T. Nakashima, and H. Kubota (1988) Opt. Lett. **13**, 120.
Nikolaus, B. and D. Grischkowsky (1983a) Appl. Phys. Lett. **42**, 1.
Nikolaus, B. and D. Grischkowsky (1983b) Appl. Phys. Lett. **43**, 228.
Ohmori, Y., Y. Sasaki, and T. Edahiro (1983) Trans. IECE Jpn. **E-66**, 146.
Owyoung, A., R.W. Hellwarth, and N. George (1972) Phys. Rev. B **5**, 628.
Palfrey, S.L. and D. Grischkowsky (1985) Opt. Lett. **10**, 562.
Payne, D.N. and W.A. Gambling (1975) Electron. Lett. **11**, 176.
Roskos, H., A. Seilmeier, W. Kaiser, and J.D. Harvey (1987) Opt. Commun. **61**, 81.
Rothenberg, J.E. and D. Grischkowsky (1989) Phys. Rev. Lett. **62**, 531.
Schadt, D. and B. Jaskorzynska (1987) J. Opt. Soc. Am. B **4**, 856.
Schadt, D., B. Jaskorzynska, and U. Osterberg (1986) J. Opt. Soc. Am. B **3**, 1257.
Shank, C.V., R.L. Fork, R. Yen, R.H. Stolen, and W.J. Tomlinson (1982) Appl. Phys. Lett. **40**, 761.
Shapiro, S.L. and H.P. Broida (1967) Phys. Rev. **154**, 129.
Shimizu, F. (1967) Phys. Rev. Lett. **19**, 1097.
Smith, R.G. (1972) Appl. Opt. **11**, 2489.
Stolen, R.H. (1979a) IEEE J. Quantum Electron. **QE-15**, 1157.
Stolen, R.H. (1979b) Nonlinear properties of optical fibers. In *Optical Fiber Telecommunications*, S.E. Miller and A.G. Chynoweth eds., chapter 5. Academic Press, New York.
Stolen, R.H. and E.P. Ippen (1973) Appl. Phys. Lett. **22**, 276.
Stolen, R.H. and A.M. Johnson (1986) IEEE J. Quantum Electron. **QE-22**, 2154.
Stolen, R.H. and C. Lin (1978) Phys. Rev. A **17**, 1448.
Stolen, R.H., E.P. Ippen, and A.R. Tynes (1972) Appl. Phys. Lett. **20**, 62.
Stolen, R.H., V. Ramaswamy, P. Kaiser, and W. Pleibel (1978) Appl. Phys. Lett. **33**, 699.
Stolen, R.H., C. Lee, and R.K. Jain (1984a) J. Opt. Soc. Am. B **1**, 652.
Stolen, R.H., W. Pleibel, and J.R. Simpson (1984b) IEEE J. Lightwave Technol. **LT-2**, 639.
Stolen, R.H., C.V. Shank, and W.J. Tomlinson (1984c) Procedure for calculating optical pulse compression from fiber-grating combinations. In *Ultrafast Phenomena IV*, D.H. Auston and K.B. Eisenthal, eds., p. 46. Springer-Verlag, Berlin.
Stolz, B., U. Osterberg, A.S.L. Gomes, W. Sibbett, and J.R. Taylor (1986) IEEE J. Lightwave Technol. (1986) **LT-4**, 55.
Strickland, D. and G. Mourou (1985) Opt. Commun. **56**, 219.
Suzuki, T. and T. Fukumoto (1976) Electron. Commun. Jpn. **59-C(3)**, 117.
Tai, K. and A. Tomita (1986a) Appl. Phys. Lett. **48**, 309.
Tai, K. and A. Tomita (1986b) Appl. Phys. Lett. **48**, 1033.
Thurston, R.N., J.P. Heritage, A.M. Weiner, and W.J. Tomlinson (1986) IEEE J. Quantum Electron. **QE-22**, 682.
Tomlinson, W.J. and W.H. Knox (1987) J. Opt. Soc. Am. B **4**, 1404.
Tomlinson, W.J., R.H. Stolen, and C.V. Shank (1984) J. Opt. Soc. Am. B **1**, 139.
Tomlinson, W.J., R.H. Stolen, and A.M. Johnson (1985) Opt. Lett. **10**, 457.
Treacy, E.B. (1968) Phys. Lett. **28A**, 34.
Treacy, E.B. (1969) IEEE J. Quantum Electron. **QE-5**, 454.
Ueda, Y. and K. Shimoda (1967) Japan. J. Appl. Phys. **6**, 628.
Valk, B., W. Hodel, and H.P. Weber (1984) Opt. Commun. **50**, 63.
Valk, B., W. Hodel, and H.P. Weber (1985) Opt. Commun. **54**, 363.
Weiner, A.M., J.P. Heritage, and R.N. Thurston (1986) Opt. Lett. **11**, 153.

Weiner, A.M., J.P. Heritage, and R.H. Stolen (1988) J. Opt. Soc. Am. B **5**, 364.
Weingarten, K.J., M.J.W. Rodwell, and D.M. Bloom (1988) IEEE J. Quantum Electron. **QE-24**, 198.
Wright, J.V. and B.P. Nelson (1977) Electron. Lett. **13**, 361.
Yang, T.Y., P.P. Ho, A. Katz, R.R. Alfano, and R.A. Ferrante (1985) Appl. Opt. **24**, 2021.
Zel'dovich, B.Y. and I.I. Sobel'man (1971) JETP Lett. **13**, 129.
Zhao, W. and E. Bourkoff (1988) IEEE J. Quantum Electron. **QE-24**, 365.
Zysset, B., W. Hodel, P. Beaud, and H.P. Weber (1986) Opt. Lett. **11**, 156.

# Part II
## New Developments

# 11
# Coherence Properties of the Supercontinuum Source

I. Zeylikovich and R.R. Alfano

## 1. Introduction

One of the salient features of laser radiation is *coherence* which is revealed by interference in the form of fringes. Coherence phenomena can be observed in the temporal and spatial domains. The *Michelson* interferometer can be used to measure the temporal coherence, and the spatial coherence can be observed in a *Young's* double-slit experiment (Born and Wolf, 1964). The supercontinuum is a novel nonlinear optical phenomena characterized by a dramatic "white-light" spectrum which can be generated in various *media* (Alfano and Shapiro, 1970). There are diverse applications for the supercontinuum source which depend upon coherence, such as optical coherence tomography (Hartl et al., 2001), optical frequency metrology (Diddams et al., 2000), communications (Takara, 2002), and ultrashort pulse generation (Baltuska et al., 2002). The contrast of the supercontinuum frequency comb longitudinal modes generated in fiber depends on coherence degradation (Nakazawa et al., 1998) which is related to a radio frequency noise component over a broadband frequency region of the supercontinuum. The coherent nature of the supercontinuum generation process is important for ensuring the spectral mode structure of the frequency comb associated with laser pulses to be transferred coherently to the supercontinuum. The complex degree of mutual coherence was defined for independent supercontinuum sources (Dudley and Coen, 2002). Recently, the supercontinuum mutual coherence was quantified by interference between the supercontinuum generated from two separated photonic crystal fibers (PCFs) (Gu et al., 2003) and by means of a time-delay pulsed method of supercontinuum trains generated through a tapered fiber (Lu and Knox, 2004). In the experimental setups (Gu et al., 2003; Lu and Knox, 2004), a fixed delay between two interferometer's beams was used. The broadband noise in microstructure fiber, related to the mutual coherence, was studied experimentally and by numerical simulations (Corwin et al., 2003).

This chapter describes some of the recent research works related to the coherence properties of the supercontinuum generated from bulk and fiber media.

## 2. Background

The total field at point $P$ is obtained by a superposition of two waves $E_1(t)$ and $E_2(t)$ of frequency $\omega$ propagating from point sources $S_1$ and $S_2$. The field at $P$ is given by

$$E_P(t) = E_1 \exp i[\omega(t - r_1/c) + \varphi_1(t)] + E_2 \exp i[\omega(t - r_2/c) + \varphi_2(t)], \tag{1}$$

where $\varphi_1(t)$ and $\varphi_2(t)$ are the phases of the two waves and $r_1$ and $r_2$ are the distances from $P$ to $S_1$ and $S_2$, respectively. When the phase difference $\varphi_1(t) - \varphi_2(t)$ is constant, the two sources are *mutually coherent*. When the phase quantity $\varphi_1(t) - \varphi_2(t)$ varies with time in a random fashion, then the two sources are *mutually incoherent* and destroy the interference.

The degree of coherence is obtained from the total field at point $P$. The intensity at $P$ for stationary fields is given by

$$I_P(r_1, r_2) = \langle E_P(t) E_P{}^*(t) \rangle, \tag{2}$$

where $I_1 = \langle |E_1|^2 \rangle$ and $I_2 = \langle |E_2|^2 \rangle$ are the intensities at $P$ due to $S_1$ and $S_2$. The angle brackets denote the time average. The intensity at $P$ is given by (Born and Wolf, 1964)

$$I_P(\tau) = I_1 + I_2 + 2\,\mathrm{Re}\{\Gamma_{12}(\tau)\}, \tag{3}$$

where $\tau = (r_1 - r_2)/c$ and $\Gamma_{12}(\tau) = \langle E_1(t + \tau) E_2^*(t) \rangle$ is termed the *mutual coherence function.* $\Gamma_{12}(\tau)$ is given as

$$\Gamma_{12}(\tau) = |\Gamma_{12}(0)| \exp[i(2\pi\nu\tau + \psi_{12})], \tag{4}$$

where $2\pi\nu\tau = (2\pi/\lambda)(|r_1 - r_2|)$ and $\psi_{12} = \arg[\Gamma_{12}(\tau)]$. Experiments for $\Gamma_{12}(\tau)$ are restricted to small path differences defined by $\Delta l << c/\Delta\nu$. The function $\Gamma_{12}(0)$ is termed the *mutual intensity*. The function $\Gamma_{11}(\tau) = \langle E_1(t) E_1^*(t + \tau) \rangle$ is known as the *autocorrelation function* or the *self-coherence function*.

Equation (3) is given as

$$I_P(\tau) = I_1 + I_2 + 2|\Gamma_{12}(\tau)| \cos(2\pi\nu\tau + \psi_{12}). \tag{5}$$

The *complex degree of coherence* is defined as

$$\gamma_{12}(\tau) = \Gamma_{12}(\tau) \big/ [\Gamma_{11}(0)\Gamma_{22}(0)]^{1/2} = \Gamma_{12}(\tau) \big/ (I_1 I_2)^{1/2}. \tag{6}$$

The intensity at $P$ is written as

$$I_P(\tau) = I_1 + I_2 + 2(I_1 I_2)^{1/2} |\gamma_{12}(\tau)| \cos(2\pi\nu\tau + \psi_{12}). \tag{7}$$

The visibility of the interference fringes, $V$, is defined as

$$V = (I_{\max} - I_{\min}) \big/ (I_{\max} + I_{\min}), \tag{8}$$

which becomes

$$V = \left[ 2(I_1 I_2)^{1/2} \big/ (I_1 + I_2) \right] |\gamma_{12}(\tau)|. \tag{9}$$

A qualitative description of some of the basic experiments which illustrate the coherence effects follows. It should be emphasized that the effects of coherence in a radiation field are all contained in the complex function $\gamma_{12}(\tau)$. It is useful to separate the coherence effects into two categories. The first category, termed temporal coherence, results from the finite spectral bandwidth of the radiation, $\Delta\nu$. The second category, termed spatial coherence, results from angular source size $\theta$. The region of high spatial coherence is defined by the transverse coherence length $l_t = \lambda/\theta$. Thus, $\gamma_{11}(\tau)$ (or, simply, $\gamma(\tau)$) is a measure of temporal coherence and $\gamma_{12}(0)$ (or, simply, $\mu_{12}$) measures spatial coherence effects. The free space coherence length $l_c = c\tau_c$ is measured as the full-width-half-maximum (FWHM) of the $|\gamma(\tau)|$-function and is defined by the spectral bandwidth $\Delta\nu$ ($\tau_c \sim 1/\Delta\nu$). The coherence length of the supercontinuum is short and of the order of a few microns. It is not necessarily true that the coherence length is always inversely proportional to the entire spectral width $\Delta\nu$ of the supercontinuum and/or the entire spectrum can be used to produce the shortest pulse duration. For example, the soliton's time jitter and its associated changes in the supercontinuum spectrum as the result of the pulse noise can cause decoherence in a portion of the entire supercontinuum spectrum.

The supercontinuum is an unusual "white-light" source because of its distinction with a conventional white-light source (Alfano and Shapiro, 1970). The supercontinuum has a high degree of spatial coherence resulting in a highly collimating beam. Moreover, the frequency and time are well correlated in the supercontinuum pulse produced by the self-phase modulation (SPM) process. The chirped supercontinuum pulse spectrum ($\omega$ versus $t$) can be compressed to the ultrashort pulse due to high spectral phase correlation.

Significant progress in femtosecond (fs) pulse generation from mode-locked lasers has made it possible to generate optical pulses below 20 fs which are of a few cycles in duration (Nisoli et al., 1996; Baltuska et al., 2002). This achievement has resulted in a growing interest in controlling the phase of the underlying carrier wave with respect to the envelope profile (Jones et al., 2000; Apolonski et al., 2000). The supercontinuum pulses have become an important tool in precision optical frequency measurements (Hartl et al., 2001), and in the generation of attosecond pulses (Baltuska et al., 2003).

The electric field of an ultrashort pulse in a laser pulse train is given by

$$E(t) = A(t)\cos(\omega_0 t + \varphi). \tag{10}$$

The fields depend on the carrier-envelope phase (CEP) $\varphi$, determining the position of the carrier wave (oscillating at frequency $\omega_0$) with respect to the amplitude envelope $A(t)$. Due to cavity or material dispersion ($n(\lambda)$) the group velocity $v_g \neq v_p$ (the phase velocity), the CEP is shifted with each successive laser pulse by

$$\Delta\varphi = (1/v_g - 1/v_p)L\omega_0 = (n_g - n)L\omega_0/c, \tag{11}$$

where $L$ is of round-trip cavity length, and group index is $n_g = n + \omega\, \partial n/\partial\omega$.

For a light pulse traveling in a nonlinear Kerr media where the index $n = n_0 + n_2 I(t)$ is of length $l$, the net $\Delta\varphi$ shift becomes

$$\Delta\varphi = (\omega\, \partial n/\partial\omega - I(t)\omega\, \partial n_2/\partial\omega)(\ell\omega/c), \tag{12}$$

which can be written as

$$\Delta\varphi = \delta\varphi^0 + \delta\varphi^{NL}. \tag{13}$$

In the frequency domain, $\Delta\varphi$ results in offset frequency $f_{CE}$ from the exact repetition rate $f_{\text{rep}}$. The frequency of each individual laser mode $f_m$ is given by

$$f_m = mf_{\text{rep}} + f_{CE}, \tag{14}$$

where $m$ is the mode number and $f_{\text{rep}} = 1/\tau$ is the repetition frequency of the pulse train with time $\tau$ between pulses. The offset can be rewritten as

$$\Delta\varphi = 2\pi\, f_{CE}/f_{rep}. \tag{15}$$

The linear dispersion does not effect $f_{CE}$ whereas $\delta\varphi^{NL}$ changes the pulse-to-pulse phase, and $f_{CE}$ causes additional noise, jitter, and CEP coherence degradation. The pulse-to-pulse evolution of the CEP can be measured and stabilized by the laser cavity feedback control using the supercontinuum in a $f$-to-$2f$ interferometer such that the CEP coherence is maintained (Jones et al., 2000). Carrier-envelope coherence time was used to quantitatively characterize CEP stability (Fortier et al., 2002). A mode-locked laser pulse train can produce a phase-locked frequency comb spectrally limited by femtosecond pulse duration. The coherent supercontinuum generation is needed to produce a spectral comb *spanning an octave.* The supercontinuum generation process is particularly important to ensure that the phase coherence is transferred from laser pulses to supercontinuum pulses.

## 3. Coherence of Supercontinuum Generated in a Bulk Media

The mutual coherence of the supercontinuum pulses independently generated in a bulk media ($CaF_2$, glasses) was tested by performing an experiment related to the double-source interference, such as was done by Bellini and Hansch (2000). Two supercontinuum pulses were independently generated at different lateral positions in the $CaF_2$ plate by two phase-locked laser pulses (see Figure 11.1). When the two pump pulses were adjusted for zero relative delay, clear and stable interference fringes were produced in space by the two white-light continua, generating independently, indicating that supercontinuum sources were highly phase-correlated. The interference pattern was spectrally dispersed with a planar diffraction grating and a lens. It was possible to produce stable fringe patterns of high contrast over the entire spectrum demonstrating the high supercontinuum pulses' mutual (spectral) coherence over the entire visible spectrum.

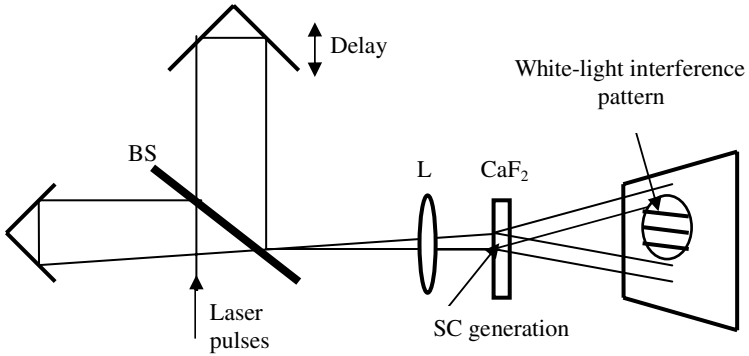


FIGURE 11.1. Experimental setup for testing the phase lock between two "white-light" continuum pulses. The infrared pulses from the laser are split by a 50% beam splitter (BS) and focused with a variable relative delay by lens L onto a thin $CaF_2$ plate. Interference fringes between the two emerging continua are detected on a screen in the far field.

There is a substantial difference between the Bellini–Hansch (BH) approach and the Young- or Michelson-type experiments. In such cases two spatial portions of the same beam or two time-delayed replicas of the *same* pulse are recombined to produce interference. In the Bellini–Hansch experiment the interference fringes appear because of the spatio-temporal superposition of two white-light pulses that are independently generated at two separate positions of the $CaF_2$ plate by split pulses. These supercontinuum pulses were expected to be highly uncorrelated. However, the Bellini–Hansch experiment has shown that the phase relations of the pump pulses were transferred to the supercontinuum pulses producing stable interference fringes.

In addition, the collinear generation of supercontinuum pulses in bulk media was demonstrated using time-delayed pulses from the visible down to the near-infrared, demonstrating that the mutual coherence of the pump pulses is fully transferred to the two supercontinua pulses (Corsi et al., 2003).

To characterize interference between independent supercontinuum pulses the mutual (spectral) coherence function was introduced by Dudley and Coen (2002). In optical coherence tomography (OCT) (Hartl et al., 2001), the high-axial resolution depends on the interference with the pair of the *same* supercontinuum pulses (separated into the reference and sample pulses). The resulting interference pattern depends on time-delay interference that is averaged over multiple pairs. To characterize this type of interference in the time domain, the degree of temporal coherence ($|\gamma(\tau)|$-function) can be used.

The "self-coherence" properties of the supercontinuum generated in a thin plate of different solid materials were experimentally investigated using a diffraction-grating-based interferometer (Zeylikovich and Alfano, 2003).

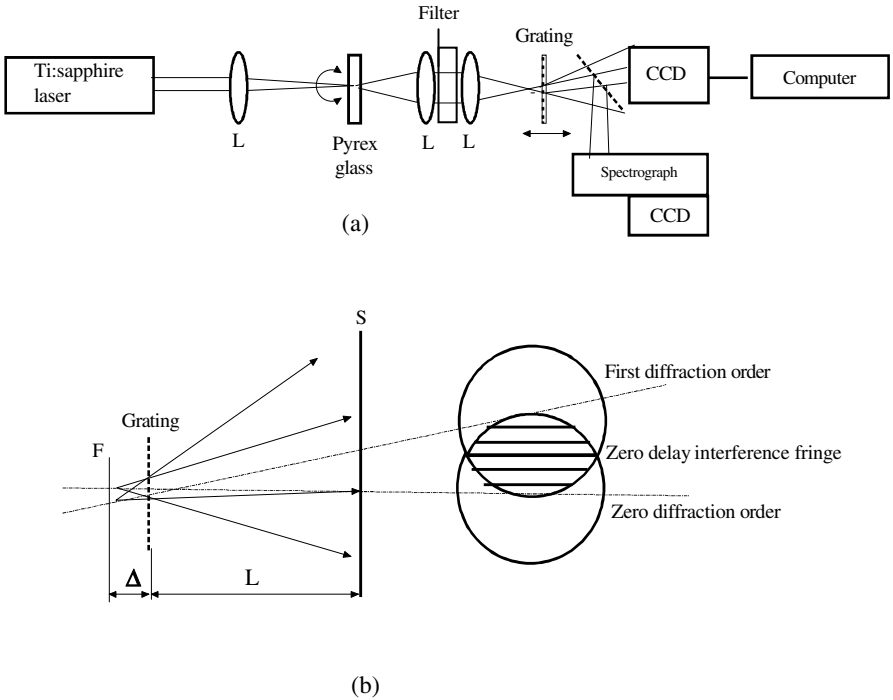


FIGURE 11.2. (a) Experimental setup for measuring spatial-temporal coherence of the supercontinuum generation; and (b) a diagram of the diffraction grating based interferometer focused by a 10-cm focal length lens into plane-parallel plates of $CaF_2$, sapphire, BK-7.

This interferometer does not require a reference beam and is not sensitive to vibration. The experimental setup to explore the coherence of the supercontinuum source is shown schematically in Figure 11.2(a). A mode-locked Ti : sapphire amplifier system provides 200-fs pulses with a repetition rate of 250 kHz and about 20 MW peak power. The output of the Ti : sapphire laser centered at 800 nm is fused silica, and pyrex glass. A broadband supercontinuum extending from 400 nm to 850 nm is produced in the 9-mm thickness pyrex glass plate (PGP). To achieve stable supercontinuum generation the PGP is rotated at 2 Hz. The supercontinuum out of the plate is collimated by the fused silica lens and is focused by a 3-cm focal-length fused silica lens into the diffraction grating (100 lines/mm). Diffraction grating (DG) is placed near the focus of the lens and interference fringes appear by the interference of zero and first diffraction orders. The interference pattern is captured by the 14-bits charge coupled device (CCD) camera. The optimal interferometric fringes are shown in Figure 11.3(a)(insert) together with an intensity distribution in the $x$-direction perpendicular to the interference fringes. The

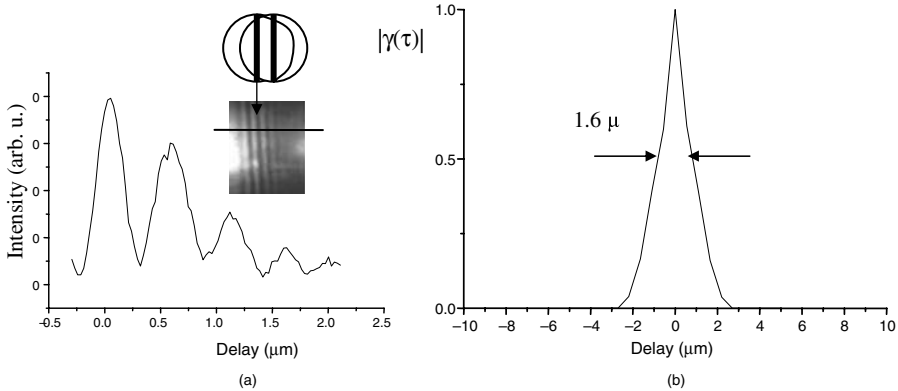


FIGURE 11.3. Interferometric fringes are shown in (a) together with an intensity distribution in the $x$-direction perpendicular to the interference fringes. The degree of temporal coherence is shown in (b).

fringe visibility is given by Eq. (9) and can be rewritten as

$$V = V_0|\gamma_{12}(\tau)|, \tag{16}$$

where $V_0 = [2(I_1I_2)^{1/2}/(I_1 + I_2)]$, and $I_1$ and $I_2$ are the zero and first diffraction orders' intensities. The degree of *spatial* coherence $|\mu_{12}| = |\gamma_{12}(0)|$ can be obtained measuring the fringe visibility at zero path difference ($V(0)$). Since $|\gamma_{12}(\tau)| = |\mu_{12}||\gamma(\tau)|$ (where $|\gamma(\tau)| = |\gamma_{11}(\tau)|$ is the degree of temporal coherence, $|\gamma(0)| = 1$), and from Eq. (16) $|\mu_{12}|$ can be obtained as

$$|\mu_{12}| = V(0)/V_0. \tag{17}$$

Using Eqs. (16) and (17), $|\gamma(\tau)|$ is given as

$$|\gamma(\tau)| = V(\tau)/|\mu_{12}|V_0 = V(\tau)/V(0). \tag{18}$$

Measuring the visibility $V(x)$ of the interference fringes at different $x$-positions, the function $V(\tau)$ can be calculated using Eq. (18).

The degree of spatial coherence $|\mu_{12}|$ of about 0.34 was calculated by Eq. (17) using the intensity distribution shown in Figure 11.3(a) (for zero delay and for zero and first diffraction orders wavefronts shift ($\delta X$) of half of beam diameter). The degree of temporal coherence was calculated by Eq. (18) and by using the intensity distribution shown in Figure 11.3(a) (for different time delays). The result is shown in Figure 11.3(b).

The free-space coherence length $l_c$ of the supercontinuum source is defined by the FWHM of the $|\gamma(\tau)|$ and is about 1.6 $\mu$m. The $l_c$ is given by (Hartl et al., 2001)

$$\ell_c = [2\ln(2)/\pi](\lambda_0^2/\Delta\lambda), \tag{19}$$

where $\Delta\lambda$ is the spectral bandwidth.

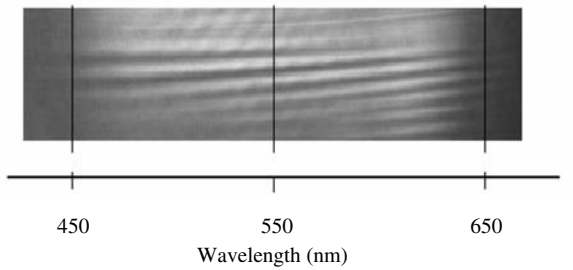


FIGURE 11.4. Supercontinuum spectral interference fringes from a pyrex glass plate.

The spectrum of the supercontinuum source had a bandwidth $\Delta\lambda$ of about 140 nm centered at 550 nm. To achieve a flat spectrum distribution along a bandwidth $\Delta\lambda$ the very high intensity part of the entire spectrum was cut off above 650 nm by the short pass filter. A "blue" part of the spectrum of about 450 nm was limited by the sensitivity of the CCD detector. The $l_c$ was calculated to be about 0.95 $\mu$m which is significantly less than the experimental 1.6 $\mu$m. The "effective" spectral bandwidth $(\Delta\lambda)_{\text{eff}}$ of the supercontinuum source was estimated to be 83 nm (using Eq. (19)). To explain the reduction of the spectral bandwidth the degree of *spatial* coherence over the entire visible spectrum was measured.

The interferometer was combined with the spectrograph and the interference fringes were set parallel to the dispersion direction of the spectrograph by rotating the DG by 90°. The interference spectrum was registered by the CCD camera. The spectral interference is shown in Figure 11.4. The intensity distributions at different path differences were taken in the direction perpendicular to the spectrograph dispersion and correspond to the wavelengths specified in the caption. Using these intensity distributions the degree of spectral *spatial* coherence $|\mu_{12}(\lambda)|$ was calculated using the intensity distribution shown in Figure 11.4 at a zero path difference of 0.45 at 550 nm, of 0.31 at 650 nm, and of 0.19 at 450 nm. The average of these numbers, of about 0.31, is closed to the $|\mu_{12}| = 0.34$. The degradation of the $|\mu_{12}|$ can be associated with spectral phase and amplitude fluctuations.

## 4. Coherence of Supercontinuum in Photonic Crystal Fibers (PCFs)

### 4.1 Supercontinuum Generation in PCFs

The supercontinuum generation is sensitive to input pulse noise which is of particular importance for applications requiring stability over an octave-

spanning supercontinuum sources, for such applications as metrology which requires highly coherent supercontinuum light with limited pulse-to-pulse variations and reduced timing jitter. The fluctuations in both the temporal and spectral properties were studied by Dudley and Coen (2002a,b) using numerical simulations of supercontinuum generation in PCFs in the presence of noise on the input pulse. By quantifying the phase fluctuations using the mutual degree of coherence, the influence of the input pulse wavelength and duration on the supercontinuum coherence was calculated, allowing optimal experimental conditions for coherent supercontinuum generation to be identified. Quantum noise was modeled phenomenologically by including in the input field a noise seed of one photon per mode with random phase. Simulation parameters were used for a 10-cm tapered fused-silica strand of 2.5-μm diameter with a Zero Dispersion Wavelength at 780 nm, in which supercontinuums spanning more than an octave were generated. Dudley and Coen (2002a) simulations were first carried out with 10-kW peak power, 150-fs duration (FWHM) hyperbolic secant input pulses injected at 850 nm in the anomalous dispersion regime.

The simulations allow the physical origin of several major spectral and temporal features to be identified. In particular, with an anomalous-dispersion regime input, nonlinear and dispersive interactions lead to rapid temporal oscillations owing to ultrafast modulation instability (MI) which initiates a multisoliton generation. These solitons separate temporally from the residual input pulse by different amounts that are due to group-velocity walk-off. The Dudley and Coen (2002b) results also show that the supercontinuum pulses that are generated are affected by significant spectral and temporal jitter from run to run. As well as causing significant averaging of any integrated temporal or spectral characteristics that would be experimentally measured, this jitter is associated with coherence degradation caused by severe fluctuations in the spectral phase at each wavelength.

The modulus of the complex degree of first-order coherence calculated over a finite bandwidth at each wavelength in the supercontinuum is given by (Dudley and Coen, 2002a)

$$\left|g_{12}^{(1)}(\lambda, t_1 - t_2)\right| = \left|\left\langle E_1^*(\lambda, t_1) E_2(\lambda, t_2)\right\rangle\right| \Big/ \left[\left\langle \left|E_1(\lambda, t_1)\right|^2 \right\rangle \left\langle \left|E_2(\lambda, t_2)\right|^2 \right\rangle\right]^{1/2}. \quad (20)$$

The angle brackets denote an ensemble average over independently generated supercontinuum pairs $[E_1(\lambda, t)E_2(\lambda, t)]$ and $t$ is the time measured at the resolution time scale of the spectrometer. The ensemble average was applied to the results of many simulations with different random quantum noise.

The coherence, $|g_{12}^{(1)}|$ at $t_1 - t_2 = 0$, was calculated which would correspond to measuring the fringe visibility in a two independently generated supercontinuum sources' interference. During the initial stage of evolution, at $z =$ 2 cm, the input pulse undergoes significant compression and associated spectral broadening and $|g_{12}^{(1)}| \approx 1$ over most of the supercontinuum spectrum. For $z = 5$ cm, where the effects of MI and pulse breakup were clearly manifested on the temporal intensity profile, there was significant coherence degradation,

with a reduced $|g_{12}^{(1)}|$. The coherence degradation also increases for longer $z$ = 10 cm at the fiber output, $|g_{12}^{(1)}| << 1$ over most of the supercontinuum.

Superior coherence properties were shown to be expected for supercontinuum generated with shorter input pulses where SPM plays a more significant role in the spectral broadening and the effects of MI are reduced. This result was confirmed for 150-fs input pulses with those obtained using shorter input pulse durations of 100 fs and 50 fs. Although the spectral broadening in all cases were comparable, MI on the temporal profile is less apparent as the input pulse duration was reduced, and shorter input pulses were clearly seen to lead to an improved coherence, with $|g_{12}^{(1)}| \approx 1$ over more than an octave for the shortest input pulses of 50 fs. In addition, for a pulse with an input wavelength of 740 nm in the normal-dispersion regime in which MI was completely inhibited, there was negligible coherence degradation. The generated spectral width of 350 nm at the 20-dB level was, however, significantly less than that obtained with an anomalous-dispersion regime pump. The significant coherence degradation observed at 780 nm (the ZDW) and 820 nm (anomalous dispersion) was consistent with the increased influence of MI at these longer wavelengths. For frequency metrology application, it is clear that supercontinuum must be generated where coherence degradation is minimized and where supercontinuum spans over an octave.

## 4.2 Supercontinuum Coherence Properties in a PCF

The mechanisms responsible for supercontinuum coherence degradation near and far from the ZDW are still not completely understood. Both temporal and spectral coherence time-delay resolved measurements provide more complete information on supercontinuum coherence that is important for different applications. The supercontinuum temporal and mutual coherence degradation near and far from the ZDW with a novel approach for producing spectral interference in the fiber output was investigated (Zeylikovich et al., 2005). The experimental setup is shown in Figure 11.5. An Er : fiber oscillator/amplifier/frequency-doubling system (IMRA femtolite "C" series) provides 120-fs pulses centered at 1560 nm and 90-fs pulses centered at 780 nm with a repetition rate of 48 MHz and about 40/20 mW average power at 1560/780 nm. Pulses were coupled into a 1.5 m-long section of PCF (purchased from Crystal Fibre A/S). The ZDW was located at 740 nm.

The fiber consisted of a fused silica core with a diameter of 2 $\mu$m, embedded in a fused silica cladding of air-filled cylinders parallel to the core in a hexagonal pattern. Spectra of the fiber output were analyzed using an optical spectrum analyzer (OSA, ANDO AQ-6317). The fiber output in time domain was studied using the rapid scanning autocorrelator (FR-103XL) that utilizes a background-free, second-harmonic generation (SHG) for the measurement of the pulse intensity autocorrelation function. The coherence length of the supercontinuum light was measured using a diffraction-grating-based interferometric autocorrelator (Zeylikovich et al., 1995).

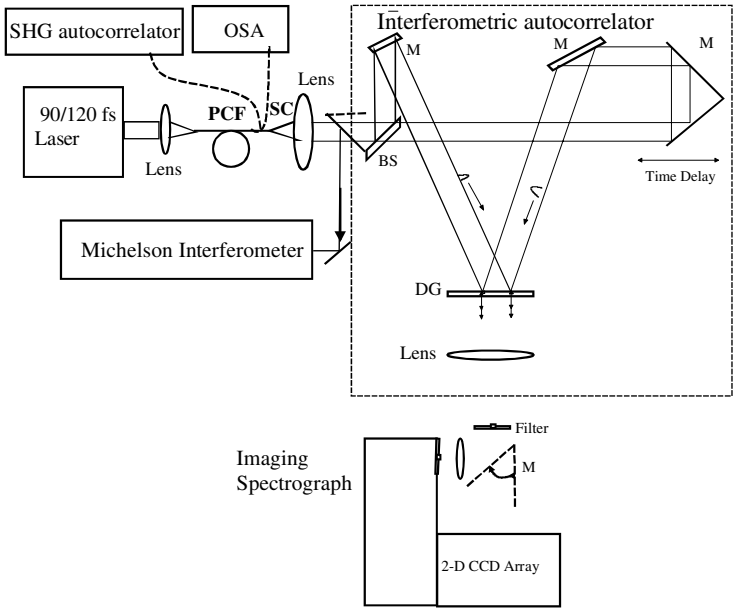


FIGURE 11.5. The experimental setup for spectra and spectral-temporal coherence of the supercontinuum generation measurements. M, mirrors; BS, beam splitter, DG, diffraction grating; OSA, the optical spectrum analyzer.

The soliton number $N$ is an integer closest to the parameter (Agrawal, 2001) $A_0 = (\gamma P_0 T_0^2/|\beta_2|)^{1/2}$, where $\gamma = n_2\omega/cA_{\text{eff}}$ is the nonlinear coefficient equal to ~0.1 $W^{-1}m^{-1}$ at 800 nm, $P_0$ is the peak power, $T_0 = T_{\text{FWHM}}/1.76$ is the pulse duration, and $\beta_2$ is the group velocity dispersion coefficient (~ –0.015 $ps^2/m$ at 800 nm).

At 22-W peak power, distinct Stokes and anti-Stokes Raman peaks at 785 mm and 778 mm were observed, respectively, followed by the generation of the strong distinct second component at 772 nm and the third anti-Stokes component (see Figure 11.6). As the power was increased to 45 W, a second separate peak split off from the pump. The generation of a second soliton peak was accompanied by the appearance of a blue-shifted peak around 677 nm. Increasing the power from 45 W to 90 W pronounced the first soliton frequency shift up to 50 nm, followed by the 12-nm shift of the blue-shifted peak with the power increasing. As the input power was increased further to 140 W, the spectral peak at 830 nm was split into two spectral peaks at 812 nm and 856 nm. The temporal behavior of the solitons was obtained using a SHG autocorrelator. One was used to measure the solitons' time-delay (depending from the pump peak power) and jitter. The autocorrelation results show the appearance of new pulses (solitons) generated in the fiber that propagate at different speed. The results show run-to-run variations in the structure of the observed temporal intensity. The estimated value of the

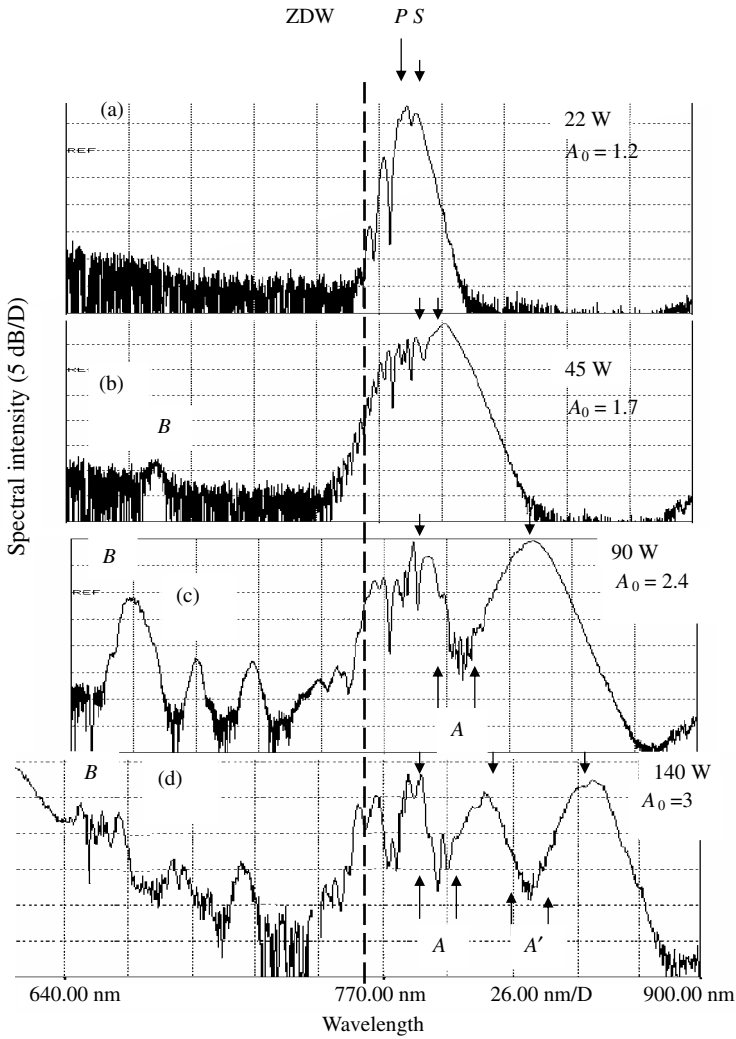


FIGURE 11.6. Recorded spectra at a pump wavelength of 780 nm ($P$) for different peak powers coming out of the fiber. $S$ and ↓ indicate solitons spectral peaks. Spectral-domain interference of the corresponding soliton spectral bands are shown as the labeled features $A$ and $A'$.

observed jitter $\Delta t$ is about 0.1 ps. A time-integrated measurement of the jitter averages out the jitter that occurs on a time scale shorter than the device integration time.

### 4.2.1 Supercontinuum Self- and Mutual Coherence in the PCF

The coherence length of the supercontinuum light for the 140 W peak power was measured by a diffraction-grating-based autocorrelator (Zeylikovich et

al. 1995). The measured $l_c$ was about 12 $\mu$m in good agreement with the Michelson interferometer measurements. The theoretical $l_c$ is given by Eq. (19) which is derived for a transform-limited Gaussian pulse. The spectrum of the supercontinuum pulse extends over 100 nm. The "effective" spectral bandwidth $(\Delta\lambda)_{\text{eff}}$ of the supercontinuum source (with the equivalent Gaussian spectrum bandwidth) was estimated to be 20 nm giving, from Eq. (19), a theoretical coherence length of 12 $\mu$m. To explain this difference between the estimated "effective" spectrum bandwidth (~20 nm) and the experimental value of the supercontinuum spectrum bandwidth (~100 nm), the experiments were performed using the spectrograph combined with the autocorrelator. The near zero-delay interferometric region produced by the DG-based autocorrelator was focused perpendicular to the spectrograph entrance slit. A portion of the time-delayed interference spectrum was registered by the CCD camera (Figure 11.5). The two-dimensional spectral interference is shown in Figure 11.7(b)–(e). The spectra (Figure 11.7(d), (e)) reflect interference in the normal dispersion region while Figure 11.7(b) and (c) are in the anomalous dispersion region.

The condition for maximum intensity of the two-dimensional spectral interference is given by

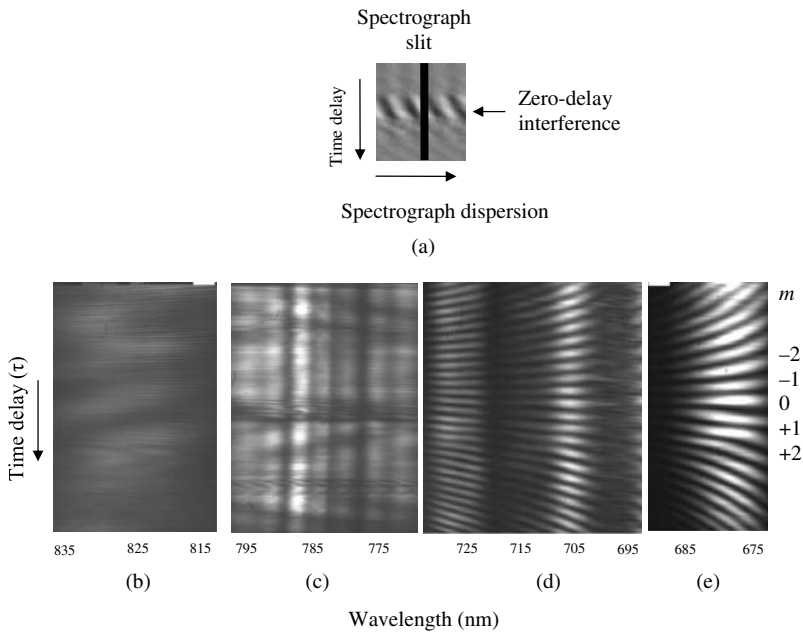


FIGURE 11.7. The two-dimensional time-delay resolved spectral interference results: (a) the spectrograph entrance slit together with the near zero-delay interferometric region (rotated horizontally); (b)–(e) two-dimensional time-delay resolved spectral interference.

$$\omega\tau = 2m\pi, \qquad \text{where} \quad m = 0, \pm 1, \pm 2, \ldots \tag{21}$$

Integer numbers $m = 0, \pm 1, \pm 2, \pm 3$ are interference orders. Figure 11.7 has a wavelength scale along the $x$-axis. The fringes should then appear linear, oriented under the certain angle to the $x$-axis (as observed in Figure 7(d)). The angle between the $m$th interference fringe and the $x$-axis is given by

$$\tan \alpha_m = mD/K, \tag{22}$$

where $D = d\lambda/dx$ is a spectrograph dispersion and $K$ is a calibration coefficient.

The distance $\delta y$ between two interference fringes along the $y$-direction is

$$\delta y = c\delta\tau = \lambda,$$

so that it should increase with increasing $\lambda$ and this is opposite to what is observed in Figure 11.7(d) and (e). The blue-shifted spectral components (nonsolitonic radiation (NSR)) produce fringes in the regions of Figure 11.7(d) and (e). It is assumed, that a dispersive wave (Dudley and Coen, 2002a) was a starting process for the NSR. Under certain pump power, the dispersive wave was parametrically coupling with the soliton through the four-wave mixing. In this case, the four waves are generated at well-defined angles. In addition, when an intense ultrashort laser pulse propagates through a medium, it distorts the atomic and molecular configuration which in turn changes the refractive index. This effect changes the phase, amplitude, and frequency of the incident laser pulse. The phase change can cause a frequency sweep within the pulse envelope, producing SPM and a well-defined temporal chirp. Both of these processes can change the spectral interference fringe shape and spectral period. A detailed analysis is needed to explain the shape of fringes observed in Figure 11.7(d) and (e).

The spectral interference shown in Figure 11.7(d), (e) clearly shows the high degree of spectral coherence for the NSR (Figure 11.7(e), (d)), and the coherence degradation in the pump (Figure 11.7 (c)), and the soliton's spectral (Figure 11.7(b)) regions. The spectral coherence degradation observed in Figure 11.7(b), (c) is associated with run-to-run fluctuations in the spectral phase at each wavelength, and temporal coherence degradation is associated with the temporal jitter.

Clarification is needed to distinguish the "same" pulse spectral coherence and the "pulse-to-pulse" mutual coherence shown by the Bellini–Hansch experiment. In OCT (Hartl et al., 2001), the high-axial resolution depends on the interference with the pair of the same supercontinuum pulses (separated into the reference and sample pulses). The resulting interference pattern depends on time-delay interference that is averaged over multiple pairs. If a single pulse spectral interference is considered (without averaging over multiple input pulses), then $V(\lambda) = 1$ which reflects the fact that a light pulse is always self-coherent. The soliton's time jitter and associated changes in the supercontinuum spectra as a result of input pulse noise cause decoherence.

In this case, $\Delta\lambda$ used for the $l_c$ calculation needs to be estimated by the FWHM of the spectrally coherent regions (Figure 11.7(e) and (d)).

### 4.2.2 Mutual (Axial) Supercontinuum Coherence in the PCF

Two time-delayed femtosecond pump pulses propagating axially in the PCF with the group velocity $\upsilon_g$, produce two independent supercontinuum pulses (Zeylikovich et al., 2005), as shown in Figure 11.8. The $E_1(t)$ and $E_2(t-\tau)$ are amplitudes of the generated supercontinuum pulses, separated in time by the fixed time interval $\tau$. The $G_1(\omega, z)$ and $G_2(\omega, z-\upsilon_g\tau)\exp(-i\omega\tau)$ are the spectral amplitudes of these dual-pulses generated in fiber at lengths $z$ and $z-\upsilon_g\tau$. At the output of fiber, the dual-pulses produce spectral interference patterns with intensity of $I(\omega, \tau)$, where wavelength peaks depend upon time delay:

$$I(\omega,\tau)=\left\langle\int_0^L\left|G_1(\omega,z)+G_2(\omega,z-\upsilon_g\tau)\exp(-i\omega\tau)\right|^2dz\right\rangle$$
$$=\left[\langle I_1(\omega)\rangle+\langle I_2(\omega)\rangle\right]\left[1+K\left|g_{12}(\omega,\tau)\right|\cos(\omega\tau-\delta)\right], \qquad (23)$$

where

$$\delta=\arg g_{12}(\omega,\tau),\quad I_1(\omega)=\int_0^L|G_1(\omega,z)|^2dz,\quad I_2(\omega)=\int_0^L|G_2(\omega,z)|^2dz,$$

and $K|g_{12}(\omega, \tau)|$ is the contrast of the multiple-frequency channels. The coefficient $K$ is given by

$$K=2\left[\langle I_1(\omega)\rangle\langle I_2(\omega)\rangle\right]^{1/2}\Big/\left[\langle I_1(\omega)\rangle+\langle I_2(\omega)\rangle\right],$$

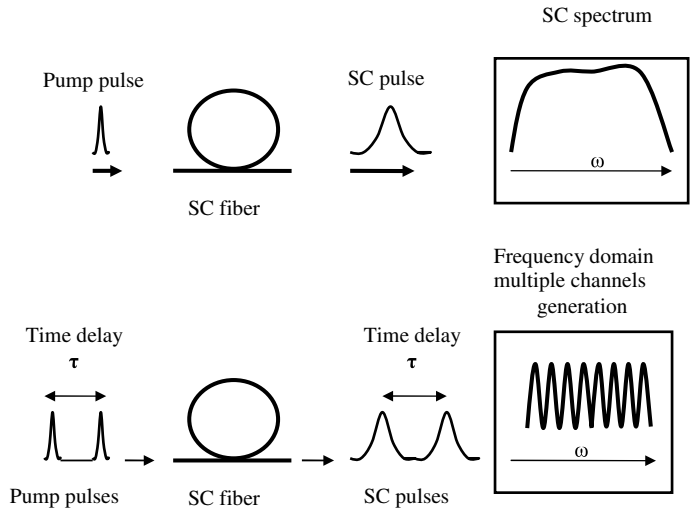


Figure 11.8. Multiple frequency channels generation setups. Spectra of single and dual pulses.

and the complex degree of mutual (axial) coherence between the independent axial supercontinuum sources is

$$g_{12}(\omega,\tau)=\left\langle \int_0^L G_1(\omega,z)G_2{}^*(\omega,z-v_g\tau)\,dz \right\rangle \Big/ \left[\langle I_1(\omega)\rangle\langle I_2(\omega)\rangle\right]^{1/2}, \qquad (24)$$

where $L$ is the fiber length. The angle brackets denote an ensemble average over independently generated pairs of supercontinuum spectra.

In the spectral domain, the period of the spectral interference fringes is $\Omega = 1/\tau$. The frequency interval can be changed by variation of the time delay $\tau$. The output supercontinuum spectrum from the PCF for the 120-fs pulses centered at 1560 nm with 500-W peak power is shown in Figure 11.8(a). The parameter $A_0$ was calculated to be 1.6 ($N = 2$) for $\gamma \sim 0.05\,\mathrm{W}^{-1}\,\mathrm{m}^{-1}$, ZDW $\lambda = 740$ nm, and $|\beta_2| \sim 0.2\,\mathrm{ps}^2/\mathrm{m}$ at 1550 nm.

The output spectrum for two pump pulses under the same conditions as Figure 11.9(a), separated by the time-delay $\tau \sim 6.7$ ps, is shown in Figure 11.9(b). The spectrum now consists of numerous well-defined frequency peaks. The use of two pump pulses did not change the spectrum envelope. In this case, the degree of spectral coherence (DSC) of the generated soliton was high ($|g_{12}(\omega, \tau)| \sim 0.98$), which is demonstrated by the high contrast of the spectral interference (Figure 11.9(b)). It is assumed that the high DSC of the soliton is due to the fact that the pump wavelength is far from the ZDW ($\lambda = 740$ nm). In this case, the generated supercontinuum is much less sensitive to noise on the input pulse and coherence degradation.

The corresponding spectra generated by two 90-fs pulses at 780 nm near the ZDW separated by $\tau \sim 3.3$ s is shown in Figure 11.9(c). The high contrast ($|g_{12}(\omega, \tau)| \sim 0.8$) spectral interference in Figure 11.9(c) is observed only in the region close to the pump wavelength, and the low contrast ($|g_{12}(\omega, \tau)| \sim 0.05$) is observed in the soliton's spectral region. The increase in two pulses' time-delay up to 6.6 ps led to the generation of the spectrum shown in Figure 11.9(d), which is associated only with self-phase modulation accompanied by the high DSC ($|g_{12}(\omega, \tau)| \sim 0.8$). The use of two delayed pump pulses near the ZDW significantly changed the generated spectrum, as distinct from the two pump pulses spectrum envelope at 1550 nm.

Numerical simulations (Dudley and Coen, 2002a) show that the main source for the soliton's temporal jitter arises from the modulation instability MI effects in the presence of input pulse noise and results in low coherence. The MI bandwidth $B$ and soliton order $N$ depends inversely on the amount of group velocity dispersion (GVD), $|\beta_2|$. The GVD increases for larger wavelengths, thereby $B$ and $N$ in turn decrease. The $B$ and $N$ can be calculated from the relationships (Agrawal, 2001):

$$B = 2(\gamma P_0/|\beta_2|)^{1/2} \qquad \text{and} \qquad N = \left(\gamma P_0 T_0^2/|\beta_2|\right)^{1/2}. \qquad (25)$$

Since $(\gamma/|\beta_2|)^{1/2}$ for 800 nm is approximately five times greater than for the 1550 nm wavelength, the soliton's temporal jitter is much larger for the 800 nm pump when compared with the 1550 nm pump wavelength.

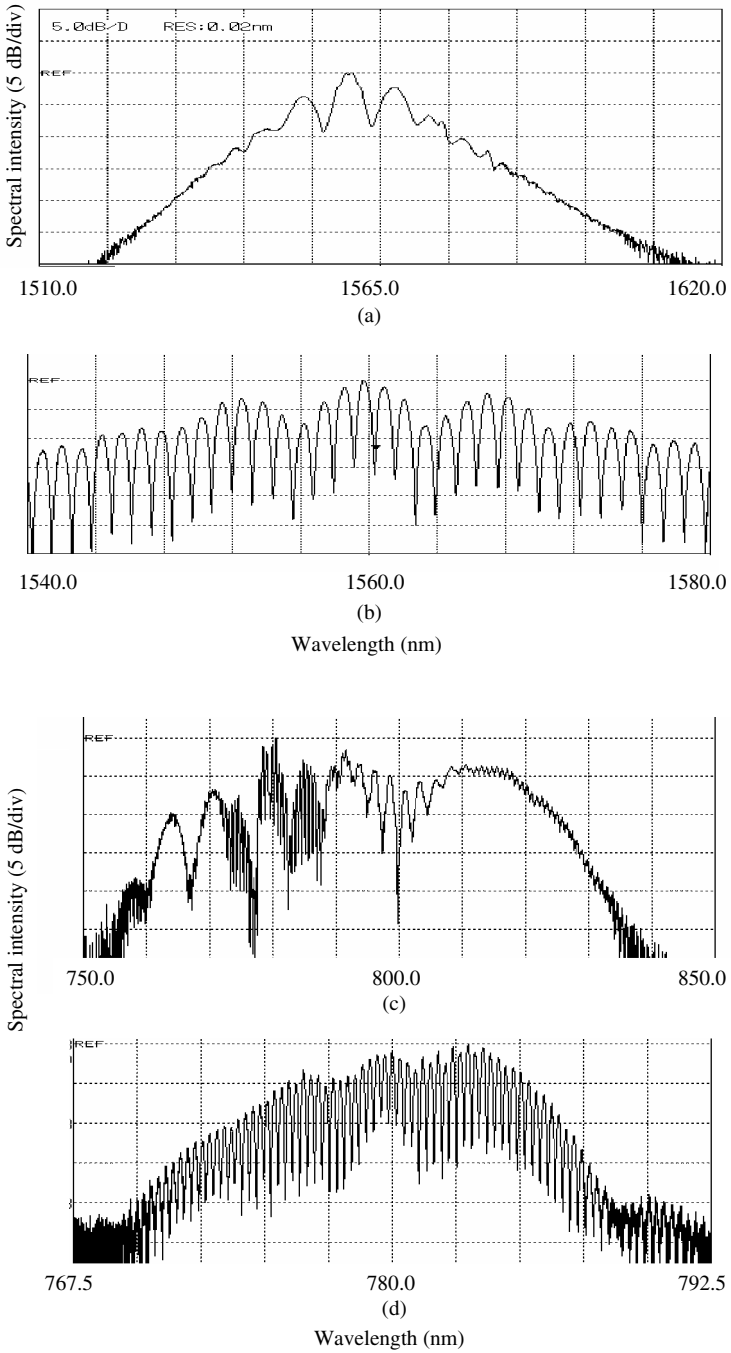


FIGURE 11.9. Recorded spectra at pump wavelengths of: (a) 1560 nm using a single pulse; (b) two pump pulses separated in time by 6.7 ps; (c) 780 nm using two pump pulses separated in time by 3.3 ps; and (d) 6.6 ps.

H. Takara (2002) used picosecond lasers with a repetition rate of ~10 GHz to create multiple optical carriers for the wavelength division multiplexing (WDM) network. It is much simpler to produce a broadband supercontinuum by femtosecond pulses; however, the repetition rate of femtosecond lasers is limited (~100 MHz). This sets up a frequency separation limit between the frequency channels, being no more than 100 MHz. This range is not enough to separate the channels for the WDM network and then transmit information. In our approach, the coherent generation of a large number of frequency channels, at 100 GHz appropriate for the WDM network, is demonstrated by a pair of time-delayed pump pulses.

## 5. Conclusion

This chapter presents some of the salient properties related to the coherence of the supercontinuum laser source generated in bulk and fibers. In fibers with an input anomalous-dispersion region, the supercontinuum pulses that are generated are affected by significant spectral and temporal jitter from run to run, due to MI on the temporal profile and multiple solitons generation producing coherence degradation. The soliton's time jitter, and associated changes in the supercontinuum spectra as a result of input pulse noise, cause decoherence in a portion of the entire supercontinuum spectrum and, as a consequence, the coherence length of the supercontinuum is inversely proportional to the coherent ("effective") spectral bandwidth (not to the entire spectrum). The solitons' spectra have a low coherence when the soliton's wavelength is close to the ZDW and a high degree of spectral coherence when the soliton's wavelength is far from the ZDW. Excellent coherent properties can be achieved for input pulses of duration ~50 fs (or less), with a fiber's length shorter than 5 cm, and/or propagating in the normal-dispersion region. The method of spectral interferometry is a convenient way of quantifying the coherence degradation across supercontinuum spectra generated in fibers and bulk media. The coherent supercontinuum generation of a large number of frequency channels at 100 GHz appropriate for the WDM network has been demonstrated using a pair of time-delayed pump pulses. The well-defined correlation of the frequency versus time behavior in the supercontinuum over a large frequency bandwidth will play an important role in many diverse applications which depend upon coherence.

### References

Agrawal, G.P. (2001) *Nonlinear Fiber Optics.* Academic Press, New York.

Alfano, R.R. and S.L. Shapiro (1970a) Emission in the region 4000 to 7000 Å via four photon coupling in glass. Phys. Rev. Lett. **24**, 584–587.

Alfano, R.R. and S.L. Shapiro (1970b) Observation of self-phase modulation and small-scale filaments in crystals and glasses. Phys. Rev. Lett. **24**, 592–594.

Alfano, R.R. and S.L. Shapiro (1970c) Direct distortion of electronic clouds of rare-gas atoms in intense electric fields. Phys. Rev. Lett. **24**, 1217–1220.

Apolonski, A., A. Poppe, G. Tempea, C. Spielman, T. Udem, R. Holzwarth, T.W. Hansch, and F. Krausz (2000) Controlling the phase evolution of few-cycle light pulses. Phys. Rev. Lett. **90**, 740–743.

Baltuska, A., T. Fuji, and T. Kobayashi (2002) Visible pulse compression to 4 fs by optical parametrical amplification and programmable dispersion control. Opt. Lett. **27**, 306–308.

Baltuska, A., M. Uiberacker, E. Goulielmakis, R. Kienberger, V.S. Yakovlev, T. Udem, T.W. Hansch, and F. Krausz (2003) Phase-controlled amplification of few-cycle laser pulses. IEEE J. Sel. Topics Quantum Electron. **9**, 972–987.

Bellini, M. and T.W. Hansch (2000) Phased-locked white-light continuum pulses: Toward a universal optical frequency-comb synthesizer. Opt. Lett. **25**, 1049–1051.

Born, M. and E. Wolf (1964) *Principles of Optics*. Pergamon Press, Oxford.

Corsi, C., A. Tortora, and M. Bellini (2003) Mutual coherence of supercontinuum pulses collinearly generated in bulk media. Appl. Phys. B **77**, 285–290.

Corwin, K.L., N.R. Newbury, J.M. Dudley, S. Coen, S.A. Diddams, K. Weber, and R.S. Windeler (2003) Fundamental noise limitations to supercontinuum generation in microstuctured fiber. Phys. Rev. Lett. **90**, 113904.

Diddams, S.A., D.J. Jones, J. Ye, S.T. Cundiff, J.L. Hall, J.K. Ranka, R.S. Windeler, R. Holzwarth, T. Udem, and T.W. Hänsch (2000) Direct link between microwave and optical frequencies with a 300 THz femtosecond laser comb. Phys. Rev. Lett. **84**, 5102–5105.

Dudley, J.M. and S. Coen (2002a) Numerical simulation and coherence properties of supercontinuum generation in photonic crystal and tapered optical fibers. IEEE J. Sel. Topics Quantum Electron. **8**, 651–659.

Dudley, J.M. and S. Coen (2002b) Coherence properties of supercontinuum spectra generated in photonic crystal and tapered optical fibers. Opt. Lett. **27**, 1180–1182.

Fortier, T.M., D.J. Jones, J. Ye, S. Cundiff, and R.S. Windeler (2002) Long-term carrier-envelope phase coherence. Opt. Lett. **27**, 1436–1438.

Gu, X., M. Kimmel, A.P. Shreenath, R. Trebino, J.M. Dudley, S. Coen, and R. Windeler (2003) Experimental studies of the coherence of microstructure-fiber supercontinuum. Opt. Express **11**, 2697–2703.

Hartl, I., X.D. Li, C. Chudoba, R.K. Ghanta, T.H. Ko, J.G. Fujimoto, J.K. Ranka, and R.S. Windeler (2001) Ultrahigh-resolution optical coherence tomography using continuum generation in air–silica microstructure optical fiber. Opt. Lett. **26**, 608–610.

Jones, D.J., S.A. Diddams, J.K. Ranka, A. Stentz, R.S. Windeler, J.L. Hall, and S.T. Cundiff (2000) Carrier-envelope phase control of femtosecond mode-locked lasers and direct optical frequency synthesis. Science **288**, 635–639.

Lu, F. and W.H. Knox (2004) Generation of a broadband continuum with spectral coherence in tapered single-mode optical fibers. Opt. Express **12**, 347–353.

Nakazawa, M., K. Tamura, H. Kubbota, and E. Yoshida (1998) Coherence degradation in the process of supercontinuum generation in an optical fiber. Opt. Fiber Technol. **4**, 215–223.

Nisoli, M., S. De Silvestri, and O. Svelto (1996) Generation of high energy 10 fs pulses by a new pulse compression technique. Appl. Phys. Lett. **68**, 2793–2795.

Takara, H. (2002) Multiple optical carrier generation from a supercontinuum source. Opt. & Photonics News **13**, 48–51.

Zeylikovich, I., Q.D. Liu, G. Bai, N. Zhadin, A. Gorokhovsky, and R.R. Alfano (1995) Interferometric 2D imaging amplitude correlator for ultrashort pulses. Opt. Commun. **115**, 485–490.

Zeylikovich, I. and R.R. Alfano (2003) Coherence properties of the supercontinuum source. Appl. Phys. B **77**, 265–268.

Zeylikovich, I., V. Kartazaev, and R.R. Alfano (2005) Spectral, temporal and coherence properties of supercontinuum generation in microstructure fiber. J. Opt. Soc. Am. B **22**, 1453–1460.

# 12
# Supercontinuum Generation in Materials (Solids, Liquids, Gases, Air)

## Summary

This chapter highlights some of the key research papers studying the generation of supercontinuum in a variety of materials (solids, liquids, and gases) since the advent of available femtosecond mode-locked lasers. The focus of most of this research was on extending and controlling the spectral broadening and the involvement of self-focusing to change the spatial profile. Three types of femtosecond lasers have been primarily used in supercontinuum generation: Ti : sapphire lasers operating at about 800 nm, $Cr^{4+}$ : forsterite lasers operating at about 1200 nm, and fiber lasers operating at about 1500 nm. The supercontinuum spectral extending over 300 nm to 4500 nm has been demonstrated in materials. Polarization excitation can be used to control and modify the supercontinuum generation and broadening.

One of the major aims of many of the research papers presented here was to create an ideal "white light" continuum laser source. The width of the continuum spectral band was found to increase with band gap energies of the materials, where $CaF_2$ and LiF are among the best for solids, water for liquids, and argon for gases. The supercontinuum appears to be a "universal phenomenon" created in all transparent Kerr $\chi_3$ materials using intense ultrashort laser excitation pulses with duration in the picosecond to femtosecond range.

## Updated References

Tortora, A., C. Corsi, and M. Bellini (2004) Comb-like supercontinuum generation in bulk media. Appl. Phys. Lett. **85**, No. 7, 1113.

Hovhannisyan, D. and K. Stepanyan (2004) Computational modeling of supercontinuum generation in fused silica by a femtosecond laser pulse of a few optical cycles. Microwave and Optical Technology Letters **42**, No.1, 60.

Schroeder, H. and S.L. Chin (2004) Visualization of the evolution of multiple filaments in methanol. Opt. Commun. **234**, Nos. 1–6, 399.

Rodriguez, M., R. Bourayou, G. Mejean, J. Kasparian, J. Yu, E. Salmon, A. Scholz, B. Stecklum, J. Eisloffel, U. Laux, A.P. Hatzes, R. Sauerbrey, L. Woste, and J.P.

Wolf (2004) Kilometer-range nonlinear propagation of femtosecond laser pulses—Art. no. 036607. Phys. Rev. E **6903**, No. 3, Part 2, 6607.
Luo, Q., S.A. Hosseini, B. Ferland, and S.L. Chin (2004) Backward time-resolved spectroscopy from filament induced by ultrafast intense laser pulses. Opt. Commun. **233**, Nos. 4–6, 411.
Corsi, C., A. Tortora, and M. Bellini (2004) Generation of a variable linear array of phase-coherent supercontinuum sources. Appl. Phys. B **78**, Nos. 3–4, 299.
Boyraz, O., T. Indukuri, and B. Jalali (2004) Self-phase-modulation induced spectral broadening in silicon waveguides. Opt. Express **12**, No. 5, 829.
Dharmadhikari, A.K., F.A. Rajgara, N.C.S. Reddy, A.S. Sandhu, and D. Mathur (2004) Highly efficient white light generation from barium fluoride. Opt. Express **12**, No. 4, 695.
Zhang, J.Y., C.K. Lee, J.Y. Huang, and C.L. Pan (2004) Sub-femto-joule sensitive single-shot OPA-XFROG and its application in study of white-light supercontinuum generation. Opt. Express **12**, No. 4, 574.
Liu, W., S.A. Hosseini, Q. Luo, B. Ferland, S.L. Chin, O.G. Kosareva, N.A. Panov, and V.P. Kandidov (2004) Experimental observation and simulations of the self-action of white light laser pulse propagating in air. New J. Phys. **6**, 6.
Khan, N. and N. Mariun (2004) Observation of discrete supercontinuum spectra from a multi-pulse pumped distributed feedback dye laser. Appl. Phys. B **78**, No. 2, 179.
Grant, C.D., A.M. Schwartzberg, Y.Y. Yang, S.W. Chen, and J.Z. Zhang (2004) Ultrafast study of electronic relaxation dynamics in Au-11 nanoclusters. Chem. Phys. Lett. **383**, Nos. 1–2, 31.
Cook, K., A.K. Kar, and R.A. Lamb (2003) White-light supercontinuum interference of self-focused filaments in water. Appl. Phys. Lett. **83**, No. 19, 3861.
Zheltikov, A. (2003) Supercontinuum generation. Appl. Phys. B **77**, Nos. 2–3, 143.
Kandidov, V.P., O.G. Kosareva, I.S. Golubtsov, W. Liu, A. Becker, N. Akozbek, C.M. Bowden, and S.L. Chin (2003) Self-transformation of a powerful femtosecond laser pulse into a white-light laser pulse in bulk optical media (or supercontinuum generation). Appl. Phys. B **77**, Nos. 2–3, 149.
Fang, X.J. and T. Kobayashi (2003) Evolution of a super-broadened spectrum in a filament generated by an ultrashort intense laser pulse in fused silica. Appl. Phys. B **77**, Nos. 2–3, 167.
Akozbek, N., A. Becker, M. Scalora, S.L. Chin, and C.M. Bowden (2003) Continuum generation of the third-harmonic pulse generated by an intense femtosecond IR laser pulse in air. Appl. Phys. B **77**, Nos. 2–3, 177.
Kolesik, M., G. Katona, J.V. Moloney, and E.M. Wright (2003) Theory and simulation of supercontinuum generation in transparent bulk media. Appl. Phys. B **77**, Nos. 2–3, 185.
Weigand, R., H. Crespo, A. Dos Santos, and P. Balcou (2003) Time-resolved study of the spectral characteristics of supercontinuum pulses propagating in scattering media. Appl. Phys. B **77**, Nos. 2–3, 253.
Corsi, C., A. Tortora, and M. Bellini (2003) Mutual coherence of supercontinuum pulses collinearly generated in bulk media. Appl. Phys. B **77**, Nos. 2–3, 285.
Srivastava, A. and D. Goswami (2003) Control of supercontinuum generation with polarization of incident laser pulses. Appl. Phys. B **77**, Nos. 2–3, 325.
Golubtsov, I.S., V.P. Kandidov, and O.G. Kosareva (2003) Initial phase modulation of a high-power femtosecond laser pulse as a tool for controlling its filamen-

tation and generation of a supercontinuum in air. Quantum Electron. **33**, No. 6, 525.

Liu, W., S.L. Chin, O. Kosareva, I.S. Golubtsov, and V.P. Kandidov (2003) Multiple refocusing of a femtosecond laser pulse in a dispersive liquid (methanol). Opt. Commun. **225**, Nos. 1–3, 193.

Kalosha, V.P. and J. Herrmann (2003) Ultrawide spectral broadening and compression of single extremely short pulses in the visible, UV-VUV, and middle infrared by high-order stimulated Raman scattering. Phys. Rev. A **68**, No. 2, 023812.

Nguyen, N.T., A. Saliminia, W. Liu, S.L. Chin, and R. Vallee (2003) Optical breakdown versus filamentation in fused silica by use of femtosecond infrared laser pulses. Opt. Lett. **28**, No. 17, 1591.

Kolesik, M., G. Katona, J.V. Moloney, and E.M. Wright (2003) Physical factors limiting the spectral extent and band gap dependence of supercontinuum generation. Phys. Rev. Lett. **9104**, No. 4, 3905.

Liu, W., O. Kosareva, I.S. Golubtsov, A. Iwasaki, A. Becker, V.P. Kandidov, and S.L. Chin (2003) Femtosecond laser pulse filamentation versus optical breakdown in $H_2O$. Appl. Phys. B **76**, No. 3, 215.

Iwasaki, A., N. Akozbek, B. Ferland, Q. Luo, G. Roy, C.M. Bowden, and S.L. Chin (2003) A LIDAR technique to measure the filament length generated by a high-peak power femtosecond laser pulse in air. Appl. Phys. B **76**, No. 3, 231.

Kandidov, V.P., O.G. Kosareva, and A.A. Koltun (2003) Nonlinear-optical transformation of a high-power femtosecond laser pulse in air. Quantum Electron. **33**, No. 1, 69.

Skupin, S., U. Peschel, C. Etrich, L. Leine, F. Lederer, and D. Michaelis (2003) Simulation of femtosecond pulse propagation in air. Opt. Quantum Electron. **35**, No. 4, 573.

Saliminia, A., N.T. Nguyen, M.C. Nadeau, S. Petit, S.L. Chin, and R. Vallee (2003) Writing optical waveguides in fused silica using 1 kHz femtosecond infrared pulses. J. Appl. Phys. **93**, No. 7, 3724.

Tzankov, P., T. Fiebig, and I. Buchvarov (2003) Tunable femtosecond pulses in the near-ultraviolet from ultrabroadband parametric amplification. Appl. Phys. Lett. **82**, No. 4, 517.

Yang, H., J. Zhang, J. Zhang, L.Z. Zhao, Y.J. Li, H. Teng, Y.T. Li, Z.H. Wang, Z.L. Chen, Z.Y. Wei, J.X. Ma, W. Yu, Z.M. Sheng (2003) Third-order harmonic generation by self-guided femtosecond pulses in air. Phys. Rev. E **67**, No. 1, Part 2, 5401.

Naumov, S., E. Sorokin, V.L. Kalashnikov, G. Tempea, and I.T. Sorokina (2003) Self-starting five optical cycle pulse generation in $Cr^{4+}$: YAG laser. Appl. Phys. B **76**, No. 1, 1.

Kolesik, M., J.V. Moloney, and M. Mlejnek (2002) Unidirectional optical pulse propagation equation. Phys. Rev. Lett. **8928**, No. 28, 3902.

Xiao, J., Z.Y. Wang, and Z.Z. Xu (2002) Carrier shock and frequency conversion of a few-cycle pulse laser propagating in a non-resonant two-level atom medium. Chinese Phys. **11**, No. 12, 1276.

Kim, K.Y., I. Alexeev, and H.M. Milchberg (2002) Single-shot measurement of laser-induced double step ionization of helium. Opt. Express **10**, No. 26, 1563.

Liu, W., O. Kosareva, I.S. Golubtsov, A. Iwasaki, A. Becker, V.P. Kandidov, and S.L. Chin (2002) Random deflection of the white light beam during self-focusing and filamentation of a femtosecond laser pulse in water. Appl. Phy. B **75**, Nos. 4–5, 595.

Bartels, A. and H. Kurz (2002) Generation of a broadband continuum by a Ti: sapphire femtosecond oscillator with a 1-GHz repetition rate. Opt. Lett. **27**, No. 20, 1839.

Tate, J. and D.W. Schumacher (2002) A novel study of supercontinuum generation. Appl. Phys. B **74**, Supplement 1, S57.

Golubtsov, I.S. and O.G. Kosareva (2002) Influence of various physical factors on the generation of conical emission in the propagation of high-power femtosecond laser pulses in air. J. Opt. Technol. **69**, No. 7, 462.

Popescu, F. and A.S. Chirkin (2002) Self- and cross-phase modulation of ultrashort light pulses in an inertial Kerr medium: Spectral control of squeezed light. J. Opt. B **4**, No. 3, 184.

Schumacher, D. (2002) Controlling continuum generation. Opt. Lett. **27**, No. 6, 451.

Osvay, K., G. Kurdi, J. Klebniczki, M. Csatari, and I.N. Ross (2002) Demonstration of high gain amplification of femtosecond ultraviolet laser pulses. Appl. Phys. Lett. **80**, No. 10, 1704.

Akozbek, N., C.M. Bowden, and S.L. Chin (2002) Propagation dynamics of ultrashort high-power laser pulses in air: Supercontinuum generation and transverse ring formation. J. Mod. Opt. **49**, Nos. 3–4, 475.

Tzankov, P., I. Buchvarov, and T. Fiebig (2002) Broadband optical parametric amplification in the near UV-VIS. Opt. Commun. **203**, Nos. 1–2, 107.

Midorikawa, K., H. Kawano, A. Suda, C. Nagura, and M. Obara (2002) Polarization properties of ultrafast white-light continuum generated in condensed media. Appl. Phys. Lett. **80**, No. 6, 923.

Liu, W., S. Petit, A. Becker, N. Akozbek, C.M. Bowden, and S.L. Chin (2002) Intensity clamping of a femtosecond laser pulse in condensed matter. Opt Commun. **202**, Nos. 1–3, 189.

Lorenc, M., M. Ziolek, R. Naskrecki, J. Karolczak, J. Kubicki, and A. Maciejewski (2002) Artifacts in femtosecond transient absorption spectroscopy. Appl. Phys. B **74**, No. 1, 19.

Tzortzakis, S., L. Sudrie, M. Franco, B. Prade, and A. Mysyrowicz (2001) Self-guided propagation of ultrashort IR laser pulses in fused silica. Phys. Rev. Lett. **87**, No. 21, 213902-1.

Brunel, M., L. Mess, G. Gouesbet, and G. Gréhan (2001) Cerenkov-based radiation from superluminal excitation in microdroplets by ultrashort pulses. Opt. Lett. **26**, No. 20, 1621.

Weigand, R., M. Wittmann, and J.M. Guerra (2001) Generation of femtosecond pulses by two-photon pumping supercontinuum-seeded collinear traveling wave amplification in a dye solution. Appl. Phys. B **73**, No. 3, 201.

Kolesik, M., J.V. Moloney, and E.M. Wright (2001) Polarization dynamics of femtosecond pulses propagating in air. Phys. Rev. E **6404**, No. 4, Part 2, 6607.

Xiao, J., Z.Y. Wang, and Z.Z. Xu (2001) Spectrum of a few-cycle laser pulse propagating in a two-level atom medium. Chinese Phys. **10**, No. 10, 941.

Hovhannisyan, D.L. (2001) Analytic solution of the wave equation describing dispersion-free propagation of a femtosecond laser pulse in a medium with a cubic and fifth-order nonlinearity. Opt. Commun. **196**, Nos. 1–6, 103.

Wang, S.F., Y.D. Qin, H. Yang, D.L. Wang, C.J. Zhu, and G.H. Gong (2001) Dynamics of ionization-enhanced spectral expansion in water induced by an intense femtosecond laser beam. Chinese Phys. **10**, No. 8, 735.

Huber, R., H. Satzger, W. Zinth, and J. Wachtveitl (2001) Noncollinear optical parametric amplifiers with output parameters improved by the application of a white light continuum generated in $CaF_2$. Opt. Commun. **194**, Nos. 4–6, 443.

Akozbek, N., M. Scalora, C.M. Bowden, and S.L. Chin (2001) White-light continuum generation and filamentation during the propagation of ultra-short laser pulses in air. Opt. Commun. **191**, Nos. 3–6, 353.

Yu, J., D. Mondelain, G. Ange, R. Volk, S. Niedermeier, J.P. Wolf, J. Kasparian, and R. Sauerbrey (2001) Backward supercontinuum emission from a filament generated by ultrashort laser pulses in air. Opt. Lett. **26**, No. 8, 533.

Ell, R., U. Morgner, F.X. Kärtner, J.G. Fujimoto, E.P. Ippen, V. Scheuer, G. Angelow, T. Tschudi, M.J. Lederer, A. Boiko, and B. Luther-Davies (2001) Generation of 5-fs pulses and octave-spanning spectra directly from a Ti–sapphire laser. Opt. Lett. **26**, No. 6, 373.

Watanabe, A. and K. Itoh (2001) Spatial coherence of supercontinuum emitted from multiple filaments. Jpn. J. Appl. Phys. Part 1 **40**, No. 2A, 592.

Linkforman, J.-P., M. Mehendale, D.M. Villeneuve, M. Joffre, and P.B. Corkum (2001) Conversion of high-power 15-fs visible pulses to the mid infrared. Opt. Lett. **26**, No. 2, 99.

Bespalov, V.G., S.A. Kozlov, V.N. Krylov, G. Seifang, D.I. Stasel'ko, and Y.A. Shpolyansky (2000) Generation of femtosecond spectral supercontinuum in optical media with electron and electron-vibrational nonlinearities. Izv. Akad. Nauksssr Ser. Fiz. **64**, No. 10, 1938.

Farztdinov, V.M., R. Schanz, S.A. Kovalenko, and N.P. Ernsting (2000) Relaxation of optically excited *p*-nitroaniline: Semiempirical quantum-chemical calculations compared to femtosecond experimental results. J. Phys. Chem. A **104**, No. 49, 11486.

Liu, C.S. and V.K. Tripathi (2000) Laser frequency upshift, self-defocusing, and ring formation in tunnel ionizing gases and plasmas. Phys. Plasmas **7**, No. 11, 4360.

Kasparian, J., R. Sauerbrey, D. Mondelain, S. Niedermeier, J. Yu, J.P. Wolf, Y.B. Andre, M. Franco, B. Prade, S. Tzortzakis, A. Mysyrowicz, M. Rodriguez, H. Wille, and L. Woste (2000) Infrared extension of the supercontinuum generated by femtosecond terawatt laser pulses propagating in the atmosphere. Opt. Lett. **25**, No. 18, 1397.

Sandhu, A.S., S. Banerjee, and D. Goswami (2000) Suppression of supercontinuum generation with circularly polarized light. Opt. Commun. **181**, Nos. 1–3, 101.

Qin, Y.D., C.J. Zhu, H. Yang, and Q.H. Gong (2000) Supercontinuum generation in atmospheric-pressure nitrogen using a tightly focused intense femtosecond laser beam. Chinese Phys. Lett. **17**, No. 6, 413.

Bespalov, V.G., S.A. Kozlov, and Y.A. Shpolyanskii (2000) Method for analyzing the propagation dynamics of femtosecond pulses with a continuum spectrum in transparent optical media. J. Opt. Technol. **67**, No. 4, 303.

Gaeta, A.L. (2000) Catastrophic collapse of ultrashort pulses. Phys. Rev. Lett. **84**, No. 16, 3582.

Petit, S., A. Talebpour, A. Proulx, and S.L. Chin (2000) Some consequences during the propagation of an intense femtosecond laser pulse in transparent optical media: A strongly deformed white-light laser. Laser Phys. **10**, No. 1, 93.

Watanabe, W., Y. Masuda, H. Arimoto, and K. Itoh (1999) Coherent array of white-light continuum generated by microlens array. Opt. Rev. **6**, No. 3, 167.

Efimov, O.M., L.B. Glebov, S. Grantham, and M. Richardson (1999) Photoionization of silicate glasses exposed to IR femtosecond pulses. J. Non-Cryst. Solids **253**, Nos. 1–3, 58.

Kondo, Y., K. Miura, T. Suzuki, H. Inouye, T. Mitsuyu, and K. Hirao (1999) Three-dimensional arrays of crystallites within glass by using non-resonant femtosecond pulses. J. Non-Cryst. Solids **253**, Nos. 1–3, 143.

Chin, S.L., A. Brodeur, S. Petit, O.G. Kosareva, and V.P. Kandidov (1999) Filamentation and supercontinuum generation during the propagation of powerful ultrashort laser pulses in optical media (white light laser). J. Nonlinear Opt. Phys. Mater. **8**, No. 1, 121.

Brodeur, A. and S.L. Chin (1999) Ultrafast white-light continuum generation and self-focusing in transparent condensed media. J. Opt. Soc. Am. B **16**, No. 4, 637.

Morozov, V.B., A.N. Olenin, and V.G. Tunkin (1999) Transformation of strong picosecond pulses in radiation with an extended quasirotational spectrum during self-focusing in high-pressure hydrogen. J. Exper. Theoret. Phys. **88**, No. 2, 263.

Kawano, H., T. Mori, Y. Hirakawa, and T. Imasaka (1999) Stimulated Raman scattering and four-wave Raman mixing seeded by a supercontinuum generated in dibromomethane using picosecond and femtosecond laser sources. Opt. Commun. **160**, Nos. 4–6, 277.

Chin, S.L., S. Petit, F. Borne, and K. Miyazaki (1999) The white light supercontinuum is indeed an ultrafast white light laser. Jpn. J. Appl. Phys., Part 2 **38**, No. 2A, L126.

Zozulya, A.A., S.A. Diddams, A.G. van Engen, and T.S. Clement (1999) Propagation dynamics of intense femtosecond pulses: Multiple splitting, coalescence, and continuum generation. Phys. Rev. Lett. **82**, No. 7, 1430.

Bespalov, V.G., S.A. Kozlov, Y.A. Shpolyanskii, and A.N. Sutyagin (1998) Spectral superbroadening of high-power femtosecond laser pulses and their time compression down to one period of the light field. J. Opt. Technol. **65**, No. 10, 823.

Mlejnek, M., E.M. Wright, and J.V. Moloney (1998) Femtosecond pulse propagation in argon: A pressure dependence study. Phys. Rev. E **58**, No. 4, 4903.

Brodeur, A. and S.L. Chin (1998) Band-gap dependence of the ultrafast white-light continuum. Phys. Rev. Lett. **80**, No. 20, 4406.

Mori, T., Y. Hirakawa, and T. Imasaka (1998) Role of a supercontinuum in the generation of rotational Raman emission based on stimulated Raman gain and four-wave Raman mixing. Opt. Commun. **148**, Nos. 1–3, 110.

Mogilevtsev, D., T.A. Birks, and P.St.J. Russell (1998) Group-velocity dispersion in photonic crystal fibers. Opt. Lett. **23**, No. 21, 1662.

Akopyan, A.A. and D.L. Oganesyan (1997) Analytic solution of the wave equation describing dispersion-free propagation of a femtosecond laser pulse in a medium with a cubic nonlinearity. Quantum Electron. **27**, No. 7, 605.

Efimov, O.M., K. Gabel, S.V. Garnov, L.B. Glebov, S. Grantham, M. Richardson, and M.J. Soileau (1998) Color-center generation in silicate glasses exposed to infrared femtosecond pulses. J. Opt. Soc. Am. B **15**, No. 1, 193.

Krylov, V., O. Ollikainen, J. Gallus, U. Wild, A. Rebane, and A. Kalintsev (1998) Efficient noncollinear parametric amplification of weak femtosecond pulses in the visible and near-infrared spectral range. Opt. Lett. **23**, No. 2, 100.

Spielmann, C., N.H. Burnett, S. Sartania, R. Koppitsch, M. Schnurer, C. Kan, M. Lenzner, P. Wobrauschek, and F. Krausz (1997) Generation of coherent X-rays in the water window using 5-femtosecond laser pulses. Science, **278,** No. 5338, 661.

Zhang, W.L., Q.Y. Wang, Q.R. Xing, L. Chai, and K.M. Yoo (1997) Ultra-broad band supercontinuum produced by terawatt femtosecond laser. Sci. China Ser. A **40**, No. 5, 534.

Krylov, V., A. Rebane, D. Erni, O. Ollikainen, U. Wild, V. Bespalov, and D. Staselko (1996) Stimulated Raman amplification of femtosecond pulses in hydrogen gas. Opt. Lett. **21**, No. 24, 2005.

Ranka, J.K., R.W. Schirmer, and A.L. Gaeta (1996) Observation of pulse splitting in nonlinear dispersive media. Phys. Rev. Lett. **77**, No. 18, 3783.

Silva, L.O.E., J.T. Mendonca, and G. Figueira (1996) Full wave theory of Fermi photon acceleration. Phys. Scripta **T63**, 288.

Brodeur, A., F.A. Ilkov, and S.L. Chin (1996) Beam filamentation and the white light continuum divergence. Opt. Commun. **129**, Nos. 3–4, 193.

Ting, A., K. Krushelnick, H.R. Burris, A. Fisher, C. Manka, and C.I. Moore (1996) Backscattered supercontinuum emission from high-intensity laser-plasma interactions. Opt. Lett. **21**, No. 15, 1096.

Gross, B. and J.T. Manassah (1996) Effects of spatio-temporal coupling on pulse propagation in nonlinear defocusing medium. Opt. Commun. **126**, Nos. 4–6, 269.

Chin, S.L. and S. Lagace (1996) Generation of $H_2$, $O_2$, and $H_2O_2$ from water by the use of intense femtosecond laser pulses and the possibility of laser sterilization. Appl. Opt. **35**, No. 6, 907.

Nibbering, E.T.J., P.F. Curley, G. Grillon, B.S. Prade, M.A. Franco, F. Salin, and A. Mysyrowicz (1996) Conical emission from self-guided femtosecond pulses in air. Opt. Lett. **21**, No. 1, 62.

Nishioka, H., W. Odajima, K. Ueda, and H. Takuma (1995) Ultrabroadband flat continuum generation in multichannel propagation of terrawatt Ti:sapphire laser pulses. Opt. Lett. **20**, No. 24, 2505.

Rodriguez, G., J.P. Roberts, and A.J. Taylor (1994) Ti:sapphire based ultrafast pump-probe laser source in the violet and ultraviolet. Proc. SPIE **2116**, 219.

Noskov, V.I. (1993) Geometrization of electrodynamics in a super-continuum model in connection with conformal invariance. Russian Phys. J. **36**, No. 6, 598.

Ilkov, F.A., V. Francois, and S.L. Chin (1994) Supercontinuum generation in a $CO_2$ gas in the presence of ionization. Proc. SPIE **2041**, 127.

Belenov, E.M. and I.P. Prokopovich (1993) Two-photon Raman processes in spectral ultrabroadening of intense ultrashort light pulses. Quantum Electron. **23**, No. 6, 497.

Ilkov, F.A., L.Sh. Ilkova, and S.L. Chin (1993) Supercontinuum generation versus optical breakdown in $CO_2$ gas. Opt. Lett. **18**, No. 9, 681.

Francois, V., F.A. Ilkov, and S.L. Chin (1993) Experimental study of the supercontinuum spectral width evolution in $CO_2$ gas. Opt. Commun. **99**, Nos. 3–4, 241.

Xing, Q., K.M. Yoo, and R.R. Alfano (1993) Self-bending of light. Opt. Lett. **18**, No. 7, 479.

Francois, V., F.A. Ilkov, and S.L. Chin (1992) Supercontinuum generation in $CO_2$ gas accompanied by optical breakdown. J. Phys. B **25**, No. 11, 2709.

Karlsson, M., D. Anderson, M. Desaix, and M. Lisak (1991) Dynamic effects of Kerr nonlinearity and spatial diffraction on self-phase modulation of optical pulses. Opt. Lett. **16**, No. 18, 1373.

Zhu, S.-B., J.-B. Zhu, and G.W. Robinson (1991) Molecular-dynamics study of liquid water in strong laser fields. Phys. Rev. A **44**, No. 4, 2602.

Blok, V.R. and M. Krochik (1991) Transient Raman gain stimulated by a noise pump. Phys. A **170**, No. 2, 355.

Nguyen Dai Hung and Y.H. Meyer (1990) A compact Fabry–Perot tuned 1 ps dye laser. Opt. Commun. **79**, Nos. 3–4, 215.

Fedorov, M.V., M.Y. Ivanov, and P.B. Lerner (1990) Interaction of atoms with supershort laser pulses and the generation of the supercontinuum. J. Phys. B **23**, No. 15, 2505.

Fedorov, M.V. and M.Yu. Ivanov (1990) Coherence and interference in a Rydberg atom in a strong laser field: Excitation, ionization, and emission of light. J. Opt. Soc. Am. B **7**, No. 4, 569.

Golub, I. (1990) Optical characteristics of supercontinuum generation. Opt. Lett. **15**, No. 6, 305.

Gosnell, T.R., A.J. Taylor, and D.P. Greene (1990) Supercontinuum generation at 248 nm using high-pressure gases. Opt. Lett. **15**, No. 2, 130.

Adair, R., L.L. Chase, and S.A. Payne (1989) Nonlinear refractive index of optical crystals. Phys. Rev. B **39**, No. 5, 3337.

# 13
# Supercontinuum Generation in Microstructure Fibers

## Summary

Over the past four years, there has been a surge of activity in the supercontinuum field since the introduction of various types of microstructure fibers. The main reason for this great interest worldwide is the low femtosecond pulse energies (~1 nJ) required to generate the supercontinuum. The pulses from femtosecond oscillators can conveniently be used to produce supercontinuum. The microstructure fibers provide a micron to submicron size guide over a long distance for a femtosecond pulse to travel along. In comparison to supercontinuum generated in bulk media, there is a limited interaction length, ~5 cm for supercontinuum. In addition, self-focusing (beam breakup) in bulk requires larger energies in the 100 $\mu$J to mJ range for supercontinuum production. Also, the fibers have unique dispersion characteristics which provide for zero dispersion, and anomalous dispersion (negative) regions to keep the supercontinuum and pump femtosecond pulses from spreading and overlapping over a longer distance to interact further and extend the supercontinuum broadening.

There are several different types of microstructure fibers being used to produce supercontinuum. The most commonly used are: photonic crystal fibers (PCFs), birefringent photonic crystal fiber, tapered fibers, hollow (holey) fiber arrays, simple and multiple submicron size core fibers, and doped silica fibers.

The PCF has a central region of pure silica core surrounded by lower index air holes. Light is guided by total internal reflection and in a step index fiber due to the refractive index difference between core and air holes. An elliptically shaped core instead of a circular core induces a high birefringence which can preserve the state of polarization of the pump and supercontinuum pulses traveling in the fiber. A tapered silica fiber consists of a long, narrow waist region, ~2 $\mu$m, connected on both sides by larger size diameter fibers. High intensity can be produced in the waist region.

The most commonly used femtosecond laser sources for supercontinuum generation in fibers are: Ti : sapphire, $Cr^{4+}$ : forsterite, erbium fiber, and ytter-

bium fiber lasers. For the erbium fiber laser pulses of 60 fs, 200 pJ at 1560 nm, produces a supercontinuum over an octave spanning from 400 to 1750 nm in (SF6) silica fiber. For a $Cr^{4+}$: forsterite laser pulse of 30 fs, 0.6 nJ at 1250 nm, produces a supercontinuum from 1 $\mu$m to 2 $\mu$m in nonlinear glass fiber. Using a Ti : sapphire laser pulse of 4 nJ at 800 nm in a tapered fiber of 2 $\mu$m diameter and 90 mm in length, a supercontinuum over two octaves broad was generated covering 370 to 1545 nm. For Ti : sapphire pulses of 150 fs, 10 nJ at 820 nm, can produce a supercontinuum in the ultraviolet in a silica hollow fiber. Using two cascaded hollow fibers filled with argon of 60 cm length with pulse compression, the shortest pulses of 3.8 fs of 100 $\mu$J were achieved with the supercontinuum spanning over 500 THz (400 nm to 1000 nm) using 25 fs, $\frac{1}{2}$ mJ pump pulses from the Ti : sapphire amplifier system operating at 1 kHz.

In microstructural fibers, when pump wavelength lies in an anomalous dispersion region, it is the solitons that initiate the formation of the continuum. In a normal dispersion region, self-phase modulation is the process that initiates the continuum generation. The combination of four-wave mixing and Raman processes extends the spectral width of the continuum. In that regard, the pulse duration of an ultrafast laser determines the operational mechanisms —for 10 fs to 1000 fs laser pulses, self-phase modulation and soliton generation dominates; while for pulses >30 ps, stimulated Raman and four-wave mixing play a major role in extending the spectra. The supercontinuum spectra can span more than a two optical octave bandwidth spread from 380 nm to 1600 nm using 200 fs pulses with energy in the tens of nanojoules. The span over an octave (i.e., 450 nm to 900 nm) is important in controlling the phase of the carrier wave inside the pulse envelope of a mode-locked pulse train using the *f* and 2*f* waves from a supercontinuum in an interferometer.

The selected references in this chapter describe some of the salient features of supercontinuum generation and applications using microstructure fibers.

## Updated References

Konorov, S.O., E.E. Serebryannikov, A.M. Zheltikov, P. Zhou, A.P. Tarasevitch, and D. von der Linde (2004) Generation of femtosecond anti-Stokes pulses through phase-matched parametric four-wave mixing in a photonic crystal fiber. Opt. Lett. **29**, No. 13, 1545.

Katayama, T. and H. Kawaguchi (2004) Supercontinuum generation and pulse compression in short fibers for optical pulses generated by 1.5 $\mu$m optical parametric oscillator. Japanese J. Appl. Phys. Part 2 **43**, No. 6A, L712.

[Anon] (2004) Single-mode white-light supercontinuum source is compact. Laser Focus World **40**, No. 6, 11.

Espinasse, P. (2004) Microstructured fibers enable supercontinuum generation. oemagazine, The SPIE Magazine of Photonic Technologies and Applications **4**, No. 8, 11.

Cheng, C.F., X.F. Wang, and B. Lu (2004) Nonlinear propagation and supercontinuum generation of a femtosecond pulse in photonic crystal fibers. Acta Phys. Sinica **53**, No. 6, 1826.

Li, S.G., X.D. Liu, and L.T. Hou (2004) Vector analysis of dispersion for the fundamental cladding mode in photonic crystal fibers. Acta Phys. Sinica **53**, No. 6, 1873.

Kolesik, M., E. Wright, and J. Moloney (2004) Simulation of femtosecond pulse propagation in sub-micron diameter tapered fibers. Appl. Phys. B **79**, No. 3, 293.

Konorov, S.O., A.B. Fedotov, W. Boutu, E.E. Serebryannikov, D.A. Sidorov-Biryukov, Y.N. Kondrat'ev, V.S. Shevandin, K.V. Dukel'skii, A.V. Khokhlov, and A.M. Zheltikov (2004) Frequency conversion of subnanojoule femtosecond pulses in microstructure fibers. Opt. Spectrosc. **96**, No. 4, 575.

Nan, Y., C. Lou, J. Wang, T. Wang, and L. Huo (2004) Signal-to-noise ratio improvement of a supercontinuum continuous-wave optical source using a dispersion-imbalanced nonlinear optical loop mirror. Appl. Phys. B **79**, No. 1, 61.

Konorov, S.O., A.B. Fedotov, V.P. Mitrokhin, D.A. Sidorov-Biryukov, Y.N. Kondrat'ev, V.S. Shevandin, K.V. Dukel'skii, A.V. Khokhlov, and A.M. Zheltikov (2004) Polarization-controlled spectral transformation of unamplified femtosecond pulses in multiple waveguide channels of a photonic-crystal fiber. Laser Phys. **14**, No. 5, 760.

Konorov, S.O., I. Bugar, D.A. Sidorov-Biryukov, D. Chorvat, Y.N. Kondrat'ev, V.S. Shevandin, K.V. Dukel'skii, A.V. Khokhlov, A.B. Fedotov, F. Uherek, V.B. Morozov, V.A. Makarov, D. Chorvat, and A.M. Zheltikov (2004) Chirp-controlled anti-Stokes frequency conversion of femtosecond pulses in photonic–crystal fibers. Laser Phys. **14**, No. 5, 772.

Hu, M.L., C.Y. Wang, Y.F. Li, Z. Wang, X.C. Ni, C. Lu, S.G. Li, L.T. Hou, and G.Y. Zhou (2004) Supercontinuum generation and transmission in a random distributed microstructure fiber. Laser Phys. **14**, No. 5, 776.

Konorov, S.O., A.A. Ivanov, D.A. Akimov, M.V. Alfimov, A.A. Podshivalov, Y.N. Kondrat'ev, V.S. Shevandin, K.V. Dukel'skii, A.V. Khokhlov, and A.M. Zheltikov (2004) Cross-phase modulation control of ultrashort pulses spectrally transformed in photonic-crystal fibers. Laser Phys. **14**, No. 5, 791.

Zheltikov, A.M. (2004) Nonlinear optics of microstructure fibers. Phys.–Uspekhi **47**, No. 1, 69.

Saitoh, K. and M. Koshiba (2004) Highly nonlinear dispersion-flattened photonic crystal fibers for supercontinuum generation in a telecommunication window. Opt. Express **12**, No. 10, 2027.

Washburn, B.R. and N.R. Newbury (2004) Phase, timing, and amplitude noise on supercontinua generated in microstructure fiber. Opt. Express **12**, No. 10, 2166.

Hu, M.L., C.Y. Wang, L. Chai, and A.M. Zheltikov (2004) Frequency-tunable anti-Stokes line emission by eigenmodes of a birefringent microstructure fiber. Opt. Express **12**, No. 9, 1932.

Courvoisier, C., A. Mussot, R. Bendoula, T. Sylvestre, J.G. Reyes, G. Tribillon, B. Wacogne, T. Gharbi, and H. Maillotte (2004) Broadband supercontinuum in a microchip-laser-pumped conventional fiber: Toward biomedical applications. Laser Phys. **14**, No. 4, 507.

Tausenev, A.V. and P.G. Kryukov (2004) Raman-converter-diode-pumped continuous-wave femtosecond Er-doped fibre laser. Quantum Electron. **34**, No. 2, 106.

Zhang, R., J. Teipel, X.P. Zhang, D. Nau, and H. Giessen (2004) Group velocity dispersion of tapered fibers immersed in different liquids. Opt. Express **12**, No. 8, 1700.

Zheng, Y., Y.P. Zhang, X.J. Huang, L. Wang, Y.Y. Wang, K.N. Zhou, X.D. Wang, Y. Guo, X.F. Yuan, G.Y. Zhou, L.T. Hou, Z.Y. Hou, G.Z. Xing, and J.Q. Yao (2004) Supercontinuum generation with 15-fs pump pulses in a microstructured fibre with random cladding and core distributions. Chinese Phys. Lett. **21**, No. 4, 750.

Hilligsoe, K.M., T.V. Andersen, H.N. Paulsen, C.K. Nielsen, K. Molmer, S. Keiding, R. Kristiansen, K.P. Hansen, and J.J. Larsen (2004) Supercontinuum generation in a photonic crystal fiber with two zero dispersion wavelengths. Opt. Express **12**, No. 6, 1045.

Sansone, G., G. Steinmeyer, C. Vozzi, S. Stagira, M. Nisoli, S. De Silvestri, K. Starke, D. Ristau, B. Schenkel, J. Biegert, A. Gosteva, and U. Keller (2004) Mirror dispersion control of a hollow fiber supercontinuum. Appl. Phys. B **78**, No. 5, 551.

Konorov, S.O., D.A. Akimov, A.A. Ivanov, M.V. Alfimov, and A.M. Zheltikov (2004) Microstructure fibers as frequency-tunable sources of ultrashort chirped pulses for coherent nonlinear spectroscopy. Appl. Phys. B **78**, No. 5, 565.

Kawanishi, S., T. Yamamoto, H. Kubota, M. Tanaka, and S.I. Yamaguchi (2004) Dispersion controlled and polarization maintaining photonic crystal fibers for high performance network systems. IEICE Trans. Electron. **E87C**, No. 3, 336.

Konorov, S.O., E.E. Serebryannikov, A.M. Zheltikov, P. Zhou, A.P. Tarasevitch, and D. von der Linde (2004) Mode-controlled colors from microstructure fibers. Opt. Express **12**, No. 5, 730.

Zhu, Z.M. and T.G. Brown (2004) Experimental studies of polarization properties of supercontinua generated in a birefringent photonic crystal fiber. Opt. Express **12**, No. 5, 791.

Zheltikov, A.M. (2004) Microstructure fibers: A new phase of nonlinear optics. Laser Phys. **14**, No. 2, 119.

Haverkamp, N. and H.R. Telle (2004) Complex intensity modulation transfer function for supercontinuum generation in microstructure fibers. Opt. Express **12**, No. 4, 582.

Nicholson, J.W. and M.F. Yan (2004) Cross-coherence measurements of supercontinua generated in highly-nonlinear, dispersion shifted fiber at 1550 nm. Opt. Express **12**, No. 4, 679.

Zhu, Z.M. and T.G. Brown (2004) Effect of frequency chirping on supercontinuum generation in photonic crystal fibers. Opt. Express **12**, No. 4, 689.

Kobtsev, S.M., S.V. Kukarin, and N.V. Fateev (2003) Generation of a polarised supercontinuum in small-diameter quasi-elliptic fibres. Quantum Electron. **33**, No. 12, 1085.

Li, S.G., Y.L. Ji, G.Y. Zhou, L.T. Hou, Q.Y. Wang, M.L. Hu, Y.F. Li, Z.Y. Wei, J. Zhang, and X.D. Liu (2004) Supercontinuum generation in holey microstructure fibers by femtosecond laser pulses. Acta Phys. Sinica **53**, No. 2, 478.

Zhao, J., L.K. Chen, C.K. Chan, and C. Lin (2004) Analysis of performance optimization in supercontinuum sources. Opt. Lett. **29**, No. 5, 489.

Yamamoto, T., H. Kubota, S. Kawanishi, M. Tanaka, and S.I. Yamaguchi (2004) Highly nonlinear dispersion-flattened polarization-maintaining photonic crystal fiber in 1.55 $\mu$m region. IEICE Trans. Electron. **E87C**, No. 2, 250.

Zhang, W., Y. Wang, J.D. Peng, and X.M. Liu (2004) Broadband high power continuous wave fiber Raman source and its applications. Opt. Commun. **231**, Nos. 1–6, 371.

Zhu, Z.M. and T.G. Brown (2004) Polarization properties of supercontinuum spectra generated in birefringent photonic crystal fibers. J. Opt. Soc. Am. B **21**, No. 2, 249.

Cristiani, I., R. Tediosi, L. Tartara, and V. Degiorgio (2004) Dispersive wave generation by solitons in microstructured optical fibers. Opt. Express **12**, No. 1, 124.

Wadsworth, W.J., N. Joly, J.C. Knight, T.A. Birks, F. Biancalana, and P.S.J. Russell (2004) Supercontinuum and four-wave mixing with Q-switched pulses in endlessly single-mode photonic crystal fibres. Opt. Express **12**, No. 2, 299.

Hori, T., J. Takayanagi, N. Nishizawa, and T. Goto (2004) Flatly broadened, wideband and low noise supercontinuum generation in highly nonlinear hybrid fiber. Opt. Express **12**, No. 2, 317.

Lu, F. and W.H. Knox (2004) Generation of a broadband continuum with high spectral coherence in tapered single-mode optical fibers. Opt. Express **12**, No. 2, 347.

Konorov, S.O., A.B. Fedotov, W. Boutu, E.E. Serebryannikov, D.A. Sidorov-Biryutcov, Y.N. Kondrat'ev, V.S. Shevandin, K.V. Dukel'skii, A.V. Khokhlov, and A.M. Zheltikov (2004) Multiplex frequency conversion of subnanojoule femtosecond pulses in microstructure fibers. Laser Phys. **14**, No. 1, 100.

Washburn, B.R., S.A. Diddams, N.R. Newbury, J.W. Nicholson, M.F. Yan, and C.G. Jorgensen (2004) Phase-locked, erbium-fiber-laser-based frequency comb in the near infrared. Opt. Lett. **29**, No. 3, 250.

Konorov, S.O., A.A. Ivanov, M.V. Alfimov, A.B. Fedotov, Y.N. Kondrat'ev, V.S. Shevandin, K.V. Dukel'skii, A.V. Khokhlov, A.A. Podshivalov, A.N. Petrov, D.A. Sidorov-Biryukov, and A.M. Zheltikov (2003) Generation of radiation tunable between 350 and 600 nm and nonlinear-optical spectral transformation of femtosecond Cr : forsterite-laser pulses in submicron fused silica channels of a microstructure. Quantum Electron. **33**, No. 11, 989.

Bagayev, S.N., V.I. Denisov, V.F. Zakharyash, V.M. Klementyev, I.I. Korel', S.A. Kuznetsov, V.S. Pivtsov, and S.V. Chepurov (2003) Study of the spectral characteristics of a femtosecond Ti : sapphire laser after propagation of its radiation through a tapered fibre. Quantum Electron. **33**, No. 10, 883.

Proulx, A., J.M. Menard, N. Ho, J.M. Laniel, R. Vallee, and C. Pare (2003) Intensity and polarization dependences of the supercontinuum generation in birefringent and highly nonlinear microstructured fibers. Opt. Express **11**, No. 25, 3338.

Hundertmark, H., D. Kracht, D. Wandt, C. Fallnich, V.V.R.K. Kumar, A.K. George, J.C. Knight, and P.S. Russell (2003) Supercontinuum generation with 200 pJ laser pulses in an extruded SF6 fiber at 1560 nm. Opt. Express **11**, No. 24, 3196.

Kano, H. and H. Hamaguchi (2003) Characterization of a supercontinuum generated from a photonic crystal fiber and its application to coherent Raman spectroscopy. Opt. Lett. **28**, No. 23, 2360.

Druon, F., N. Sanner, G. Lucas-Leclin, P. Georges, K.P. Hansen, and A. Petersson (2003) Self-compression and Raman soliton generation in a photonic crystal fiber of 100-fs pulses produced by a diode-pumped Yb-doped oscillator. Appl. Opt. **42**, No. 33, 6768.

Schreiber, T., J. Limpert, H. Zellmer, A. Tunnermann, and K.P. Hansen (2003) High average power supercontinuum generation in photonic crystal fibers. Opt. Commun. **228**, Nos. 1–3, 71.

Mollenauer, L.F. (2003) Nonlinear optics in fibers. Science **302**, No. 5647, 996.

Biancalana, F., D.V. Skryabin, and P.S. Russell (2003) Four-wave mixing instabilities in photonic-crystal and tapered fibers—Art. no. 046603. Phys. Rev. E, **6804**, No. 4, 6603.

Nikolov, N.I., T. Sorensen, O. Bang, and A. Bjarklev (2003) Improving efficiency of supercontinuum generation in photonic crystal fibers by direct degenerate four-wave mixing. J. Opt. Soc. Am. B **20**, No. 11, 2329.

Hori, T., N. Nishizawa, T. Goto, and M. Yoshida (2003) Wideband and nonmechanical sonogram measurement by use of an electronically controlled, wavelength-tunable, femtosecond soliton pulse. J. Opt. Soc. Am. B **20**, No. 11, 2410.

Gonzalez-Herraez, M., S. Martin-Lopez, P. Corredera, M.L. Hernanz, and P.R. Horche (2003) Supercontinuum generation using a continuous-wave Raman fiber laser. Opt. Commun. **226**, Nos. 1–6, 323.

Schenkel, B., J. Biegert, U. Keller, C. Vozzi, M. Nisoli, G. Sansone, S. Stagira, S. De Silvestri, and O. Svelto (2003) Generation of 3.8-fs pulses from adaptive compression of a cascaded hollow fiber supercontinuum. Opt. Lett. **28**, No. 20, 1987.

Zheltikov, A.M. (2003) The physical limit for the waveguide enhancement of nonlinear-optical processes. Opt. Spectrosc. **95**, No. 3, 410.

Corwin, K.L., N.R. Newbury, J.M. Dudley, S. Coen, S.A. Diddams, B.R. Washburn, K. Weber, and R.S. Windeler (2003) Fundamental amplitude noise limitations to supercontinuum spectra generated in a microstructured fiber. Appl. Phys. B **77**, No. 4, 467.

Zheltikov, A.M. (2003) Limiting efficiencies of nonlinear-optical processes in microstructure fibers. J. Exper. Theoret. Phys. **97**, No. 3, 505.

Sorokin, E., V.L. Kalashnikov, S. Naumov, J. Teipel, F. Warken, H. Giessen, and I.T. Sorokina (2003) Intra- and extra-cavity spectral broadening and continuum generation at 1.5 $\mu$m using compact low-energy femtosecond Cr : YAG laser. Appl. Phys. B **77**, Nos. 2–3, 197.

Prabhu, M., A. Taniguchi, S. Hirose, J. Lu, M. Musha, A. Shirakawa, and K. Ueda (2003) Supercontinuum generation using Raman fiber laser. Appl. Phys. B **77**, Nos. 2–3, 205.

Nicholson, J.W., A.K. Abeeluck, C. Headley, M.F. Yan, and C.G. Jorgensen (2003) Pulsed and continuous-wave supercontinuum generation in highly nonlinear, dispersion-shifted fibers. Appl. Phys. B **77**, Nos. 2–3, 211.

Petrov, G.I., V.V. Yakovlev, and N.I. Minkovski (2003) Near-infrared continuum generation of femtosecond and picosecond pulses in doped optical fibers. Appl. Phys. B **77**, Nos. 2–3, 219.

Husakou, A.V. and J. Herrmann (2003) Supercontinuum generation in photonic crystal fibers made from highly nonlinear glasses. Appl. Phys. B **77**, Nos. 2–3, 227.

Town, G.E., T. Funaba, T. Ryan, and K. Lyytikainen (2003) Optical supercontinuum generation from nanosecond pump pulses in an irregularly microstructured air-silica optical fiber. Appl. Phys. B **77**, Nos. 2–3, 235.

Cao, Q., X. Gu, E. Zeek, M. Kimmel, R. Trebino, J. Dudley, and R.S. Windeler (2003) Measurement of the intensity and phase of supercontinuum from an 8-mm-long microstructure fiber. Appl. Phys. B **77**, Nos. 2–3, 239.

Teipel, J., K. Franke, D. Turke, F. Warken, D. Meiser, M. Leuschner, and H. Giessen (2003) Characteristics of supercontinuum generation in tapered fibers using femtosecond laser pulses. Appl. Phys. B **77**, Nos. 2–3, 245.

McFerran, J.J. and A.N. Luiten (2003) Uniform oscillations of supercontinua. Appl. Phys. B **77**, Nos. 2–3, 259.

Corwin, K.L., N.R. Newbury, J.M. Dudley, S. Coen, S.A. Diddams, B.R. Washburn, K. Weber, and R.S. Windeler (2003) Fundamental amplitude noise limitations to supercontinuum spectra generated in a microstructured fiber. Appl. Phys. B **77**, Nos. 2–3, 269.

Ames, J.N., S. Ghosh, R.S. Windeler, A.L. Gaeta, and S.T. Cundiff (2003) Excess noise generation during spectral broadening in a microstructured fiber. Appl. Phys. B **77**, Nos. 2–3, 279.

Price, J.H.V., T.M. Monro, K. Furusawa, W. Belardi, J.C. Baggett, S. Coyle, C. Netti, J.J. Baumberg, R. Paschotta, and D.J. Richardson (2003) UV generation in a pure-silica holey fiber. Appl. Phys. B **77**, Nos. 2–3, 291.

Akimov, D.A., M. Schmitt, R. Maksimenka, K.V. Dukel'skii, Y.N. Kondrat'ev, A.V. Khokhlov, V.S. Shevandin, W. Kiefer, and A.M. Zheltikov (2003) Supercontinuum generation in a multiple-submicron-core microstructure fiber: Toward limiting waveguide enhancement of nonlinear-optical processes. Appl. Phys. B **77**, Nos. 2–3, 299.

Tartara, L., I. Cristiani, and V. Degiorgio (2003) Blue light and infrared continuum generation by soliton fission in a microstructured fiber. Appl. Phys. B **77**, Nos. 2–3, 307.

Fedotov, A.B., I. Bugar, D.A. Sidorov-Biryukov, E.E. Serebryannikov, D. Chorvat, M. Scalora, D. Chorvat, and A.M. Zheltikov (2003) Pump-depleting four-wave mixing in supercontinuum-generating microstructure fibers. Appl. Phys. B **77**, Nos. 2–3, 313.

Kalashnikov, V.L., P. Dombi, T. Fuji, W.J. Wadsworth, J.C. Knight, P.S.J. Russell, R.S. Windeler, and A. Apolonski (2003) Maximization of supercontinua in photonic crystal fibers by using double pulses and polarization effects. Appl. Phys. B **77**, Nos. 2–3, 319.

Shpolyanskiy, Y.A., D.L. Belov, M.A. Bakhtin, and S.A. Kozlov (2003) Analytic study of continuum spectrum pulse dynamics in optical waveguides. Appl. Phys. B **77**, Nos. 2–3, 349.

Akimov, D.A., E.E. Serebryannikov, A.M. Zheltikov, M. Schmitt, R. Maksimenka, W. Kiefer, K.V. Dukel'skii, V.S. Shevandin, and Y.N. Kondrat'ev (2003) Efficient anti-Stokes generation through phase-matched four-wave mixing in higher-order modes of a microstructure fiber. Opt. Lett. **28**, No. 20, 1948.

Konorov, S.O., A.A. Ivanov, M.V. Alfimov, A.B. Fedotov, Y.N. Kondrat'ev, V.S. Shevandin, K.V. Dukel'skii, A.V. Khokhlov, A.A. Podshivalov, A.N. Petrov, D.A. Sidorov-Biryukov, and A.M. Zheltikov (2003) Generation of frequency-tunable radiation within the wavelength range of 350–600 nm through nonlinear-optical spectral transformation of femtosecond Cr : forsterite-laser pulses in submicron fused silica threads of a microstructure fiber. Laser Phys. **13**, No. 9, 1170.

Fedotov, A.B., I. Bugar, D.A. Sidorov-Biryukov, E.E. Serebryannikov, D. Chorvat, M. Scalora, D. Chorvat, and A.M. Zheltikov (2003) Nonlinear-optical spectral transformation of ultrashort pulses in microstructure fibers: Extending the capabilities of femtosecond laser sources. Laser Phys. **13**, No. 9, 1222.

Konorov, S.O. and A.M. Zheltikov (2003) Frequency conversion of subnanojoule femtosecond laser pulses in a microstructure fiber for photochromism initiation. Opt. Express **11**, No. 19, 2440.

Mussot, A., T. Sylvestre, L. Provino, and H. Maillotte (2003) Generation of a broad-band single-mode supercontinuum in a conventional dispersion-shifted fiber by use of a subnanosecond microchip laser. Opt. Lett. **28**, No. 19, 1820.

Feng, X., T.M. Monro, P. Petropoulos, V. Finazzi, and D. Hewak (2003) Solid microstructured optical fiber. Opt. Express **11**, No. 18, 2225.

Hilligsoe, K.M., H.N. Paulsen, J. Thogersen, S.R. Keiding, and J.J. Larsen (2003) Initial steps of supercontinuum generation in photonic crystal fibers. J. Opt. Soc. Am. B **20**, No. 9, 1887.

Kolevatova, O.A., A.N. Naumov, and A.M. Zheltikov (2003) Phase-matching conditions for third-harmonic generation revised to include group-delay effects and nonlinear phase shifts. Laser Phys. **13**, No. 8, 1040.

Matsuura, M. and N. Kishi (2003) Continuum spectrum generation utilizing adiabatic compression in Raman amplifier for multi-wavelength pulse source. Opt. Express **11**, No. 16, 1856.

Li, S.G., L.T. Hou, Y.L. Ji, and G.Y. Zhou (2003) Supercontinuum generation in holey microstructure fibres with random cladding distribution by femtosecond laser pulses. Chinese Phys. Lett. **20**, No. 8, 1300.

Jasapara, J., T.H. Her, R. Bise, R. Windeler, and D.J. DiGiovanni (2003) Group-velocity dispersion measurements in a photonic bandgap fiber. J. Opt. Soc. Am. B **20**, No. 8, 1611.

Akimov, D.A., A.A. Ivanov, M.V. Alfimov, A.B. Fedotov, T.A. Birks, W.J. Wadsworth, P.S. Russell, O.A. Kolevatova, S.O. Konorov, A.A. Podshivalov, A. Petrov, D.A. Sidorov-Biryukov, and A.M. Zheltikov (2003) Frequency conversion of femtosecond Cr : forsterite-laser pulses in a tapered fibre. Quantum Electron. **33**, No. 4, 317.

Thomann, I., A. Bartels, K.L. Corwin, N.R. Newbury, L. Hollberg, S.A. Diddams, J.W. Nicholson, and M.F. Yan (2003) 420-MHz Cr : forsterite femtosecond ring laser and continuum generation in the 1–2-$\mu$m range. Opt. Lett. **28**, No. 15, 1368.

Reeves, W.H., D.V. Skryabin, F. Biancalana, J.C. Knight, P.S. Russell, F.G. Omenetto, A. Efimov, and A.J. Taylor (2003) Transformation and control of ultra-short pulses in dispersion-engineered photonic crystal fibres. Nature **424**, No. 6948, 511.

Yamamoto, T., H. Kubota, S. Kawanishi, M. Tanaka, and S. Yamaguchi (2003) Supercontinuum generation at 1.55 $\mu$m in a dispersion-flattened polarization-maintaining photonic crystal fiber. Opt. Express **11**, No. 13, 1537.

Fedotov, A.B., P. Zhou, Y.N. Kondrat'ev, S.O. Konorov, E.A. Vlasova, D.A. Sidorov-Biryukov, V.S. Shevandin, K.V. Dukel'skii, A.V. Khokhlov, S.N. Bagayev, V.B. Smirnov, A.P. Tarasevitch, D. von der Linde, and A.M. Zheltikov (2003) Frequency up-conversion of spectrally sliced mode-separable supercontinuum emission from microstructure fibers. Laser Phys. **13**, No. 6, 816.

Akimov, D.A., A.A. Ivanov, A.N. Naumov, O.A. Kolevatova, M.V. Alfimov, T.A. Birks, W.J. Wadsworth, P.S.J. Russell, A.A. Podshivalov, and A.M. Zheltikov (2003) Generation of a spectrally asymmetric third harmonic with unamplified 30-fs Cr : forsterite laser pulses in a tapered fiber. Appl. Phys. B **76**, No. 5, 515.

Sone, H., M. Imai, Y. Imai, and Y. Harada (2003) The effect of input azimuth of cross-phase-modulated soliton pulses on supercontinuum generation in a dispersion-flattened/decreasing fiber with low birefringence. IEICE Trans. Electron. **E86C**, No. 5, 714.

Schenkel, B., J. Biegert, U. Keller, M. Nisoli, G. Sansone, S. Stagira, C. Vozzi, S. De Silvestri, and O. Svelto (2003) Adaptive pulse compression to 3.7 fs of a cascaded hollow fiber supercontinuum. CLEO 2002—Conference on Lasers and Electro-Optics, 2006.

Konorov, S.O., O.A. Kolevatova, A.B. Fedotov, E.E. Serebryannikov, D.A. Sidorov-Biryukov, J.M. Mikhailova, A.N. Naumov, V.I. Beloglazov, N.B. Skibina, L.A. Mel'nikov, and A.V. Shcherbakov, and A.M. Zheltikov (2003) Waveguide modes of electromagnetic radiation in hollow-core microstructure and photonic-crystal fibers. J. Exper. Theoret. Phys. **96**, No. 5, 857.

Arkhireev, V.A., A.E. Korolev, D.A. Nolan, and V.V. Solov'ev (2003) High-efficiency generation of a supercontinuum in an optical fiber. Opt. Spectrosc. **94**, No. 4, 632.

Sone, H., M. Imai, Y. Imai, and Y. Harada (2003) The effect of input azimuth of cross-phase-modulated soliton pulses on supercontinuum generation in a dispersion-

flattened/decreasing fiber with low birefringence. IEICE Trans. Electron. **E86C**, No. 5, 714.

Newbury, N.R., B.R. Washburn, K.L. Corwin, and R.S. Windeler (2003) Noise amplification during supercontinuum generation in microstructure fiber. Opt. Lett. **28**, No. 11, 944.

Cucinotta, A., F. Poli, S. Selleri, L. Vincetti, and M. Zoboli (2003) Amplification properties of $Er^{3+}$-doped photonic crystal fibers. J. Lightwave Technol. **21**, No. 3, 782.

Efimov, A. and A.J. Taylor (2003) Nonlinear generation of very high-order UV modes in microstructured fibers. Opt. Express **11**, No. 8, 910.

Fedotov, A.B., P. Zhou, M.L. Hu, Y.F. Li, E.E. Serebryannikov, K.V. Dukel'skii, Y.N. Kondrat'ev, V.S. Shevandin, A.P. Tarasevitch, D.A. Sidorov-Biryukov, C.Y. Wang, D. von der Linde, and A.M. Zheltikov (2003) Laser micromachining of microstructure fibers with femtosecond pulses. Laser Phys. **13**, No. 4, 657.

Lehtonen, M., G. Genty, H. Ludvigsen, and M. Kaivola (2003) Supercontinuum generation in a highly birefringent microstructured fiber. Appl. Phys. Lett. **82**, No. 14, 2197.

Nicholson, J.W., M.F. Yan, P. Wisk, J. Fleming, F. DiMarcello, E. Monberg, A. Yablon, C. Jorgensen, and T. Veng (2003) All-fiber, octave-spanning supercontinuum. Opt. Lett. **28**, No. 8, 643.

Corwin, K.L., N.R. Newbury, J.M. Dudley, S. Coen, S.A. Diddams, K. Weber, and R.S. Windeler (2003) Fundamental noise limitations to supercontinuum generation in microstructure fiber—art. no. 113904. Phys. Rev. Lett. **9011**, No. 11, 3904.

Akimov, D.A., M.V. Alfimov, A.A. Ivanov, A.B. Fedotov, T.A. Birks, W.J. Wadsworth, P.S. Russell, S.O. Konorov, O.A. Kolevatova, A.A. Podshivalov, and A.M. Zheltikov (2003) Doubly phase-matched cascaded parametric wave mixing of ultrashort laser pulses. JETP Lett. **77**, No. 1, 7.

Sorokin, E., S. Naumov, V.L. Kalashnikov, I.T. Sorokina, J. Teipel, D. Meiser, and H. Giessen (2003) Spectral broadening of 50 fs Cr : YAG pulses around 1.5 $\mu$m in the tapered fiber. CLEO 2003—Conference on Lasers and Electro-Optics, June 2003, Baltimore, Maryland.

Adachi, M., M. Hirasawa, A. Suguro, N. Karasawa, S. Kobayashi, R. Morita, and M. Yamashita (2003) Spectral-phase characterization and adapted compensation of strongly chirped pulses for a tapered fiber. Jpn. J. Appl. Phys. Part 2 **42**, No. 1A–B, L24.

Seefeldt, M., A. Heuer, and R. Menzel (2003) Compact white-light source with an average output power of 2.4 W and 900 nm spectral bandwidth. Opt. Commun. **216**, Nos. 1–3, 199.

Fang, X.J., N. Karasawa, R. Morita, R.S. Windeler, and M. Yamashita (2003) Nonlinear propagation of a few optical cycle pulses in a photonic crystal fiber—Experimental and theoretical studies beyond the slowly varying-envelope approximation. IEEE Photon. Technol. Lett. **15**, No. 2, 233.

Melchor, G.M., M.A. Granados, and G.H. Corro (2002) On the problem of ideal amplification of optical solitons. Quantum Electron. **32**, No. 11, 1020.

Tartara, L., I. Cristiani, V. Degiorgio, F. Carbone, D. Faccio, and M. Romagnoli (2002) Nonlinear propagation of ultrashort laser pulses in a microstructured fiber. J. Nonlinear Opt. Phys. Mater. **11**, No. 4, 409.

Nisoli, M., G. Sansone, S. Stagira, C. Vozzi, S. De Silvestri, and O. Svelto (2002) Ultrabroadband continuum generation by hollow-fiber cascading. Appl. Phys. B **75**, Nos. 6–7, 601.

Fedotov, A.B., P. Zhou, A.N. Naumov, V.V. Temnov, V.I. Beloglazov, N.B. Skibina, L.A. Mel'nikov, A.V. Shcherbakov, A.P. Tarasevitch, D. von der Linde, and A.M. Zheltikov (2002) Spectral broadening of 40-fs Ti : sapphire laser pulses in photonic-molecule modes of a cobweb-microstructure fiber. Appl. Phys. B **75**, Nos. 6–7, 621.

Sanders, S.T. (2002) Wavelength-agile fiber laser using group-velocity dispersion of pulsed super-continua and application to broadband absorption spectroscopy. Appl. Phys. B **75**, Nos. 6–7, 799.

Tartara, L., I. Cristiani, V. Degiorgio, F. Carbone, D. Faccio, M. Romagnoli, and W. Belardi (2003) Phase-matched nonlinear interactions in a holey fiber induced by infrared super-continuum generation. Opt. Commun. **215**, Nos. 1–3, 191.

Fedotov, A.B., P. Zhou, Y.N. Kondrat'ev, S.N. Bagayev, V.S. Shevandin, K.V. Dukel'skii, A.V. Khokhlov, V.B. Smirnov, A.P. Tarasevitch, D. von der Linde, and A.M. Zheltikov (2002) Spatial and spectral filtering of supercontinuum emission generated in microstructure fibres. Quantum Electron. **32**, No. 9, 828.

Ozeki, Y., K. Taira, K. Aiso, Y. Takushima, and K. Kikuchi (2002) Highly flat supercontinuum generation from 2 ps pulses using 1-km-long erbium-doped fibre amplifier. Electron. Lett. **38**, No. 25, 1642.

Fedotov, A.B., P. Zhou, A.P. Tarasevitch, K.V. Dukel'skii, Y.N. Kondrat'ev, V.S. Shevandin, V.B. Smirnov, D. von der Linde, and A.M. Zheltikov (2002) Microstructure-fiber sources of mode-separable supercontinuum emission for wave-mixing spectroscopy. J. Raman Spectrosc. **33**, Nos. 11–12, 888.

Kumar, V.V.R.K., A.K. George, W.H. Reeves, J.C. Knight, P.S. Russell, F.G. Omenetto, and A.J. Taylor (2002) Extruded soft glass photonic crystal fiber for ultrabroad supercontinuum generation. Opt. Express **10**, No. 25, 1520.

Fedotov, A.B., P. Zhou, Y.N. Kondrat'ev, S.N. Bagayev, V.S. Shevandin, K.V. Dukel'skii, V.B. Smirnov, A.P. Tarasevitch, D. von der Linde, and A.M. Zheltikov (2002) The mode structure and spectral properties of supercontinuum emission from microstructure fibers. J. Exper. Theoret. Phys. **95**, No. 5, 851.

Harbold, J.M., F.O. Ilday, F.W. Wise, T.A. Birks, J. Wadsworth, and Z. Chen (2002) Long-wavelength continuum generation about the second dispersion zero of a tapered fiber. Opt. Lett. **27**, No. 17, 1558.

Boyraz, O. and M.N. Islam (2002) A multiwavelength CW source based on longitudinal mode-carving of supercontinuum generated in fibers and noise performance. J. Lightwave Technol. **20**, No. 8, 1493.

Ortigosa-Blanch, A., J.C. Knight, and P.S.J. Russell (2002) Pulse breaking and supercontinuum generation with 200-fs pump pulses in photonic crystal fibers. J. Opt. Soc. Am. B **19**, No. 11, 2567.

Nishizawa, N. and T. Goto (2002) Characteristics of pulse trapping by use of ultrashort soliton pulses in optical fibers across the zero-dispersion wavelength. Opt. Express **10**, No. 21, 1151.

Dudley, J.M., X. Gu, L. Xu, M. Kimmel, E. Zeek, P. O'Shea, R. Trebino, S. Coen, and R.S. Windeler (2002) Cross-correlation frequency resolved optical gating analysis of broadband continuum generation in photonic crystal fiber: Simulations and experiments. Opt. Express **10**, No. 21, 1215.

Genty, G., M. Lehtonen, H. Ludvigsen, J. Broeng, and M. Kaivola (2002) Spectral broadening of femtosecond pulses into continuum radiation in microstructured fibers. Opt. Express **10**, No. 20, 1083.

Champert, P.A., S.V. Popov, M.A. Solodyankin, and J.R. Taylor (2002) Multiwatt average power continua generation in holey fibers pumped by kilowatt peak power seeded ytterbium fiber amplifier. Appl. Phys. Lett. **81**, No. 12, 2157.

Naumov, A.N., A.B. Fedotov, I. Bugar, D. Chorvat, V.I. Beloglazov, S.O. Konorov, L.A. Mel'nikov, N.B. Skibina, D.A. Sidorov-Biryukov, E.A. Vlasova, V.B. Morozov, A.V. Shcherbakov, D. Chorvat, and A.M. Zheltikov (2002) Supercontinuum generation in photonic-molecule modes of microstructure cobweb fibers and photonic-crystal fibers with femtosecond pulses of tunable 1.1–1.5-$\mu$m radiation. Laser Phys. **12**, No. 8, 1191.

Wadsworth, W.J., A. Ortigosa-Blanch, J.C. Knight, T.A. Birks, T.P.M. Man, and P.S. Russell (2002) Supercontinuum generation in photonic crystal fibers and optical fiber tapers: A novel light source. J. Opt. Soc. Am. B **19**, No. 9, 2148.

Fedotov, A.B., A.N. Naumov, A.M. Zheltikov, I. Bugar, D. Chorvat, A.P. Tarasevitch, and D. von der Linde (2002) Frequency-tunable supercontinuum generation in photonic-crystal fibers by femtosecond pulses of an optical parametric amplifier. J. Opt. Soc. Am. B **19**, No. 9, 2156.

Apolonski, A., B. Povazay, A. Unterhuber, W. Drexler, W.J. Wadsworth, J.C. Knight, and P.S. Russell (2002) Spectral shaping of supercontinuum in a cobweb photonic-crystal fiber with sub-20-fs pulses. J. Opt. Soc. Am. B **19**, No. 9, 2165.

Husakou, A.V. and J. Herrmann (2002) Supercontinuum generation, four-wave mixing, and fission of higher-order solitons in photonic-crystal fibers. J. Opt. Soc. Am. B **19**, No. 9, 2171.

Olsson, B.E. and D.J. Blumenthal (2002) Pulse restoration by filtering of self phase modulation broadened optical spectrum, J. Lightwave Technol. **20**, No. 7, 1113.

Reeves, W.H., J.C. Knight, and P.St.J. Russell (2002) Demonstration of ultra-flattened dispersion in photonic crystal fibers. Opt. Express **10**, No. 14, 609.

Gaeta, A.L. (2002) Nonlinear propagation and continuum generation in microstructured optical fibers. Opt. Lett. **27**, No. 11, 924.

Sone, H., T. Arai, M. Imai, and Y. Imai (2002) Modal birefringence dependent supercontinuum due to cross-phase modulation in a dispersion-flattened/decreasing fiber. Opt. Rev. **9**, No. 3, 89.

Igarashi, K., S. Saito, M. Kishi, and M. Tsuchiya (2002) Broad-band and extremely flat supercontinuum generation via optical parametric gain extended spectrally by fourth-order dispersion in anomalous-dispersion-flattened fibers. IEEE J. Sel. Topics Quantum Electron. **8**, No. 3, 521.

Dudley, J.M. and S. Coen (2002) Numerical simulations and coherence properties of supercontinuum generation in photonic crystal and tapered optical fibers. IEEE J. Sel. Topics Quantum Electron. **8**, No. 3, 651.

Fedotov, A.B., A.N. Naumov, I. Bugar, D. Chorvat, D.A. Sidorov-Biryukov, and A.M. Zheltikov (2002) Supercontinuum generation in photonic-molecule modes of microstructure fibers. IEEE J. Sel. Topics Quantum Electron. **8**, No. 3, 665.

Washburn, B.R., S.E. Ralph, and R.S. Windeler (2002) Ultrashort pulse propagation in air–silica microstructure fiber. Opt. Express **10**, No. 13, 575.

Dudley, J.M. and S. Coen (2002) Coherence properties of supercontinuum spectra generated in photonic crystal and tapered optical fibers. Opt. Lett. **27**, No. 13, 1180.

Saitoh, K. and M. Koshiba (2002) Full-vectorial imaginary-distance beam propagation method based on a finite element scheme: Application to photonic crystal fibers. IEEE J. Quantum Electron. **38**, No. 7, 927.

Price, J.H.V., K. Furusawa, T.M. Monro, L. Lefort, and D.J. Richardson (2002) Tunable, femtosecond pulse source operating in the range 1.06–1.33 $\mu$m based on a $Yb^{3+}$-doped holey fiber amplifier. J. Opt. Soc. Am. B **19**, No. 6, 1286.

Wu, Y., C.Y. Lou, M. Han, T. Wang, and Y.Z. Gao (2002) Effects of pulse chirp on supercontinuum produced in dispersion decreasing fibre. Chinese Phys. **11**, No. 6, 578.

Fedotov, A.B., I. Bugar, A.N. Naumov, D. Chorvat, D.A. Sidorov-Biryukov, and A.M. Zheltikov (2002) Light confinement and supercontinuum generation switching in photonic-molecule modes of a microstructure fiber. JETP Lett. **75**, No. 7, 304.

Price, J.H.V., W. Belardi, T.M. Monro, A. Malinowski, A. Piper, and D.J. Richardson (2002) Soliton transmission and supercontinuum generation in holey fiber, using a diode pumped Ytterbium fiber source. Opt. Express **10**, No. 8, 382.

Watanabe, S. and F. Futami (2002) All-optical wavelength conversion using ultra-fast nonlinearities in optical fiber. IEICE Trans. Electron. **E85C**, No. 4, 889.

Herrmann, J., U. Griebner, N. Zhavoronkov, A. Husakou, D. Nickel, J.C. Knight, W.J. Wadsworth, P.S.J. Russell, and G. Korn (2002) Experimental evidence for supercontinuum generation by fission of higher-order solitons in photonic fibers. Phys. Rev. Lett. **88**, No. 17, 3901–1.

Coen, S., A.H.L. Chau, R. Leonhardt, J.D. Harvey, J.C. Knight, W.J. Wadsworth, and P.S.J. Russell (2002) Supercontinuum generation by stimulated Raman scattering and parametric four-wave mixing in photonic crystal fibers. J. Opt. Soc. Am. B **19**, No. 4, 753.

Dudley, J.M., L. Provino, N. Grossard, H. Maillotte, R.S. Windeler, B.J. Eggleton, and S. Coen (2002) Supercontinuum generation in air–silica microstructured fibers with nanosecond and femtosecond pulse pumping. J. Opt. Soc. Am. B **19**, No. 4, 765.

Akimov, D.A., A.A. Ivanov, M.V. Alfimov, S.N. Bagayev, T.A. Birks, W.J. Wadsworth, P.S. Russell, A.B. Fedotov, V.S. Pivtsov, A.A. Podshivalov, and A.M. Zheltikov (2002) Two-octave spectral broadening of subnanojoule Cr : forsterite femtosecond laser pulses in tapered fibers. Appl. Phys. B **74**, Nos. 4–5, 307.

Schumacher, D. (2002) Controlling continuum generation. Opt. Lett. **27**, No. 6, 451.

Nishizawa, N. and T. Goto (2002) Trapped pulse generation by femotosecond soliton pulse in birefringent fibers. Opt. Express **10**, No. 5, 256.

Spalter, S., H.Y. Hwang, J. Zimmermann, G. Lenz, T. Katsufuji, S.-W. Cheong, and R.E. Slusher (2002) Strong self-phase modulation in planar chalcogenide glass waveguides. Opt. Lett. **27**, No. 5, 363.

Cormack, I.G., D.T. Reid, W.J. Wadsworth, J.C. Knight, and P.St.J. Russell (2002) Observation of soliton self-frequency shift in photonic crystal fibre. Electron. Lett. **38**, No. 4, 167.

Tartara, L., I. Cristiani, and V. Degiorgio (2002) Blue light and infrared continuum generation in a highly nonlinear holey fiber. CLEO 2002—Conference on Lasers and Electro-Optics, May 2002, Long Beach, California, p. CTuU2.

Dianov, E.M. and P.G. Kryukov (2001) Generation of a supercontinuum in fibres by a continuous train of ultrashort pulses. Quantum Electron. **31**, No. 10, 877.

Holzwarth, R., M. Zimmermann, T. Udem, T.W. Hansch, P. Russbuldt, K. Gabel, R. Poprawe, J.C. Knight, W.J. Wadsworth, and P.S.J. Russell (2001) White-light frequency comb generation with a diode-pumped Cr : LiSAF laser. Opt. Lett. **26**, No. 17, 1376.

Nishizawa, N. and T. Goto (2001) Widely wavelength-tunable ultrashort pulse generation using polarization maintaining optical fibers. IEEE J. Sel. Topics Quantum Electron. **7**, No. 4, 518.

Sharping, J.E., M. Fiorentino, A. Coker, P. Kumar, and R.S. Windeler (2001) Four-wave mixing in microstructure fiber. Opt. Lett. **26**, No. 14, 1048.

Mori, K., H. Takara, and S. Kawanishi (2001) Analysis and design of supercontinuum pulse generation in a single-mode optical fiber. J. Opt. Soc. Am. B **18**, No. 12, 1780.

Prabhu, M., N.S. Kim, and K. Ueda (2001) Efficient broadband supercontinuum generation in 1483.4 nm range pumped by high power Raman fiber laser. Laser Phys. **11**, No. 11, 1240.

Husakou, A.V. and J. Herrmann (2001) Supercontinuum generation of higher-order solitons by fission in photonic crystal fibers—Art. no. 203901. Phys. Rev. Lett. **87**, No. 20, 3901–1.

Coen, S., A.H.L. Chan, R. Leonhardt, J.D. Harvey, J.C. Knight, W.J. Wadsworth, and P.S.J. Russell (2001) White-light supercontinuum generation with 60-ps pump pulses in a photonic crystal fiber. Opt. Lett. **26**, No. 17, 1356.

Clark, S.W., F.Ö. Ilday, and F.W. Wise (2001) Fiber delivery of femtosecond pulses from a Ti:sapphire laser. Opt. Lett. **26**, No. 17, 1320.

Lee, J., G.H. Song, U.-C. Paek, and Y.G. Seo (2001) Design and fabrication of a nonzero-dispersion fiber with a maximally flat dispersion spectrum. IEEE Photon. Technol. Lett. **13**, No. 4, 317.

Husakou, A.V., V.P. Kalosha, and J. Herrmann (2001) Supercontinuum generation and pulse compression in hollow waveguides. Opt. Lett. **26**, No. 13, 1022.

Liu, X., C. Xu, W.H. Knox, J.K. Chandalia, B.J. Eggleton, S.G. Kosinski, and R.S. Windeler (2001) Soliton self-frequency shift in a short tapered air–silica microstructure fiber. Opt. Lett. **26**, No. 6, 358.

Nishizawa, N., and T. Goto (2001) Widely broadened supercontinuum generation using highly nonlinear dispersion shifted fibers and femtosecond fiber laser. Jpn. J. Appl. Phys. **40**, L365.

Boyraz, O., J. Kim, M.N. Islam, F. Coppinger, and B. Jalali (2000) 10 Gb/s multiple wavelength, coherent short pulse source based on spectral carving of supercontinuum generated in fibers. J. Lightwave Technol. **18**, No. 12, 2167.

[Anon] (2000) Tapered standard fiber produces supercontinuum. Laser Focus World **36**, No. 11, 11.

Birks, T.A., W.J. Wadsworth, and P.S. Russell (2000) Supercontinuum generation in tapered fibers. Opt. Lett. **25**, No. 19, 1415.

Yu, C.X., H.A. Haus, E.P. Ippen, W.S. Wong, and A. Sysoliatin (2000) Gigahertz-repetition-rate mode-locked fiber laser for continuum generation. Opt. Lett. **25**, No. 19, 1418.

Tamura, K.R., H. Kubota, and M. Nakazawa (2000) Fundamentals of stable continuum generation at high repetition rates. IEEE J. Quantum Electron. **36**, No. 7, 773.

Ferrando, A., E. Silvestre, J.J. Miret, and P. Andres (2000) Vector description of higher-order modes in photonic crystal fibers. J. Opt. Soc. Am. A **17**, No. 7, 1333.

Prabhu, M., N.S. Kim, and K. Ueda (2000) Ultra-broadband CW supercontinuum generation centered at 1483.4 nm from Brillouin/Raman fiber laser. Jpn. J. Appl. Phys. Part 2 **39**, No. 4A, L291.

Wu, J., Y.H. Li, C.Y. Lou, and Y.H. Gao (2000) Theoretical and experimental study of supercontinuum generation in the dispersion-shifted fiber. Int. J. Infrared Millimeter Waves **21**, No. 7, 1085.

Fedotov, A.B., A.M. Zheltikov, A.A. Ivanov, M.V. Alfimov, D. Chorvat, V.I. Beloglazov, L.A. Mel'nikov, N.B. Skibina, A.P. Tarasevitch, and D. von der Linde (2000) Supercontinuum-generating holey fibers as new broadband sources for spectroscopic applications. Laser Phys. **10**, No. 3, 723.

Koch, F., S.V. Chernikov, and J.R. Taylor (2000) Characterization of dispersion in components for ultrafast lasers. Opt. Commun. **180**, Nos. 1–3, 133.

Homoelle, D. and A. Gaeta (2000) Nonlinear propagation dynamics of an ultrashort pulse in a hollow waveguide. Opt. Lett. **25**, No. 10, 761.

Wadsworth, W.J., J.C. Knight, A. Ortigosa-Blanch, J. Arriaga, E. Silvestre, and P.St.J. Russell (2000) Soliton effects in photonic crystal fibres at 850 nm. Electron. Lett. **36**, No. 1, 53.

Ranka, J.K., R.S. Windeler, and A.J. Stentz (2000) Visible continuum generation in air–silica microstructure optical fibers with anomalous dispersion at 800 nm. Opt. Lett. **25**, No. 1, 25.

Ranka, J.K., R.S. Windeler, and A.J. Stentz (2000) Optical properties of high-delta air–silica microstructure optical fibers. Opt. Lett. **25**, No. 11, 796.

Monro, T.M., D.J. Richardson, N.G.R. Broderick, and P.J. Bennett (2000) Modeling large air fraction holey optical fibers. J. Lightwave Technol. **18**, No. 1, 50.

Nishizawa, N., R. Okamura, and T. Goto (2000) Widely wavelength tunable ultrashort soliton pulse and anti-Stokes pulse generation for wavelengths of 1.32–1.75 $\mu$m. Jpn. J. Appl. Phys. **39**, L409.

Nowak, G.A., J. Kim, and M.N. Islam (1999) Stable supercontinuum generation in short lengths of conventional dispersion-shifted fiber. Appl. Opt. **38**, No. 36, 7364.

Kubota, H., K.R. Tamura, and M. Nakazawa (1999) Analyses of coherence-maintained ultrashort optical pulse trains and supercontinuum generation in the presence of soliton-amplified spontaneous-emission interaction. J. Opt. Soc. Am. B **16**, No. 12, 2223.

Okuno, T., M. Onishi, T. Kashiwada, S. Ishikawa, and M. Nishimura (1999) Silica-based functional fibers with enhanced nonlinearity and their applications. IEEE J. Sel. Topics Quantum Electron. **5**, No. 5, 1385.

Bakhshi, B. and P.A. Andrekson (1999) Dual-wavelength 10-GHz actively mode-locked erbium fiber laser. IEEE Photon. Technol. Lett. **11**, No. 11, 1387.

Mogilevtsev, D., T.A. Birks, and P.St.J. Russell (1999) Localized function method for modeling defect modes in 2-D photonic crystals. J. Lightwave Technol. **17**, No. 11, 2078.

Broderick, N.G.R., T.M. Monro, P.J. Bennett, and D.J. Richardson (1999) Nonlinearity in holey optical fibers: Measurement and future opportunities. Opt. Lett. **24**, No. 20, 1395.

Shimizu, N., K. Mori, T. Ishibashi, and Y. Yamabayashi (1999) Quantum efficiency of InP/InGaAs uni-travelling-carrier photodiodes at 1.55–1.7 $\mu$m measured using supercontinuum generation in optical fiber. Jpn. J. Appl. Phys. Part 1 **38**, No. 4B, 2573.

Futami, F., Y. Takushima, and K. Kikuchi (1999) Generation of wideband and flat supercontinuum over a 280-nm spectral range from a dispersion-flattened optical fiber with normal group-velocity dispersion. IEICE Trans. Electron. **E82C**, No. 8, 1531.

Futami, F., Y. Takushima, and K. Kikuchi (1999) Generation of wideband and flat supercontinuum over a 280-nm spectral range from a dispersion-flattened optical

fiber with normal group-velocity dispersion. IEICE Trans. Commun. **E82B**, No. 8, 1265.

Tamura, K.R. and M. Nakazawa (1999) Femtosecond soliton generation over a 32-nm wavelength range using a dispersion-flattened dispersion-decreasing fiber. IEEE Photon. Technol. Lett. **11**, No. 3, 319.

Ferrando, A., E. Silvestre, J.J. Miret, and P. Andres (1999) Full-vector analysis of a realistic photonic crystal fiber. Opt. Lett. **24**, No. 5, 276.

Nishizawa, N., R. Okamura, and T. Goto (1999) Analysis of widely wavelength tunable femtosecond soliton pulse generation using optical fibers. Jpn. J. Appl. Phys. **38**, 4768.

Xu, L., N. Karasawa, N. Nakagawa, R. Morita, H. Shigekawa, and M. Yamashita (1999) Experimental generation of an ultra-broad spectrum based on induced-phase modulation in a single-mode glass fiber. Opt. Commun. **162**, Nos. 4–6, 256.

Takushima, Y. and K. Kikuchi (1999) 10-GHz, over 20-channel multiwavelength pulse source by slicing supercontinuum spectrum generated in normal-dispersion fiber. IEEE Photon. Technol. Lett. **11**, No. 3, 322.

Knight, J.C., J. Broeng, T.A. Birks, and P.St.J. Russell (1998) Photonic band gap guidance in optical fibers. Science **282**, No. 5393, 1476.

Lewis, S.A.E., S.V. Chernikov, and J.R. Taylor (1998) Ultra-broad-bandwidth spectral continuum generation in fibre Raman amplifier. Electron. Lett. **34**, No. 23, 2267.

Takushima, Y., F. Futami, and K. Kikuchi (1998) Generation of over 140-nm-wide supercontinuum from a normal dispersion fiber by using a mode-locked semiconductor laser source. IEEE Photon. Technol. Lett. **10**, No. 11, 1560.

Mogilevtsev, D., T.A. Birks, and P.St.J. Russell (1998) Group-velocity disperion in photonic crystal fibers. Opt. Lett. **23**, No. 21, 1662.

Takiguchi, K., S. Kawanishi, H. Takara, A. Himeno, and K. Hattori (1998) Dispersion slope equalizer for dispersion shifted fiber using a lattice-form programmable optical filter on a planar lightwave circuit. J. Lightwave Technol. **16**, No. 9, 1647.

Kang, J.U. and R. Posey (1998) Demonstration of supercontinuum generation in a long-cavity fiber ring laser. Opt. Lett. **23**, No. 17, 1375.

Sotobayashi, H. and K. Kitayama (1998) 325nm bandwidth supercontinuum generation at 10 Gbit/s using dispersion-flattened and non-decreasing normal dispersion fibre with pulse compression technique. Electron. Lett. **34**, No. 13, 1336.

Nakazawa, M., K. Tamura, H. Kubota, and E. Yoshida (1998) Coherence degradation in the process of supercontinuum generation in an optical fiber. Opt. Fiber Technol. **4**, No. 2, 215.

Calvani, R., R. Caponi, and E. Grazioli (1998) Femtosecond transform-limited pulse generation by compensating for the linear chirp of SPM spectra in dispersion shifted fibers. Fiber Integrated Opt. **17**, No. 1, 41.

Mori, K., H. Takara, S. Kawanishi, M. Saruwatari, and T. Morioka (1997) Flatly broadened supercontinuum spectrum generated in a dispersion decreasing fibre with convex dispersion profile. Electron. Lett. **33**, No. 21, 1806.

Nibbering, E.T.J., O. Duhr, and G. Korn (1997) Generation of intense tunable 20-fs pulses near 400 nm by use of a gas-filled hollow waveguide. Opt. Lett. **22**, No. 17, 1335.

Kawanishi, S., K. Uchiyama, H. Takara, T. Morioka, M. Yamada, and T. Kanamori (1997) Nearly transform-limited 1.4 $\mu$m picosecond pulse generation by supercon-

tinuum and pulse amplification in Tm-doped optical amplifier. Electron. Lett. **33**, No. 18, 1553.

Okuno, T., M. Onishi, and M. Nishimura (1998) Generation of ultra-broad-band supercontinuum by dispersion-flattened and decreasing fiber. IEEE Photon. Technol. Lett. **10**, No. 1, 72.

Chernikov, S.V., Y. Zhu, J.R. Taylor, and V.P. Gapontsev (1997) Supercontinuum self-*Q*-switched ytterbium fiber laser. Opt. Lett. **22**, No. 5, 298.

Tamura, K., E. Yoshida, and M. Nakazawa (1996) Generation of 10 GHz pulse trains at 16 wavelengths by spectrally slicing a high power femtosecond source. Electron. Lett. **32**, No. 18, 1691.

Manassah, J.T. and B. Gross (1995) Propagation of femtosecond pulses in a fiber amplifier. Opt. Commun. **122**, Nos. 1–3, 71.

Calvani, R., R. Caponi, C. Naddeo, and D. Roccato (1995) Subpicosecond pulses at 2.5 GHz from filtered supercontinuum in a fiber pumped by a chirp compensated gain-switched DFB laser. Electron. Lett. **31**, No. 19, 1685.

Mori, K., T. Morioka, and M. Saruwatari (1995) Ultrawide spectral range group-velocity dispersion measurement utilizing supercontinuum in an optical-fiber pumped by a 1.5 μm compact laser source. IEEE Trans. Instrumentation Measurement **44**, No. 3, 712.

Elgin, J.N., T. Brabec, and S.M.J. Kelly (1995) A perturbative theory of soliton propagation in the presence of third order dispersion. Opt. Commun. **114**, Nos. 3–4, 321.

Akhmediev, N. and M. Karlsson (1995) Cherenkov radiation emitted by solitons in optical fibers. Phys. Rev. A **51**, No. 3, 2602.

Morioka, K., K. Mori, S. Kawanishi, and M. Saruwatari (1994) Pulse-width tunable, self-frequency conversion of short optical pulses over 200 nm based on supercontinuum generation. Electron. Lett. **30**, No. 23, 1960.

Wang, Q.Z., Q.D. Liu, D. Liu, P.P. Ho, and R.R. Alfano (1994) High-resolution spectra of self-phase modulation in optical fibers. J. Opt. Soc. Am. B **11**, No. 6, 1084.

Takara, H., S. Kawanishi, T. Morioka, K. Mori, and M. Saruwatari (1994) 100 Gbit/s optical waveform measurement with 0.6 ps resolution optical sampling using subpicosecond supercontinuum pulses. Electron. Lett. **30**, No. 14, 1152.

Mori, K., T. Morioka, and M. Saruwatari (1994) Ultra-wide spectral range group velocity dispersion measurement of single-mode fibers using LD-pumped supercontinuum in an optical fiber. Conference Proceedings. 10th Anniversary. IMTC/94. Advanced Technologies in I & M. 1994 IEEE Instrumentation and Measurement Technolgy Conference (Cat. No. 94CH3424-9): (Vol 2) 1036.

Mori, K., T. Morioka, J.M. Jacob, and M. Saruwatari (1994) 1.4–1.7 $\mu$m, <2 ps white pulse generation for multiwavelength pulse source using supercontinuum in a single-mode optical fiber. 1994 Conference on Precision Electromagnetic Measurements Digest (Cat. No. 94CH3449-6): 497.

Dumais, P., F. Gonthier, S. Lacroix, J. Bures, A. Villeneuve, P.G.J. Wigley, and G.I. Stegeman (1993) Enhanced self-phase modulation in tapered fibers. Opt. Lett. **18**, No. 23, 1996.

Mori, K., T. Morioka, and M. Saruwatari (1993) Group velocity dispersion measurement using supercontinuum picosecond pulses generated in an optical fibre. Electron. Lett. **29**, No. 11, 987.

Gross, B. and J.T. Manassah (1992) Supercontinuum in the anomalous group-velocity dispersion region. J. Opt. Soc. Am. B **9**, No. 10, 1813.

Wang, J.-K., Y. Siegal, C. Lu, and E. Mazur (1992) Generation of dual-wavelength, synchronized, tunable, high energy, femtosecond laser pulses with nearly perfect Gaussian spatial profile. Opt. Commun. **91**, Nos. 1–2, 77.

Lucek, J.K. and K.J. Blow (1992) Soliton self-frequency shift in telecommunications fiber. Phys. Rev. A **45**, No. 9, 6666.

Gross, B. and J.T. Manassah (1991) The spectral distribution and the frequency shift of the supercontinuum. Phys. Lett. A **160**, No. 3, 261.

Islam, M.N., G. Sucha, I. Bar-Joseph, M. Wegener, J.P. Gordon, and D.S. Chemla (1989) Femtosecond distributed soliton spectrum in fibers. J, Opt. Soc. Am. B **6**, No. 6, 1149.

Beaud, P., W. Hodel, B. Zysset, and H.P. Weber (1987) Ultrashort pulse propagation, pulse breakup, and fundamental soliton formation in a single-mode optical fiber. IEEE J. Quantum Electron. **QE-23**, No. 11, 1938.

Wai, P.K.A., C.R. Menyuk, Y.C. Lee, and H.H. Chen (1986) Nonlinear pulse propagation in the neighborhood of the zero-dispersion wavelength of monomode optical fibers. Opt. Lett. **11**, No. 7, 464.

*Note*: Most recently (2005), researchers (A. Abeeluck, K. Brar, and J. Bouteiller) at Lucent Technology produced SC with a bandwidth of 100 nm in a highly nonlinear fiber of length 1 km and a bandwidth of 245 nm for 4.5 km length using a continuous wave pump diode–Raman fiber laser. The SC was attributed to a combination of stimulated Raman and four wave mixing.

# 14
# Supercontinuum in Wavelength Division Multiplex Telecommunication

## Summary

The increasing demand for large capacity optical communication needs to incorporate both wavelength and time multiplexing. The supercontinuum offers both capabilities. Major advances in multiple wavelengths, division multiplexing for communication applications, have been achieved by several Japanese groups using the supercontinuum. This chapter highlights the references of researchers who are working toward achieving the transfer of extremely large amounts of coded information to meet tomorrow's demands. The supercontinuum produced by pulses from mode-locked lasers offers an effective way to obtain both the wavelength and time channels, because of the ease of generating thousands of optical frequencies and maintaining coherence from pulse to pulse.

Multi-terabits/s (3.24 Tbits/s) transmission over 80 km distances has been achieved using only a limited number of wavelength channels ~81 from the supercontinuum. A 1.5 ps pulse from a mode-locked diode laser combined with an erbium amplifier produces the supercontinuum which is multiplexed to 40 Gbits/s from time multiplexing the pulse train from 10 GHz to 40 GHz.

There are many challenges to overcome to improve speed—such as reducing a bit period time to ~1 ps and increasing the number of coherent wavelengths in the supercontinuum, generated by femtosecond pulses from compact high repetition rate mode-locked lasers. One needs to use 30 fs pulses at a bit period time of ~1 ps and thousands of wavelengths coding from the supercontinuum to achieve pentabits/s transmitted over tens of kilometers.

## Updated References

Sato, K. (2004) Key enabling technologies for future networks. Opt. Photon. News **15**, No. 5, 34.

Koga, M., T. Morioka, and Y. Miyamoto (2004) Next generation optical communication technologies for realizing bandwidth abundant networking capability. Opt. Rev. **11**, No. 2, 87.

Nan, Y., C. Lou, J. Wang, T. Wang, and L. Huo (2004) Signal-to-noise ratio improvement of a supercontinuum continuous-wave optical source using a dispersion-imbalanced nonlinear optical loop mirror. Appl. Phys. B **79**, No. 1, 61.

Dixit, N. and R. Vijaya (2004) Performance evaluation of a multi-wavelength gigahertz optical source for wavelength division multiplexed transmission. Opt. Commun. **235**, Nos. 1–3, 89.

Yusoff, Z., P. Petropoulos, K. Furusawa, T.M. Monro, and D.J. Richardson (2003) A 36-channel × 10-GHz spectrally sliced pulse source based on supercontinuum generation in normally dispersive highly nonlinear holey fiber. IEEE Photon. Technol. Lett. **15**, No. 12, 1689.

Lasri, J., P. Devgan, R.Y. Tang, J.E. Sharping, and P. Kumar (2003) A microstructure-fiber-based 10-GHz synchronized tunable optical parametric oscillator in the 1550-nm regime. IEEE Photon. Technol. Lett. **15**, No. 8, 1058.

Shah, D.D., N. Dixit, and R. Vijaya (2003) A multi-wavelength optical source for synchronous and asynchronous data transfer at a minimum of 16 × 10 Gbps. Opt. Fiber Technol. **9**, No. 3, 149.

Takara, H., T. Ohara, and K. Sato (2003) Over 1000 km DWDM transmission with supercontinuum multi-carrier source. Electron. Lett. **39**, No. 14, 1078.

Wang, J.P., Y. Wu, C.Y. Lou, and Y.Z. Gao (2003) A study of optical pulse characters extracted from supercontinuum by filters. Microwave Opt. Technol. Lett. **37**, No. 5, 387.

Mori, K., K. Sato, H. Takara, and T. Ohara (2003) Supercontinuum lightwave source generating 50 GHz spaced optical ITU grid seamlessly over S-, C- and L-bands. Electron. Lett. **39**, No. 6, 544.

Chou, J., Y. Han, and B. Jalali (2003) Adaptive RF-photonic arbitrary waveform generator. IEEE Photon. Technol. Lett. **15**, No. 4, 581.

Takara, H., H. Masuda, K. Mori, K. Sato, Y. Inoue, T. Ohara, A. Mori, M. Kohtoku, Y. Miyamoto, T. Morioka, and S. Kawanishi (2003) 124 nm seamless bandwidth, 313 × 10 Gbit/s DWDM transmission. Electron. Lett. **39**, No. 4, 382.

Shah, J. (2003) Optical CDMA. Opt. Photon. News, **14**, No. 4, 42.

Sotobayashi, H., W. Chujo, and K. Kitayama (2002) Photonic gateway: Multiplexing format conversions of OCDM-to-WDM and WDM-to-OCDM at 40 Gb/s (4 × 10 Gb/s). J. Lightwave Technol. **20**, No. 12, 2022.

Sotobayashi, H., W. Chujo, A. Konishi, and T. Ozeki (2002) Wavelength-band generation and transmission of 3.24-Tbit/s (81-channel WDMX 40-Gbit/s) carrier-suppressed return-to-zero format by use of a single supercontinuum source for frequency standardization. J. Opt. Soc. Am. B **19**, No. 11, 2803.

Sotobayashi, H., W. Chirio, and K. Kitayama (2002) Photonic gateway: TDM-to-WDM-to-TDM conversion and reconversion at 40 Gbit/s (4 channels × 10 Gbits/s). J. Opt. Soc. Am. B **19**, No. 11, 2810.

Wang, B.C., V. Baby, L. Xu, I. Glesk, and P.R. Prucnal (2002) 173-ps wavelength switching of four WDM channels using an OTDM channel selector. IEEE Photon. Technol. Lett. **14**, No. 11, 1620.

Schmid, R.P., T. Schneider, and J. Reif (2002) Femtosecond all-optical wavelength and time demultiplexer for OTDM/WDM systems. Appl. Phys. B **74**, S205.

Taccheo, S., and K. Ennser (2002) Investigation of amplitude noise and timing jitter of supercontinuum spectrum-sliced pulses. IEEE Photon. Technol. Lett. **14**, No. 8, 1100.

Sotobayashi, H., W. Chujo, and K. Kitayama (2002) Transparent virtual optical code/wavelength path network. IEEE J. Sel. Topics Quantum Electron. **8**, No. 3, 699.

Kovsh, D., L. Liu, B. Bakhshi, A. Pilipetskii, E.A. Golovchenko, and N. Bergano (2002) Reducing interchannel crosstalk in long-haul DWDM systems. IEEE J. Sel. Topics Quantum Electron. **8**, No. 3, 597.

Takada, K., M. Abe, T. Shibata, and K. Okamoto (2002) GHz-spaced 4200-channel two-stage tandem demultiplexer for ultra-multi-wavelength light source using supercontinuum generation. Electron. Lett. **38**, No. 12, 572.

Dixit, N., D.D. Shah, and R. Vijaya (2002) Optimization study for the generation of high-bit-rate spectrally enriched pulses for WDM applications. Opt. Commun. **205**, Nos. 4–6, 281.

Boscolo, S., S.K. Turitsyn, and K.J. Blow (2002) Study of the operating regime for all-optical passive 2R regeneration of dispersion-managed RZ data at 40 Gb/s using in-line NOLMs. IEEE Photon. Technol. Lett. **14**, No. 1, 30.

Takara, H. (2002) Multiple optical carrier generation from a supercontinuum source. Opt. Photon. News **13**, No. 3, 48.

Yamada, E., H. Takara, T. Ohara, K. Sato, K. Jinguji, Y. Inoue, T. Shibata, and T. Morioka (2001) 106 channel × 10 Gbit/s, 640 km DWDM transmission with 25 GHz spacing with supercontinuum multi-carrier source. Electron. Lett. **37**, No. 25, 1534.

Onohara, K., H. Sotobayashi, K. Kitayama, and W. Chujo (2001) Photonic time-slot and wavelength-grid interchange for 10-Gb/s packet switching. IEEE Photon. Technol. Lett. **13**, No. 10, 1121.

Sotobayashi, H., W. Chujo, and T. Ozeki (2001) Wideband tunable wavelength conversion of 10-Gbit/s return-to-zero signals by optical time gating of a highly chirped rectangular supercontinuum light source. Opt. Lett. **26**, No. 17, 1314.

Du Mouza, L., E. Seve, H. Mardoyan, and S. Wabnitz (2001) High-order dispersion-managed solitons for dense wavelength-division multiplexed transmissions. Opt. Lett. **26**, No. 15, 1128.

Sotobayashi, H., W. Chujo, and K. Kitayama (2001) 1.52 Tbit/s OCDM/WDM (4 OCDM × 19 WDM × 20 Gbit/s) transmission experiment. Electron. Lett. **37**, No. 11, 700.

Sotobayashi, H., W. Chujo, and T. Ozeki (2001) 80 Gbit/s simultaneous photonic demultiplexing based on OTDM-to-WDM conversion by four-wave mixing with supercontinuum light source. Electron. Lett. **37**, No. 10, 640.

Kawanishi, S. (2001) High bit rate transmission over 1 Tbit/s. IEICE Trans. Commun. **E84B**, No. 5, 1135.

Watanabe, S. and F. Futami (2001) All-optical signal processing using highly-nonlinear optical fibers. IEICE Trans. Commun. **E84B**, No. 5, 1179.

Kawanishi, S. (2001) High bit rate transmission over 1 Tbit/s. IEICE Trans. Electron. **E84C**, No. 5, 509.

Watanabe, S. and F. Futami (2001) All-optical signal processing using highly-nonlinear optical fibers. IEICE Trans. Electron. **E84C**, No. 5, 553.

Yamada, E., H. Takara, T. Ohara, K. Sato, T. Morioka, K. Jinguji, M. Itoh, and M. Ishii (2001) 150 channel supercontinuum CW optical source with high SNR and precise 25 GHz spacing for 10 Gbit/s DWDM systems. Electron. Lett. **37**, No. 5, 304.

Boivin, L. and B.C. Collings (2001) Invited paper—Spectrum slicing of coherent sources in optical communications. Opt. Fiber Technol. **7**, No. 1, 1.

Futami, F. and K. Kikuchi (2001) Low-noise multiwavelength transmitter using spectrum-sliced supercontinuum generated from a normal group-velocity dispersion fiber. IEEE Photon. Technol. Lett. **13**, No. 1, 73.

Sotobayashi, H., A. Konishi, W. Chujo, and T. Ozeki (2001) Simultaneously generated 3.24 Tbit/s (81 WDM × 40 Gbit/s) carrier suppressed RZ transmission using a single supercontinuum source. Proceedings of the 27th European Conference on Optical Communication 2001, ECOC '01, Vol. 1, 56.

Sotobayashi, H., K. Kitayama, and W. Chujo (2001) 40 Gbit/s photonic packet compression and decompression by supercontinuum generation. Electron. Lett. **37**, No. 2, 110.

Prabhu, M., T. Saitou, A. Taniguchi, M. Musha, L. Jianren, J. Xu, K.-I. Ueda, and N.S. Kim (2001) High-efficiency broadband supercontinuum generation centered at 1483.4 nm using Raman fiber laser. Optical Fiber Communication Conference and Exhibit, 2001. OFC 2001, Vol. 3, WP3-1.

Arai, T., H. Sone, M. Imai, and Y. Imai (2001) Enhancement of supercontinuum spectrum generation due to cross-phase modulation in a dispersion-flattened/decreasing fiber. Optical Fiber Communication Conference and Exhibit, 2001. OFC 2001, Vol. 3, WDD13-1.

Taccheo, S. (2001) Amplitude noise and timing jitter of pulses generated by supercontinuum spectrum-slicing for data-regeneration and TDM/WDM applications. Optical Fiber Communication Conference and Exhibit, 2001. OFC 2001, Vol. 3, WP2-2.

Yamada, E., H. Takara, T. Ohara, K. Sato, T. Morioka, K. Jinguji, M. Itoh, and M. Ishii (2001) A high SNR, 150 ch supercontinuum CW optical source with precise 25 GHz spacing for 10 Gbit/s DWDM systems. Optical Fiber Communication Conference and Exhibit, 2001. OFC 2001, Vol. 1, ME2-1.

Sotobayashi, H., K. Kitayama, and W. Chujo (2000) Photonic compression and decompression of 40 Gbit/s packet by supercontinuum generation. OSA Trends in Optics and Photonics Series, Volume on Optical Amplifiers and Their Applications 2000, Vol. 44, 196.

Saruwatari, M. (2000) All-optical signal processing for terabit/second optical transmission. IEEE J. Sel. Topics Quantum Electron. **6**, No. 6, 1363.

Boivin, L., S. Taccheo, C.R. Doerr, L.W. Stulz, R. Monnard, W. Lin, and W.C. Fang (2000) A supercontinuum source based on an electroabsorption-modulated laser for long distance DWDM transmission. IEEE Photon. Technol. Lett. **12**, No. 12, 1695.

Takara, H., T. Ohara, K. Mori, K. Sato, E. Yamada, Y. Inoue, T. Shibata, M. Abe, T. Morioka, and K.I. Sato (2000) More than 1000 channel optical frequency chain generation from single supercontinuum source with 12.5 GHz channel spacing. Electron. Lett. **36**, No. 25, 2089.

Sato, K.I. (2000) Photonic transport networks based on wavelength division multiplexing technologies. Philos. Trans. Roy. Soc. London, Ser. A **358**, No. 1773, 2265.

Yu, J.J., X.Y. Zheng, C. Peucheret, A.T. Clausen, H.N. Poulsen, and P. Jeppesen (2000) All-optical wavelength conversion of short pulses and NRZ signals based on a nonlinear optical loop mirror. J. Lightwave Technol. **18**, No. 7, 1007.

Tamura, K.R., H. Kubota, and M. Nakazawa (2000) Fundamentals of stable continuum generation at high repetition rates. IEEE J. Quantum Electron. **36**, No. 7, 773.

Hashimoto, T., H. Sotobayashi, K. Kitayama, and W. Chujo (2000) Photonic conversion of OC-192OTDM-to-4 × OC-48WDM by supercontinuum generation. Electron. Lett. **36**, No. 13, 1133.

Wada, N., H. Sotobayashi, and K. Kitayama (2000) 2.5 Gbit/s time-spread/wavelength-hop optical code division multiplexing using fibre Bragg grating with supercontinuum light source. Electron. Lett. **36**, No. 9, 815.

Yegnanarayanan, S., A.S. Bhushan, and B. Jalali (2000) Fast wavelength-hopping time-spreading encoding/decoding for optical CDMA. IEEE Photon. Technol. Lett. **12**, No. 5, 573.

Boivin, L., S. Taccheo, C.R. Doerr, P. Schiffer, L.W. Stulz, R. Monnard, and W. Lin (2000) 400 Gbit/s transmission over 544 km from spectrum-sliced supercontinuum source. Electron. Lett. **36**, No. 4, 335.

Sotobayashi, H. and K. Kitayama (1999) Observation of phase conservation in multiwavelength binary phase shift-keying pulse-sequence generation at 10 Gbits/s by use of a spectrum-sliced supercontinuum in an optical fiber. Opt. Lett. **24**, No. 24, 1820.

Yamabayashi, Y. and M. Nakazawa (1999) Terabit transmission technology. NTT Rev. **11**, No. 4, 23.

Kawanishi, S., H. Takara, K. Uchiyama, I. Shake, and K. Mori (1999) 3 Tbit/s (160 Gbit/s × 19 channel) optical TDM and WDM transmission experiment. Electron. Lett. **35**, No. 10, 826.

Kawanishi, S., H. Takara, K. Uchiyama, I. Shake, and K. Mori (1999) 3 Tbit/s (160 Gbit/s × 19 channel) transmission by optical TDM and WDM. LEOS Newsletter **13**, No. 5, 7.

Bhushan, A.S., F. Coppinger, S. Yegnanarayanan, and B. Jalali (1999) Nondispersive wavelength-division sampling. Opt. Lett. **24**, No. 11, 738.

Mikulla, B., L. Leng, S. Sears, and B.C. Collings, M. Arend, and K. Bergman (1999) Broad-band high-repetition-rate source for spectrally sliced WDM. IEEE Photon. Technol. Lett. **11**, No. 4, 418.

Takushima, Y. and K. Kikuchi (1999) 10-GHz, over 20-channel multiwavelength pulse source by slicing supercontinuum spectrum generated in normal-dispersion fiber. IEEE Photon Technol Lett. **11**, No. 3, 322.

Sotobayashi, H. and K. Kitayama (1999) Broadcast-and-select OCDM/WDM network using 10 Gbit/s spectrum-sliced supercontinuum BPSK pulse code sequences. Electron. Lett. **35**, No. 22, 1966.

Sotobayashi, H. and K. Kitayama (1999) Observation of phase conservation in a pulse sequence at 10 Gb/s in a semiconductor optical amplifier wavelength converter by four-wave mixing. IEEE Photon. Technol. Lett. **11**, No. 1, 45.

Takushima, Y., F. Futami, and K. Kikuchi (1998) Generation of over 140-nm-wide supercontinuum form a normal dispersion fiber by using a mode-locked semiconductor laser source. IEEE Photon. Technol. Lett. **10**, No. 11, 1560.

Chan, V.W.S., K.L. Hall, E. Modiano, and K.A. Rauschenbach (1998) Architectures and technologies for high-speed optical data networks. J. Lightwave Technol. **16**, No. 12, 2146.

Sotobayashi, H. and K. Kitayama (1998) 325 nm bandwidth supercontinuum generation at 10 Gbit/s using dispersion-flattened and non-decreasing normal dispersion fibre with pulse compression technique. Electron. Lett. **34**, No. 13, 1336.

Kawanishi, S., H. Takara, K. Uchiyama, I. Shake, O. Kamatani, and H. Takahashi (1997) 1.4 Tbit/s (200 Gbit/s × 7 ch) 50 km optical transmission experiment. Electron. Lett. **33**, No. 20, 1716.

Guy, M.J., S.V. Chernikov, and J.R. Taylor (1997) A duration-tunable, multiwavelength pulse source for OTDM and WDM communications systems. IEEE Photon. Technol. Lett. **9**, No. 7, 1017.

Breuer, D., and K. Petermann (1997) Comparison of NRZ- and RZ-modulation format for 40-Gb/s TDM standard-fiber systems. IEEE Photon. Technol. Lett. **9**, No. 3, 398.

Takiguchi, K., S. Kawanishi, H. Takara, O. Kamatani, K. Uchiyama, A. Himeno, and K. Jinguji (1996) Dispersion slope equalising experiment using planar lightwave circuit for 200 Gbit/s time-division-multiplexed transmission. Electron. Lett. **32**, No. 22, 2083.

Morioka, T., H. Takara, S. Kawanishi, O. Kamatani, K. Takiguchi, K. Uchiyama, M. Saruwatari, H. Takahashi, M. Yamada, T. Kanamori, and H. Ono (1996) 1 Tbit/s (100 Gbit/s × 10 channel) OTDM/WDM transmission using a single supercontinuum WDM source. Electron. Lett. **32**, No. 10, 906.

Morioka, T., H. Takara, S. Kawanishi, T. Kitoh, and M. Saruwatari (1996) Error-free 500 Gbit/s all-optical demultiplexing using low-noise, low-jitter supercontinuum short pulses. Electron. Lett. **32**, No. 9, 833.

Morioka, T., K. Okamoto, M. Ishii, and M. Saruwatari (1996) Low-noise, pulsewidth tunable picosecond to femtosecond pulse generation by spectral filtering of wideband supercontinuum with variable bandwidth arrayed-waveguide grating filters. Electron. Lett. **32**, No. 9, 836.

Morioka, T., S. Kawanishi, H. Takara, O. Kamatani, M. Yamada, T. Kanamori, K. Uchiyama, and M. Saruwatari (1996) 100 Gbit/s × 4 ch, 100 km repeaterless TDM-WDM transmission using a single supercontinuum source. Electron. Lett. **32**, No. 5, 468.

Morioka, T., K. Uchiyama, S. Kawanishi, S. Suzuki, and M. Saruwatari (1995) Multiwavelength picosecond pulse source with low jitter and high optical frequency stability based on 200 nm supercontinuum filtering. Electron. Lett. **31**, No. 13, 1064.

Kawanishi, S., H. Takara, T. Morioka, O. Kamatani, and M. Saruwatari (1995) 200 Gbit/s, 100 km time-division-multiplexed optical-transmission using supercontinuum pulses with prescaled PLL timing extraction and all-optical demultiplexing. Electron. Lett. **31**, No. 10, 816.

Morioka, T., S. Kawanishi, H. Takara, and O. Kamatani (1995) Penalty-free, 100 Gbit/s optical-transmission of less-than-2 ps supercontinuum transform-limited pulses over 40 km, Electron. Lett. **31**, No. 2, 124.

Morioka, K., K. Mori, S. Kawanishi, and M. Saruwatari (1994) Pulse-width tunable, self-frequency conversion of short optical pulses over 200 nm based on supercontinuum generation. Electron. Lett. **30**, No. 23, 1960.

Morioka, T., S. Kawanishi, H. Takara, and M. Saruwatari (1994) Multiple-output, 100 Gbit/s all-optical demultiplexer based on multichannel four-wave mixing pumped by a linearly-chirped square pulse. Electron. Lett. **30**, No. 23, 1959.

Morioka, T., S. Kawanishi, K. Mori, and M. Saruwatari (1994) Transform-limited, femtosecond WDM pulse generation by spectral filtering of gigahertz supercontinuum. Electron. Lett. **30**, No. 14, 1166.

Morioka, T., S. Kawanishi, K. Mori, and M. Saruwatari (1994) Nearly penalty-free, <4 ps supercontinuum Gbit/s pulse generation over 1535–1560 nm. Electron. Lett. **30**, No. 10, 790.

Morioka, T., K. Mori, S. Kawanishi, and M. Saruwatari (1994) Multi-WDM-channel, Gbit/s pulse generation from a single laser source utilizing LD-pumped supercontinuum in optical fibers. IEEE Photon. Technol. Lett. **6**, No. 3, 365.

Morioka, T., K. Mori, and M. Saruwatari (1993) More than 100-wavelength-channel picosecond optical pulse generation from single laser source using supercontinuum in optical fibres. Electron. Lett. **29**, No. 10, 862.

Lucek, J.K. and K.J. Blow (1992) Soliton self-frequency shift in telecommunications fiber. Phys. Rev. A **45**, No. 9, 6666.

# 15
# Femtosecond Pump: Supercontinuum Probe for Applications in Semiconductors, Biology, and Chemistry


## Summary

Immediately following the supercontinuum discovery in 1969, it was realized that the supercontinuum, then called a "white light continuum," was an ideal light flash for probing transient phenomena upon photoexcitation of materials. This discovery of the picosecond continuum advanced conventional flash lamp and nanosecond laser photolysis by over one thousand-fold in time resolution for chemistry and biological applications. Soon afterward, carrier and phonon dynamics in semiconductors and dielectrics were investigated on the picosecond and nanosecond time scales to obtain information on intra- and intervalley hot electron transitions which involved nonradiative vibrational and optical phonon dynamics. With the advent of femtosecond mode-locked pulse lasers (CPM dye and later Ti:sapphire), the supercontinuum generated by femtosecond pulses was extended into the femtosecond time scale to probe events with even finer time resolution, for better understanding the underlying fundamental processes of the excitation that live in materials.

This chapter gives a selected sample of references to the numerous research works probing faster processes in biology, chemistry, and solid state physics using a femtosecond pump–supercontinuum probe approach.

In chemistry, femtosecond photo-induced intramolecular electron transfer, charge transfer, and the effect of solute–solvent dynamics on the absorption transitions of the solute are being studied on femtosecond to picosecond time scales. The cooling dynamics of the "hot" excited solute in the $S_1$ state results in a 50-fs internal conversion in the $S_1$ state by intramolecular vibrational thermalization followed by a solute-to-solvent energy transfer on the order of ~2 ps which proceeds through the hydrogen bonds. The ultrafast electron transfer injected from the excited dye to a $TiO_2$ semiconductor nanoparticle was reported to occur on a 6-fs time scale.

In the solid state, research concentrated on heavy and light hole dynamics in quantum wells, quantum dots, and bulk semiconductors, and probing quasi-particle and electron temporal behavior near Fermi levels of Fermi

liquids and non-Fermi liquid states in superconductors. The relaxation of photoexcited electrons near the Fermi level of metallic silver nanoparticles occurs with complex relaxation behavior for times ~670 fs to 4 ps. In porous silicon, coherent optical phonons were attributed to the large 500-fs component of the transmission component arising from the size of crystallized regions. The nonequilibrium carriers at the semicondutor–metal interface occur on the femtosecond scale for a carrier to penetrate through the Schottky barrier.

In the biological chemistry area, the photo-isomerization dynamics was studied by Raman with a supercontinuum probe pulse with >250 fs to obtain more information between *trans*- and *cis*-forms and the charge transfer states.

The next era of pump-supercontinuum probe usage will undoubtedly be focused on ultraviolet and X-ray attosecond pump pulses with a supercontinuum to probe ever finer times and coherent processes of electron motion in atoms and the molecules and carriers' linear and angular momentum relaxation. One anticipates the study of Auger events of the electron bond rearrangments of the inner shell transitions and vacancies in atoms. The attosecond time scale of orbiting electrons about nuclei and for electron transitions between inner shells will be investigated with sub-femtosecond supercontinuum and attosecond pulse excitation to answer more on the quantum and relativistic events.

## Updated References

Katayama, T. and H. Kawaguchi (2004) Measurement of ultrafast cross-gain saturation dynamics of a semiconductor optical amplifier using two-color pump-probe technique. IEEE Photon. Technol. Lett. **16**, No. 3, 855.

Ushakov, E.N., V.A. Nadtochenko, S.P. Gromov, A.I. Vedernikov, N.A. Lobova, M.V. Alfimov, F.E. Gostev, A.N. Petrukhin, and O.M. Sarkisov (2004) Ultrafast excited state dynamics of the bi- and termolecular stilbene-viologen charge-transfer complexes assembled via host–guest interactions. Chem. Phys. **298**, Nos. 1–3, 251.

Wu, S.J., D.L. Wang, H.B. Jiang, H. Yang, Q.H. Gong, Y.L. Ji, and W. Lu (2004) Transient saturation absorption spectroscopy excited near the band gap at high excitation carrier density in GaAs. Chinese Phys. **13**, No. 1, 111.

Grant, C.D., A.M. Schwartzberg, Y.Y. Yang, S.W. Chen, and J.Z. Zhang (2004) Ultrafast study of electronic relaxation dynamics in $Au_{11}$ nanoclusters. Chem. Phys. Lett. **383**, Nos. 1–2, 31.

Kovalenko, S.A., J.L.P. Lustres, N.P. Ernsting, and W. Rettig (2003) Photoinduced electron transfer in bianthryl and cyanobianthryl in solution: The case for a high-frequency intramolecular reaction coordinate. J. Phys. Chem. A **107**, No. 48, 10228.

Wang, D.L., H.B. Jiang, S.J. Wu, H. Yang, Q.H. Gong, J.F. Xiang, and G.Z. Xu (2003) An investigation of solvent effects on the optical properties of dye IR-140 using the pump supercontinuum-probing technique. J. Opt. A **5**, No. 5, 515.

Chekalin, S., V. Kompanets, M. Kurdoglyan, A. Oraevsky, N. Starodubtsev, V. Sundstrom, and A. Yartsev (2003) Femtosecond pump-probe investigation of primary photo-induced processes in C-60-Sn nanostructures. Synthetic Metals, **139**, No. 3, 799.

Lee, S.M., B.K. Rhee, M. Choi, and S.H. Park (2003) Optical parametric spectral broadening of picosecond laser pulses in beta-barium borate. Appl. Phys. Lett. **83**, No. 9, 1722.

Dobryakov, A.L., S.A. Kovalenko, and N.P. Ernsting (2003) Electronic and vibrational coherence effects in broadband transient absorption spectroscopy with chirped supercontinuum probing. J. Chem. Phys. **119**, No. 2, 988.

Wang, D.L., J.F. Xiang, H.B. Jiang, G.Z. Xu, and Q.H. Gong (2003) Photo-induced electron transfer between dye IR-140 and $TiO_2$ colloids by femtosecond pump supercontinuum probing. J. Opt. A **5**, No. 2, 123.

Wang, D.L., H. Yang, H.B. Jiang, Q.H. Gong, Q.F. Zhang, and J.L. Wu (2002) Optical transient relaxation of an Ag–BaO composite thin film with a supercontinuum probe. Chinese Phys. Lett. **19**, No. 8, 1115.

Fujita, K., C. Yasumoto, and K. Hirao (2002) Photochemical reactions of samarium ions in sodium borate glasses irradiated with near-infrared femtosecond laser pulses. J. Lumin. **98**, Nos. 1–4, 317.

Huber, R., J.E. Moser, M. Gratzel, and J. Wachtveitl (2002) Real-time observation of photo-induced adiabatic electron transfer in strongly coupled dye/semiconductor colloidal systems with a 6 fs time constant. J. Phys. Chem. B **106**, No. 25, 6494.

Zhang, Q.F., D.L. Wang, Q.H. Gong, and J.L. Wu (2002) Investigation on transient relaxation in Ag–BaO composite thin film with pump supercontinuum-probe technique. J. Phys. D **35**, No. 12, 1326.

Lozovik, Y.E., A.L. Dobryakov, S.A. Kovalenko, S.P. Merkulova, S.Y. Volkov, and M. Willander (2002) Study of localization of carriers in disordered semiconductors by femtosecond spectroscopy. Laser Phys. **12**, No. 4, 802.

Wang, D.L., H.B. Jiang, H. Yang, C.L. Liu, Q.H. Gong, J.F. Xiang, and G.Z. Xu (2002) Investigation on photoexcited dynamics of IR-140 dye in ethanol by femtosecond supercontinuum-probing technique. J. Opt. A **4**, No. 2, 155.

Vinogradov, E.A., A.L. Dobryakov, Y.E. Lozovik, and Y.A. Matveets (2001) Femtosecond photoresponse of structures with the Schottky barrier. Laser Phys. **11**, No. 11, 1147.

Kovalenko, S.A., R. Schanz, H. Hennig, and N.P. Ernsting (2001) Cooling dynamics of an optically excited molecular probe in solution from femtosecond broadband transient absorption spectroscopy. J. Chem. Phys. **115**, No. 7, 3256.

Richardson, C.J.K., J.B. Spicer, R.D. Huber, and W.H.W. Lee (2001) Direct detection of ultrafast thermal transients by use of a chirped, supercontinuum white-light pulse. Opt. Lett. **26**, No. 14, 1105.

Palit, D.K., A.K. Singh, A.C. Bhasikuttan, and J.P. Mittal (2001) Relaxation dynamics in the excited states of LDS-821 in solution. J. Phys. Chem. A **105**, No. 26, 6294.

Kovalenko, S.A., N. Eilers-Konig, T.A. Senyushkina, and N.P. Ernsting (2001) Charge transfer and solvation of betaine-30 in polar solvents—A femtosecond broadband transient absorption study. J. Phys. Chem. A **105**, No. 20, 4834.

Farztdinov, V.M., R. Schanz, S.A. Kovalenko, and N.P. Ernsting (2000) Relaxation of optically excited *p*-nitroaniline: Semiempirical quantum-chemical calculations compared to femtosecond experimental results. J. Phys. Chem. A **104**, No. 49, 11486.

Dobryakov, A.L., S.A. Kovalenko, V.M. Farztdinov, S.P. Merkulova, N.P. Ernsting, and Y.E. Lozovik (2000) Ultrafast relaxation in $YBa_2Cu_3O_7$-delta on the femtosecond scale: Luttinger or two-dimensional Fermi liquid picture? Solid State Commun. **116**, No. 8, 437.

Kovalenko, S.A., R. Schanz, V.M. Farztdinov, H. Hennig, and N.P. Ernsting (2000) Femtosecond relaxation of photoexcited para-nitroaniline: Solvation, charge transfer, internal conversion and cooling. Chem. Phys. Lett. **323**, Nos. 3–4, 312.

Dobryakov, A.L., V.A. Karavanskii, S.A. Kovalenko, S.P. Merkulova, and Y.E. Lozovik (2000) Observation of coherent phonon states in porous silicon films. JETP Lett. **71**, No. 7, 298.

Yoshizawa, M., M. Kubo, and M. Kurosawa (2000) Ultrafast photoisomerization in DCM dye observed by new femtosecond Raman spectroscopy. J. Lumin. **87–9**, 739.

Vinogradov, E.A., C.C. Davis, A.L. Dobryakov, Y.E. Lozovik, and I.I. Smolyaninov (2000) Electron injection dynamics through the Schottky barrier. Laser Phys. **10**, No. 1, 76.

Yoshizawa, M. and M. Kurosawa (2000) Femtosecond time-resolved Raman spectroscopy using stimulated Raman scattering—Art. no. 013808. Phys. Rev. A **6001**, No. 1, 3808.

Farztdinov, V.M., S.A. Kovalenko, Y.E. Lozovik, D.V. Lisin, Y.A. Matveets, T.S. Zhuravleva, V.M. Geskin, L.M. Zemtsov, V.V. Kozlov, and G. Marowsky (2000) Ultrafast optical response of carbon films. J. Phys. Chem. B **104**, No. 2, 220.

Farztdinov, V.M., A.L. Dobryakov, S.A. Kovalenko, D.V. Lisin, S.P. Merkulova, F. Pudonin, and Y.E. Lozovik (1999) Ultrafast phenomena in copper films. Phys. Scripta **60**, No. 6, 579.

Kovalenko, S.A., A.L. Dobryakov, V.A. Karavanskii, D.V. Lisin, S.P. Merkulova, and Y.E. Lozovik (1999) Femtosecond spectroscopy of porous silicon. Phys. Scripta **60**, No. 6, 589.

Dobryakov, A.L. and Y.E. Lozovik (1999) A new optical method for measuring the electron–phonon interaction parameter lambda <Omega(2)> using the spectral dependence of the relaxation rate. JETP Lett. **70**, No. 5, 329.

Lozovik, Y.E., A.V. Klyuchnik, and S.P. Merkulova (1999) Nanolocal optical study and nanolithography using scanning probe microscope. Laser Phys. **9**, Nos. 2, 552.

Lozovik, Y.E., S.A. Kovalenko, A.L. Dobryakov, V.M. Farztdinov, Y.A. Matveets, S.P. Merkulova, and N.P. Ernsting (1999) Fermi liquid study on femtosecond scale. Laser Phys. **9**, No. 2, 557.

Lochschmidt, A., N. Eilers-Konig, N. Heineking, and N.P. Ernsting (1999) Femtosecond photodissociation dynamics of bis(julolidine) disulfide in polar and apolar solvents. J. Phys. Chem. A **103**, No. 12, 1776.

Kovalenko, S.A., A.L. Dobryakov, J. Ruthmann, and N.P. Ernsting (1999) Femtosecond spectroscopy of condensed phases with chirped supercontinuum probing. Phys. Rev. A **59**, No. 3, 2369.

Vinogradov, E.A., V.M. Farztdinov, S.A. Kovalenko, A.L. Dobryakov, Y.E. Lozovik, and Y.A. Matveets (1999) Femtosecond dynamics of A(2)B(6)-metal microcavity polaritons. Laser Phys. **9**, No. 1, 215.

Zhuravleva, T.S., S.A. Kovalenko, Y.E. Lozovik, Y.A. Matveets, V.M. Farztdinov, A.L. Dobryakov, A.V. Nazarenko, L.M. Zemtsov, V.V. Kozlov, G.P. Karpacheva, and G. Marowsky (1998) Ultrafast optical response of IR-treated polyacrylonitrile films. Polymers Adv. Technol. **9**, Nos. 10–11, 613.

Kovalenko, S.A., J. Ruthmann, and N.P. Ernsting (1998) Femtosecond hole-burning spectroscopy with stimulated emission pumping and supercontinuum probing. J. Chem. Phys. **109**, No. 5, 1894.

Vinogradov, E.A., V.M. Farztdinov, A.L. Dobryakov, S.A. Kovalenko, Y.E. Lozovik, and Y.A. Matveets (1998) Ultrafast dynamics and parametric excitations of microcavity modes. Laser Phys. **8**, No. 3, 620.

Freiberg, A., J.A. Jackson, S. Lin, and N.W. Woodbury (1998) Subpicosecond pump-supercontinuum probe spectroscopy of LH2 photosynthetic antenna proteins at low temperature. J. Phys. Chem. A **102**, No. 23, 4372.

Vinogradov, E.A., V.M. Farztdinov, A.L. Dobryakov, S.A. Kovalenko, Y.E. Lozovik, and Y.A. Matveets (1998) Femtosecond spectroscopy of semiconductor microcavity polaritons. Laser Phys. **8**, No. 1, 316.

Farztdinov, V.M., S.A. Kovalenko, Y.A. Matveets, N.F. Starodubtsev, and G. Marowsky (1998) The slowing-down of ultrafast relaxation in C-60 films at high femtosecond pump intensities. Appl. Phys. B **66**, No. 2, 225.

Kovalenko, S.A., J. Ruthmann, and N.P. Ernsting (1997) Ultrafast Stokes shift and excited-state transient absorption of coumarin 153 in solution. Chem. Phys. Lett. **271**, Nos. 1–3, 40.

Dobryakov, A.L., N.P. Ernsting, S.A. Kovalenko, and Y.E. Lozovik (1997) New method of non-Fermi liquid study by pump-supercontinuum probe femtosecond spectroscopy. Laser Phys. **7**, No. 2, 397.

Kovalenko, S.A., N.P. Ernsting, and J. Ruthmann (1997) Femtosecond Stokes shift in styryl dyes: Solvation or intramolecular relaxation? J. Chem. Phys. **106**, No. 9, 3504.

Bultmann, T. and N.P. Ernsting (1996) Competition between geminate recombination and solvation of polar radicals following ultrafast photodissociation of bis(*p*-aminophenyl) disulfide. J. Phys. Chem. **100**, No. 50, 19417.

Lozovik, Y.E. A.L. Dobryakov, N.P. Ernsting, and S.A. Kovalenko (1996) New method of non-Fermi liquid study by pump-supercontinuum probe femtosecond spectroscopy. Phys. Lett. A **223**, No. 4, 303.

Kovalenko, S.A., N.P. Ernsting, and J. Ruthmann (1996) Femtosecond hole-burning spectroscopy of the dye DCM in solution: The transition from the locally excited to a charge-transfer state. Chem. Phys. Lett. 258, Nos. 3–4, 445.

Rodriguez, G., J.P. Roberts, and A.J. Taylor (1994) Ultraviolet ultrafast pump-probe laser based on a Ti:sapphire laser system. Opt. Lett. **19**, No. 15, 1146.

Martin, M.M., P. Plaza, N. Dai Hung, Y.H. Meyer, J. Bourson, and B. Valeur (1993) Photoejection of cations from complexes with a crown-ether-linked merocyanine evidenced by ultrafast spectroscopy. Chem. Phys. Lett. **202**, No. 5, 425.

# 16
# Supercontinuum in Optical Coherence Tomography


## Summary

This chapter presents references to research in ultrahigh resolution optical coherence tomography (OCT) imaging using the supercontinuum source. The images are formed from the backscatter ballistic light from refractive index changes inside the materials, primarily tissues. The axial resolution of the OCT images is dependent on the bandwidth of the illumination source. The supercontinuum is the best and most convenient way to produce the widest bandwidth for OCT. Presently, the longitudinal resolutions of 2.5 $\mu$m in air and ~2 $\mu$m in tissue have been achieved using the supercontinuum in OCT. The high transmission zone for deep penetration of tissue for imaging is from 700 nm to 1300 nm. Laser sources being used at different central wavelengths which cover the absorption regions of tissue for OCT imaging are: Ti : sapphire (centered at 800 nm), neodymium glass (centered at 1060 nm), $Cr^{4+}$: forsterite (centered at 1300 nm), and $Cr^{4+}$ : YAG (centered at 1500 nm). A compact handheld OCT unit, including a femtosecond source, microstructure supercontinuum fibers, transmission fibers, and scanning units for remote diagnoses of tissues and structures of surfaces, is under development and investigation for medical and nonmedical applications.


## Updated References


Shi, K.B., P. Li, S.Z., Yin, and Z.W. Liu (2004) Chromatic confocal microscopy using supercontinuum light. Opt. Express **12**, No. 10, 2096.

Unterhuber, A., B. Povazay, K. Bizheva, B. Hermann, H. Sattmann, A. Stingl, T. Le, M. Seefeld, R. Menzel, M. Preusser, H. Budka, C. Schubert, H. Reitsamer, P.K. Ahnelt, J.E. Morgan, A. Cowey, and W. Drexler (2004) Advances in broad bandwidth light sources for ultrahigh resolution optical coherence tomography. Phys. Medicine Biol. **49**, No. 7, 1235.

Wojtkowski, M., V.J. Srinivasan, T.H. Ko, J.G. Fujimoto, A. Kowalczyk, and J.S. Duker (2004) Ultrahigh-resolution, high-speed, Fourier domain optical coherence tomography and methods for dispersion compensation. Opt. Express **12**, No. 11, 2404.

Drexler, W. (2004) Ultrahigh-resolution optical coherence tomography. J. Biomedical Opt. **9**, No. 1, 47.

Bourquin, S., A.D. Aguirre, I. Hartl, P. Hsiung, T.H. Ko, J.G. Fujimoto, T.A. Birks, W.J. Wadsworth, U. Bunting, and D. Kopf (2003) Ultrahigh resolution real time OCT imaging using a compact femtosecond Nd : Glass laser and nonlinear fiber. Opt. Express **11**, No. 24, 3290.

Corwin, K.L., N.R. Newbury, J.M. Dudley, S. Coen, S.A. Diddams, B.R. Washburn, K. Weber, and R.S. Windeler (2003) Fundamental amplitude noise limitations to supercontinuum spectra generated in a microstructured fiber. Appl. Phys. B **77**, Nos. 2–3, 269.

Sorokin, E., V.L. Kalashnikov, S. Naumov, J. Teipel, F. Warken, H. Giessen, and, I.T. Sorokina (2003) Intra- and extra-cavity spectral broadening and continuum generation at 1.5 $\mu$m using compact low-energy femtosecond Cr : YAG laser. Appl. Phys. B **77**, Nos. 2–3, 197.

Wang, Y.M., J.S. Nelson, Z.P, Chen, B.J. Reiser, R.S. Chuck, and R.S. Windeler (2003) Optimal wavelength for ultrahigh-resolution optical coherence tomography. Opt. Express **11**, No. 12, 1411.

Wang, Y.M., Y.H. Zhao, J.S. Nelson, Z.P. Chen, and R.S. Windeler (2003) Ultrahigh-resolution optical coherence tomography by broadband continuum generation from a photonic crystal fiber. Opt. Lett. **28**, No. 3, 182.

Marks, D.L., A.L. Oldenburg, J.J. Reynolds, and S.A. Boppart (2002) Study of an ultrahigh-numerical-aperture fiber continuum generation source for optical coherence tomography. Opt. Lett. **27**, No. 22, 2010.

Povazay, B., K. Bizheva, A. Unterhuber, B. Hermann, H. Sattmann, A.F. Fercher, W. Drexler, A. Apolonski, W.J. Wadsworth, J.C. Knight, P.S.J. Russell, M. Vetterlein, and E. Scherzer (2002) Submicrometer axial resolution optical coherence tomography. Opt. Lett. **27**, No. 20, 1800.

Kowalevicz, Jr., A.M., T.R. Schibli, F.X. Kartner, and J.G. Fujimoto (2002) Ultralow-threshold Kerr-lens mode-locked Ti : $Al_2O_3$ laser. Opt. Lett. **27**, No. 22, 2037.

Hartl, I., X.D. Li, C. Chudoba, R.K. Ghanta, T.H. Ko, J.G. Fujimoto, J.K. Ranka, and R.S. Windeler (2001) Ultrahigh-resolution optical coherence tomography using continuum generation in an air–silica microstructure optical fiber. Opt. Lett. **26**, No. 9, 608.

Watanabe, W. and K. Itoh (2000) Coherence spectrotomography: Optical spectroscopic tomography with low-coherence interferometry. Opt. Rev. **7**, No. 5, 406.

# 17
# Supercontinuum in Femtosecond Carrier-Envelope Phase Stabilization

## Summary

One of the newest uses of the supercontinuum in conjunction with a mode-locked laser is in metrology, to achieve better, more accurate clocks and timing. There is a worldwide effort to produce more accurate measurements of frequency where the fractional change in frequency $\Delta f/f \sim 10^{-16}$ to $10^{-18}$ is sorted. Pulses from mode-locked lasers have been used in the past as a frequency comb since the mode under laser profile is spaced by exact multiples of the repetition frequency $f_{rep} = c/2nL$. The repetition rate of pulse circulating in the cavity, ~40 MHz to 1 GHz, depends on the laser cavity length, $L$.

As ultrafast pulses generated by mode-locked lasers become shorter in time duration, ~20 fs, the relative phase between the peak of the envelope and the underlying carrier wave becomes important for the phase stabilization of optical frequencies in the pulses to make more accurate frequency measurements and intense pulses for nonlinear optical effects. The control of the carrier-envelope phase (CEP) in a mode-lock laser pulse train with the help of the supercontinuum results in more accurate techniques for frequency metrology for clocking and enhanced optical nonlinear applications.

There are two parts in a laser pulse—an envelope profile and a carrier wave. The carrier wave propagates with phase velocity, $V_p$, and the envelope profile propagates with group velocity, $V_g$. These velocities are usually different because of dispersion given by $n(\lambda)$. The maximum electric strength depends on the exact portion of the carrier wave electric field with regard to the pulse envelope here called carrier-envelope offset (CEO).

The references to papers in this chapter describe how to phase stabilize the laser pulse in a mode-locked train. A good number of researchers use the supercontinuum to accomplish this feat.

Due to cavity dispersion, $V_g \neq V_p$, the laser pulse envelope profile is not fixed to the underlying carrier frequency but shifted. There is a change of phase called the CEP slip $\Delta\varphi_{CEO}$, between the carrier phase and envelope peak for each successive phase in the mode-locked train, which is given by

$$\Delta\varphi_{\mathrm{CEO}} = \left(\frac{1}{V_g} - \frac{1}{V_p}\right) l_0 \omega_c = (n_g - n)\frac{l_0 \omega_c}{c}.$$

In the frequency domain, $\Delta\varphi_{\mathrm{CEO}}$ results in offset frequency $f_{\mathrm{CEO}}$ from the exact repetition frequency $f_{\mathrm{rep}}$. The comb frequency of the pulse in the $m$th mode is given by

$$f_m = mf_{\mathrm{rep}} + f_{\mathrm{CEO}}.$$

The most common scheme to obtain $f_{\mathrm{CEO}}$ is to beat $f_{2m}$ with $2f_m$ in an interferometer. This is where the supercontinuum comes into play. The comb consists of lines located at $f_m = mf_{\mathrm{rep}} + f_{\mathrm{CEO}}$ at the low-frequency portion of the supercontinuum spectrum and at $f_{2m}$ at the high-frequency portion of the supercontinuum spectrum. The mode at $f_{2m}$ is combined with the doubled frequency of supercontinuum at $f_m$ given by $2f_m = 2mf_{\mathrm{rep}} + 2f_{\mathrm{CEO}}$. This process is described at $f$ to $2f$ heterodyne techniques. Beating these waves in the comb at $f_{2m}$ and $2f_m$ by heterodyning gives

$$2fm - f_{2m} = 2(mf_{\mathrm{rep}} + f_{\mathrm{CEO}}) - (2mf_{\mathrm{rep}} + f_{\mathrm{CEO}}) = f_{\mathrm{CEO}}.$$

The difference between $f_{2m} = 2mf_{\mathrm{rep}} + f_{\mathrm{CEO}}$ and $2f_m$ is $f_{\mathrm{CEO}}$. One can adjust $f_{\mathrm{CEO}}$ toward zero. The one octave frequency span in the supercontinuum is used where the red (say at 1040 nm) is doubled by second harmonic generation (SHG) and the blue (say at 520 nm) is used in an interferometer to obtain the offset $f_{\mathrm{CEO}}$ and $\Delta\varphi_{\mathrm{CEO}}$ change. To do this, the laser cavity length and mirror alignment are adjusted to compensate for $f_{\mathrm{CEO}}$. The laser pulse from a mode-locked laser train is spectrally broadened to form the supercontinuum in a microstructural fiber. The output is fed into an $f$ to $2f$ interferometer loop, where the supercontinuum is split into a red pulse and a blue pulse spaced by $2f$. The red pulse is first converted by SHG in the loop and combined to be heterodyned with the blue portion of the supercontinuum at the interferometer loop. The combined beam is filtered with 10 nm bandwidth filters (at 520 nm).

The output of a mode-locked laser have pulses spaced by a repetition rate, $f_{\mathrm{rep}}$. These pulses form a comb of optical frequencies given by the mode under the spectral timing and clocking with the accuracy of $\Delta f/f \sim 10^{-14}$, see Chapter 19. The difference is that the phase velocity of the carrier wave and the group velocity of envelope causes a carrier-envelope frequency offset shift, $f_{\mathrm{CEO}}$. The offset frequency is controlled and deleted by heterodyning beating. The offset frequency offset can be stabilized and adjusted using a feedback loop to adjust either the intensity of pulse or a cavity mirror alignment. The adjustment of $\varphi_{\mathrm{CEO}}$ can make the peak of a carrier field coincide with the peak of the envelope to produce a more reproductable pulse to pulse with a higher intense field in the train for nonlinear optics and atomic physics applications. The phase stabilization can be used to control and achieve attosecond jitter resolution for probing the electron motions in atoms. It has been found that

one of the key processes to achieve attosecond pulse reproductability for CEO is the supercontinuum where $f$ to $2f$ waves in the supercontinuum are beaten together in an interferometer with a feedback loop.

## Updated References

Tortora, A., C. Corsi, and M. Bellini (2004) Comb-like supercontinuum generation in bulk media. Appl. Phys. Lett. **85**, No. 7, 1113.

McFerran, J.J., M. Marić, and A.N. Luiten (2004) Efficient detection and control of the carrier-envelope offset frequency in a self-referencing optical frequency synthesizer. Appl. Phys. B **79**, No. 1, 39.

Hundertmark, H., D. Kracht, M. Engelbrecht, D. Wandt, and C. Fallnich (2004) Stable sub-85 fs passively mode-locked Erbium-fiber oscillator with tunable repetition rate. Opt. Express **12**, No. 14, 3178.

Fang, X.J. and T. Kobayashi (2004) Self-stabilization of the carrier-envelope phase of an optical parametric amplifier verified with a photonic crystal fiber. Opt. Lett. **29**, No. 11, 1282.

Hundertmark, H., D. Wandt, C. Fallnich, N. Haverkamp, and H.R. Telle (2004) Phase-locked carrier-envelope-offset frequency at 1560 nm. Opt. Express **12**, No. 5, 770.

O'Keeffe, K., P. Jochl, H. Drexel, V. Grill, F. Krausz, and M. Lezius (2004) Carrier-envelope phase measurement using a nonphase stable laser. Appl. Phys. B **78**, No. 5, 583.

Washburn, B.R., S.A. Diddams, N.R. Newbury, J.W. Nicholson, M.F. Yan, and C.E. Jorgensen (2004) Phase-locked, erbium-fiber-laser-based frequency comb in the near infrared. Opt. Lett. **29**, No. 3, 250.

Gu, X., M. Kimmel, A.P. Shreenath, R. Trebino, J.M. Dudley, S. Coen, and R.S. Windeler (2003) Experimental studies of the coherence of microstructure-fiber supercontinuum. Opt. Express **11**, No. 21, 2697.

Ye, J., H. Schnatz, and L.W. Hollberg (2003) Optical frequency combs: From frequency metrology to optical phase control. IEEE J. Sel. Topics Quantum Electron. **9**, No. 4, 1041.

Schibli, T.R., O. Kuzucu, J.W. Kim, E.P. Ippen, J.G. Fujimoto, F.X. Kaertner, V. Scheuer, and G. Angelow (2003) Toward single-cycle laser systems. IEEE J. Sel. Topics Quantum Electron. **9**, No. 4, 990.

Holman, K.W., R.J. Jones, A. Marian, S.T. Cundiff, and J. Ye (2003) Detailed studies and control of intensity-related dynamics of femtosecond frequency combs from mode-locked Ti : sapphire lasers. IEEE J. Sel. Topics Quantum Electron. **9**, No. 4, 1018.

Kobayashi, Y., Z.Y. Wei, M. Kakehata, H. Takada, and K. Torizuka (2003) Relative carrier-envelope-offset phase control between independent femtosecond light sources. IEEE J. Sel. Topics Quantum Electron. **9**, No. 4, 1011.

Diddams, S.A., A. Bartels, T.M. Ramond, C.W. Oates, S. Bize, E.A. Curtis, J.C. Bergquist, and L. Hollberg (2003) Design and control of femtosecond lasers for optical clocks and the synthesis of low-noise optical and microwave signals. IEEE J. Sel. Topics Quantum Electron. **9**, No. 4, 1072.

Fortier, T.M., D.J. Jones, J. Ye, and S.T. Cundiff (2003) Highly phase stable mode-locked lasers. IEEE J. Sel. Topics Quantum Electron. **9**, No. 4, 1002.

Baltuska, A., M. Uiberacker, E. Goulielmakis, R. Kienberger, V.S. Yakovlev, T. Udem, T.W. Hansch, and F. Krausz (2003) Phase-controlled amplification of few-cycle laser pulses. IEEE J. Sel. Topics Quantum Electron. **9**, No. 4, 972.

Holman, K.W., R.J. Jones, A. Marian, S.T. Cundiff, and J. Ye (2003) Intensity-related dynamics of femtosecond frequency combs. Opt. Lett. **28**, No. 10, 851.

Ell, R., W. Seitz, U. Morgner, T.R. Schibli, and F.X. Kartner (2003) Carrier-envelope phase dynamics of synchronized mode-locked lasers. Opt. Commun. **220**, Nos. 1–3, 211.

Helbing, F.W., G. Steinmeyer, and U. Keller (2003) Carrier-envelope control of femtosecond lasers with attosecond timing jitter. Laser Phys. **13**, No. 4, 644.

Tauser, F., A. Leitenstorfer, and W. Zinth (2003) Amplified femtosecond pulses from an Er : fiber system: Nonlinear pulse shortening and self-referencing detection of the carrier-envelope phase evolution. Opt. Express **11**, No. 6, 594.

Buckbaum, P.H. (2003) Ultrafast control. Nature **421**, No. 6923, 593.

Baltuska, A., Th. Udem, M. Uiberacker, M. Hentschel, E. Goulielmakis, Ch. Gohie, R. Holzwarth, V.S. Yakovlev, A. Scrinzi, T.W. Hänsch, and F. Krausz (2003) Attosecond control of electronic processes by intense light fields. Nature **421**, No. 6923, 611.

Cundiff, S.T. and J. Ye (2003) Colloquium: Femtosecond optical frequency combs. Rev. Mod. Phys. **75**, No. 1, 325.

Zeng, Z.N., R.X. Li, W. Yu, and Z.Z. Xu (2003) Effect of the carrier-envelope phase of the driving laser field on the high-order harmonic attosecond pulse—Art. no. 013815. Phys. Rev. A **6701**, No. 1, 3815.

Hong, K.H., T.J. Yu, Y.S. Lee, and C.H. Nam (2003) Measurement of the shot-to-shot carrier-envelope phase slip of femtosecond laser pulses, J. Korean Phys. Soc. **42**, No. 1, 101.

Wei, Z.Y., Y. Kobayashi, and K. Torizuka (2002) Relative carrier-envelope phase dynamics between passively synchronized Ti : sapphire and Cr : forsterite lasers. Opt. Lett. **27**, No. 23, 2121.

Fortier, T.M., D.J. Jones, J. Ye, S.T. Cundiff, and R.S. Windeler (2002) Long-term carrier-envelope phase coherence. Opt. Lett. **27**, No. 16, 1436.

Baltuska, A., T. Fuji, and T. Kobayashi (2002) Self-referencing of the carrier-envelope slip in a 6-fs visible parametric amplifier. Opt. Lett. **27**, No. 14, 1241.

Cundiff, S.T. (2002) Phase stabilization of ultrashort optical pulses. J. Phys. D **35**, No. 8, R43.

Fortier, T.M., J. Ye, S.T. Cundiff, and R.S. Windeler (2002) Nonlinear phase noise generated in air-silica microstructure fiber and its effect on carrier-envelope phase. Opt. Lett. **27**, No. 6, 445.

Mücke, O.D., T. Tritschler, M. Wegener, U. Morgner, and F.X. Kärtner (2002) Determining the carrier-envelope offset frequency of 5-fs pulses with extreme nonlinear optics in ZnO. Opt. Lett. **27**, No. 23, 2127.

Ye, J., S.T. Cundiff, S. Foreman, T.M. Fortier, J.L. Hall, K.W. Holman, D.J. Jones, J.D. Jost, H.C. Kapteyn, K.A.H.V. Leeuwen, L.S. Ma, M.M. Murnane, J.L. Peng, and R.K. Shelton (2002) Phase-coherent synthesis of optical frequencies and waveforms. Appl. Phy. B **74**, Supplement 1, S27.

Holzwarth, R., M. Zimmermann, T. Udem, T.W. Hansch, P. Russbuldt, K. Gabel, R. Poprawe, J.C. Knight, W.J. Wadsworth, and P.S.J. Russell (2001) White-light frequency comb generation with a diode-pumped Cr : LiSAF laser. Opt. Lett. **26**, No. 17, 1376.

Cundiff, S.T., J. Ye, and J.L. Hall (2001) Optical frequency synthesis based on mode-locked lasers. Rev. Sci. Instrum. **72**, No. 10, 3749.

Holzwarth, R., M. Zimmermann, T. Udem, and T.W. Hänsch (2001) Optical clockworks and the measurement of laser frequencies with a mode-locked frequency comb. IEEE J. Quantum Electron. **37**, No. 12, 1493.

Brabec, T. and F. Krausz (2000) Intense few-cycle laser fields: Frontiers of nonlinear optics. Rev. Mod. Phys. **72**, No. 2, 545–591.

Apolonski, A., A. Poppe, G. Tempea, C. Spielmann, T. Udem, R. Holzwarth, T.W. Hänsch, and F. Krausz (2000) Controlling the phase evolution of few-cycle light pulses. Phys. Rev. Lett. **85**, No. 4, 740.

Bellini, M. and T.W. Hänsch (2000) Phase-locked white-light continuum pulses: Toward a universal optical frequency-comb synthesizer. Opt. Lett. **25**, No. 14, 1049.

Jones, D.J., S.A. Diddams, J.K. Ranka, A. Stentz, R.S. Windeler, J.L. Hall, and S. Cundiff (2000) Carrier-envelope phase control of femtosecond mode-locked lasers and direct optical frequency synthesis. Science **288**, No. 5466, 635.

Telle, H.R., G. Steinmeyer, A.E. Dunlop, J. Stenger, D.H. Sutter, and U. Keller (1999) Carrier-envelope offset phase control: A novel concept for absolute optical frequency measurement and ultrashort pulse generation. Appl. Phys. B **69**, No. 4, 327.

Reichert, J., R. Holzwarth, T. Udem, and T.W. Hänsch (1999) Measuring the frequency of light with mode-locked lasers. Opt. Commun. **172**, Nos. 1–6, 59.

*Note*: Venteon and Femtolaser, Inc., are two companies that offer CEP-stabilized femtosecond Ti:sapphire lasers using SC.

# 18
# Supercontinuum in Ultrafast Pulse Compression

## Summary

The ultrawide spectral width of the supercontinuum supports the frequencies required to produce the ultimate short pulse. The references in this chapter demonstrate how the supercontinuum can be used to generate sub-10-fs ultrashort pulses using pulse compression. Pulses as short as 3.8 fs with energies up to 15 $\mu$J have been generated using the supercontinuum, using two cascaded hollow fibers with adaptive pulse compression. The supercontinuum spanned from 530 nm to 1000 nm. Using sub-10-fs pulses, care is needed to prevent a time broadening effect when traveling through optics (lenses, prisms, plates, and coated dielectric mirrors) and air itself. One needs to reverse chirp the pulses to compensate for time-broadening effects in materials. With spectrally wider supercontinuum pulses, compression down to 1 fs and possibly even into attosecond regions may be possible over the next decade using uv pulses.

## Updated References

Dudley, J.M. and S. Coen (2004) Fundamental limits to few-cycle pulse generation from compression of supercontinuum spectra generated in photonic crystal fiber. Opt. Express **12**, No. 11, 2423.

Katayama, T. and H. Kawaguchi (2004) Supercontinuum generation and pulse compression in short fibers for optical pulses generated by 1.5 $\mu$m optical parametric oscillator. Jpn. J. Appl. Phys., Part 2 **43**, No. 6A, L712.

Spanner, M., M. Pshenichnikov, V. Olvo, and M. Ivanov (2003) Controlled supercontinuum generation for optimal pulse compression: A time-warp analysis of nonlinear propagation of ultra-broad-band pulses. Appl. Phys. B **77**, Nos. 2–3, 329.

Schenkel, B., J. Biegert, U. Keller, C. Vozzi, M. Nisoli, G. Sansone, S. Stagira, S. De Silvestri, and O. Svelto (2003) Generation of 3.8-fs pulses from adaptive compression of a cascaded hollow fiber supercontinuum. Opt. Lett. **28**, No. 20, 1987.

Seres, J., A. Muller, E. Seres, K. O'Keefe, M. Lenner, R.F. Herzog, D. Kaplan, C. Spielmann, and F. Krausz (2003) Sub-10-fs, terawatt-scale Ti : sapphire laser system. Opt. Lett. **28**, No. 19, 1832.

Ledingham, K.W.D., P. McKenna, and R.P. Singhal (2003) Applications for nuclear phenomena generated by ultra-intense lasers. Science **300**, 1107.

Rozanov, N.N. (2003) On the diffraction of ultrashort pulses. Opt. Spectrosc. **95**, No. 2, 299.

Schibli, T.R., O. Kuzucu, J.W. Kim, E.P. Ippen, J.G. Fujimoto, F.X. Kaertner, V. Scheuer, and G. Angelow (2003) Toward single-cycle laser systems. IEEE J. Sel. Topics Quantum Electron. **9**, No. 4, 990.

Schibli, T.R., J. Kim, O. Kuzucu, J.T. Gopinath, S.N. Tandon, G.S. Petrich, L.A. Kolodziejski, J.G. Fujimoto, E.P. Ippen, and F.X. Kaertner (2003) Attosecond active synchronization of passively mode-locked lasers by balanced cross correlation. Opt. Lett. **28**, No. 11, 947.

Spanner, M., M.Y. Ivanov, V. Kalosha, and J. Hermann (2003) Tunable optimal compression of ultrabroadband pulses by cross-phase modulation. Opt. Lett. **28**, No. 9, 749.

Chang, G.Q., T.B. Norris, and H.G. Winful (2003) Optimization of supercontinuum generation in photonic crystal fibers for pulse compression. Opt. Lett. **28**, No. 7, 546.

Inoue, J., H. Sotobayashi, and W. Chujo (2002) Sub-picosecond transform-limited 160 Gbit/s optical pulse compression using supercontinuum generation. IEICE Trans. Electron. **E85C**, No. 9, 1718.

Tsuchiya, M., K. Igarashi, S. Saito, and M. Kishi (2002) Sub-100-fs higher-order soliton compression in dispersion-flattened fibers. IEICE Trans. Electron. **E85C**, No. 1, 141.

Steinmeyer, G., L. Gallmann, F.W. Helbing, and U. Keller (2001) New directions in sub-10-fs optical pulse generation. C.R. Acad. Sci. Ser. IV **2**, No. 10, 1389.

Husakou, A.V., V.P. Kalosha, and J. Herrmann (2001) Supercontinuum generation and pulse compression in hollow waveguides. Opt. Lett. **26**, No. 13, 1022.

Tsuchiya, M., K. Igarashi, R. Yatsu, K. Taira, K.Y. Koay, and M. Kishi (2001) Sub-100-fs SDPF optical soliton compressor for diode laser pulses. Opt. Quantum Electron. **33**, 751.

Igarashi, K., M. Kishi, and M. Tsuchiya (2001) Higher-order soliton compression of optical pulses from 5 ps to 20 fs by a 15.1-m-long single-stage step-like dispersion profiled fiber. Jpn. J. Appl. Phys. **40**, Part 1, No. 11, 6426.

Han, M., C.Y. Lou, Y. Wu, G.Q. Chang, Y.Z. Gao, and Y.H. Li (2000) Generation of pedestal-free 10 GHz pulses from a comb-like dispersion profiled fiber compressor and its application in supercontinuum generation. Chinese Phys. Lett. **17**, No. 11, 806.

Yatsu, R., K. Taira, and M. Tsuchiya (1999) High-quality sub-100-fs optical pulse generation by fiber-optic soliton compression of gain-switched distributed-feedback laser-diode pulses in conjunction with nonlinear optical fiber loops. Opt. Lett. **24**, No. 16, 1172.

Lenzer, M., M. Schnurer, C. Spielmann, and F. Krausz (1998) Extreme nonlinear optics with few-cycle laser pulses. IEICE Trans. Electron. **E81C**, No. 2, 112.

Nisoli, M., S. De Silvestri, O. Svelto, R. Szipocs, K. Ferencz, C. Spielmann, S. Sartania, and F. Krausz (1997) Compression of high-energy laser pulses below 5 fs. Opt. Lett. **22**, No. 8, 522.

Baltuska, A., Z. Wei, M.S. Pshenichnikov, D.A. Wiersma, and R. Szipocs (1997) All solid-state cavity-dumped sub-5-fs laser. Appl. Phys. B **65**, 175.

Nisoli, M., S. De Silvestri, and O. Svelto (1996) Generation of high-energy 10-fs pulses by a new pulse compression technique. Appl. Phys. Lett. **68**, No. 20, 2793.

# 19
# Supercontinuum in Time and Frequency Metrology

## Summary

The references in this chapter extends the concept using the supercontinuum for phase stabilization of mode-locked lasers described in Chapter 17. As shown by the research references, there is a push to produce more accurate measurements of frequency to develop clocks with instability down to ~$10^{-17}$ at 1 s. State-of-the-art standards, based on atoms, ions, and molecules, exhibit excellent stability to achieve ultrahigh reproducibility and accuracy for clocks. The new concept added to past clock technology is based on "femtosecond optical frequency comb generation" with regular spaced sharp lines at well-defined frequencies. The pulse from a stabilized mode-locked laser is ideal for a "frequency comb." The mode spectrum of the femtosecond laser with the supercontinuum can generate optical pulse spanning over two octaves in bandwidth over the visible and near infrared. The optical heterodyning portion of the supercontinuum produces added stability for frequency measurement with a fractional frequency noise on order of $6 \times 10^{-16}$ in 1 s of averaging over the 300 THz bandwidth. With a $10^{-18}$ frequency accuracy, small gravity changes can easily be detected.

## Updated References

McFerran, J.J., M. Marić, and A.N. Luiten (2004) Efficient detection and control of the carrier-envelope offset frequency in a self-referencing optical frequency synthesizer. Appl. Phys. B **79**, No. 1, 39.

Washburn, B.R. and N.R. Newbury (2004) Phase, timing, and amplitude noise on supercontinua generated in microstructure fiber. Opt. Express **12**, No. 10, 2166.

Washburn, B.R., S.A. Diddams, N.R. Newbury, J.W. Nicholson, M.F. Yan, and C.G. Jorgensen (2004) Phase-locked, erbium-fiber-laser-based frequency comb in the near infrared. Opt. Lett. **29**, No. 3, 250.

Haverkamp, N. and H.R. Telle (2004) Complex intensity modulation transfer function for supercontinuum generation in microstructure fibers. Opt. Express **12**, No. 4, 582.

Amy-Klein, A., A. Goncharov, C. Daussy, C. Grain, O. Lopez, G. Santarelli, and C. Chardonnet (2004) Absolute frequency measurement in the 28-THz spectral region

with a femtosecond laser comb and a long-distance optical link to a primary standard. Appl. Phys. B **78**, No. 1, 25.

Naumov, A.N. and A.M. Zheltikov (2003) Frequency-time and time-space mappings with broadband and supercontinuum chirped pulses in coherent wave mixing and pump-probe techniques. Appl. Phys. B **77** Nos. 2–3, 369.

Ye, J., H. Schnatz, and L.W. Hollberg (2003) Optical frequency combs: From frequency metrology to optical phase control. IEEE J. Sel. Topics Quantum Electron. **9**, No. 4, 1041.

Baltuška, A., M. Uiberacker, E. Goulielmakis, R. Kienberger V.S. Yakovlev, T. Udem, T.W. Hänsch, and F. Krausz (2003) Phase-controlled amplification of few-cycle laser pulses. IEEE J. Sel. Topics Quantum Electron. **9**, No. 4, 972.

Ma, L.S., M. Zucco, S. Picard, L. Robertsson, and R.S. Windeler (2003) A new method to determine the absolute mode number of a mode-locked femtosecond-laser comb used for absolute optical frequency measurements. IEEE J. Sel. Topics Quantum Electron. **9**, No. 4, 1066.

Diddams, S.A., A. Bartels, T.M. Ramond, C.W. Oates, S. Bize, E.A. Curtis, J.C. Bergquist, and L. Hollberg (2003) Design and control of femtosecond lasers for optical clocks and the synthesis of low-noise optical and microwave signals. IEEE J. Sel. Topics Quantum Electron. **9**, No. 4, 1072.

Helbing, F.W., G. Steinmeyer, and U. Keller (2003) Carrier-envelope offset phase-locking with attosecond timing jitter. IEEE J. Sel. Topics Quantum Electron. **9**, No. 4, 1030.

Ye, J., J.L. Peng, R.J. Jones, K.W. Holman, J.L. Hall, D.J. Jones, S.A. Diddams, J. Kitching, S. Bize, J.C. Bergquist, L.W. Hollberg, L. Robertsson, and L.S. Ma (2003) Delivery of high-stability optical and microwave frequency standards over an optical fiber network. J. Opt. Soc. Am. B **20**, No. 7, 1459.

Jones, D.J., K.W. Holman, M. Notcutt, J. Ye, J. Chandalia, L.A. Jiang, E.P. Ippen, and H. Yokoyama (2003) Ultralow-jitter, 1550-nm mode-locked semiconductor laser synchronized to a visible optical frequency standard. Opt. Lett. **28**, No. 10, 813.

Park, S.T., E.B. Kim, J.Y. Yeom, and T.H. Yoon (2003) Optical frequency synthesizer with femtosecond mode-locked laser with zero carrier-offset frequency. J. Korean Phys. Soc. **42**, No. 5, 622.

Bartels, A., S.A. Diddams, T.M. Ramond, and L. Hollberg (2003) Mode-locked laser pulse trains with subfemtosecond timing jitter synchronized to an optical reference oscillator. Opt. Lett. **28**, No. 8, 663.

Hall, J.L. and J. Ye (2003) Optical frequency standards and measurement. IEEE Trans. Instrum. Meas. **52**, No. 2, 227.

Ma, L.S., L. Robertsson, S. Picard, J.M. Chartier, H. Karlsson, E. Prieto, and R.S. Windeler (2003) The BIPM laser standards at 633 nm and 532 nm simultaneously linked to the SI second using a femtosecond laser in an optical clock configuration. IEEE Trans. Instrum. Meas. **52**, No. 2, 232.

Helbing, F.W., G. Steinmeyer, and U. Keller (2003) Carrier-envelope control of femtosecond lasers with attosecond timing jitter. Laser Phys. **13**, No. 4, 644.

Tanaka, U., J.C. Bergquist, S. Bize, S.A. Diddams, R.E. Drullinger, L. Hollberg, W.M. Itano, C.E. Tanner, and D.J. Wineland (2003) Optical frequency standards based on the Hg-199(+) ion. IEEE Trans. Instrum. Meas. **52**, No. 2, 245.

Tanaka, U., S. Bize, C.E. Tanner, R.E. Drullinger, S.A. Diddams, L. Hollberg, W.M. Itano, D.J. Wineland, and J.C. Bergquist (2003) The Hg-199(+) single ion optical clock: Recent progress. J. Phys. B **36**, No. 3, 545.

Cundiff, S.T. and J. Ye (2003) Colloquium: Femtosecond optical frequency combs. Rev. Mod. Phys. **75**, No. 1, 325.

Ramond, T.M., S.A. Diddams, L. Hollberg, and A. Bartels (2002) Phase-coherent link from optical to microwave frequencies by means of the broadband continuum from a 1-GHz Ti : sapphire femtosecond oscillator. Opt. Lett. **27**, No. 20, 1842.

Ye, J., S.T. Cundiff, S. Foreman, T.M. Fortier, J.L. Hall, K.W. Holman, D.J. Jones, J.D. Jost, H.C. Kapteyn, K.A.H.V. Leeuwen, L.S. Ma, M.M. Murnane, J.L. Peng, and R.K. Shelton (2002) Phase-coherent synthesis of optical frequencies and waveforms. Appl. Phys. B **74**, Suppl. 1, S27.

Bagayev, S.N., V.S. Pivtsov, and A.M. Zheltikov (2002) Frequency stabilisation of femtosecond frequency combs with a reference laser. Quantum Electron. **32**, No. 4, 311.

Zheltikov, A.M. (2002) Nonlinear-optical stabilization of femtosecond frequency combs with a laser anchor. Laser Phys. **12**, No. 5, 878.

Cundiff, S.T. (2002) Phase stabilization of ultrashort optical pulses. J. Phys. D **35**, No. 8, R43.

Diddams, S.A., L. Hollberg, L.S. Ma, and L. Robertsson (2002) Femtosecond-laser-based optical clockwork with instability $\leq 6.3 \times 10^{-16}$ in 1 s. Opt. Lett. **27**, No. 1, 58.

Udem, Th., R. Holzwarth, and T.W. Hänsch (2002) Optical frequency metrology. Nature **416**, No. 6877, 233.

Hall, J.L., J. Ye, S.A. Diddams, L.S. Ma, S.T. Cundiff, and D.J. Jones (2001) Ultrasensitive spectroscopy, the ultrastable lasers, the ultrafast lasers, and the seriously nonlinear fiber: A new alliance for physics and metrology. IEEE J. Quantum Electron. **37**, No. 12, 1482.

Hollberg, L., C.W. Oates, E.A. Curtis, E.N. Ivanov, S.A. Diddams, T. Udem, H.G. Robinson, J.C. Bergquist, R.J. Rafac, W.M. Itano, R.E. Drullinger, and D.J. Wineland (2001) Optical frequency standards and measurements. IEEE J. Quantum Electron. **37**, No. 12, 1502.

Bagayev, S.N., A.K. Dmitriyev, S.V. Chepurov, A.S. Dychkov, V.M. Klementyev, D.B. Kolker, S.A. Kuznetsov, Y.A. Matyugin, M.V. Okhapkin, V.S. Pivtsov, M.N. Skvortsov, V.F. Zakharyash, T.A Birks, W.J. Wadsworth, P.S. Russell, and A.M. Zheltikov (2001) Femtosecond frequency combs stabilized with an He–Ne/$CH_4$ laser: Toward a femtosecond optical clock. Laser Phys. **11**, No. 12, 1270.

Diddams, S.A., D.J. Jones, J. Ye, S.T. Cundiff, J.L. Hall, J.K. Ranka, and R.S. Windeler (2001) Direct RF to optical frequency measurements with a femtosecond laser comb. IEEE Trans. Instrum. Meas. **50**, No. 2, 552.

Jones, R.J. and J.C. Diels (2001) Stabilization of femtosecond lasers for optical frequency metrology and direct optical to radio frequency synthesis. Phys. Rev. Lett. **86**, No. 15, 3288.

Bellini, M. and T.W. Hänsch (2000) Phase-locked white-light continuum pulses: Toward a universal optical frequency-comb synthesizer. Opt. Lett. **25**, No. 14, 1049.

Holzwarth, R., Th. Udem, T.W. Hänsch, J.C. Knight, W.J. Wadsworth, and P.St.J. Russell (2000) Optical frequency synthesizer for recision spectroscopy. Phys. Rev. Lett. **85**, No. 11, 2264.

Imai, K., M. Kourogi, and M. Ohtsu (1998) 30-THz span optical frequency comb generation by self-phase modulation in an optical fiber. IEEE J. Quantum Electron. **34**, 54.

# 20
# Supercontinuum in Atmospheric Science


## Summary

Intense ultrafast laser pulses propagating in air can self-guide in the form of channels and produce supercontinuum "white light" filaments over distances greater than 20 m. The spatial stabilization is attributed to the balance between defocusing processes of diffraction and Kerr self-focusing from the plasma created in the air by the laser pulse. In the guided channel the production of the supercontinuum is the onset fingerprint of the trapping process. An intense ultrashort laser pulse of ~10 mJ to 350 mJ of ~70 fs duration self-focuses to ~80 $\mu$m to produce the supercontinuum in air in the form of long filaments.

The research references in this chapter describe the generation of the supercontinuum in the form of filaments in the air from water droplets and ionized plasma, and present various applications of the supercontinuum to atmospheric science. These supercontinuum pulses are transmitted through fog and cloud for free space wireless optical communications and imaging used for remote sensing of pollutants and aerosols, and range finding. The production of well-defined ionized trails in air at a distance has potential uses such as controlling lightning, inducing rain, and creating an ionized pathway for missiles to follow for defensive and offensive military applications.


## Updated References


Rodriguez, M., R. Bourayou, G. Mejean, J. Kasparian, J. Yu, E. Salmon, A. Scholz, B. Stecklum, J. Eisloffel, U. Laux, A.P. Hatzes, R. Sauerbrey, L. Woste, and J.P. Wolf (2004) Kilometer-range nonlinear propagation of femtosecond laser pulses—Art. no. 036607. Phys. Rev. E **6903**, No. 3, Part 2, 6607.

Luo, Q., S.A. Hosseini, B. Ferland, and S.L. Chin (2004) Backward time-resolved spectroscopy from filament induced by ultrafast intense laser pulses. Opt. Commun. **233**, Nos. 4–6, 411.

Fibich, G., S. Eisenmann, B. Ilan, and A. Zigler (2004) Control of multiple filamentation in air. Opt. Lett. **29**, No. 15, 1772.

Mejean, G., J. Kasparian, E. Salmon, J. Yu, J.P. Wolf, R. Bourayou, R. Sauerbrey, M. Rodriguez, L. Woste, H. Lehmann, B. Stecklum, U. Laux, J. Eisloffel, A. Scholz, and A.P. Hatzes (2003) Towards a supercontinuum-based infrared lidar. Appl. Phys. B **77**, Nos. 2–3, 357.

Gaeta, A. (2003) Collapsing light really shines. Science **301**, 54.

Kasparian, J., M. Rodriguez, G. Mejean, J. Yu, E. Salmon, H. Wille, R. Bourayou, S. Frey, Y.-B. Andre, A. Mysyrowicz, R. Sauerbrey, J.-P. Wolf, and L. Woste (2003) White-light filaments for atmospheric analysis. Science **301**, No. 5629, 61.

Courvoisier, F., V. Boutou, J. Kasparian, E. Salmon, G. Méjean, J. Yu, and J.-P. Wolf (2003) Ultraintense light filaments transmitted through clouds. Appl. Phys. Lett. **83**, No. 2, 213.

Lerner E. (2003) Penetrating the fog. Industrial Physicist **9**, No. 5.

Chin, S.L., S. Petit, W. Liu, A. Iwasaki, M.-C. Nadeau, V.P. Kandidov, O.G. Kosareva, and K.Yu. Andrianov (2002) Interference of transverse rings in multifilamentation of powerful femtosecond laser pulses in air. Opt. Commun. **210**, 329.

Borrmann, S. and J. Curtius (2002) Lasing on a cloudy afternoon. Nature **418**, 826.

Favre, C., V. Boutou, S.C. Hill, W. Zimmer, M. Krenz, H. Lambrecht, J. Yu, R.K. Chang, L. Woeste, and J.-P. Wolf (2002) White-light nanosource with directional emission. Phys. Rev. Lett. **89**, No. 3, 035002-1.

Galvez, M.C., M. Fujita, N. Inoue, R. Moriki, Y. Izawa, and C. Yamanaka (2002) Three-wavelength backscatter measurement of clouds and aerosols using a white light lidar system. Jpn. J. Appl. Phys. Part 2 **41**, No. 3A, L284.

Brunel, M., L. Mess, G. Gouesbet, and G. Grehan (2001) Cerenkov-based radiation from superluminal excitation in microdroplets by ultrashort pulses. Opt. Lett. **26**, No. 20, 1621.

Berge, L. and A. Couairon (2001) Gas-induced solitons. Phys. Rev. Lett. **86**, No. 6, 1003.

Rairoux, P., H. Schillinger, S. Niedermeier, M. Rodriguez, F. Ronneberger, R. Sauerbrey, B. Stein, D. Waite, C. Wedekind, H. Wille, L. Woste, and C. Ziener (2000) Remote sensing of the atmosphere using ultrashort laser pulses. Appl. Phys. B **71**, No. 4, 573.

Braun, A., G. Korn, X. Liu, D. Du, J. Squier, and G. Mourou (1995) Self-channeling of high-peak-power femtosecond laser pulses in air. Opt. Lett. **20**, No. 1, 73.

# 21
# Coherence of the Supercontinuum

## Summary

Coherence is one of the key properties of light. Since the spectrum of the supercontinuum is extremely broad, its coherence length can be rather short, ~1.6 $\mu$m (Chapter 11), which is ideal for optical coherence tomography (OCT) (Chapter 16). The references in this chapter describe the phase coherence of the supercontinuum pulses produced in bulk and fiber media using femtosecond laser pulses.

The coherence properties of the supercontinuum are important for many applications: OCT, frequency combs, generation of intense pulses, and stabilization of a pulse-to-pulse phase relationship, attosecond jitter, and control of quantum states; to name a few important ones.

The supercontinuum generation is a way to broaden the spectrum of a pulse to more than an octave for a wide spanned frequency comb as mentioned in Chapters 17 and 19. The coherent nature of the supercontinuum generation process is important to ensure that the spectral line structure for the frequency comb from the mode-locked laser pulse is transferred coherently to the supercontinuum. The degree coherence of the supercontinuum is quantified using the mutual and self-coherence functions using interferometers or Young's two-source type interference arrangements. The distinct interference fringes observed in the overlap region of the two spectra suggest that some coherence of the pump pulses is maintained during the supercontinuum generation from bulk or fiber medium. The coherence properties of the supercontinuum improves for a small fiber interaction distance, ~2 cm, for short pump pulses, ~50 fs, and for the normal dispersion region where self-phase modulation plays a significant role in the absence of modulation instability, higher soliton generation or fission, amplification spontaneous emission, four-wave mixing, or stimulated Raman. It was found that dispersion decreasing fibers (DDF) maintain their coherence better than other dispersion flat fibers; dispersion shifted fiber as the supercontinuum broadening occurs for DDF through a single soliton compression.

A mode-locked laser pulse train can produce a self-referencing phase-locked femtosecond frequency comb. The spectral extent is limited by a pulse duration of ~50 fs. The supercontinuum is needed to produce a wider spectral for the comb. A phase-locked supercontinuum pulse can be generated from a train of these phase-locked pulses. In mode-locked lasers, the same pulse is circulating in the cavity to produce these pulse trains. The supercontinuum generation process is particularly important to ensure that the phase coherence is transferred from pumping pulses to the supercontinuum and that the phase-locking is maintained. As long as only a single filament is maintained in bulk medium, interference fringes can be observed.

The use of two nonoverlapping intense supercontinuum femtosecond pulses separated in time by $\tau$, measured in picoseconds, can produce an interference pattern in the spectral domain where multiple wavelength channels are produced for multiple wavelength multiplexing application (Chapter 11) in the 50 GHz range, ideal for wavelength discussion multiplexing (WDM) communication (see Chapter 14).

From the references in this chapter, the mutual coherence of the pump pulses from mode-locked femtosecond lasers can be transferred to the supercontinuum pulses using either bulk or fiber medium. The degree of coherence is >0.8. The phase relationship between the supercontinuum pulses and with itself are retained and robust.

The temporal, spectral, and coherence properties of femtosecond supercontinuum pulses can be used to control the spatiotemporal behavior of optical excitations in materials. The coherent control of a quantum system by one or more time-delayed chirped supercontinuum pulses may allow one to manipulate the quantum states and alter the radiative and nonradiative pathway and decay routes of excitations in chemical, semiconductor, quantum dots, nanocrystals, and biological systems. The quantum control of the transient populations and excitations can be achieved by changing the sign of chirp, polarizations, time sequence, and relative phase shape of the supercontinuum pulses. In this manner, the interference among the states can be changed. One of the goals in controlling matter with light is to achieve the largest desired contrast between different energy pathways of an optically excited state or excitation, say, between internal conversion and energy transfer routes in the primary events that occur in photosynthesis or vision.

## Updated References

Ni, X., C. Wang, X. Liang, M. Al-Rubaiee, and R.R. Alfano (2004) Fresnel diffraction supercontinuum generation. IEEE J. Sel. Topics Quantum Electron. **10**, No. 5, 1229.

Zeylikovich, I., U. Kartazayeu, and R.R. Alfano (2004) Spectral, temporal and coherence properties of supercontinuum generation in a photonic crystal fiber. Frontiers in Optics 2004, The 88th Annual Meeting, Optical Society of America. FWG6, 91.

Zeylikovich, I., U. Kartazayeu, and R.R. Alfano (2004) Supercontinuum multiple frequency channel generation for WDM system. Frontiers in Optics 2004, The 88th Annual Meeting, Optical Society of America. FWH26, 95.

Konorov, S.O., D.A. Akimov, A.A. Ivanov, M.V. Alfimov, and A.M. Zheltikov (2004) Microstructure fibers as frequency-tunable sources of ultrashort chirped pulses for coherent nonlinear spectroscopy. Appl. Phys. B **37**, No. 5, 565.

Nicholson, J.W. and M.F. Yan (2004) Cross-coherence measurements of supercontinua generated in highly-nonlinear, dispersion shifted fiber at 1550 nm. Opt. Express **12**, No. 4, 679.

Lu, F. and W.H. Knox (2004) Generation of a broadband continuum with high spectral coherence in tapered single-mode optical fibers. Opt. Express **12**, No. 2, 347.

Corsi, C., A. Tortora, and M. Bellini (2004) Generation of a variable linear array of phase-coherent supercontinuum sources. Appl. Phys. B **78**, Nos. 3–4, 299.

Kano, H. and H. Hamaguchi (2003) Characterization of a supercontinuum generated from a photonic crystal fiber and its application to coherent Raman spectroscopy. Opt. Lett. **28**, No. 23, 2360.

Gu, X., M. Kimmel, A.P. Shreenath, R. Trebino, J.M. Dudley, S. Coen, and R.S. Windeler (2003) Experimental studies of the coherence of microstructure-fiber supercontinuum. Opt. Express **11**, No. 21, 2697.

Zeylikovich, I. and R.R. Alfano (2003) Coherence properties of the supercontinuum source. Appl. Phys. B **77**, Nos. 2–3, 265.

Corsi, C., A. Tortora, and M. Bellini (2003) Mutual coherence of supercontinuum pulses collinearly generated in bulk media. Appl. Phys. B **77**, Nos. 2–3, 285.

Kim, K.Y., I. Alexeev, and H.M. Milchberg (2002) Single-shot supercontinuum spectral interferometry. Appl. Phys. Lett. **81**, No. 22, 4124.

Dudley, J.M. and S. Coen (2002) Coherence properties of supercontinuum spectra generated in photonic crystal and tapered optical fibers. Opt. Lett. **27**, No. 13, 1180.

Dudley, J.M. and S. Coen (2002) Numerical simulations and coherence properties of supercontinuum generation in photonic crystal and tapered optical fibers. IEEE J. Sel. Topics Quantum Electron. **8**, No. 3, 651.

Nishioka, H., H. Koutaka, and K. Ueda (2001) Quantum interference effects in a femtosecond-dephasing medium. Opt. Express **8**, No. 11, 617.

Smith, E.D.J., N. Wada, W. Chujo, and D.D. Sampson (2001) High resolution OCDR using 1.55 $\mu$m supercontinuum source and quadrature spectral detection. Electron. Lett. **37**, No. 21, 1305.

Kubota, H., K. Tamura, and M. Nakazawa (1999) Analyses of coherence-maintained ultrashort optical pulse trains and supercontinuum generation in the presence of soliton-amplified spontaneous-emission interaction. J. Opt. Soc. Am. B **16**, No. 12, 2223.

Nakazawa, M., K. Tamura, H. Kubota, and E. Yoshida (1998) Coherence degradation in the process of supercontinuum generation in an optical fiber. Opt. Fiber Technol. **4**, No. 2, 215.

Zeylikovich, I., V. Kartazaev, and R.R. Alfano (2005) Spectral, temporal and coherence properties of supercontinuum generation in microstructure fiber. J. Opt. Soc. Am. B **22**, No. 7, 1453.

Lee, T.-W. and S.K. Gray (2005) Controlled spatiotemporal excitation of metal nanoparticles with picosecond optical pulses. Phys. Rev. B **71**, No. 3, 035423-1.

Flores, S.C. and V.S. Batista (2004) Model study of coherent-control of the femtosecond primary event of vision. J. Phys. Chem. B **108**, No. 21, 6745.

Dela Cruz, J.M., I. Pastirk, M. Comstock, and M. Dantus (2004) Multiphoton intrapulse interference. Coherent control through scattering tissue. Opt. Express **12**, No. 17, 4144.

Dantus, M. and V.V. Lozovoy (2004) Experimental coherent laser control of physicochemical processes. Chem. Rev. **104**, No. 4, 1813.

Ozgur, U., C.-W. Lee, and H.O. Everitt (2001) Control of coherent acoustic phonons in semiconductor quantum wells. Phys. Rev. Lett. **86**, No. 24, 5604.

Marie, X., P. Le Jeune, T. Amand, M. Brousseau, J. Barrau, and M. Paillard (1997) Coherent control of the optical orientation of excitons in quantum wells. Phys. Rev. Lett. **79**, No. 17, 3222.

Bonadeo, N.H., J. Erland, D. Gammon, D. Park, D.S. Katzer, and D.G. Steel (1998) Coherent optical control of the quantum state of a single quantum dot. Science **282**, No. 5393, 1473.

# Index


**A**bsorbance changes, induced, 440
Absorption coefficient, 441
Absorption lines, 67
Absorption spectroscopy, time resolved, 356–365, 377–383
ac Stark shift, 323, 327
Aerosols, 522
Amplification length, 145
Amplitude filters, 233–238
Anomalous dispersion, 19, 101–103
Antiferromagnetic crystals, 58–62
Anti-Stokes broadening, 25
Atmospheric remote sensing, 393–395
Atmospheric science, 522
Attoseconds, 506, 517, 524
Auger events, 506
Autocorrelation function, 454
Autocorrelation trace, interferometric, 439, 440

**B**eam radius, normalized, 192
Biology applications, 505

**C**$aF_2$, 456, 473
Carrier envelope phase (CEP), 455, 456, 512
CARS (coherent anti-Stokes Raman scattering), 384–385
CEO, 512
CG (chirped Gaussian pulses), 235
Charge transfer, 505
Chemistry, 505
Chirp coefficient, 38
  linear, 187
Chirp "linearization," 419
Chirped Gaussian (CG) pulses, 235
Chirps
  impressed, 399
  initial, 82
  linear, 100, 386–388, 406
  nonlinearity-induced, 112
  pump, 149–150
  Stokes, 149–150
Chlorine dioxide, 371–372
Clocks, 519
Coherence, 453, 454, 461, 524, 525
Coherence length, 464, 465
Coherent anti-Stokes Raman scattering (CARS), 384–385
Coherent control, 506, 525
Colliding-pulse mode-locked (CPM) laser, 341, 402
Comb frequency, 513, 519
Compression ratio, 236–237
Compressors
  double-pass fiber-grating pulse, 414
  ideal, 410
  quadratic, 410
Computational switches, optical, 393
Conical emission, 332–334
Continuous wave, *see* CW *entries*
Continuum generation, *see* Supercontinuum generation
Controlling matter, 525
Copropagating pulses
  coupled nonlinear equations of, 118–121
  induced-frequency shift of, 137–141
Coupled nonlinear equations of copropagating pulses, 118–121
CPM (colliding-pulse mode-locked) laser, 341, 402
$Cr^{4+}$ lasers, 473, 481, 482, 510

Cross-phase modulation (XPM) (*see* IPM), 33, 83, 110–113, 117–118
  applications for ultrashort pulse technology, 175–178
  harmonic cross-modulation, 159–164
  induced focusing by, 168–171
  modulation instability induced by, 171–175
  optical wave breaking due to, 127–131
  pump-probe experiments, 131–144
  with second harmonic generation, 33, 159–164
  spectral broadening induced by, 141–144
  stimulated four-photon mixing and, 164–168
  with stimulated Raman scattering, 144–159
  theory of, 118–131
Cubic phase distortion, 433
CW (continuous wave) laser beam, 12–14
CW mode-locked (CWML) laser, 402–403

**D**ABCO vapor, 339
  internal conversion rates in, 352–356
Dark soliton, 305, 315–317
Defocusing medium, 191
Degradation of coherence, 462, 468
Degree of coherence, 454, 459
Derivative nonlinear Schrödinger (DNS) equation, 297
DFDL (distributed feedback dye laser), 340
Differential spectral reflectance (DSR) error, 395
Diffraction length, Rayleigh, 197
Diffraction ring pattern, 13
Dispersion
  anomalous, 19, 101–103
  group velocity, *see* Group velocity dispersion
  normal, 100–101
Dispersion-dominant regime, 96–97
Dispersion length, 145
Dispersionless medium, 238–251
  analytical solution for SPM in, 288–294
  self-focusing in, 238–242
  self-steepened pulse in, 242–251
Dispersive effect, 3
Dispersive nonlinear regime, 97–99
Distance measurements, 391–392
Distributed feedback dye laser (DFDL), 340
DNS (derivative nonlinear Schrödinger) equation, 297
Double-pass fiber-grating pulse compressor, 414
Double-pass grating-pair delay line, 407, 408
DSR (differential spectral reflectance error), 395
Dual pulse interference, 467, 525

**E**arly self-steepening, 297–301
Electric field, 88
Electric field envelope, 36
Electric field intensity, 199–200
Electric vector, 311
Electron heating, nonequilibrium, 380
Electron transfer, photoinduced, 380–381
Electronic resonances in crystals, supercontinuum near, 62–67
Electrostriction, 7, 42
Excimer amplifier system, 340–343
Excitation spectroscopy, time-resolved, 383–385
Expansion parameter, 15

**F**ast Fourier transform (FFT) method, 99
Femtosecond light pulses, 2
Femtosecond pulse compression, 432–444
Femtosecond Raman pulses, 157–159
$\Delta f/f$, 513, 519
FFT (fast Fourier transform) method, 99
Fiber, *see also* Optical fiber *entries*
Fiber-grating compressor parameters, 413

Fiber length regimes, limiting, 412
Fiber Raman amplification soliton laser (FRASL), 150–155
Fibers, 481, 518, 524
Filaments, 422
Filter transform, 233–238
Focusing, induced, *see* Induced focusing
Focusing medium, 191
Four-photon parametric generation (FPPG), 33
Fourier transform, fast (FFT) method, 99
Four wave mixing, 524
Fractional change in frequency, 512, 513, 519
FRASL (fiber Raman amplification soliton laser), 150–155
Free space wireless, 522
Frequency comb, 519, 524, 525
Frequency modulation, 9
Frequency shift, 37
  maximum, 38
*f* to 2*f,* 482, 513, 514

**G**aseous continua
  spatial characteristics of, 332–334
  spectral characteristics of, 328–332
Gases
  saturation of nonlinear response in, 327–328
  self-focusing in, 318–335
Gaussian pulses, 120
  chirped (CG), 235
Generation of supercontinuum, 473, 505
Glass optical fibers, supercontinuum in, 51–54
Graded index profile, 189
Grating constant, 410
Grating pair, 432
  double, 433
Grating separation, 411–412
Grating transform, 188
Group delay dispersion, 435
Group delay time, 389
Group velocity, 512
Group velocity dispersion (GVD), 81, 345, 386, 463, 512
  effects of, 127–131
  negative, 401, 409
  nonlinear wave equation with, 87–90
  positive, 409
Group velocity mismatch, 111–113
GVD, *see* Group velocity dispersion

**H**emoproteins, 382–383
Holes, 505
Holey fiber, 481
Horn-shaped pulse, 26–27
Hot carriers, 505
Hyperpolarizabilities, 330

**I**deal compressors, 410
Imaging, three-dimensional, 392–393
Index of refraction, *see* Refractive indexes
Induced absorbance changes, 440
Induced focusing, 263–269
  by cross-phase modulation, 168–171
Induced-frequency shift of copropagating pulses, 137–141
Induced nonlinear effects, 251–280
Induced-phase modulation (IPM) (*see* XPM), 33, 83, 131, 251–255
  based optical computational switches, 393
  of generated second harmonic pulse, 272–280
  Raman amplification and, 255–259
  spectral broadening enhancement by, 132–137
Induced polarization, 4
Induced pulse compression, 259–263
Induced self-steepening, 269–272
Induced transient optical density, 377–379
Induced ultrafast supercontinuum pulse (IUSP), 134
Infrared (IR) laser pulses, 3, 383, 384
Infrared supercontinuum generation, 347–352
Integrated intensity, 61
Interference, 10, 453
Interference fringes, 454, 525

Interference pattern of supercontinuum, 220–226
Interferometric autocorrelation trace, 439, 440
Iodine photodissociation in solution, 380
Ionization, multiphoton, 320–324
IPM, *see* Induced-phase modulation
IR, *see* Infrared *entries*
IUSP (induced ultrafast supercontinuum pulse), 134

**J**itter, 524

**K**eldysh theory, 323
Kerr distance, 145
Kerr gate, optical (OKG), 67, 175
Kerr index of refraction, 186
Kerr liquids, 27
Kerr medium, 456, 473, 522
  optical, 403–408
Kerr phase shifter (KPS), 393, 394
Kinetic spectroscopy, 338
  promising directions for, 372–373
Kink, 305, 315–317
KPS (Kerr phase shifter), 393, 394

**L**aser beams, *see* Lasers
Laser heating, 7
Laser pulses
  femtosecond, 2
  infrared, 3, 383, 384
  picosecond, 2
Lasers, 1, 473, 481, 482, 510
  soliton, 102–103
Lattice defects, transient, 380
Librational frequencies, 6
Lidar equation, 393
LIF, 473
Light pulses, *see* Laser pulses
Linear and angular momentum, 506
Linear chirp coefficient, 187
"Linearization," chirp, 419
Longitudinal phase, 205–207
Longitudinal self-focusing, 301
Low-intensity pulses, 186–207

**M**axwell's equations, 35, 87–88, 184–185; *see also* Wave equation
Metrology, 519
Microstructure fibers, 481, 518, 524
Mie scattering, 395
Mode-locked lasers, 40
Modulation
  cross-phase, *see* Cross-phase modulation
  frequency, 9
  induced-phase, *see* Induced-phase modulation
  phase, 9
  self-phase, *see* Self-phase modulation
Modulation frequency, 37–38, 330
Modulation instability (MI), 171–175, 301–303, 461, 462, 470
Molecular redistribution, 7
Multiphoton ionization, 320–324
Multiple scale method, 118, 208–211
Mutual coherence function, 454
Mutual coherent, 454, 462, 467
Mutual incoherent, 454

**N**anocrystals, 525
Nonequilibrium electron heating, 380
Nonlinear effects, induced, 251–280
Nonlinear pulse propagation, 408–422
Nonlinear refractive index, 35, 88
Nonlinear response in gases, saturation of, 327–328
Nonlinear Schrödinger equation (NSE), 98, 297, 408
  approximations leading to extended, 310–315
  derivative, 297
Nonlinear wave equation, 208
  with group velocity dispersion, 87–90
Nonlinearity-dominant regime, 97
Nonlinearity-induced chirps, 112
Nonpolarization-preserving fiber, 425
NOT gate, 393, 394
NSE, *see* Nonlinear Schrödinger equation

**O**ctave spanning, 456, 482, 513, 519
OD (induced transient optical density), 377–379

OKG (optical Kerr gate), 67, 175
OMA (optical multichannel analyzer), 332
Optical amplification of probe pulses, 142–144
Optical coherence tomography (OCT), 457, 510, 524
Optical computational switches, 393
Optical density, induced transient, 377–379
Optical fiber loss, 395
Optical fiber measurements, 395
Optical fibers, *see also* Fiber *entries*
  supercontinuum in, 51–54
Optical-field-induced refractive indexes, 4–8
Optical grating, *see* Grating *entries*
Optical Kerr gate (OKG), 67, 175
Optical Kerr medium, 403–408
Optical multichannel analyzer (OMA), 332
Optical nonlinearities, kinetics of, 396
Optical pulse compression, 385–391
  femtosecond, 432–444
  picosecond, 403–432
  in single-mode fibers, 399–444
Optical pulses, *see also* Pulse *entries*
  self-steepening of, 295–317
Optical wave-breaking, 421–422
  due to cross-phase modulation, 127–131
Optical wireless, 522

**P**arabolic graded index medium, 189–195
Peak intensity, 61
Pentabits/s, 498
Phase conjugation, Raman-induced (RIPC), 385
Phase difference, 10
Phase distortion, cubic, 433
Phase factor, time-dependent, 53
Phase increment, 21–23
Phase modulation, 9
Phase shift, 434
Photodissociation, iodine, in solution, 380
Photoexcitation, 337–339
Photoinduced electron transfer, 380–381
Photonic crystal fibers (PCF), 453, 460, 462, 468, 481
Photoreaction of rhodopsin, 381–382
Photorefraction, 7
Photosynthesis, 525
Photosynthesis process, 381
Picosecond laser pulses, 2
Picosecond optical pulse compression, 403–432
Picosecond Raman pulses, 155–157
Plasma density changes, 320
Polarization, induced, 4
Polarization-preserving fiber, 425
Polarization vector, 311
Pollutants, 522
Power spectrum, 11
Probe pulses, optical amplification of, 142–144
Probe spectral distribution, 206–207
Propagation equation, 92–96
Propagation regimes, 96–99
Pulse amplitude, 212–215
Pulse comoving coordinate, 186
Pulse compression, 91, 188–189, 517
  induced, 259–263
  optical, *see* Optical pulse compression
  stimulated Raman scattering and, 422–432
Pulse-compression switch, 176–178
Pulse compression techniques, 385–391
Pulse envelope, 35–36
Pulse phase, 216–219
Pulse propagation, 92–96
  nonlinear, 408–422
Pulse steepening, 208–238
Pulse walk-off, *see* Walk-off *entries*
Pulsed quasi-monochromatic field, 5
Pulses
  copropagating, *see* Copropagating pulses
  Gaussian, *see* Gaussian pulses
  horn-shaped, 26–27
  laser, *see* Laser pulses
  light, *see* Laser pulses
  low-intensity, 186–207
  optical, *see* Optical pulse *entries*
  probe, 142–144
  pump, 104–110

Pulses (*cont.*)
Raman, *see* Raman pulses
ultrashort, *see* Ultrashort pulse *entries*
Pump chirps, 149–150
Pump loss distance, 146
Pump-probe cross-phase modulation experiments, 131–144
Pump pulses, 104–110

**Q**uadratic compressors, 410
Quantum dots, 505, 525
Quantum effects, 506, 525
Quantum mechanical treatment of supercontinuum, 280–285
Quasi-linear partial differential equations, 211–212
Quasi-monochromatic field, pulsed, 5
Quasi-particles, 505
Quasi-solitons, 308
Quasi-steady-state self-focusing, 20–24

**R**aman amplification, 255–259
Raman gain, 425
Raman gain spectrum, 104
Raman-induced phase conjugation (RIPC), 385
Raman process, walk-off and, 146–149
Raman pulses, 104–110
femtosecond, 157–159
picosecond, 155–157
Raman scattering
coherent anti-Stokes (CARS), 384–385
stimulated, *see* Stimulated Raman scattering *entries*
Raman transitions, 6
Rare-gas liquids and solids, supercontinuum in, 54–58
Rayleigh diffraction length, 197, 242
Rayleigh wing spectrum, 8
Refractive indexes, 92–93
graded, 190
Kerr, 186
nonlinear, 35, 88
optical-field-induced, 4–8
total, 35
Relativistic events, 506
Relaxation time responses, 42
Remote sensing, atmospheric, 393–395
Replica holes, formation of, 442–443
Resonant structure, 3
Rhodopsin, photoreaction of, 381–382
RIPC (Raman-induced phase conjugation), 385

**S**alt concentration dependence, 68–72
Saturation, 326
of nonlinear response in gases, 327–328
Schrödinger equation, nonlinear, *see* Nonlinear Schrödinger equation
Second harmonic generation (SHG), 48
Second harmonic generation cross-phase modulation (SHG-XPM), 33, 159–164
Second harmonic pulse, generated, IPM of, 272–280
Self-coherence, 457, 464, 524
Self-coherence function, 454, 524
Self-focusing, 2–3, 80–81, 328–335, 404, 481, 522
in dispersionless medium, 238–242
in gases, 318–335
longitudinal, 301
quasi-steady-state, 20–24
self-phase modulation and, 20–28
transient, self-phase modulation with, 26–28
Self-focusing distance, normalized, 197–198
Self-phase modulation (SPM), 1–4, 33, 83, 117, 386
analytical solution for, 288–294
in bulk homogeneous material, 195–202
experimental arrangement for, 40–41
higher-order effects on, 80–82
local generation and propagation of, 74–78
measurement of, 400

more rigorous theory of, 14–19
in parabolic graded index medium, 189–195
pulse duration reduction, 78–80
review of conventional theory, 186–187
self-focusing and, 20–28
simple theory of, 8–14
simplified model, 34–40
spectral distribution predicted by, 187
-spectral maximum shift, 231–233
temporal and spatial, 29
temporal behavior of, 73–80
temporal distribution of, 73–74
with transient self-focusing, 26–28
in unbounded media, 324–326
Self-steepened pulse in dispersionless medium, 242–251
Self-steepening, 81–82, 215
early, 297–301
induced, 269–272
of optical pulses, 295–317
Self-steepening effect, 14–19
Semiconductors, 505
coherent transients in, 359
supercontinuum in, 47–49
supercontinuum spectroscopy of, 379–380
SFPM, *see* Stimulated four-photon mixing
SHG (second harmonic generation), 48, 513
SHG-XPM (second harmonic generation cross-phase modulation), 33, 159–164
Shock-forming distance, 302
Shortest pulse duration, 517
Silicon-intensified target (SIT) camera, 41
Single-mode fibers, pulse compression in, 399–444
SIT (silicon-intensified target) camera, 41
Slowly varying amplitude (SVA), 118
Slowly varying envelope approximation (SVEA), 367
Soliton compression, 401
Soliton laser, 102–103
Solitonlike solutions, 303–307
Solitons, 98, 297, 305, 307, 463, 468, 470
dark, 305, 315–317
fundamental, 102
quasi-solitons, 308
Solute-solvent, 505
Spatial coherence, 453, 459, 460
Spectral broadening
asymmetric, 106–109
more rigorous theory of, 14–19
self-induced, 1–3
simple theory of, 8–14
of ultrashort pulses, 24–26
XPM-induced, 141–144
Spectral broadening enhancement, 121–127
by induced-phase modulation, 132–137
Spectral coherence, 466
Spectral distribution, 226–231
probe, 206–207
Spectral extents, 227
Spectral intensity, 226
Spectral interference, 465
Spectroscopy
coherent anti-Stokes Raman scattering, 384–385
kinetic, *see* Kinetic spectroscopy
supercontinuum, of semiconductors, 379–380
time-resolved absorption, 356–365, 377–383
time-resolved excitation, 383–385
ultrafast, 2
SPM, 462, 482, 513; *see also* Self-phase modulation
SRS, *see* Stimulated Raman scattering *entries*
Stark shift, ac, 323, 327
Stimulated four-photon mixing (SFPM), 164
cross-phase modulation and, 164–168
Stimulated Raman scattering (SRS), 33, 104–110, 347–348, 417
cross-phase modulation with, 144–159
pulse compression and, 422–432
Stimulated Raman scattering
cross-phase modulation (SRS-XPM), 33

Streak camera, 79, 133, 163, 385
Stokes and anti-Stokes shifts, maximum, 17
Stokes-anti-Stokes asymmetry, 11
Stokes broadening, 24
Stokes chirps, 149–150
Stokes wave, 349
Superbroadening, *see* Spectral broadening
Supercontinuum
  gaseous, *see* Gaseous continua
  interference pattern of, 220–226
  present and future applications of, 377–396
  quantum mechanical treatment of, 280–285
  thermal focusing effects on, 202–207
  ultraviolet, 356–372
Supercontinuum generation, 33, 184–185, 453, 456, 473, 481
  in antiferromagnetic crystals, 58–62
  in calcite, 43–46
  in carbon tetrachloride, 50
  in condensed matter, 33–83
  near electronic resonances in crystals, 62–67
  enhancement of, in water, 67–73
  experimental, 34
  in gases, 318–335
  in glasses, 43
  infrared, 347–352
  in liquids, 49–51
  in optical fibers, 51–54
  in phosphoric acid, 50
  in polyphosphoric acid, 50–51
  in potassium bromide, 47
  in quartz, 43
  in rare-gas liquids and solids, 54–58
  in semiconductors, 47–49
  in sodium chloride, 43
  in solids, 41–49
  threshold power for, 330
  ultraviolet, 343–347
  in water, 50
Supercontinuum laser, 470, 481
Supercontinuum spectroscopy of semiconductors, 379–380
Supercontinuum sweep rate, 366
Susceptibility, 4
SVA (slowly varying amplitude), 118
SVEA (slowly varying envelope approximation), 367
Sweep rate, supercontinuum, 366
Switches, optical computational, 393

**T**emperature gradient, 204
Temporal coherence, 455, 459, 462
Temporal tuning, 429–430
Terabits/s, 498, 519
Thallium chloride molecules, 345–346
Thermal focusing effects on supercontinuum, 202–207
Third harmonic generation (THG), 48
Three-dimensional imaging, 392–393
Threshold gain, 174
Threshold power for continuum generation, 330
Time-dependent phase factor, 53
Time division multiplexing, 498
Time-resolved absorption spectroscopy, 356–365, 377–383
Time-resolved excitation spectroscopy, 383–385
Time-resolved infrared spectral photography (TRISP), 347–352
  application of, 352–356
Trans-cis forms, 506
Transverse coherence, 455
TRISP, *see* Time-resolved infrared spectral photography

**U** curve, 20–21
Ultimate clocks, 419
Ultrafast spectroscopic studies, 2
Ultrafast supercontinuum pulse (USP), 134
Ultrashort pulse technology, cross-phase modulation in, 175–178
Ultrashort pulses, spectral super-broadening of, 24–26
Ultraviolet, 506, 517
Ultraviolet supercontinuum generation, 343–347
Uncertainty relation, 386
USP (ultrafast supercontinuum pulse), 134

UV (ultraviolet) supercontinuum generation, 343–347

**V**isibility, 454, 459
Vision, 525

**W**alk-off, 122
  Raman process and, 146–149
Walk-off distance, 145
Wave equation, 8–9
  nonlinear, *see* Nonlinear wave equation
Wavelength division multiplexing (WDM), 470, 498, 525
Wavelength division multiplexing (WDM) systems, 395
White light, 455, 522
White light continuum, 505

**X**OR gate, 393, 394
XPM, *see* Cross-phase modulation, Induced-phase modulation
X-ray attosecond, 506

**Y**oung experiments, 457, 524
Young/Michelson interferometric system, 222–224
Young visibility function, 293

**Z**ero dispersion wavelength (ZDW), 461, 468